

NASA/CR–2015-218704/Volume I



Subsonic Ultra Green Aircraft Research: Phase II – Volume I – Truss Braced Wing Design Exploration

*Marty K. Bradley, Christopher K. Droney, and Timothy J. Allen
Boeing Research and Technology, Huntington Beach, California*

April 2015

NASA STI Program . . . in Profile

Since its founding, NASA has been dedicated to the advancement of aeronautics and space science. The NASA scientific and technical information (STI) program plays a key part in helping NASA maintain this important role.

The NASA STI program operates under the auspices of the Agency Chief Information Officer. It collects, organizes, provides for archiving, and disseminates NASA's STI. The NASA STI program provides access to the NTRS Registered and its public interface, the NASA Technical Reports Server, thus providing one of the largest collections of aeronautical and space science STI in the world. Results are published in both non-NASA channels and by NASA in the NASA STI Report Series, which includes the following report types:

- **TECHNICAL PUBLICATION.** Reports of completed research or a major significant phase of research that present the results of NASA Programs and include extensive data or theoretical analysis. Includes compilations of significant scientific and technical data and information deemed to be of continuing reference value. NASA counter-part of peer-reviewed formal professional papers but has less stringent limitations on manuscript length and extent of graphic presentations.
- **TECHNICAL MEMORANDUM.** Scientific and technical findings that are preliminary or of specialized interest, e.g., quick release reports, working papers, and bibliographies that contain minimal annotation. Does not contain extensive analysis.
- **CONTRACTOR REPORT.** Scientific and technical findings by NASA-sponsored contractors and grantees.

- **CONFERENCE PUBLICATION.** Collected papers from scientific and technical conferences, symposia, seminars, or other meetings sponsored or co-sponsored by NASA.
- **SPECIAL PUBLICATION.** Scientific, technical, or historical information from NASA programs, projects, and missions, often concerned with subjects having substantial public interest.
- **TECHNICAL TRANSLATION.** English-language translations of foreign scientific and technical material pertinent to NASA's mission.

Specialized services also include organizing and publishing research results, distributing specialized research announcements and feeds, providing information desk and personal search support, and enabling data exchange services.

For more information about the NASA STI program, see the following:

- Access the NASA STI program home page at <http://www.sti.nasa.gov>
- E-mail your question to help@sti.nasa.gov
- Phone the NASA STI Information Desk at 757-864-9658
- Write to:
NASA STI Information Desk
Mail Stop 148
NASA Langley Research Center
Hampton, VA 23681-2199

NASA/CR–2015-218704/Volume I



Subsonic Ultra Green Aircraft Research: Phase II – Volume I – Truss Braced Wing Design Exploration

*Marty K. Bradley, Christopher K. Droney, and Timothy J. Allen
Boeing Research and Technology, Huntington Beach, California*

National Aeronautics and
Space Administration

Langley Research Center
Hampton, Virginia 23681-2199

Prepared for Langley Research Center
under Contract NNL08AA16B

April 2015

The use of trademarks or names of manufacturers in this report is for accurate reporting and does not constitute an official endorsement, either expressed or implied, of such products or manufacturers by the National Aeronautics and Space Administration.

Available from:

NASA STI Program / Mail Stop 148
NASA Langley Research Center
Hampton, VA 23681-2199
Fax: 757-864-6500

1.0 Introduction

In 2009-2010, Boeing conducted the Subsonic Ultra Green Aircraft Research (SUGAR) study for NASA. In this study, Boeing identified and analyzed advanced concepts and technologies for aircraft that would fly in the 2030-2035 timeframe. Large possible improvements in fuel burn, emissions, and noise were identified and roadmaps developed for key technologies. Specific recommendations for future work were made in the Boeing Phase I Final Report (1), many of which are addressed in Phase II:

- Conduct additional design and analysis of hybrid electric gas turbine propulsion
- Conduct a comprehensive study of high aspect ratio truss braced wings
- Consider additional noise technologies (partially addressed as part of hybrid electric tasks)
- Conduct a follow-on study to consider the synergistic benefits of methane and/or hydrogen fuel

Considering the recommendations of Boeing and the other contractor teams, as well as program objectives, NASA developed these Research Objectives for Phase II:

- Experimental and Higher-Fidelity Exploration of Key Technologies to investigate the prioritized technology challenges identified in Phase I and begin moving toward the realization of the proposed vehicle concept(s) capabilities that would enable an entry into service (EIS) in the 2030-2035 timeframe, market permitting
- N+3 Advanced Vehicle Concept Study to further explore, refine, and otherwise update the preferred N+3 advanced vehicle and component concept(s) identified and developed during Phase I
- N+4 Advanced Vehicle Concept Study to leverage the substantial investment of Phase I and study the effect of additional technology development time beyond that assumed in Phase I

Boeing structured the SUGAR Phase II program to address the recommendations from Phase I as well as the research objectives provided by NASA. Three major tasks, corresponding to the Research Objectives, are included in the Phase II effort. Subtasks are organized and grouped by technical area (Figure 1.1).

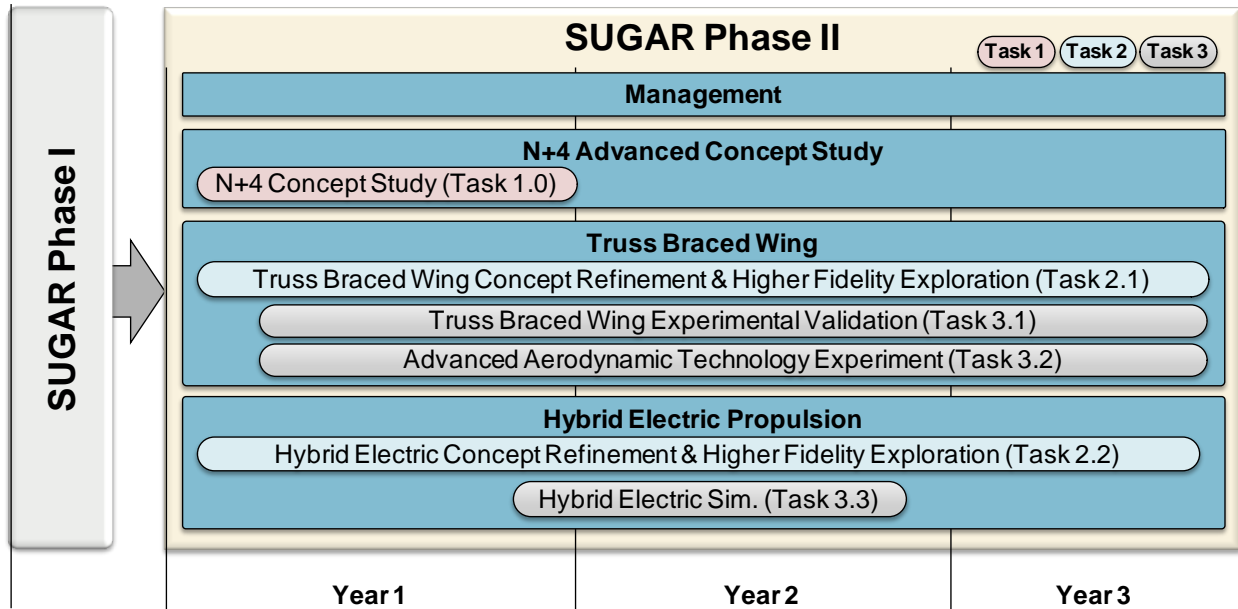


Figure 1.1 – SUGAR Phase II Tasks and Groupings

The SUGAR team from Phase I consisted of Boeing Research and Technology, Boeing Commercial Airplanes, General Electric, and Georgia Tech. In Phase II (depicted in Figure 1.2), the team was expanded to include Virginia Tech, NextGen Aeronautics, and Microcraft to enhance the technical capabilities and to build hardware to support the testing of the truss braced wing tasks.

This is the Final Report for Tasks 2.1, 3.1, and 3.2. Task 1 is fully documented in the Task 1 final report (2) and the Hybrid Electric Tasks 2.2 and 3.3 are fully documented in a separate Final Report (Volume II – Hybrid Electric Design Exploration). A separate test report for Task 3.1 provides additional information (Volume III - Truss Braced Wing Aeroelastic Test Report). Documentation for the testing in Task 3.2 is included in this report.

In Phase I of the SUGAR study, a preliminary analysis was performed on a truss braced wing configuration with N+3 technologies. The study showed that these configurations have potential for reduced fuel burn depending on the weight and aerodynamic performance of the wing. It was recommended exiting Phase I that a comprehensive study of high aspect ratio strut braced wings be performed.

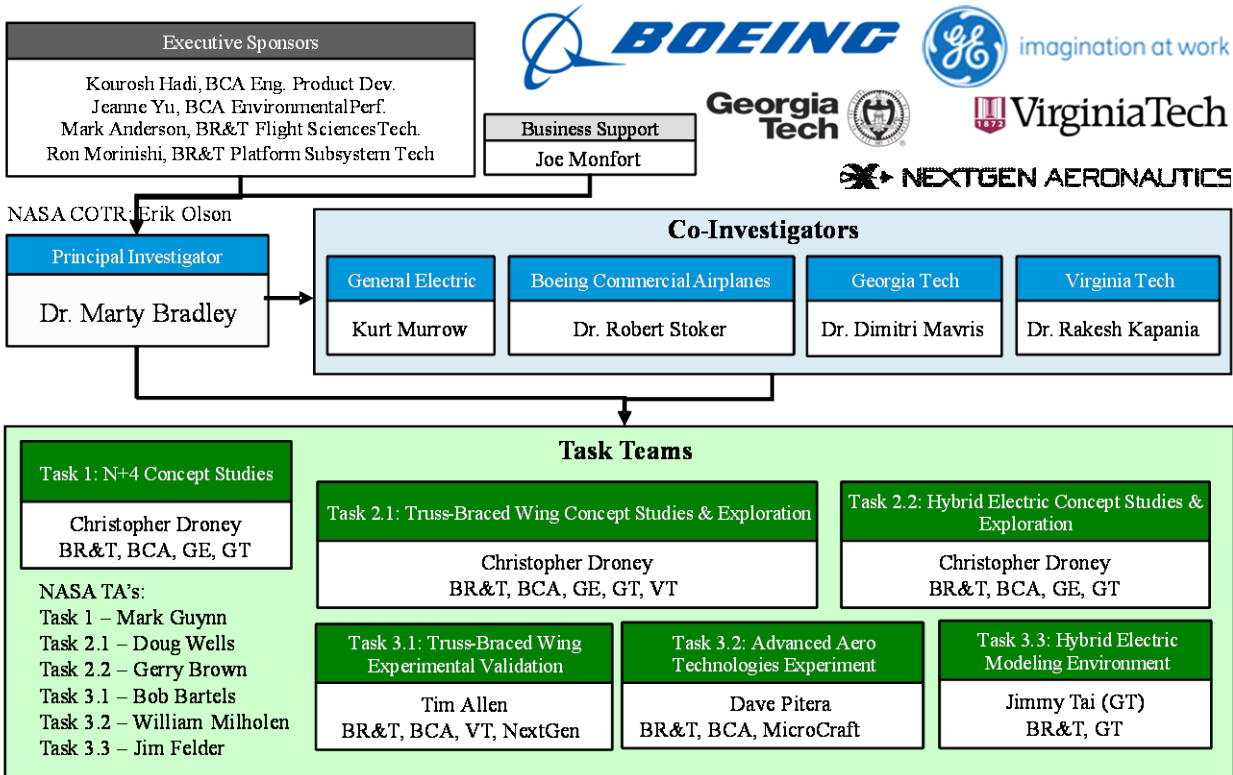


Figure 1.2 – SUGAR Phase II Team Structure

To reduce uncertainty in the performance of TBW configurations, the SUGAR Phase II team investigated the structural, aeroelastic, and control challenges that remained unaddressed in Phase I. The following analyses and tests were used to reduce TBW performance uncertainty:

- 2D airfoil research to bound multidisciplinary optimization compressibility levels
- Configuration landing gear and strut integration refinement
- Detailed MDO for design space exploration and configuration down select
- High fidelity 3D wing analysis
- 2D wind tunnel tests to validate laminar flow assumptions
- Detailed aeroelastic FEM for flutter analysis and to determine control surface rigid to elastic ratios
- Aeroelastic wind tunnel test to demonstrate flutter margin and/or active aeroelastic suppression

The work was structured into the subtasks shown in Figure 1.3, which also includes an airport compatibility study and updated technology development roadmapping. The approach and results are discussed in the sections that follow.

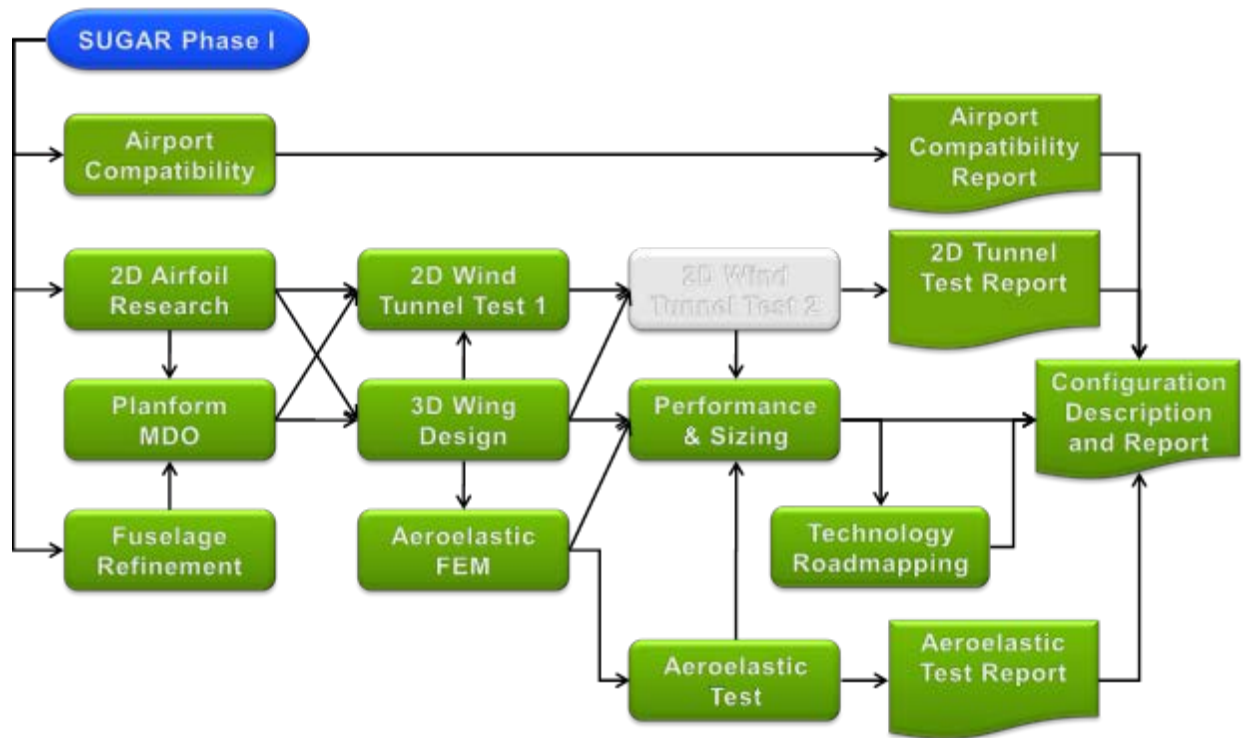


Figure 1.3 – Truss Braced Wing Task Flow

2.0 Truss-Braced Wing Concept Exploration

The iterative nature of airplane development can make for confusing documentation as trades are performed at various stages of development. For clarity, this document breaks the configuration development into three sections.

Section 2.1, *Configuration Basis, Design Trades, and Evolution*, focuses on the trades and logic that lead to the air vehicle's current embodiment. All data contained within is intended to document the mid-iteration trades and should not be correlated to the final configuration performance unless specifically noted.

Section 2.2, *Configuration Description*, details the final configuration in detail. This section represents the vehicle as analyzed for vehicle performance.

Section 2.3, *Configuration Analysis and Final Performance*, contains the analysis results and performance data for the vehicle described in the previous section.

The technology plans and roadmaps are included in Section 2.4.

2.1 Configuration Basis, Design Trades, and Evolution

Design trades and configuration basis are described in the following sections. The data contained within are not representative of the final configuration unless specifically noted.

2.1.1 Assumptions and Definitions

The coordination and planning process for the SUGAR study has highlighted how similar looking configurations can be different in design intent. Georgia Tech and Virginia Tech have experience optimizing truss braced wings, however the underlying assumptions used in their previous vehicle optimizations are different than those envisioned by The Boeing Company. This section will describe many of these options and define the vocabulary used within this report for different TBW structural layouts. It will also illustrate which options are considered the baseline for this study and why those options were chosen. Some, but not all of these baseline decisions are traded in this study.

2.1.1.1 Primary Wing and Jury Strut Definitions

Truss braced concepts are comprised of a wing, primary wing struts, jury struts, and a truss support structure (in this case the fuselage). Primary wing struts and jury struts are distinguished by their intended purpose. Primary wing struts are intended to effect wing bending loads, typically relieving wing box load and transferring it into the lower fuselage carry thru or to change load direction. Jury struts are intended to force buckling modes to higher frequencies thus stabilizing the wing and/or primary wing struts. Figure 2.1 illustrates the distinction between strut element types. A configuration with a single primary wing strut it is typically considered a strut braced wing rather than a truss braced wing. Sometimes the structural element connecting a

wing to an engine is referred to as a strut; for clarity, this study will refer to this element as a pylon

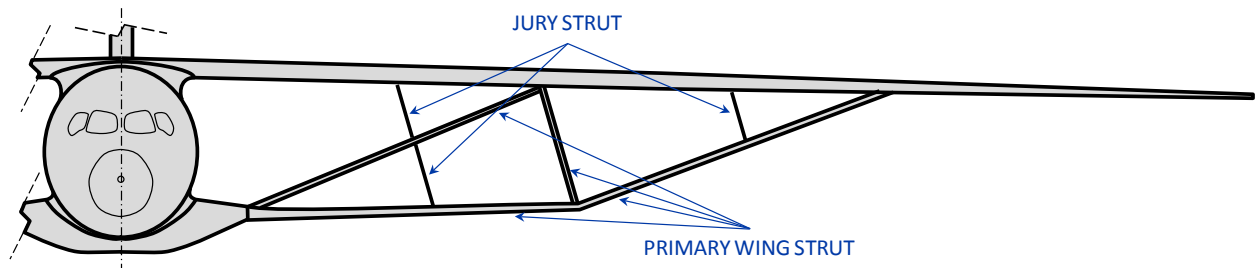


Figure 2.1 – Example Geometry Showing Strut Definitions

2.1.1.2 Constraints for Number of Strut Elements

There are countless variations on the number and layout of strut elements for a truss braced wing. Figure 2.1 shows a configuration with four primary wing struts and three jury struts. The complexity of the wing structure and manufacturing is assumed to be proportional to the number of primary and jury wing struts. For simplicity, and based on previous studies by Virginia Tech and Georgia Tech, a single strut was selected for the baseline 765-095 (SUGAR High) configuration. A strut option was traded (referred to as a “V” strut for this study) which has two streamwise coplanar primary struts with an optional fairing covering a portion of each strut or both struts in their entirety (see Figure 2.2). Zero, one, and two jury struts were considered in a trade study.

2.1.1.3 Wing to Fuselage Attachment

The attachment of the wing to the fuselage is assumed to be handled by a conventional trapezoidal panel similar to heritage Boeing high wing aircraft developed in Long Beach. This attachment scheme assumes the primary wing strut will not carry the entire wing bending load leaving a portion to be carried across the centerline by the wing box. Alternatively, the wing could be pinned at the side of body forcing all wing loads to be carried by the strut. It is possible that the pinned attachment is not a significant penalty and could speed manufacturing. This structural option should be traded but has not been addressed by this study.

2.1.1.4 Strut Attachment Constraints

One end of the primary wing strut is assumed to attach to the wing box, somewhere between the front and rear spars, at an optimum percentage of the semispan, both of which were traded by a wing planform MDO. The other end is assumed to attach to the fuselage and share the forward attachment structure of the main landing gear trunnion. Jury struts are assumed to attach to the primary struts providing stabilization without breaking the primary load path. The other end of the jury strut will be allowed to extend to any primary structure on the fuselage or wing. It is assumed for the baseline that all the strut endpoints are attached with a universal joint or pin joint, however, a moment carrying attachment was traded in the wing planform MDO.

2.1.1.5 Lifting Struts

For this phase of the study it is assumed that the strut will not carry any lift loads. It is foreseen that the optimum lift carried by the primary wing strut would be non-zero; however, interference drag in regions where the lifting strut comes in close proximity to the wing will likely be severe. It may be a vehicle benefit to have lift carried by the gear pylon and the strut root but it is seen as a second order effect. This study focuses on developing a global understanding of the species; the optimum lift to be carried by the strut and gear pylon is a design detail to be considered in a subsequent study.

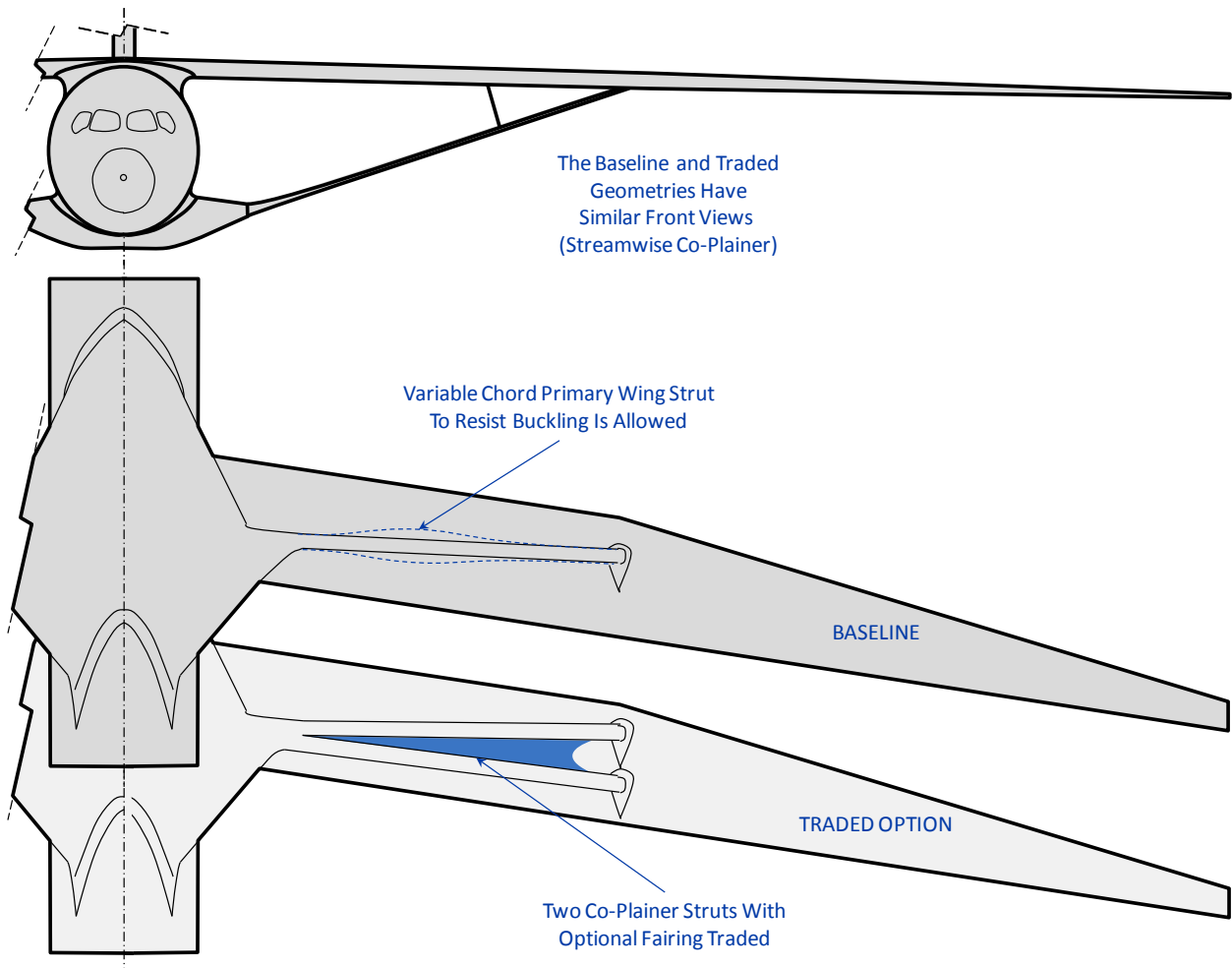


Figure 2.2 – Allowed Arrangements for Wing Struts

2.1.2 Design Considerations

This section contains design considerations that must be attributed to aircraft with high wings, strut braced wings, and high span wings. These topics are not intended to be all inclusive; additional design considerations may apply. In addition, the sources for these topics are limited to government regulation. Airframe manufacturers maintain a proprietary set of design requirements and objectives that can increase the levels of safety set forth by external regulation.

2.1.2.1 High Wing

High wing aircraft configurations are not typically used for twin aisle aircraft or single aisle aircraft larger than regional sizes. These configurations will require special attention in the areas of vertical crash loads and ditching.

Vertical Crash Loads

A substantial portion of an airplane's weight is comprised by its wing, which for a low wing aircraft involved in a vertical crash, is one of the first components to come in contact with the ground. In this scenario, the fuselage needs to react only the payload and its own inertial loads. For a high wing aircraft, the fuselage is the first component to touch the ground and it must additionally react the wing deceleration load. An erroneous common perception is that the wing must not be allowed to deform the fuselage.

The Federal Aviation Administration (FAA) states that "neither 14 CFR 25.561 nor any other part 25 requirements address the structural capability of the airframe as a whole in a crash landing" (3). The FAA continues by stating that structural deformation of the fuselage is allowed, but it must maintain a survivable volume for the passengers while protecting them from the release of internal items of mass including seats, overhead bins, and support structure. The aircraft should "provide a level of crash survivability equivalent to that of conventional large transport category airplanes" (3).

These requirements may impact the design of a high wing aircraft. The weight impact would depend on the structural arrangement and finalized configuration weights thus it is not quantified in this document. It may be beneficial to space the landing gear and wing carry thru structure longitudinally. The landing gear is largely rigid structure when stowed and in a vertical crash could create a pinch point if the wingbox is directly overhead.

From a fuselage crushing perspective, the truss braced wing may have some advantages over a traditional high wing as the strut support structure would impact the ground first. This would lift the outboard wing while pushing them outboard. This could reduce the amount of structure required to maintain a survivable volume but may come with additional penalties (portions of the wing box that contain fuel must retain the fuel in a crash for example).

Ditching

Occasionally, an aircraft is required to make an emergency landing on water (referred to as ditching). In this situation, it is required (4) to provide adequate exit capacity and time for evacuation. Traditionally, low wing configurations rely on the buoyancy of the wing fuel tanks to aide in flotation and provide stability to the aircraft. A high wing configuration must rely primarily on the buoyancy of the fuselage to float and thus, would float lower in the water than a conventional airplane.

Special care will be required to ensure the high wing aircraft floats with (likely the forward) exit doors above the waterline for a time duration that accommodates evacuation with water leakage rates consistent with probable structural damage. Openings for aircraft systems will also have to be accounted for which may drive their location in the airplane. Aft fuselage skin gauges may be set by ditching requirements. Overall, care will be required to meet ditching requirements but they are foreseen as manageable.

2.1.2.2 Truss Braced Wing

The truss braced wing configuration will require special attention as it is not explicitly covered under the current regulations. Areas of which require attention include bird strike and damage tolerant design.

Bird Strike

The current FAA requirements specify strike protection for 4 and 8 pound birds at several different speed conditions. The JAR requirements hold the entire airframe to continued safe flight after a 4 pound bird strike. It is unclear how this requirement will be levied against the strut braced wing configuration. Interpretation of the rules will be required and an FAA/JAR harmonization activity is currently underway. The weight of the bird has less contribution to the energy of impact than the speed of the bird (function of cruise speed). The current embodiment of the truss braced wing design has a low cruise speed however, higher speed configurations are being discussed.

Two approaches exist for meeting the bird strike constraints. One approach is to absorb the energy with aircraft structure ensuring that sufficient load path remains after impact to handle a reduced set of flight loads. An alternate approach is to deflect the bird energy by means of a deflector. Based on experience with vertical tails which absorb bird strike energy with structure, the strut will likely require a bird deflecting strategy. This deflector could be constructed with composite or metallic materials depending on bird energy and volume available.

The jury strut is of greater concern due to its small size. Two approaches should be traded, a bird deflector similar to that envisioned for the strut, or an aircraft design that is damage tolerant which can operate without the jury strut at reduced load. The current SUGAR designs ignore bird strike but acknowledge the design criteria's potential impact to the final configuration.

Damage Tolerant Design Criteria

Current design rules require a damage tolerant design for primary aircraft structure. This regulation can be satisfied by a trade between inspection intervals and redundancy in the load paths. The design standard essentially requires structure to be rated to limit load with damage that could be overlooked for one inspection interval. Thus, an increase in inspection frequency or more structural redundancy, both provide contribution to operating cost, will need to be

traded for the truss braced wing. The wing struts are particularly vulnerable because the structure is relatively small and highly loaded.

Traditional approaches to damage tolerant design will need to be employed when detailed strut design begins. With appropriately tailored structural geometry, the struts and their fittings should be capable of meeting this requirement.

2.1.2.3 High Span Wings

Several design considerations stem from having wings of significant span. These primarily include the areas of stability and control and airport compatibility.

Stability and Control

Stability and control challenges come in the form of high and low speed considerations.

High Speed Considerations

The 765-095 is targeted at commercial airline operation and will spend most of its time in the cruise configuration at speeds high enough to require considerable attention to stability margins. Relaxed stability can contribute to drag savings but requires care that the actuator size and rates are achievable and that increased weight and complexity are properly traded with the benefits. Relaxed high speed stability must not adversely affect the trim and control power required during other flight phases.

The supercritical wings suggested for the design have large pitching moments compared to conventional wings. This increases the trimming load required from the horizontal tail and offsets some of the tail off L/D gains. Additionally, aft loaded supercritical wings can have stall patterns with the final break occurring near the trailing edge which can lead to large pitch up and / or non-symmetrical conditions.

Another consideration is that the normal response of the shocks to small local changes in the freestream flow combined with the proposed flexible structure could require a potential need for local spanwise control of the flexible structure and the possibility of very high actuation rate requirements.

Stability levels of straight wings at these speeds have not been subject to significant flight test, so the wind tunnel or CFD to flight test correlations have not been established. This will be a significant risk that will need to be mitigated in a risk reduction program. Empirical data should only be used with great care.

Low Speed Considerations

The bank angle for wing tip strike, gust loads during ground roll, bumps on taxiways, or perhaps just the sink rate at touchdown may be factors in how flexible the wing can be. As previously noted, the stall characteristics may not be as consistent as current designs. In all configurations,

the wing stiffness (or control laws) will need to assure a symmetrical configuration through the pull, stall, and prevent any sudden disturbance from developing post stall. The control system could be used to configure the wing to ease the stall characteristics but each new function adds risk and complexity.

Meeting the crosswind and steady heading sideslip requirements requires max lift coefficient and AOA at max lift coefficient to drop off gently and predictably with increasing sideslip. Highly optimized conventional wings tend to drop off quickly and have had issues with the full rudder steady heading sideslip demonstrations. The FAA / JAA harmonization process lower the speeds that these demonstrations are required. Any future reduction in the speeds would require flat max lift coefficient versus beta curves.

Spoilers will most likely be required for high cruise speeds (where aileron effectiveness is low behind shocks) and low speed operation near the ground (where large amounts of control are required by gusts). Spoilers will be required for most of the slowdown / go down maneuvers.

Stopping these very efficient aircraft may also be a significant challenge. Currently spoilers and reverse thrust are used to supplement the brakes and flap drag. Both spoiler and reverse thrust create large turbulent flow fields, RTO or landing conditions may limit the flexibility of the wing-strut-body combination.

Airport Compatibility

Aircraft wingspans have been growing over the years. The trend is driven by the continuous need for improving aircraft performance to meet airlines' operating (economics) challenges and to reduce environmental impacts. As shown in Figure 2.3, each aircraft family has experienced wingspan growth to the limit of its airport design category:

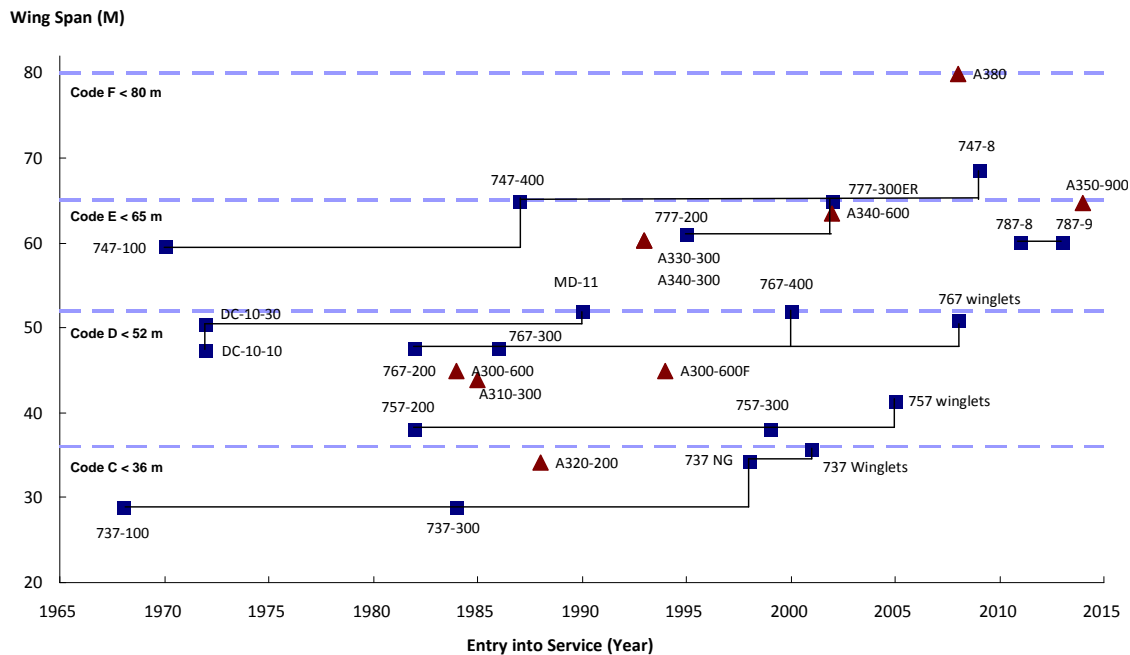


Figure 2.3 – Aircraft Wingspan Growth Trend

Airport's airside (the aircraft maneuvering area of an airport) are built to support ground operations and to meet the servicing needs of aircraft operations. Airside layout and functionality is largely determined by the operational and physical characteristics of the most demanding aircraft that uses the facility. Aircraft wingspan is one of the most critical aircraft physical characteristics, impacting all geometrical separations in the airside areas where movement or servicing of aircraft is anticipated (such as runway to runway, runway to taxiway, taxiway to taxiway, taxiway to object separations, etc.). Other aircraft operational and physical characteristics, such as tail height and outer main gear wheel span, also have impacts to layout and functionality of various airside components at airports. The following section will discuss airport compatibility issues related only to aircraft wingspan.

The areas impacted by the aircraft wingspan are depicted in Figure 2.4 and listed:

- runway – runway separation
- runway – object separation
- runway – taxiway separation
- taxiway – taxiway / taxilane separation
- taxiway / taxilane – object separation
- aircraft parking position (with and without jet bridge)
- de-icing facilities
- engine run-up pad (open or partially enclosed pad)
- aircraft hangars



Figure 2.4 – Areas Impacted by Aircraft Wingspan

Airport Design Criteria and Potential Impacts of High Wingspan

To ensure safe operation of airports as well as aircraft, each country or state enforces a set of airport design criteria by either adopting standards established by the International Civil Aviation Organization (ICAO) or by establishing their own standards. ICAO publishes a set of airport design standards (5), while the Federal Aviation Administration (FAA) in the United States establishes similar standards (6). These standards documents contain airport design criteria expressed by way of an airport reference coding system which relates to the operational and physical characteristics of the airplanes that the airport intends to serve through the airport reference coding. It is important to note that these standards are not intended to limit operations, but to provide guidelines that will accommodate a family of aircraft so as to avoid the need to make infrastructure changes each time a new aircraft begins operations into an airport.

ICAO’s airport reference coding classifies an airport based on aircraft reference field length, wingspan and outer landing gear wheel span, while the FAA uses aircraft approach speed, wingspan, and tail height as classification parameters. This section intends to address only aircraft wingspan; therefore, only classification criteria relating to wingspan will be discussed herein. Table 2.1 shows the relationship between aircraft code letter and wingspan.

Table 2.1 – Airport Reference Code Letter

ICAO Aerodrome Reference Code Letter ¹		FAA Airport Reference Code Letter ²	
Code Letter	Wingspan meters (ft)	Airplane Design Group	Wingspan feet (meters)
A	Up to but not including 15m (49)	I	< 49 (15 m)
B	15m up to but not including 24m (78.7)	II	49 – < 79 (24.1)
C	24m up to but not including 36m (118.1)	III	79 – < 118 (36)
D	36m up to but not including 52m (170.6)	IV	118- < 171 (52.1)
E	52m up to but not including 65m (213.3)	V	171- < 214 (65.2)
F	65m up to but not including 80m (262.5)	VI	214- < 262 (79.9)

An airport should be designed and constructed to meet these design standards established for its airport reference Code Letter category, unless otherwise approved by its jurisdictional aviation authority. Table 2.2 lists the taxiway minimum separation distance established by ICAO.

Table 2.2 – ICAO Airport Design Standards

Code Letter	Runway – Taxiway Centerline Separation (m)								Taxiway-Taxiway Centerline Separation (m)	Taxiway – Object Separation (m)	Taxilane – Object Separation (m)	Clearance on Aircraft Stands (m)
	Instrument Runway Code Letter Number				Non-Instrument Runway Code Letter Number							
	1	2	3	4	1	2	3	4				
A	82.5	82.5	-	-	37.5	47.5	-	-	23.75	16.25	12	3
B	87	87	-	-	42	52	-	-	33.5	21.5	16.5	3
C	-	-	168	-	-	-	93	-	44	26	24.5	4.5
D	-	-	176	176	-	-	101	101	66.5	40.5	36	7.5
E	-	-	-	182.5	-	-	-	107.5	80	47.5	42.5	7.5
F	-	-	-	190	-	-	-	115	97.5	57.5	50.5	7.5

Source: ICAO Annex 14, Volume 1, Aerodrome Design and Operations

Item shown in *orange* indicate separation distances that are allowed by ICAO however, non-instrument approaches (non-instrument runways) are rare at commercial aviation airports.

Unless otherwise approved by the jurisdictional aviation authority, not meeting these design standards could, generally, cause:

¹ Only the second component of the ICAO Aerodrome Reference Code Letter is shown here. The first component is a Code Number from 1 to 4 that relates to the airplane reference field length. Besides the wingspan, the outer main gear wheel span is the other determinant of the Code Letter.

² Only the first component of the FAA Airport Reference Code Number (the airplane design group code) is shown. The second component, called the aircraft approach category (which ranges from categories A to E) is based on the aircraft approach speed. Besides the wingspan, the tail height is the other determinant of the airplane design group.

- Aircraft whose wingspan is larger than the airport reference Code Letter to which an airport is currently designed to be rejected for operations at the airport
- Special operational restrictions to be imposed. Such restrictions could be in various forms:
 - temporarily closing a parallel taxiway while the larger aircraft is on the adjoining runway or taxiway
 - disallowing the larger aircraft from using a particular runway or taxiway
 - limiting the aircraft wingspans on adjacent operational areas
 - declaring only a limited time frame for such an operation

Any restriction, regardless of form, will disrupt normal operations at an airport, and may cause flight delays and airport capacity / throughput reduction.

Due to budget and / or space availability, not every area of an airport will be designed and built to one airport reference Code Letter. Especially at terminal aprons where aircraft park, the parking stands (including stands with jet bridges and remote stands without jet bridges) are sized to accommodate particular sizes of aircraft to maximize capacity and maintain a safe apron circulation and space for Ground Service Equipment (GSE) storage and staging. A larger wingspan aircraft attempting to park in a smaller parking stand, generally, will cause:

- closure or restrictions on adjacent parking stands to smaller wingspan aircraft
- restrictions on apron circulation (e.g., apron taxilanes, service roads)
- reduction in size or relocation of GSE storage and staging area
- delay and capacity reduction in the airport terminal area as a combined effect of operational restrictions and the reduced passenger capacity of larger wingspan aircraft (compared with the same capacity aircraft with smaller wingspans)

Design standards for several other wingspan-impacted areas are not listed in Table 2.2, but they include runway-runway separation, runway-object separation, de-icing facilities, and aircraft hangars.

Runway to runway and runway to object separation are also related to wake vortex (the turbulence that forms behind an aircraft as it passes through the air, the most important of which are wingtip vortices which can remain in the air for up to three minutes after the passage of an aircraft). A non-infrastructure impact from an increase in the wake vortex turbulence is the separation between aircraft on arrival and departure. As the turbulence increases, greater separation is required, negatively impacting the throughput, and potentially overall airport capacity. The wake vortex turbulence is related to aircraft weight and wingspan – turbulence increases as the weight goes up, and decreases with increases to the span.

De-icing facilities, engine run-up pads (especially partially enclosed pads), and aircraft hangars will also be impacted by an increased wingspan. Most likely many of these will not be wide enough to accommodate increased wingspans and it is expected that modifications to these facilities will be required. Further study is required to determine the impact of these changes

Impacts of SUGAR Aircraft Wingspan on Airports Worldwide³

The SUGAR program identified a 737-like aircraft as the study aircraft. Its wings incorporate a unique folding wing design mechanism. The unfolded wingspan (approximately 52m) will stay within the ICAO Code Letter D wingspan limit and the folded wingspan (approximately 36m) will stay within the Code Letter C wingspan limit.

This SUGAR aircraft intends to operate with its wings unfolded on the runway and folded whenever the aircraft is off the runway. The SUGAR aircraft wings will be compatible with the ICAO Code Letter D runway environment (including runway to parallel taxiway separations), and Code Letter C taxiways and parking aprons. Since the airports are traditionally designed for an unfolded wing, the SUGAR aircraft will have design and operational incompatibility on ICAO Code Letter C airport runways as well as with hangars and aprons when the wing is unfolded (mechanical malfunction or maintenance that requires the wings to be unfolded).

This study has analyzed the worldwide airport class distribution by traffic and has examined runway-to-taxiway separations at 100 Code Letter C airports which are within the top 115 Code Letter C airports by traffic. The following sections discuss the findings.

Worldwide Airport Distribution by Traffic

This study analyzed the worldwide airport reference coding distribution by scheduled flights as reported in the Official Airline Guide (OAG) through February 2012. It should be noted that the OAG database used in the study records only scheduled flights, without visibility of most freighter and all charter operations. Moreover, the database accuracy mainly relies on the reporting airlines. The study included a total of 2,313 commercial airports worldwide. As shown on Figure 2.5, 58.5 percent of studied airports worldwide support only Code Letter C aircraft traffic; 18.7 percent serve Code Letter D traffic; 21.4 percent serve Code Letter E traffic; and only 1.4 percent serves Code Letter F traffic.

³ This study focuses on wingspan impact to ICAO Code C airports. It is expected that the conclusions reached in this study will be transferable to other aircraft families.

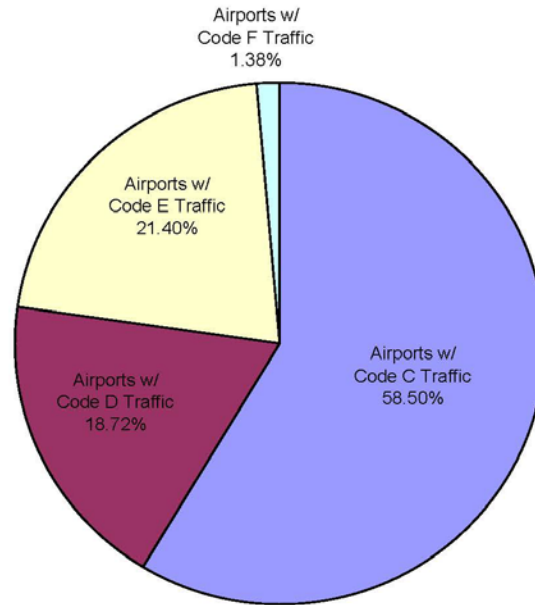


Figure 2.5 – Worldwide Airport Distribution by Traffic⁴

It should be noted that the airport distribution discussed above is based on aircraft that the airports served both in the past and serves at the time of this study. It does not reflect the airport class that its physical geometry can accommodate. For simplicity, this study only considers, for example, that an increase in wingspan on a Code Letter C aircraft will have more visible impacts on those airports with Code Letter C traffic (not on Code Letters D through F traffic) as of the time of the study.

Wingspan Impacts on Runway-to-Taxiway Separations

This study examined runway and taxiway centerline separations at 100 Code Letter C airports. These airports serve aircraft not larger than Code Letter C and are within the top 115 Code Letter C airports by traffic (15 of the top 115 airports did not have clear enough images in Google Earth to make measurements). The study was based on the latest images provided by Google Earth Pro. It is found that, out of these 100 airports, 75 percent of the airports have runway and taxiway centerline separations above the ICAO Code Letter C and D requirements (or FAA Airport Reference Code (ARC)⁵ III and IV standards⁶). This finding indicates that the SUGAR aircraft’s unfolded wingspan of 52m may not cause significant impacts on the runway system at the top

⁴ Code Letter C aircraft included in the analysis are 717, 727, 737, MD80, MD90, DC-3 to -7B, A318, A319, A320, A321, TU-134, YAK-42. Regional jet and turboprop Code Letter C aircraft are not included. Code Letters D-F aircraft included in the analysis are 707, 720, 747, 757, 767, 777, MD11, DC-7C, DC-8, DC-10, A310, A300, A330, A340, A380, IL-76, IL-96, TU-204, AN-124, TU-154, TU-204

⁵ The FAA ARC consists of two components. The second component, depicted by letters from A to D, is the aircraft approach category which relates to aircraft approach speed. The first component, depicted by a Roman numeral from I to VI, is the airplane design group which relates to airplane wingspan or tail height, whichever is the most restrictive.

⁶ Out of the 100 airports studied, 18 are US airports. US airports follow the FAA standards, published in AC 150/5300-13, “Airport Design”. The FAA standards are different from the ICAO standards as shown on Table 2. In terms of runway-to-taxiway separations, the FAA standards are less demanding. Airport design groups III and IV require 400 feet (120 m) runway and taxiway centerline separations by FAA criteria.

100 Code Letter C airports worldwide (by number of operations). However, the extent of wingspan impact on the runway system at the remaining Code Letter C airports will vary by airport, due to the uniqueness of each airport and its jurisdictional aviation authority. It should be noted that this study classified the airports into different categories (Code Letters) only by way of the aircraft that are serving the airport. The ICAO / FAA standards are the minimum design standards and airports may have over-designed their infrastructure in anticipation of future growth. Additionally, this study examined the airports based on today's ICAO / FAA standards. In many cases, these have been gradually reduced over the years from the criteria that were effective at the time of the design / construction of a given airport.

Wingspan Impacts on Other Areas

The SUGAR aircraft will be expected to maintain a Code Letter C wingspan (folded) while it is off the runway. Because this aircraft will operate in areas designed and operated to accommodate an ICAO Code C wingspan we will need to convince the airport authorities worldwide that once in the folded position, the aircraft will have a fail-safe and fool-proof means to maintain the folded condition, even if there is a loss of power, or any other system breakdown. Without full disclosure of the on-board fold and unfold systems, airports will be forced to declare that they cannot accept an aircraft whose span might inadvertently become Code D when all of the clearances and separations that allow the aircraft to even be on the airport are based on a folded span.

Potential Issues with the SUGAR Aircraft Folding Wings

As mentioned above, a major potential issue with the SUGAR aircraft folding wings will be human acceptance, especially, by the airports and their jurisdictional aviation authorities. The SUGAR aircraft, by its unfolded wingspan, will be identified as Code Letter D aircraft. It is unknown whether the SUGAR aircraft will be accepted by individual jurisdictional aviation authorities and / or the airport operators as a Code Letter C aircraft for taxiing and parking, until after such time as a similar folding wing aircraft has been introduced into commercial service and accepted by the authorities.

Secondly, the dual status of the SUGAR aircraft (hybrid Code C/D) will create challenges to Air Traffic Control (ATC) and airport operational controllers (ground controllers). ATC and airport ground controllers will need to employ two sets of standards (Code Letter D during approach and departure, and Code Letter C standards everywhere else) to direct the SUGAR aircraft maneuvering at an airport. Any inadvertent folding wing mechanism failure or any irregular changes required from the routine folding-unfolding configuration will need to be addressed at every operational level. Our early attempts with the 777 wing fold (the aircraft was referred to as the 767-X at the time) faced a very skeptical airport audience. Their belief was that any mechanical system will be prone to break-downs and failures, so they implied that they would

require full span compatibility for the aircraft on their airports. Early disclosure of the fold / unfold process will be required by airports and aviation authorities in order for the aircraft to be accepted.

In cold climate areas, aircraft de-icing is normally conducted at the gate before departure and / or at a designated de-icing apron located somewhere between the gate and the runway. To ensure that wing-folding area is free of ice during unfolding, ATC procedures may require maintaining an unfolded-wing configuration after de-icing, or perhaps some on-board anti-icing feature may be required. Our thought process at the time was that even though de-icing was then (and still is now) primarily achieved by de-icing at the gate, that a secondary de-icing would be provided as the aircraft neared its departure threshold, at which time the wings would be fully in the unfolded position. While this may seem to be only a back-up system, many airlines / airports use this technique today, due to the problem of dispatched aircraft running short on their holdover times. When an aircraft in the takeoff queue is within a few minutes of the ice-preventative effectiveness of their last de-icing, a secondary de-icing vehicle is often pre-positioned near a threshold to apply a final de-icing treatment. This practice will probably become a requirement for folding wing aircraft once they are deployed to the world's airports.

Georgia Tech Airport Compatibility Dashboard

Compared to current transport aircraft, the wing span of the SUGAR concept is potentially much longer for the same aircraft weight/seat class. This increase in span is critical to the advantages of the design. Practically, the operation of the SUGAR concept may be limited by existing airport infrastructure parameters, and thus may have access to only a subset of airports. Several potential limiting parameters include runway width, taxiway width, runway-taxiway separation, taxiway-object separation and separations at gate, as illustrated in Figure 2.4

Runway width can impose limitations depending on the undercarriage width, and runway-taxiway separation depends on the wing span. The wing folding mechanism can be used to mitigate the problems with taxiway-object separation and separations at gate. Aircraft weight is another potential limiting factor, however, it is assumed the weight of a SUGAR concept can be accommodated by the runway of the airport design group number selected based on the wing span.

Objective

The purpose of this task was to provide a parametric-based analysis for wing span/fold location for a constraint analysis based on runway widths and lengths and minimum taxiway-runway separation. Utilizing this information, the user can determine the number of United States airports that are accessible by a variable span SUGAR aircraft with and without a wing fold, as a function of the fold location and fold angle. This information can be used to aid in preliminary

decision making as regards the desired exploration space for more integrated design of a wing fold mechanism at multiple potential aircraft sizes.

The outcome of this task is a dashboard analysis tool, constructed in MS Excel that utilizes collected airport data, combined with aircraft-level aspects of the wing design to determine the accessible United States airports. Below, the data sources will be described, along with any necessary assumptions employed, followed by a physical description of the dashboard components. Finally, a sample use-case will be provided to demonstrate how the tool can be implemented to perform the objective.

Description of Data Structure

The dashboard is a data-driven tool, based on several available and specifically collected or computed sets of information. The data are provided in the 'Runway Data', 'Wing Fold', 'OAG Feb 2012 Twy-Rwy' tabs within the dashboard.

The Runway Data tab contains a collection of United States airport runways, including their latitude and longitudinal locations. This information is used to demonstrate the available airports on a map of the contiguous United States. This data also contains effective runway lengths and runway widths, used to determine which U.S. runways meet the criteria selected in the dashboard. Runway length is important because takeoff distance, although not directly related to the wing span, has to be considered in the airport compatibility study.

The Wing Fold data tab contains the first-order computations of the wing geometry, which allow the dashboard to dynamically display changes in wingspan, fold length, and fold angle.

The OAG Feb 2012 Twy-Rwy tab contains the runway-taxiway separation information. This data was obtained through the use of publically available internet mapping software, which allowed for the examination of specific airports to manually measure the runway-taxiway separation for the top 90% of United States airports based on total operations. The real runway-taxiway separation of an airport can be more (and sometimes less) than the one required for its airport design group number assigned per the airport design specifications. The SUGAR concept may be able to operate at an airport of lower airport design group number, and those runway-taxiway separation data have to be measured directly from the airport satellite photos. Some airports do not have a taxiway, and in that case the runway-taxiway separation will be represented by the distance between the runway centerline and the closest parallel taxi line in the apron or ramp. This information is ultimately used at the dashboard level to determine the percentage of airports for a given airport ICAO Code that meet the necessary runway-taxiway separation criterion.

Dashboard Architecture

This dashboard is made in Excel, and it does not use macros to ensure compatibility with other versions of excel. The user-interface of the dashboard is located in the ‘Dashboard’ tab. The Dashboard is arranged into three sections: the Runways, Wing Fold, and Runway-Taxiway sections. Each of these is impacted in certain ways by the inputs: wing span, fold length, fold angle, runway length, and runway width. These inputs are provided by the user based on the specific analysis scenario, and can be varied dynamically to provide instantaneous tradeoff results. In general, the color-coding on the dashboard uses a red/green paradigm, where red designates dissatisfaction of the filtering criteria, and green implies satisfaction. Some inputs are provided as a range (minimum and maximum) whereas others are provided as specific values. These are summarized in Table 2.3.

Table 2.3 – User inputs to the dashboard.

Variable	Units	Type	Minimum	Maximum
Wingspan	Feet	Single-Value	36	326
Fold Length	Feet	Single-Value	0	30
Fold Angle	Degrees	Single-Value	0	135
Runway Length	Feet	Range	0	15000
Runway Width	Feet	Range	0	320

The Runways section of the dashboard is shown in Figure 2.6. The inputs to the Runways section are runway length and (required) runway width. This section lets the user filter from a list of over 5,700 domestic runways of the continental United States by runway length and width. The user can choose to include or exclude tower-less and military airports. The runway width should be selected based on the undercarriage width. However, the undercarriage width usually is not known during the conceptual design stage. Instead, the user can provide an estimate of a reasonable range for the undercarriage width, and examine the impact of that range on the number of domestic runways that the SUGAR concept can operate on with a certain wing-fold design.

	Runway Length (ft)		Runway Width (ft)	
<i>Lower Limit</i>	3245	◀ ▶	81	◀ ▶
<i>Upper Limit</i>	8187	◀ ▶	289	◀ ▶

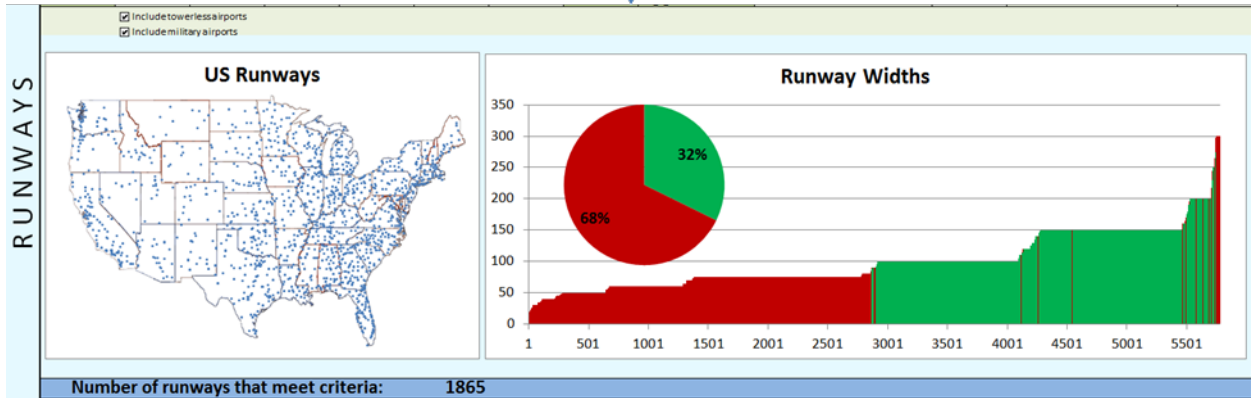


Figure 2.6 – The Runways section of the dashboard.

The Wing Fold section is shown in Figure 2.7. The inputs to the Wing Fold section are wing span, fold length and fold angle. The wing span input refers to the unfolded wing span. The fold length refers to the length of the folded section from the point of the fold to the tip of the wing. The fold angle is an absolute value measured as the exterior angle from the span-wise axis of the aircraft to the wing-fold section. The wing span *after* folding will be calculated based on the wing design inputs provided.

Wingspan (ft)	Fold length (ft)	Fold angle (deg)
220	16	90

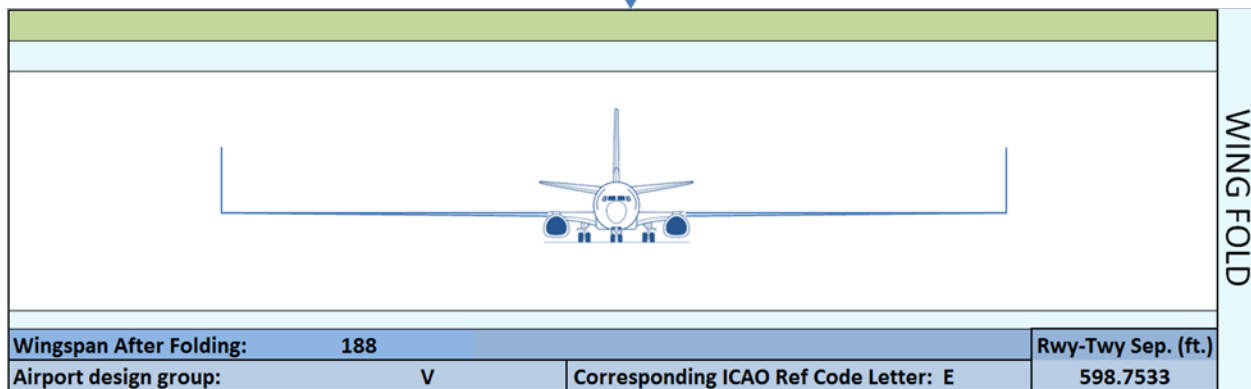


Figure 2.7 – The Wing Fold section of the dashboard.

The airport design group number for the resulting aircraft configuration is computed and shown. This design group number is also based on the wing span *after* folding. The ICAO Reference Code Letter is also provided. This information is then used to lookup the minimum runway-taxiway separation for these aircraft based on Table 2.2.

The Runway-Taxiway section is shown in Figure 2.8. The input to the Runway-Taxiway section is the minimum required runway-taxiway separation (provided in feet), determined from the ICAO reference letter that corresponds to the specified aircraft configuration. Again, all comparisons are performed on the wingspan *after* folding to demonstrate the increased compatibility from wing-fold implementation.

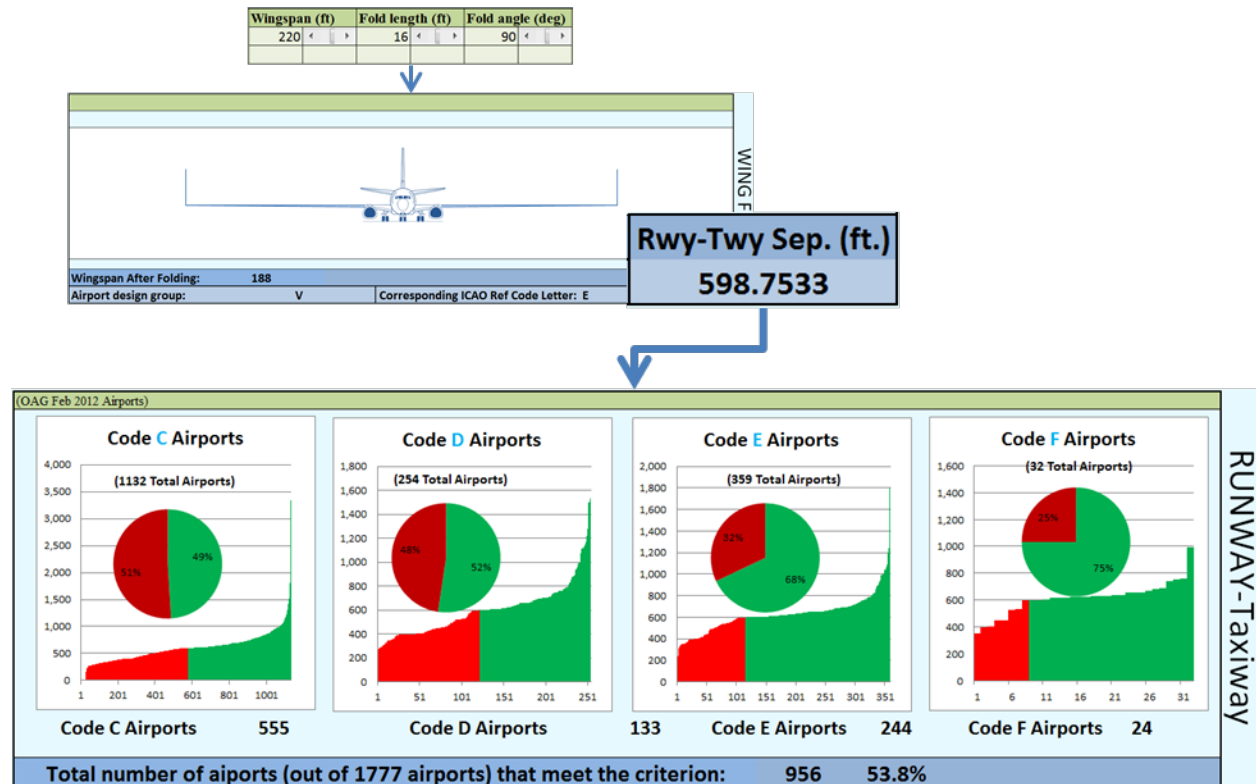


Figure 2.8 – The Runway-Taxiway section of the dashboard.

This section uses the minimum separation to filter a list of 1777 airports worldwide of Code C, D, E and F. The filter results are provided for each of the airport codes as a percentage of airports that meet the minimum runway-taxiway separation distances for the specified configuration. The airport design specifications including ICAO Annex 14, Aerodromes, and FAA Advisory Circular 50/5300-13, Airport Design, provide the guidelines and rules for selection/determination of the proper airport design group number, runway width and runway-taxiway separation. (5) (6)

Sample Use Case

As an example, a use-case is provided to demonstrate how the dashboard should be utilized. The example is based on the SUGAR High (N+3 Advanced High Span) aircraft (1). The particular configuration has a Maximum Take-Off Weight (MTOW) of approximately 140,100 lbs. (not a dashboard input but provided for reference) and a wingspan of 215 feet. The Takeoff Field Length (TOFL) trades identified a minimum TOFL of 8,190 feet. For aircraft of this weight, per Advisory Circular 150/5300, the minimum runway width for this type of aircraft is 200 feet. (6) The

maximum is unconstrained, as this use-case will assume that there is no max limit on runway width that the aircraft can operate on. These input values were provided to the dashboard to produce the baseline front-view geometry shown in Figure 2.9.

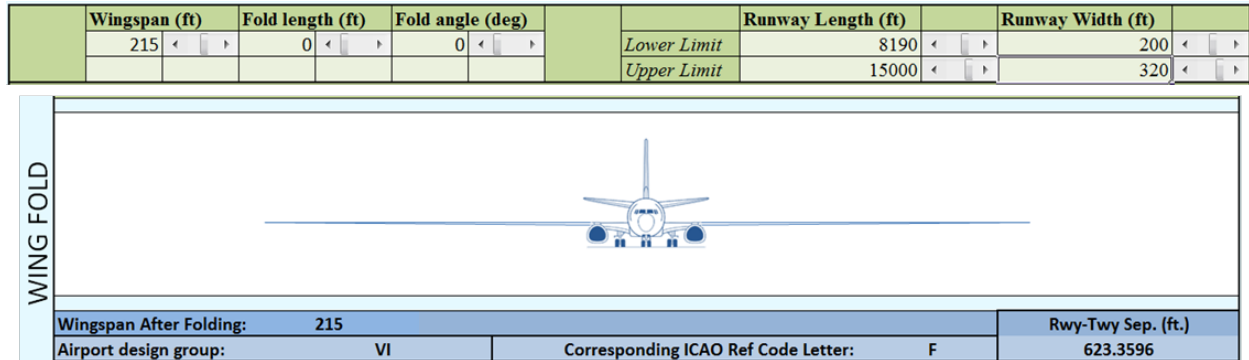


Figure 2.9 – Baseline front-view of the use-case SUGAR Volt aircraft.

Analyzing the United States airports that conform to the runway length and width specifications shows that only a negligible percentage of airports (19) airports in the continental United States can operate this concept. The spatial distribution of these airports (shown in Figure 2.10) covers many of the metro-plex regions when compared to the 21 areas identified by the FAA (6) in Figure 2.11, with the most notable omission being the Denver, CO region, and the Pacific Northwest.

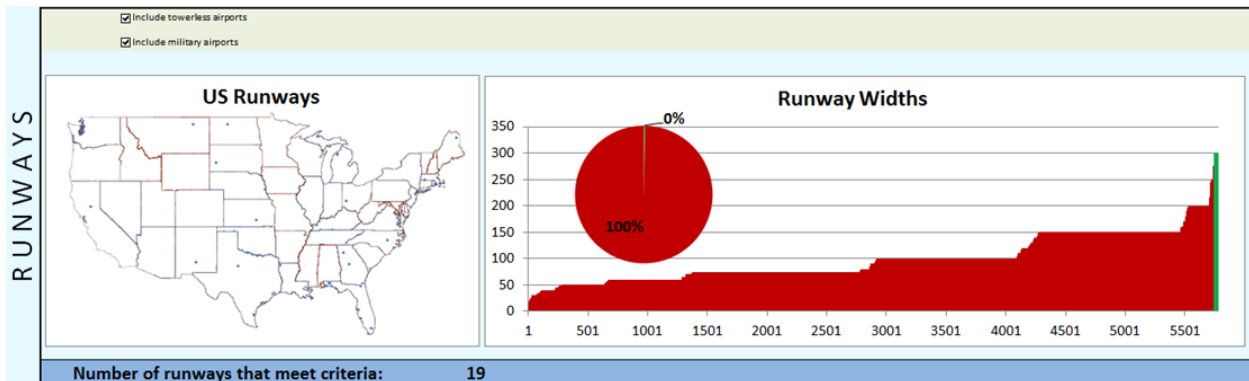


Figure 2.10 – Runway-view shows the number of U.S. runways that meet the specified minimum width



Figure 2.11 – FAA Metroplex regions (7)

The airport design group and ICAO Reference Code Letter are VI and F respectively for the baseline configuration. These designations correspond to a minimum runway-taxiway separation of approximately 623 feet. This information is used to determine the percentage (out of 1,777) of OAG airports that support this runway-taxiway separation. The input specifications result in 40.6% of airports (721) supporting the minimum runway-taxiway separation required to operate the aircraft without a wing-fold. Twenty-two of these airports are United States airports, as summarized in Figure 2.12.

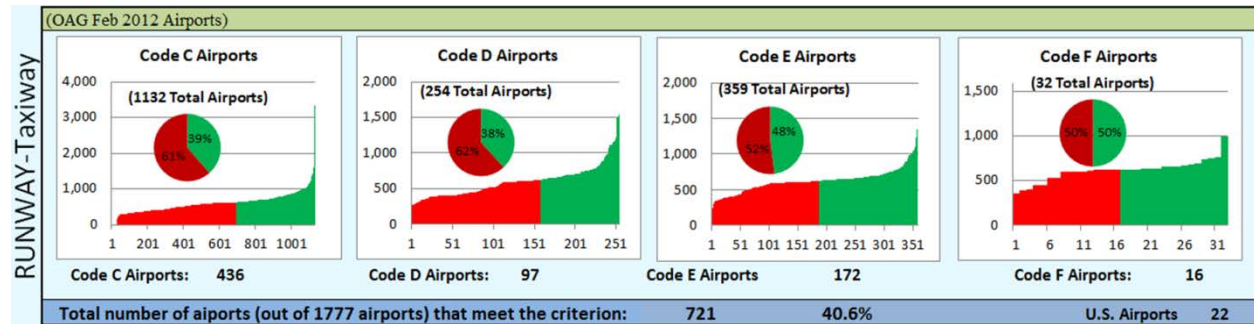


Figure 2.12 – Breakdown of 1,777 OAG airports with respect to the runway-taxiway separation criteria.

To examine the potential impact of adding a wing-fold, the user can select a reasonable baseline fold angle and examine the impact of varying the fold length. In the interest of simplicity, the baseline fold angle will be 90 degrees for this use-case, as shown in Figure 2.13.

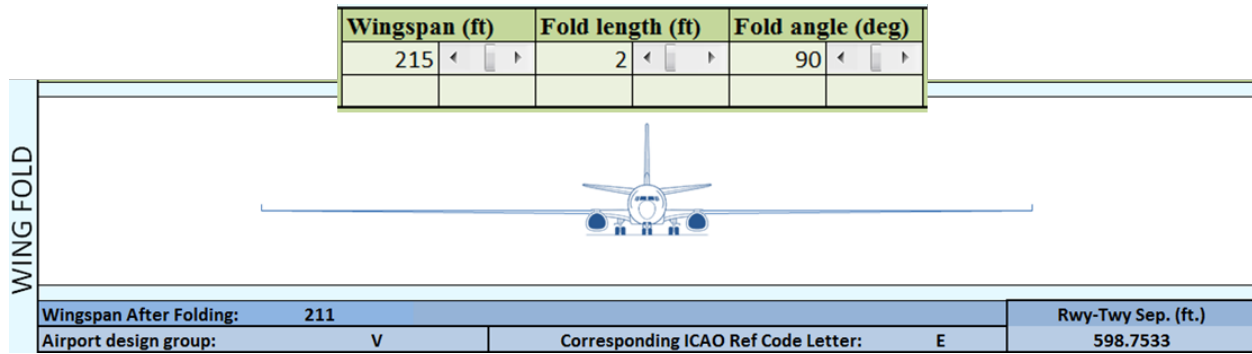


Figure 2.13 – Folded configuration changes the airport design group and minimum runway-taxiway separation.

Varying the fold length shows that there is an immediate change in the design group with a fold length of only 2 feet. The change occurs in the airport design group, which affects the minimum runway-taxiway separation. This change adds over 200 OAG airports with the necessary minimum runway-taxiway separation, and increases the number of United States airports from 22 to 34. Further increasing the fold length to 24 feet provides another change to the airport design group, adding an additional 100 of the OAG airports and the number of U.S. airports enabled by the wing-fold increases to 38. Therefore, the user could reasonably conclude that wing-folds within the vicinity of 2 and 24 feet should be targeted for further exploration. If consideration is warranted, the user can trade the location of the fold (i.e. – the length) by changing the angle of the fold (reducing the range of motion required to fold the wing) to achieve a similar effective span as shown in Figure 2.14.

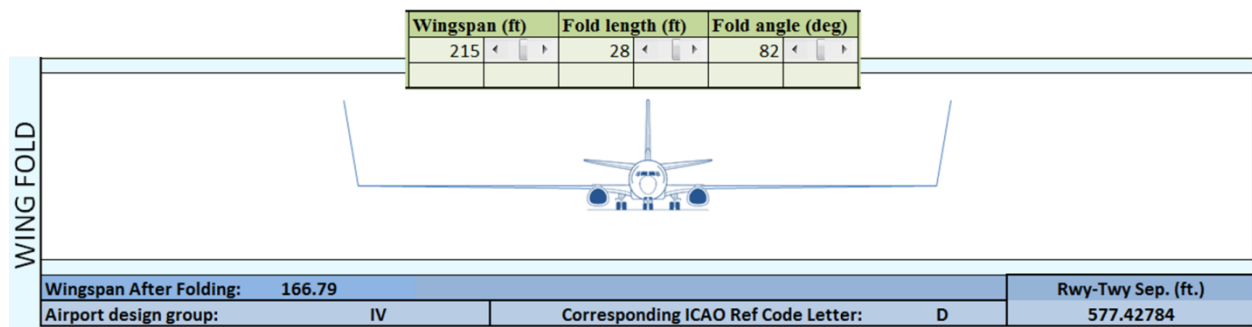


Figure 2.14 – Similar wingspan after folding can be achieved by trading fold length for fold angle.

2.1.3 Vehicle Design Evolution

The initial release of the 765-095 SUGAR High configuration was generated under the first phase of the SUGAR program. The fuselage and empennage arrangement for the configuration are typical for a high wing transport, but the wing, landing gear and their integration with the rest of the vehicle occupied unexplored design territory.

Phase II revised the initial release with many geometry refinements; several of these were the product of a detailed integration exercise between the fuselage, landing gear, and wing strut. These changes resulted in configuration Revision A.

Revision A was used to initiate a planform and strut Multi-Disciplinary Optimization (MDO). The results of the optimization were used to derive Revision B. A high speed wing design, which set wing thickness distribution and airfoil shape, was then generated by Boeing for the resulting planform. This design was released as Revision C which, in turn, was used as the starting point for an increased fidelity high speed aerodynamic analysis, a low speed aerodynamics design, and an aeroelastic Finite Element Analysis (FEM). The resulting updates were rolled into the final configuration released for this phase of the strut braced wing study, Revision D. This process is illustrated in Figure 2.15.

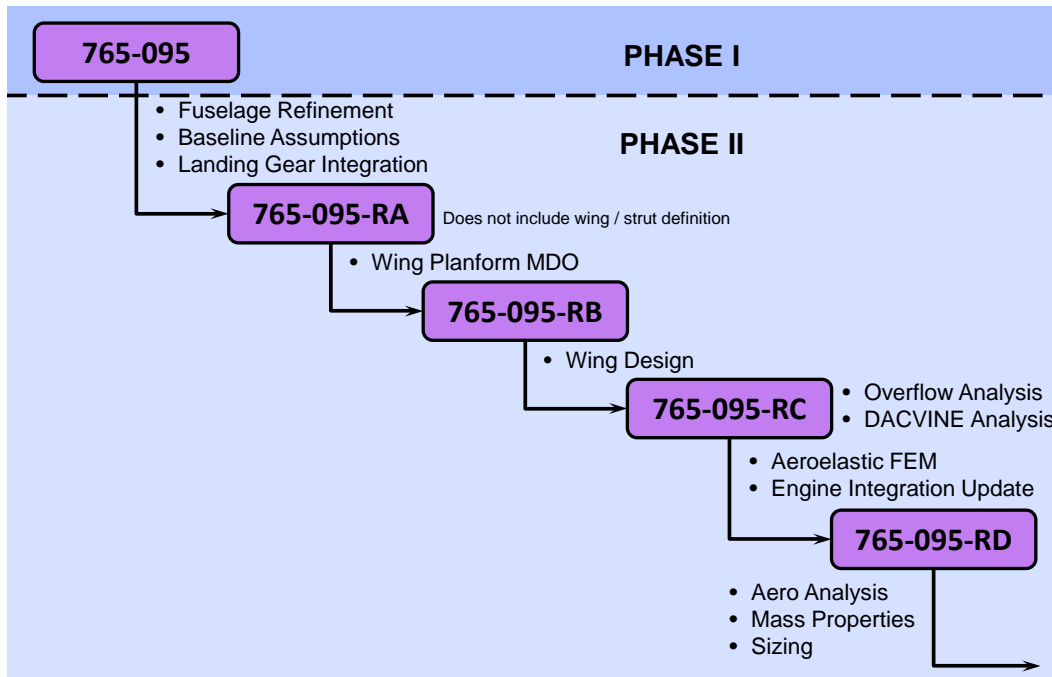


Figure 2.15 – Configuration Evolution

2.1.4 Wing Planform Development

Georgia Tech and Virginia Tech have, in partnership, developed a design environment which utilizes structures, aerodynamics, mass properties, and performance tools to explore the truss braced wing design space. This capability was leveraged to determine a starting point for the SUGAR program. In summary, the effort was comprised of a coordination effort to baseline assumptions and requirements, an airfoil design task, and a strut and wing planform optimization led by the university team.

2.1.4.1 Model Analysis Coordination

In order to minimize any discrepancy in analysis constraints or methods, Boeing, Virginia Tech, and Georgia Tech discussed the truss braced wing MDO procedure used within the university design environment. Changes and constraints requested by Boeing are documented:

- Interference drag for the wing and jury struts was calculated from a database of CFD data that was run outside the MDO environment
- Mach Ratio effects from the body were incorporated into the MDO environment.
- Excrescence drag was included for this MDO.
- Lifting struts were assumed to be outside the scope of this study. Previous studies have shown that more optimum lift distributions can be achieved with a lifting strut. Boeing experts believe that the interference drag penalty of a lifting strut in close proximity to the wing will be severe and may not have been captured by the previous university CFD analysis.
- Advanced Material Properties (quasi-isotropic):
 - $E=10.5$ MSI
 - $G=3.9$ MSI
 - $\nu=0.325$
 - Ultimate Strain Allowable 4500 micro In/In
 - Density = .057 lb/in³
- A pseudo-dynamic gust is included in the MDO by factoring static gust loads by 1.0 between wing root and truss brace. Outboard of truss brace a linear interpolation from 1.0 (inboard) to 1.4 (at the wing tip) is used.
- The design speed envelope of the airplane is illustrated in Figure 2.16.

2.1.4.2 Boeing 2D Airfoil Design

Advancements in design tools and computing resources have enabled three-dimensional wing design to become the standard at The Boeing Company. The SUGAR Phase II team included a two-dimensional design task for the sole purpose of constraining local wing sections to thicknesses that are appropriate for the drag divergence Mach number of interest, Mach 0.70. Previous studies have shown that sectional lift coefficients are not likely to increase past 0.8. In order to press the state-of-the-art designs, it was decided to attempt to attain a sectional lift coefficient of 0.9. Experience from the Phase I effort led the team to push the cruise altitude to 43,000 feet.

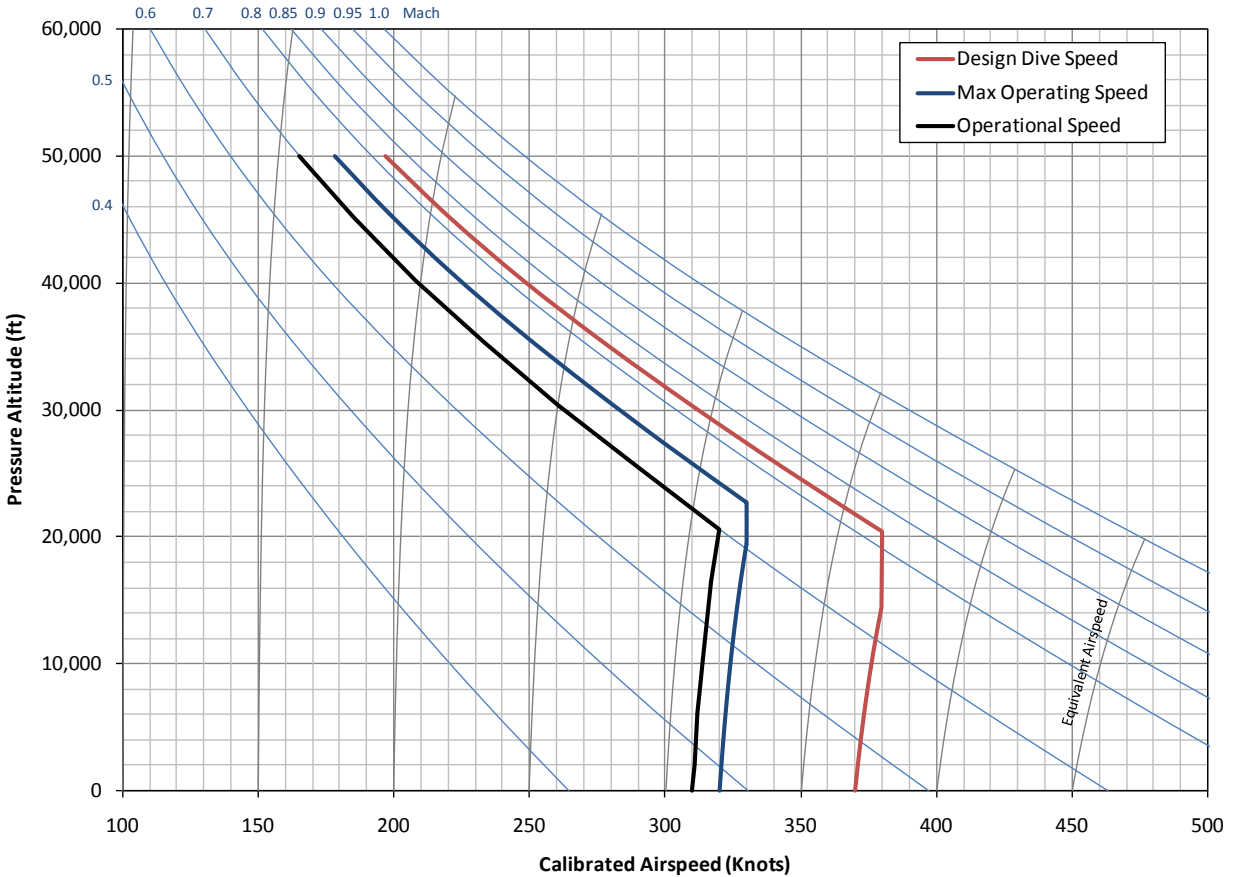


Figure 2.16 – Design Speed Envelope

Airfoil Design Tools

Boeing utilizes both commercial codes and internally developed applications to design and analyze aircraft geometry. The design process and tools used for a specific problem are specifically tailored using recent code developments, user familiarity, and code applicability. For this project, several analysis codes were used.

CDISC – Inverse Design

The Constrained Direct Iterative Surface Curvature (CDISC) program is an aerodynamic-design tool for defining surfaces that match a prescribed pressure distribution. It uses streamline curvature theory to adjust an existing geometry to the target pressure distribution. It was developed as a stand-alone program by NASA that can easily be used in conjunction with various flow solvers and includes the capability to specify various geometry constraints (such as spanwise/chordwise curvature, thickness, etc.). The prevalent uses include the common suite of Navier Stokes codes: OVERFLOW, CFL3D, TLNS3D and USM3D. For the 2-D airfoil design done in this study, CDISC was coupled to CFL3D.

Overflow –Analysis

Overflow is an overset grid flow solver for simulating fluid flow around solid bodies. It is a compressible 3-D flow solver that solves the time-dependent, Reynolds-averaged, Navier-Stokes equations using multiple overset structured grids and has several turbulence models available. For the 2-D analysis done in this study Overflow was used with the S-A turbulence model.

CFL3D – Coupled to CDISC Inverse Design

CFL3D is a Reynolds-averaged, thin-layer, Navier-Stokes flow solver for structured grids. It is used here coupled to CDISC inverse design and used for its robustness, speed and ease of use compared to Overflow. It was run with the Baldwin-Barth turbulence model which gave a good match to the pressure distribution predicted by Overflow.

Methodology, Constraints, and Resulting Airfoil Characteristics

Two approaches were used for generating airfoil data for this task. The turbulent airfoil design was chosen from a library based on historical experience. The airfoil chosen was designed for a higher Mach number and lower lift coefficient than the task requirements thus adjustments to the data were made based on internal methods to account for the differences. The design for an upper surface laminar airfoil was seeded from the turbulent airfoil. The process used an inverse design method to maintain a pre-determined, favorable pressure gradient on the upper surface from just aft of the leading edge terminating at a shock whose location was prescribed as far aft as deemed reasonable based on engineering judgment and previous experience. The section lift was maintained as well as the maximum thickness of the airfoil. The inverse design was performed using CDISC and CFL3D. The resulting airfoil had a lower surface pressure ramp that was favorable for laminar flow, even though it was not specifically addressed in the design process, so a lower surface laminar design could use the same airfoil shape allowing the trade study to focus on high lift leading edge devices. The airfoils will be referred to as follows:

- T1 – Turbulent Baseline Airfoil
- L1 – Upper Surface Laminar

Once the airfoil shapes were defined, Overflow was used to conduct 2D angle of attack and Mach number sweeps using the RANS S-A turbulence model. The resulting data was used to generate curves of sectional drag coefficient vs. Mach number for a fixed lift coefficient. Drag divergence is defined as the point where the slope of this curve reaches 0.1. The three designed airfoils drag divergence characteristics are shown in Figure 2.17.

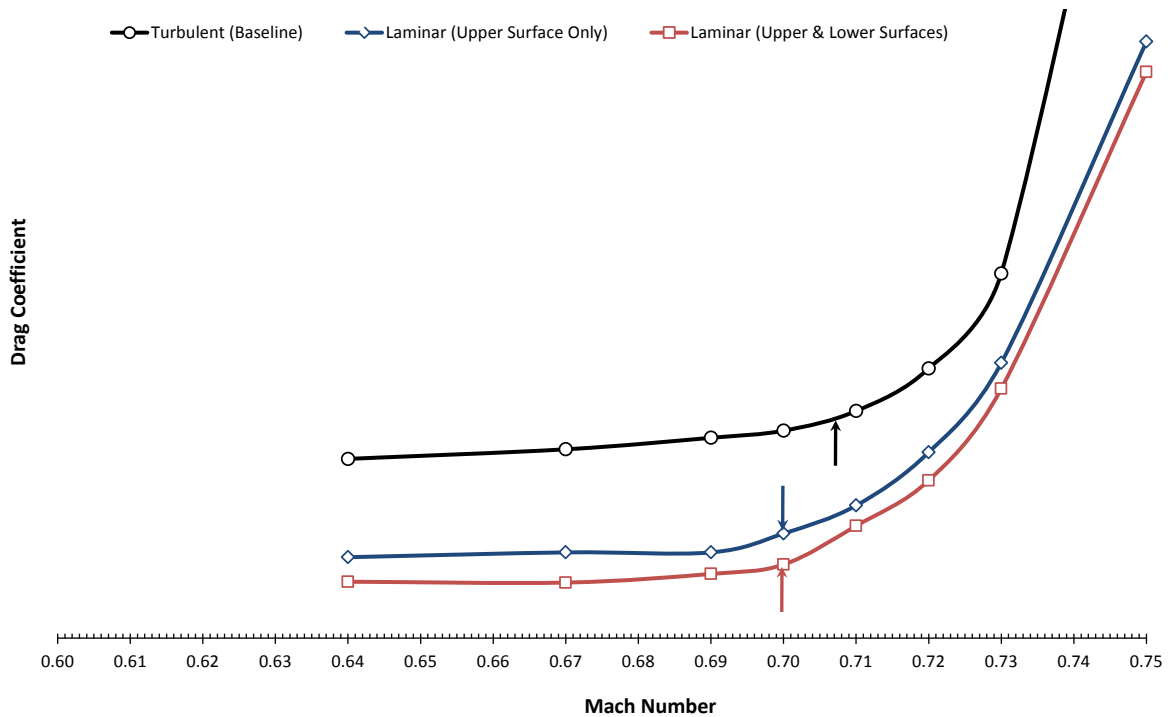


Figure 2.17 – Airfoil Drag Divergence

In parallel to calculating divergence Mach number, a Boeing proprietary process was used to estimate the lift coefficient for buffet onset at various Mach numbers. The lift coefficient was then divided by the FAA required 1.3g margin to determine the maximum operational lift coefficient for the section. The Korn factor was then calculated at both the drag divergence and the buffet limit points; the lowest Korn factor was then chosen for distribution to the university MDO team.

There are two inherent assumptions in the approach used for this task. The first assumption is that the divergence Mach number can be approximated by the Korn equation. For the purposes of this study, this assumption is reasonable. The second (and likely invalid) assumption is that the buffet boundary follows the Korn equation. If buffet boundary is used to constrain the Korn factor, the result would be overly conservative as cruise lift coefficient decreases, but would allow for wings that were all technically viable at or below cruise lift coefficient of 0.9. For this study, a buffet constrained Korn factor was used. The resulting airfoil characteristics are shown in Table 2.4.

Table 2.4 – Airfoil Characteristics

	(T1) Turbulent	(L1) Upper Surface Laminar	(L1) Both Surfaces Laminar
Thickness (%)	0.133	0.12	0.12
Camber (%)	2.3	2.3	2.3
M_{Design}	0.7	0.7	0.7
$C_{lDesign}$	0.9	0.9	0.9
M_{dd}	0.707	0.6997	0.6997
KA	0.929	0.915	0.916
Estimated $C_{lbuffer}$	1.29	1.24	1.25
Laminar Run (%)	N/A	54	54 / 40

2.1.4.3 SUGAR TBW Configuration Multi-Disciplinary Optimization

The aircraft design space was explored using the university MDO environment. The performance requirements, tool background, and trades are covered in the following sections.

SUGAR TBW Configuration and Design Requirements

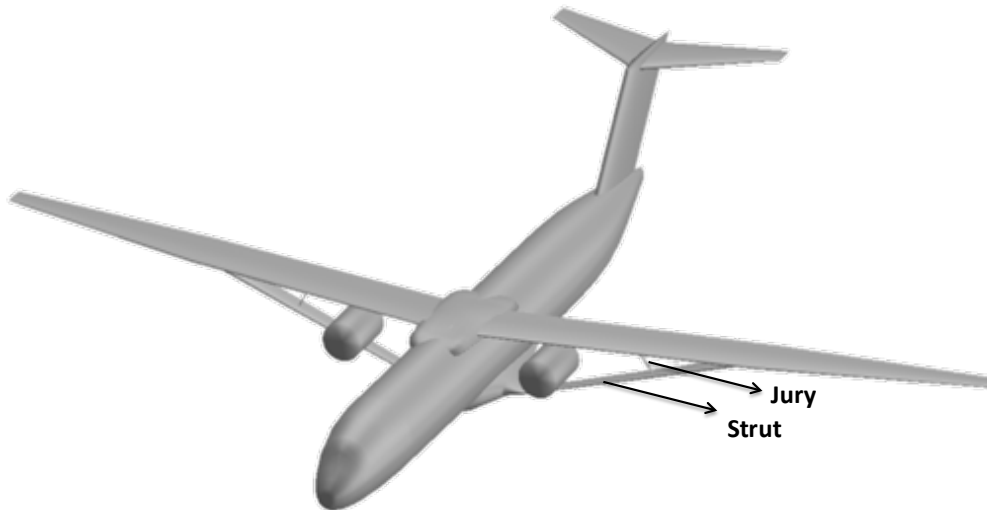


Figure 2.18 – SUGAR TBW concept

This airplane has a conventional wing-tail arrangement with a fuselage, a high wing, and a T-tail. For enhanced takeoff and low speed flight performance, slats and flaps are provided. The fuselage accommodates a mixed seat arrangement of 12 first class and 142 economy class seats. The fuselage geometry had been refined from that of the Phase I configuration by Boeing and was utilized in this MDO study. Aerodynamically shaped landing gear pods are attached under the belly of the fuselage, providing a structurally efficient integration of the strut. Two advanced high bypass ratio engines are attached under the wing.

The target payload and range capability of the TBW aircraft is depicted in Figure 2.19. The aircraft is required to fly longer than 900 nm distance carrying the maximum payload of 46,000 lbs. This maximum range at the maximum payload is labeled Pt1 in the payload range envelope, which is the intersection of the maximum zero fuel weight limit line and the MTOW limit line. With the design payload, defined as 154 passengers with 200 lbs per passenger, the aircraft must be capable of achieving at least 3,500 nm range. This maximum range at the full cabin loading is labeled Pt2 in the payload range envelope. In addition, total available onboard fuel volume must be greater than mission fuel required for Pt2 mission by 10 percent. Pt3 represents an average mission determined from the Boeing Phase I study, at which the vehicle is anticipated to operate most frequently.

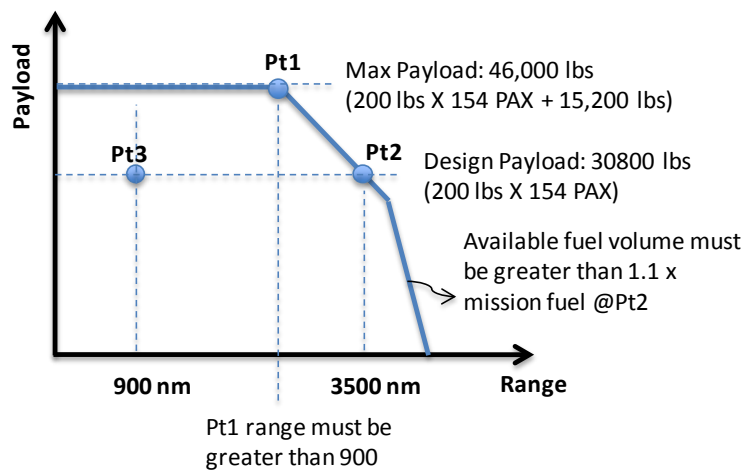


Figure 2.19 – Payload and range capabilities for SUGAR TBW aircraft

Range performance was evaluated with the N+3 mission profile utilized in Boeing SUGAR Phase I study. The reference profile is illustrated in Figure 2.20. Initially, the aircraft climbs out for minimum fuel burn with no restrictions in terms of speed and altitude, cruise-climbs at Mach 0.7, maintaining optimum altitude, and descends at maximum L/D. Reserve fuel includes 3% of trip fuel and 200 nm of a divert segment with a 10 minute hold.

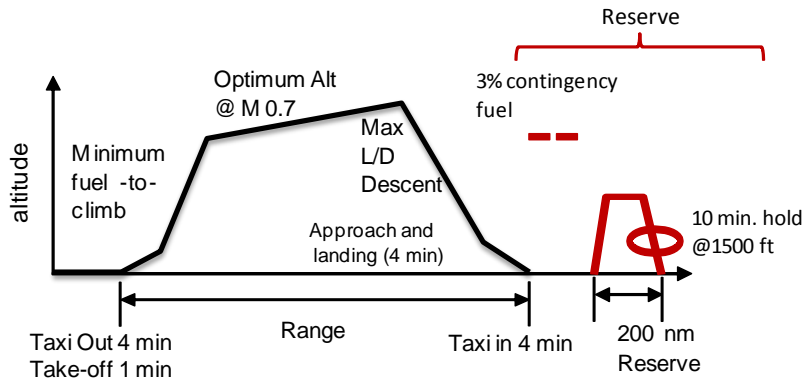


Figure 2.20 – Mission profile applied to SUGAR TBW MDO

The aircraft was optimized for minimum block fuel at the average mission (Pt3 mission), calculated with this mission profile above. Block fuel is defined as total fuel consumption from takeoff to touchdown at landing excluding taxi-in and reserve fuel in this study. The aircraft is required to meet a set of design requirements, which are listed in Table 2.5.

Table 2.5 – SUGAR TBW Design Goals

Response	Design Goal
Block Fuel of Pt3 mission	Minimize
Max range of Pt2 mission	> 3,500 (nm)
Max range of Pt1 mission	> 900 (nm)
Time to climb, 35k ft MTOW	< 30 (min.)
Distance to climb, 35k ft MTOW	< 200 (nm)
Ps at initial cruise altitude of Pt2 mission	> 300 (ft/min)
2nd segment climb excess thrust of Pt2 mission	> 0 (lbs)
Missed approach climb excess thrust of Pt2 mission	> 0 (lbs)
TOFL (ft) of Pt2 mission	< 8,190
Approach speed (knots) of Pt2 mission	< 135
Mission fuel@ design payload of Pt2 mission	< 0.9 * Available Fuel Weight (lbs)
Wing tip clearance angle at max. tail down	(>7(deg) minimum, >9 preferred)
Engine clearance to fuselage	> engine diameter (ft)
Strut/wing attachment location	< wing folding location 118/2 (ft)
Skin thickness to OML depth	< 0.4

TBW Tool and Test Configuration Description

A TBW design and analysis environment developed by Virginia Tech was adapted as the primary tool for the SUGAR MDO study. The original TBW MDAO framework was implemented in ModelCenter with a number of contributing analyses such as aerodynamic analysis and structural analysis developed to analyze TBW configurations, as well as conventional tube-wing configurations. For more details regarding the analysis modules not described in this paper,

please refer to Ref (8). In order to address design elements specific to the SUGAR configuration, as well as to improve analysis fidelity, a number of modifications were applied to the original TBW tool with Boeing support. These modifications included modules for aerodynamic analysis, structural analysis, propulsion system modeling, and tail sizing. Each of these modules is discussed in greater detail in the following sections.

Aerodynamic analysis

Aerodynamic analysis modules were updated to account for the effect of the fuselage on the airflow over the wing. An empirical equation provided by Boeing that related Mach number at wing leading edge to spanwise location along the wing was implemented. Figure 2.21 depicts variation of M-ratio, defined as ratio of wing leading edge Mach number to free stream Mach number used for this study.

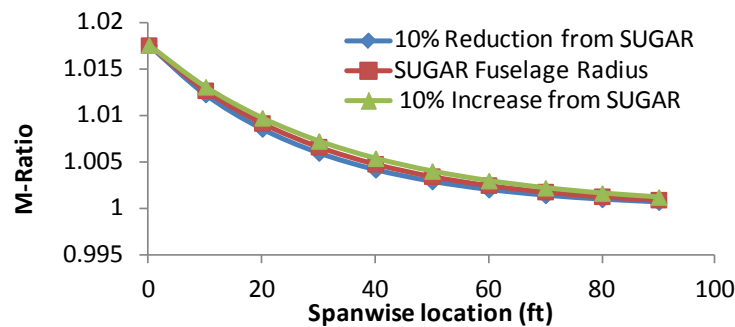


Figure 2.21 – Ratio of wing leading edge Mach number to free stream Mach number

Structure Analysis

The structural analysis module was updated to handle different boundary conditions and to enable the modeling of dynamic gust loads. Boeing had expressed significant interest in understanding the tradeoffs of using pin-joints for the strut and truss assembly. The use of pin-joints can have a favorable influence on the fabrication, assembly and maintenance of the truss structure. The sizing of such a structure required the ability to model the joints between wing and truss members using pin-joints or ball-joints. Pin-joints allow the transmission of all force components and all moment components except the one along the axis of the pin. Ball joints allow the transmission of all force components without any moment transfer. The code was modified so that a simple flag in the input deck could be changed to select one of the three conditions at each connection: rigid joint, pin-joint and ball-joint. A similar flag for the boundary condition on the wing and strut allowed the selection between fixed and pinned boundary condition.

The structural sizing code developed at Virginia Tech used quasi-steady load definitions. In other words, the influence of a dynamic gust on stress levels could not be taken into account. Boeing considered this to be an important effect for the design studies, and suggested that in order to include the influence of dynamic gust in a quasi-steady load definition, an additional scaling

factor be used for the loads from the wing-strut joint to the wing tip. The scaling was defined to be linear from 1.0 at the wing-strut intersection, to $(1.0+x)$ at the wing tip, where 'x' is a factor defined by Boeing. The structural sizing code was modified to include this scaling influence. The wing structure analyses were conducted based on advanced material properties provided by Boeing.

Propulsion System Model

The propulsion module was revised based on gFan+ engine data supplied from GE. This module was used for the configuration analysis and optimization. Thereafter, one configuration was down-selected and the effect of cruise Mach number was analyzed. For this purpose, Georgia Tech developed engine decks for each Mach number considered, in addition to using the gFan+ engine data from General Electric.

Tail Sizing

A new tail sizing module was incorporated into the MDO environment. The analysis commences with repositioning the wing to align 25% MAC with a target longitudinal location provided by Boeing for a proper static margin. The horizontal tail and vertical tail areas are calculated based on a surrogate model derived from a dataset generated by Boeing using a proprietary tool. The estimates required tail volume coefficients for a number of input parameters such as wing span, fuselage length, spanwise engine location, CG excursions due to fuel burn and payload, and length of tail moment arms. Once tail areas are calculated, the vertical tail location is adjusted such that the aft spar of the horizontal tail connects to a fuselage frame at a specific location. Subsequently, the horizontal tail is relocated such that the aft spars of the horizontal tail are aligned with the aft spar of the vertical tail. Since this adjustment changes length of tail moment arms, the process iterates until it converges.

In addition to those major disciplinary codes, the TBW MDO environment evolved through incorporation of numerous minor enhancements such as wing tip clearance angle analysis, the inclusion of engine location as a design variable, and automated wing repositioning to align 25% MAC to a target longitudinal location. The weight analysis module was updated to estimate changes in aircraft center of gravity due to fuel burn, required for the tail sizing module. While the design environment featured numerous modifications to improve its fidelity, there were several areas in which additional improvement is particularly desirable. In particular, the landing gear pod drag estimation featured lower fidelity than other parts of the environment, and no analysis of flutter was included in the MDO framework. These areas of deficiency are expected to be assessed in detail in subsequent tasks as part of higher fidelity analyses and tests conducted by Boeing.

In order to support tool development, the team developed a set of test configurations as test beds. Those test configurations have been matured along with tool enhancement as depicted in Figure 2.22.

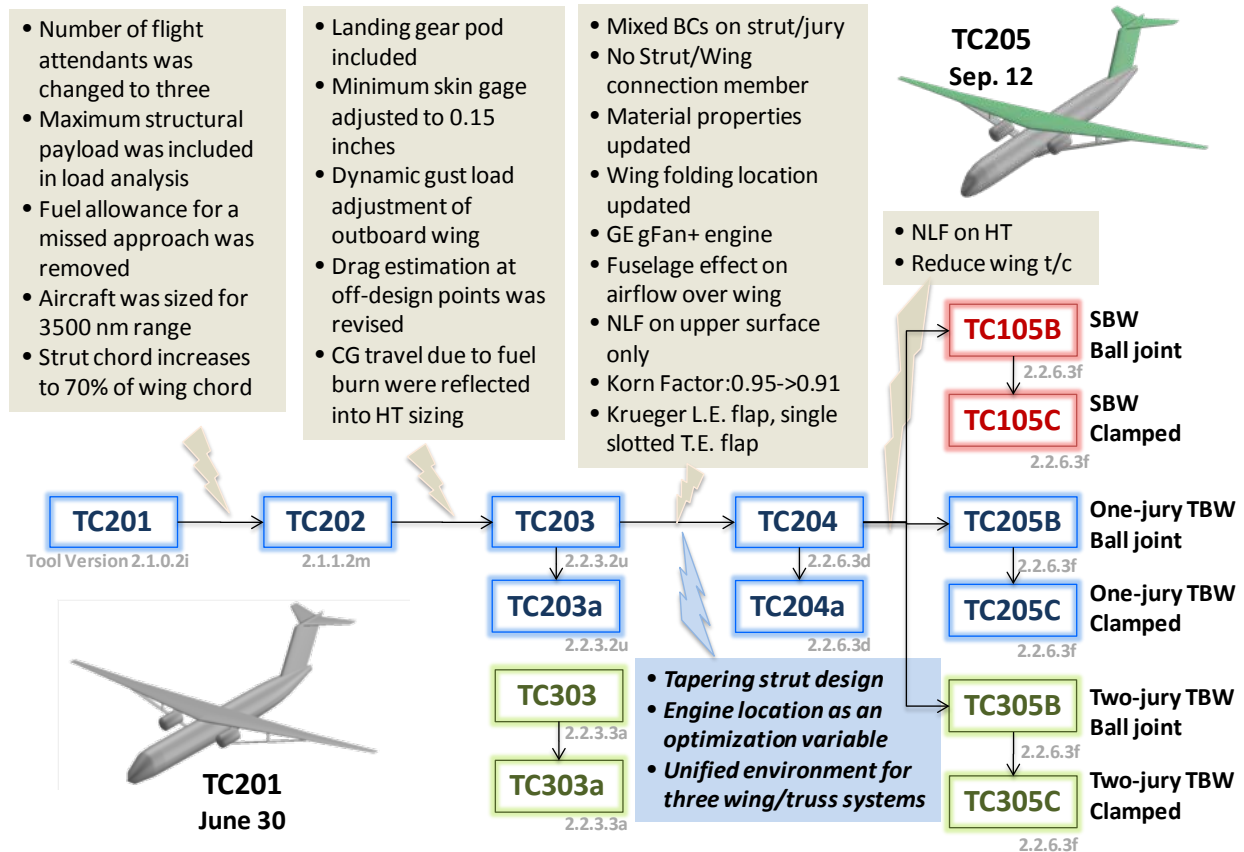


Figure 2.22 – Test Configuration and Tool Evolution

SUGAR MDO Approach

Compared with a conventional cantilever wing configuration, the TBW configuration has a significantly larger design space, because of myriads of possible truss system designs. In addition, wing natural laminar flow (NLF) design options add another dimension into the already complicated design space. The overwhelming scope of the TBW MDO is managed with a staged approach illustrated in Figure 2.23. The Stage 1 study is aimed at identifying the most suitable TBW architecture among three candidates:

- C100 Series: Also referred to as strut braced wing (SBW), this configuration has only a strut per side to support the main wing
- C200 Series: Also referred to as One-Jury TBW, this configuration has a strut and a jury connecting the strut and the main wing per side
- C300 Series: Also referred to as Two-Jury TBW, this configuration has a strut and two juries connecting the strut and the main wing per side

For each candidate, two different boundary conditions for the truss structures were investigated. For the first condition, one end of the strut and jury members was considered to be ball-jointed and the other end clamped (rigidly joined). For the second condition, both ends were considered to be clamped (rigid joint)

The Stage 2 study is aimed at investigating alternative natural laminar flow options in conjunction with high lifting system options based on the best TBW architecture selected from Stage 1.

The Stage 3 study is aimed at refining a TBW configuration selected from Stage 2 from the air-vehicle integration point of view through an iterative, experienced human-in-the-loop process, leading up to a final configuration for subsequent research activities including detailed OML lofting and higher fidelity analyses and tests, which will be conducted by Boeing.

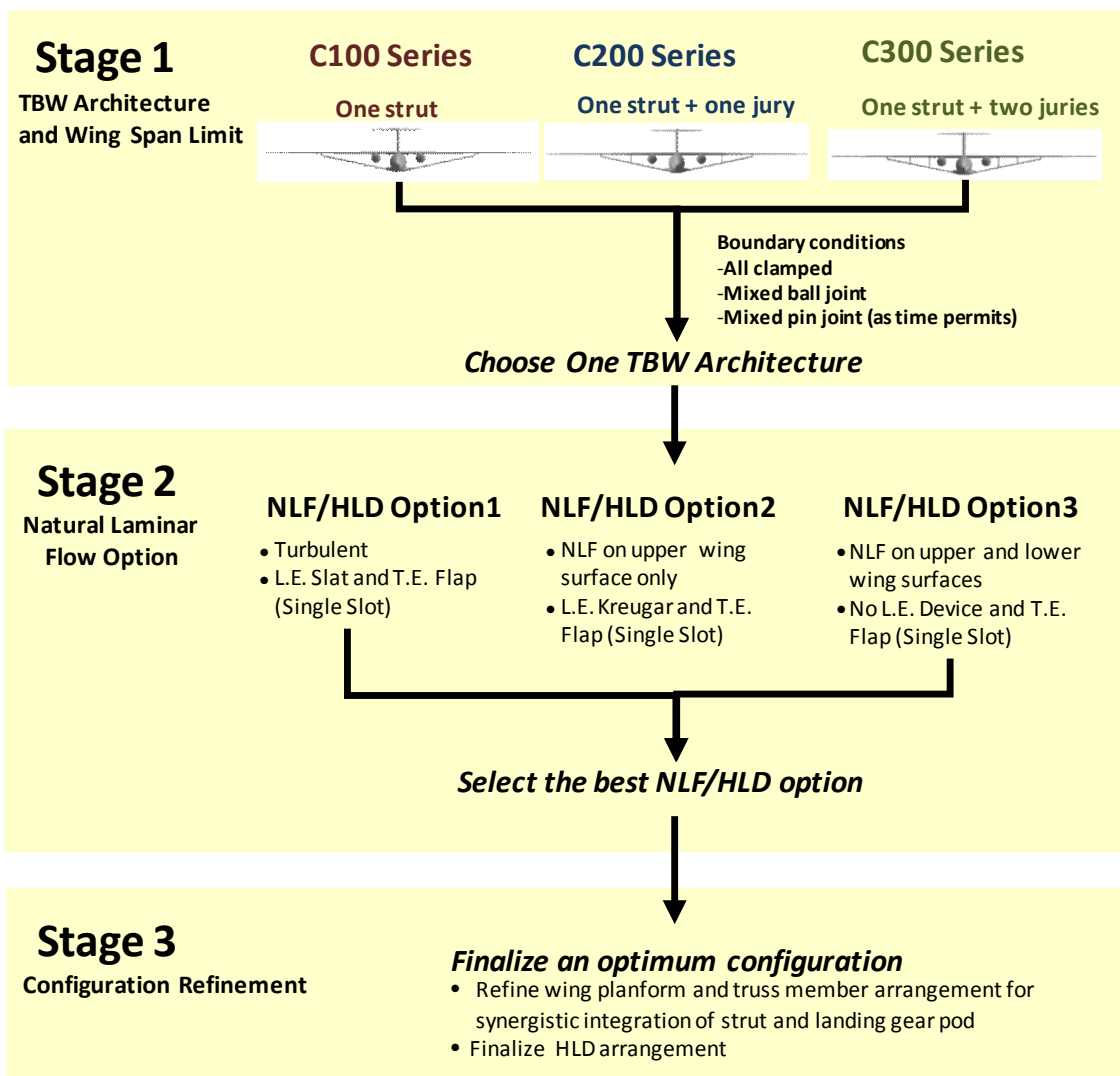


Figure 2.23 – SUGAR MDO approach

The optimization process was commenced from a “baseline” or “test” configuration satisfying most (but not necessarily all) of the constraints of the optimization problem. From this test configuration, two parallel branches of optimization were simultaneously begun. The first branch, shown on the left in Figure 2.24, exclusively utilized Design Explorer as the optimization tool. A suitably wide range was allowed for each design variable so as to provide a sufficiently broad design space for the optimizer to operate in. This is shown by the dotted black line in the left column of Figure 2.24. The results from this optimization run were then analyzed for optimality (with respect to minimization of the objective function) and feasibility (with respect to satisfying of all problem constraints). In particular, the obtained solution was checked for design variables, which may have finished at either their respective upper or lower bounds. In this case, the solution lay on at least one face of the hypercube representing the allowable design space. In case of such an occurrence, the design variable bounds for the concerned variables were adjusted, following which a subsequent optimization run was commenced. This procedure was continued until a solution was obtained for which infringement on the design variable bounds was either eliminated or minimized. Mathematically, such a solution represents at least a local optimum, i.e. there exists a finite design space neighborhood in the vicinity of the solution where the objective function value is higher than that for the solution. The run-time for Design Explorer is strongly related to the number of design variables being considered for the optimization. The MDO analyses carried out at Georgia Tech considered strut-braced wing (SBW), truss-braced wing (TBW) with one jury support, and truss-braced wing (TBW) with two jury supports, featuring a progressively increasing number of design variables that were necessary to define the more complicated geometry involved. Typical Design Explorer run-times recorded for a single MDO were in the range of 2-3 days.

The second branch of the optimization, shown on the right in Figure 2.24, utilized Darwin as the optimization tool. Darwin utilizes genetic algorithm based optimization, and is better suited for multi-modal design spaces. However, Darwin has a significantly longer run-time than Design Explorer (run-times of the order of days were not uncommon), and hence the second branch uses Darwin only as its first step. The “top” solutions obtained from using Darwin were used as starting points for subsequent optimization searches using Design Explorer, as shown in the figure.

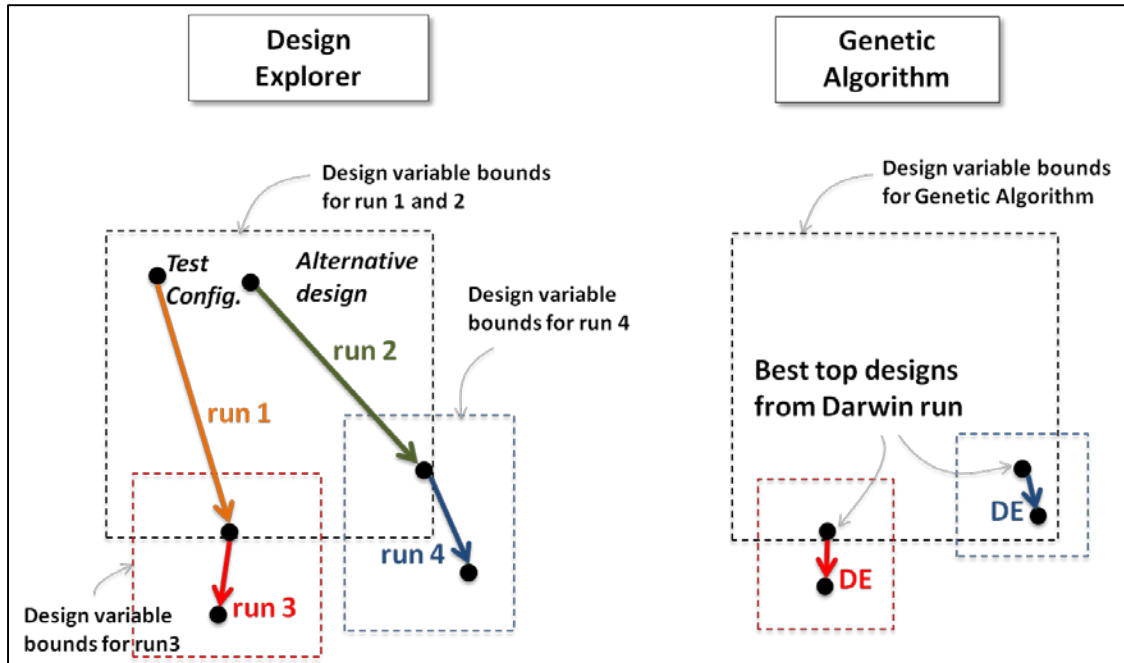


Figure 2.24 – Optimization approach for MDO study

It should also be mentioned that in the initial stages of the MDO study, the sensitivities of the responses to certain initially selected design variables were analyzed. If the effect of a design variable on system level responses was found to be insufficient to warrant further consideration, the design variable was dropped from subsequent optimizations, which thus featured a reduced dimensionality of the design space. For example, at the initial stages of the study, the sweep angles of the inboard and outboard sections of the wing were considered separately. However, a sensitivity analysis showed that the effect of the outboard wing sweep angle on the system metrics was negligibly small. As a result, the outboard wing section sweep angle was set to equal the inboard wing section sweep angle, with only the latter being retained as an active design variable. The design variables utilized in this MDO study are listed in Table 2.6.

Table 2.6 – SUGAR TBW MDO Design Variables

Group	Variables	Definition	C100	C200	C300
Wing	Sw	Wing reference area	X	X	X
	TR_inbd	Taper ratio of the inboard section	X	X	X
	TR_outbd	Taper ratio of the outboard section	X	X	X
	AR	Aspect ratio	X	X	X
	TOC_r	Wing thickness to Chord at the root	X	X	X
	TOC_b	Wing thickness to Chord at the break	X	X	X
	TOC_t	Wing thickness to Chord at the tip	X	X	X
	Eta	Wing break location in percent span	X	X	X
	Lambda_inbd	Wing 0.25 chord sweep of the inboard wing section	X	X	X
	Lambda_outbd	Wing 0.25 chord sweep of the outboard wing section	X	X	X
	Strut	CR_r_strut	Strut chord at the root as a fraction of wing chord at the planform break	X	X
CR_j1_strut		Strut chord at jury 1 intersection as a fraction of wing chord at the planform break		X	X
CR_j2_strut		Strut chord at jury 2 intersection as a fraction of wing chord at the planform break			X
CR_b_strut		Strut chord at the tip intersection as a fraction of wing chord at the planform break	X	X	X
TOC_r_strut		Strut thickness to chord at the root	X	X	X
TOC_j1_strut		Strut thickness to chord at jury 1 intersection		X	X
TOC_j2_strut		Strut thickness to chord at jury 2 intersection			X
TOC_b_strut		Strut Thickness to chord at the tip	X	X	X
Jury	CR_jury_1	Jury 1 chord as a fraction of strut chord at Jury1/Strut intersection		X	X
	CR_jury_2	Jury 2 chord as a fraction of strut chord at Jury2/Strut intersection			X
	TOC_jury_1	Thickness to chord ratio of jury 1		X	X
	TOC_jury_2	Thickness to chord ratio of jury 2			X
	eta_jury_1_strut	Ratio of position of jury 1 on strut to wing junction (wing break), 0 at centerline, 1 at wing break		X	X
	eta_jury_2_strut	Ratio of position of jury 2 on strut to wing junction (wing break), 0 at centerline, 1 at wing break			X
	eta_jury_1_wing	Ratio of position of jury 1 on wing to wing break, 0 at centerline, 1 at wing break eta		X	X
	eta_jury_2_wing	Ratio of position of jury 2 on wing to wing break, 0 at centerline, 1 at wing break eta			X
Prop.	dMaxRequiredThrust	Max thrust at SLS per an engine	X	X	X
	Yeng	Spanwise engine location / wing semi-span	X	X	X
	DesignRange	Pt2 mission range	X	X	X

Results and Observations

Stage 1: Down Selection of TBW Architecture

A preliminary MDO study indicated that optimum designs are commonly featured with extremely slender wings, confirming that TBW configuration offers a sizable aerodynamic efficiency improvement through a significant increase in wing aspect ratio. An optimization process may drive a design to an extreme to gain a minuscule, additional improvement in the objective function incurring significant penalties or potential technical issues in other design criteria. For instance, a long and slender wing may reduce the number of serviceable airports, and it may also become more vulnerable to aeroelastic instability. Therefore, the dominance of very high AR wing designs warrants the need for investigating the sensitivity of fuel burn with respect to wing span.

To this end, three TBW architectures are optimized for different span limits, and the results are summarized in Figure 2.25. Comparison of the optimum configurations led to a few observations:

- For a given wing span, adding a jury leads to a higher AR, less swept, and smaller wing requiring a higher engine thrust, which results in a higher wing loading and a higher thrust-to-weight ratio.
- A larger span allows a higher optimum wing aspect ratio, which is well expected.

In addition to the span constraint, the take-off field length and maximum range of Pt1 appeared to be the active constraints for all optimum designs. The available fuel volume and the maximum range of Pt2 constraints also became active for a few cases.

Total wing and truss weights of the optimum TBW configurations are compared in Figure 2.26, which clearly indicates that a longer span (or higher aspect ratio) wing is heavier. For the same wing span limit, it is evident that adding a jury leads to a lighter wing. However, the two jury TBW configuration provides only a marginal benefit in wing weight reduction relative to one jury TBW. Aerodynamic efficiency generally improves as the span constraint is relaxed as shown in Figure 2.27, which compares lift-to-drag ratio at a representative cruise condition. Adding a jury increases drag, resulting in degradation in aerodynamic efficiency for most cases. Such drag penalties are found to be substantial for a two jury TBW, outweighing the weight benefit. Maximum Take-off weight (MTOW) is compared in Figure 2.28. Overall, MTOW increases as the wing span constraint is relaxed.

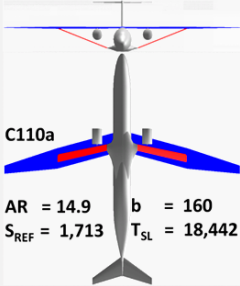
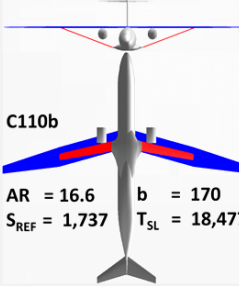
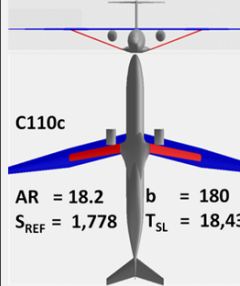
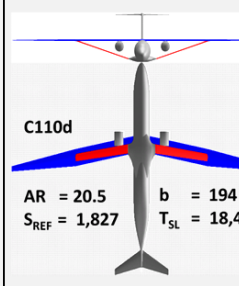
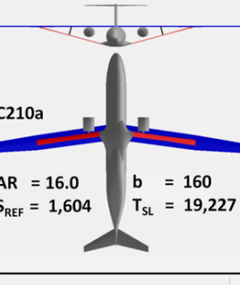
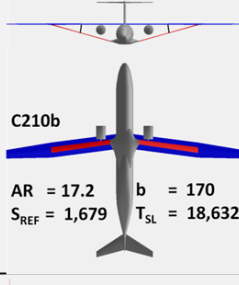
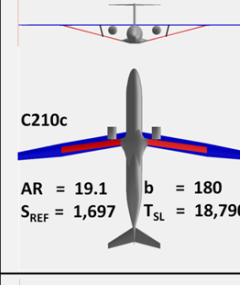
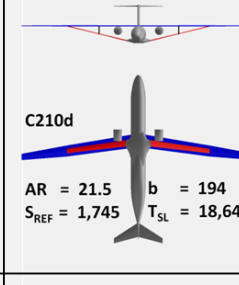
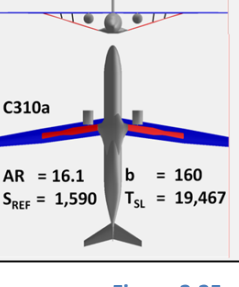
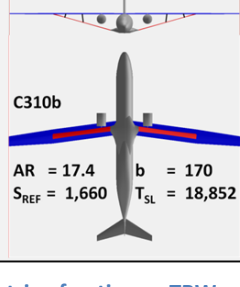
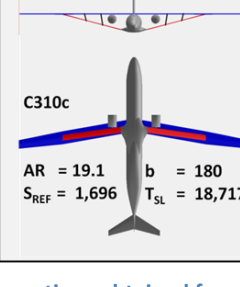
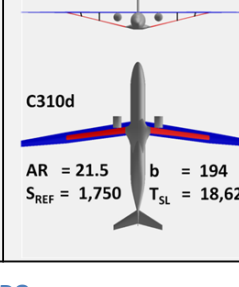
	b < 160	b < 170	b < 180	unconstrained
C100 (SBW)	 <p>C110a AR = 14.9 b = 160 S_{REF} = 1,713 T_{SL} = 18,442</p>	 <p>C110b AR = 16.6 b = 170 S_{REF} = 1,737 T_{SL} = 18,477</p>	 <p>C110c AR = 18.2 b = 180 S_{REF} = 1,778 T_{SL} = 18,430</p>	 <p>C110d AR = 20.5 b = 194 S_{REF} = 1,827 T_{SL} = 18,477</p>
C200 (1-jury)	 <p>C210a AR = 16.0 b = 160 S_{REF} = 1,604 T_{SL} = 19,227</p>	 <p>C210b AR = 17.2 b = 170 S_{REF} = 1,679 T_{SL} = 18,632</p>	 <p>C210c AR = 19.1 b = 180 S_{REF} = 1,697 T_{SL} = 18,790</p>	 <p>C210d AR = 21.5 b = 194 S_{REF} = 1,745 T_{SL} = 18,641</p>
C300 (2-jury)	 <p>C310a AR = 16.1 b = 160 S_{REF} = 1,590 T_{SL} = 19,467</p>	 <p>C310b AR = 17.4 b = 170 S_{REF} = 1,660 T_{SL} = 18,852</p>	 <p>C310c AR = 19.1 b = 180 S_{REF} = 1,696 T_{SL} = 18,717</p>	 <p>C310d AR = 21.5 b = 194 S_{REF} = 1,750 T_{SL} = 18,621</p>

Figure 2.25 – Matrix of optimum TBW configurations obtained from MDO

The one-jury TBW appeared to be the architecture that offers the best fuel efficiency for the SUGAR mission throughout all span limits investigated in this study as shown in Figure 2.29. Overall, relaxation of the span constraint results in higher fuel efficiency. However, the benefit quickly diminishes after the span reaches 170 ft, offering less than 1.4% fuel burn improvement for any further increase in wing span. Therefore, a one-jury TBW with 170 ft span, designated as C210b, was selected as a baseline for the Stage 2 MDO study that is aimed at investigating the effect of alternative natural laminar flow options.

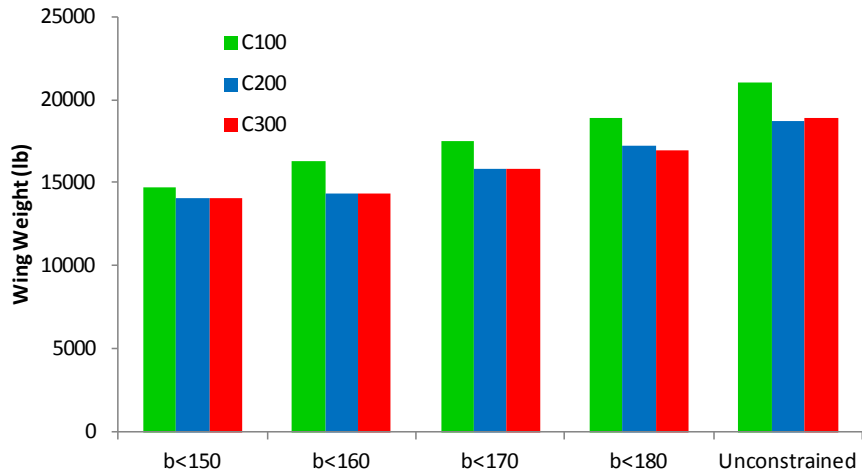


Figure 2.26 – Comparison of total wing truss system weight

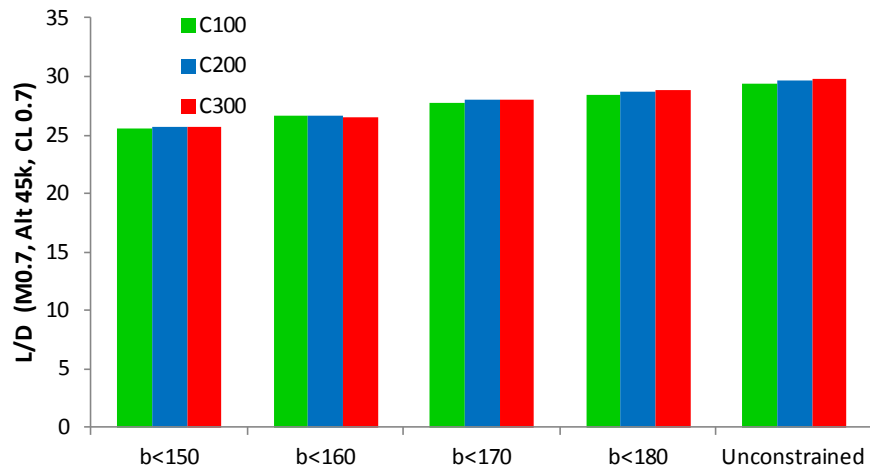


Figure 2.27 – Comparison of lift-to-drag ratio

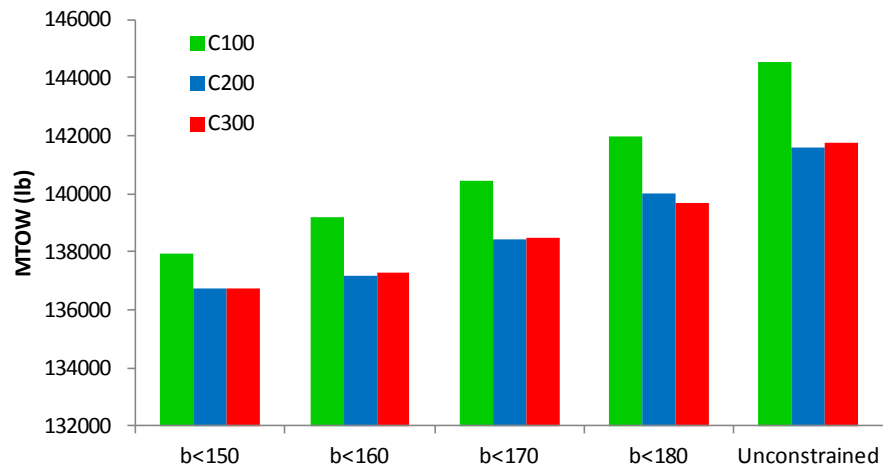


Figure 2.28 – Comparison of maximum take-off weight

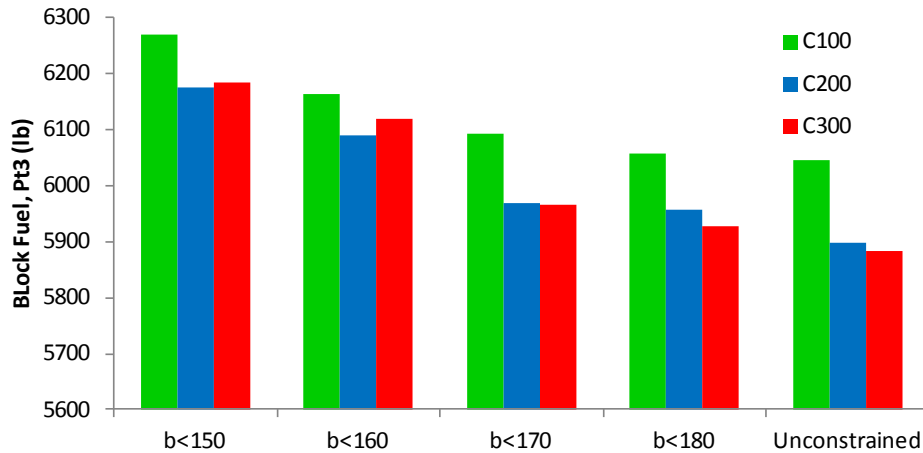


Figure 2.29 – Comparison of block fuel weight

Stage 2: Down-selection of NLF Option

The MDO study also analyzed the effect of natural laminar flow (NLF) on the aircraft metrics of interest and objective function (block fuel for Pt3 mission). The NLF analysis was performed in conjunction with an analysis of various high-lift device (HLD) options. The NLF-HLD configurations of interest are described in Table 2.7.

Table 2.7 – SUGAR MDO NLF Options and Associated HLD System

	Wing NLF Option	HLD	Korn Factor
C210	NLF on upper surface only	L.E. Kruegar + T.E. Flap (Single Slot) Clmax : 1.80/2.40 (TO/LD)	0.91
C211	Turbulent	L.E. Slat + T.E. Flap (Single Slot) Clmax : 1.96/2.90 (TO/LD)	0.925
C212	NLF on upper and lower surfaces	No L.E. Device + T.E. Flap (Single Slot) Clmax : 1.62/1.96 (TO/LD)	0.91

During the Stage 1 study, low speed performance metrics including take-off and landing field length, approach speed, and second segment climb rate were calculated with a simple empirical method embedded in FLOPS, which does not require detailed low speed aerodynamic data. The Stage 2 study employed the more detailed field performance analysis method available in FLOPS in order to more accurately propagate the effect of HLD options to aircraft field performance. Low speed aerodynamics for the HLD options were predicted offline through the use of a higher fidelity aerodynamics tool, and the resulting low speed drag polars and lift coefficient vs. angle of attack (CL vs. α) curves were incorporated into the TBW tool.

As shown in Table 2.7, the first configuration, the C210 series, featured natural laminar flow only on the upper surface of the wing. In addition, it is equipped with a leading-edge Krueger flap and a single-slot trailing-edge flap as high-lift devices. The second configuration, the C211 series,

featured fully turbulent flow over both the upper and lower surfaces of the wing. For this configuration, a leading-edge slat and a single-slot trailing-edge flap were considered as high-lift devices. Finally, the third configuration, the C212 series, featured NLF on both the upper and lower surfaces of the wing. No leading-edge high-lift device was considered, and this configuration featured only a single-slot trailing-edge flap. The different HLD options give different maximum lift coefficient values for the aircraft that affect only its takeoff and landing performance, respectively through takeoff field length (TOFL) and landing approach speed (VAPP). The NLF condition affects the cruise performance, through the variation of skin friction drag, and thus has an effect on the objective function (block fuel). Additionally, the extent of NLF, given by the location of transition from laminar to turbulent flow in percentage of wing chord was also varied during the analysis. Optimum configurations obtained for three NLF options are shown in Figure 2.30.

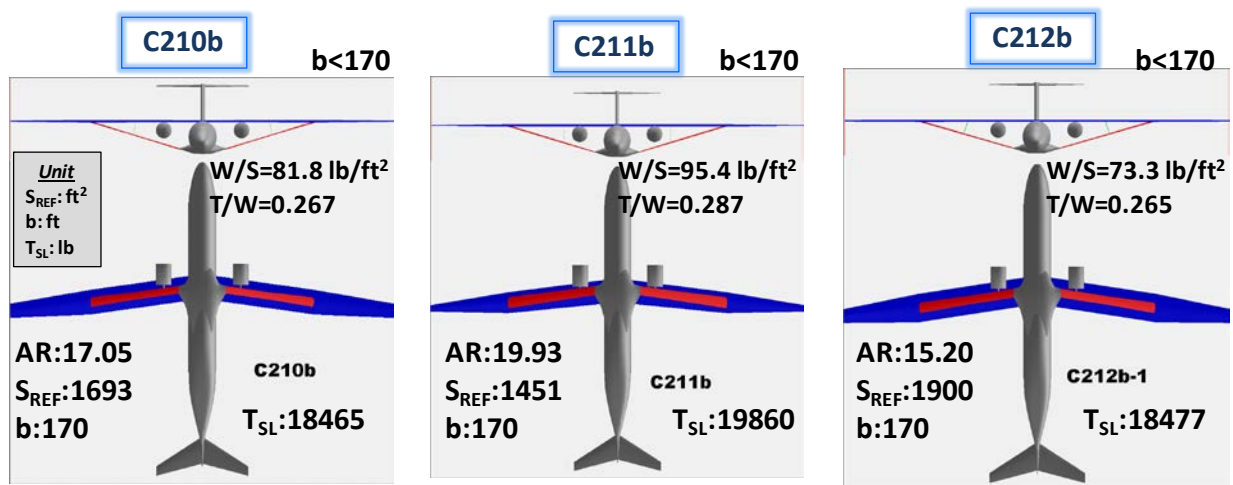


Figure 2.30 – Optimum TBW configurations obtained for different NLF options

Figure 2.31 shows a comparison of the aerodynamic efficiencies of the optimized designs for each category. The lift-to-drag (L/D) ratio, used as a measure of the aerodynamic efficiency, was evaluated at 45,000 ft, Mach 0.70 and a lift coefficient of 0.70. Owing to the reduction in skin friction drag, the C212 configuration (NLF on both upper and lower surface) has the best aerodynamic efficiency, while the 211 configuration (fully turbulent flow) has the lowest. Within the same configuration, the aerodynamic efficiency is seen to be higher when the span constraint is relaxed to 180 ft as compared to 170 ft. This is expected, since the higher span limit allows for a higher aspect ratio that results in improved aerodynamic efficiency. Within the C210 and C212 series, it is also seen that the aerodynamic efficiency is positively related to the extent of NLF, with a delayed transition to turbulent flow allowing for higher efficiencies.

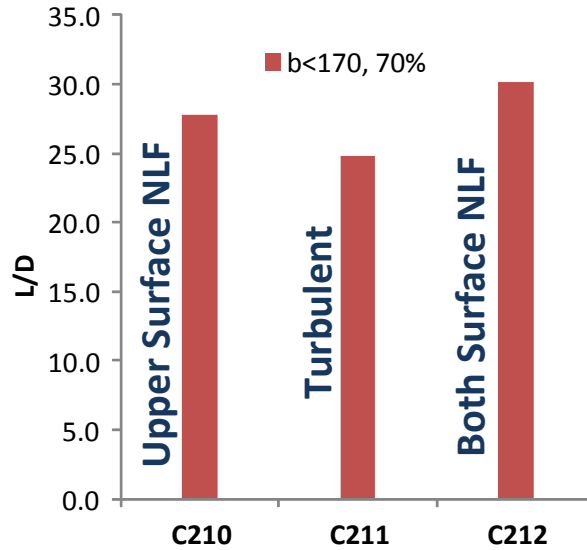


Figure 2.31 – Aerodynamic efficiency of NLF configurations

Figure 2.32 shows the block fuel of the Pt3 (900 nmi) mission for the three configurations. Among the three NLF configurations, the C212 series has the best block fuel performance on account of the largest reduction in skin friction drag owing to natural laminar flow on both upper and lower wing surfaces. For the same reason, the C211 series (all turbulent flow) suffers the most significant block fuel penalty. For the C211 series (all turbulent flow), the block fuel performance is seen to improve when the wing-span constraint is relaxed from 170 ft to 180 ft. Further, within the C210 and C212 series, the block fuel performance is improved as the allowable extent of NLF (prior to transition to turbulent flow) is increased.

It was found that the take-off field length constraint is one of the main drivers for the C210 series (NLF on wing upper surface) and the C212 series (NLF on both upper and lower surface), rendering significantly low wing loadings as depicted in Figure 2.30. C212b wing loading is as low as 73 lb/ft². C210b wing loading is slightly higher but only 82 lb/ft². The C212 series outfitted with a trailing edge flap only is found to have only little room to improve take-off maximum lift coefficient. The C210 series were re-examined with hypothetical improvements to take-off maximum lift coefficient.

The investigation indicates that the C210 series (NLF on wing upper surface) can be as fuel efficient as C212 series (NLF on both upper and lower surface) if maximum lift coefficient of 2.2 is achieved as illustrated in Figure 2.33. A subsequent study on low speed aerodynamics confirmed that maximum lift coefficient of 2.2 is achievable by increasing the flap area and take-off flap deflection angle while maintaining a sufficient margin for the second segment climb performance requirement as depicted in Figure 2.34. Based on Stage 1 and 2 studies, the NLF on wing upper surface option with a 170 ft wing span and take off $C_{L_{max}}$ of 2.2, labeled as C210b2.2, was selected as the baseline for further refinement.

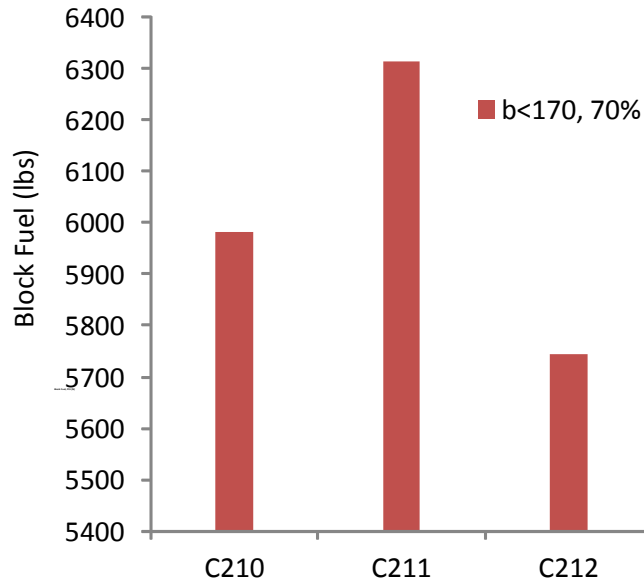


Figure 2.32 – Pt3 block fuel for NLF configurations

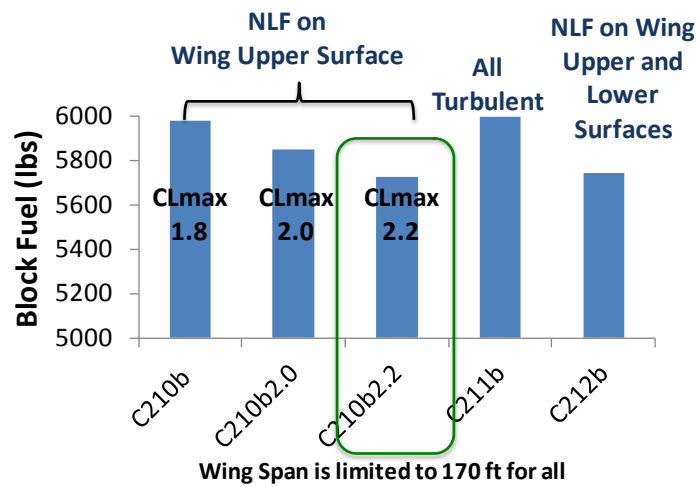


Figure 2.33 – Block fuel improvement of C210 series by increasing maximum lift coefficient

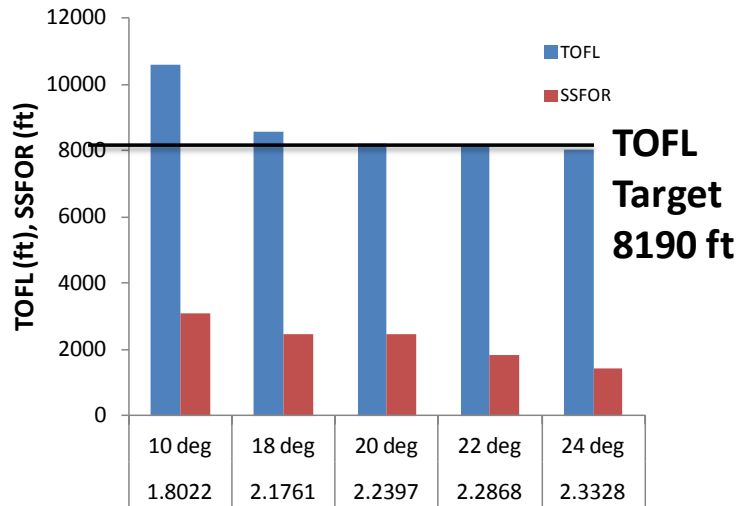


Figure 2.34 – TOFL and second segment climb excess thrust for varying flap deflection angles

Stage 3: Refinement of Down-selected Configuration

C210b2.2 has been further refined addressing potential air-vehicle integration issues, which could not be fully assessed within the MDO framework. First, high lift device arrangement was adjusted to extend the leading edge flap to the tip of the wing. With a revised low speed polar, C201b2.2 was re-optimized while wing area and aspect ratio were fixed. Subsequently, Boeing conducted a preliminary OML and wing structure integration study, and finalized wing sweep and taper ratio of the inboard and outboard wing sections. And finally, wing anhedral angle was set to 1.5 deg to ensure appropriate stability characteristics of the aircraft, and the rest of the still active design variables were re-optimized, which formed the final TBW configuration (C401c) from the MDO study. Since this refinement was applied to a limited subset of the design space, changes in Pt3 mission block fuel during the process were found to be inconsequential as shown in Figure 2.36.

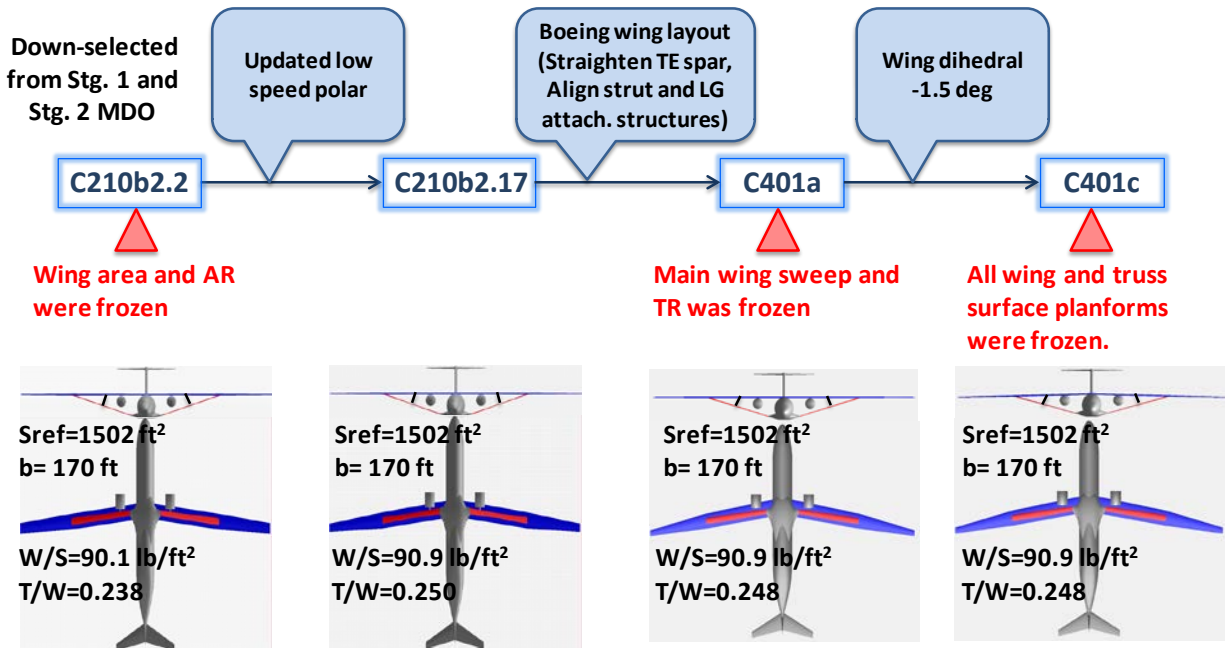


Figure 2.35 – Configuration refinement overview

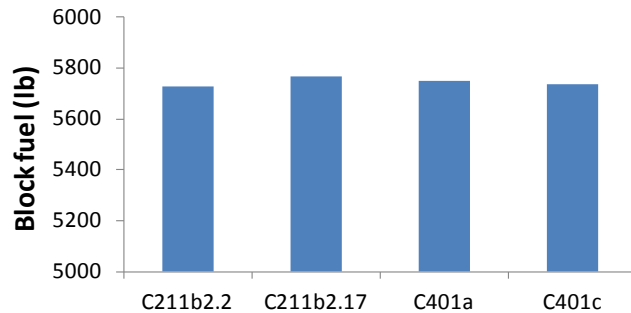


Figure 2.36 – Changes in Pt3 Mission block fuel during Stage 3

Cruise Speed Sensitivity Study

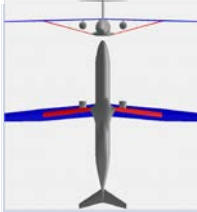
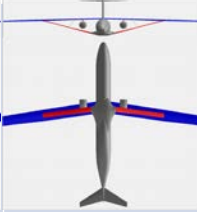
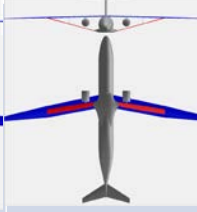
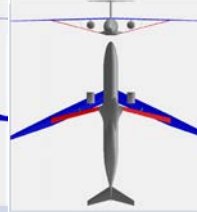
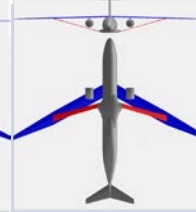
The effect of the cruise Mach number was investigated in conjunction with the impact on aircraft cost. Prior to this, all optimizations had been performed at a default cruise Mach number of 0.70. For this analysis however, the environment was modified slightly to allow for aerodynamic lookup tables to be generated for varying cruise Mach numbers.

The effect of cruise Mach number on the block fuel performance of an optimized TBW-aircraft was analyzed across the Mach number range 0.60 – 0.80 (in increments of 0.05), which is the range in which configurations of this nature may be expected to operate. Also, for each Mach number, a custom engine deck was generated using a nonproprietary version of NPSS gFan+ engine model, which Georgia Tech developed to closely represent GE gFan+ model based on public domain data (1). Georgia Tech gFan+ engines were designed for alternate cruise speeds as follows:

- Aerodynamic design point Bypass Ratio was held constant at 13
- Engine sizing points and conditions were held constant except for cruise Mach and altitude
- Design point Fan Pressure Ratio (FPR), Low Pressure Compressor Pressure Ratio (LPCPR), were adjusted to optimize propulsive efficiency for alternate cruise Mach by adjusting OPR to account for lower/higher total temperature at lower/higher cruise Mach number
- Sizing the engine for lower cruise Mach numbers, allowing for higher cruise OPR, yielding some TSFC reduction in addition to benefits from reduced flight speed

For each Mach number, the Pt3 mission block fuel was set as the objective function for the optimizer, and the geometric and performance constraints outlined in Table 2.5 were applied to this study as before. ModelCenter’s Design Explorer optimizer was then used to carry out the optimization. The optimum designs for alternate cruise speed were summarized in Table 2.8.

Table 2.8 – Summary of optimum designs for alternate cruise speeds

	M60-GT	M65-GT	M70-GE (C401c)	M75-GT	M80-GT
					
Wing area (sq.ft.)	1,598	1,620	1,502	1,453	1,533
Taper ratio	0.98/0.68	0.95/0.83	0.89/0.39	0.83/0.38	0.99/0.30
AR	17.63	17.87	19.24	19.88	17.15
TOC (%)	8.00/11.54/11.21	8.75/11.75/11.82	8.00/10.45/9.46	9.61/10.38/8.56	8.54/9.15/8.41
Wing sweep (deg)	5	8.5	11.5	24.9	28.8
Max. Thrust (lb)	15,218	15,150	16,716	18,168	18,459
MTOW (lb)	134,722	135,224	136,443	140,083	141,779
Wing Weight (lb)	14,796.7	15,243.8	15,532.2	18,281.5	18,617.1
Block fuel, Pt. 3 (lb)	5,478.4	5,531.6	5,740.4	5,843.3	6,159.5
T / W	0.226	0.224	0.254	0.259	0.260
W / S (lb/sq.ft.)	84.31	83.47	90.84	96.41	92.48
L / D	28.28	27.04	27.29	25.30	21.84
TSFC (1/hr)	0.41365	0.42755	0.46850	0.47208	0.49440

Certain trends in the design variables were evident from the optimized designs. As expected, the wing sweep increases progressively with increase of Mach number. In addition, for the higher Mach numbers, the outboard section of the wing is more tapered and has a lower thickness-to-

chord ratio. As expected, for the higher Mach numbers, the thrust requirement is higher, and there is a monotonic reduction in the cruise L/D. On account of the monotonic increase in aircraft gross weight coupled with a much smaller variation in wing planform area, the higher Mach number designs also have a slightly higher wing loading.

For each of the designs shown in Table 2.8, all of the constraints were satisfied, and there were minor variations in the actual constraint values.

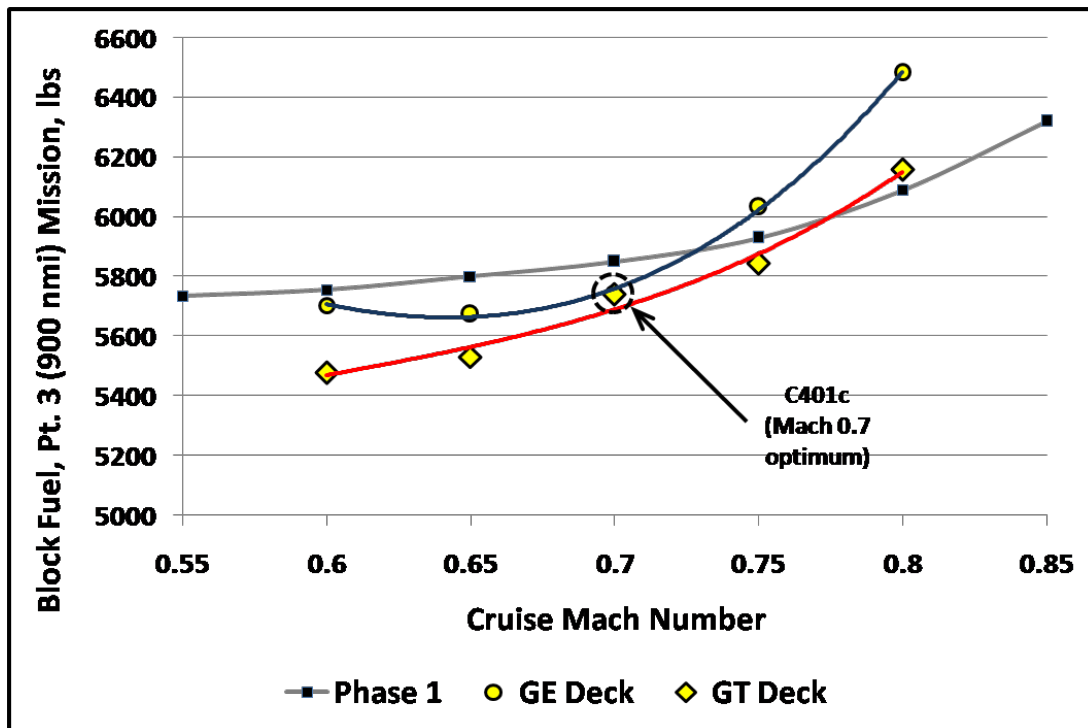


Figure 2.37 – Effect of cruise Mach number of Pt. 3 mission fuel burn

In addition to an analysis of the variation of aircraft geometry with increasing cruise Mach number, a key observation of this work was the variation in the Pt. 3 mission block fuel, which is shown in Figure 2.37. The gray curve represents the results obtained from the Boeing SUGAR Phase 1 Report (1), and these are included here for comparison purposes.

The optimal designs denoted by the blue curve represent designs that all use the GE gFan+ engine deck (for Mach 0.70). Since the cruise Mach number range is from 0.60 – 0.80, for all but one of the designs (i.e. Mach 0.70), the engine deck represents an off-design operating point for the engine. The resulting penalty in block fuel performance is clear from the shape of the blue curve below and above the design operating Mach number of Mach 0.70.

The red curve denotes optimal designs obtained using custom GT engine decks for each relevant Mach number of interest. In other words, each airplane is optimized with an engine model

designed for cruise operation at the corresponding Mach number. The results obtained clearly show an increasing trend in block fuel as the cruise Mach number is increased.

It should be noted that the previously obtained C401c design (within dotted circle) is the design point that is common to both the curves, since the gFan+ engine is optimized for a cruise Mach number of 0.70, which also happens to be the actual cruise Mach number for this design.

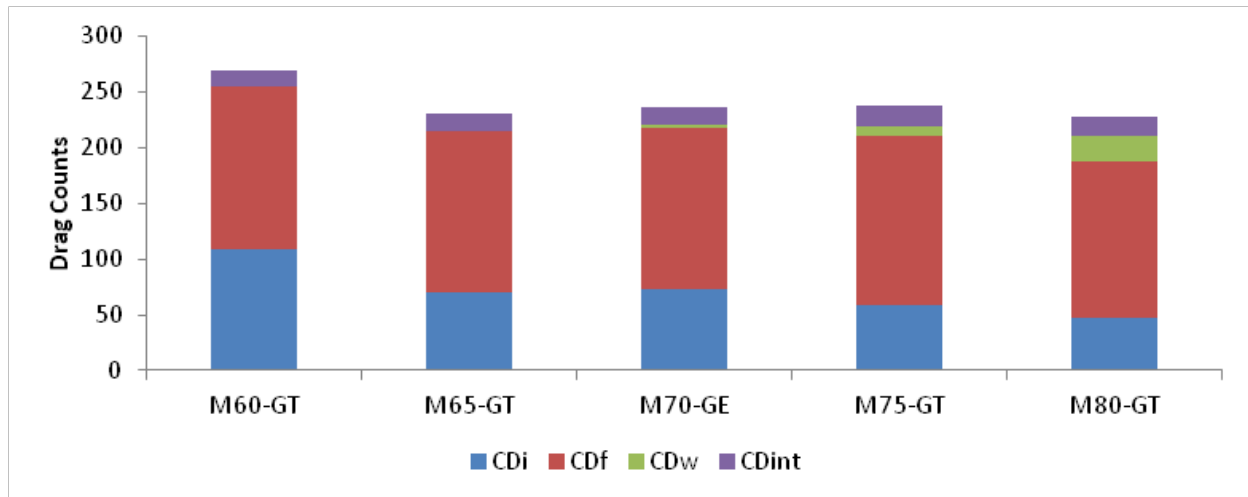


Figure 2.38 – Comparison of drag breakdown

It can be seen that the slope of the red curve is higher than that of the gray curve. This can be explained by a consideration of the aerodynamic drag breakdown of the TBW optimal designs. Figure 2.38 shows the breakdown of the aerodynamic drag of each design into induced (CDi) drag, friction drag (CDf), wave drag (CDw) and interference drag (CDint). The induced drag coefficient reduces with increasing Mach number due to a reduction in the lift coefficient at cruise. The interference drag is reasonably constant across the Mach number range considered, and as expected, the wave drag is negligible for the lower Mach numbers but is significant as the Mach number increases.

The sharp increase in the wave drag originates from the fact that the landing gear pod is fixed relative to the fuselage of the aircraft for all the designs. The optimization affects the design of the wing, strut and juries, but not that of the fuselage or the landing gear pod. Now, as the cruise Mach number is increased, the optimizer naturally increases the sweep angle of the wings to reduce the wing wave drag contribution. However, as a result of the fixed position and geometry of the landing gear pod, the strut-pod attachment point is fixed, and this prevents the strut from being swept back as much as the wing. As a result the strut sweep angle is considerably less than that of the wing at the higher Mach numbers (e.g., Mach 0.60 compared to Mach 0.80, as shown in Figure 2.39 and this results in the strut encountering higher wave drag at the higher Mach numbers. This higher drag ultimately results in a higher fuel burn over the Pt.3 mission.

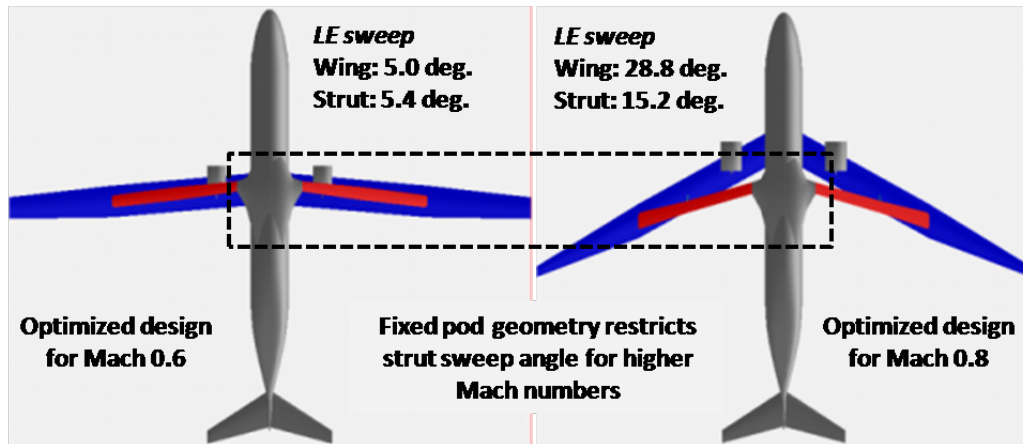


Figure 2.39 – Geometric constraint of the strut due to the fixed attachment to the landing gear pod

Design Optimization with Respect to Direct Operating Cost

Cost estimating capability was achieved through the addition of the program Aircraft Life Cycle Cost Analysis, or ALCCA (9). This program, originally written by NASA and modified within the ASDL, performs bottom up cost estimation of aircraft, both for manufacturers and airlines. Within this project, the primary metric of interest was the airline's direct operating cost (DOC), as it served a useful parameter for optimization.

In order to determine the direct operating cost for a given vehicle, ALCCA calculated numerous cost components and summed them together. This can be decomposed into the cash DOC and the ownership costs. The Cash DOC reflects operating costs associated with each flight, and include the fuel, crew salary, and maintenance costs. The other major component of the DOC is the ownership cost, which includes costs not related to usage but to ownership of the vehicle itself. This includes depreciation, hull insurance, and financing. The overall DOC is calculated by finding each of these cost components.

Within the cash DOC the cost of maintenance depends largely on the cost per hour for maintenance and the amount of time spend on maintenance. This comes from inputs given by the user that define values such as the hourly rate paid to maintenance personnel, and the expected amount of maintenance, such as mean time between failures and mean time to repair. Similar to maintenance costs, flight crew costs depend largely on inputs such salaries and the amount of time they work. Like maintenance, these values were based on defaults programmed into ALCCA, as they could be expected to be similar to typical values for current aircraft.

The cost of fuel was based on the quantity of fuel consumed, and the cost per gallon of fuel. The cost per gallon of fuel is a straightforward value that is simply input by the user, and can be based on the current cost of aircraft fuel. The other required value for this estimate, the fuel consumed, was not an input, and instead was based on the block fuel value, as calculated by the MDO based on the vehicle and specified mission profile.

The other major component of the DOC, ownership cost, was the sum of financing, depreciation, and insurance, all of which depended predominantly on the value of the vehicle itself. This value was determined using ALCCA's estimate of the vehicle's manufacturing cost. Consequently, this was one of the most difficult aspects of the cost estimate. ALCCA's manufacturing cost estimation is based on regressions from historical data, and uses the weights of various components of the aircraft, such as wings, fuselage, vertical tail, horizontal tail, and engines. It also requires a breakdown of materials used in these components, as well as values that characterize the learning curve (which governs the rate at which the production cost goes down as successive units are produced). ALCCA's estimate also reflects the total number of units manufactured, since investment costs are ameliorated across all vehicles produced. The profile of production rate is also considered. To provide the information required for ALCCA to make its estimates, data came from three places. For values that were already determined by the MDO, these were used as inputs. Where possible, values not given by the MDO were estimated based on records for comparable vehicles. In the case of inputs for which no information was available, ALCCA's default estimates were used.

Examples of ALCCA inputs for which the MDO provided information include the weight breakdown of the vehicle. As the weights of the various components of the aircraft have a strong influence on the manufacturing cost estimated by ALCCA, the fact that these values were based on the results of the MDO increased confidence in ALCCA's manufacturing cost estimate. In the case of the material breakdown of each major vehicle component, values from the Boeing 737-800 were used. Values from the Boeing 737-800 were also used for estimates related to the manufacturing program, such as the number of years of development preceding the production of the first unit, cost of the engines, the rate of return of the manufacturer, and the learning curves. All other manufacturing variables were defaulted to ALCCA's built in values. This included the number of units produced, and the profile of production rate on a month by month basis.

Of the various cost components of the DOC, fuel costs and depreciation were the highest, followed by flight crew. This was followed by the cost of maintenance, which represented a much smaller part of the overall DOC. Because of this, the DOC was most sensitive to factors affecting fuel burn and manufacturing cost. Because the fuel cost is based on block fuel and the cost per gallon of that fuel, the DOC was very sensitive to the cost of fuel. This matches prevailing expectations about the DOC, and supports the underlying premise of this project, namely that focusing on fuel efficiency can positively affect the overall cost of operating the vehicle. The other major component of the DOC was the depreciation cost. This was close enough to fuel costs that depending on the price per gallon of fuel and on the cruise speed given, depreciation could be larger or smaller than the fuel cost. Because depreciation was based on the manufacturer's price, the overall DOC was sensitive to everything that influenced the manufacturer's price. While the cost of designing and manufacturing an aircraft is typically hard to predict and features a great

deal of uncertainty, ALCCA represents one of the best available options for predicting these values. Whatever uncertainty may be associated with the depreciation cost of the vehicle, it is doubtful that it could be known with much greater confidence within the scope of this project. The weight components in particular increase confidence in the value determined by ALCCA for depreciation costs, as these were taken directly from the MDO rather than from some comparable vehicle. The cost of the flight crew can also be considered to be reliable due to the simplicity of the equations with which it is found. This can also be said of the maintenance costs, which at any rate has much less influence on the DOC, due to its small size.

After optimizing based on minimization of the block fuel for the five different cruise Mach numbers of 0.6, 0.65, 0.7, 0.75, and 0.8, the process was repeated for all five Mach numbers using direct operating cost as the metric of interest. For each of the two sets of five optimum designs, fuel consumption, empty weight, and aircraft price all showed trends of increasing with increasing Mach number as shown in Figure 2.40, Figure 2.41, and Figure 2.42, respectively. This makes sense, as it reflects the fact that at higher Mach numbers more fuel is required, as well as larger wings to support the increased take-off gross weight. This is reflected in the acquisition price of the vehicle, which is strongly influenced by the weight of the vehicle.

The two approaches converged on similar designs, but in no cases did they converge on a single design that was considered the best by both metrics. With respect to fuel burn, the designs found by minimizing fuel burn featured lower block fuel than those optimized with respect to DOC. The reverse was true when looking at the DOC of the optimum vehicles that were found; for each Mach number the designs found by minimizing DOC had lower values for DOC than those found by minimizing for fuel burn. It is also of note that the plots showed a kink in the trend for Mach = 0.75. This merits further investigation to identify the cause of this anomaly.

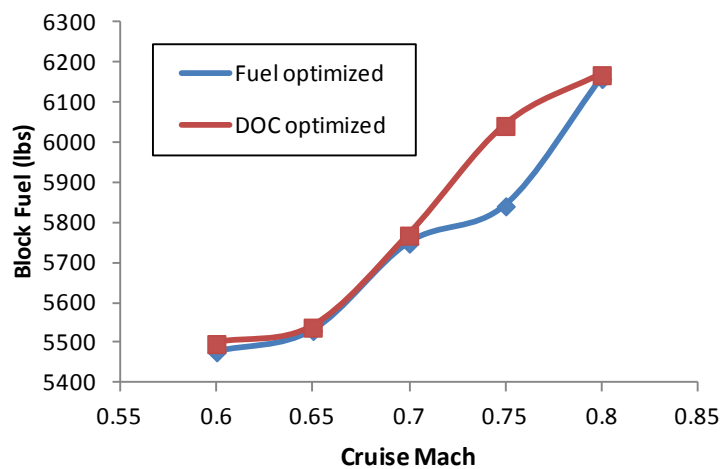


Figure 2.40 – Comparison of block fuel between the fuel burn optimum and the DOC optimum

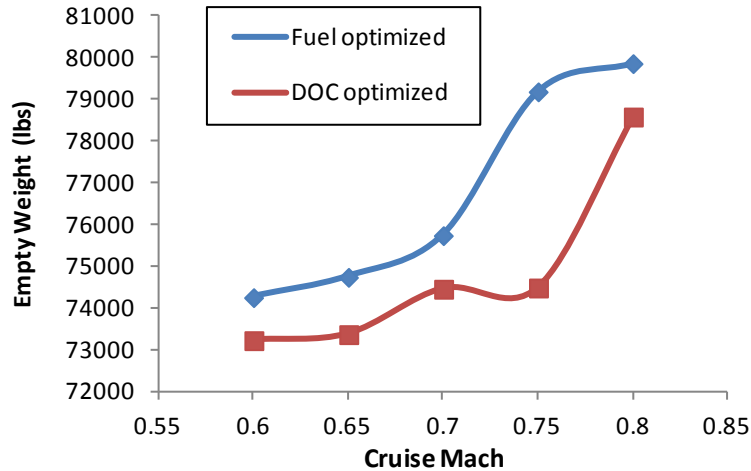


Figure 2.41 – Comparison of empty weight between the fuel burn optimum and the DOC optimum

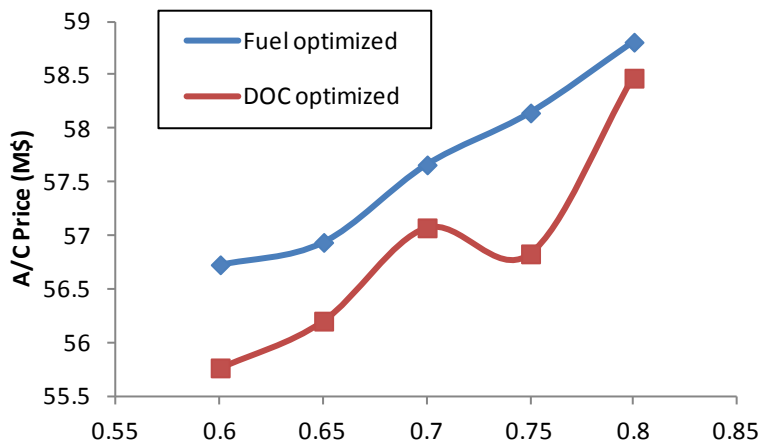


Figure 2.42 – Comparison of aircraft price between the fuel burn optimum and the DOC optimum

The percent difference for each design variable was compared for each of the two designs found at each Mach number in Figure 2.33. This does not reveal any clear trends, suggesting that despite the similarity in output parameters between the two sets of optimums, the designs achieve their optimums in different ways. This suggests that within the design space exist many similarly desirable local optima. This corresponds to what has been found throughout this investigation, where the existence of many local variables with similar optimality has been detected consistently. Perhaps the only trend seen when looking at the percent difference between the two sets of designs at each Mach number is that the variation between the design variables decreases as Mach number increases. One interpretation of this is that as the requirements become more demanding at higher Mach numbers, the feasible design space shrinks down and allows a smaller range for each of the design variables that can be used.

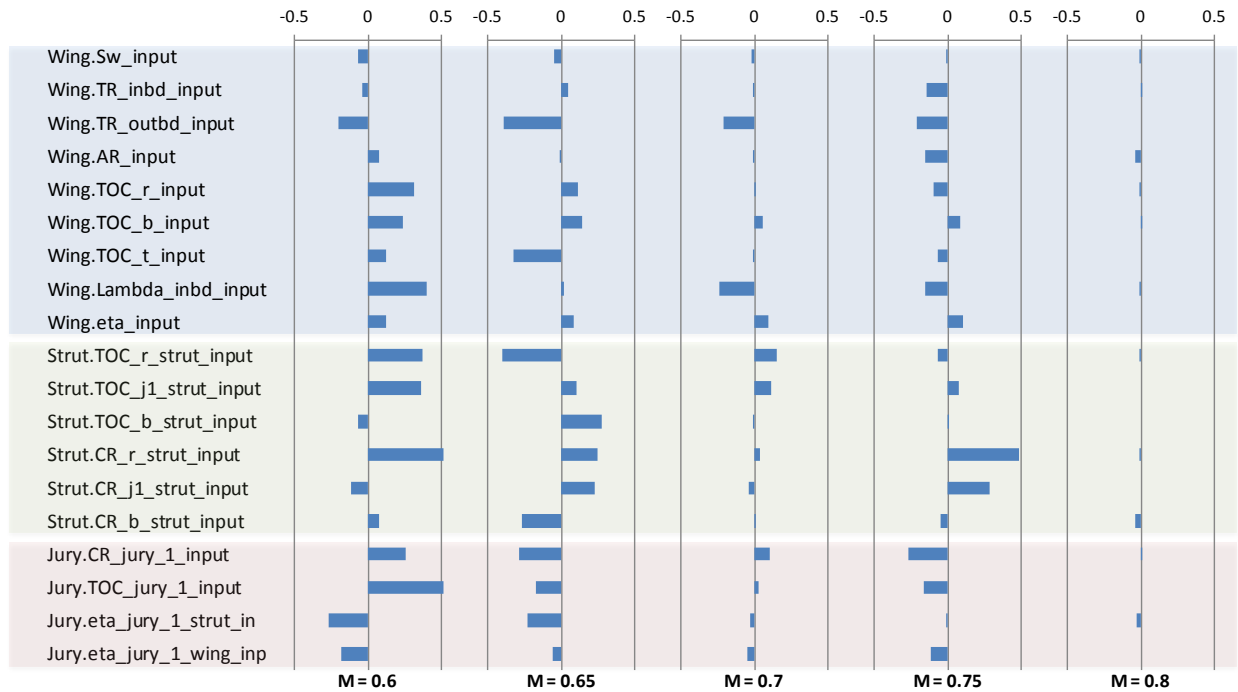


Figure 2.43 – Changes of design variables between the fuel burn optimum and the DOC optimum

Various metrics related to operating costs were considered under two scenarios, one in which the cost of jet fuel is \$3.40, and the other in which the cost of jet fuel was \$5.18. These fuel cost assumptions were obtained from a forecast by the U.S. Energy Information Administration (EIA) (10), in which EIA projected jet fuel cost to 2035 with three different scenarios - "low oil price", "reference", and "high oil price". The lower and higher jet fuel costs respectively represent EIA's projection for year 2035 under "reference" and "high oil price" scenarios. As shown in Figure 2.44, the total DOC decreases with increasing Mach number, but the cash DOC remains relatively constant as shown in Figure 2.45.

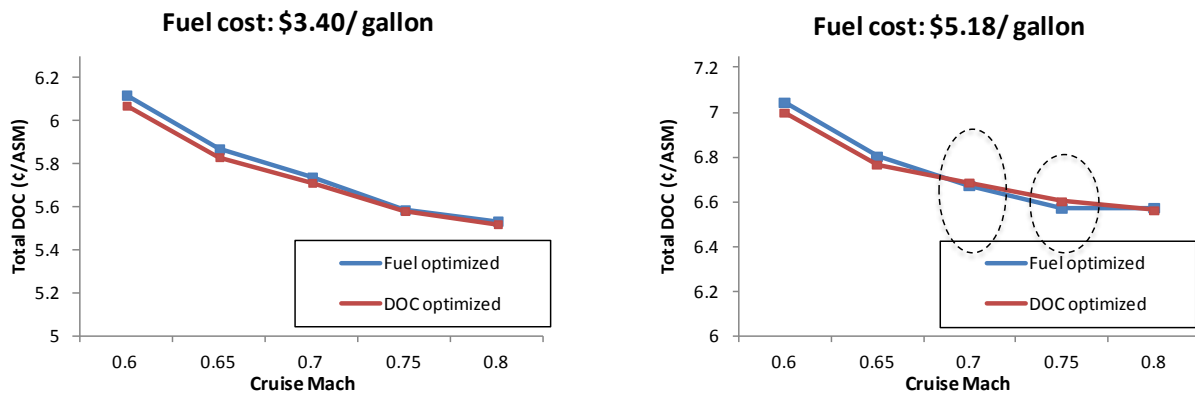


Figure 2.44 – Total DOC for two fuel cost assumption

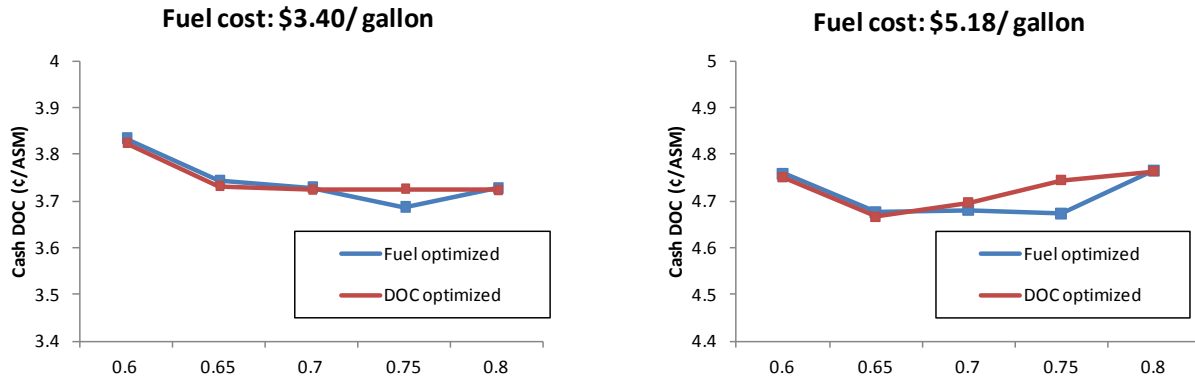


Figure 2.45 – Cash DOC for two fuel cost assumption

Greater insight into these trends can be found by looking at the various components of DOC. The DOC breakdown shows that fuel and depreciation are the largest components, followed by crew costs, followed by all remaining cost components combined as shown in Figure 2.46.

The cost of all fuel used increases with increasing Mach number, since more fuel is used at higher cruise Mach numbers. Conversely, ownership costs and crew costs go down with increasing cruise Mach number since crews are paid for fewer hours per flight, and ownership costs are spread out over a greater number of flights. The relationship between the productivity and cruise speed is shown in Figure 2.47. The changes in fuel costs and crew costs largely cancel each other out, which yielded a relatively constant cash DOC trend across different Mach numbers. When all cost components are considered in the plot of the total DOC, the trend associated with ownership costs factors in, and the total DOC goes down with increasing Mach number. This decreasing trend for Total DOC was somewhat surprising, as it was not expected to be monotonic but rather bucket shaped. This would reflect an optimum Mach number, where the influences of the increasing costs from fuel and decreasing costs from crew and ownership would be minimized. This still appears to be the case, but the Mach number at which the total DOC is minimized is greater than Mach 0.8 under the assumptions currently used in this investigation.

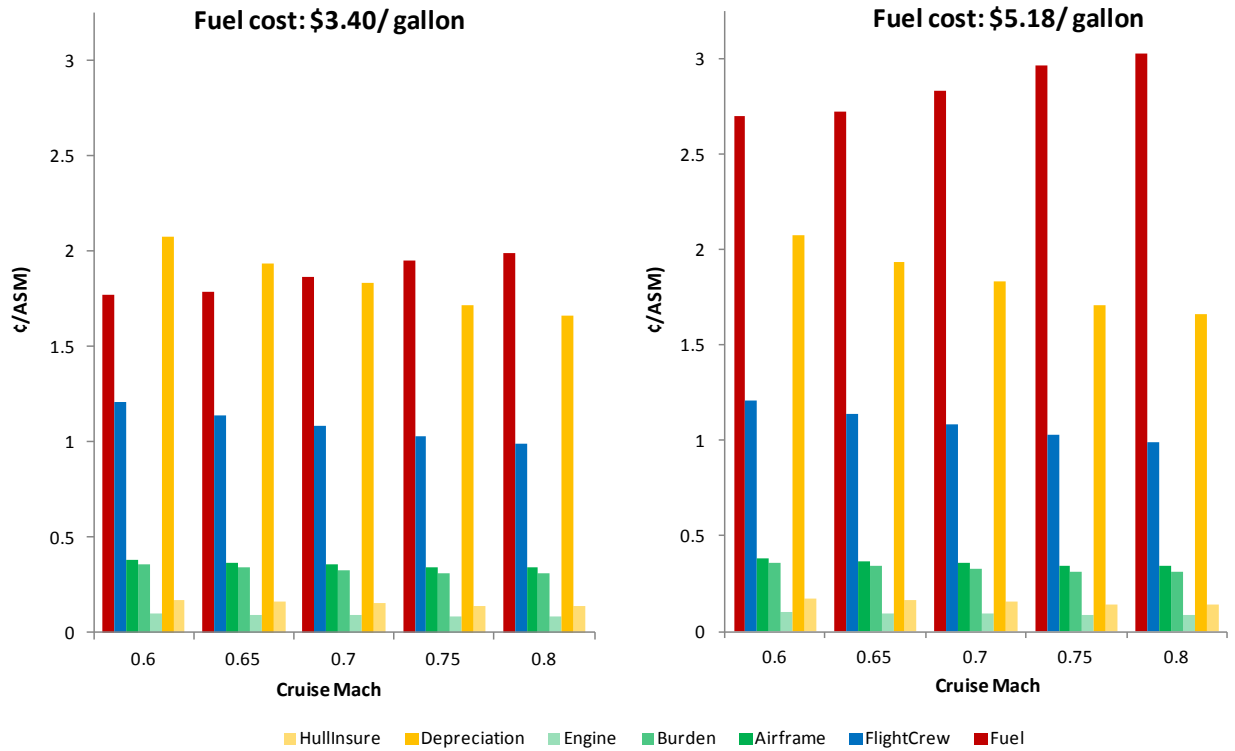


Figure 2.46 – Breakdown of total DOC

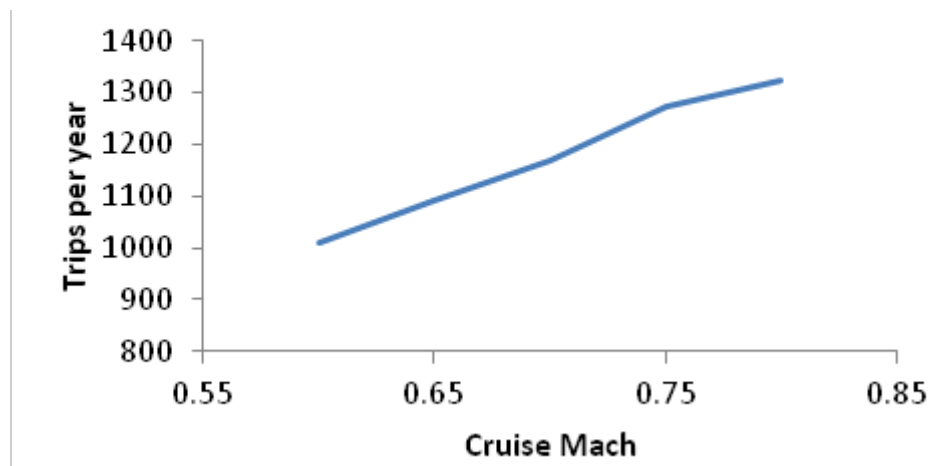


Figure 2.47 – Productivity vs. cruise speed (Number of Trips per Year; Utilization = 2,835 hrs; Mission Range = 900 nm)

It is also significant that as fuel costs go up, this increases the importance of fuel economy. The increase in fuel costs causes the fuel component to represent a greater share in the total DOC. Thus, a given percent reduction here may have a large impact on the overall DOC of the vehicle.

2.1.4.4 Multi-Disciplinary Optimization Data Used for Post Analysis

Loads and aerodynamic data developed by the MDO provided design targets for Boeing discipline experts during the development of 765-095 Revisions B and C.

Loads Data

The MDO environment included 17 different loads cases in the structural analysis. The load cases are defined in Table 2.9.

Table 2.9 – MDO Environment Load Condition Definitions

No.	Alt [ft]	Mach	n (Aero)	n (Inertia)	% fuel	Cargo	Title
1	36,000	0.70	2.5	2.5	100	Design	36K ft, M 0.7, 2.5g, TOGW
2	36,000	0.70	2.5	2.5	50	Maximum	36K ft, M 0.7, 2.5g, MZFW
3	36,000	0.70	-1.0	-1.0	100	Design	36K ft, M 0.7, -1.0g, TOGW
4	36,000	0.70	-1.0	-1.0	50	Maximum	36K ft, M 0.7, -1.0g, MZFW
5	0	0.20	0.0	2.0	100	Design	2g, Taxi Bump, TOGW
6	0	0.20		Gust	100	Design	0 ft, M 0.2, TOGW, Gust
7	0	0.20		Gust	0	Maximum	0 ft, M 0.2, MZFW, Gust
8	0	0.40		Gust	100	Design	0 ft, M 0.4, TOGW, Gust
9	0	0.40		Gust	0	Maximum	0 ft, M 0.4, MZFW, Gust
10	10,000	0.50		Gust	100	Design	10K ft, M 0.5, TOGW, Gust
11	10,000	0.50		Gust	0	Maximum	10K ft, M 0.5, MZFW, Gust
12	20,000	0.60		Gust	100	Design	20K ft, M 0.6, TOGW, Gust
13	20,000	0.60		Gust	0	Maximum	20K ft, M 0.6, MZFW, Gust
14	30,000	0.70		Gust	100	Design	30K ft, M 0.7, TOGW, Gust
15	30,000	0.70		Gust	0	Maximum	30K ft, M 0.7, MZFW, Gust
16	40,000	0.70		Gust	100	Design	40K ft, M 0.7, TOGW, Gust
17	40,000	0.70		Gust	0	Maximum	40K ft, M 0.7, MZFW, Gust

The wing loads are calculated and applied to a structural analysis module. The input nodal loads for the wing are illustrated in Figure 2.48. It should be noted that the nodal loading of the structure between the jury strut and primary wing strut are reduced due to reduced node spacing. The load at centerline is half the total node load because of model symmetry.

The external loads are used to calculate the truss member internal loads. Figure 2.49 shows the wing shear and Figure 2.50 shows the wing bending moment for all the load cases analyzed. The bending moment data for all load cases was used to determine design bending moment curves which are shown in Figure 2.51. A portion of the inboard wing is sized by global buckling due to the high compressive force imparted on the wing by the wing strut. This compressive force is illustrated in Figure 2.52 and the corresponding wing strut load in Figure 2.53.

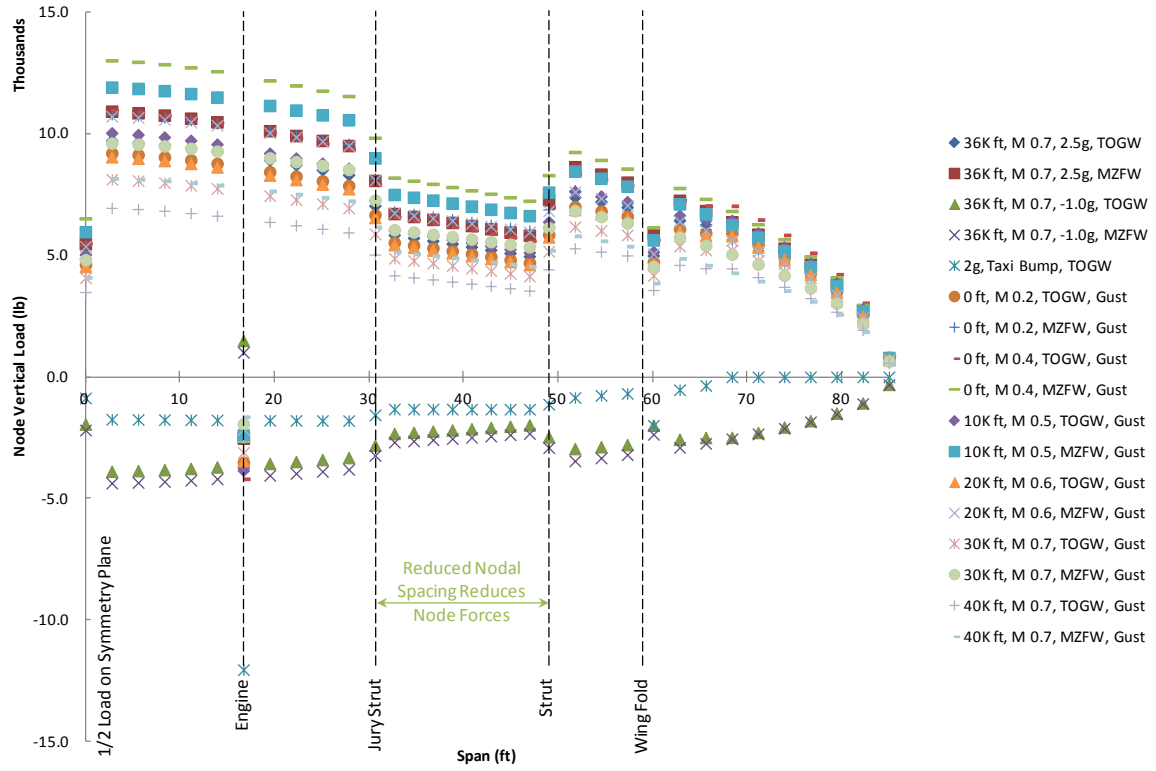


Figure 2.48 – Wing Loads (External to Truss System)

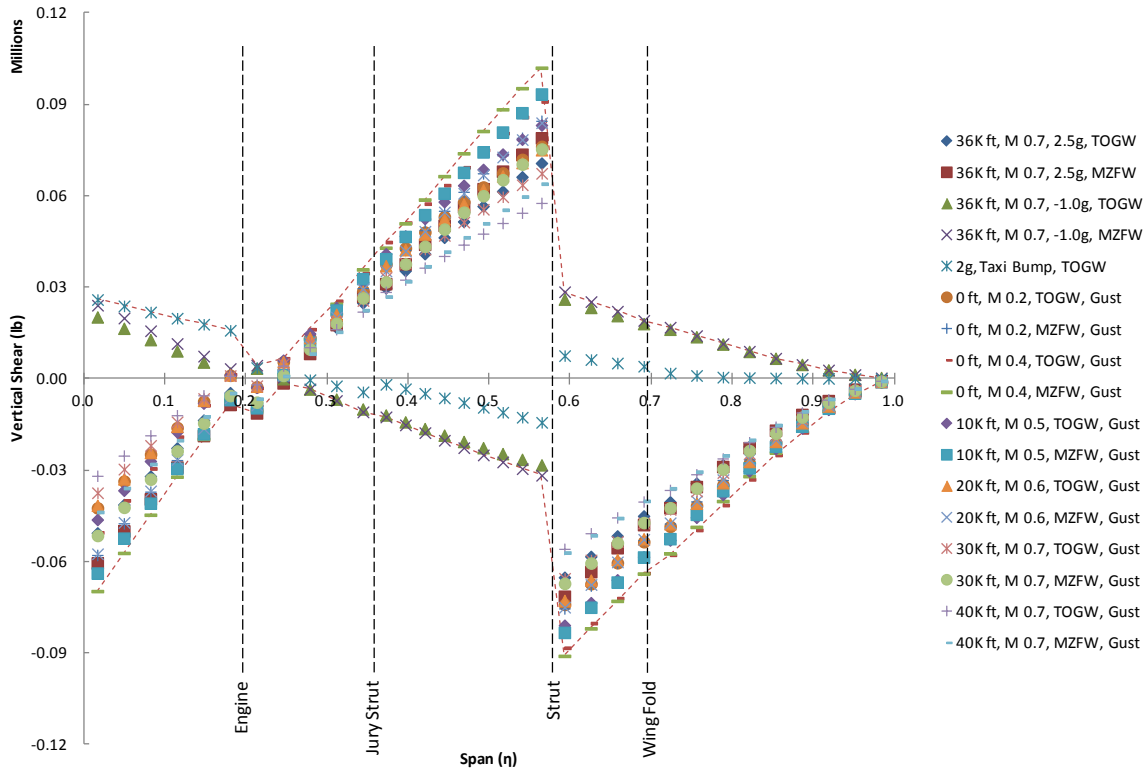


Figure 2.49 – Wing Shear

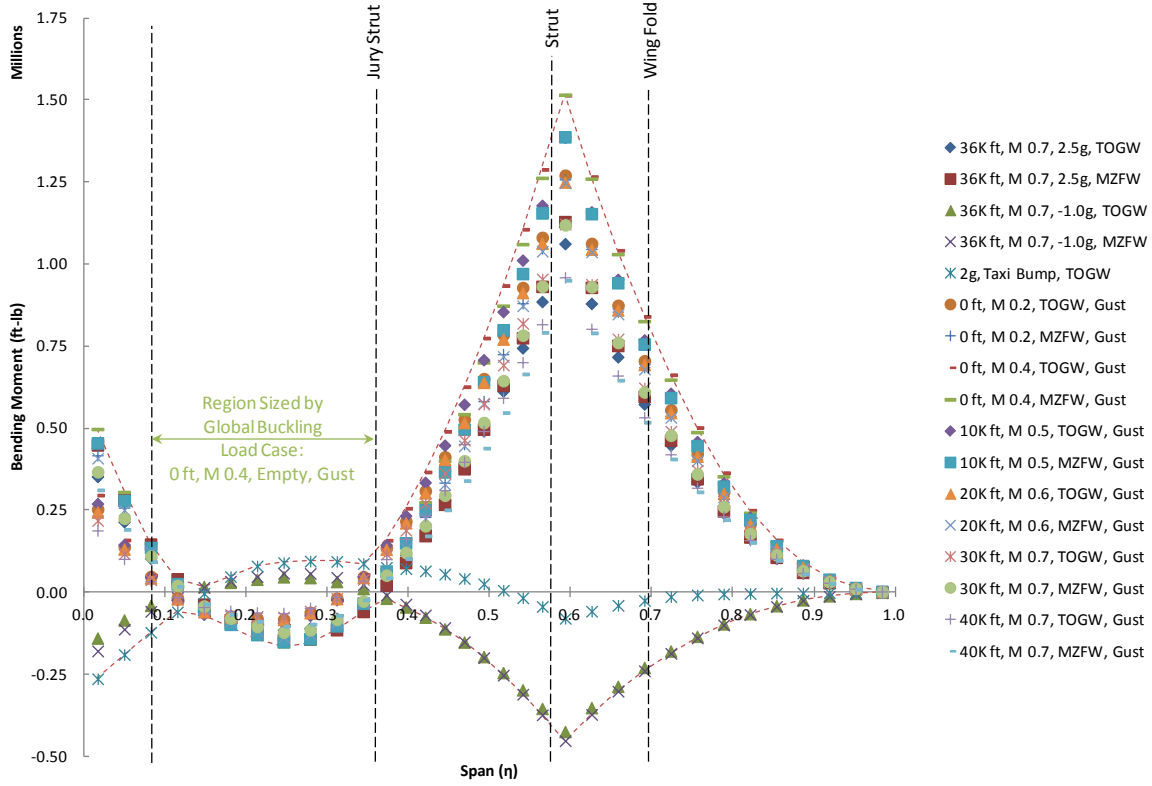


Figure 2.50 – Wing Moment

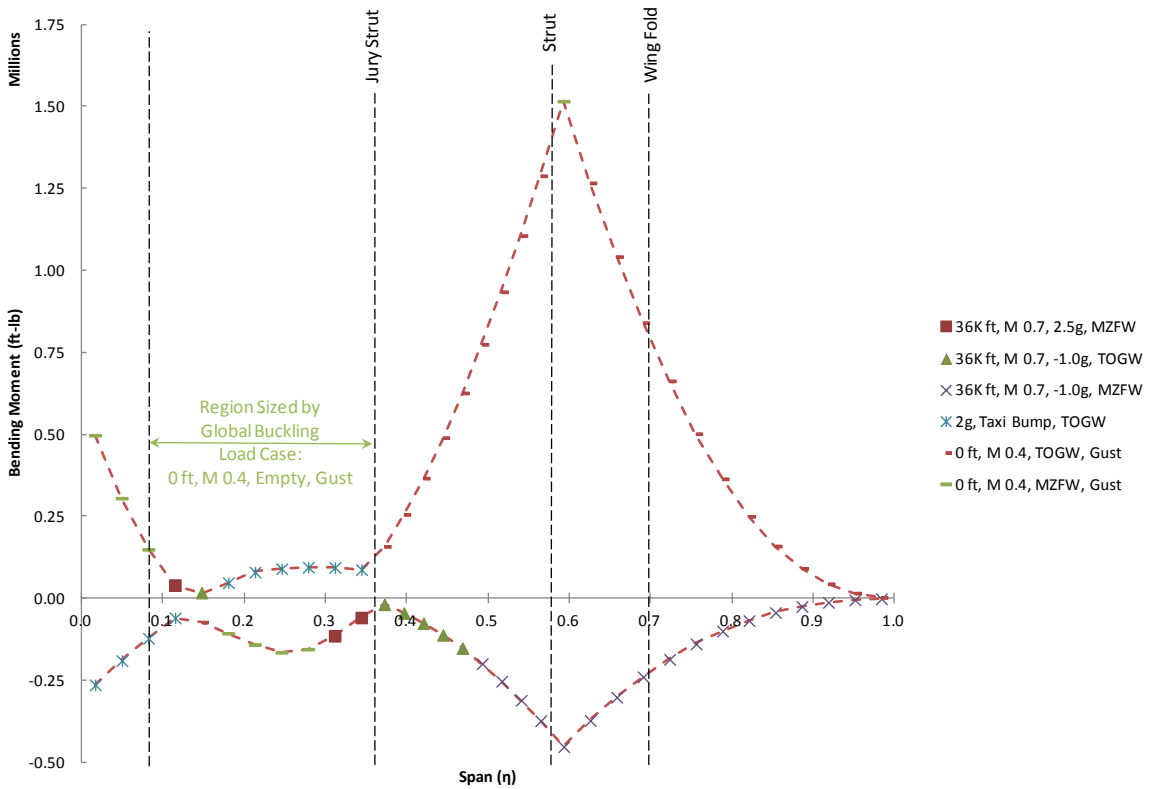


Figure 2.51 – Wing Design Moment

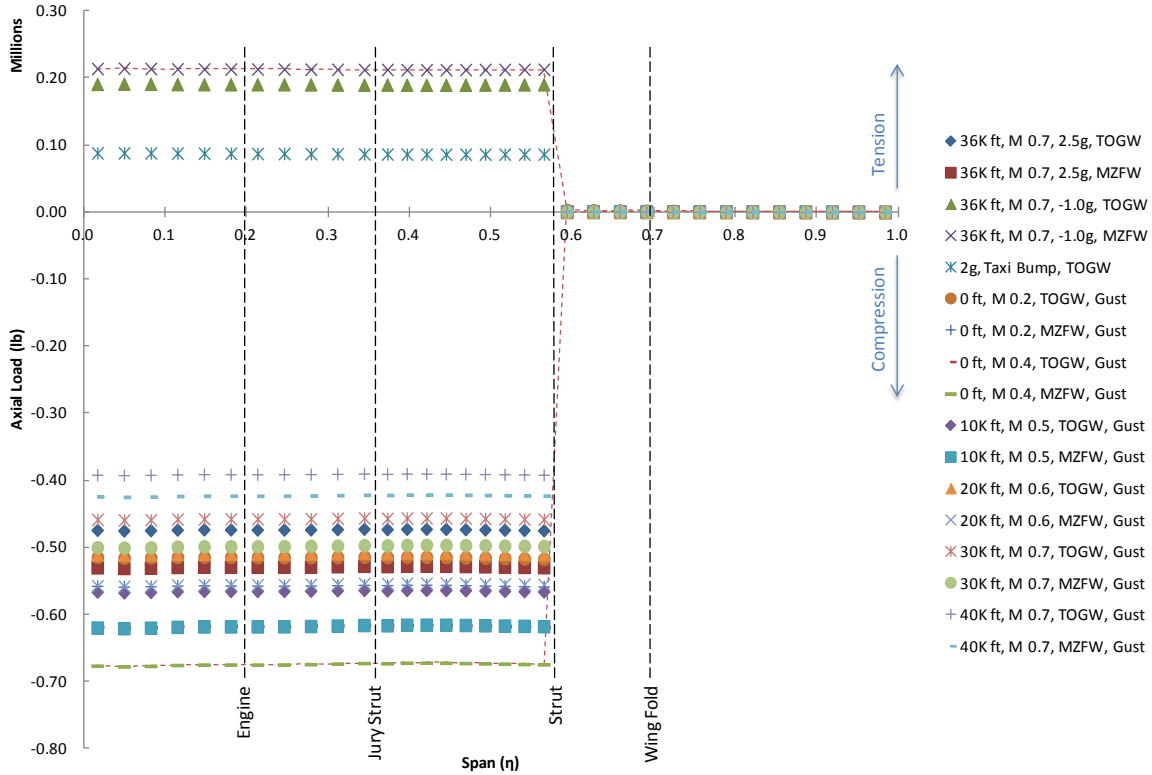


Figure 2.52 – Wing Axial Load

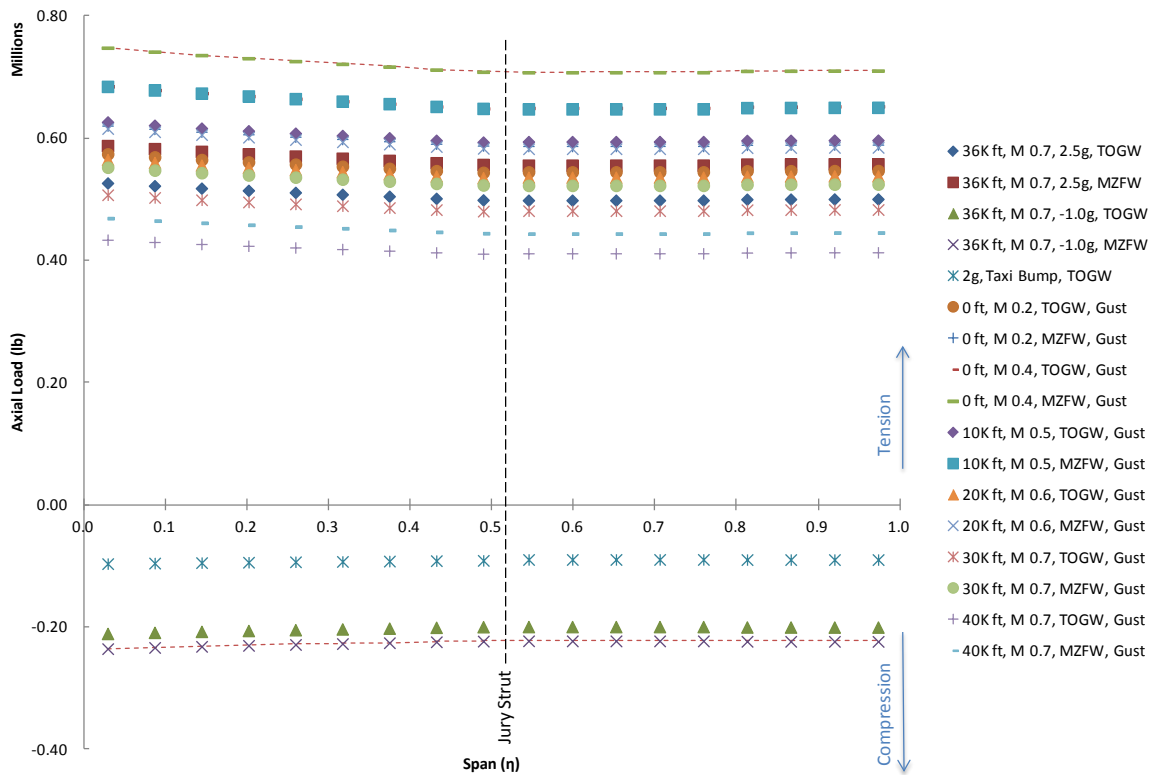


Figure 2.53 – Strut Axial Load

The loads are then used to size the structure. The physical thickness of the sized wing, wing strut, and jury strut are shown in Figure 2.54. Figure 2.55 shows which load conditions sized each node and illustrates which nodes are sized by buckling and strength (labeled bending). It should be noted that an artificial carryover constraint prevented the optimization from reducing the strut chord near its tip. A prediction of how the strut would have sized without the constraint is shown as a dashed line in Figure 2.54. The strut geometry will be refined in the aeroelastic FEM.

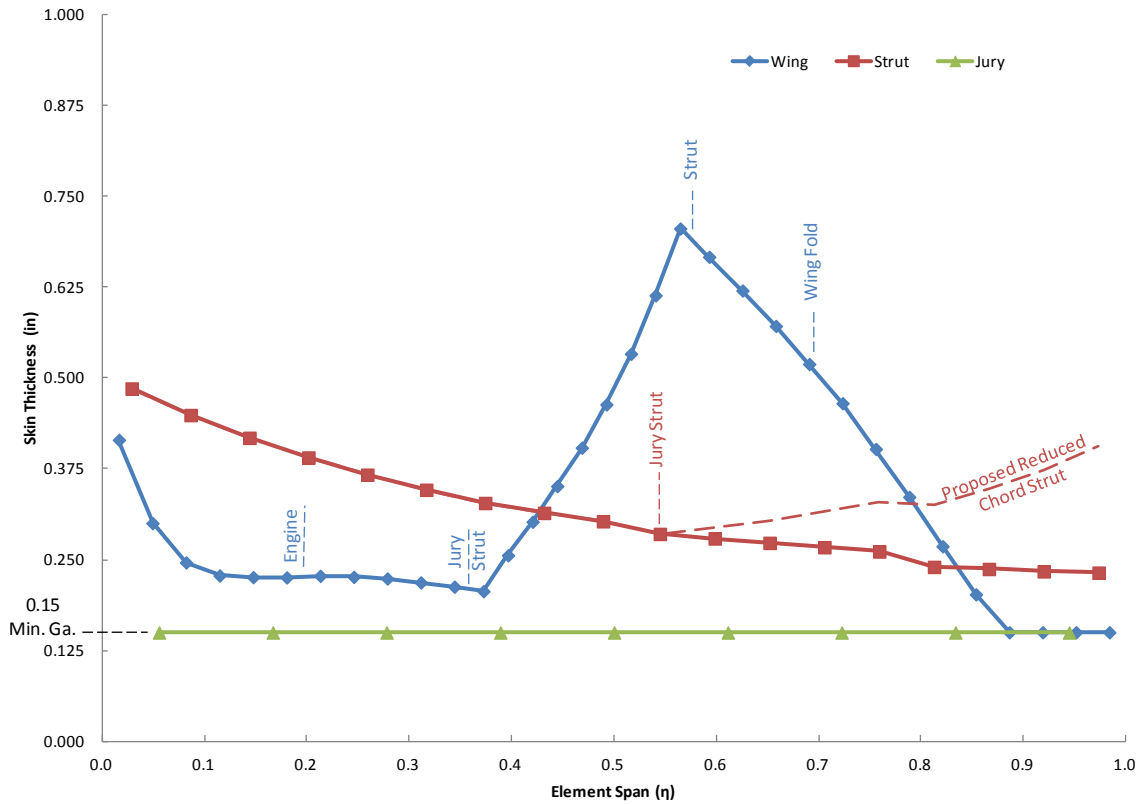


Figure 2.54 – Sized Skin Thickness

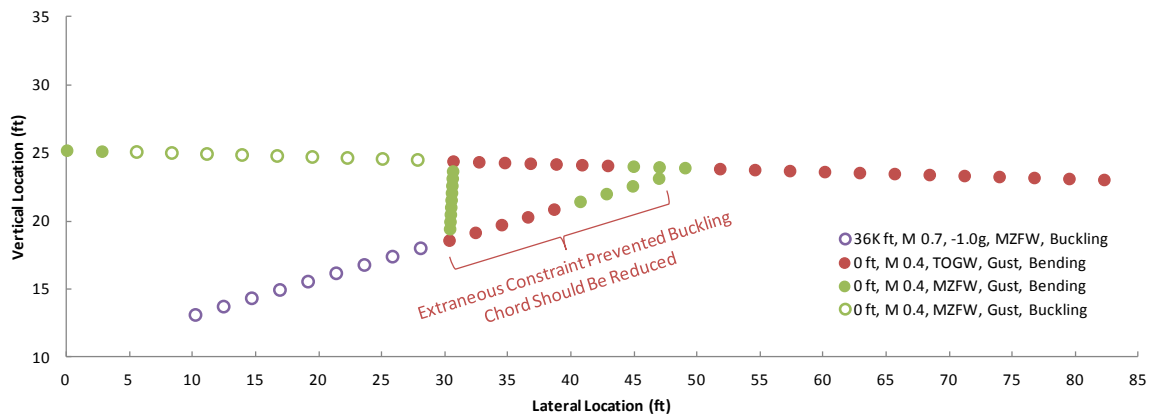


Figure 2.55 – Skin Sizing Load Cases

The resulting nodal deflections are shown for the wing in Figure 2.56 and for the entire truss in Figure 2.57. The wing tip deflection predicted by the MDO is significant when compared to conventional configurations. This is especially true if the deflection is measured from the strut junction. This is largely due to the rotation that is allowed at the strut junction (a ball or pin joint connection). If the rotation at the strut junction is accounted for, the wing deflection (though higher than typical) is reasonable. The deflections of the entire truss are plotted to scale for better perspective.

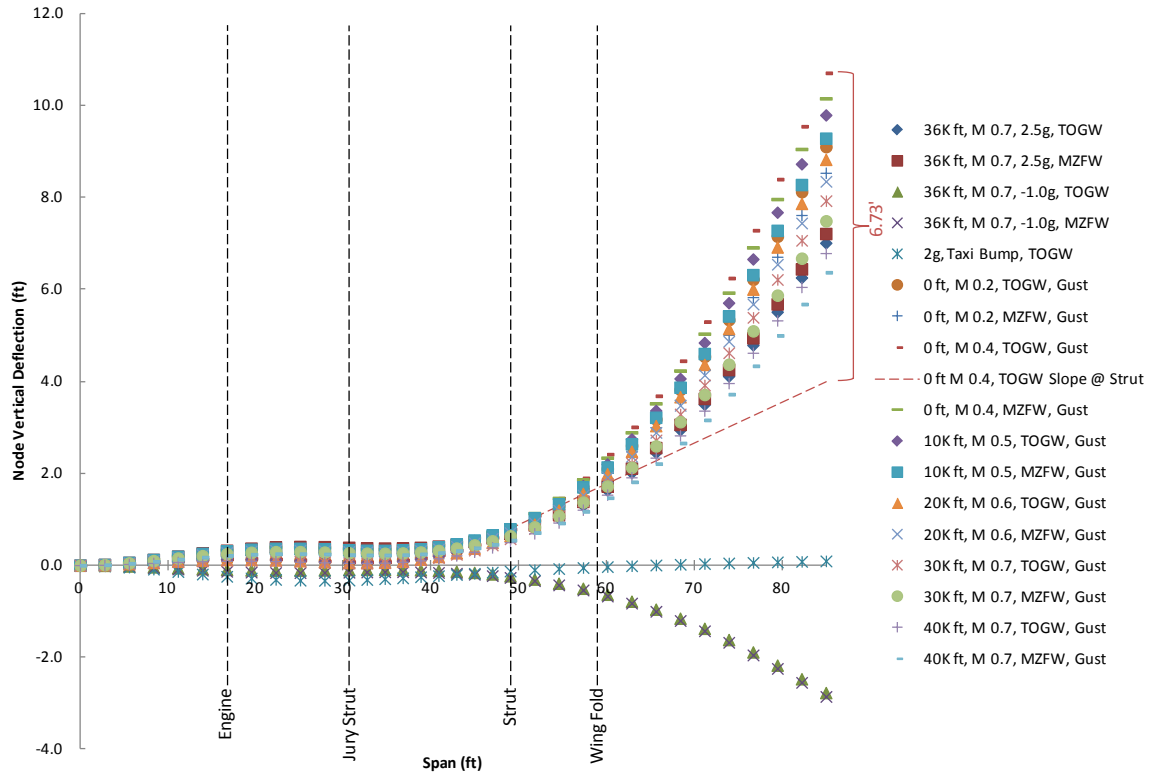


Figure 2.56 – Wing Node Deflection

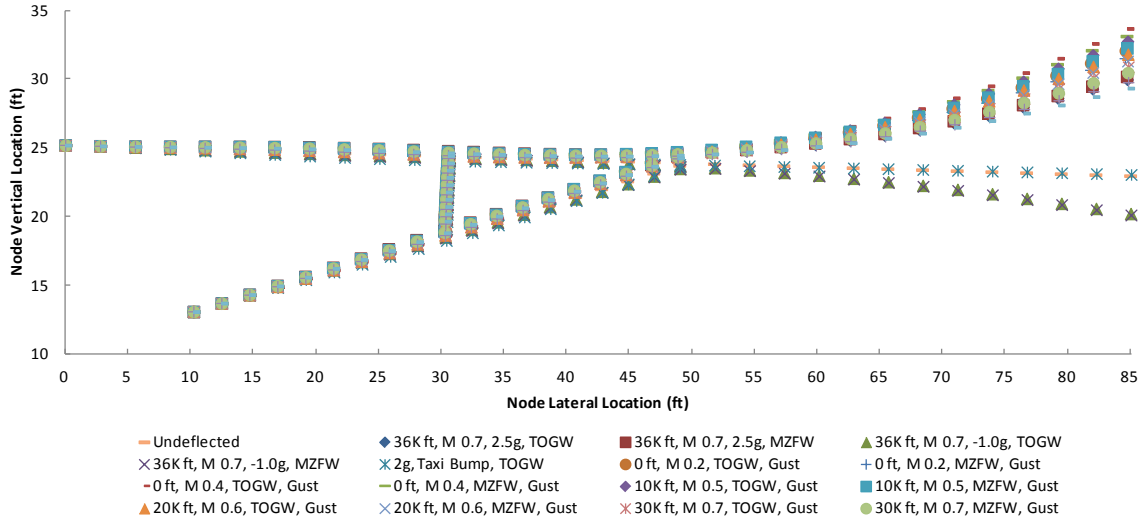


Figure 2.57 – Truss Node Deflection

Aerodynamic Data

Two pieces of aerodynamic data from the MDO environment will be used as design goals for future tasks. The wing lift distribution (Figure 2.58) and the drag divergence Mach number (Figure 2.59) will be used as targets for the high speed wing design. The lift distribution is used to trade induced drag (which tends toward an elliptic distribution) and wing structural weight (which tends toward a triangular distribution). The wing lift distribution that resulted from the MDO is shown in blue and is compared to an elliptic distribution in purple. The distribution is slightly triangular and falls within expectation. Also included is a coefficient of normal force (illustrated in red) which is approximately equal to sectional lift coefficient. The sectional lift coefficient is surprisingly flat and lends credence to a 2D starting point for design.

Additional surprises stem from the drag divergence plot. Several definitions of drag divergence exist, but no matter which is used, the results of the MDO clearly indicate the optimum speed to fly for fuel efficiency is well below divergence. One typical definition for drag divergence is when the slope of the drag due to Mach number vs. Mach number curve reaches 0.05. The MDO results in a configuration that cruises at a slope of 0.021, less than half the slope of a conventional configuration. These results are mirrored by internal Boeing analysis. For this study, a design target slope of 0.021 will be used to bound wing thickness.

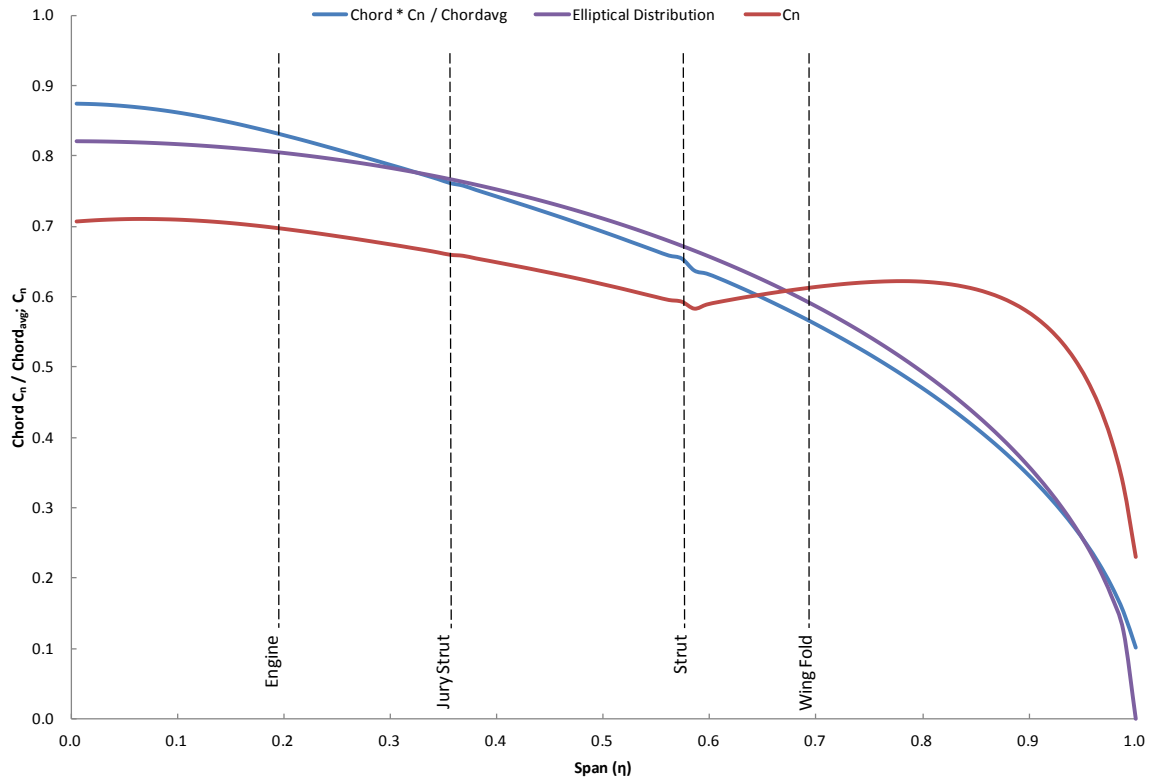


Figure 2.58 – Wing Lift Distribution

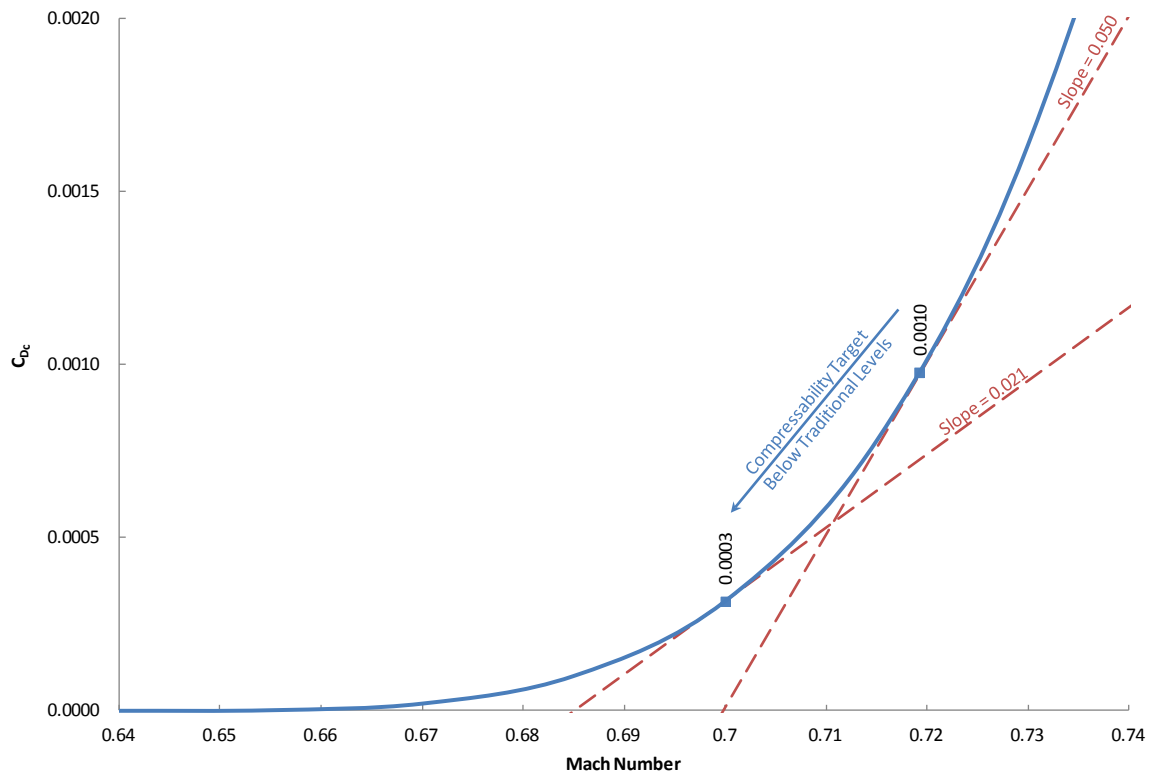


Figure 2.59 – Aircraft Drag Divergence

The university MDO predicted an optimum lift coefficient of 0.616. Based on the load data summarized earlier in this section, the wing weight was predicted to be higher than the weight predicted by the MDO environment. If the wing weight is a more significant fraction of OEW the optimum configuration will tend to fly at a higher lift coefficient than predicted by the optimization. It was estimated that the TOGW of the airplane will increase from 136,000 pounds predicted by the MDO to approximately 150,000 pounds. This increase will be accounted for by changing the design cruise lift coefficient to 0.7, a percentage change roughly equal to the change in gross weights.

2.1.5 Other Phase II Configuration Changes

2.1.5.1 Engine Integration

The baseline engine integration for 765-095-RA is illustrated in Figure 2.60. The installation is a conventional nacelle-pylon arrangement with placement constrained by the exhaust plume and wing strut interaction. Alternative arrangements are possible though do not appear attractive.

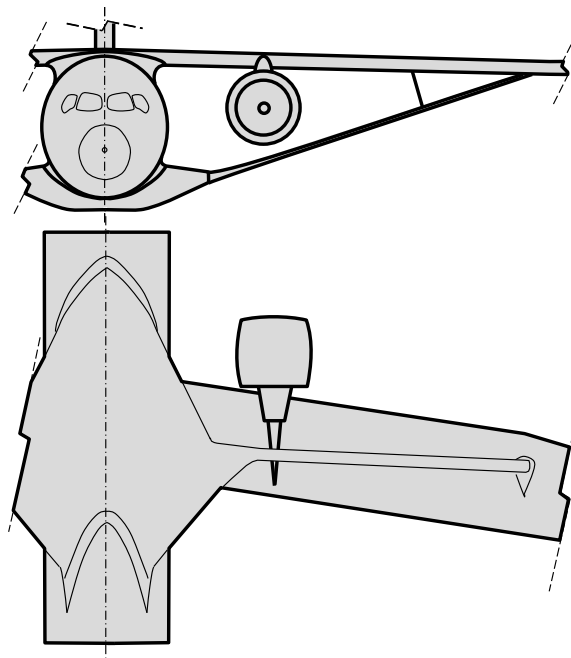


Figure 2.60 – Baseline Engine Integration

Typically, engines are located in front of the wing because this offers the best integrated solution between weight and interference drag. While there may be benefits in wetted area and pylon interference drag to moving the engine aft and closer to the wing, it is not clear that there would be a vehicle-level improvement (heritage experience points to the opposite). Moving the engine aft and closer to the wing would increase interference drag from the nacelle. Additionally, some engine placement options would interrupt the load paths, which would unnecessarily increase weight. Loading the engines fan case may reduce SFC and increase engine wear. To prevent this,

load must be ring-framed around the fan case and the engine attachments must be designed for stiffness rather than stress, as was done on the DC-10/MD-11 aircraft centerline engine. Experience has shown that it is best to avoid the situation if possible.

Another consideration is thrust reversing. Many of the integration alternatives would preclude the use of a cascade style reverser and would have to use heavier alternatives. Turbine and fan disk failures are also a concern, as primary structure would be impacted by disk debris.

Engine maintenance makes up a significant portion of direct operating cost. Airframe integration decisions that reduce serviceability, thus increasing maintenance costs, are highly undesirable. This becomes a greater concern if fuel burn decreases, as the percentage of engine maintenance on direct operating cost would increase.

Figure 2.61 shows the result of a brainstorming activity on engine and strut integration. None of the options considered appeared to have any advantage over the baseline installation though none were traded analytically. While there may be some benefits to some of the alternative engine integration concepts, the potential negative aspects make it hard to justify many of the options.

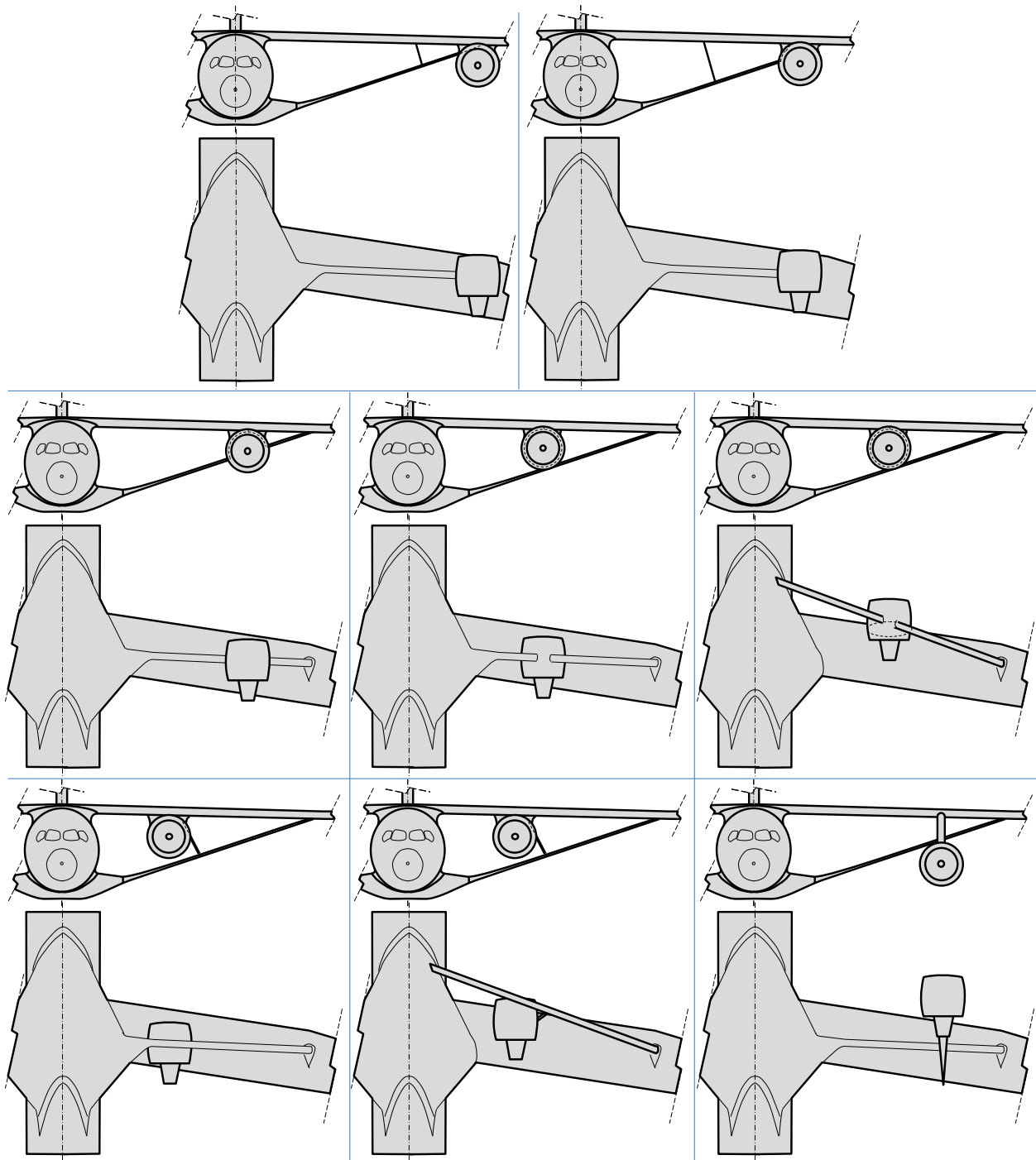


Figure 2.61 – Alternative Engine Integration Concepts

2.1.5.2 *Nose Refinement*

The nose shape of an aircraft is influenced by many factors such as aerodynamics, pilot vision, structures, internal arrangement, manufacturing, and visual appeal. The nose of 765-095 (Figure 2.62-A) was 350 inches long yielding a fineness ratio of 2.22. This fineness ratio should accommodate a divergence Mach number of about 0.87, significantly higher than what is required for a 0.70 cruise speed. The reduced nose length is traded equally for constant section

yielding no net fuselage length change. The constant section is easier and less expensive to manufacture. The nose length for 765-095-RA (Figure 2.62-B) is 250 inches and its fineness ratio is 1.59 which is still sufficient for a 0.82 cruise Mach number. The nose length was not reduced further due to interior arrangement and flight deck integration reasons. The nose camber was also reduced.

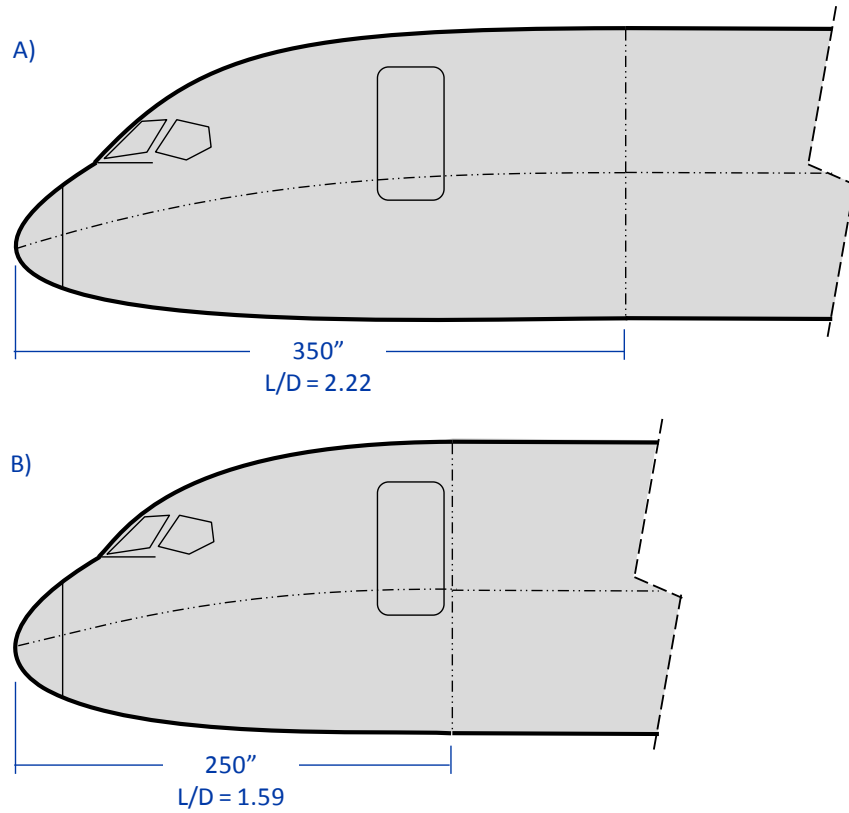


Figure 2.62 – A) 765-095 Nose Profile View; B) 765-095-RA Nose Profile View

To verify the fuselage aerodynamic performance in cruise, the fuselage OML was analyzed with the CFD++ N-S solver on a 3.5 million hybrid cell grid, using the K-Epsilon turbulence model. Figure 2.63 shows a centerline cut of local Mach number and surface pressure contours for the solution, and shows nothing adverse for the Mach 0.7, Angle of Attack 1.5°, 42,000 ft altitude condition.

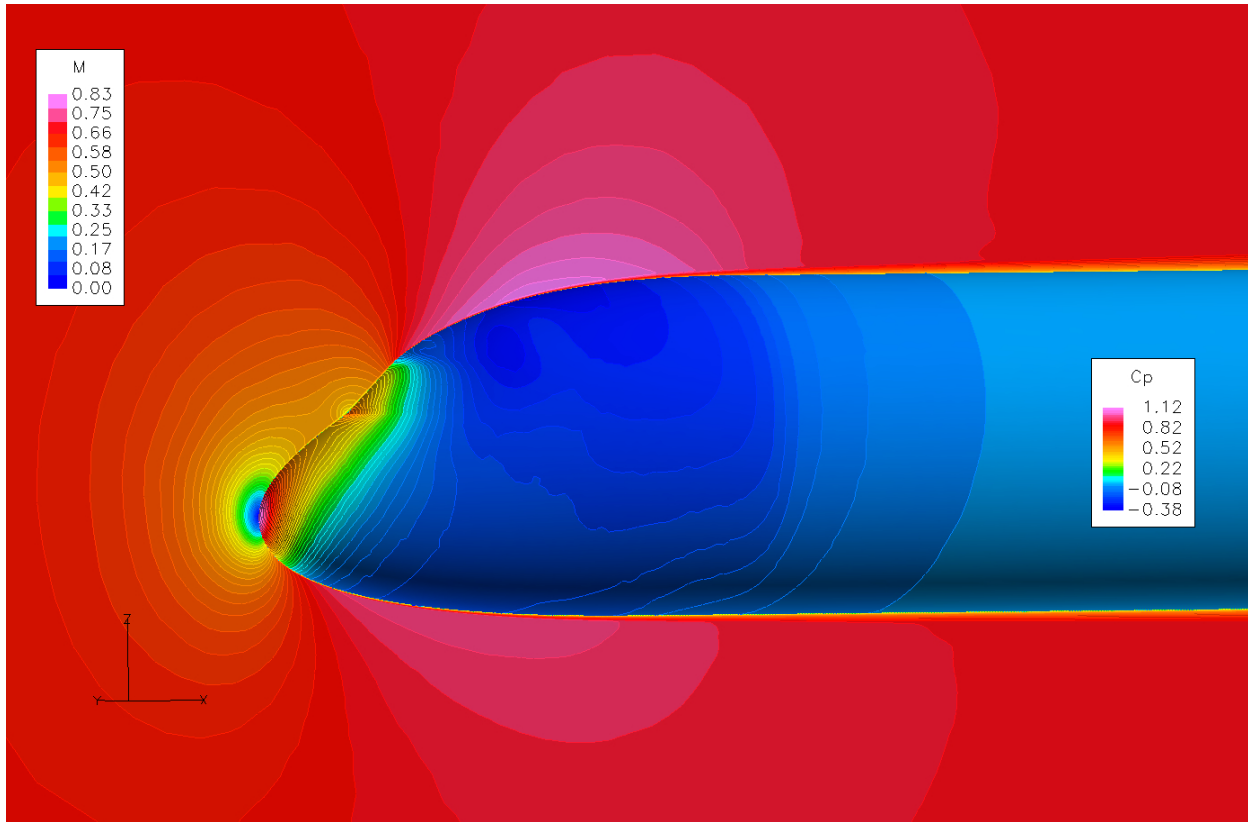


Figure 2.63 – Forward Fuselage Mach Number and Pressure Contours

2.1.5.3 Landing Gear Integration

The landing gear configuration from SUGAR Phase I (765-095), illustrated in Figure 2.64, is a body mounted installation similar to the BAE-146 which uses a collapsible link that reduces its folded length. This provides clearance for the airplane keel beam while minimizing the gear trunnion's distance from the fuselage. The gear is a trailing arm geometry which typically would be heavier than conventional arrangements but provides vehicle level advantages for some configurations because the oleo geometry and kinematics are independent from the strut geometry enabling features such as the collapsible link previously mentioned. Other advantages may include more benign loads transmitted to the rigid structure and more tolerance for poorly surfaced airfields. This integration was chosen based on experience with internal studies which focused on high wing transports and was not fully refined for the Phase I configuration as attention was diverted to understanding the species as a whole rather than detailed component integration.

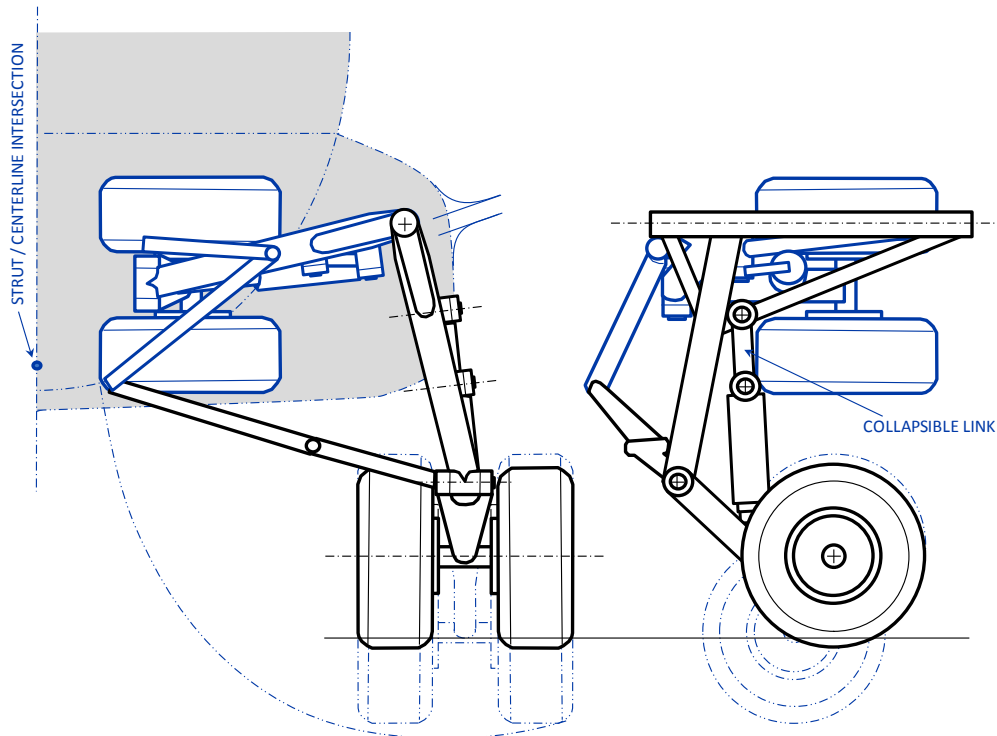


Figure 2.64 – Phase I Gear Installation (765-095)

The global understanding of truss braced wings obtained in Phase I provided many possible integration strategies that should be studied. For landing gear, in an effort to combine highly loaded structural members to increase structural efficiency, an untraded decision was made to integrate the strut carry thru with the landing gear. This integration scheme will restrict the location of the strut to fuselage junction to occur at the same location as the landing gear. The gear location falls out from the vehicle configuration and airplane CG limits, thus the fuselage strut integration location is fixed. This decision was not traded for this study and based on the FEM results, doesn't seem to impact the TBW system adversely for this Mach number. If higher speeds are studied, this integration decision should be traded.

In addition to shared heavy structure, it is perceived that the configuration would benefit from a strut integration as low on the fuselage as possible. The original gear arrangement's trunnion (the structural element aligned with the gear rotation axis which carries substantial gear loads to its attachment) integrates high on the fuselage near the passenger floor. Lowering the trunnion location would benefit the aircraft by allowing a shorter landing gear strut and an increased mechanical advantage for the wing strut thus decreasing its load or increasing the optimum strutted span.

The evolution of the landing gear arrangement through three cycles constrained by the thinking described in the previous paragraphs is illustrated in Figure 2.65 A thru D. Figure 2.65-A shows the Phase I installation. Figure 2.65-B shows a simple strut (non-trailing arm) landing gear

installed at a very low point on the fuselage facilitating the need for a stub pylon for gear attachment. This arrangement significantly shortened the landing gear strut and lowered the wing strut attachment location but left two constraints that could not be satisfied. The landing gear strut length was not sufficient for the integration of the oleo (shock absorber) and the landing gear couldn't be installed at a location that would provide adequate main gear ground track. These constraints could be met by lengthening the gear strut and moving the attachment further from the fuselage thus growing the size of the pylon.

Rather than grow the strut length, the oleo was decoupled from the gear strut allowing it to lean toward the fuselage. This cant angle enables the gear to meet the minimum gear track required for this size aircraft without growing the length of the strut (Illustrated in Figure 2.65-C). The gear arrangement was integrated with additional rigor and slowly evolved into Figure 2.65-D which takes into account the structure, kinematics and gear stowage. This evolution solves the landing gear integration within scope of the study. No detailed trades were performed during the evolution and if further vehicle refinement were to be performed it is suggested that integrations B thru D (and possibly additional to landing gear integration concepts) be explored at a higher fidelity. An unexplored possibility is that the evolution from C to D changed the geometry significantly enough that a simple strut could be optimum.

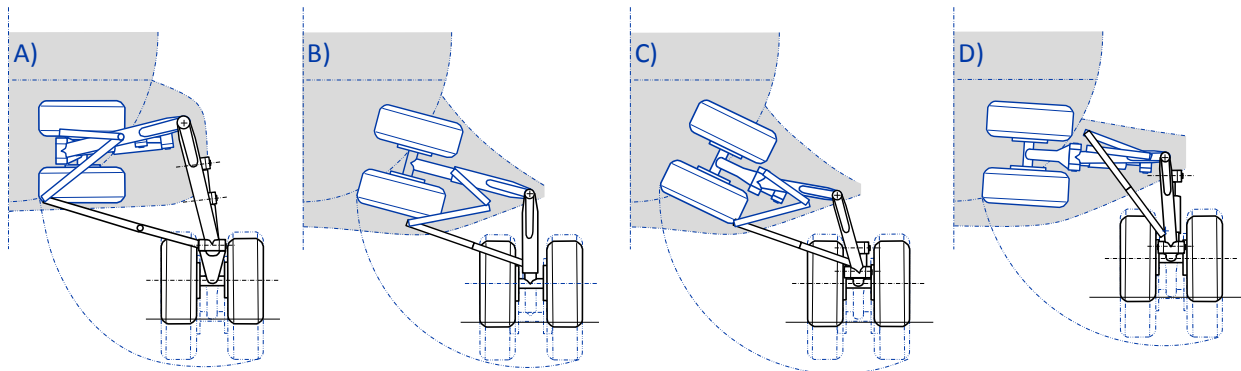


Figure 2.65 – Landing Gear Installation Progression

As previously mentioned, the goal of the landing gear and wing strut integration is to maximize the mechanical advantage the wing strut has at carrying wing loads. The evolution of the gear, assuming a consistent strut angle, would provide an additional 47.5 inches of additional strutted wing span and efficiently reuses highly loaded structure. This integration scheme does assume that reducing wing bending moment at the strut junction in favor of increasing gear pylon loads is a net benefit to the airplane. Figure 2.66 shows the final gear configuration in both front and side view. It also shows graphically the increase in strutted span (labeled “Horizontal Offset” that was achieved by the installation.

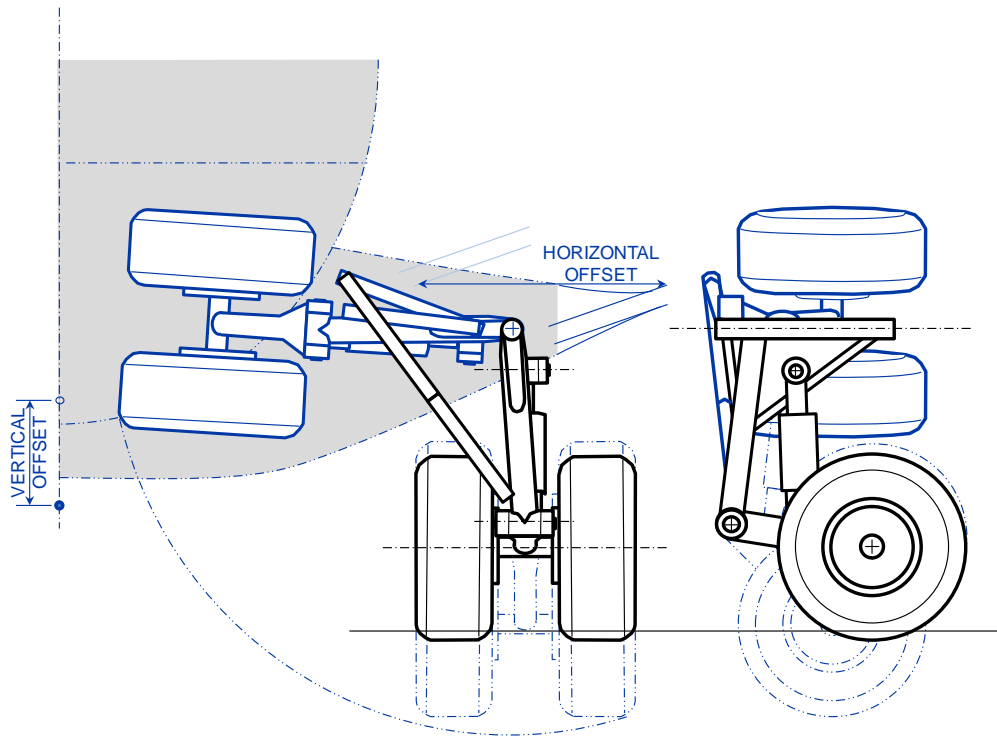


Figure 2.66 – Final Installation (765-095-RA)

The structural arrangement of the gear pylon contributes significantly to the gear arrangement selected for this study. From an external view, the pylon looks similar to a wing. This may lead to an expectation that the structure would work in a similar fashion; this is not the case. Unlike a wing, the gear pylon cannot have a lower cover panel because the gear is required to retract through the lower surface of the pylon. Figure 2.67 shows the pylon structural arrangement with each primary component labeled. There is an upper cover panel, but it cannot be extended to the centerline because the retracted gear protrudes above where the upper skin would be. The pylon structure has a forward and aft member that act as fuselage frame, pressure panel, and pylon spar. The aft member breaks forward in plan view which necessitates a longitudinal stabilization element. It also has a pylon upper skin that extends from outboard of the landing gear to the fuselage side of body. Finally, a closure panel on the tip of the pylon resists the forward and aft members from pulling apart. The following sections will illustrate the loads introduced by the wing strut and landing gear and show how those loads are intended to be handled by the pylon structure. These figures are based on design intent and do not reflect the actual load paths that the sized structure will produce.

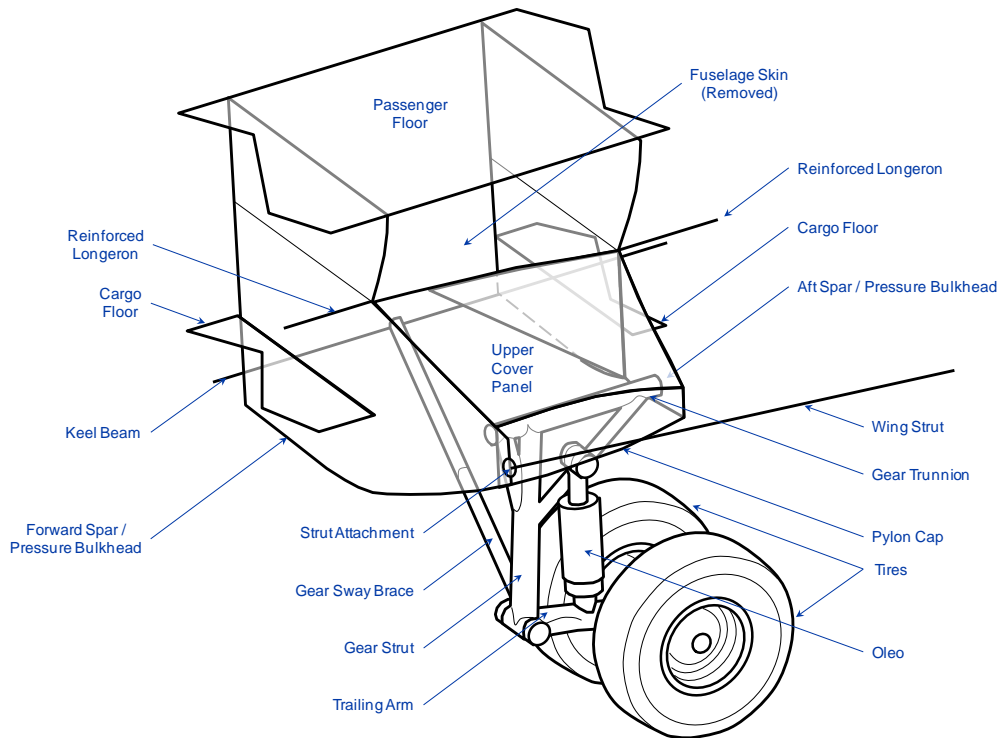


Figure 2.67 – Gear Structural Arrangement

Landing gear loads can be broken into three directions, Longitudinal, Lateral, and Vertical, each of which is handled differently by the structure. Figure 2.68 shows the intended load path for the landing gear vertical load. The load is distributed to the forward and aft spars of the gear pylon by the landing gear assembly (illustrated in blue). The majority of the landing gear load is transmitted to the rear spar due to the position of the tire relative to the trunnion attachment. The rear spar caps handle the vertical load imparted by the rear attachment of the trunnion, however the rear spar is canted forward (in plan view) and turns to align with the fuselage frames at the pylon side of body. This creates kick loads for both the upper and lower caps which are handled by the fuselage skin and longerons and a longitudinal shear member (illustrated in green) respectively. In the forward spar, the load is intended to run along the spar caps to centerline. The load in the upper cap is turned laterally toward the centerline at

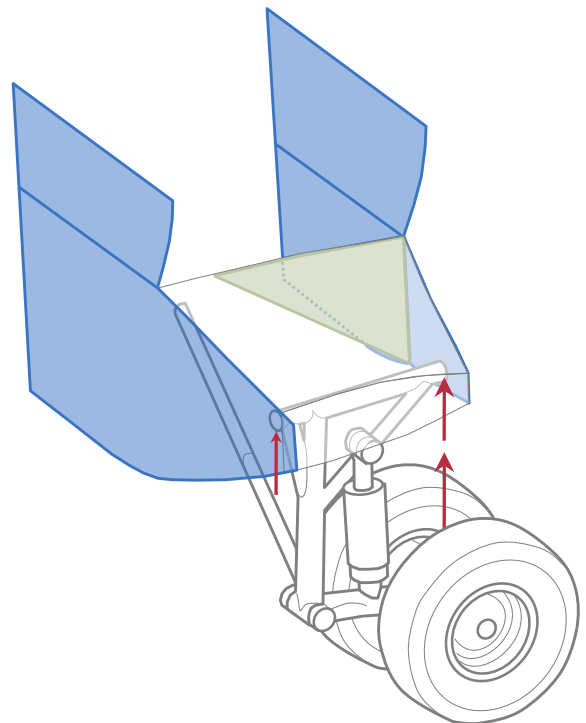


Figure 2.68 – Landing Gear Load Paths: Vertical Load

the side of body attachment which creates a kick load handled by the fuselage skin. The lower cap is turned gradually and will require stabilization members that extend upward to the fuselage frame. The current length of the trunnion is arbitrary and could be lengthened to balance the front and aft spar loads and reduce the kick loads in the aft spar through decreased turning angle.

Longitudinal loads (Figure 2.69) imparted on the landing gear are transmitted to the pylon with a torsional load that is a function of the primary loads offset from the trunnion attachment. The torsional load is handled by the same structure and in the same manner as the vertical load. The longitudinal load is reacted by the pylon upper panel (illustrated in purple) which transmits the load into the fuselage skin and longeron (not shown) via shear. This panel also stiffens the pylon in bending (vertical loads) and torsion (gear drag loads). A panel at the end of the pylon (shown in yellow) prevents the forward and aft spars from spreading apart when under load.

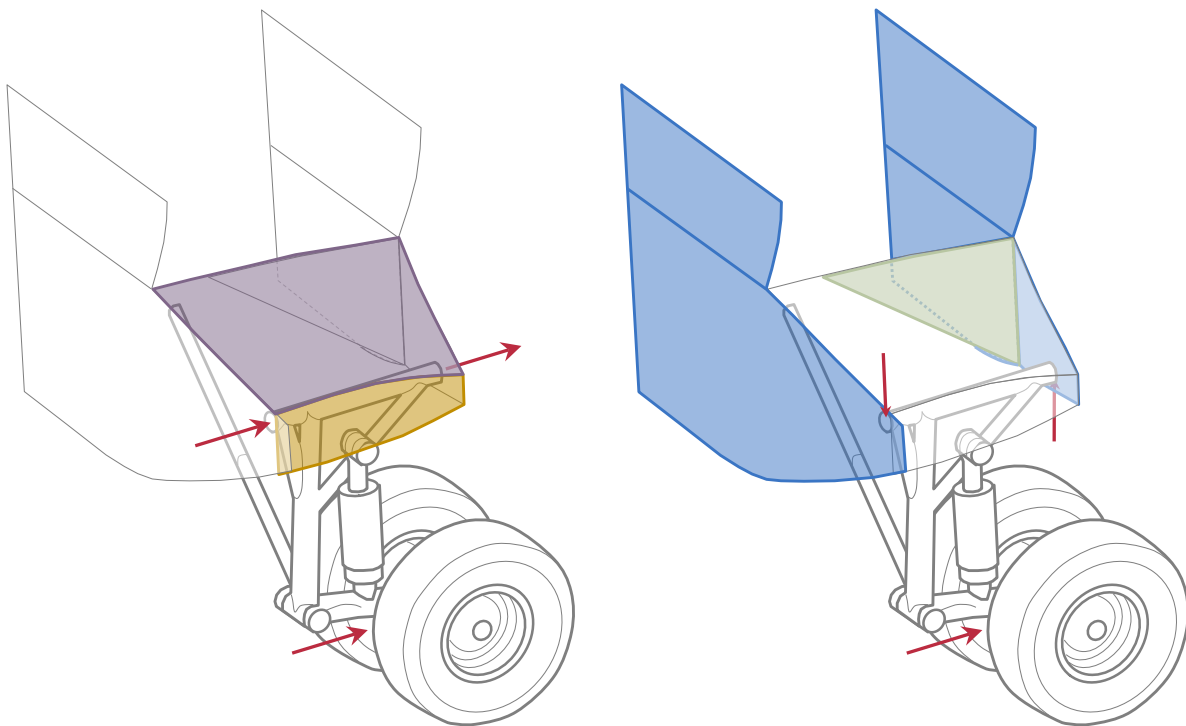


Figure 2.69 – Landing Gear Load Paths: Longitudinal Load

The load paths for lateral loads imparted on the gear are rather simple (depicted in Figure 2.70) and rely on the gear sway brace (brown) which transmits loads directly into the forward pressure bulkhead / pylon front spar (blue).

As previously mentioned, these illustrations represent the design intent only. The load will follow the path of highest stiffness which would be determined during a higher fidelity design process. This is a starting point layout that will be analyzed for the Phase II effort; no iteration is planned.

An empirical method (sensitive only to passenger cabin length) was used to estimate the longitudinal location of the landing gear. The landing gear location will be refined as more is learned about the center of gravity limits of the aircraft. As the landing gear shifts the aft fuselage loft will be revised to maintain proper tail strike clearance.

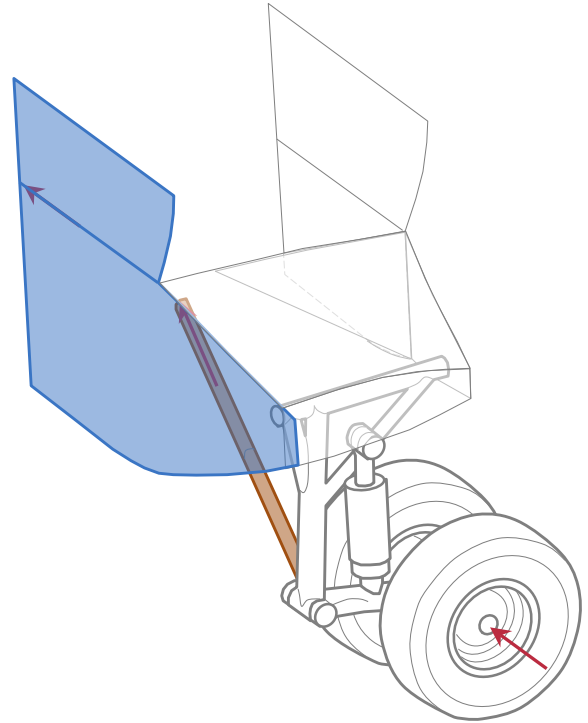


Figure 2.70 – Landing Gear Load Paths: Lateral Load

2.1.5.4 Aft Fuselage

The aft fuselage closes out the constant section with minimum drag. It must accommodate attachments for the empennage and provide adequate ground rotation for takeoff. The 765-095 configuration has higher span and lower sweep than conventional configurations which results in a higher lift curve slope. For a given wing area and gross weight, lower ground rotation angles are required to make the same lift as conventional airplanes. The tail strike angle for the 765-095 was reduced from $\sim 12.5^\circ$ to $\sim 10.5^\circ$ to account for this and the aft fuselage was re-lofted to reduce upswep drag. The ground rotation limit change was calculated by the ratio of lift curve slopes for the 765-094 and 765-095 configurations from Phase I. The change in ground rotation limit and its cascading effect on the shape of the aft fuselage is illustrated in Figure 2.71.

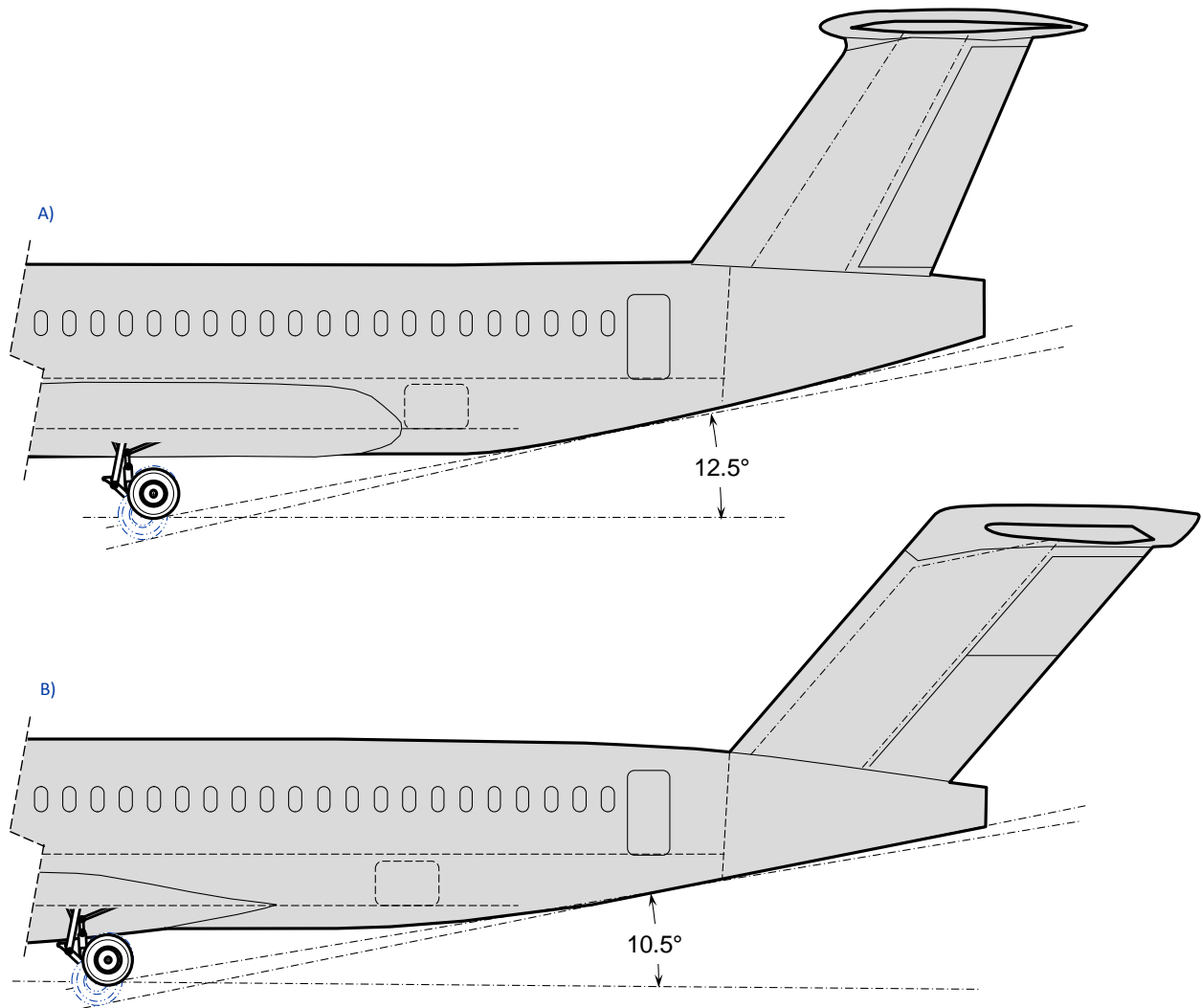


Figure 2.71 – Aft Fuselage Changes A) 765-095, B) 765-095-RC

To verify the fuselage aerodynamic performance in cruise, the fuselage OML was analyzed with the CFD++ N-S solver on a 3.5 million hybrid cell grid, using the K-Epsilon turbulence model. Figure 2.72 shows a centerline cut of local Mach number and surface pressure contours for the solution, and shows nothing adverse for the Mach 0.7, Angle of Attack 1.5°, 42,000 ft altitude condition.

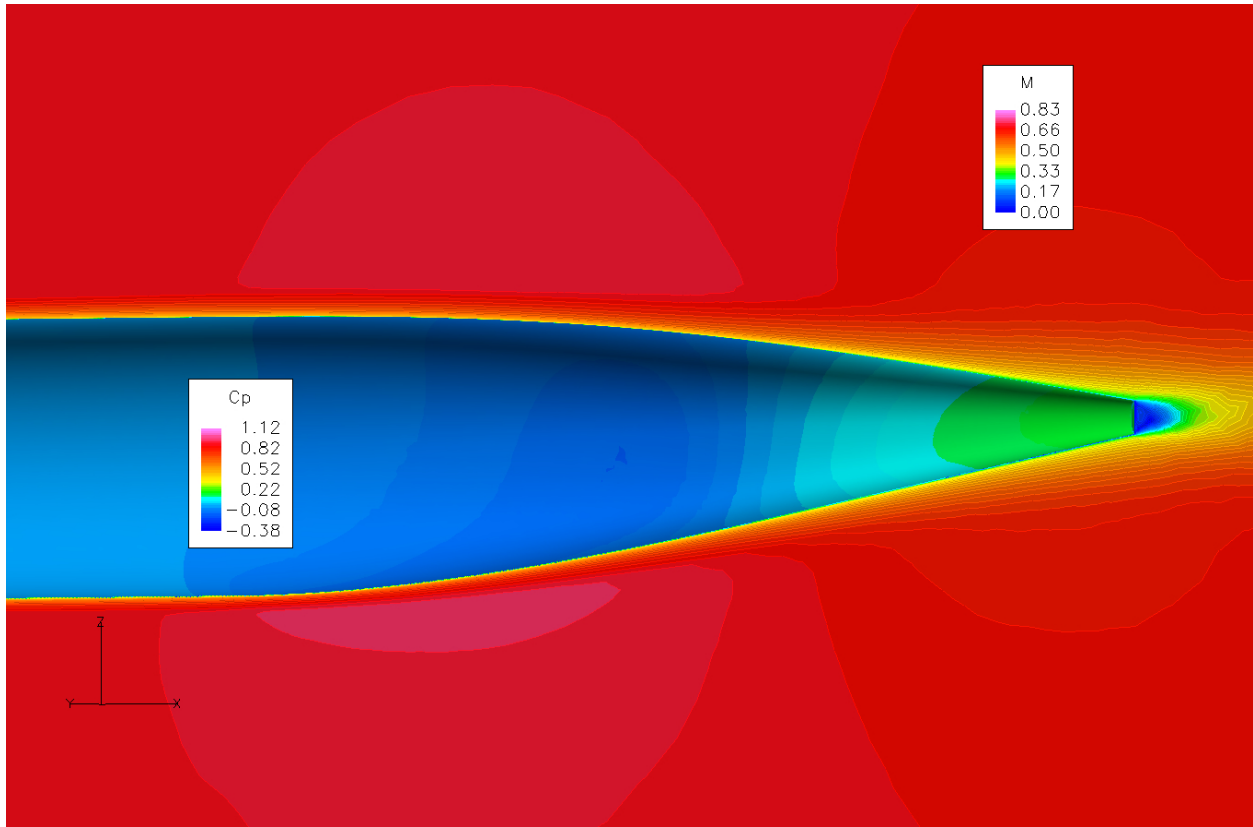


Figure 2.72 – Aft Fuselage Mach Number and Pressure Contours

2.1.5.5 Horizontal and Vertical Tail

The arrangement of the horizontal and vertical tail was updated from the initial release (Figure 2.73-A) based on Boeing's experience with small DC and MD series jets and the C-17. The vertical tail sweep was changed to increase the tail arm of the horizontal stabilizer. The horizontal stabilizer is attached to the rear spar of the vertical tail by a pin hinge at its rear spar. The horizontal forward spar is attached to a jack screw which, in turn, is attached to a diagonal structural element in the vertical tail. This accommodates movement of the entire horizontal stabilizer for trim. The vertical tail is assumed to have a single hinged rudder and both horizontal and vertical are assumed to have two spanwise segments for redundancy in the flight controls. The bullet faring shown in the initial release was replaced with a wiping surface configuration. Three degrees of anhedral is included on the horizontal tail to alleviate flutter loads which typically size portions of the vertical tail structure. The revised empennage is shown in Figure 2.73-B.

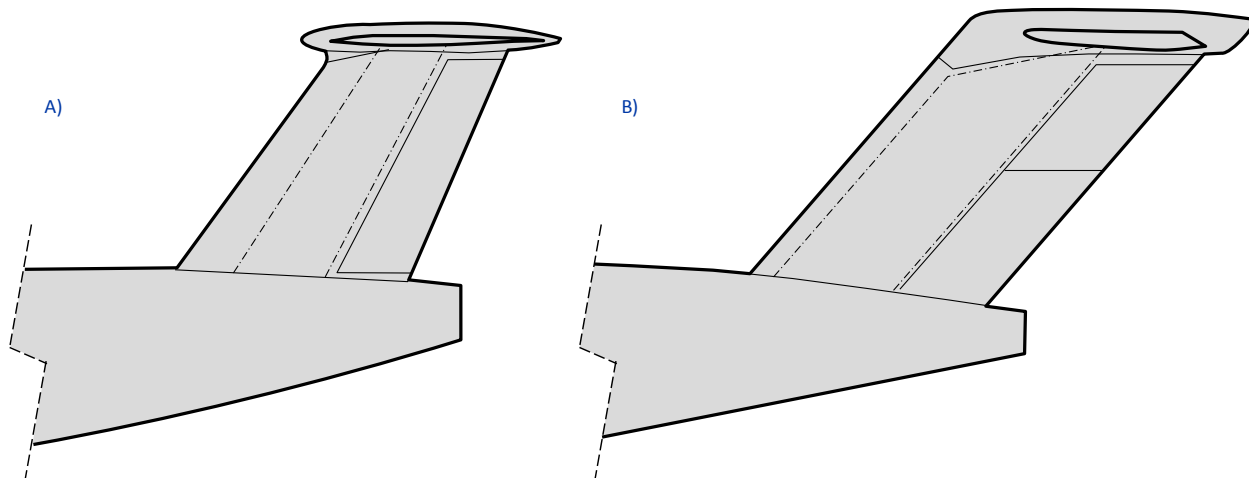


Figure 2.73 – Horizontal and Vertical Tail

2.1.6 High Speed Wing Design

At the beginning of the MDO exercise documented in Section 2.1.4.3, planform data was allowed to optimize using all variables applicable (shown in Table 2.6) resulting in configuration C210b2.17. This planform was changed as appropriate for integration and based on discipline expert review. The inboard sweep of the wing was set to align the front and rear spars with the most appropriate structure while maintaining the wing MAC at a fixed location (an empirical percentage of the passenger cabin length). The inboard taper ratio was adjusted to prevent excessive washout followed by wash in which would result from a constant chord inboard wing. The outboard wing sweep was traded in the MDO environment and the results showed the impact on fuel burn to be negligible. This allowed the outboard wing sweep to be adjusted to provide a linear rear spar at a constant percentage of chord. The rear spar and front spar are assumed to break at the side of body joint for this study. The resulting planform is depicted in Figure 2.74. It should be noted that it is assumed the strut will integrate at the planform break.

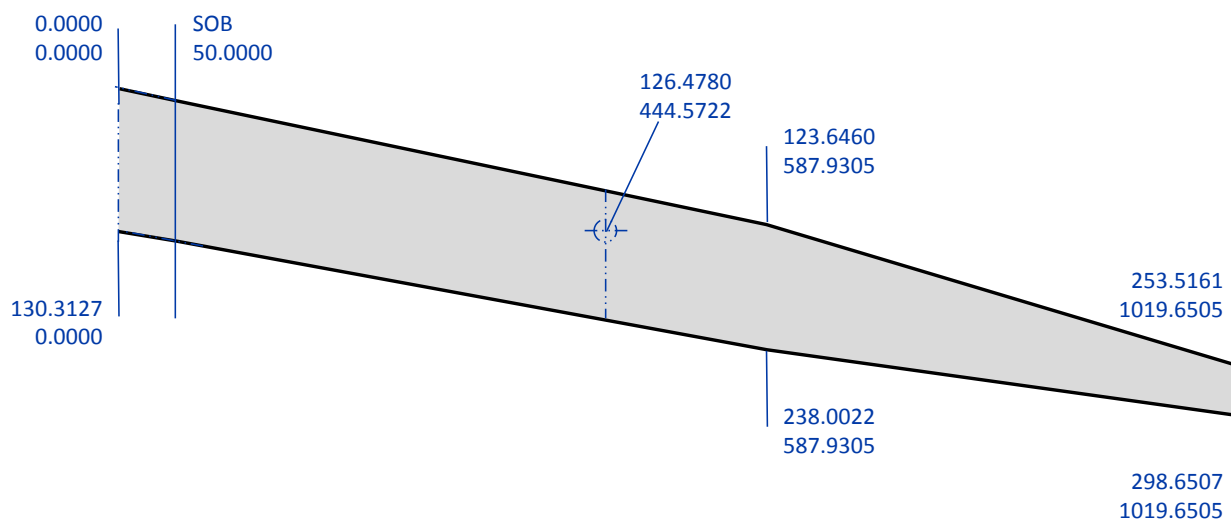


Figure 2.74 – Wing Reference Planform

In order to maintain the best possible performance after wing integration all applicable variables shown in Table 2.6 were re-optimized with exception to those shown in Table 2.10 which were driven by the wing integration, span sensitivity, and previous optimizations. The wing integration impact on fuel burn was minimal as previously shown in Figure 2.35. Anhedral was included to provide better flying qualities since wing tip clearance was not an issue at 170 feet of span.

Table 2.10 – Planform Variables Fixed by Integration

Sw
TR_inbd
TR_outbd
AR
Eta
Lambda_inbd
Lambda_outbd

Each discipline requires reference quantities based on the analysis being performed. Two tables of reference quantities are provided. Table 2.11 shows reference information in the wing reference plane (a plane coincident with the root and tip quarter chord points) while Table 2.12 shows projected reference quantities. The tables include many different formulations of reference quantities and each is used depending method requirements. This study will report all non-dimensional information using the total projected reference data unless otherwise specified.

Table 2.11 – Reference Quantities (Wing Reference Plane)

Parameter	Units	Trap	Wimp	ESDU	Total	TotExp
Area	ft.^2	1797.46	1500.81	1501.38	1477.62	1387.56
Aspect Ratio		16.078	19.256	19.249	19.559	9.418
Span	in.	2040	2040	2040	2040	969.9829
Taper Ratio		0.216	0.346	0.271	0.346	0.35
Root Chord	in.	208.6244	130.3127	166.8247	130.3127	128.9557
Tip Chord	in.	45.1346	45.1346	45.1346	45.1346	45.1346
SOB Chord	in.	200.6075		160.8574	128.9557	
Sweep LE	deg.	16.74	13.47	15.26	13.47	13.57
Sweep 25%	deg.	14.61	12.51	13.66	12.51	12.58
Sweep 50%	deg.	12.44	11.55	12.04	11.55	11.58
Sweep TE	deg.	7.99	9.61	8.73	9.61	9.56
MAC	in.	144.4348	110.286	117.6238	110.286	109.0301
Ybar	in.	400.4738	444.7246	412.3996	444.7246	471.9676
XLEmac	in.	67.214	98.9065	87.7203	98.9065	104.985
Xc/4	in.	103.3227	126.478	117.1263	126.478	132.2426

Table 2.12 – Reference Quantities (Projected)

Parameter	Units	Trap	Wimp	ESDU	Total	TotExp
Area	ft.^2	1796.84	1500.29	1500.86	1477.11	1387.09
Aspect Ratio		16.073	19.25	19.242	19.552	9.414
Span	in.	2039.3009	2039.3009	2039.3009	2039.301	969.6505
Taper Ratio		0.216	0.346	0.271	0.346	0.35
Root Chord	in.	208.6244	130.3127	166.8247	130.3127	128.9557
Tip Chord	in.	45.1346	45.1346	45.1346	45.1346	45.1346
SOB Chord	in.	200.6075		160.8574	128.9557	
Sweep LE	deg.	16.74	13.47	15.27	13.47	13.58
Sweep 25%	deg.	14.61	12.52	13.67	12.52	12.58
Sweep 50%	deg.	12.44	11.56	12.04	11.56	11.58
Sweep TE	deg.	8	9.61	8.73	9.61	9.56
MAC	in.	144.4348	110.286	117.6238	110.286	109.0301
Ybar	in.	400.3365	444.5722	412.2583	444.5722	471.8059
XLEmac	in.	67.214	98.9065	87.7203	98.9065	104.985
Xc/4	in.	103.3227	126.478	117.1263	126.478	132.2426

2.1.6.1 Preliminary Wing Design

The university MDO played a pivotal role in generating the baseline wing loft for the SUGAR program. The following data were used as design constraints:

- Airplane Drag Rise Slope at 0.7 Mach: 0.021 (rounded to 0.025)
- Wing Planform
- Wing Spanwise Loading

Boeing used Flo22 to analyze the resulting wing planform and set the wing thickness distribution and twist while accounting for body effects. It should be noted that the drag rise Mach number prediction in the method is more reliable than the level of compressibility drag it computes (based on flight tests and wind tunnel data). For this reason, the drag axis is intentionally omitted from the charts that use this method, Overflow analysis, discussed in Section 2.1.6.2, will be used for drag computation and comparison. Flo22 is computationally less expensive allowing for much iteration prior to the use of higher fidelity methods.

In order to understand what levels of compressibility could be attained, a first pass analysis was completed using a constant 10.6% thickness-to-chord ratio and the L1 airfoil documented in Section 2.1.4.2. The wing was twisted to provide an elliptic distribution, a convenient distribution for wing design comparisons. As illustrated in Figure 2.75, the constant thickness-to-chord wing provided drag divergence margin of approximately 0.02 Mach at the targeted 0.025 divergence criteria.

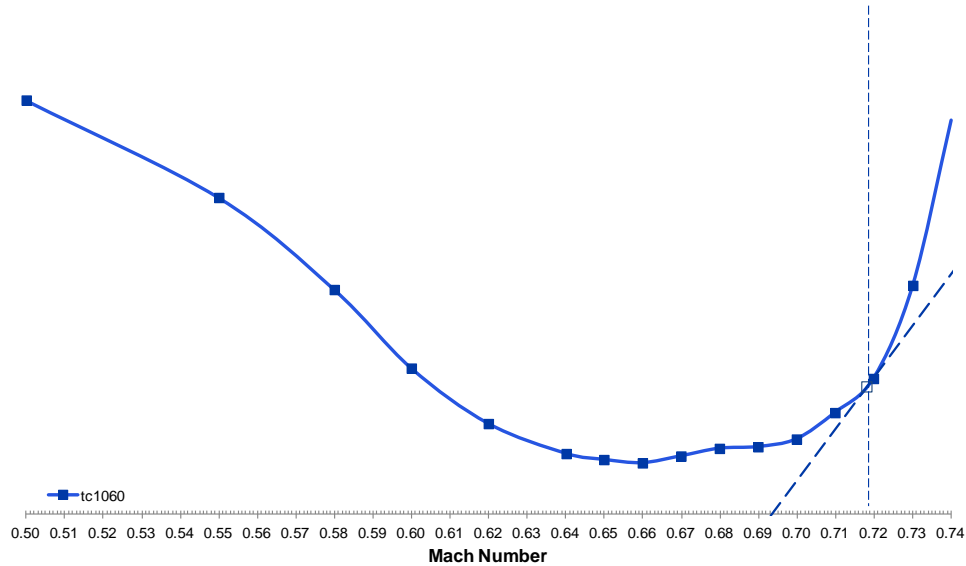


Figure 2.75 – Constant 10.6% t/c Drag Rise

Because the drag divergence requirement was exceeded, three different wing thickness distributions were generated. Discussions with Mass Properties, Structures, and Aerodynamic designers resulted in a strategy of holding wing thickness constant from the wing root to the strut attachment, holding maximum thickness-to-chord ratio constant between the strut attachment and the wing fold, and providing conventional wing thickness-to-chord distributions outboard. The tip thickness-to-chord ratio was held 1.4% lower than the max based on historical wing designs. The three wing thickness distributions generated with this strategy (tmod1 thru tmod3) start with a maximum thickness of 12% and increase by 0.5% each intending to bracket the drag divergence criteria. Table 2.13 and Figure 2.76 show each of these three wing thickness distributions as well as the University and constant 10.6% distributions.

Table 2.13 – Thickness Distributions of Various SUGAR Wing Options

eta	Univ	tc1060	tmod1	tmod2	tmod3
0.05	0.08229	0.10600	0.10674	0.11091	0.11535
0.15	0.08666	0.10600	0.10877	0.11330	0.11784
0.3	0.09333	0.10600	0.11247	0.11716	0.12185
0.45	0.09999	0.10600	0.11643	0.12128	0.12614
0.58*	0.10562	0.10600	0.12000	0.12500	0.13000
0.70	0.10242	0.10600	0.12000	0.12500	0.13000
0.80	0.09983	0.10600	0.11729	0.12229	0.12729
0.90	0.09724	0.10600	0.11314	0.11814	0.12314
1.00	0.09464	0.10600	0.10600	0.11100	0.11600

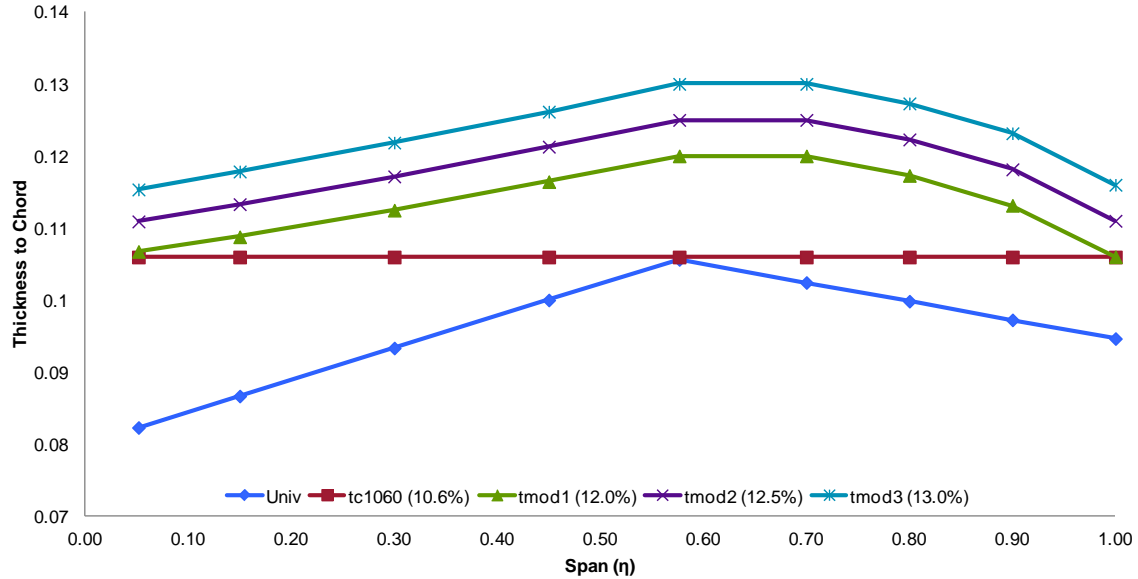


Figure 2.76 – Thickness-to-Chord of Various Airfoils

Drag divergence curves were computed for wing thicknesses tmod1 thru tmod3. These results, compared in Figure 2.77, indeed bracket the required cruise Mach Number with a drag divergence slope of 0.25 with both tmod1 and tmod2 meeting the criteria. It is expected that there will be small drag divergence knockdowns encountered for washout (to attain a more structurally favorable lift distribution) and trim. Table 2.14 shows characteristics including average exposed thickness-to-chord ratio, design lift coefficient, drag divergence Mach number, and Korn factor for each of the airfoils analyzed.

The airfoil design used in the design was originally generated for a lift coefficient of 0.9 and had a shock location at 57% chord. Since the wing design process was performed for a lift coefficient of 0.7, the shock moved forward to 55% chord for a 12% thickness-to-chord ratio. An additional airfoil exploration was performed updating design parameters to the actual wing design conditions. Airfoil L2 was generated which pushed the shock back to 62% at 12% thickness-to-chord ratio. This airfoil was designed for a lift coefficient of 0.725, the maximum sectional lift coefficient for the wing planform at a cruise lift coefficient of 0.7. A thicker section (L3) was also designed but was determined to have lower performance than L2 for this configuration.

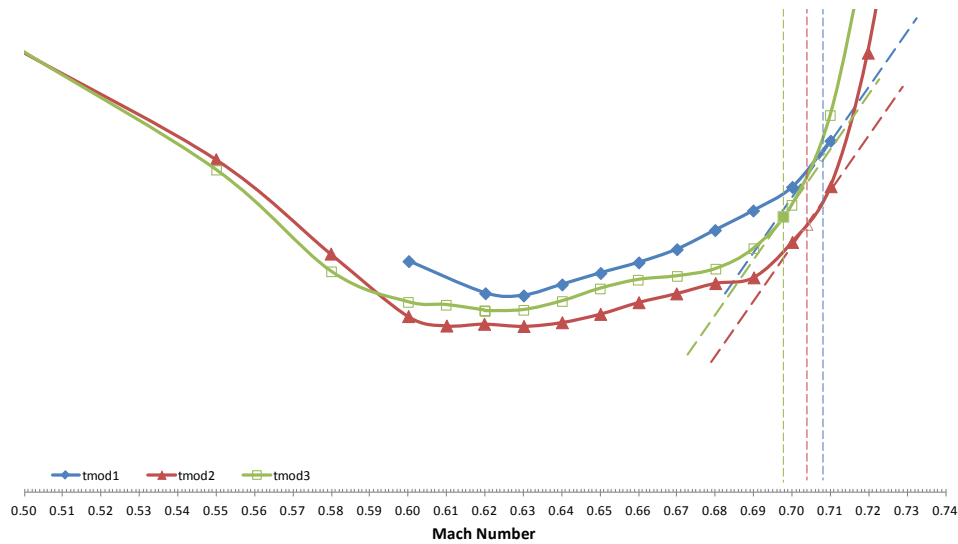


Figure 2.77 – Drag Rise for tmod1 thru tmod3

Table 2.14 – Properties for Wings tmod1 thru tmod3

	tc1060	tmod1	tmod2	tmod3
Avg. Exposed Thickness	0.1060	0.1143	0.1192	0.1240
Design CL	0.70	0.70	0.70	0.70
Divergence Mach # (@0.025 Slope)	0.7184	0.7076	0.7040	0.6980
Korn Factor (@0.025 Slope)	0.8944	0.8919	0.8932	0.8920

The wing loft was updated and named tmod2 x, which utilized the L2 airfoil using the same thickness distribution which resulted in a drag rise curve as depicted in Figure 2.78. It is shown that the new wings drag divergence Mach number decreased to 0.699 which is deemed not enough after the expected twist and trim knockdowns. A hybrid airfoil (created by averaging cross sections L1 and L2) was also run (tmod h), its drag divergence was not significantly better than tmod2 x. It should be noted that, as previously stated, the actual drag levels are not as important as the drag divergence calculation and that these results are for elliptic span loading.

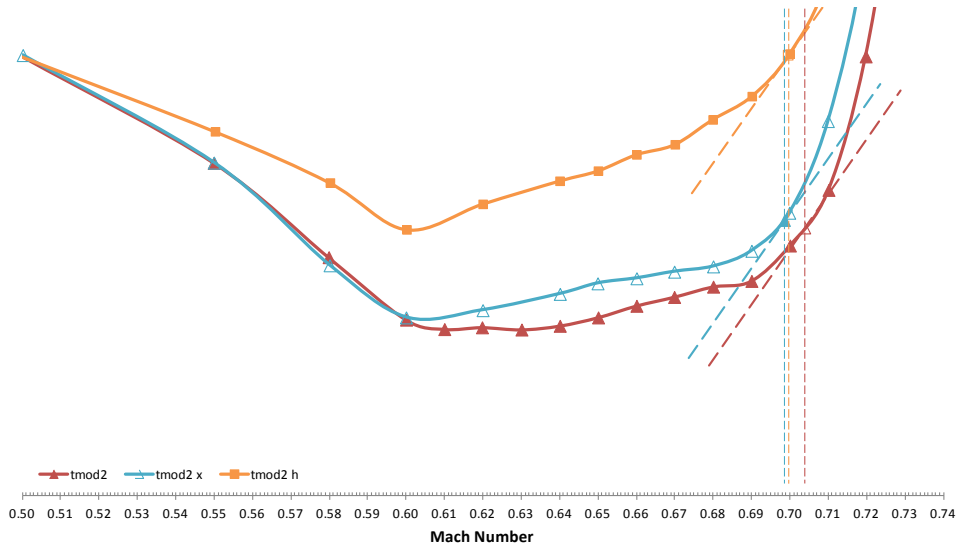


Figure 2.78 – Drag Divergence for Perturbations on Base Laminar Airfoil

The original tmod2 cross section was picked because the modified configurations would have required up to a ½% thickness penalty to recapture the drag divergence goal. Drag levels were not significantly different between all the designs because increased laminar run benefits were offset by increased compressibility drag.

Table 2.15 – Properties for Wings with Modified Airfoils

	tmod2	tmod2 x	tmod2 h
Avg. Exposed Thickness	0.1192	0.1192	0.1192
Design CL	0.70	0.70	0.70
Shock Location (%)	55	58	62
Divergence Mach # (@0.025 Slope)	0.7040	0.6986	0.6998
Korn Factor (@0.025 Slope)	0.8932	0.8878	0.8890

With the final wing cross section selected, the elliptic distribution was updated to match the university generated optimum twist distribution. A comparison between the elliptic, university, and final wing twist is shown in Figure 2.79. The wing twist schedule (airfoil twist vs. span) is illustrated in Figure 2.80. Figure 2.81 shows the effect of twist on drag divergence. The university lift distribution could not be matched in the region of the body due to the body’s influence on the wing. The finalized wing properties are summarized in Table 2.16.

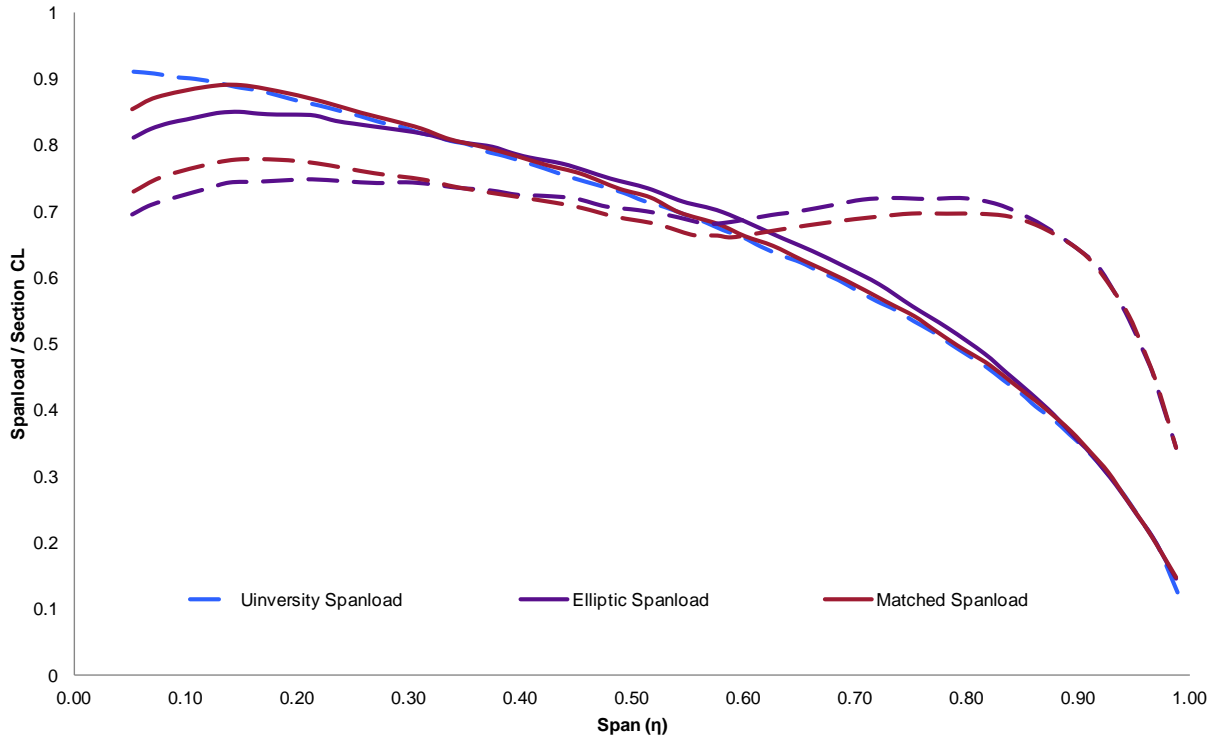


Figure 2.79 – Spanload Distribution of University Goal, Elliptic, and Boeing Wings

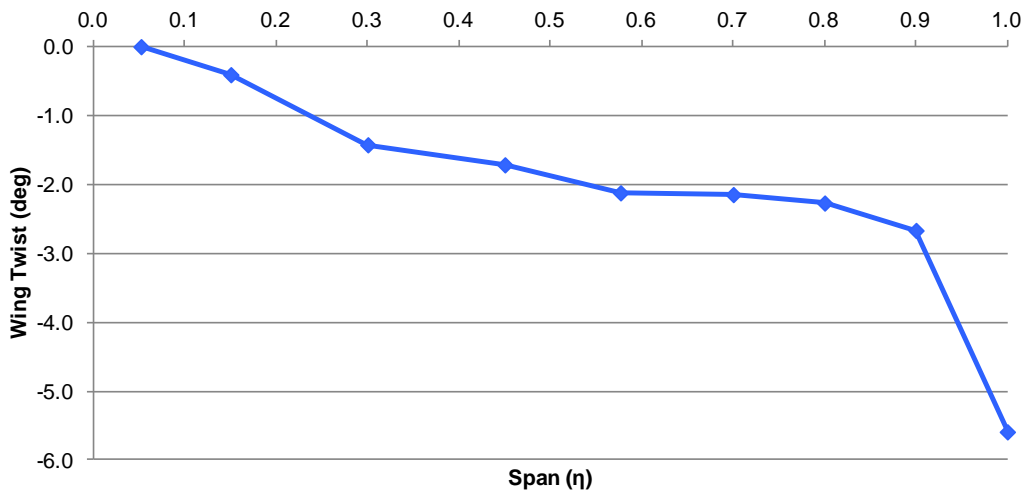


Figure 2.80 – Final SUGAR Wing Twist

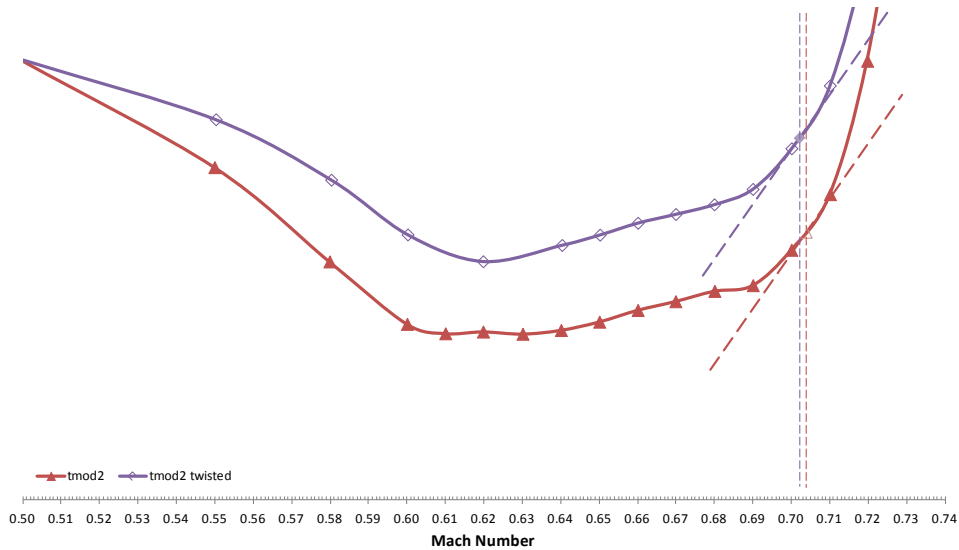


Figure 2.81 – Twist Change in Drag Rise Mach Number

Table 2.16 – Properties for Final SUGAR Wing

	tmod2	Twisted
Avg. Exposed Thickness	0.1192	0.1192
Design CL	0.70	0.70
Divergence Mach # (@0.025 Slope)	0.7040	0.7022
Korn Factor (@0.025 Slope)	0.8932	0.8914

2.1.6.2 Overflow Analysis

The wing geometry developed in Section 2.1.6.1 was analyzed using Overflow (version 2.2c) to generate data for lift and drag that could be used in the aeroelastic FEM and CASES aerodynamic build-up. Consistent with the Flo22 analysis, both the wing and body were included in the analysis. A low fidelity wing-to-body fairing was generated; the results of the CFD solution in the immediate regions around the fairing may not be representative of the finalized geometry however, the results appeared to be within reason. The overflow grid included 13 zones and contained 14.4 million points. The solution was generated with QCR enabled, the SA-RC turbulence model, and upwind differencing.

Drag rise was calculated from Mach 0.5 to 0.76, CL sweeps were generated at various Mach Numbers to calculate lift curve slope for the FEM and to determine viscous e (an input to CASES aerodynamic methods), and a drag polar was developed to determine the optimum cruise lift coefficient. These high speed solutions were calculated at a cruise altitude of 42,000 feet, 11.2 million Reynolds Number, at Mach 0.7.

The boundary conditions for the model assumed that the body was fully turbulent and that the wing was laminar on the upper surface from 8.3% span to 93.8% span. The laminar region starts at the stagnation point and propagates aft until transition. The transition location was determined by first solving a fully turbulent solution and manually inspecting the solution for pressure gradients favorable for laminar flow. These regions were updated with laminar boundary conditions and the solution was restarted. The wing tip was not included due to poor gradients and turbulent interference from the tip. The wing root region was not included because of the turbulence generated by the body. The wing lower surface transitioned to turbulent after only a few gridlines. Figure 2.82 shows examples of the laminar flow regions of the SUGAR wing for various flight conditions. Table 2.17 shows the calculated laminar flow regions for various conditions run.

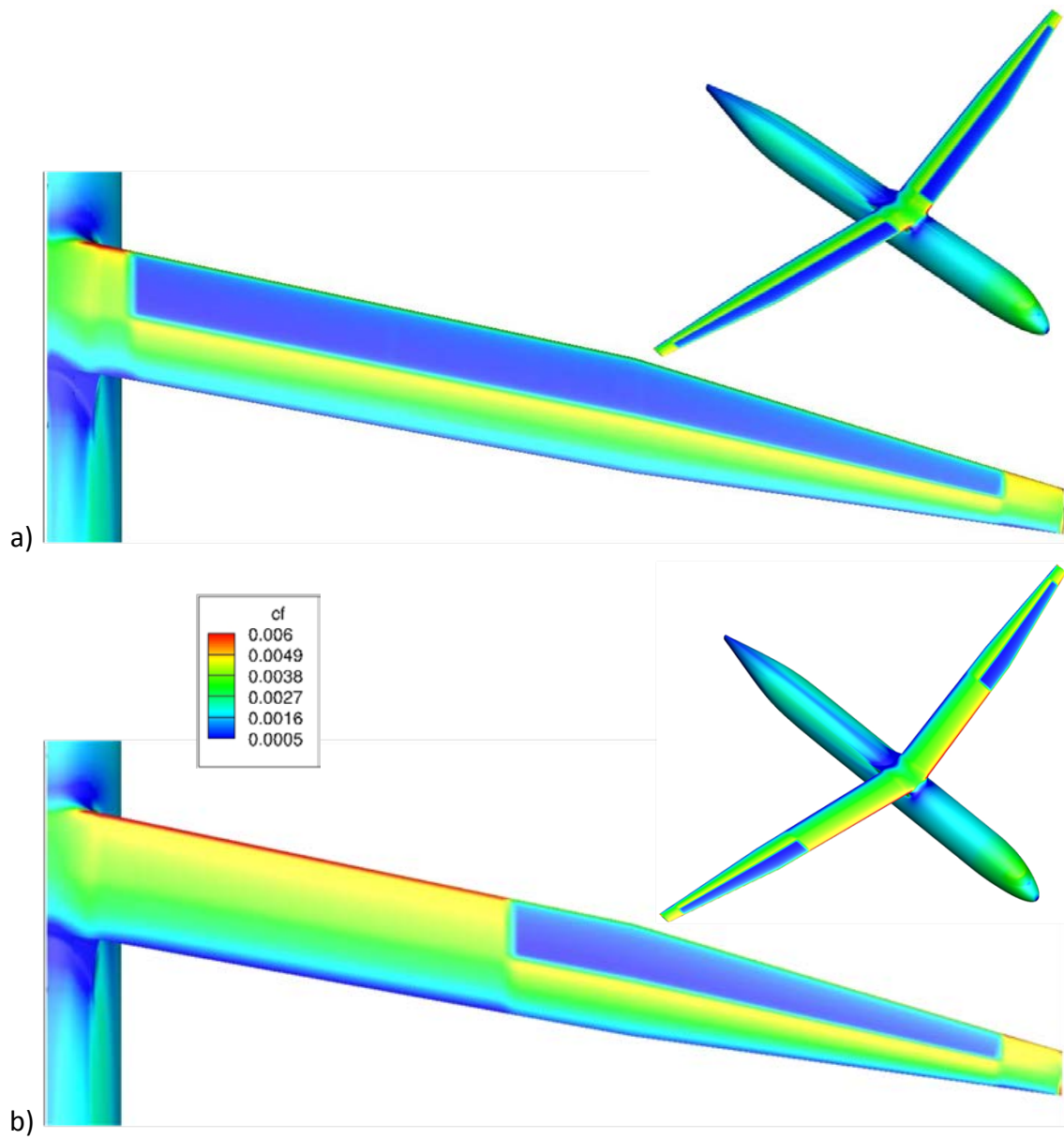


Figure 2.82 – CF Plot Depicts Regions of Laminar Flow a) Mach 0.70, CL 0.70, b) Mach 0.65, CL 0.70

Table 2.17 – Flight Conditions and Laminar Flow Extent

Mach	CL	Chordwise Extent of Laminar Flow
0.50	0.20	49.40%
0.50	0.40	49.40%
0.50	0.70	0.60%
0.60	0.70	1.00%
0.65	0.70	1.5% Inboard 49.4% Outboard
0.69	0.70	1.5% Inboard 49.4% Outboard
0.70	0.40	49.40%
0.70	0.70	49.40%
0.71	0.70	51.80%
0.74	0.70	54.20%
0.76	0.40	65.70%
0.76	0.70	65.70%

The wing drag rise was calculated via the Overflow analysis. The results are plotted in Figure 2.83 along with the final twisted wing drag rise calculated from Flo22. The turbulent curve corresponds to the Overflow results with a fully turbulent boundary condition. The fully laminar curve is calculated using input regions of laminar flow based on the turbulent results. The laminar curve with pressure drag credit only is the same solution as the full laminar curve ignoring the reduction in drag due to skin friction. The Overflow results might predict a slightly faster drag divergence Mach number than Flo22. The drag levels of the Flo22 results should be ignored.

Aerodynamic buildups calculated in CASES start with a fully turbulent assumption anchored at Mach 0.50 and book keep all Mach number induced changes in drag from the anchor point as compressibility effects. The internally calculated compressibility drag (which would follow a curve similar to the turbulent line) can be adjusted by a compressibility correction table (a function of Mach and CL). The CASES compressibility correction was calculated using the offset between turbulent and fully laminar curves such as those below. The drag increment from the cruise condition (Mach 0.7; Cl 0.7) is shown in Table 2.18. This includes the increment for the pressure and laminar skin friction coefficient (summing the turbulent, pressure, and skin friction components totals to the laminar flow compressibility drag increment).

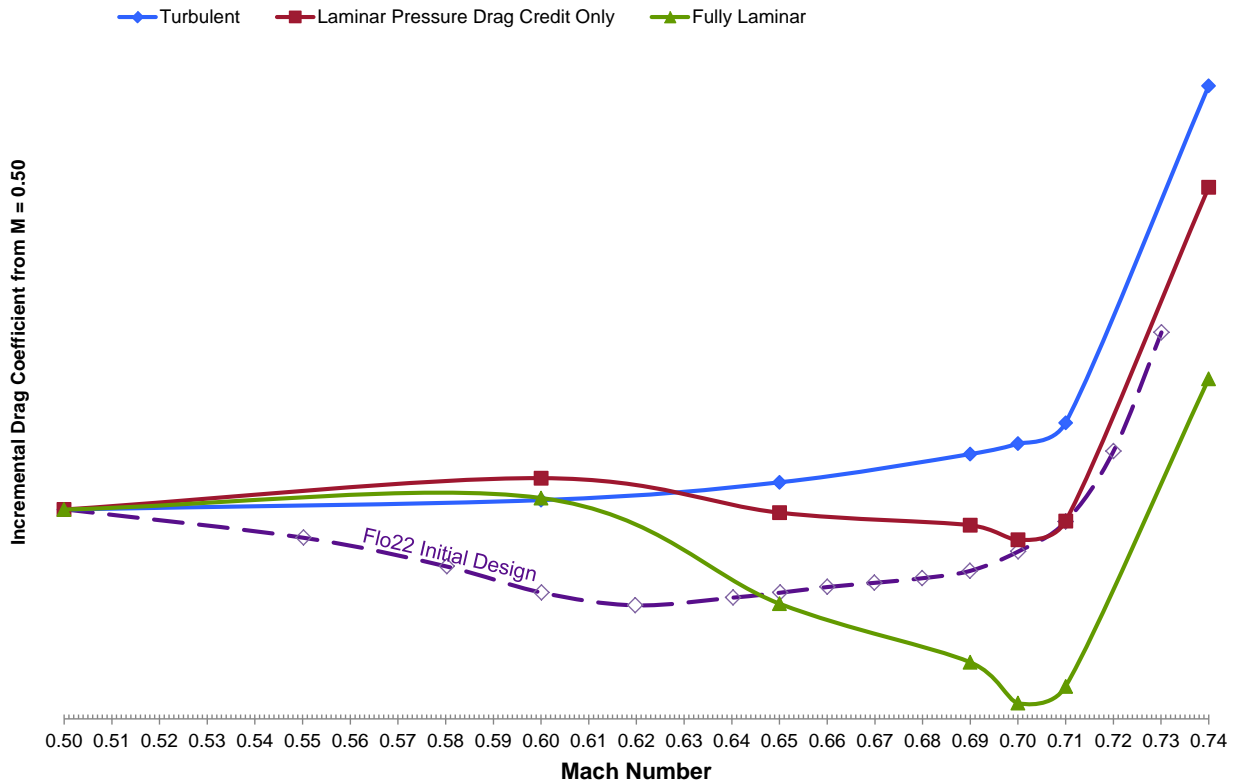


Figure 2.83 – Overflow Drag Rise CL 0.70

Table 2.18 – Drag Buildup from Turbulent Overflow Solution

Turbulent	Delta	from	0.00063
M=0.5			
Laminar Pressure	Delta		-0.00092
Laminar Cf	Delta		-0.00166
Total Drag	Delta	from	-0.00185
M=0.5			

Initial passes at aerodynamic buildups indicated that the wing may want to operate at higher lift coefficients than the initial estimate of 0.70. To verify this, the Overflow analysis was used to investigate the aircraft drag polar to higher lift coefficients. Figure 2.84 shows that even up to a lift coefficient of 0.8 the polar remains fairly linear. Lift-to-drag ratio at a lift coefficient of 0.7 is 33.05 and increases to 33.27 at a lift coefficient of 0.8. For further verification, the drag rise curve was recalculated at a lift coefficient of 0.8. Figure 2.85 shows a slight decrease in drag divergence due to the higher lift coefficient but still shows a drag divergence Mach number greater than 0.70.

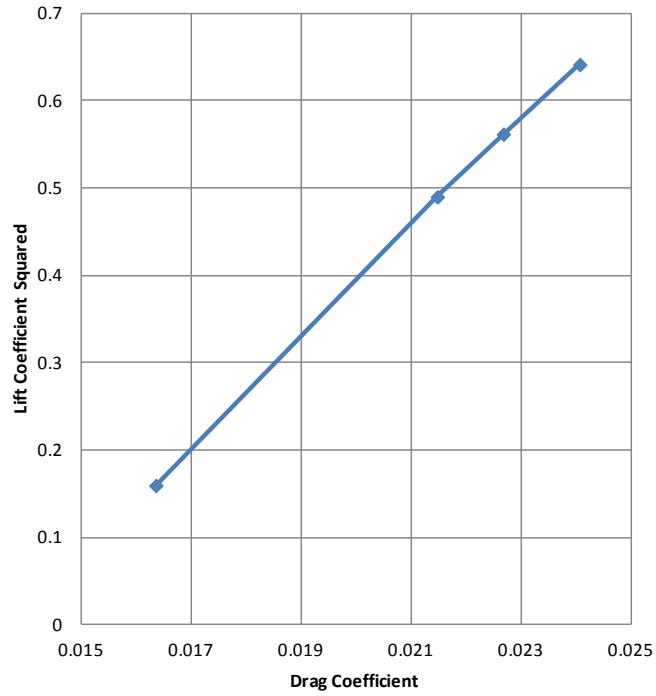


Figure 2.84 – Overflow Drag Polar at Mach 0.70

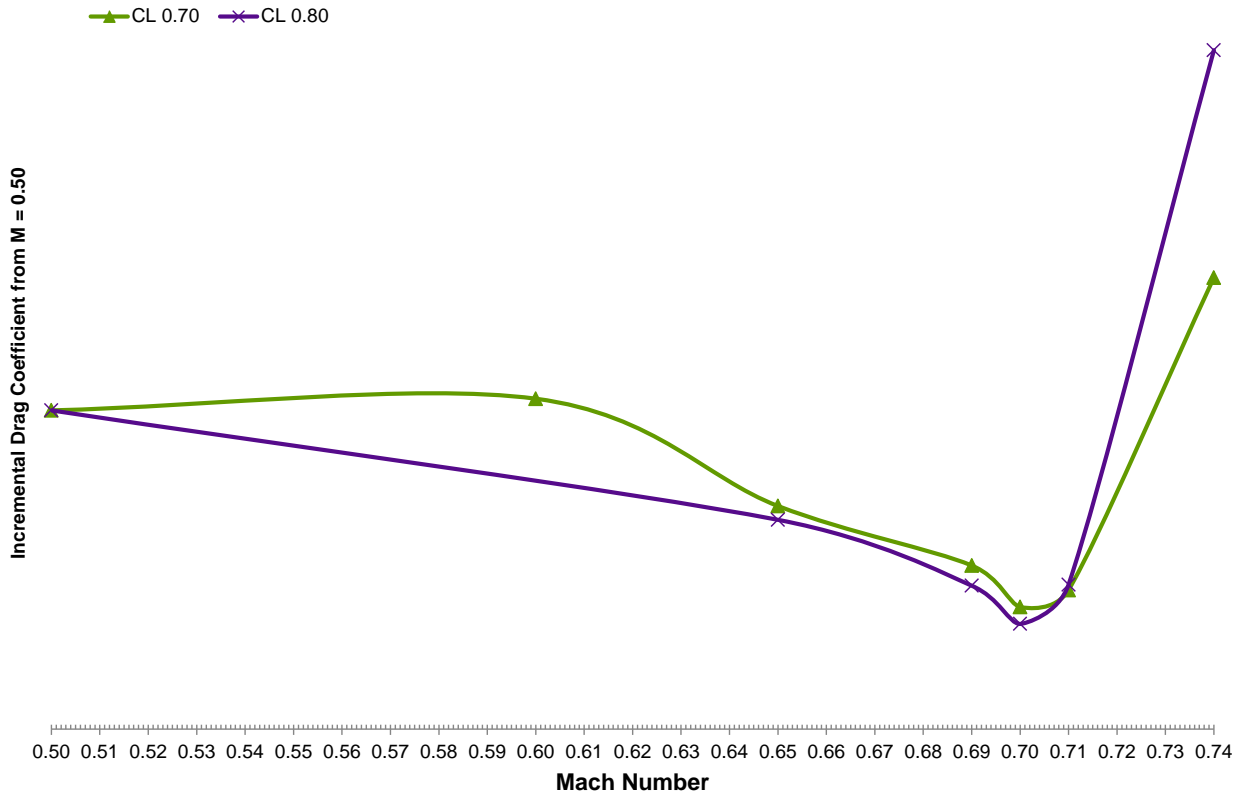


Figure 2.85 – Overflow Drag Rise at Higher CL's

CASES buildups require a viscous e at 0.50 Mach number for drag calculation. CASES empirical methods can estimate these values but the database that supports the estimation does not include aircraft in the vicinity of aspect ratio 20. To verify the calculation performed by CASES, a drag polar was generated at Mach 0.50 and includes both viscous and laminar curves. The viscous curve corresponded very closely with the CASES prediction (shown in Section 2.3.1). The CASES calculated value was not calibrated. A comparison of the laminar wing span loads and sectional lift coefficients are shown in Figure 2.86.

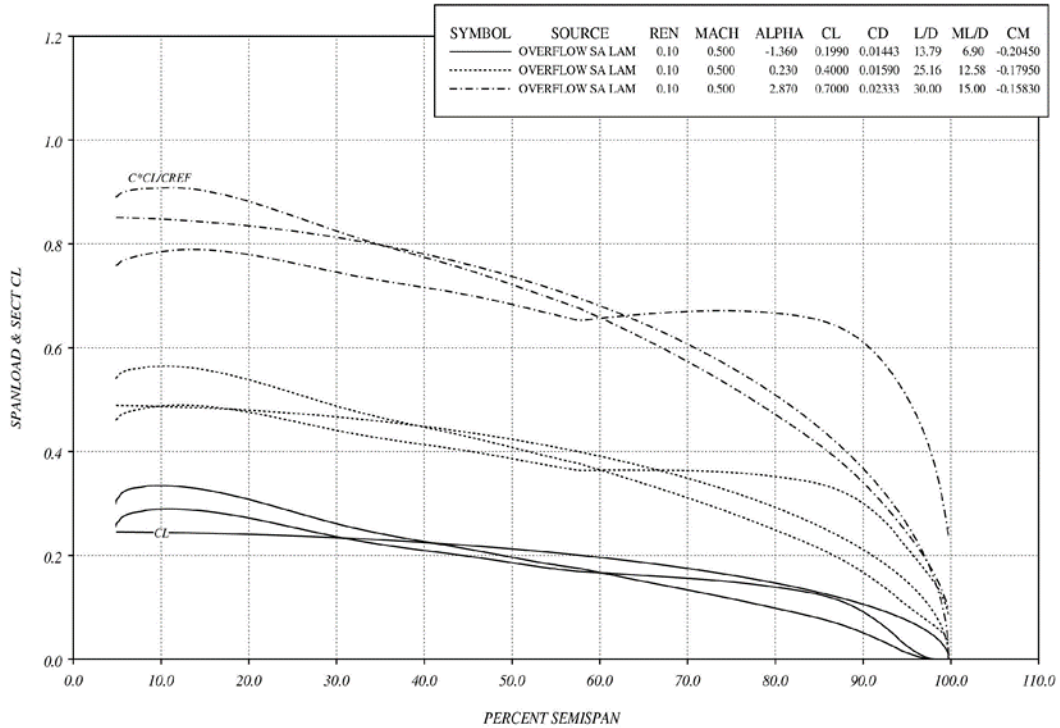


Figure 2.86 – Comparison of Span Load and Sectional Lift Coefficient Distributions for SUGAR Wing – Body

In addition to calibrating the aerodynamic buildup, the Overflow analysis was used to generate data for the aeroelastic FEM. The flight envelope of the airplane was swept from lift coefficients ranging from -0.2 to 0.8 across Mach numbers ranging from 0.5 to 0.9. The resulting lift curve slopes are shown in Figure 2.87. Spanwise aerodynamic centers were also generated.

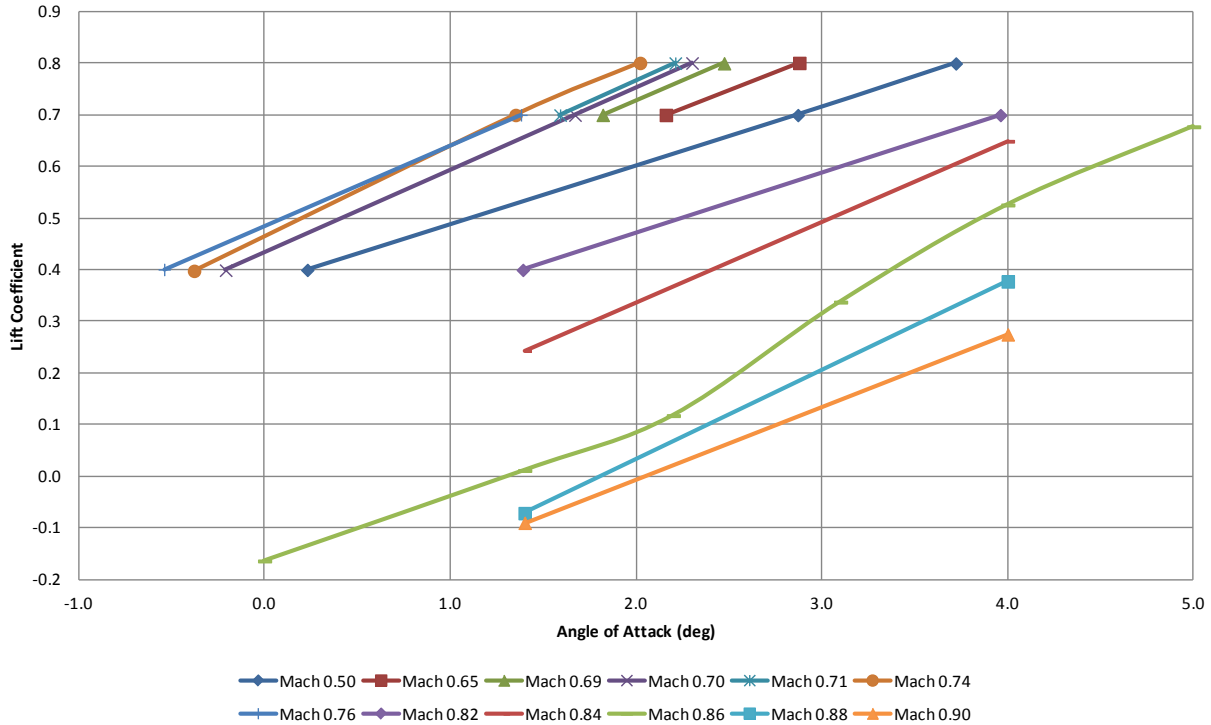


Figure 2.87 – Lift Curve Slope for Various Mach Numbers

2.1.7 Low Speed Wing Design

The high lift system design and analysis task for the truss braced wing (TBW) configuration consisted of the definition of the surface geometry and deployed rigging positions of the leading edge Krueger and trailing edge flaps followed by the estimation of the low speed lift and drag characteristics as a function of the Krueger and trailing edge flap deflections.

The Krueger and flap sectional shapes were defined using a series of non-dimensional shape parameters developed from previous high lift system design studies. The surfaced Krueger geometry was defined in two spanwise components separated by the leading edge planform break location. The single element trailing edge flap was defined in two spanwise segments albeit with continuous surfaces; this arrangement would be consistent with the flaperons located aft of each engine.

The rigged (i.e., deployed) position of the Krueger and flaps were specified in terms of their streamwise deflection and corresponding gap and overhang relative to the wing box. For the flaps a generic rigging schedule was used which was representative of a typical fowler-motion flap as a function of the deflection. Deployed flap positions were defined for streamwise deflections of 10°, 20°, and 30°. No optimization was performed on the maximum landing flap deflection or on the rigging positions (in terms of gap and overhang).

Leading edge Krueger deflections were defined for 35°, 40°, 45°, 50°, and 55° positions. For simplicity each Krueger deflection used the same gap and overhang position which was defined

using the results of previous Boeing proprietary Krueger design studies. The Krueger deployed position was then established using Boeing low speed max lift coefficient methodology. The max lift coefficient method uses solutions from the Boeing proprietary panel method code DACVINE (Douglas Aircraft Company Viscous Neumann) (11) coupled with an empirical “delta pressure coefficient peak” criteria (12). The DACVINE code is a fast, flexible, and robust panel method flow solver capable of handling complex geometries such as a complete aircraft configuration with the high lift system deployed. The code employs relatively simple surface paneling along with non-linear Kutta condition and mathematically consistent higher-order formulation. The delta pressure coefficient peak criteria was developed from a large database of 2-D high lift system wind tunnel test results coupled with an empirical flap reduction schedule which accounts for three-dimensional viscous effects on the high lift system. A flap reduction schedule was developed through correlation with proprietary 3-D full-span high lift wind tunnel test data; the correlation includes a variation to account for Reynolds Number effects. Thus, for this study the 10°, 20°, and 30° *geometric* flap deflections were simulated using equivalent *effective* flap deflections (i.e., lower) using the flap reduction schedule. Note that the flap reduction schedule only applies to the trailing edge elements; leading edge devices such as slats and Krueger flaps are analyzed using their actual geometric deflection.

Lift curves and max lift coefficient values were determined for each of the five Krueger deflections (35° to 55°) with the trailing edge flap position set at the equivalent 30° landing position. Based on these results the 50° Krueger deflection was selected as the optimum; this Krueger deflection was used for all subsequent configurations during the TBW high lift system development. Sample results from the study showing the DACVINE predicted Krueger delta pressure coefficient peak values along with the delta pressure coefficient peak criteria are given in Figure 2.88 for the 50° Krueger / 30° flap configuration.

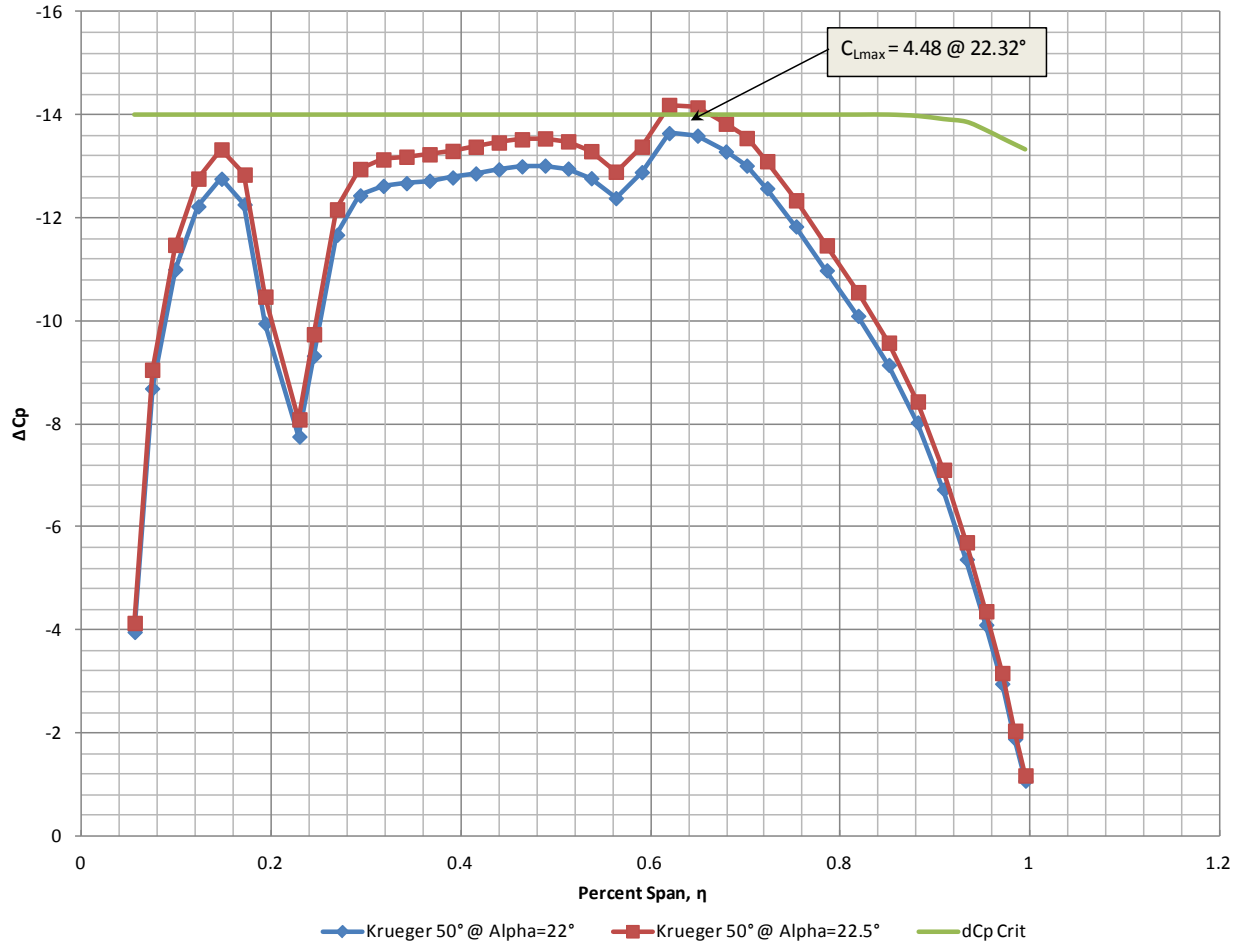


Figure 2.88 – Predicted ΔC_p -peak Levels on the 50° Leading Edge Krueger.

In addition to evaluating the effects of the Krueger and flap deflections DACVINE was also used to evaluate the effects of the engine nacelles, pylon, wing strut, and gear pods on the low speed configuration. A table showing all of the configurations evaluated during the high lift design process is shown in Figure 2.89. The reference condition used for the high lift analysis study was Mach: 0.20, Altitude: 10,000 ft. This results in an MAC and tip Reynolds number of 9.8 Million and 4 million respectively.

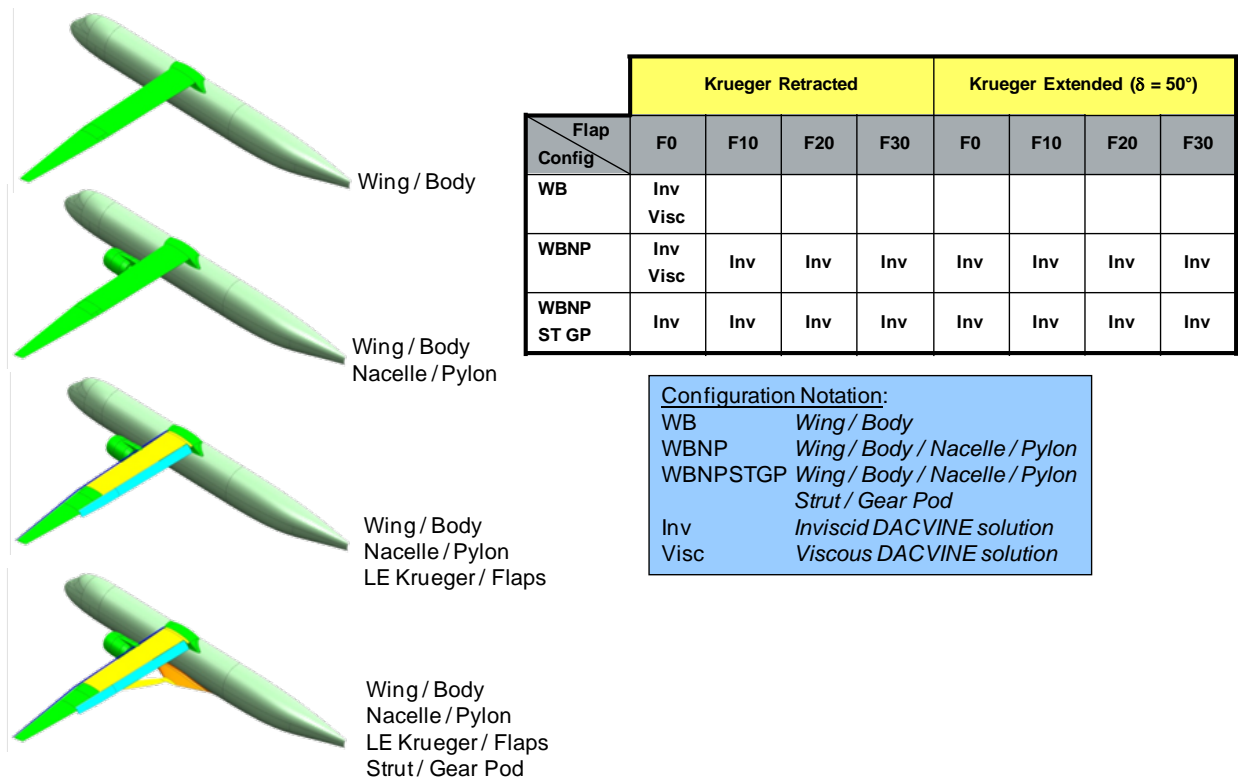


Figure 2.89 – Matrix of TBW High Lift Configurations Evaluated

The final trimmed low speed lift curves and drag polars which were used for the takeoff and landing performance estimates were built up from components which were assembled using the Boeing CASES low speed aero characteristics tool. Prior to the start of the high lift design process it was recognized that the CASES low speed database does not include data for wings with aspect ratios as high as those of the SUGAR configuration and thus the low speed aero characteristics buildup for the TBW configuration would rely heavily on the results from the DACVINE solutions. The components used for estimating the final lift curves and drag polars are shown below:

- Lift curves
 - $C_{L\alpha}$ – DACVINE predictions
 - $C_{L\alpha=0}$ – DACVINE predictions
 - C_{Lmax} – DACVINE predictions with ΔC_{Ppeak} criteria
 - $\Delta C_{Ltrim} = 5\%$ (conceptual estimate)
- Drag polars
 - C_{Do} – CASES High Speed Buildup
 - C_{Di} – DACVINE
 - C_{Dp} – Empirical Database
 - $\Delta C_{Dtrim} = 3\% C_{Dtotal}$
 - ΔC_{Dgear} – CASES Support Tables

The single element Fowler motion flap is shown in Figure 2.90 at 30° of equivalent deflection. Note that the flap span was assumed to be continuous across its entire extent which is consistent with the use of a flaperon behind the engine for high speed control. A later control surface update has broken the trailing edge flap segments to accommodate the engine pylon. Flap riggings were generated for 10, 20, and 30 degree equivalent deflections. The leading edge Krueger (rigged at 45° of deflection not the final 50° deflection) is shown in Figure 2.91. An example of the DACVINE surface grid topology (the wakes are not shown for clarity) is given in Figure 2.92.

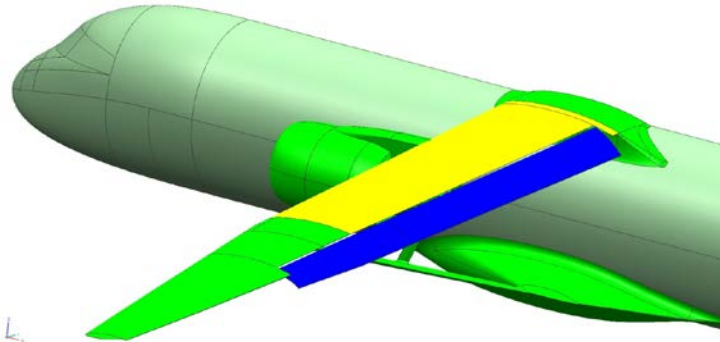


Figure 2.90 – Flap Rigged at 30 Degrees Equivalent Deflection

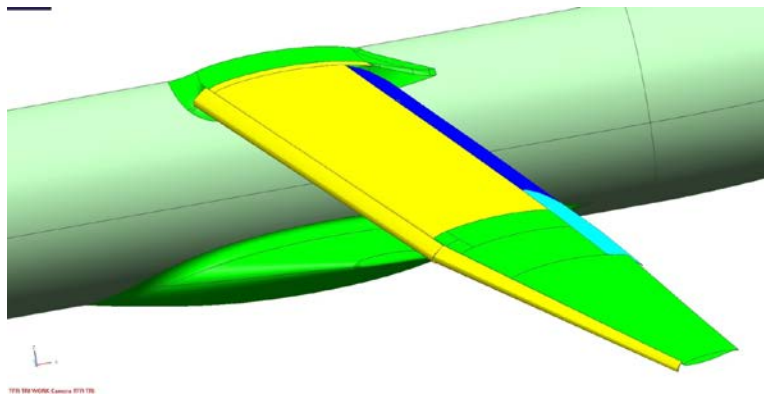


Figure 2.91 – Krueger Rigged at 45 Degrees Deflection

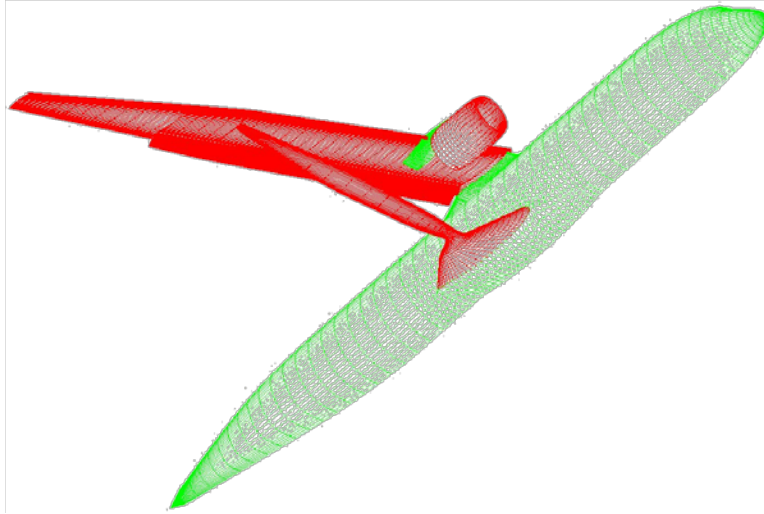


Figure 2.92 – Example of DACVINE Paneling (Lifting Surfaces in Red, Non-lifting surfaces in Green)

The resulting lift curves (ending at maximum lift coefficient for each flap/Krueger deflection) are shown in Figure 2.93 for non-lifting struts and in Figure 2.94 for lifting struts.

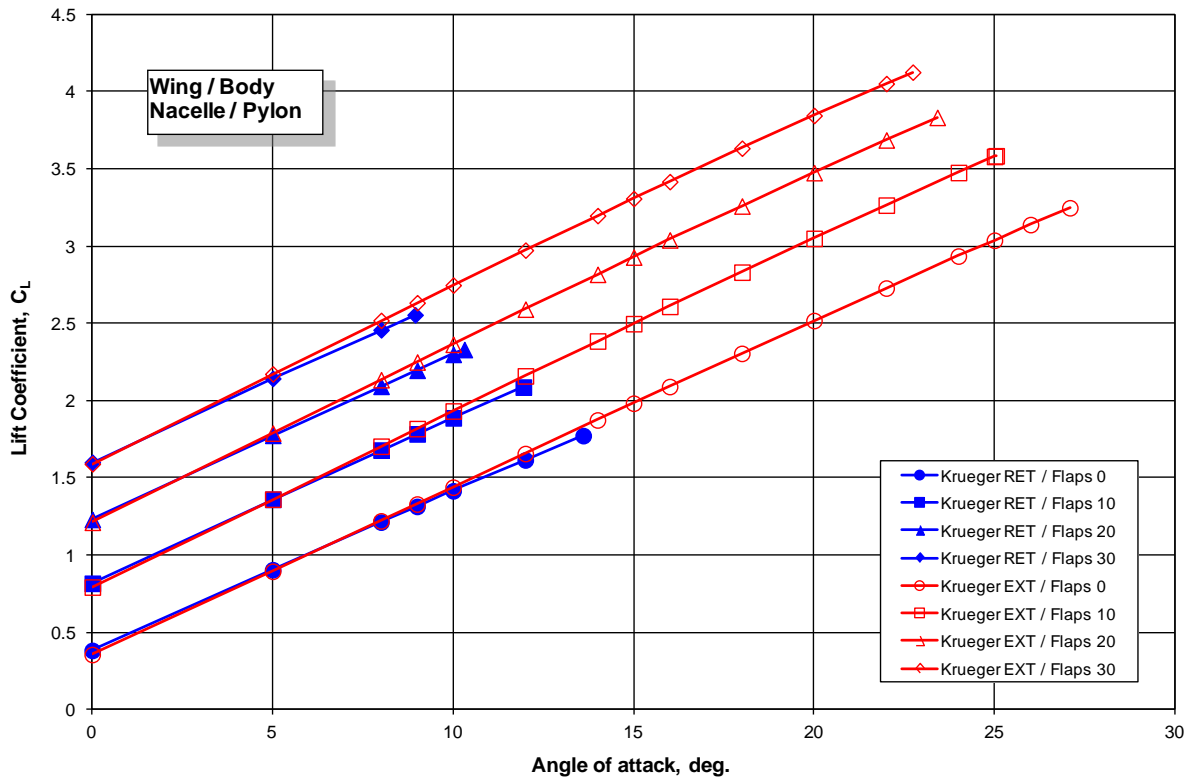


Figure 2.93 – Lift Curves for 765-095-RC; Struts and Gear Pods Non-Lifting; Mach 0.20

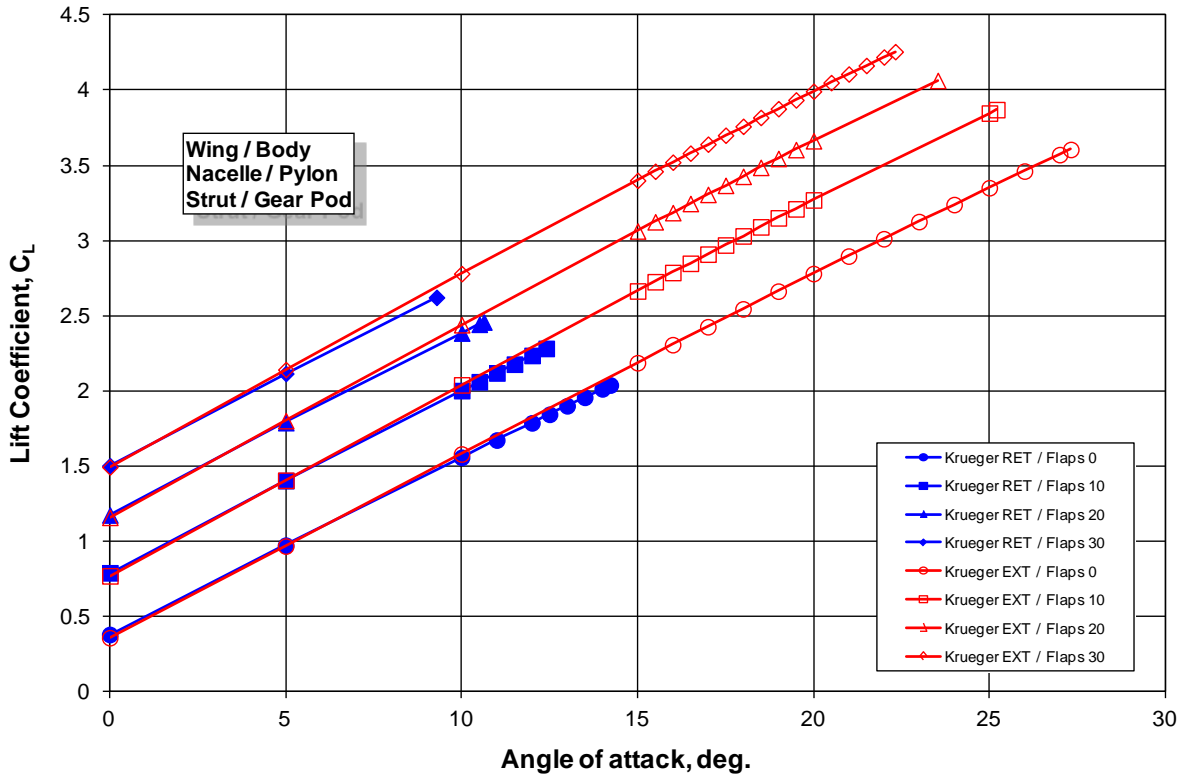


Figure 2.94 – Lift Curves for 765-095-RC with Lifting Struts and Gear Pods; Mach 0.20

2.1.8 Finite Element Model and Sizing

This activity produced a detailed finite element model (FEM) of the SUGAR aircraft, including all relevant load paths, sized to meet strength, buckling, and flutter constraints. The configuration definition was determined by the MDO and design activities described above. To determine the flutter weight penalty, the wing, strut, jury strut, and landing gear pylon were optimized with and without flutter constraints. Two distinct strut configurations were sized, one with the strut attached at the front spar and one with a V-strut attached to both the front and rear spars. The sized detailed FEM is the basis for the aeroelastic wind tunnel test described in Section 2.4.9.

2.1.8.1 Center Body FEM Description

The finite element model of the SUGAR aircraft's center fuselage consists of a detailed mesh of the fuselage center section, the landing gear pylon, and the landing gear structure; geometric and material properties for each structural element are also included.

Boeing provided the original geometry layout to Virginia Tech, who then modified it, ensuring meshable surfaces and mesh continuity. Major modifications to the original geometry include:

- Fuselage longerons: The original geometry lacked the definition of fuselage stiffening members. Upon discussion, geometry defining the position, orientation and shape of the fuselage longerons and of the landing gear pylon stiffeners was added to the model.

Mesh – Fuselage Center Section

Figure 2.95 shows various views of the fuselage center section mesh. The mesh consists of quadrilateral shell elements (QUAD4) of approximately 2 by 2 inches. At the fore and aft ends element size varies to allow mesh transition at the interface with the front and rear fuselage sections.

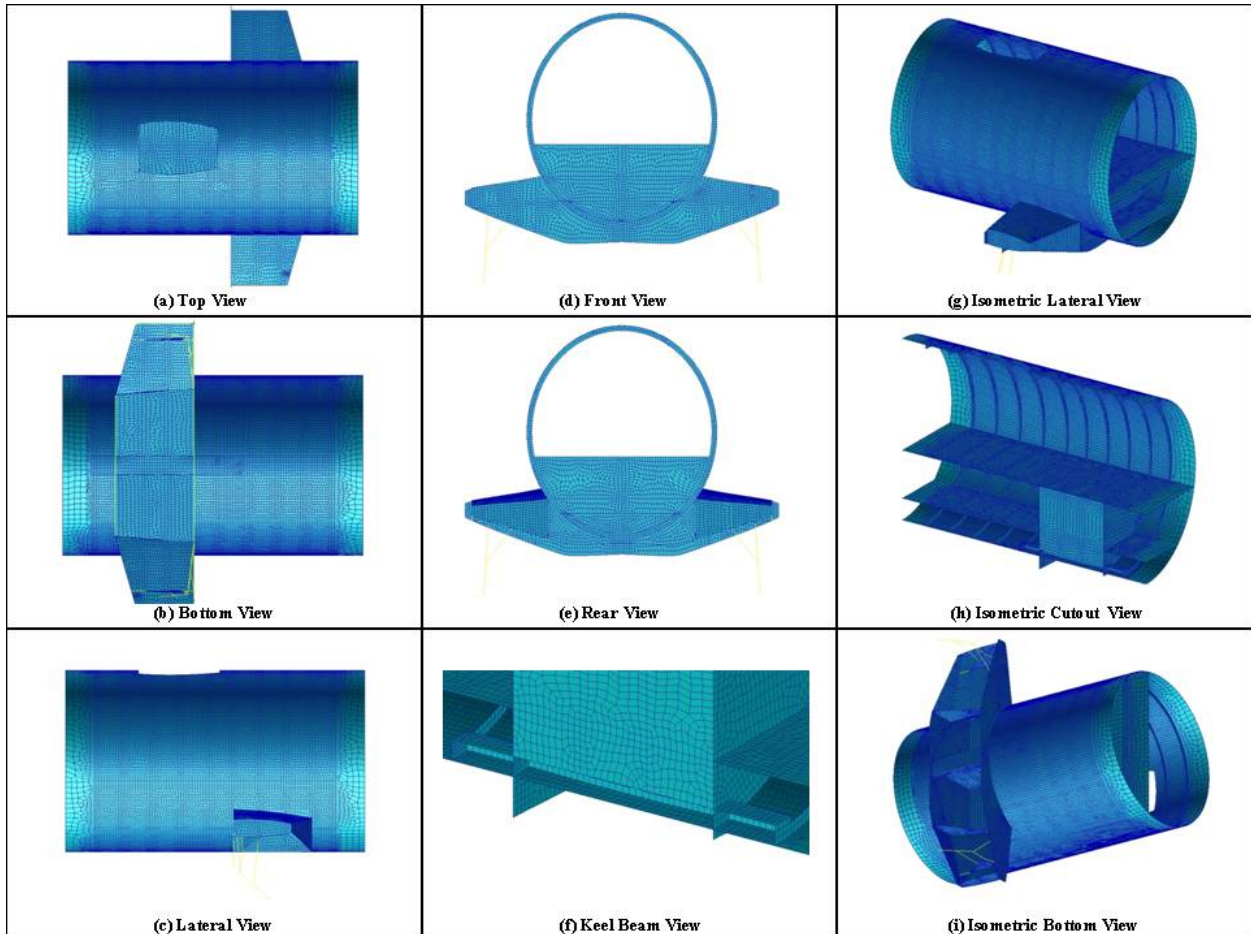


Figure 2.95 – SUGAR Aircraft Fuselage Center Section Mesh

Mesh – Landing Gear, Longerons, and Stiffeners

The landing gear, longerons, and stiffeners are modeled using beam elements (CBEAM) with appropriate cross-sections and dimensions. Figure 2.96 presents a view of the landing gear, fuselage longerons, and gear pylon stiffeners. Beam cross-sectional shapes and dimensions are described below.

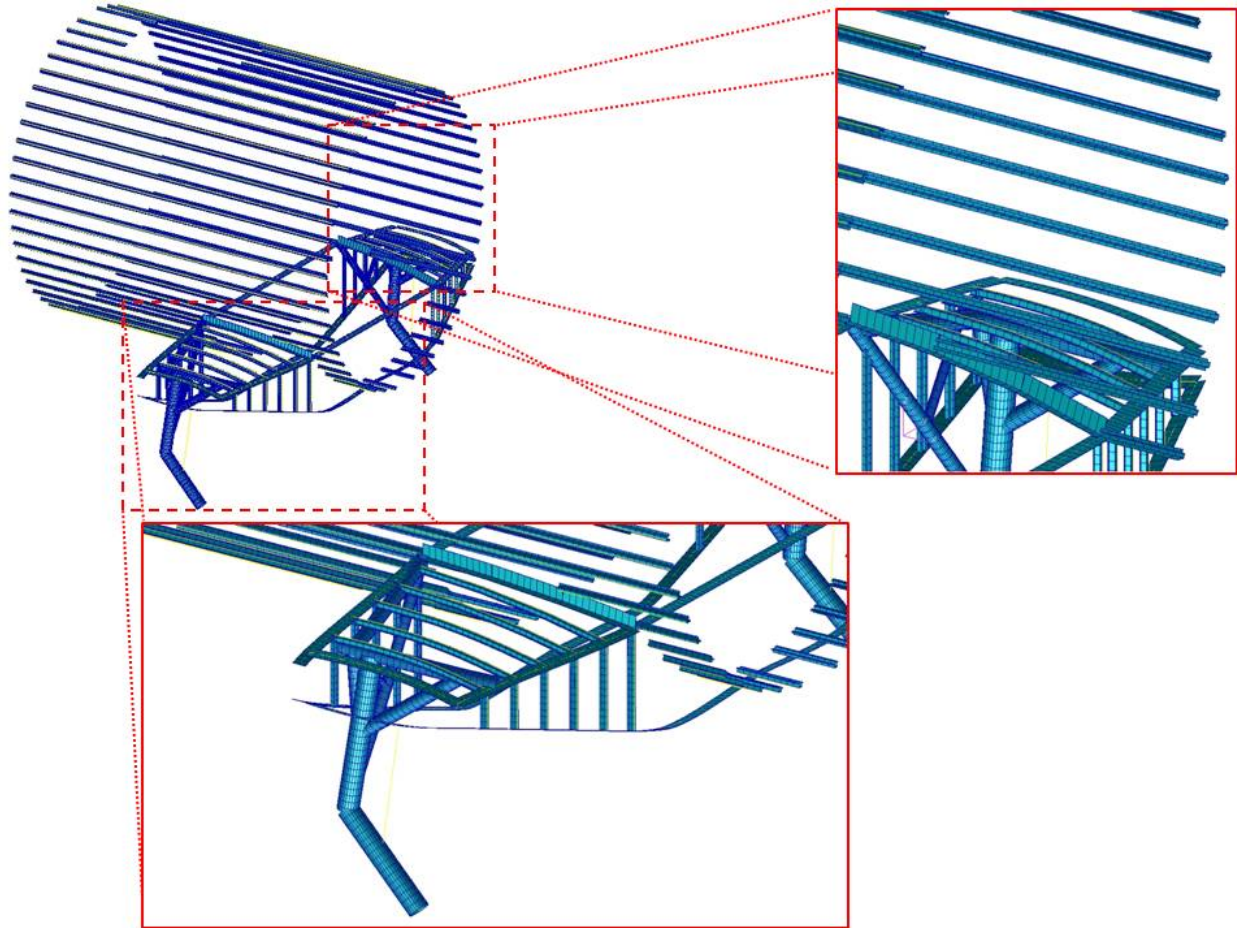


Figure 2.96 – Structure, Fuselage Longerons and Gear Pylon Stiffeners Mesh

Properties – Fuselage Skin

Fuselage skin panels are modeled using quadrilateral shell elements (QUAD4) with 10 properties associated with each element. Reference (13) shows 0.04 inches as a typical skin thickness for similar aircraft, so, initially, that constant thickness was applied to all skin elements. All skin elements located in any section – between any two consecutive frames – have the identical set of properties associated with them, which allows the whole section's thickness to change during the sizing phase.

Properties – Fuselage Frames

The frames are also modeled using quadrilateral shell elements (QUAD4), again associating 10 properties to each element. Each frame has a unique properties set, allowing their thicknesses to change independently during the sizing phase (as with the skins, the initial thicknesses were set uniformly at 0.04 inches).

Properties – Passenger Deck and Cargo Deck

The passenger deck is also modeled using quadrilateral shell elements (QUAD4), but here only two properties are defined, one in the center fuselage section, the second in the front and rear fuselage sections.

Properties – Longerons

The fuselage longerons are modeled using beam elements (CBEAM), with the cross-section shown in Figure 2.97. The values chosen for the parameters are (again citing Niu, Reference (13), as representative and typical):

- $t = 0.05$ in
- $H = 1.25$ in
- $W = 1.125$ in
- $W1 = 0.625$ in

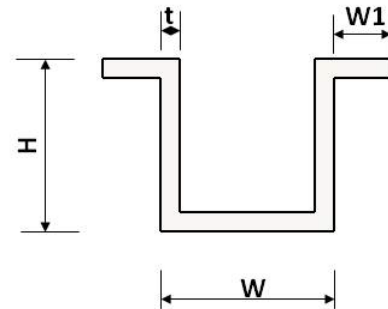


Figure 2.97 – Longerons Cross-section

The distance between consecutive longerons is approximately 10 inches. The same cross section is used to model the landing gear pylon stiffeners. Unique properties are associated to each longeron and group of stiffeners.

Properties – Spar and Rib Caps

The caps of the spars and ribs forming the landing gear pylon are modeled using beam elements (CBEAM) characterized by rectangular cross-section with thickness of 0.05 in and width of 4 in.

Properties – Landing Gear

The landing gear structure is modeled using beam elements (CBEAM) with solid circular cross-sections. The diameter of the beams varies depending on the structural element as listed in Table 2.19. The beam numbering refers to the structural layout presented in Figure 2.98.

Table 2.19 – Diameter of the beams forming the landing gear structure

Diameter (in)	Structural Part (See Figure 2.98)
6	Beam 1, Beam 2
4.4	Beam 3
4	Beam 4, Beam 5, Beam 6
3.2	Beam 7
2	Beam 8

The landing gear structure is connected to the landing gear pylon structure by three spherical joints (blue dots in Figure 2.98); this avoids stress concentrations due to the transfer of moments between the two.

The wheels are connected to the main gear leg by a hinge that allows rotation in the XZ plane (fore-aft and up-down). The shock absorber is modeled using a spring element (CELAS1), with spring constant of 40,000 lb/in.

Properties – Miscellaneous

Additional landing gear pylon structure properties model the keel beam, the front and rear spars, and the rib. The thickness of each of these structural elements changes independently during optimization.

Material Properties

Two materials are used: a generic titanium alloy for the landing gear structure and a generic aluminum alloy for the rest of the structure. The properties of these materials are listed in Table 2.20 and Table 2.21, respectively.

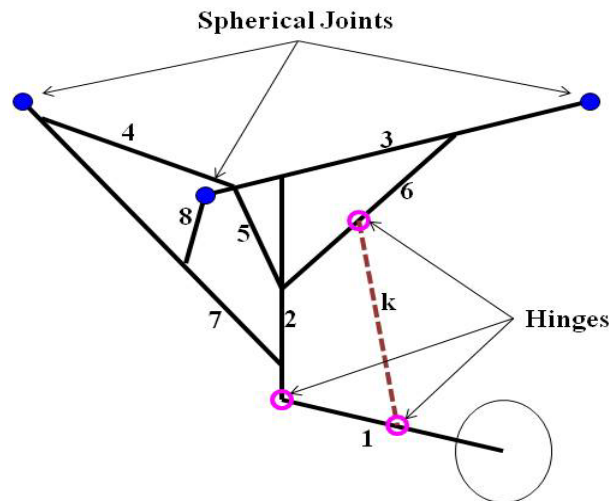


Figure 2.98 – Landing Gear Structure

Table 2.20 – Titanium Alloy Mechanical Properties

Material	Titanium Alloy
Elastic Modulus	16 Msi
Poisson's ratio	0.33
Density	0.17 lb/in ³

Table 2.21 – Aluminum Alloy Mechanical Properties

Material	Aluminum Alloy
Elastic Modulus	10.6 Msi
Poisson's ratio	0.33
Density	0.1 lb/in ³

Center Body FEM Checkout

We performed a (qualitative) preliminary static analysis on the fuselage structure to visualize the load paths for each of four distinct load cases. This ensured consistency between the results of

the applied loads and the real system of forces acting on the structure. The von Mises stress distributions for the four load cases are presented in Figure 2.99 to Figure 2.106.

The four load cases were:

- Vertical load introduced in the landing gear structure
- Lateral load introduced in the landing gear structure
- Drag load introduced in the landing gear structure
- Tension load introduced at the wing strut attachment

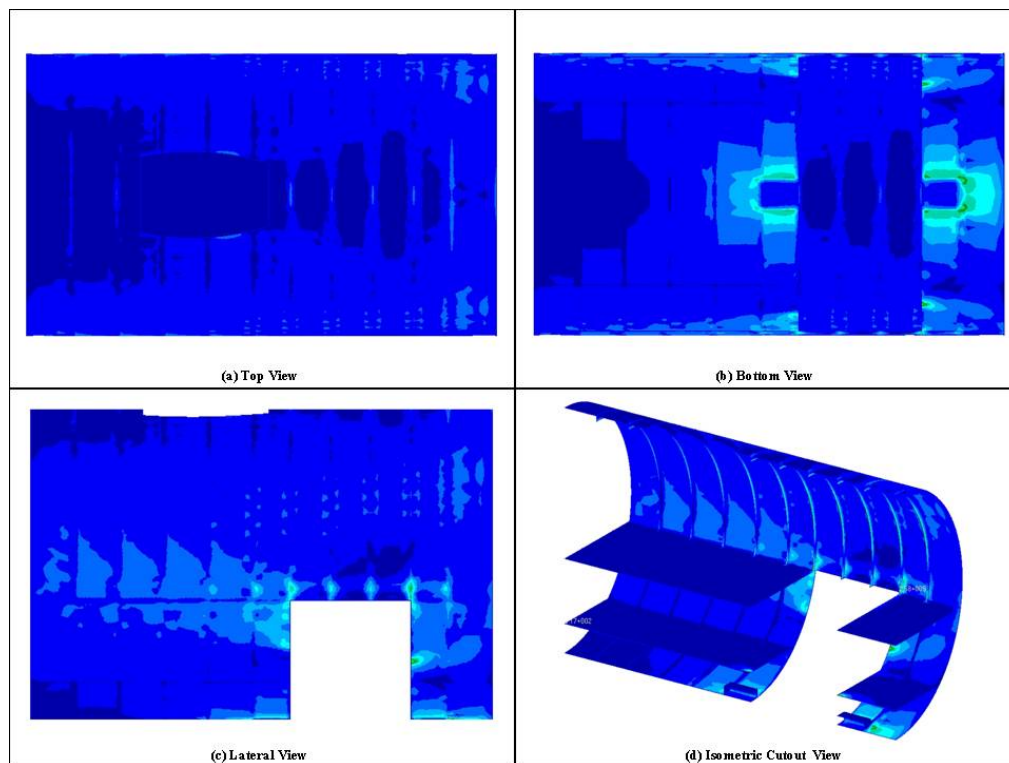


Figure 2.99 – Stress Distribution in the Center Fuselage Caused By a Landing Gear Vertical Load

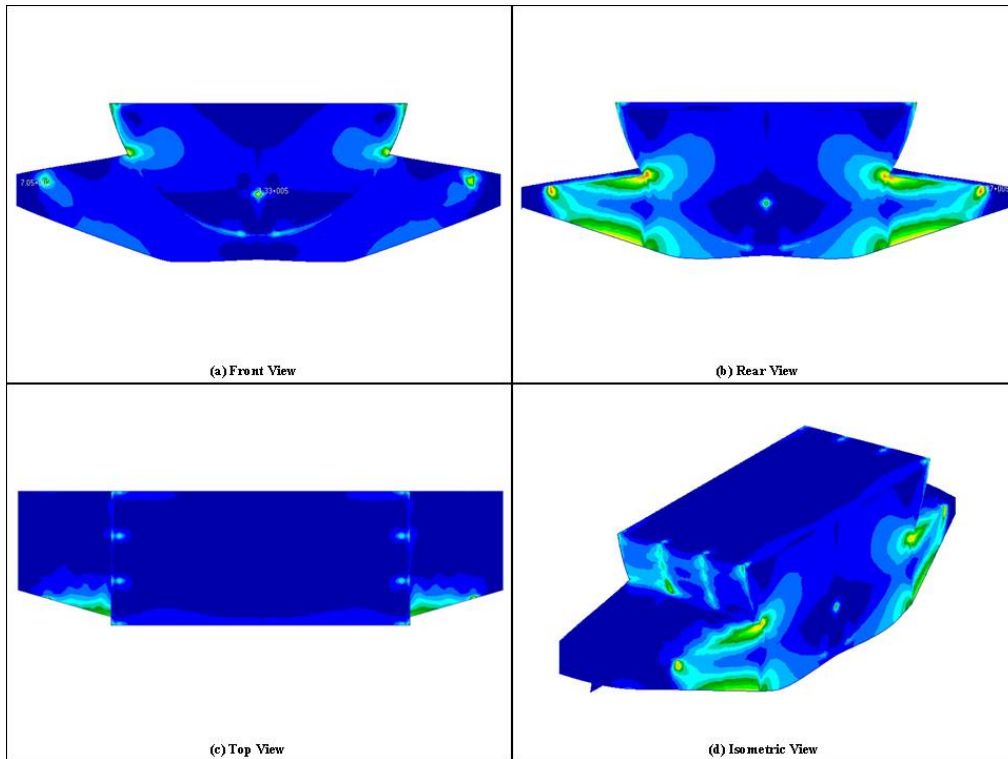


Figure 2.100 – Stress Distribution in the Gear Pylon Caused By a Landing Gear Vertical Load

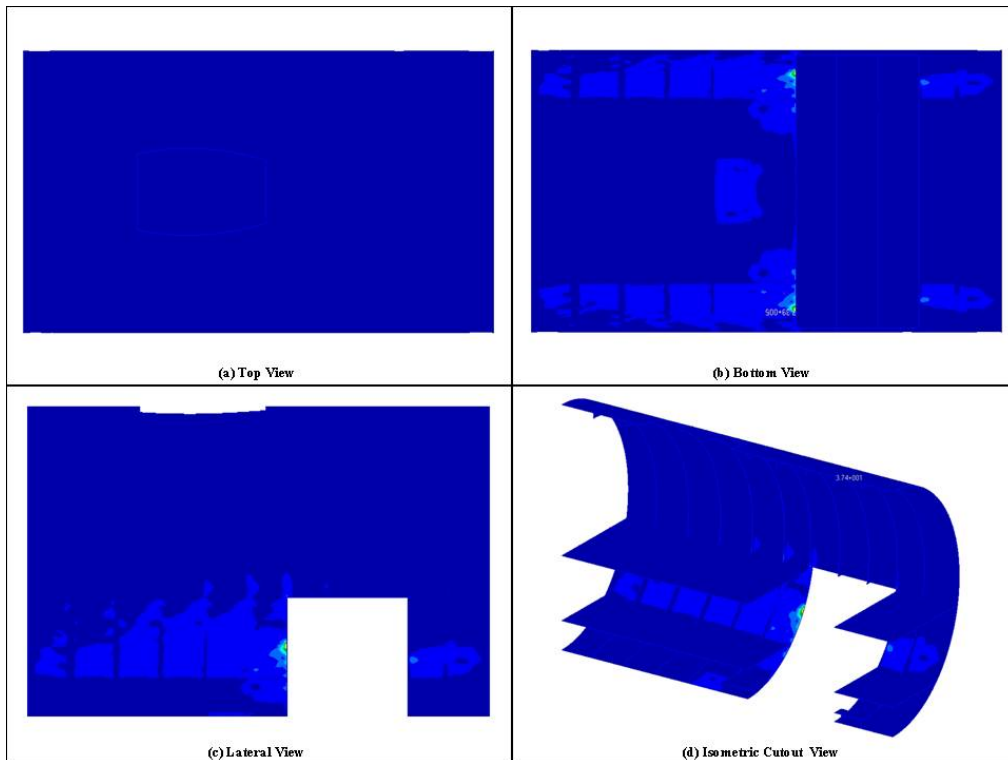


Figure 2.101 – Stress Distribution in the Center Fuselage Caused By a Landing Gear Lateral Load

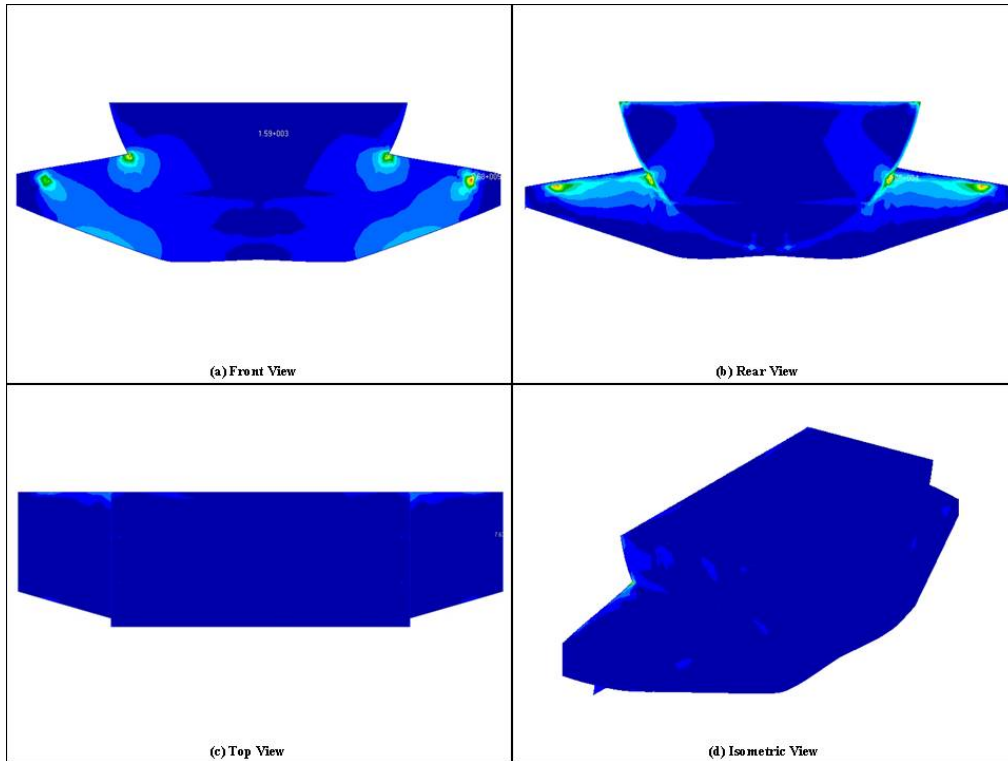


Figure 2.102 – Von Stress Distribution in the Gear Pylon Caused By a Landing Gear Lateral Load

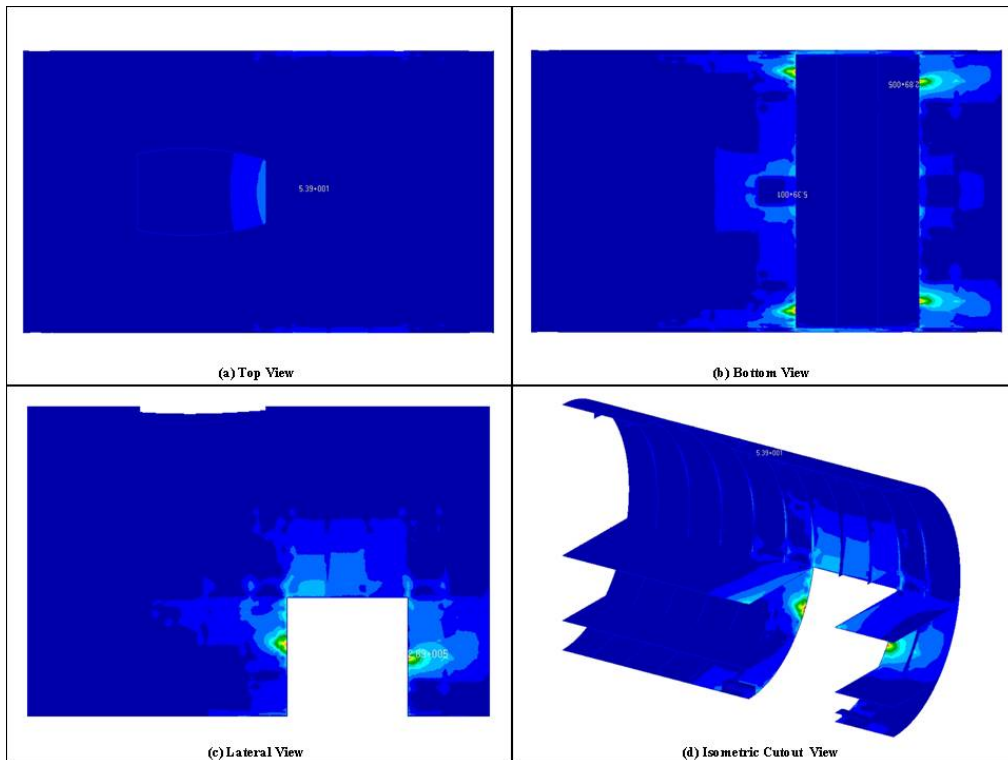


Figure 2.103 – Stress Distribution in the Center Fuselage Caused By a Landing Gear Drag Load

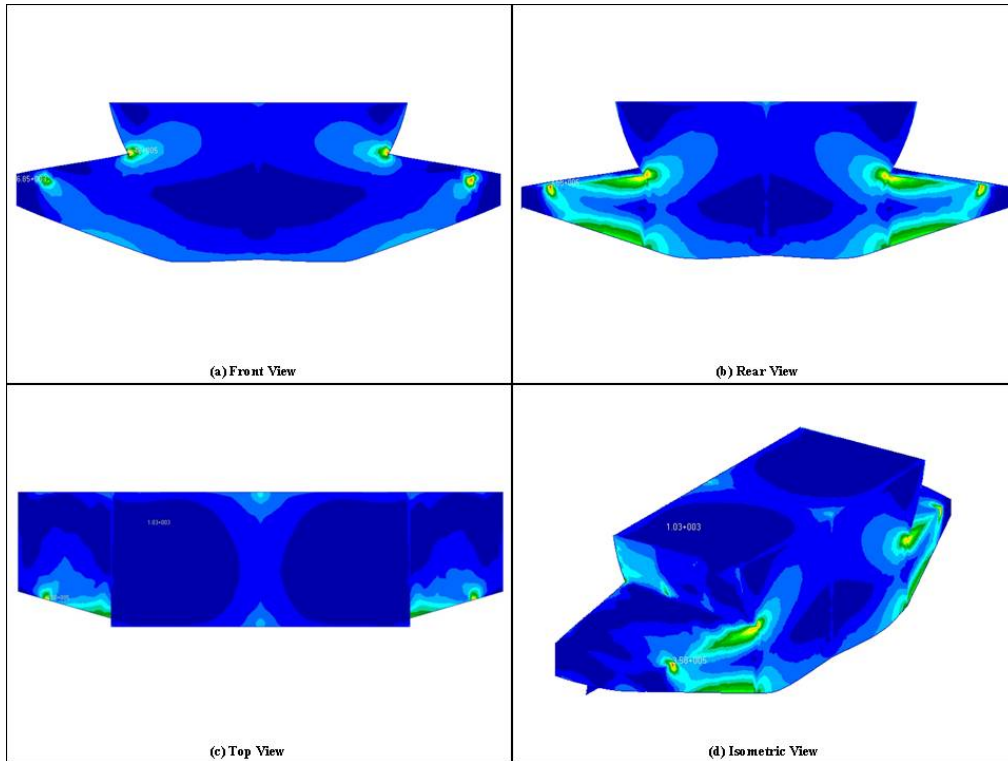


Figure 2.104 – Stress Distribution in the Gear Pylon Caused By a Landing Gear Drag Load

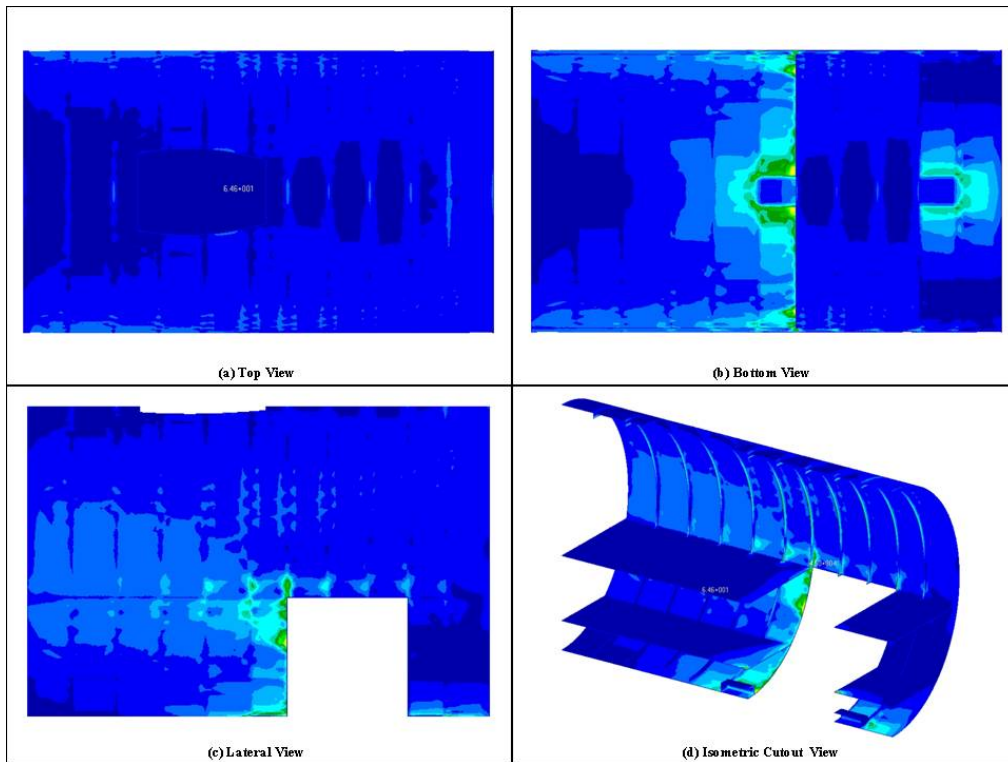


Figure 2.105 – Stress Distribution in the Center Fuselage Caused By a Wing Strut Load

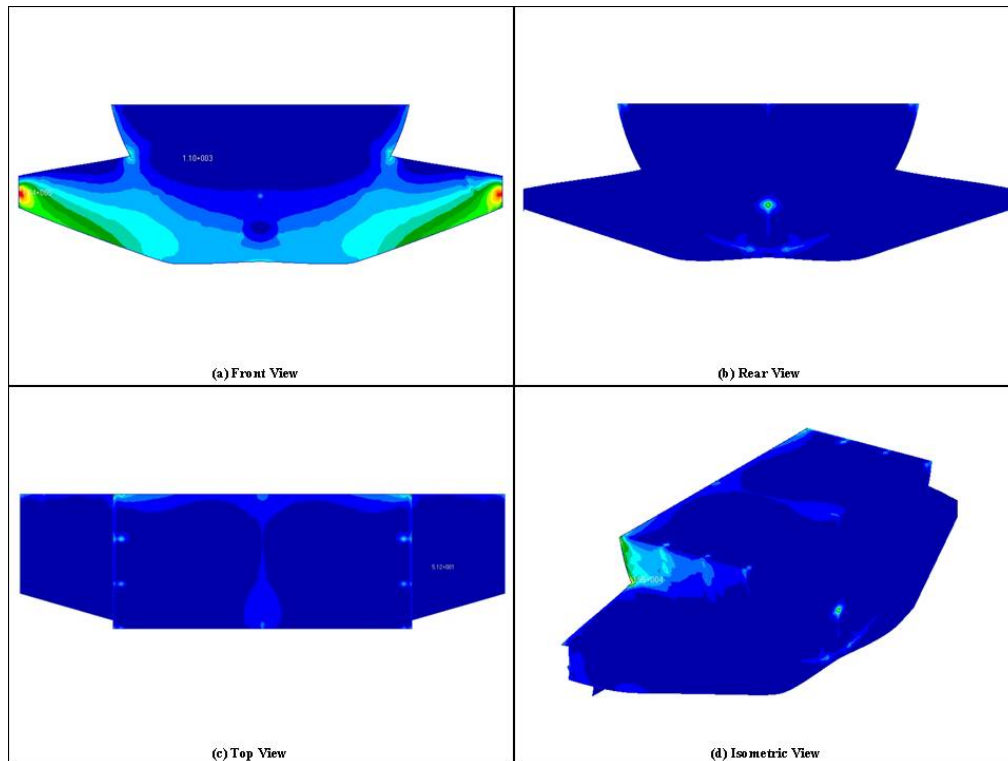


Figure 2.106 – Stress Distribution in the Gear Pylon Caused By a Wing Strut Load

2.1.8.2 Wing FEM Description

The wing FEM was generated to match the OML using Boeing’s proprietary RapidFem process which generated skins, spar webs, rib webs, spar caps, rib caps, and control surfaces. Streamwise rib spacing was set to 25 inches.

Engine/nacelle/pylon weight and air-load application grids attach to the wing using RBE3 elements. The RBE3 element attaches to the wing at the intersection of the front spar and a rib, and to the rib half way between the front and rear spars.

Control surfaces are supported at inboard and outboard hinges that react shear loads. Control surface hinge moments are reacted at the inboard hinge.

The strut and jury are modeled as box beams where the box width, depth, and skin thickness can be varied. Strut attachment to the wing and gear pylon is a pin joint reacting all 3 shear loads and torsion about the local strut beam axis. Clamped joints connect the jury to the wing and strut.

All 2D wing box elements are of composite material with the following layup used for the cover panels: Layers 1 and 7, 45 degrees; Layers 2 and 6, -45 degrees; Layers 3 and 5, 90 degrees; and Layer 4, 0 degrees. Thickness of all +/-45 degree layers and the two 90 degree layers are the same. In addition, a smeared T shaped stringer is added as layer 8 and 9 as shown in Figure 2.107. The stringer spacing is 5 inches and the stringer size scales up with the skin so the stringer is a constant 33% of the stringer plus skin area.

The 2D element lamina stiffness for all wing skins and webs, the 1D element laminate stiffness used for wing caps, strut, and jury strut, and the 3D stiffness used for the control surfaces are shown in Table 2.22.

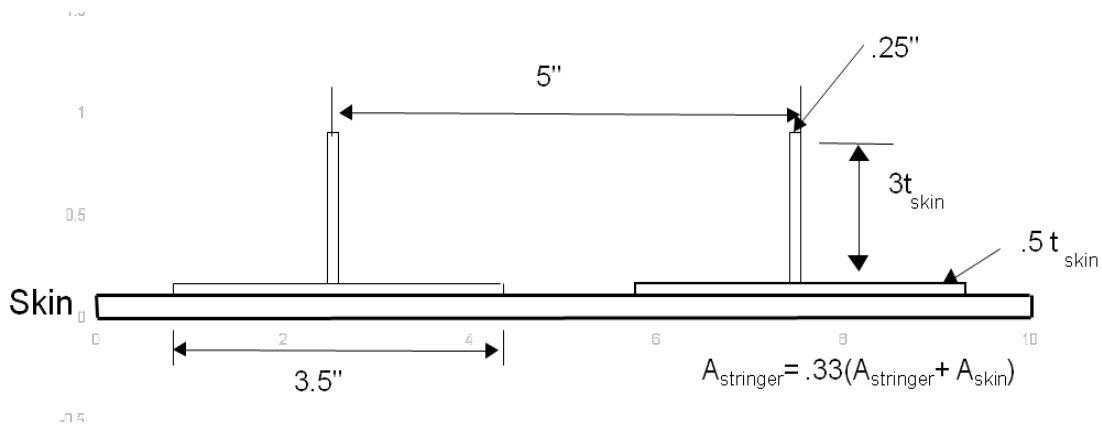


Figure 2.107 – FEM skin and stringer geometry

Table 2.22 – Wing Stiffness Properties

2D Element Lamina Stiffness		1D Cap Laminate Stiffness		3D Stiffness	
E1	2.35×10^7 lb/in ²	E	1.05×10^7 lb/in ²	E	5.00×10^6 lb/in ²
E2	1.06×10^6 lb/in ²	v	0.30	v	0.25
v	0.34	G12	4.04×10^6 lb/in ²	G12	2.00×10^6 lb/in ²
G12	8.00×10^5 lb/in ²				

2.1.8.3 Finite Element Model Integration

Integration of the FEM involved adding fuselage and tail beam elements and joining the Virginia Tech generated center body FEM to the Boeing generated wing FEM. Using rigid beam elements for the forward fuselage, aft fuselage, and tail instead of building a 3D FEM simplified the model generation and analysis. (The goal of the finite element analysis was to size the wing, and we made the assumption that the dynamics of the forward and aft fuselage and tail would not significantly impact the wing dynamics.) Body and tail aerodynamics were applied to the model through the beam elements. The forward fuselage and aft fuselage/tail attach to the 3D centerbody FEM using an RBE3 element, which adds no stiffness to the centerbody.

The wing is attached to the centerbody in three manners. The first is the primary vertical connection between the wing and fuselage, and occurs at the wing front and rear spars. Here, a frame-mounted post extends up from the fuselage and attaches to a trap panel. The trap panel extends from the post to the front and rear spars of the wing at the side-of-body rib. This arrangement is shown in Figure 2.108.

The second is the primary fore and aft connection between the wing and fuselage. Here, the grids along the fuselage wing cutout are connected, in the x direction only, to the closest grids on the wing's lower skin. This is shown in Figure 2.109.

The third is the primary lateral connection between the wing and fuselage, where the end grids of three fuselage frames are connected, in the y direction only, to grids on the wing lower skin. This is shown in Figure 2.110.

The integrated FEM with 396,240 degrees of freedom is shown in Figure 2.111. The solid element control surface arrangement is shown in Figure 2.112

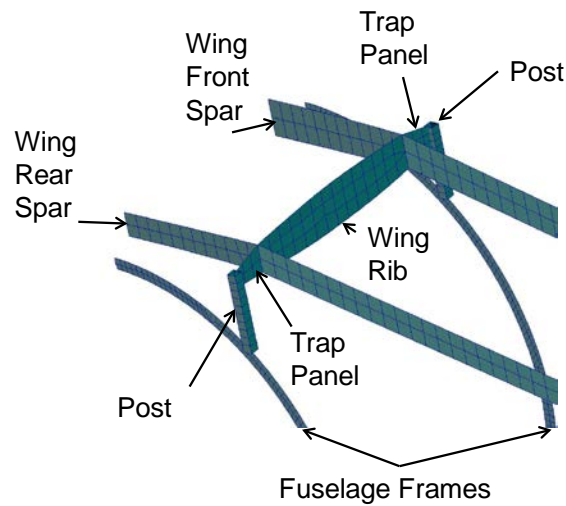


Figure 2.108 – Primary vertical connection between wing and body

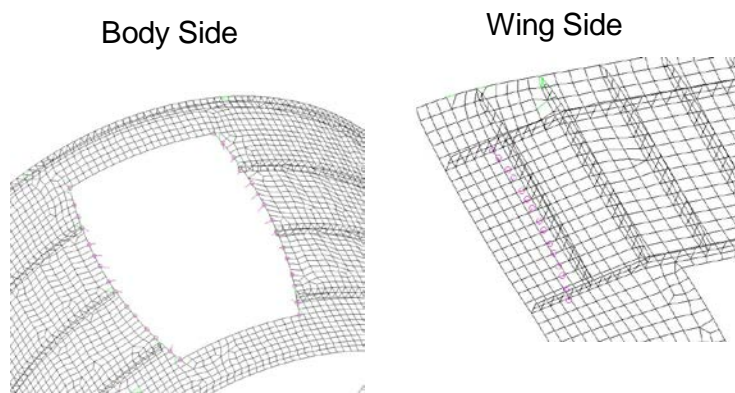


Figure 2.109 – Primary forward/aft connection between wing and body

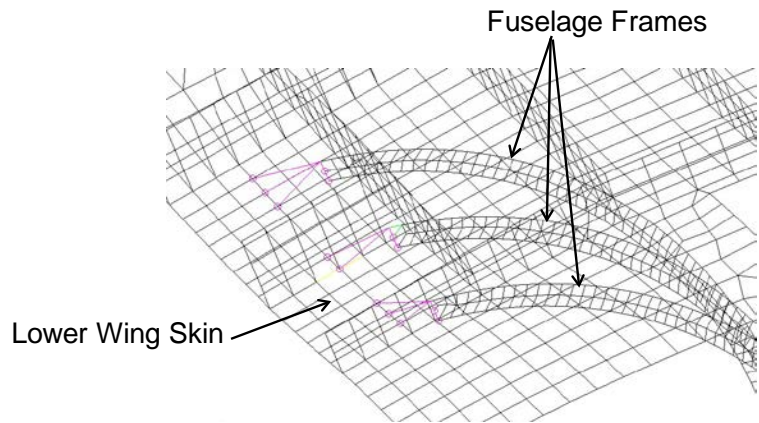


Figure 2.110 – Primary lateral connection between wing and body

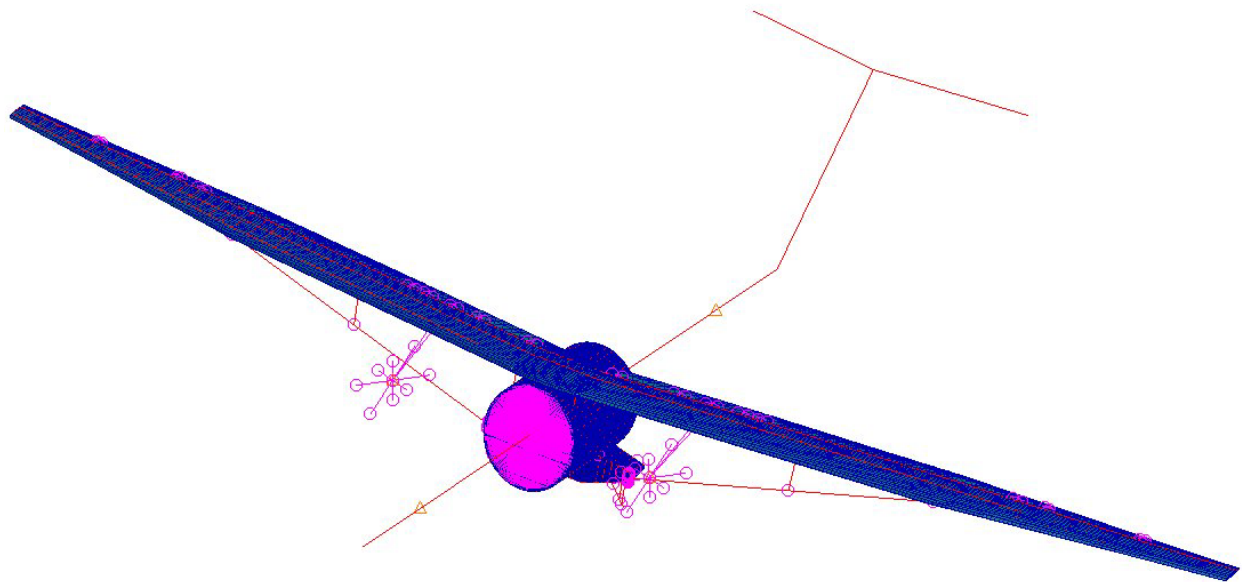


Figure 2.111 – Integrated FEM

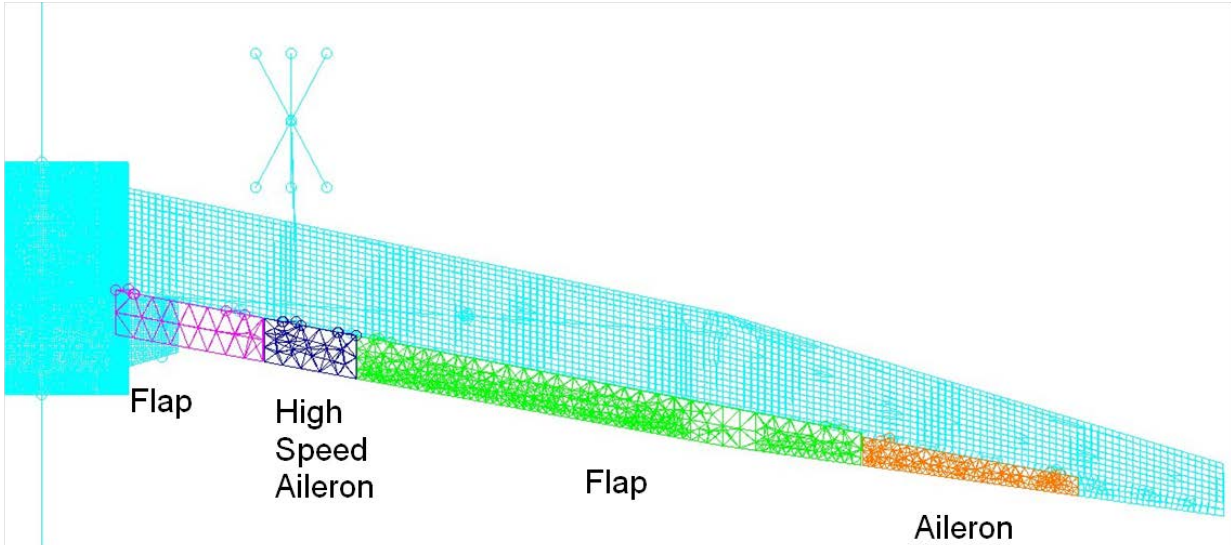


Figure 2.112 – Control Surface Arrangement

2.1.8.4 Mass Case Descriptions

The FEM includes density times volume weight for all sized structural items, which includes the wingbox and the gear pylon. The density of the composite material was increased by 17% to represent cutouts, fasteners, and other unmodeled features. All remaining weight is provided to match the vehicle group weight statement shown in Section 2.3.2, and is spread on the model as concentrated mass items. Spread weight representing Operating Weight includes the stuffed fuselage and tails, stuffed engine/nacelle/pylon, wing control surfaces, and wing systems. Spread weights representing estimated joint weights at the interfaces of the wing/strut, strut/jury, strut/landing gear pylon, strut/wing, and of the wing fold joint were included in the model.

Table 2.23 lists the fuel and payload combinations that were analyzed. Concentrated mass items were spread to represent the five distinct cases.

Table 2.23 – Payload and Fuel Combinations

Fuel	Payload
Fuel to reach MTOW from MZFW	Max to Reach MZFW
Full	Max to reach MTOW with Full Fuel
Full	None
Reserve	Max to Reach MZFW
Reserve	None

2.1.8.5 Aerodynamic Model and Corrections

The doublet lattice aerodynamic model of the SUGAR TBW configuration is shown in Figure 2.113, with panels representing the wing, body, tails, nacelles, and struts. The Overflow aerodynamic model’s grid of 14.4 million points only represented the wing and body. The Overflow results

were linearized between two conditions as listed in Table 2.24. The linear doublet lattice aerodynamics were modified, or corrected, to match the slope and intercept of the wing sectional aerodynamics from the Overflow CFD analyses. Mach numbers above the dive Mach of 0.82 are used for flutter analyses up to the 1.15 speed pad required by FAA regulations.

Overflow results showed a significant aft shift in aerodynamic center for Mach numbers above 0.82, and at Mach 0.86 exhibited non-linear behavior in the angle of attack range investigated, so in running flutter we incorporated corrections using the Overflow results. We input these corrections to Nastran as DMI WKK and FA2J matrices for static aeroelasticity runs, and as DMI WFACT matrices for flutter and dynamic gust runs.

Since the Overflow model was wing/body only, we calculated sectional lift curve slope and AC corrections using a wing/body doublet lattice model. Figure 2.114 and Figure 2.115 show the wing sectional doublet lattice lift curve slope and aerodynamic center corrected to exactly match the Overflow results.

The wing corrections calculated using the wing/body doublet lattice model are used with the full doublet lattice model, while employing the uncorrected doublet lattice on all non-wing panels.

In addition to the lift curve slope correction a lift at zero alpha was input for quasistatic aeroelastic runs at Mach 0.7, 0.76, and 0.82. The correction for lift at zero alpha was found by matching the Overflow sectional data for the $C_l = 0.7$ condition with an elastic doublet lattice run. This was done for the original unsized model, which was stiffer than the sized model.

As discussed in Section 2.1.8.8, the loads generated for the unsized model were conservatively used for all sizing. Finally, drag data were generated by interpolating the Overflow sectional data to the angle of attack for critical 2.5G and -1G conditions, and forces were generated at all wing leading edge grids to match the Overflow results.

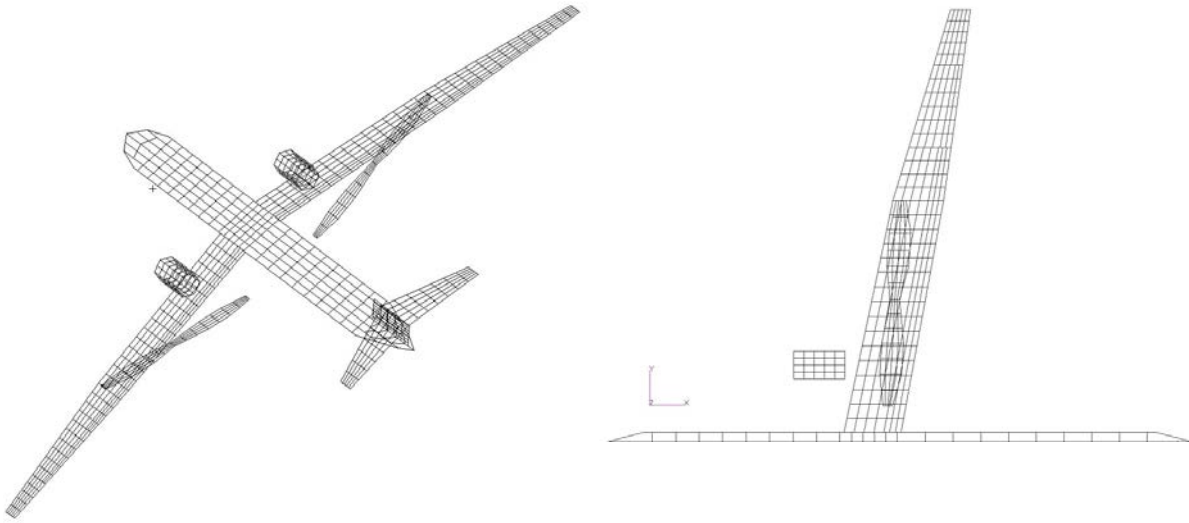


Figure 2.113 – Doublet Lattice Aerodynamic Model

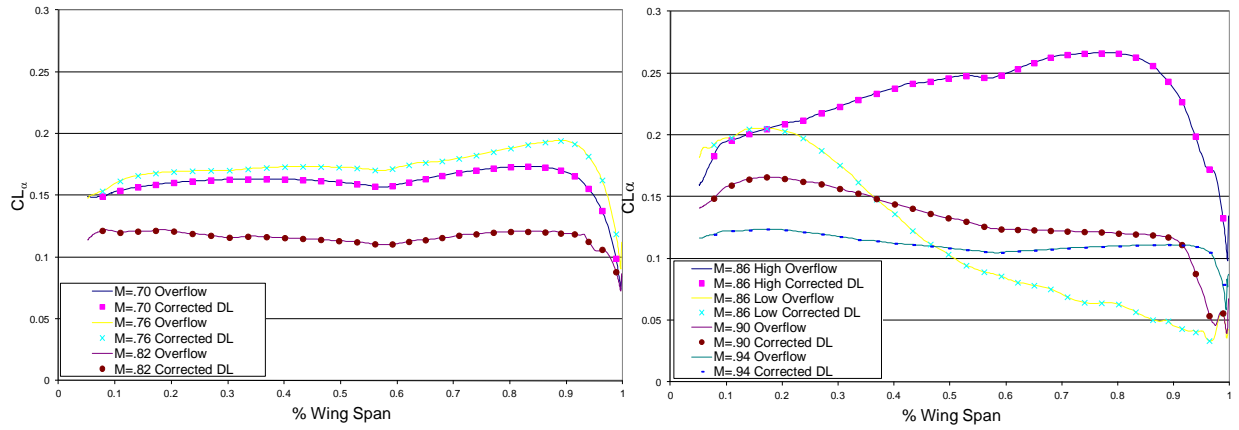


Figure 2.114 – Section Lift Curve Slope Comparison

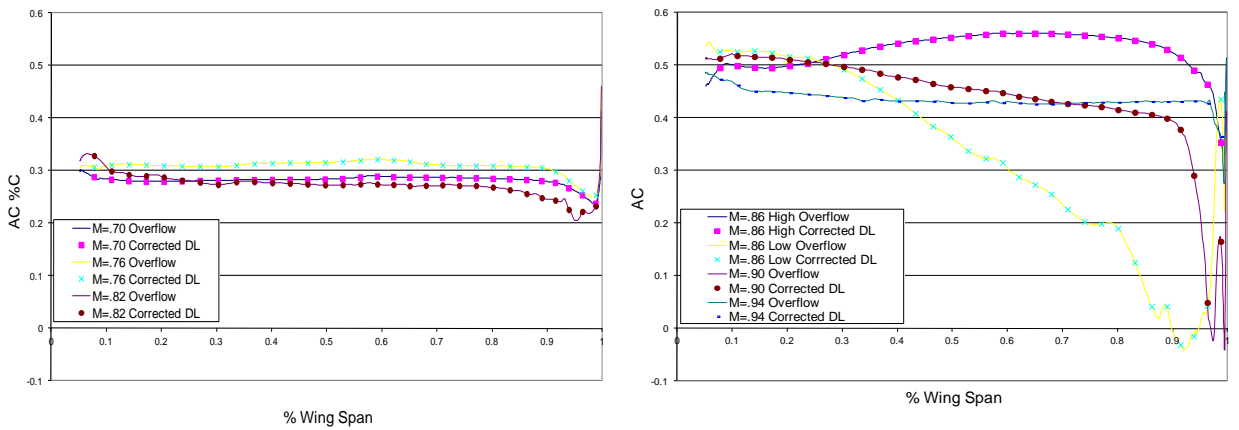


Figure 2.115 – Sectional Aerodynamic Center Comparison

Table 2.24 – Overflow Correction Conditions

Mach	Alpha 1	C_L 1	Alpha 2	C_L 2
0.70	-0.21	0.400	1.67	0.700
0.76	-0.38	0.400	1.38	0.700
0.82	1.39	0.400	3.96	0.700
0.86 Low	0.00	-0.164	2.20	0.118
0.86 High	2.20	0.118	4.00	0.526
0.90	1.40	0.104	4.00	0.255
0.94	1.40	0.010	4.00	0.304

2.1.8.6 Load Conditions

Load conditions investigated include 2.5G and -1G balance maneuvers, 2G flaps down balance maneuvers, takeoff roll, 0.5G turn, braked roll, and 1-cos dynamic gust. Flight loads were calculated in Nastran Sol 144 with the horizontal tail being used to trim the vehicle. Doublet lattice aerodynamics were corrected to match Overflow CFD results as described in the previous section. Ground conditions were calculated by finding the inertial loads required to balance input landing gear loads. Gust loads were calculated using Nastran Sol 146.

An extensive survey of 2.5G and -1G balance maneuvers was done to determine critical load conditions. Results from the survey showing 2.5G and -1G wing critical limit external and internal shear, moments, and torque loads are show in Figure 2.116.

The internal loads plots in Figure 2.116 show the large decrease in loads inboard of where the strut removes load from the wing. The bending moment drops significantly inboard of the strut attachment, nearly reaching zero at the jury, then growing slightly to the fuselage side-of-body. Torsion increases at the strut but doesn't increase much going inboard, resulting in a significant benefit at the side-of-body. Wing fore/aft bending increases inboard of the strut.

Critical 2.5G and -1G conditions are at M = 0.76, 230 KEAS with maximum payload and fuel to reach maximum takeoff weight.

A sea level 200 KEAS flaps down 2G balance maneuver was run. All trailing edge surfaces were deflected to 30 degrees except the outboard aileron.

All landing gear loads were calculated using a conservative aircraft weight of 149,294 lb. The takeoff roll ground condition load had main and nose gear loads calculated to produce 2G vertical. The turn condition had main and nose gear loads calculated to produce 0.5G lateral and 1G vertical. The braked roll condition had main gear loads calculated to produce a 0.93G deceleration and 1.17G vertical.

A survey of 1-cos discrete dynamic gust loads was completed using the criteria in Federal Airworthiness Regulations Part 25. The flight profile alleviation factor was conservatively calculated as 0.85 at sea level, increasing to 1.0 at 50,000 ft. The gust design velocities are plotted in Figure 2.117. A number of gust gradients were run to determine critical loads for each condition.

As shown in Figure 2.118, results from the gust survey showed loads less than the 2.5G and -1G steady pitch maneuvers. Since the gust loads were significantly below the steady pitch maneuvers loads, no gust conditions were included in the sizing runs.

The loads used for the sizing runs were calculated using the initial unsized model and not updated for the sized model. The wing for the sized model washes out more and provides more aeroelastic relief to the wing loads. This can be seen in Figure 2.118, which shows wing vertical bending moments of the sized wing lower than the initial unsized loads.

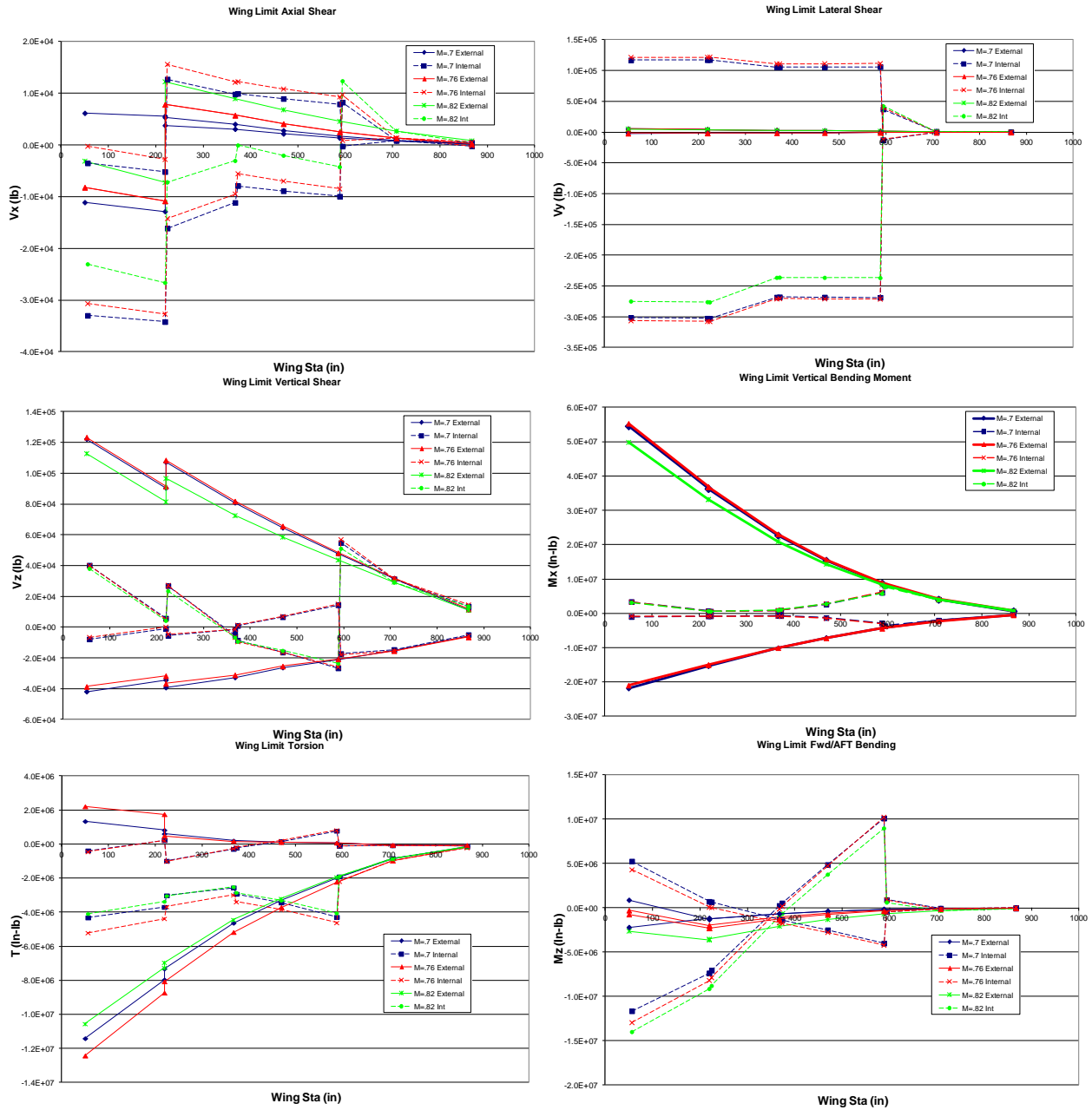


Figure 2.116 – Limit Loads 2.5 and -1G Balance Maneuvers

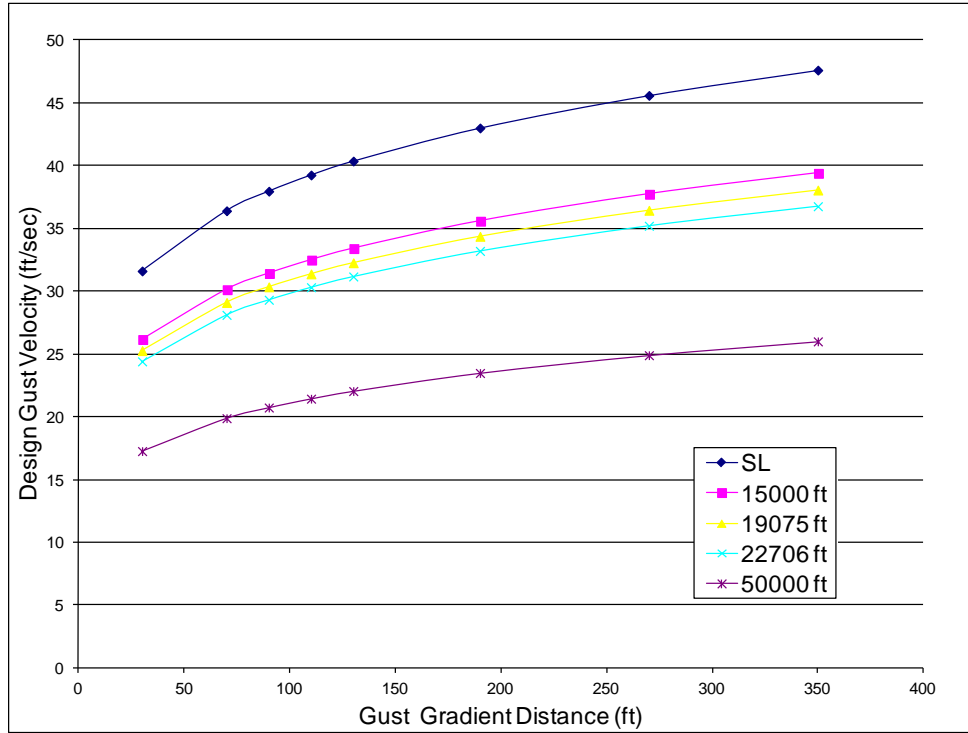


Figure 2.117 – Design Gust Velocities

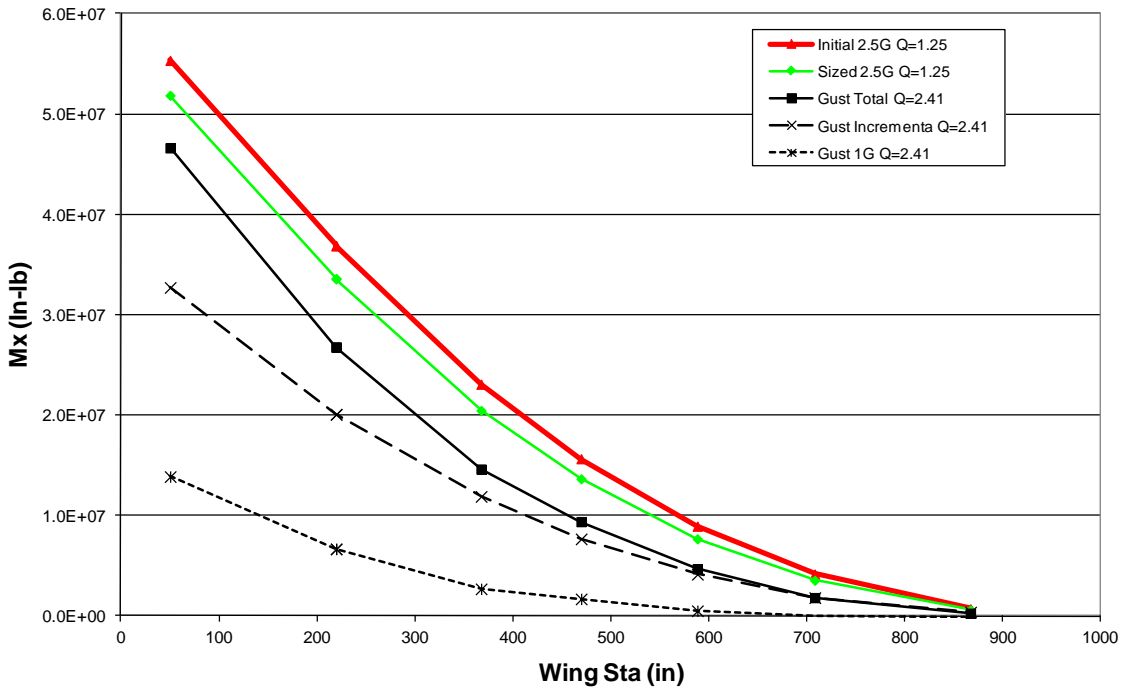


Figure 2.118 – Wing Limit Vertical Bending Moment Comparison

2.1.8.7 Structural Sizing and Optimization

Structural sizing and optimization was run using Nastran Sol 200. Sized structure includes strut, jury, landing gear pylon, wing skins, spars, ribs, and spar and rib caps. All 2D elements had the

thicknesses of 0, +/-45, and 90 degree plies as separate design variables. The strut and jury were modeled as box beam elements with design variables of the box chord, depth, and skin and spar thickness. The box depth was 0.3 times the box chord.

The strength constraint for 2D elements was lamina principal strain less than 0.0045 at ultimate load. The strength constraint for cap elements was laminate stress less than 90,000 PSI at ultimate load. The strength constraint for the strut and jury elements was laminate principal strain less than 0.0045 at ultimate load. No buckling was allowed at ultimate load. The flutter constraint was damping factor G less than 0.02. Minimum skin gage was 0.1 inch.

Structural sizing was performed on two different strut/jury configurations, Configurations 1 and 3 (so named because of how the study was set up). Configuration 1 had the strut running from the landing gear pylon attachment point to the wing front spar at 57.6% semi-span. Configuration 3 is the V strut, with one strut running from the landing gear pylon attachment point to the wing front spar at 57.6% semi-span and another strut running from the gear pylon attachment point to the rear spar at 57.6% semi-span.

Sizing on the first strut configuration was done without flutter constraints, with 1.09Vd flutter constraints, and with 1.15Vd flutter constraints to determine the flutter weight penalty. The V-strut configuration was only sized with 1.15Vd flutter constraints. An equation relating weight and strut/jury wetted area to fuel burn was minimized as the objective in the optimization runs. Using this equation Sol 200 minimized weight and strut/jury chord.

2.1.8.8 Initial Linear Results

NASTRAN Sol 200 converged on solutions for the front spar strut model with the 3 different constraints and for the V-strut model with 1.15 flutter constraints. A weight summary of these solutions is shown in Table 2.25. The results show only a 324 lb penalty for meeting 1.09Vd flutter constraints and 346 lb penalty for meeting 1.15Vd on the front spar strut model. The V-strut model shows a 381 lb weight reduction over the front spar model with the 1.15 flutter constraints.

Sized thicknesses for the wing skins and wing rib and spar webs are shown in Figure 2.119 and Figure 2.120 for strut Configuration 1 with 1.09Vd flutter constraints. The skin thickness peaks at just over 0.4 inch on the upper skin at the strut attachment location. A good bit of the lower surface is minimum gage while a smaller area of the upper skin is minimum gage. The skins also show increased thicknesses locally at the engine attachment and side of body.

Peak thickness for the wing spar webs is 1.62 inch for the rear spar at the side of body and 0.9 inch for the front spar at the strut attachment. Much of the spar webs are minimum gage except for increases at the side of body, strut attachment, control surface attachment locations, and at the tip of the wing.

Almost all of the ribs are minimum gage except for at the tip of the wing. Sized wing rib and spar cap areas are shown in Figure 2.121. Most of the caps have a minimum area of 0.1 in^2 except at the strut attachment and wing tip. The front spar caps at strut attachment peak at 4.4 in^2 .

Sized 2D and 1D element thickness and areas for the sized landing gear pylon are shown in Figure 2.122 and Figure 2.123. The landing gear pylon front spar and rear spar have local peaks at the corners of the bulkhead at the side-of-body, the max being 5.4 inch on the rear spar web. There are also increased gages at the front and rear spars where the gear loads are introduced to the gear pylon. The gear pylon 1D elements are almost all minimum gage except upper caps on the rear spar, which peaked out at 10 in^2 .

Sized strut and jury box chords are shown in Figure 2.124. The strut and jury chords shown for Configuration 1 were close to optimal for the strength-only sizing, 1.09Vd flutter constraint, and 1.15 Vd flutter constraint sizing. The strut has minimum chord at the endpoints and jury attachment, and maximum chord between the endpoints and jury attachment to resist buckling. A curve showing the configuration 3 forward and aft strut chords added together is shown for comparison. The jury chord increases linearly from the strut to a maximum value at the wing.

Figure 2.125 shows the sized strut box skin and spar thickness distributions. The skin and spar both have minimum thickness between the endpoints and the jury attachment, where the chord is maximum. The configuration 3 forward strut has larger skin thickness than the configuration 1 struts, while the configuration 3 aft strut skin thicknesses are smaller. The configuration 3 forward strut spar thickness is in line with configuration 1; the configuration 3 aft strut spar thickness is smaller.

Figure 2.126 shows the sized jury box skin and spar thickness distributions. The configuration 1 jury box skins are near constant for most of the jury but have a larger thickness at the wing. The configuration 3 front and aft jury skin thickness curves are relatively flat. The configuration 1 jury box spars increase from the strut to a maximum value at the wing, and the configuration 3 aft spar thickness is lowest of all. Maximum stress and strain results for configuration 1 with 1.09Vd flutter constraints have been included to compare with strength allowables.

Figure 2.127 shows wing upper and lower skin ultimate principal strain for the 2.5G balance maneuver for skin ply 1. The figure shows the upper surface peak minimum strain of 0.00306, and the lower surface peak maximum strain of 0.00382, both less than the allowable of 0.0045. This means the non-minimum gage wing skins are not designed by strength cases but by buckling or flutter constraints.

Figure 2.128 shows ultimate maximum principal strain for ply one of the spar and rib webs, and shows maximum combined stresses for the spar and rib caps in the 2.5G balance maneuver. The web strains and cap stresses are both significantly below the design allowable.

Figure 2.129 shows strut and jury max ultimate combined strains for the 2.5G balance maneuver. The figure shows a relatively constant strut strain, with higher values at the jury and at the wing end. Peak strain at the wing end is 0.00408, which is below the allowable of 0.0045. The jury shows low strains, peaking at a value of 0.00246.

Ground conditions produced peak loads on the landing gear pylon. Figure 2.130 shows maximum ultimate principal strain, for layer 9, on the gear pylon for the braked roll ground condition. Rear spar web regions showing peak strains at the strength allowable include near the gear load introduction location, the bottom section, and at the side-of-body corner. Also, the top of the panel supporting the gear side brace is at the allowable. Figure 2.131 shows the gear pylon caps peak ultimate combined stress for the critical braked roll condition is well below the allowable.

Flutter surveys including all modes up to 20 Hz have been completed on all mass cases at Mach numbers of 0.7, 0.76, 0.82, 0.86, 0.90, and 0.94. The surveys show critical instabilities to occur at Mach = 0.82 for two mass cases, one with full fuel and payload to reach maximum takeoff weight, the second with residual fuel and maximum payload.

The Mach trend for the 1.09Vd sized model is shown in Figure 2.132. No speeds are shown at Mach = 0.90 because no flutter was found at the maximum speed investigated. (The effect of the aft aerodynamic center shift above $M = 0.82$ can be seen.) Figure 2.133 and Figure 2.134 show the damping and frequency curves for the critical Mach = 0.82 using the sized 1.09Vd model. Results are shown for the full fuel and for residual fuel mass cases. The frequency plots include only the modes that contribute the most to the aeroelastic instability.

The results show the optimizer successfully met the flutter constraints of keeping the damping less than 0.02 for speeds below 1.09Vd. The full fuel mass case has a positive crossing for a symmetric mode at 2.75Hz. This flutter mode, shown in Figure 2.135, is primarily a coupling of bending mode 11 and torsion mode 16, shown in Figure 2.136 and Figure 2.137. The frequencies plot shows these modes converging when the damping turns positive. Much of the torsion of mode 16 occurs at the engine attachment section of the wing, where the wing is less stiff than a typical cantilevered wing. The flutter mode has significant fore/aft motion but this mode doesn't contribute to the instability as much as modes 11 and 16.

The full fuel mass case also has a positive crossing for an antisymmetric mode at 3.51Hz. This flutter mode, shown in Figure 2.138, is primarily a coupling of bending mode 15 and torsion mode 17. Like the symmetric torsion mode the antisymmetric torsion mode 17 has a lot of torsion occurring at the engine attachment section of the wing. Modes 15 and 17 are shown in Figure 2.139 and Figure 2.140.

The residual fuel mass case has two positive symmetric crossings at 2.69Hz and at 2.78Hz. These flutter modes, which are shown in Figure 2.141 and Figure 2.142, are primarily a different

combination of bending mode 12, fore/aft mode 14, and torsion mode 16. Modes 12, 14, and 16 are shown in Figure 2.143, Figure 2.144, and Figure 2.145.

Table 2.25 – Sized Structure Weight Summary

	A Config 1 No Flutter	B Config 1 1.09 V _D	C Delta (B-A)	D Config 1 1.15 V _D	E Delta (D-A)	F Config 3 1.15 V _D	G Delta (F-D)
Skins	5,558	5,700	142	5,689	131	5,581	-108
Spars	766	822	56	828	63	710	-118
Ribs	705	719	14	718	13	683	-35
Spar Caps	230	249	20	250	20	182	-70
Rib Caps	161	173	12	174	13	138	-37
Strut	787	866	78	890	103	881	-9
Jury	21	23	1	24	3	19	-5
Gear Pylon 2D	3,415	3,415	0	3,415	0	3,415	0
Gear Pylon 3D	125	125	0	125	0	125	0
Total	11,768	12,092	323	12,113	346	11,734	-382

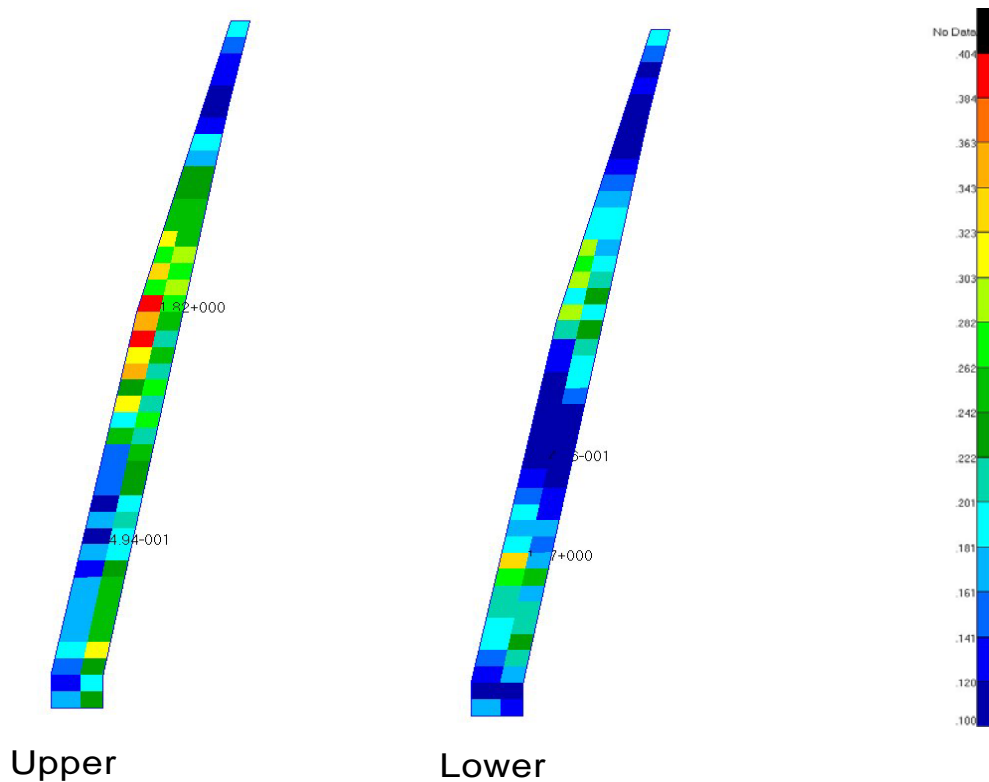


Figure 2.119 – Sized Upper and Lower Skin Thickness – Config. 1 1.09V_D

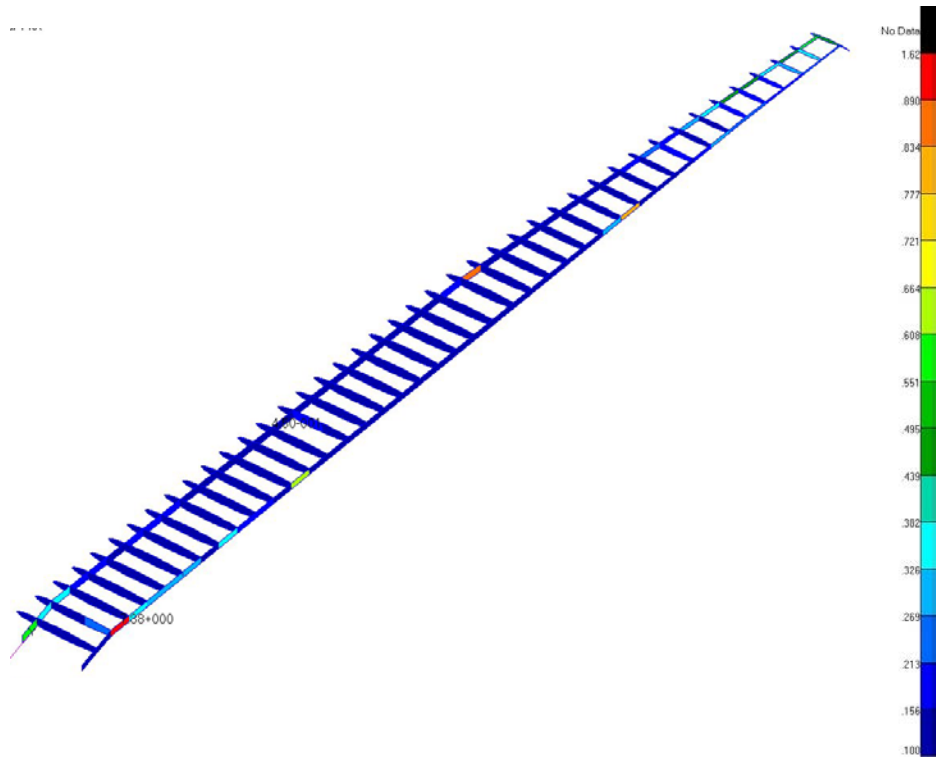


Figure 2.120 – Sized Rib and Spar Web Thickness – Config 1 1.09Vd

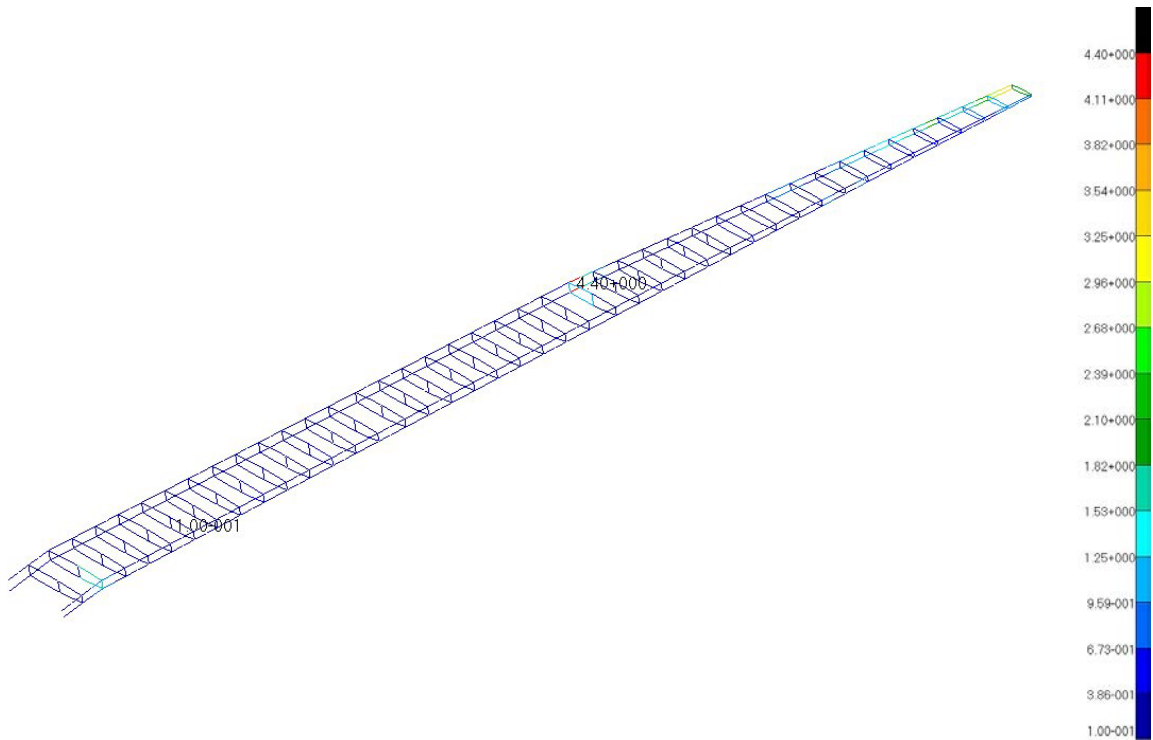


Figure 2.121 – Sized Rib and Spar Cap Area – Config 1 1.09Vd

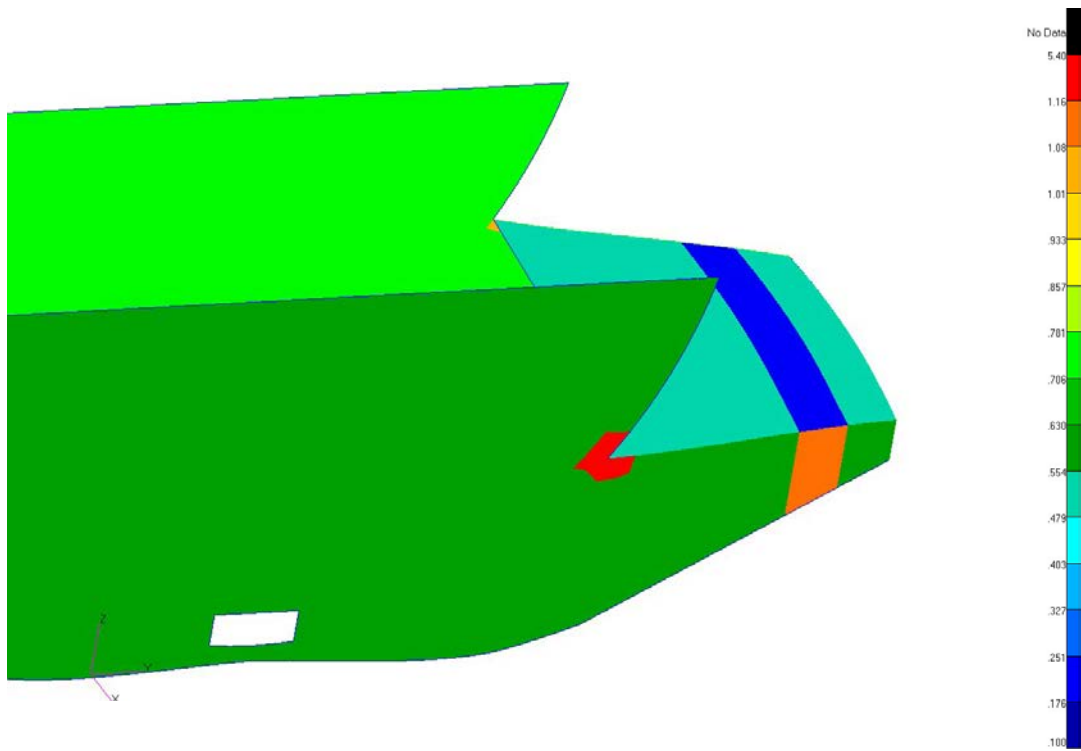


Figure 2.122 – Gear Pylon 2D Element Thickness – Config 1 1.09Vd

Patran 2010.2.3 04-Jan-13 13:36:35
Area Scalar Plot

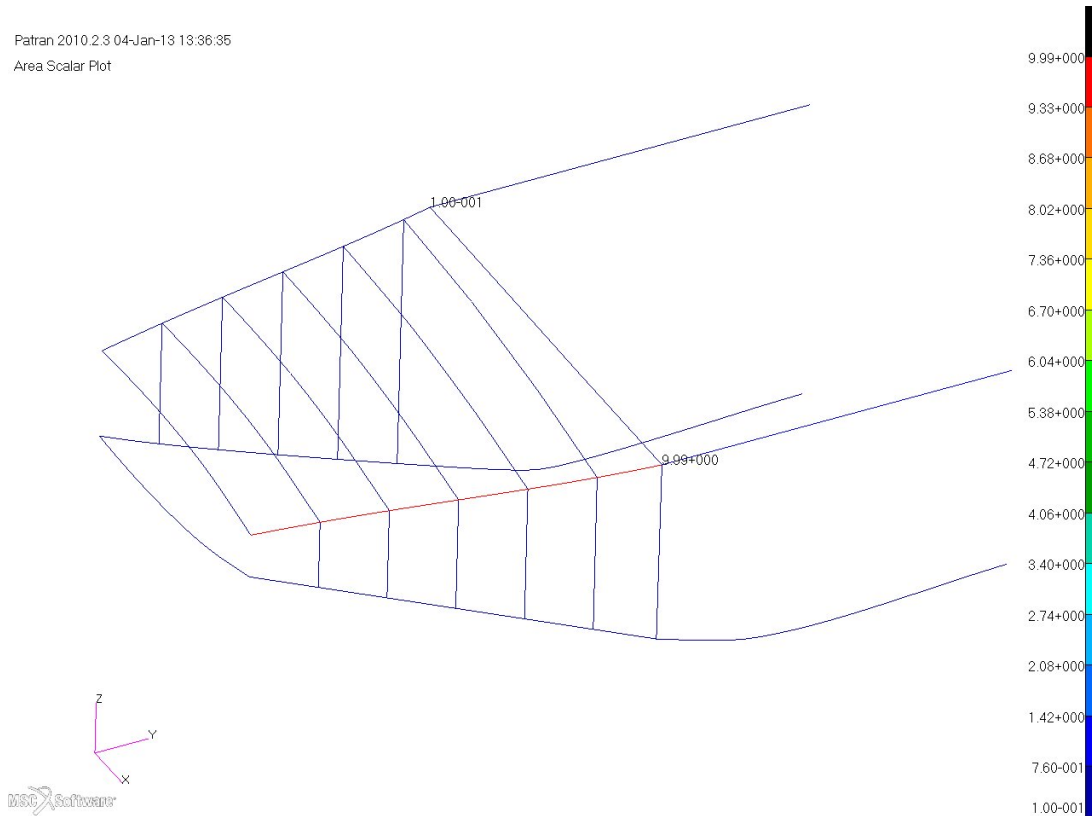


Figure 2.123 – Gear Pylon 1D Element Area – Config. 1 1.09Vd

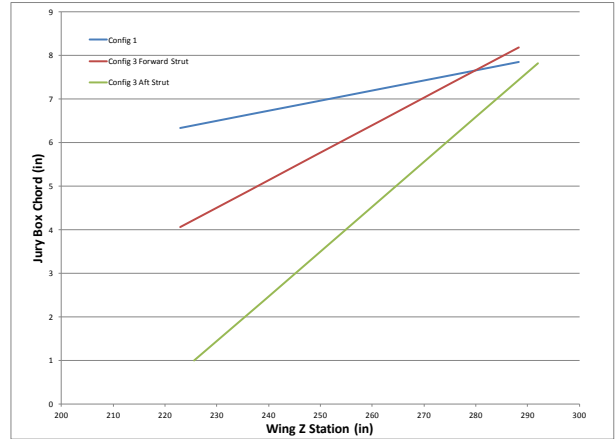
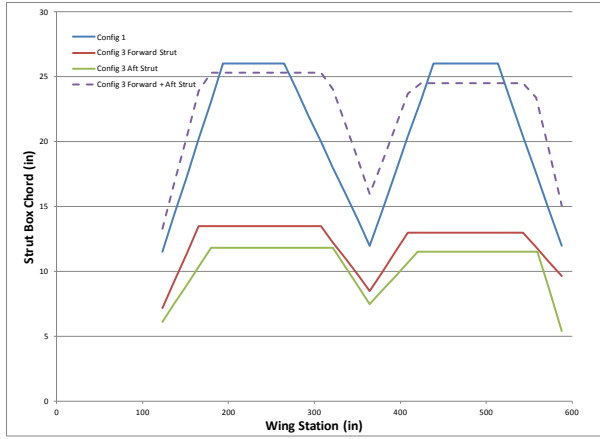


Figure 2.124 – Sized Strut and Jury Chord

SKINS

SPARS

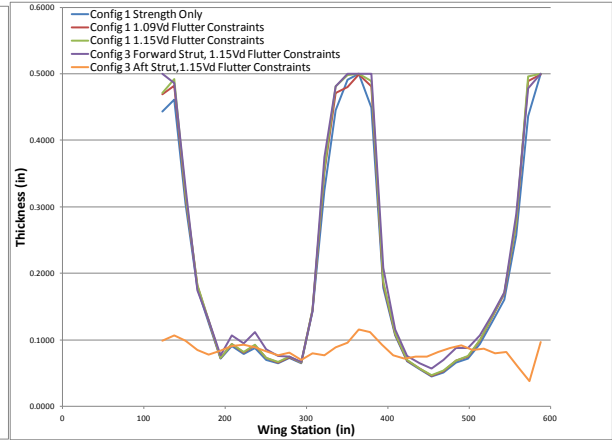
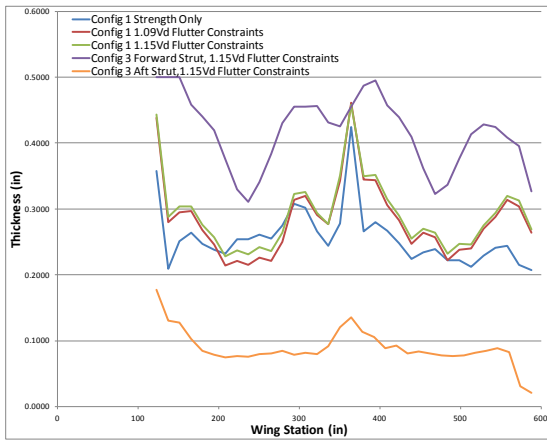


Figure 2.125 – Sized Strut Box Skin and Spar Thickness

SKINS

SPARS

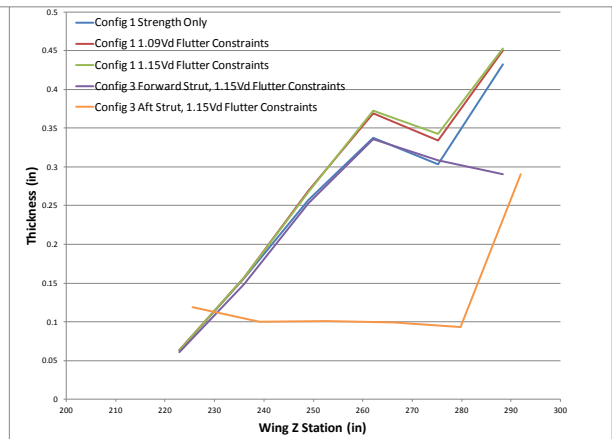
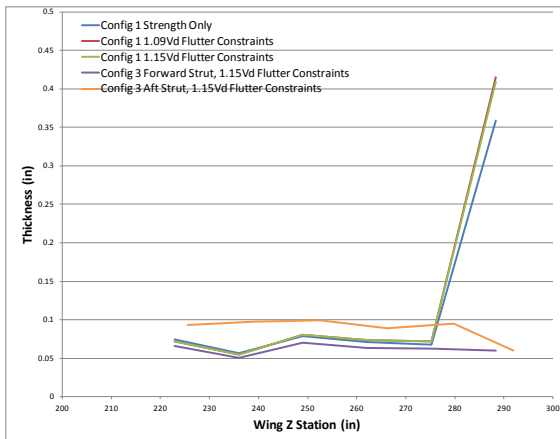


Figure 2.126 – Sized Jury Box Skin and Spar Thickness

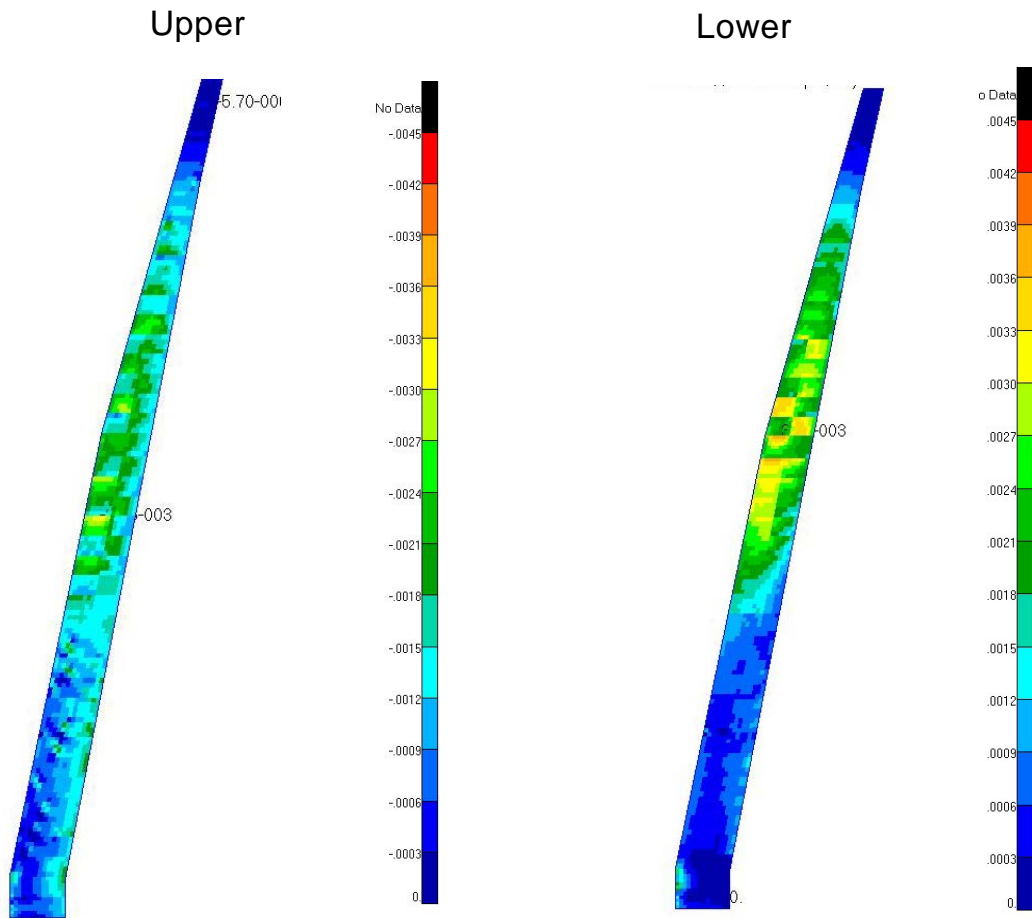


Figure 2.127 – Wing Upper and Lower Skin Ply 1 Ultimate Principal Strain – 2.5G Balance Maneuver

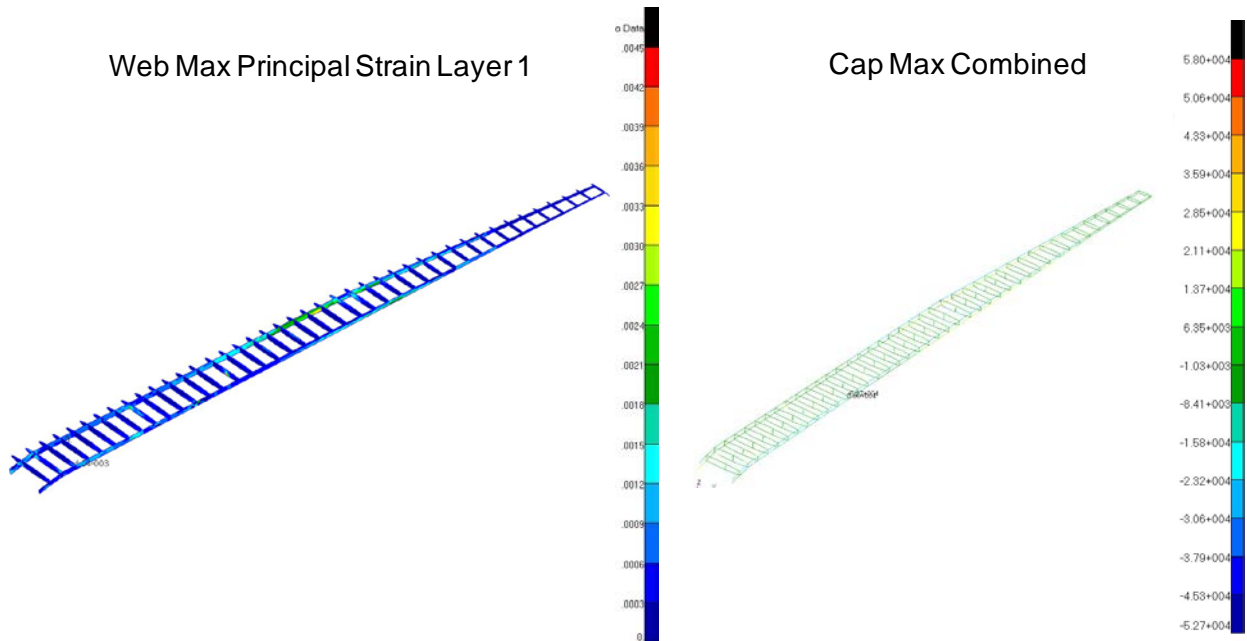


Figure 2.128 – Rib and Spar Maximum Ultimate Stress and Strain 2.5G Balance Maneuver

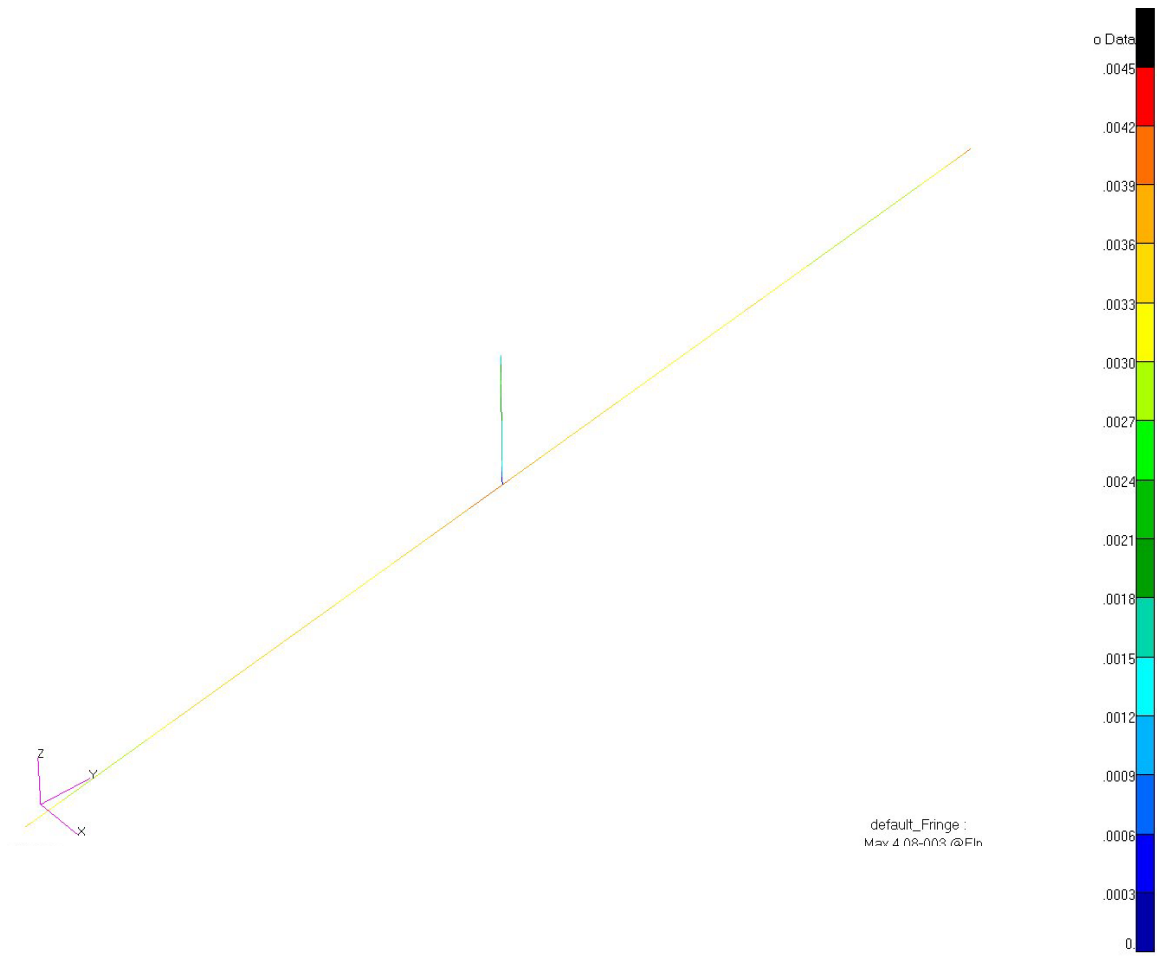


Figure 2.129 – Strut and Jury Max Ultimate Combined Strain – 2.5G Balance Maneuver

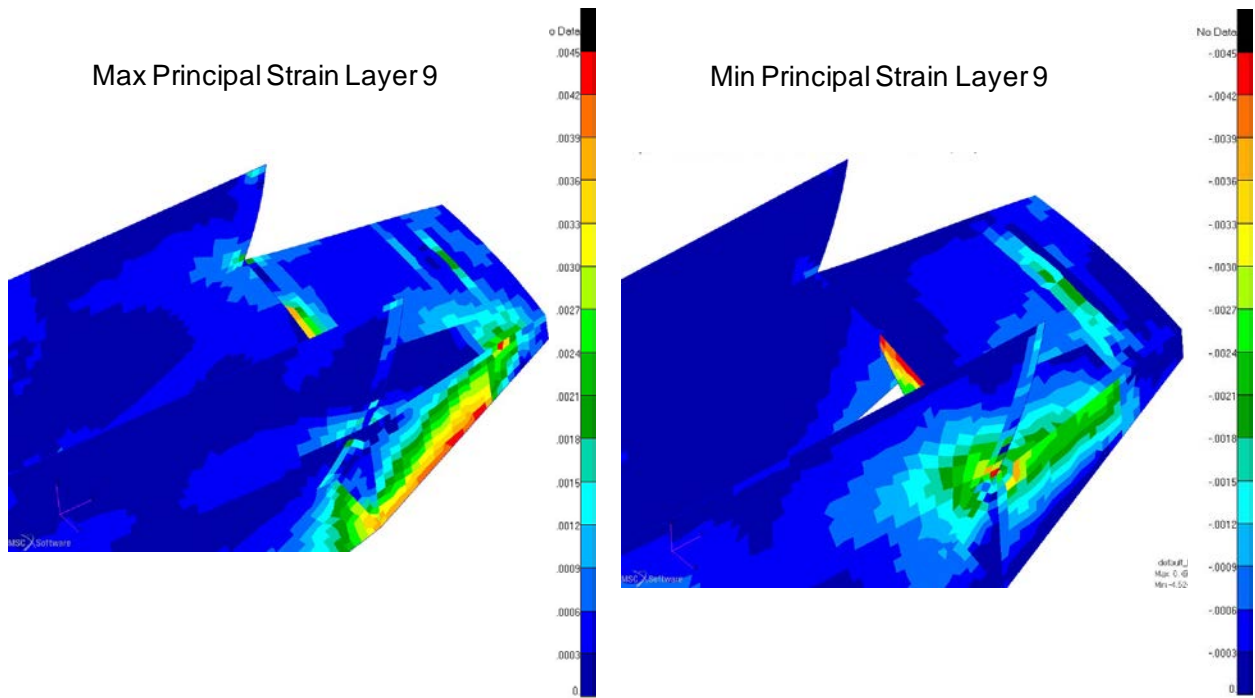


Figure 2.130 – Gear Pylon Ultimate Layer 9 Principal Strain – Braked Roll Condition

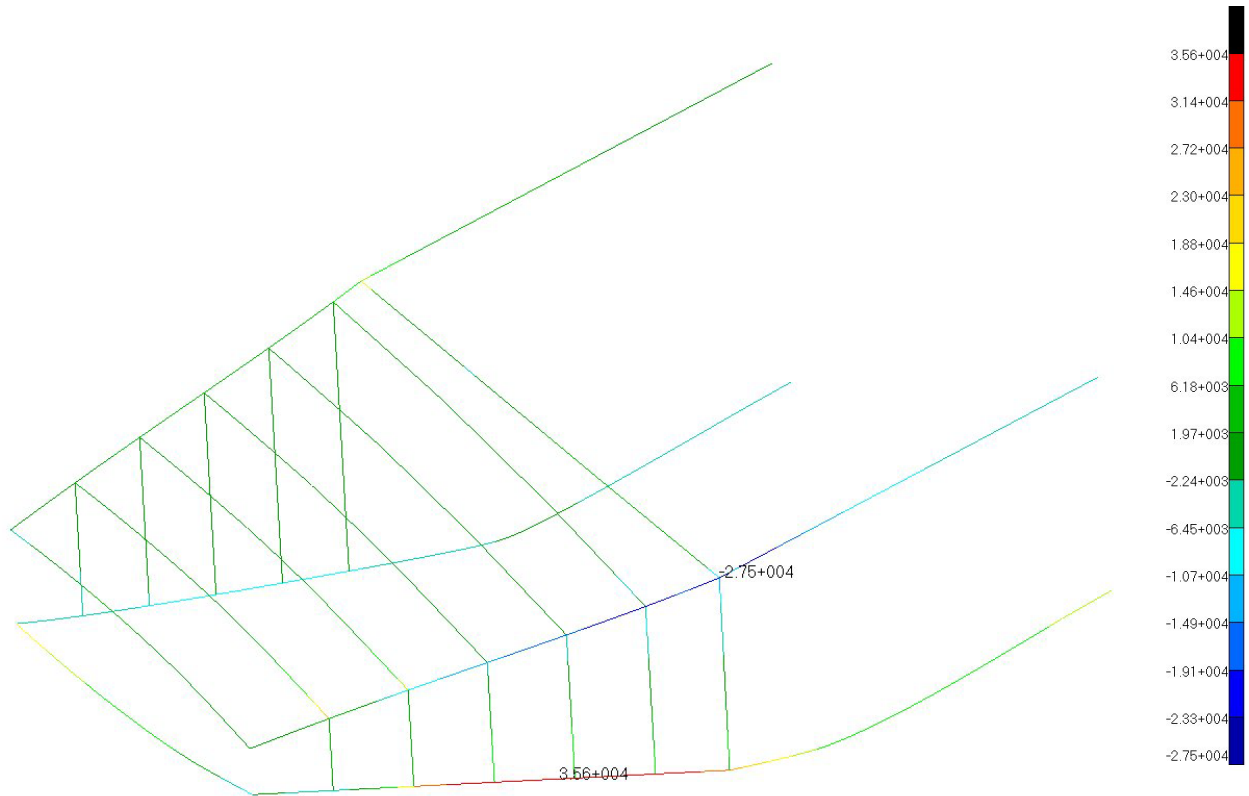


Figure 2.131 – Gear Pylon Ultimate Combined Stress – Braked Roll Condition

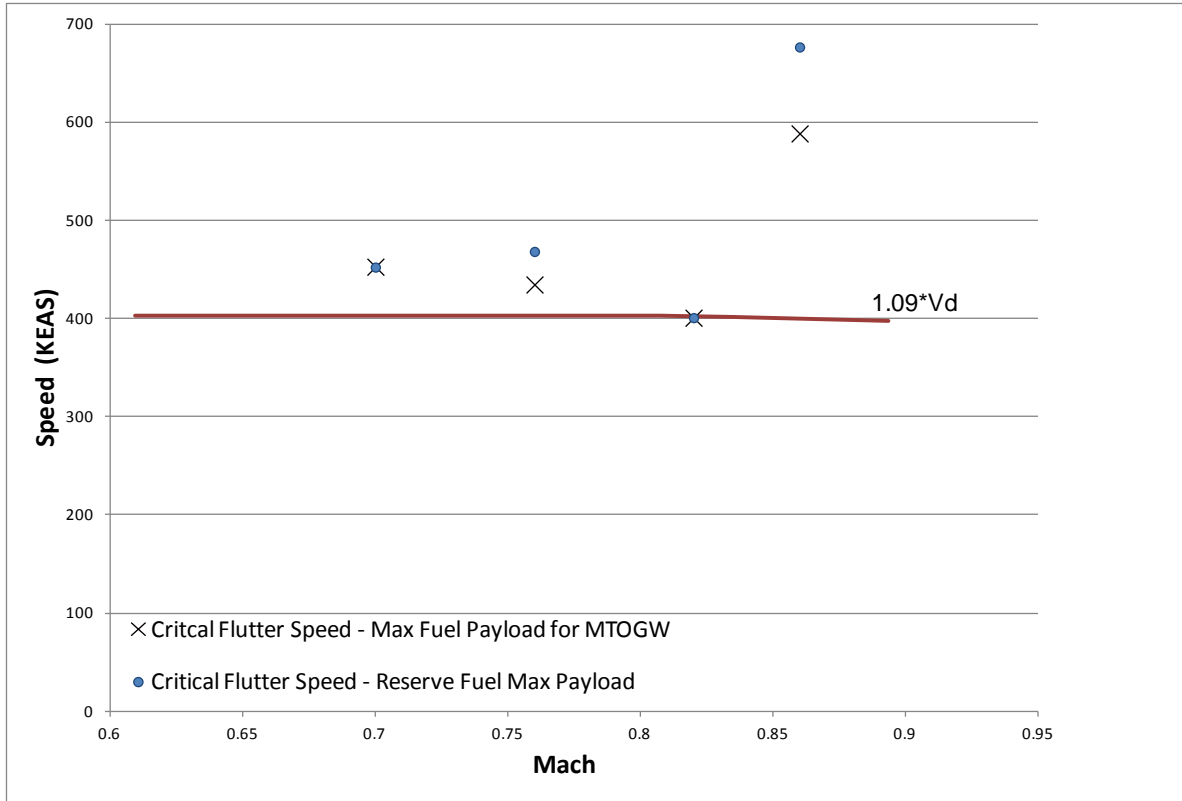


Figure 2.132 – Critical Flutter Speed Mach Trend

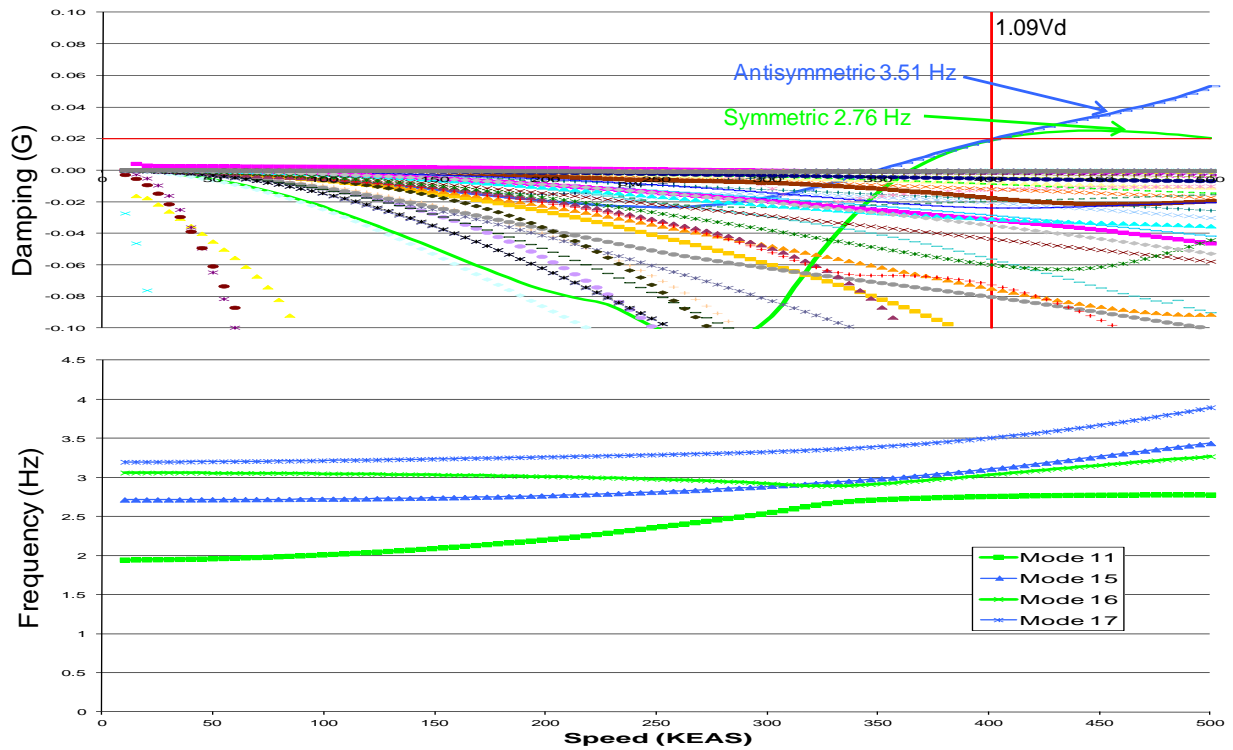


Figure 2.133 – Flutter V-G Mach=0.82, $1.09V_d$ Sized Model, Full Fuel, Payload for MTOGW

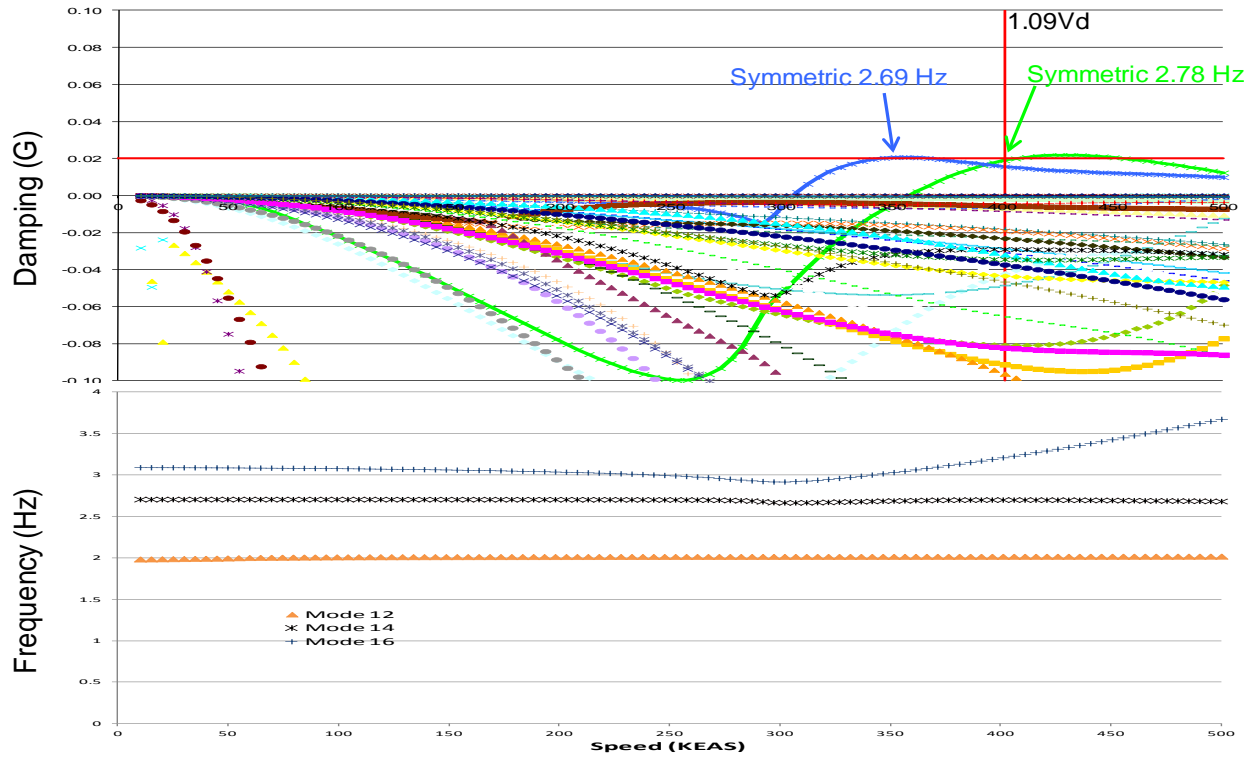


Figure 2.134 – Flutter V-G Mach=.82, 1.09Vd Sized Model, Residual Fuel, Max Payload

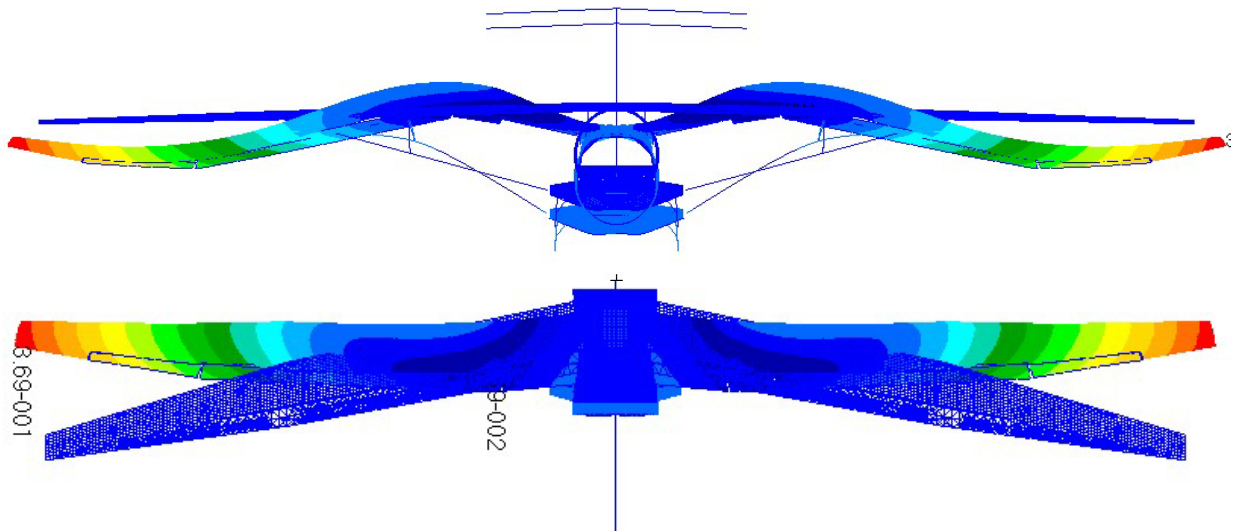


Figure 2.135 – Symmetric Flutter Mode, 1.09Vd Model, Mach=.82, Full Fuel, 401 KEAS

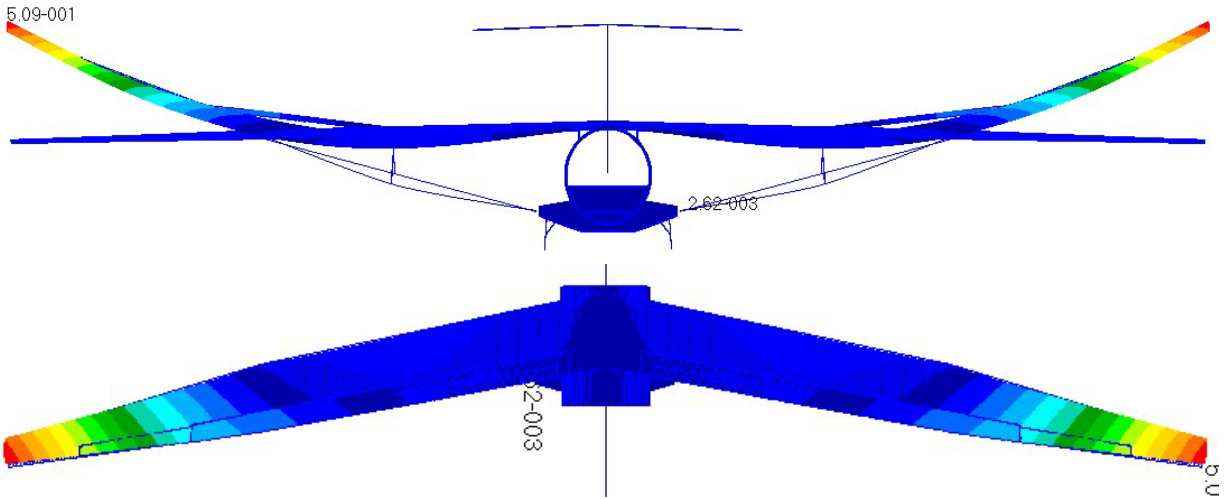


Figure 2.136 – Mode 11 1.95Hz, 1.09Vd Model, Full Fuel

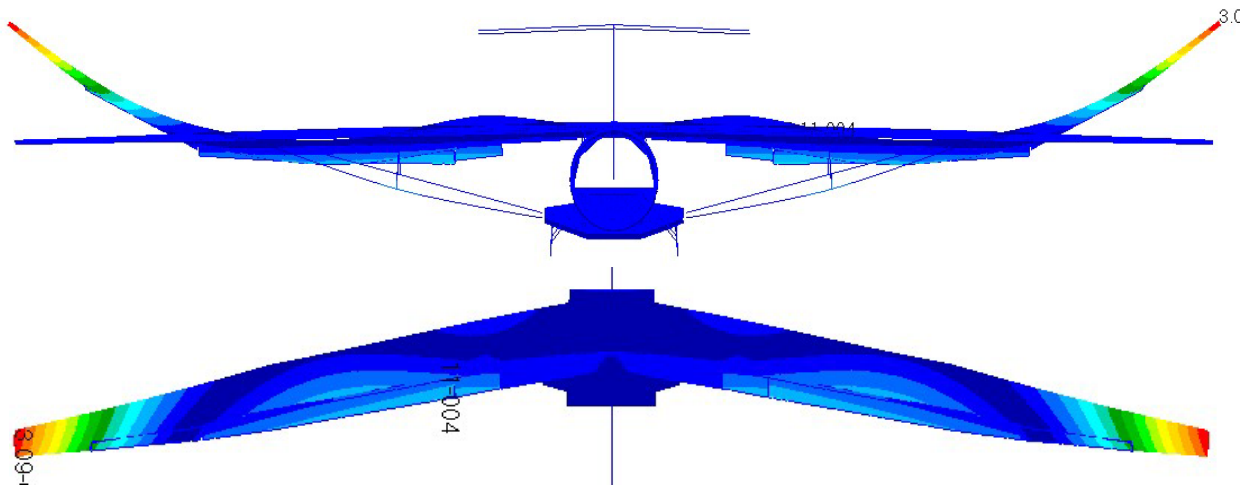


Figure 2.137 – Mode 16 3.06 Hz, 1.09Vd Model, Full Fuel

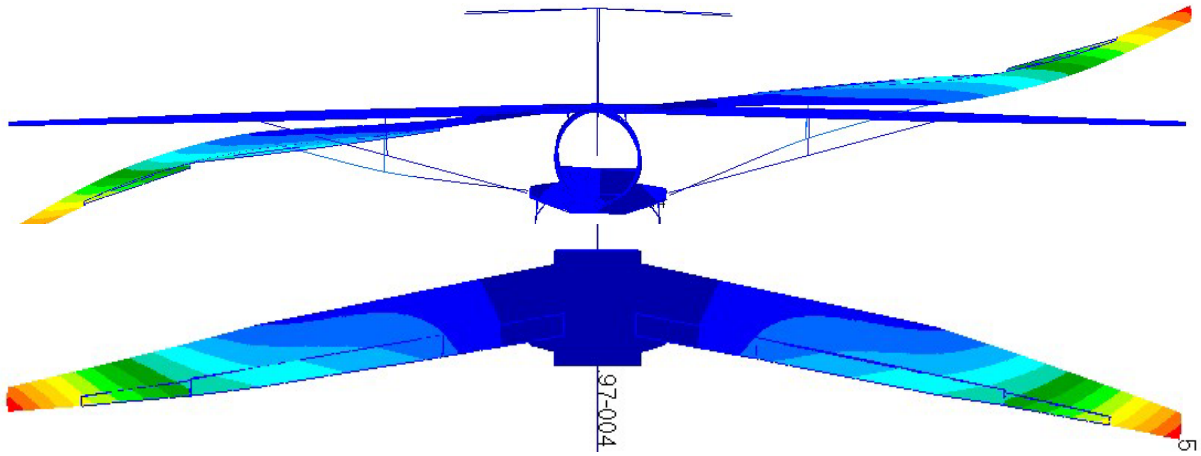


Figure 2.138 – Antisymmetric Flutter Mode, 1.09Vd Model, Mach=.82, Full Fuel

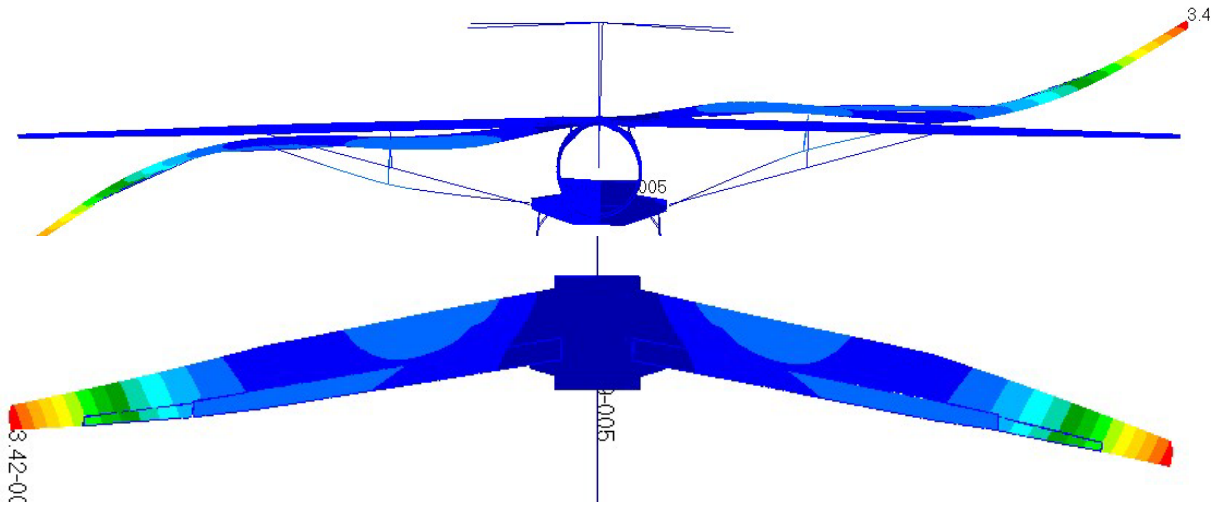


Figure 2.139 – Mode 15 2.71 Hz, 1.09Vd Model, Full Fuel

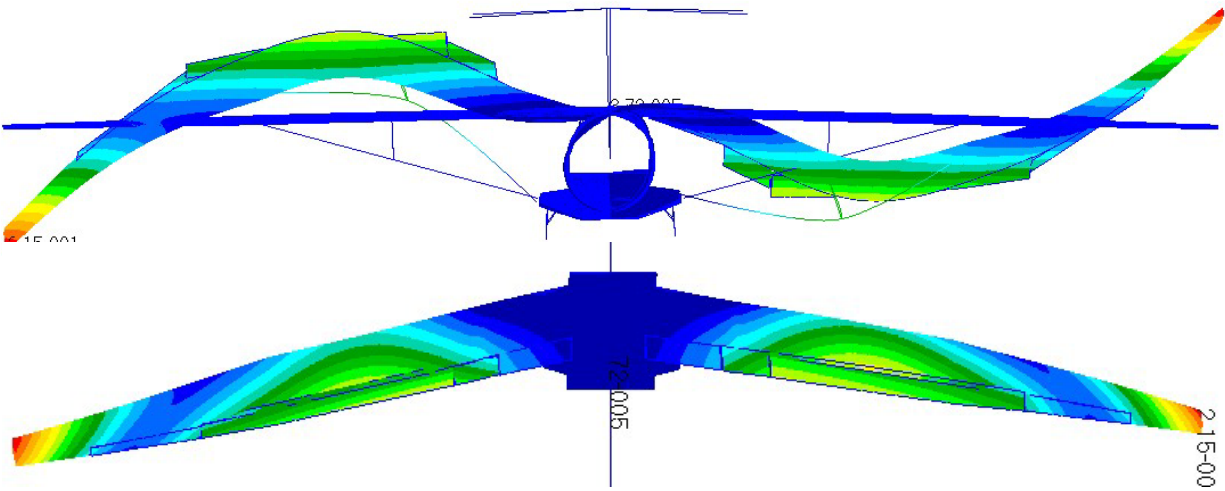


Figure 2.140 – Mode 17 3.20 Hz, 1.09Vd Model, Full Fuel



Figure 2.141 – Flutter Mode 2.70Hz, 1.09Vd Model, Residual Fuel, 356 KEAS

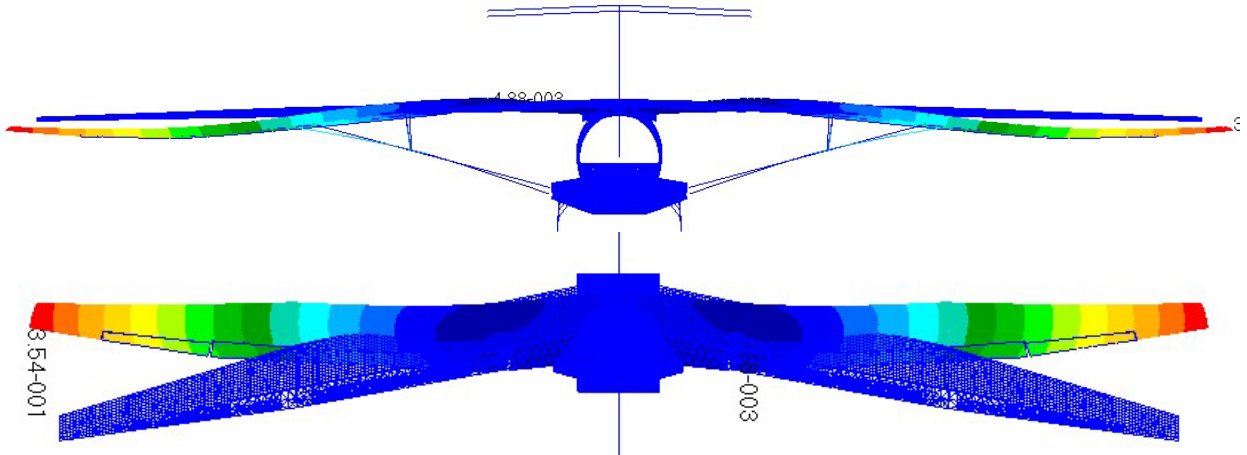


Figure 2.142 – Flutter Mode 2.78Hz, 1.09Vd Model, Residual Fuel, 401 KEAS

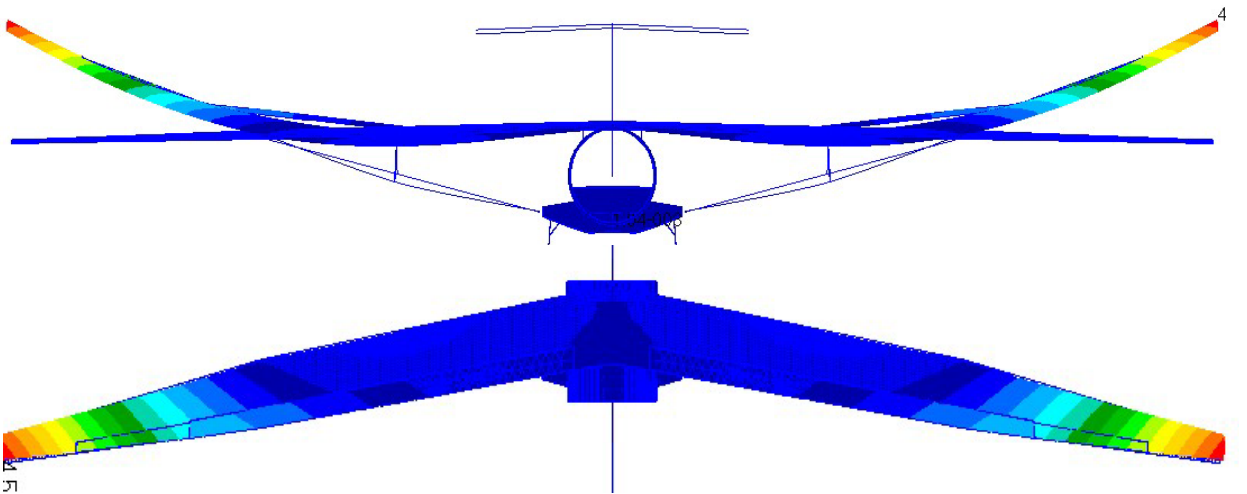


Figure 2.143 – Mode 12 1.98Hz, 1.09Vd Model, Residual Fuel

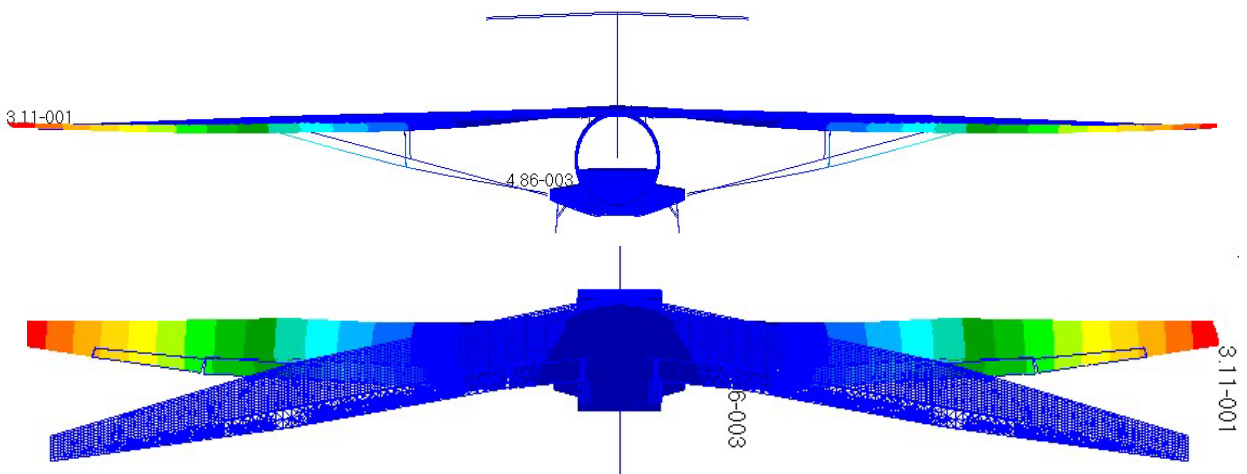


Figure 2.144 – Mode 14 2.70 Hz, 1.09Vd Model, Residual Fuel

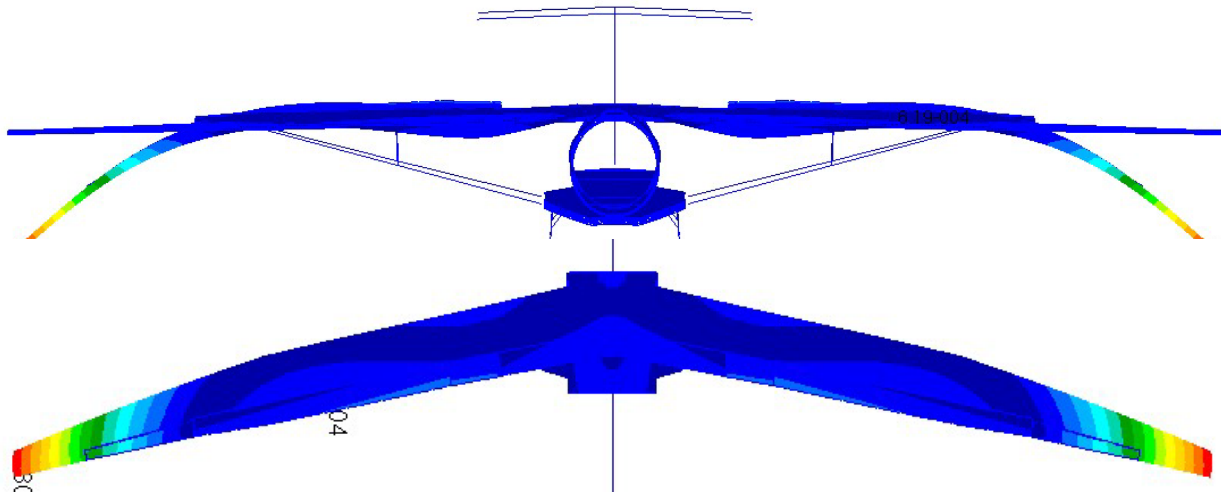


Figure 2.145 – Mode16 3.09Hz, 1.09Vd Model, Residual Fuel

2.1.8.9 Initial Linear FEM Conclusions

The results of the detailed FEM sizing analysis for this very high aspect ratio wing show a significant truss-braced configuration benefit to structural weight relative to a cantilevered wing. The weight penalty to pass flutter constraints was minimal and the V-strut configuration showed a small weight benefit over the single strut configuration. The loads and sized structure inboard of the strut both show the benefit of the truss bracing. The CFD-predicted aft shift in aerodynamic center improved flutter speeds for Mach numbers above 0.82. The loads for the 2.5G and -1G balance maneuvers were larger than those for 1-cos dynamic gusts. Buckling constraints, and where needed, flutter constraints, sized the wing, strut, and jury. The landing gear pylon was critical for strength requirements for the gear cases. The configuration 1 model sized to pass 1.09Vd flutter constraints will be the basis for the upcoming aeroelastic wind tunnel test, which will verify the conclusions of this analysis.

2.1.8.10 Full Scale Resizing Using Wind Tunnel Results

The full scale FEMs have been resized using the results from the aeroelastic test summarized in Section 3.0. The test showed that the flutter speed varied as loads on the model varied. This non-linear result has been modeled by including preload and large displacement non-linear effects in the flutter solution. Vehicle design criteria for loads to apply to the flutter analysis aren't well defined. Negative limit maneuver loads were used to resize the FEM. Transport category negative limit maneuver loads are calculated at -1G up to Vc with a linear variation to 0G at Vd. Loads calculated at Vd were used to check stability up to 1.15Vd.

The non-linear flutter method used is described in Section 3.0. To run solution 106 with large displacements on the full scale FEM, linear elements such as CBARs needed to be removed from the model. Even with most of the linear elements removed solution 106 convergence was slow.

No unsteady aerodynamic weighting factors were used in the resizing because the uncorrected doublet lattice analysis was fairly accurate at predicting test minimum flutter speeds at each angle of attack. The critical Mach for minimum flutter speed varied for each angle of attack. The flutter analysis used uncorrected doublet lattice aerodynamics at Mach = 0.75 for V_c and below and Mach = 0.8 for V_d and above.

The flutter solution in Nastran solution 200 uses a linear structures model. The sizing exercise involved constraining the linear flutter results in solution 200 such that flutter requirements were met when the non-linear preload and large displacement flutter speeds were checked for the optimized FEM.

Optimization was successful in producing a FEM which met all strength, buckling, and non-linear flutter constraints. This was done for baseline configuration 1 (Strut attached to front spar) and configuration 3 (Struts attached to both front and rear spar). Non-linear flutter results for the full fuel mass case configuration 1 active constraint antisymmetric mode is shown in Figure 2.146. This flutter mode is at the required 0 g damping at V_c and -1G. The flutter mode becomes more damped in a non-linear way as the load factor is increased from -1G to 0G and +1G. Figure 2.147 shows the non-linear results for the residual fuel mass case configuration 1 active symmetric mode. The mode meets the 0 g requirement at V_d and is less than 0.02 at 1.15 V_d . This flutter mode shows little variation in damping at V_d for different load factors. Non-linear flutter results for the residual fuel mass case configuration 3 active constraint symmetric mode is shown in Figure 2.148. Again, this mode meets the 0 g requirement at V_d and is less than 0.02 at 1.15 V_d .

Weight summaries for the resized FEMs are shown in Table 2.26. The flutter penalty for the baseline configuration has gone from 346 lb pretest to 809 lb including all post-test non-linear flutter analysis updates. The pretest configuration 3 (strut attached to both front and rear spar) sizing including flutter constraints was 381 lb lighter than configuration 1 sizing including flutter constraints. The post-test configuration 3 sizing including flutter constraints was 148 lb lighter than post-test configuration 1 sizing. The configuration 3 resized results show a decrease in wing skin weight and an increase in strut weight when compared to the configuration 1 results.

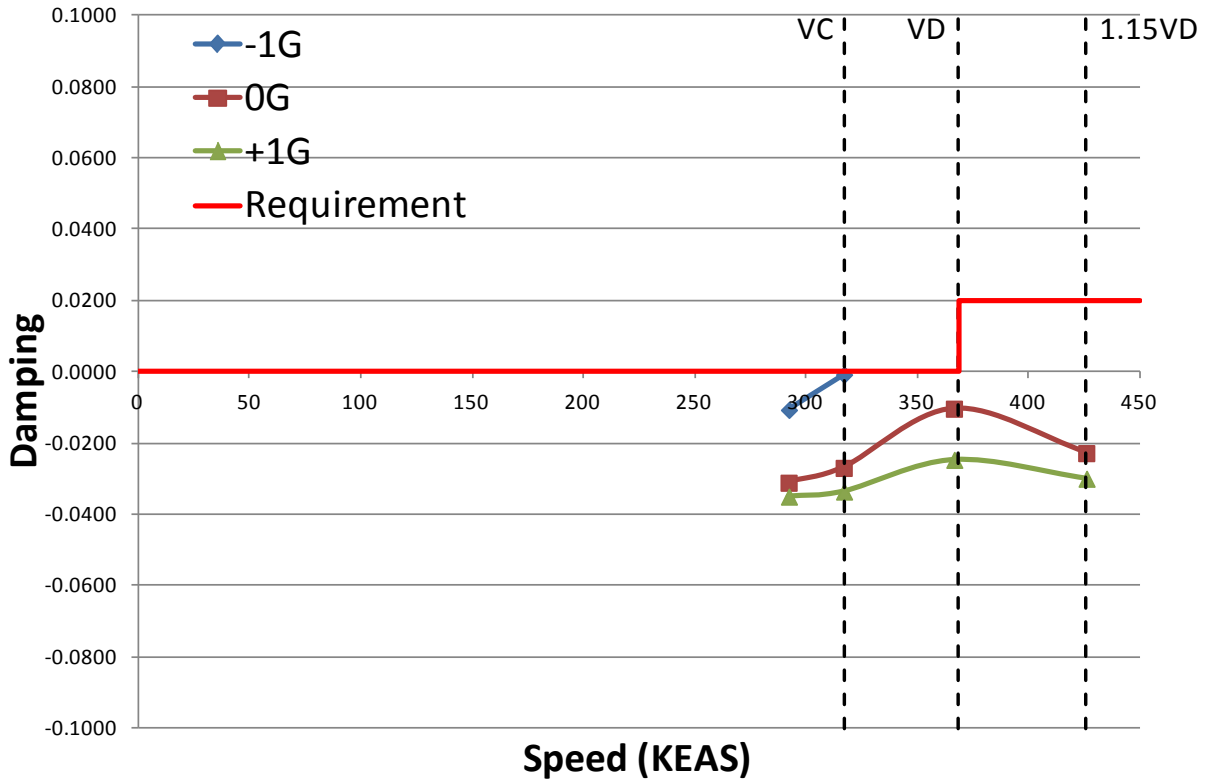


Figure 2.146 – Non-linear Flutter Results Config 1 Full Fuel

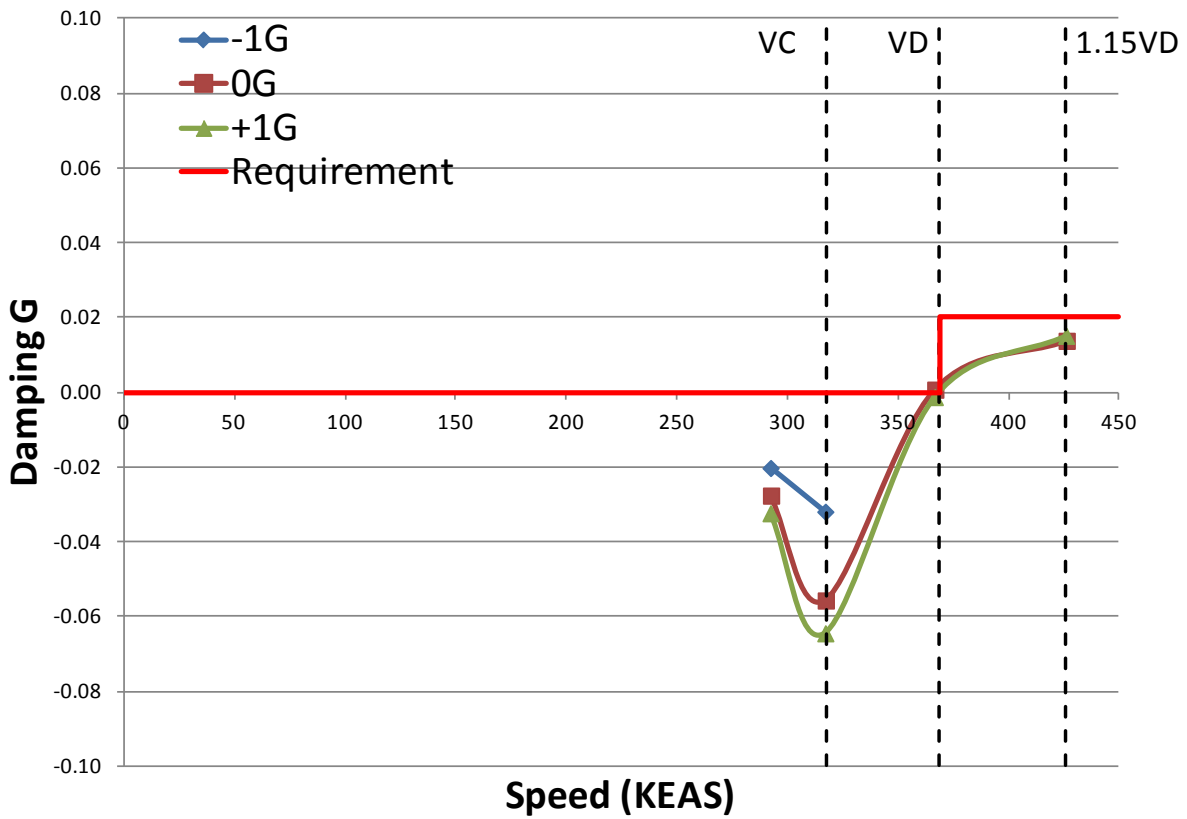


Figure 2.147 – Non-linear Flutter Results Config 1 Residual Fuel

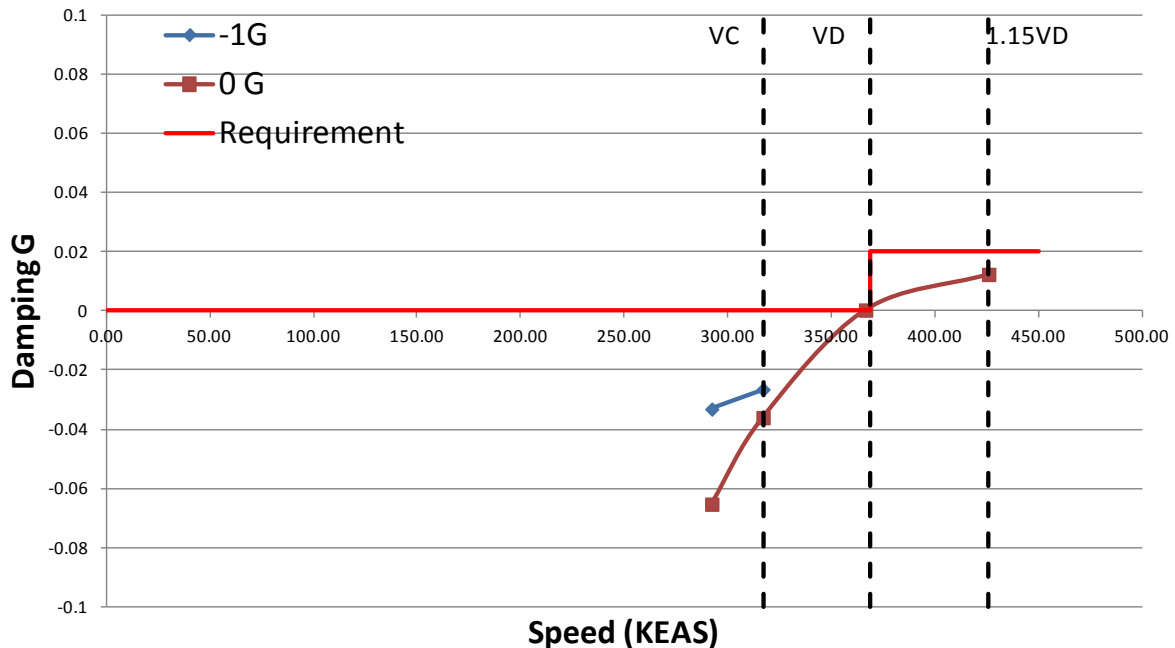


Figure 2.148 – Non-linear Flutter Results Config 3 Residual Fuel

Table 2.26 – Post Aeroelastic Test Sizing Weight Summary

	A Config 1 No Flutter	B Pretest Config 1 1.15 V _D	C Pretest Delta (B-A)	D Pretest Config 3 1.15 V _D	E Pretest Delta (D-B)	F Posttest Config 1 1.15 V _D	G Posttest Delta (F-A)	H Posttest Config 3 1.15 V _D	I Posttest Delta (H-F)
Skins	5,558	5,689	131	5,581	-108	6,031	473	5,670	-361
Spars	766	828	63	710	-118	814	48	723	-92
Ribs	705	718	13	683	-35	724	19	711	-14
Spar Caps	230	250	20	182	-70	230	1	193	-38
Rib Caps	161	174	13	138	-37	170	9	155	-15
Strut	787	890	103	881	-9	1,032	245	1,419	387
Jury	21	24	3	19	-5	36	14	20	-16
Gear Pylon 2D	3,415	3,415	0	3,415	0	3,415	0	3,415	0
Gear Pylon 3D	125	125	0	125	0	125	0	125	0
Total	11,768	12,113	346	11,734	-382	12,577	809	12,431	-149

2.1.9 Propulsion System Development and Performance

The gFan engine proposed in Phase I (1) of the program represents an advanced 2035 turbofan. In the absence of aircraft sensitivities, a 1.35 fan pressure ratio design was selected as an aggressive starting point. In phase II, Boeing provided GE with aircraft thrust requirements and fuel burn sensitivities to engine specific fuel consumption, weight and drag for the SUGAR High aircraft. These thrust requirements and sensitivities were used to generate the updated gFan+, and are summarized in Table 2.27.

Table 2.27 – Representative Thrust Requirements and Aircraft Sensitivities

Flight Condition	Thrust Requirements
Top Of Climb	3,200
Takeoff Boeing Equivalent Thrust	14,500
Engine Parameter = Fuel Burn Sensitivity	
1% SFC =	1.1 %
1,000 lb =	2.81%
2.4 lbf Nacelle Drag =	0.09%

Based on these sensitivities, GE conducted a fan pressure ratio parametric study to gain insight into the aircraft level trades between engine design parameters and center the phase II gFan+ cycle design. The SFC, weight and drag effects on fuel burn are shown in Figure 2.149 for fan pressure ratios ranging from 1.35 to 1.55. The data is representative of unique LP spool designs coupled to a rubber core having common thermodynamic characteristics across the spectrum of pressure ratios.

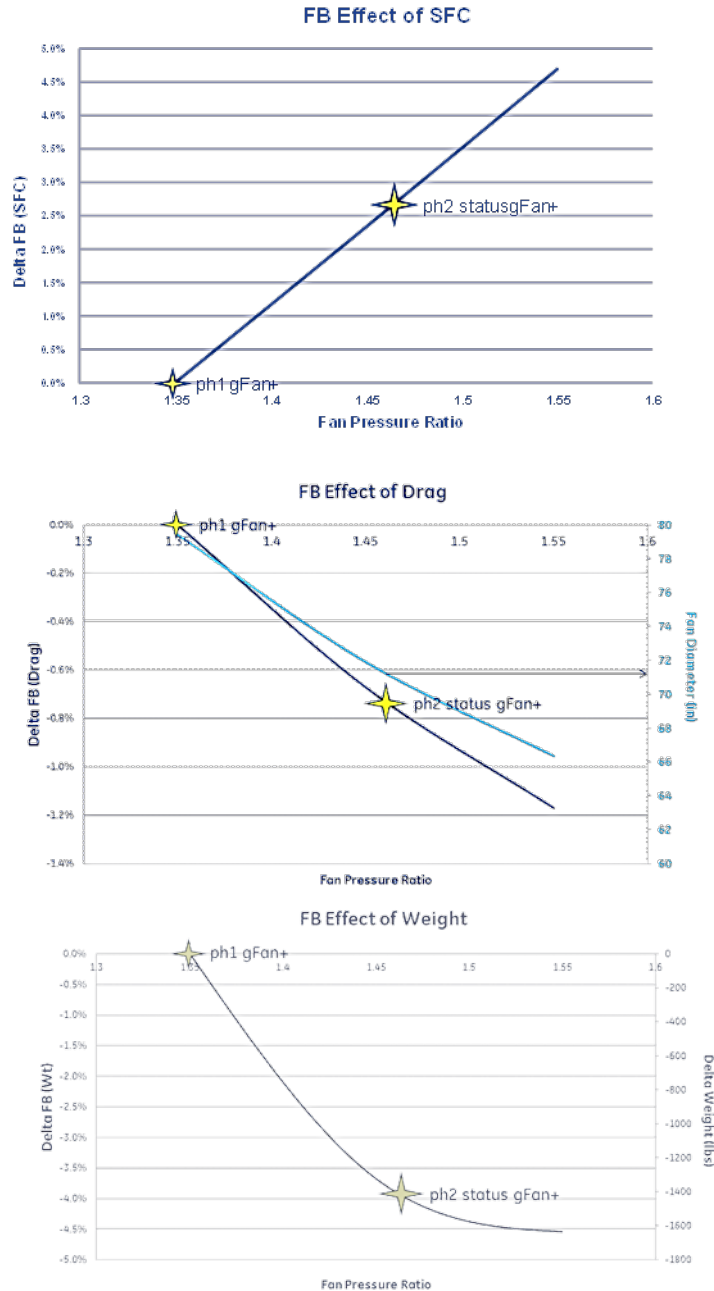


Figure 2.149 – gFan+ Fan Pressure Ratio Parametric Study

A fan pressure ratio of 1.46 was selected from the study for the gFan+, sacrificing SFC to realize a lighter weight, lower drag engine based on Figure 2.150 below. The expected fuel burn benefit resulting from the fan pressure ratio parametric, along with a refinement of component efficiencies is summarized in Figure 2.151.

The resulting gFan+ engine is described in Section 2.2.8.

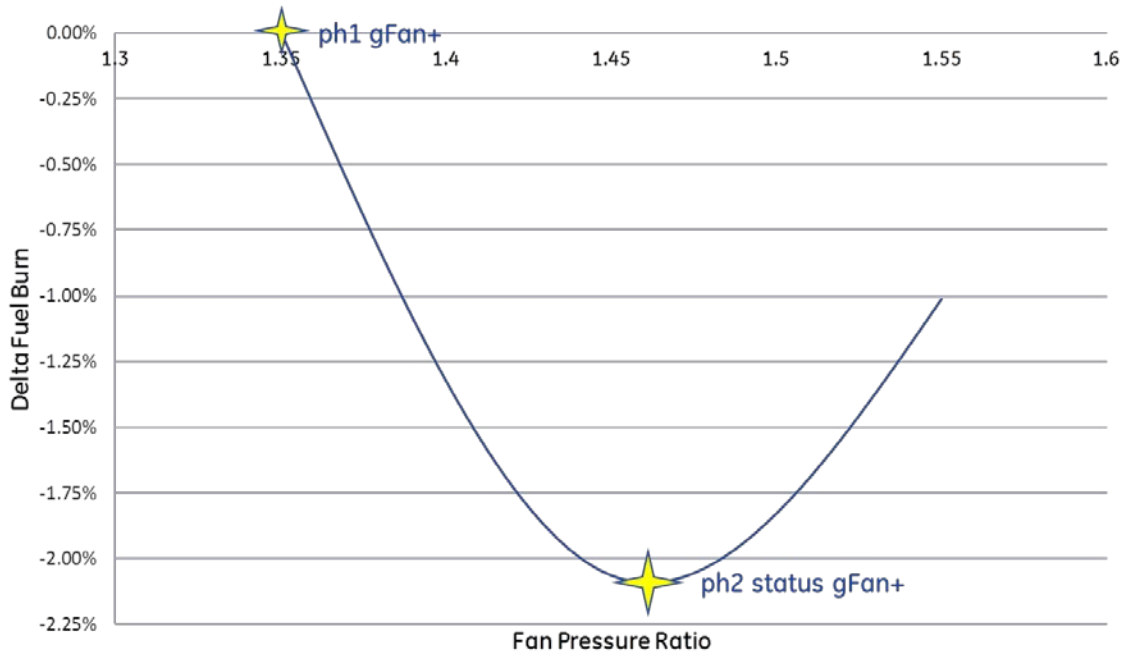


Figure 2.150 – Fan Pressure Ratio, Fuel Burn Trade

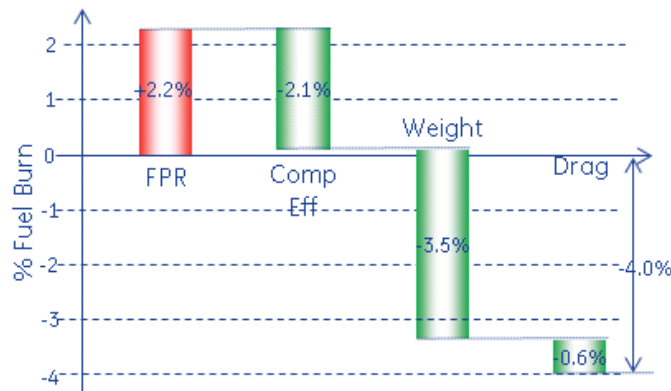


Figure 2.151 – gFan+ Fuel Burn Improvement Estimate

2.2 Configuration Description

The configuration covered in this description was generated in response to NASA Subsonic Fixed Wing N+3 design requirements (14) which initiated under a Phase I contract (1). The “SUGAR High” configuration (Model 765-095) represents a single member of a 737 class airplane family, the evolution of which is outlined in Table 2.28. It is a tube and wing configuration with a high mounted truss braced wing, twin wing mounted engines, a T-tail empennage, and pylon mounted main landing gear. The 154 passenger dual class fuselage is a 6-abreast seating arrangement, the lower lobe is bulk loaded.

The configuration description details an uncycled configuration. The final sizing is detailed in Section 2.3.3.

Table 2.28 – 765-095 Revision History

Rev.	Description of Major Changes	Date
New	SUGAR Phase I Exit	6/4/2009
A	Fuselage Refinement, Landing Gear Integration	5/2/2011
B	Wing Planform MDO	11/7/2011
C	High Speed Wing Design	1/5/2012
D	Strut Planform, Low Speed Wing Design, Engine Pylon Integration	10/8/2012

2.2.1 Integration

The aircraft general arrangement drawing, configuration walk-around, and principal characteristics are shown in Figure 2.152, Figure 2.153, and Table 2.29 respectively. An additional walk-around illustration is provided (Figure 2.154) for an un-ducted fan (UDF) version of the same airplane. The configurations are identical other than the propulsion installation thus, a general arrangement is not provided for the UDF variant. Table 2.30 shows the component axis system origins relative to the body axis.

Parameter	Units	Total Projected	Horizontal Stab.	Vertical Fin
Area	ft.^2	1477.11	296.24	297.69
Aspect Ratio		19.552	5.000	1.000
Span	in.	2039.301	461.833	207.043
Taper Ratio		0.346	0.350	1.000
Root Chord	in.	130.313	136.839	207.043
Tip Chord	in.	45.135	47.894	207.043
Sweep 25%	deg.	12.52	20.63	41.00
MAC	in.	110.286	99.504	207.043
Volume Coeff.			1.5631	0.687

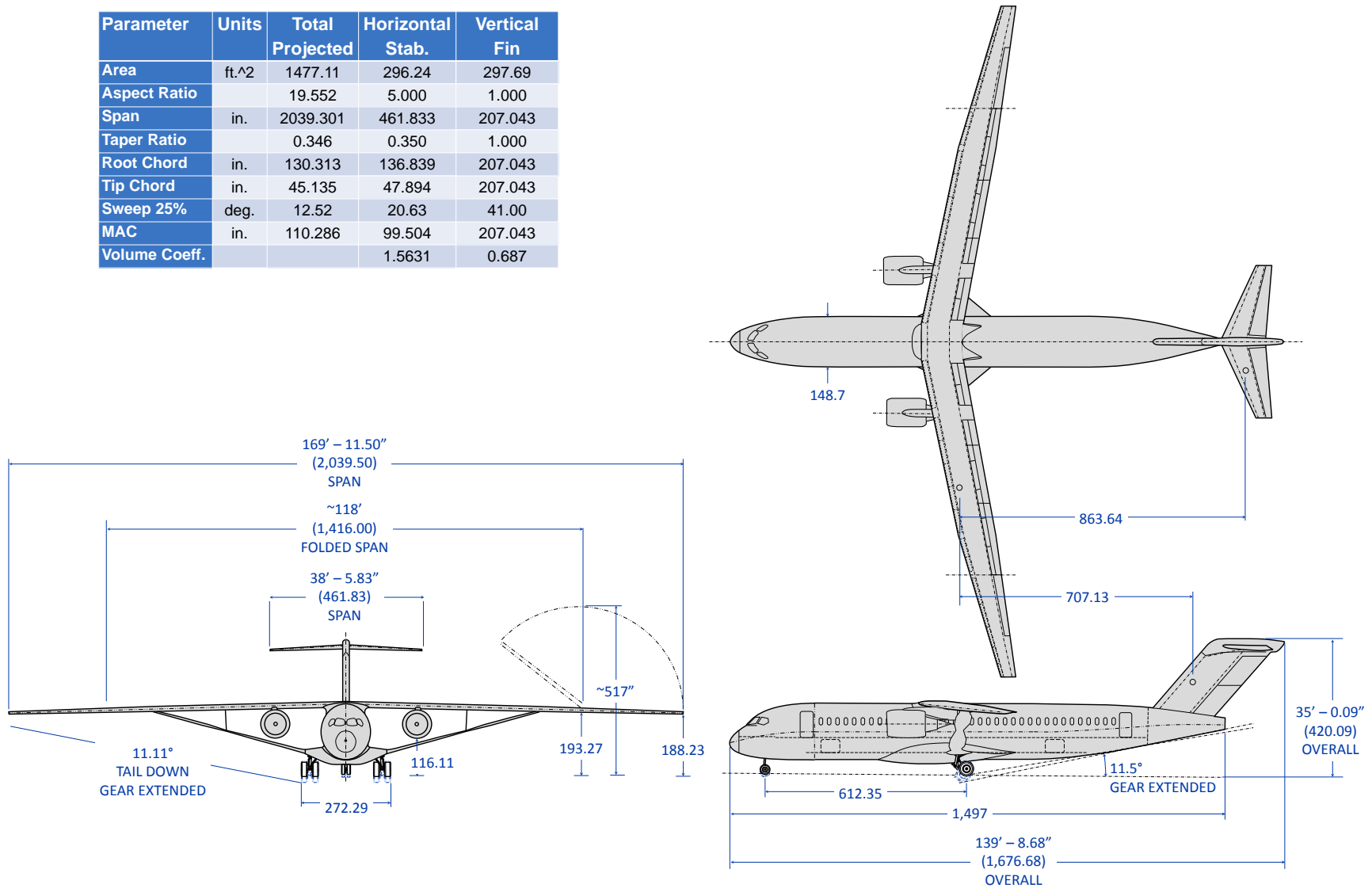


Figure 2.152 – SUGAR High (765-095-RevD) General Arrangement

154 Seats dual class

4,260 nmi DC Design Range
M 0.70 Cruise

150,000 lb MTOW
141,300 lb MLW
133,300 lb MZFW
87,300 lb OEW

Empennage
T-tail configuration

Fuselage
Single Aisle Cross Section
Advanced Stitched Composite w/ Damage Arresting Features

High Lift System
Simple Hinged Single Slot
Drooped Spoilers

Wing
Strut Braced AR 20
Natural Laminar Flow
Wing Fold at 118' Span
Krueger Flap for Bug Protection
Ply Optimized Advanced Stitched Wing Box

Landing Gear
Strut Mounted Trailing Arm

Propulsion
Ducted fan engines
23,000 lb BET
71 in. fan diameter

Figure 2.153 – SUGAR High (765-095-Rev D) Configuration Features

154 Seats dual class

3,850 nmi DC Fallout Range
M 0.70 Cruise

150,000 lb MTOW
144,900 lb MLW
136,900 lb MZFW
90,900 lb OEW

Empennage
T-tail configuration

Fuselage
Single Aisle Cross Section
Advanced Stitched Composite w/ Damage Arresting Features

High Lift System
Simple Hinged Single Slot
Drooped Spoilers

Wing
Strut Braced AR 20
Natural Laminar Flow
Wing Fold at 118' Span
Krueger Flap for Bug Protection
Ply Optimized Advanced Stitched Wing Box

Landing Gear
Strut Mounted Trailing Arm

Propulsion
Counter rotating unducted
fan engines
24,000 lb BET
144 in. fan diameter

Figure 2.154 – SUGAR High (765-095-Rev D) Unducted Fan Configuration Features

Table 2.29 – Principal Characteristics

Model 765-095 Rev. D (As Drawn)	Ducted Fan	UDF
Weights		
Maximum Takeoff Weight (MTOW)	150,000 lb	150,000 lb
Maximum Landing Weight (MLW)	141,300 lb	144,900 lb
Maximum Zero Fuel Weight (MZFW)	133,300 lb	136,900 lb
Operating Empty Weight (OEW)	87,300 lb	90,900 lb
Engine		
Engine Type	gFan+2	gFan+ UDF
Boeing Equivalent Thrust	23,000 lbf	24,000 lbf
Fan Diameter	71 in	144 in
Overall Dimensions		
Length	139.7 ft	
Height	35 ft	
Fuselage Length	124.8 ft	
Fuselage Cross Section (Height x Width)	166.5 x 148.7 in	
Passenger Cabin Length	1127 in	
Wing		
Reference Area	1477.11 ft ²	
Span	169.3 ft	
Projected Sweep	12.52 deg	
Passenger, Baggage, Fuel Capacities		
Passenger Count (Dual Class)	154	
Class Distribution (FC / EC)	12 / 142	
Cargo Capacity	Bulk	
Fuel Capacity	5,416 USG	
Landing Gear		
Wheel Base	612.35	
Main Track	272.29	
Main Tire Size	45x17R21	
Nose Tire Size	30x10.5R15	

Table 2.30 – Component Origins

Component	X	Y	Z
Fuselage	0.00	0.00	0.00
Wing	696.40	0.00	303.75
Vertical Fin	1387.96	0.00	265.21
Horizontal Stabilizer	1615.53	0.00	480.94
NLG	235.00	0.00	92.34
MLG	847.36	110.00	87.00

2.2.2 Wing

The wing is a high aspect ratio, truss braced, low sweep design optimized for a 0.70 cruise Mach number featuring natural laminar flow on the upper surface. The wing layout incorporates a fold at 118' of span to accommodate existing code C gate and taxiway infrastructure.

The leading edge is populated with full span Krueger flaps broken by the engine pylon, planform break, and the wing fold. The front spar accommodates a leading edge device chord ratio ranging from ten percent at the root to fifteen percent at the tip. The trailing edge of the wing is fitted with single slotted flaps extending from the side of body to the wing fold. A small flap segment acts as an aileron at high speed. Outboard of the wing fold there is a low speed aileron. Spoilers are assumed to cover the entire flapped span with exception of the portion reserved for the high speed aileron. These spoilers are assumed to be drooped for takeoff. The control surface and high lift system layout is the result of negotiations between low speed aerodynamics and stability and control. A drawing of this completed planform is illustrated in Figure 2.155 and the projected reference quantities are shown in Table 2.31. It should be noted that the reference quantities are displayed for a planform with no leading or trailing edge breaks at the side-of-body. A detailed wing corner point drawing is presented in Figure 2.156.

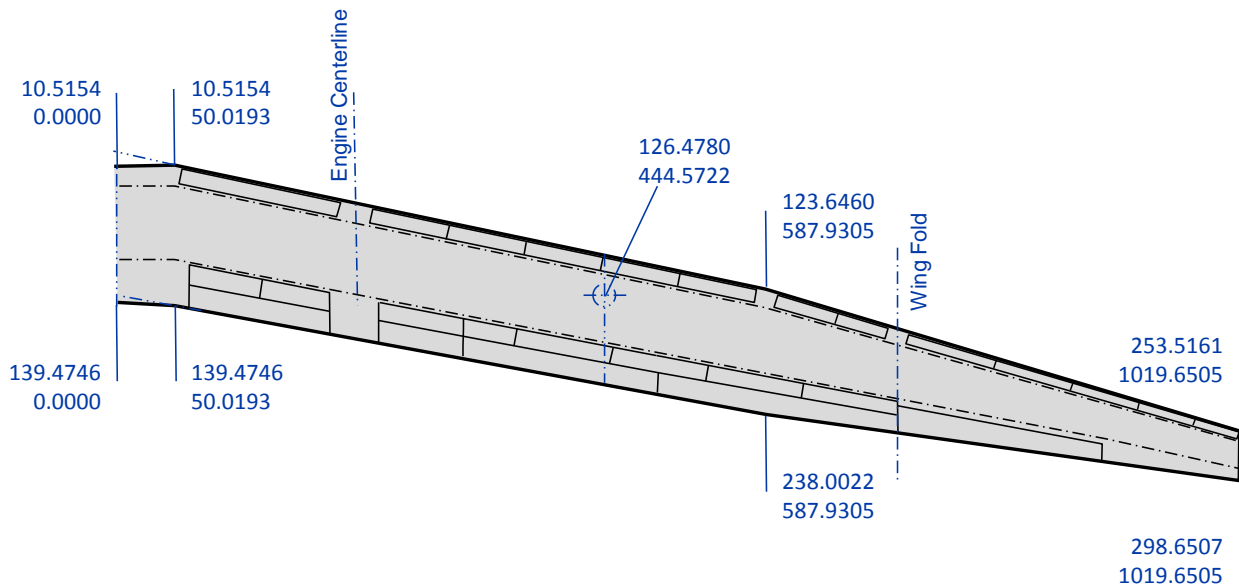


Figure 2.155 – SUGAR High (765-095 RD) Planform (Projected)

Table 2.31 – Wing Reference Geometry

Parameter	Units	Total (Projected)	Parameter	Units	Total (Projected)
Area	ft ²	1477.11	MAC	in	110.286
Aspect Ratio		19.552	Ybar	in	444.5722
Span	in	2039.301	XLEmac	in	98.9065
Taper Ratio		0.346	Xc/4	in	126.478
Root Chord	in	130.3127			
Tip Chord	in	45.1346			(Reference)
SOB Chord	in	128.9557	Krueger Area	ft ²	138.89
Sweep LE	deg	13.47	Flaperon Area	ft ²	41.73
Sweep 25%	deg	12.52	Single Slot Flap Area	ft ²	264.21
Sweep TE	deg	9.61	Aileron Area	ft ²	52.98
Dihedral	deg	-1.50	Spoiler Area	ft ²	118.81

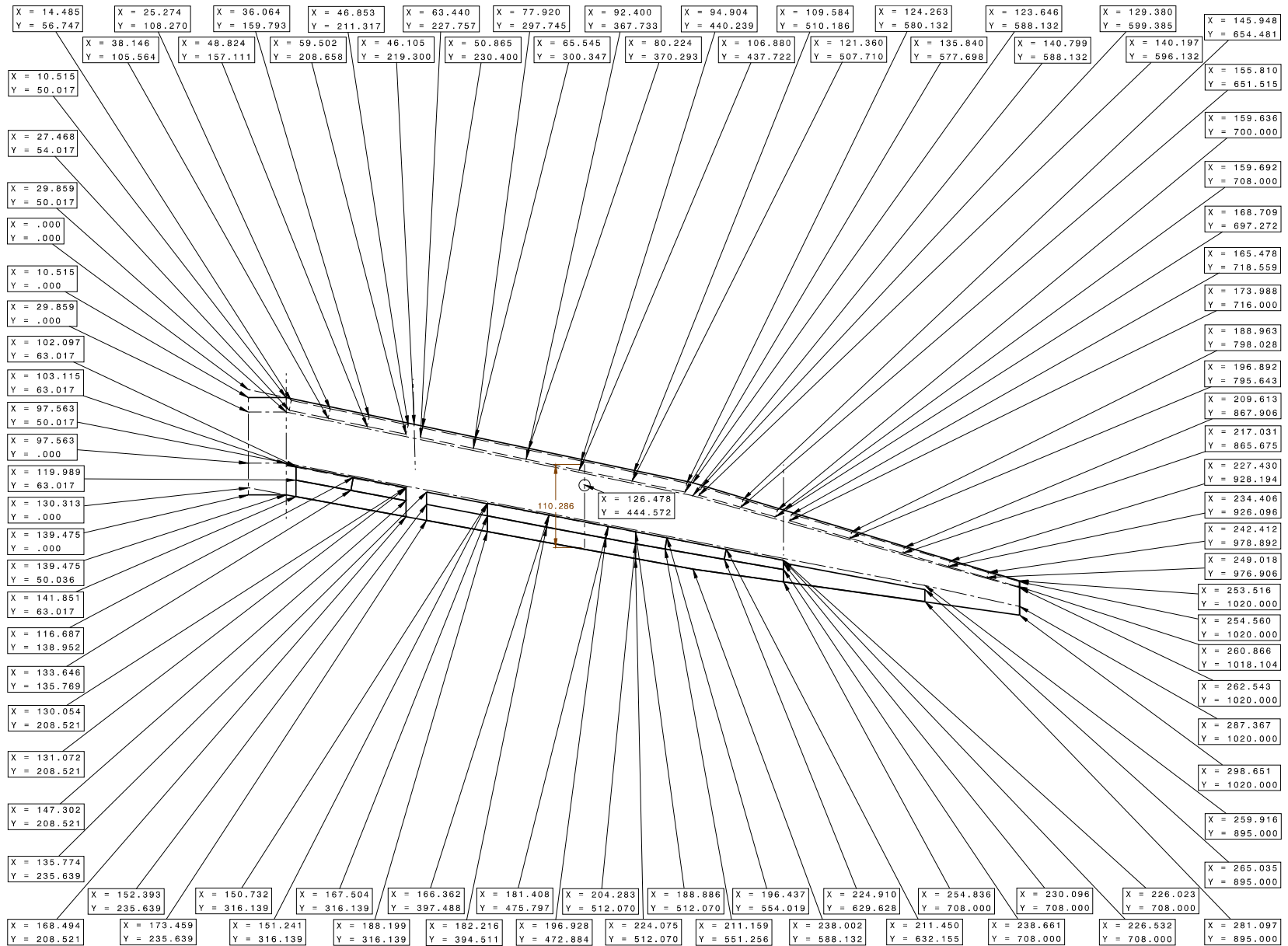


Figure 2.156 – Wing Corner Point Drawing (Wing Reference Plane)

2.2.3 Strut and Jury Strut

The main strut for the SUGAR High configuration is shaped like a bow tie because the chord is sized by buckling, which is not critical at the supported locations. The strut is 18.1 percent thick full span and uses a symmetric airfoil. The strut cross section and support fairings have not been optimized and should be considered notional. The strut box is designed to keep the bending axis straight between the three attachment points. The front spar and rear spars are at 14.8 percent chord and 70 percent chord respectively. The strut dihedral is 15.09 degrees. The strut corner points are shown in Figure 2.157. The joints for the strut are pinned (axis normal to the bending axis) while the jury strut are clamped. A future revision will transition the jury strut to a pinned connection.

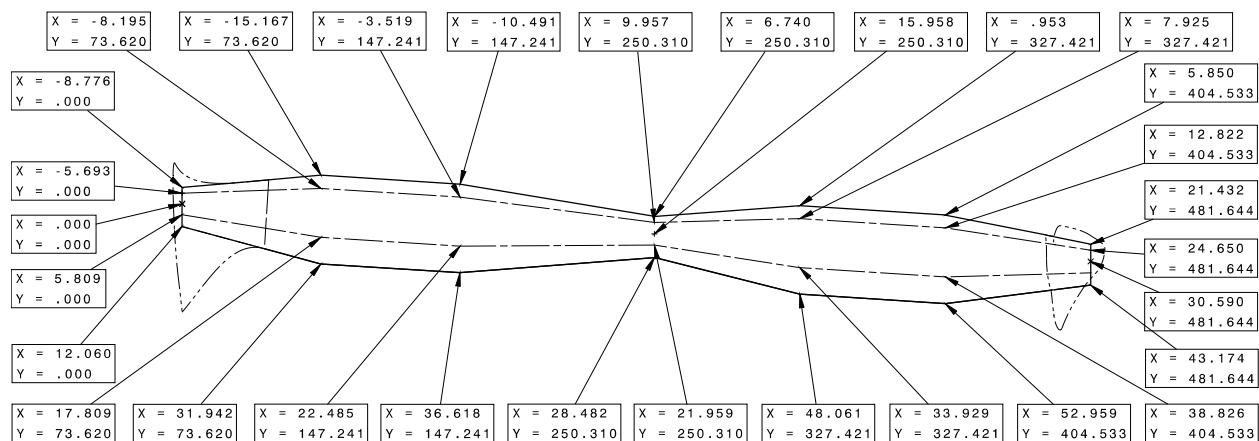


Figure 2.157 – SUGAR High (765-095 RD) Strut Corner Points

The jury strut is composed of the same airfoil as the main strut and is installed with 87.44 degrees of dihedral (the strut leans outboard in a front view). The strut tie in-chord and wing tie-in chords are 11.47 and 14.22 inches respectively. The strut has a linear chord distribution.

2.2.4 Vertical Fin

The vertical tail is arranged similarly to an MD series twin-jet. It is a two spar layout with no taper and a two surface simple hinged rudder. The front spar breaks and converges on the rear spar at the vertical tip where the horizontal stabilizer pivot is mounted. The horizontal jack screw mechanism is above the front spar. The vertical planform is illustrated in Figure 2.158 and the reference planform parameters are shown in Table 2.32.

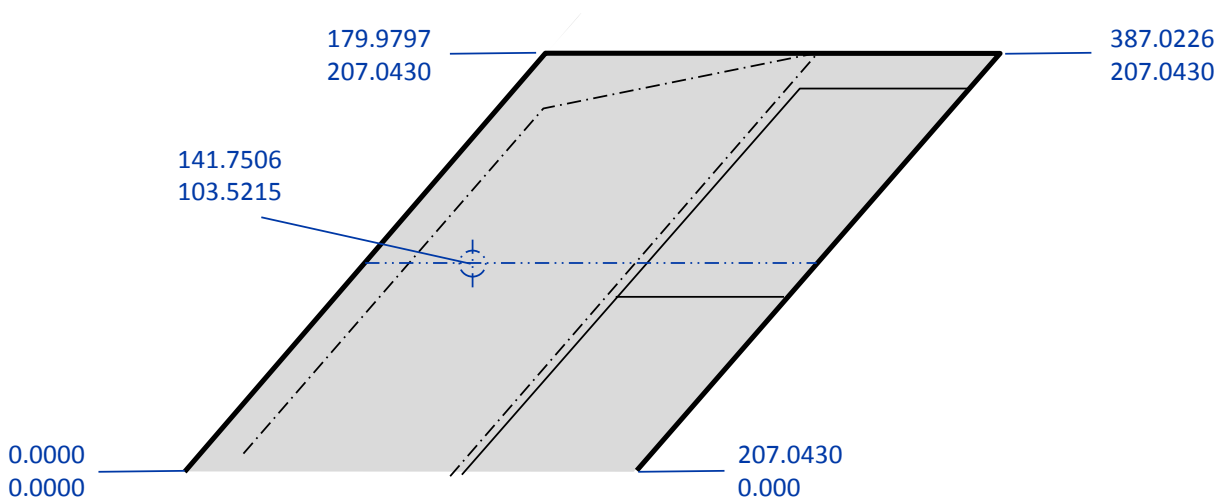


Figure 2.158 – SUGAR High (765-095 RD) Vertical Planform

Table 2.32 – SUGAR High (765-095 RD) Vertical Planform Parameters

Parameter	Units	Total (Projected)
Area	ft ²	297.69
Aspect Ratio		1.000
Span	in	207.0430
Taper Ratio		1.000
Root Chord	in	207.0430
Tip Chord	in	207.0430
Sweep LE	deg	41.00
Sweep 25%	deg	41.00
Sweep TE	deg	41.00
MAC	in	207.0430
Ybar	in	103.5215
Xc/4	in	141.7506

2.2.5 Horizontal Stabilizer

The horizontal stabilizer has a planform typical of T-tail empennage arrangements and is depicted in Figure 2.159. The stabilizer is full flying with a pivot behind and below the rear spar and a jack screw acting in front of the front spar. The elevator is split into two separate segments spanwise. The projected planform parameters are displayed in Table 2.33.

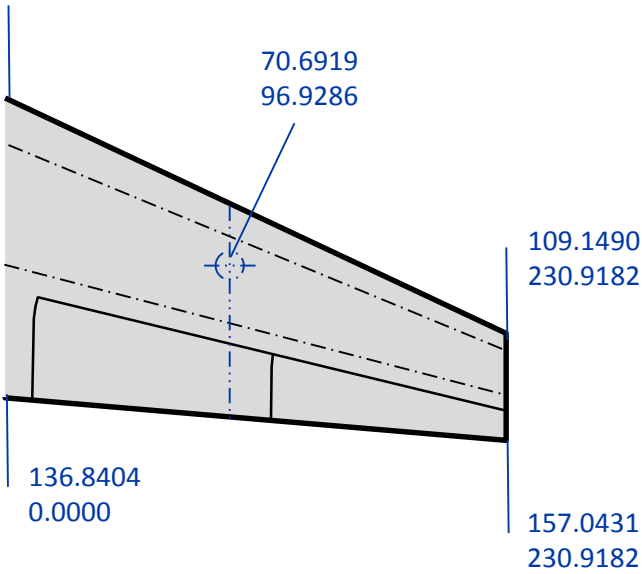


Table 2.33 – SUGAR High (765-095 RD) Horizontal Planform Parameters

Parameter	Units	Total (Projected)
Area	ft ²	296.24
Aspect Ratio		5.000
Span	in	461.8363.
Taper Ratio		0.350
Root Chord	in	136.8404
Tip Chord	in	47.8941
Sweep LE	deg	25.30
Sweep 25%	deg	20.63
Sweep TE	deg	5.00
Dihedral	deg	-3.00
MAC	in	99.5049
Ybar	in	96.9279
Xc/4	in	70.6919

Figure 2.159 – SUGAR High (765-095 RD) Horizontal Planform

2.2.6 Fuselage

The SUGAR High fuselage is a single-aisle layout with three-by-three seating. The cargo compartment is bulk loaded and is not designed for containerized cargo. The cross-section is illustrated in Figure 2.160 and a Layout of Passenger Accommodations (LOPA) is shown in Figure 2.161. The LOPA and cross-section are the same as Phase I.

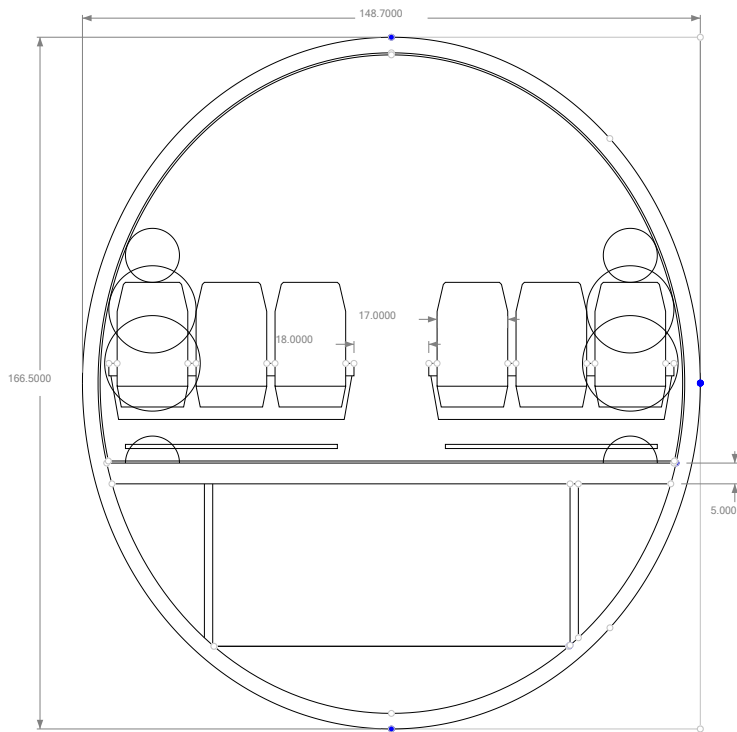
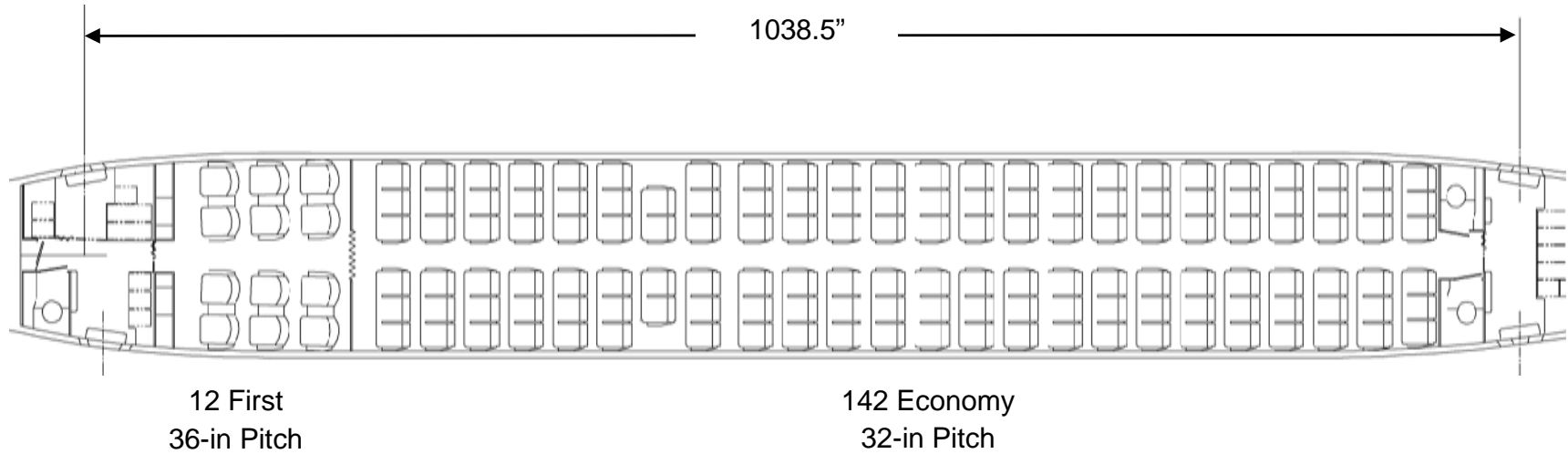


Figure 2.160 – 765-095-RevD Fuselage Cross Section

Interior Arrangement

SUGAR

IAC Short / Medium Range – Dual Class



	Class (%)	Carts (qty)	Cart Ratio (Carts/Pax)	Lavatory Ratio (Pax/Lav)	Closet Ratio (Rod-in/Pax)
First	7.79	3.0	0.250	12	4.00
Economy	92.20	7.0	0.049	71	0.00
Total	100.00	10.0	0.649	–	–

Figure 2.161 – SUGAR High (765-095) Layout of Passenger Accommodations

2.2.7 Landing Gear

The high aspect ratio, high lift curve slope configuration allows for a low static ground line. The configuration uses a levered landing gear arrangement to enable this low stance. The landing gear attaches to the gear pylon, a stub wing like structure that carries landing gear and strut loads. An overview of the kinematic arrangement is illustrated in Figure 2.162 and the ground footprint is shown in Figure 2.163

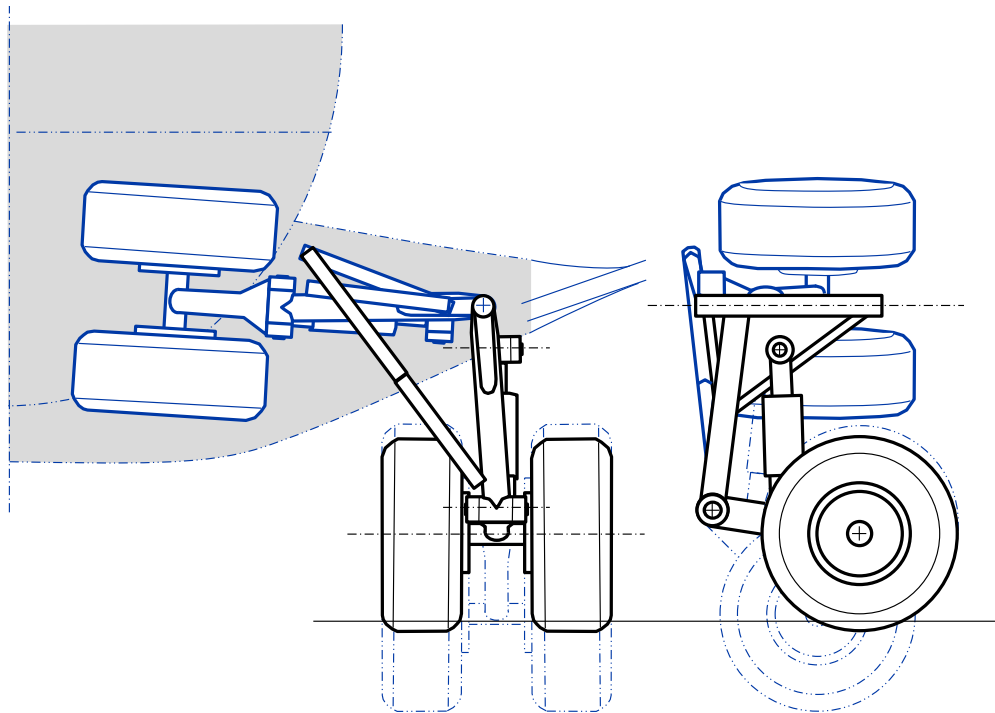


Figure 2.162 – SUGAR High (765-095 RD) Landing Gear Layout

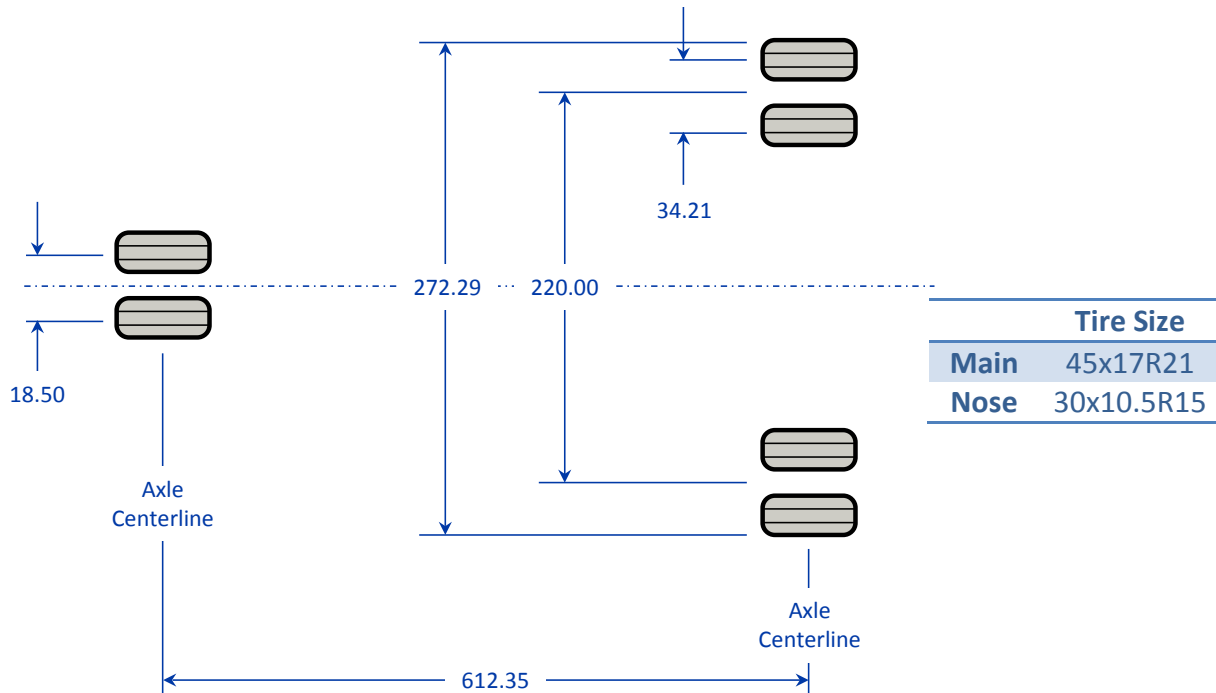


Figure 2.163 – SUGAR High (765-095 RD) Landing Gear Arrangement

2.2.8 Propulsion

GE conducted a fan pressure ratio parametric study to gain insight into the aircraft level trades between engine design parameters and center the phase II gFan+ cycle design. In 2011, a fan pressure ratio of 1.46 was selected from the study for the gFan+, sacrificing SFC to realize a lighter weight, lower drag engine based on vehicle level sensitivities. A conceptual layout of the gFan+ was performed at the optimum fan pressure ratio and is shown in Figure 2.164. A summary of the propulsion system key characteristics is provided in Table 2.34

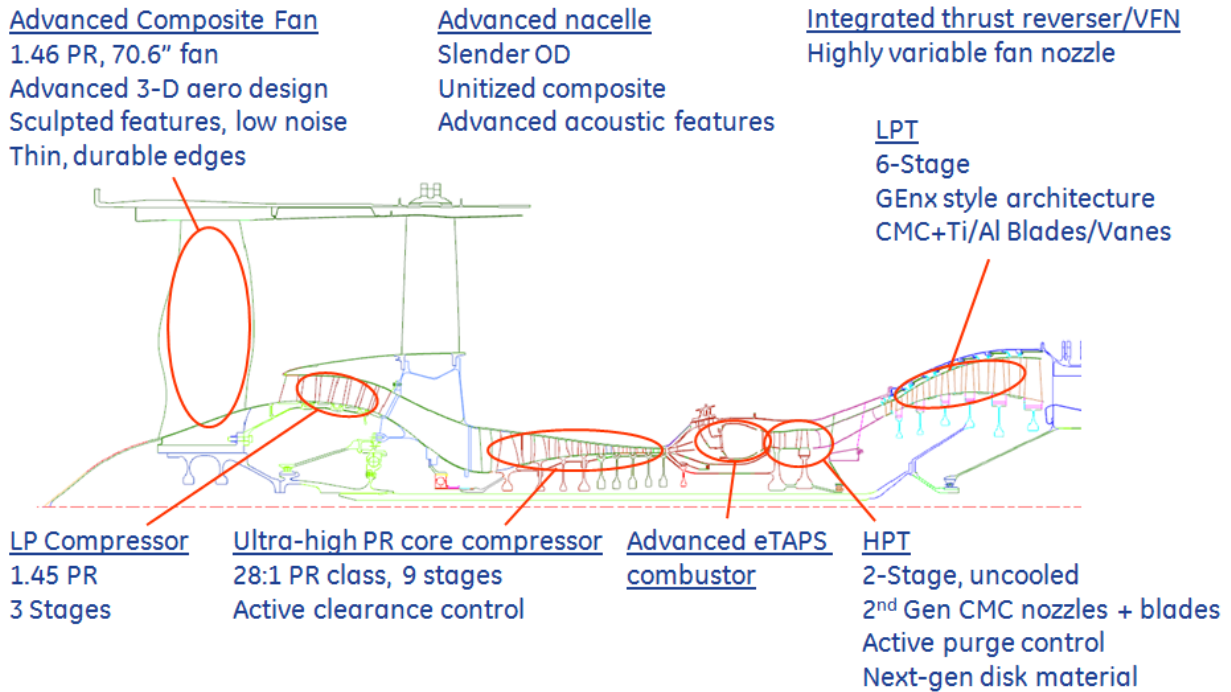


Figure 2.164 – gFan+ Concept Layout

Table 2.34 – gFan+ Key Characteristics

JP+2035GT+DF

Fan Diameter	70.6	In
Length	129	In
Propulsion System Weight	6335	lbm

		SFC
Performance	Thrust (lbf)	(lbm/lbf/hr)
SLS	21943	0.220
Takeoff	16592	0.295
Top of Climb	3931	0.467
Cruise	3145	0.455

In 2012, GE was tasked with designing an Unducted Fan (UDF) architecture for the Truss Braced Wing airframe. The thrust requirements and corresponding aircraft remain unchanged and can be found in Table 2.27. The additional room under the wing due to the engine’s high mount location on the fuselage makes it well suited to unducted fan propulsor concepts. The ultra-low pressure ratio of UDF propulsors enables substantial improvements to propulsive efficiency relative to its ducted counterpart. The counter rotating fans on the UDF run at a nearly constant speed over the course of the mission and necessitate a change to the gFan+ power plant architecture. A second spool was introduced to achieve gFan+ overall pressure ratio levels and

to maintain operability at lower power settings. The UDF architecture shares core technologies and materials with the gFan+ advanced turbofan. Furthermore, the UDF propulsor diameter of 144 inches was derived from the LNG+2045GT+SOFC+UDF architecture designed for N+4 studies. A conceptual layout of the gFan+ UDF was produced to achieve optimal overall efficiency and is shown in Figure 2.165. A summary of the propulsion system key characteristics is provided in Table 2.35.

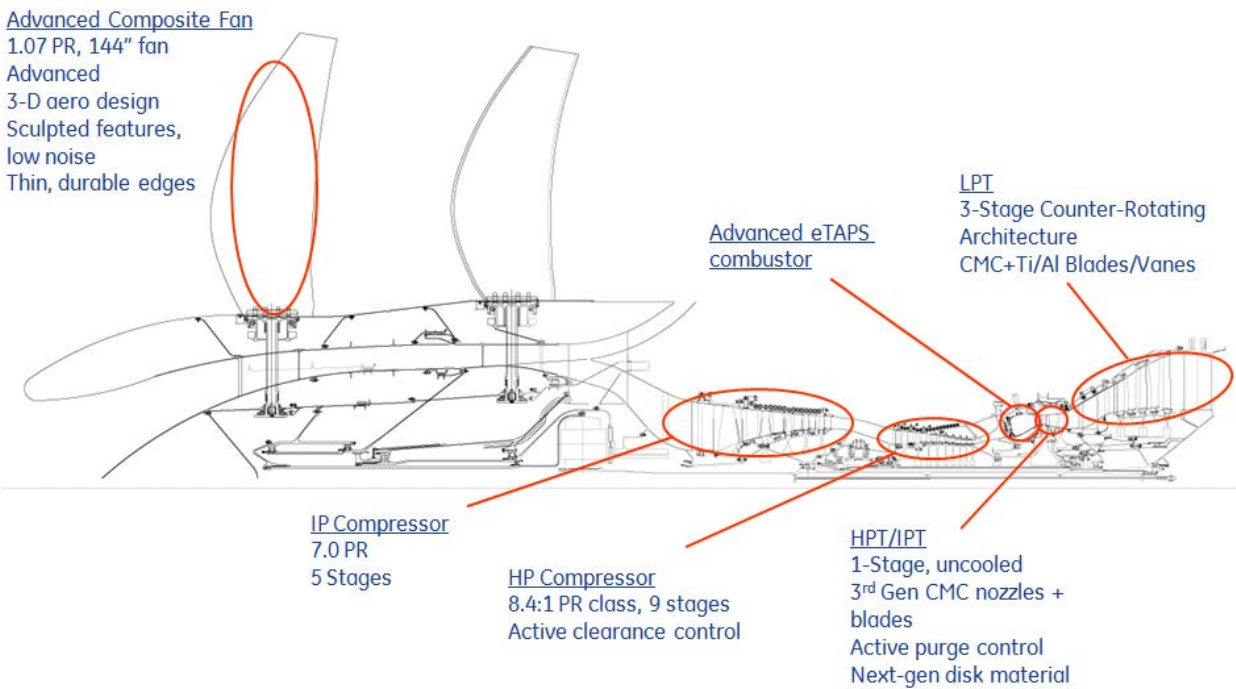


Figure 2.165 – gFan+ UDF Concept Layout

Table 2.35 – gFan+ UDF Key Characteristics

gFan+ UDF		
Fan Diameter	144	In
Length	189	In
Propulsion System Weight	8011	lbm

Performance	Thrust (lbf)	SFC (lbm/lbf/hr)
SLS	24809	0.152
Takeoff	16079	0.239
Top of Climb	3981	0.415
Cruise	3181	0.416

2.3 Configuration Analysis and Final Performance

This section includes the discipline analyses of the configuration documented in Section 2.2. The results of the analysis are not used in the synthesis of the SUGAR High configuration but would be incorporated in a next configuration cycle.

2.3.1 Aerodynamics

High Speed:

Computer Aided Sizing and Evaluation System (CASES) cruise drag bookkeeping is shown in Figure 2.166. Parasite drag represents the incompressible zero-lift drag. Induced drag accounts for the drag due to lift based on airplane efficiency factor at $M=0.50$. Compressibility drag is a function of both Mach and lift coefficient while trim drag accounts for pitching moment on the configuration.

Using CASES accounting and incorporating the wing-body CFD solutions, high speed aerodynamic buildup for the 765-095 Rev D is shown in Table 2.36 and is summarized in Figure 2.167.

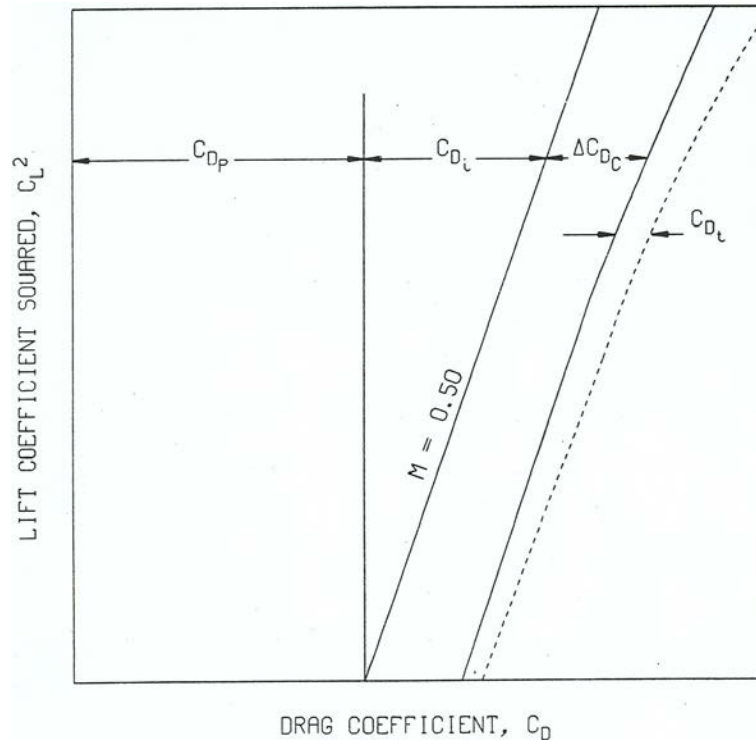


Figure 2.166 – CASES Standard Buildup: $C_D = C_{Dp} + C_{Di} + C_{Dc} + C_{Dtrim}$

It should be noted that NLF/Riblets does not include the wing NLF benefit. Wing upper surface NLF was included in the higher order wing design and bookkept under airplane compressibility drag. Negative Compressibility in the bookkeeping is due to the effect of laminar flow above Mach 0.50 as illustrated by Figure 2.83.

The aerodynamic characteristics reflect the design Mach number of 0.71 for current air traffic management integration. The resulting high speed data is shown in Figure 2.168. The figure illustrates the maximum aerodynamic efficiency (M^*L/D) occurring at the design cruise Mach (0.71) and C_L (0.75).

Table 2.36 – 765-095 Rev D High Speed Buildup

CONFIGURATION	765-095 Rev D	765-095 Rev D UDF
WING AREA	1477	1477
SWEEP (DEG)	12.58	12.58
T/C-AVE	0.154	0.154
AIRFOIL TYPE	SUPERCRT. DTE	SUPERCRT. DTE
F BUILD-UP (FT2)		
FUSELAGE	8.6959	8.6959
WING	10.1543	10.1543
STRUT / JURY	2.8963	2.8963
FLAP SUPPORT	0.2519	0.2519
HORIZONTAL	1.8904	1.8904
VERTICAL	1.7194	1.7194
N&P	1.9020	0.0000
CANOPY	0.0405	0.0405
GEAR PODS	3.0872	3.0872
NLF	-2.4115	-2.4115
RIBLETS	-1.1814	-0.9300
EXCRESCENCE	2.6450	2.5521
STRUTS C_{DC}	0.5900	0.5900
UPSWEEP	0.3414	0.3414
WING TWIST	0.1640	0.1640
TURBULENT CDC INCREMENT	-1.5656	-1.39000
FUSELAGE BUMP	0.3675	0.3675
F-TOTAL (FT2)	29.5873	28.0194
E-VISC	0.931	0.931
CRUISE CD BUILD-UP		
M-CRUISE	0.71	0.71
CL-CRUISE	0.75	0.75
CRUISE ALTITUDE	42000	42000
CD0	0.02003	0.01897
CDI	0.00981	0.00981
CDC	-0.00063	-0.00062
CDTRIM	0.00060	0.00057
CDTOT	0.02981	0.02873
L/D	25.159	26.107
M L/D	17.863	18.536

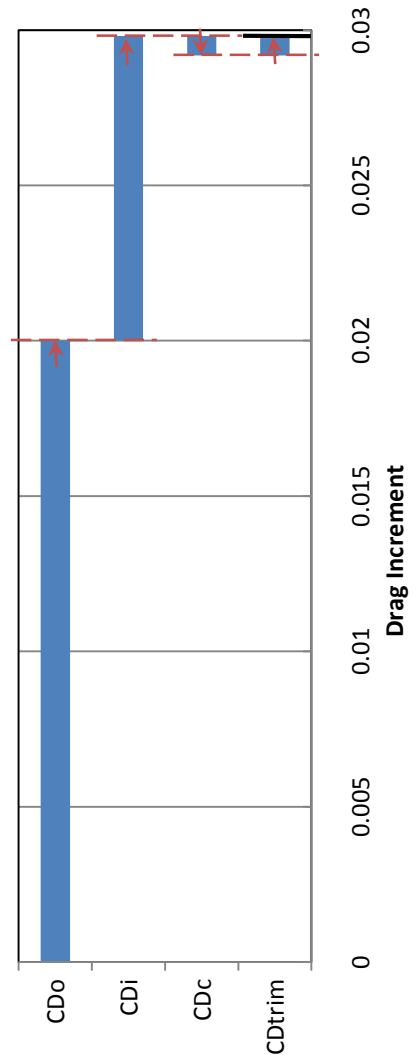


Figure 2.167 – 765-095 Rev D High Speed Buildup (UDF Not Shown)

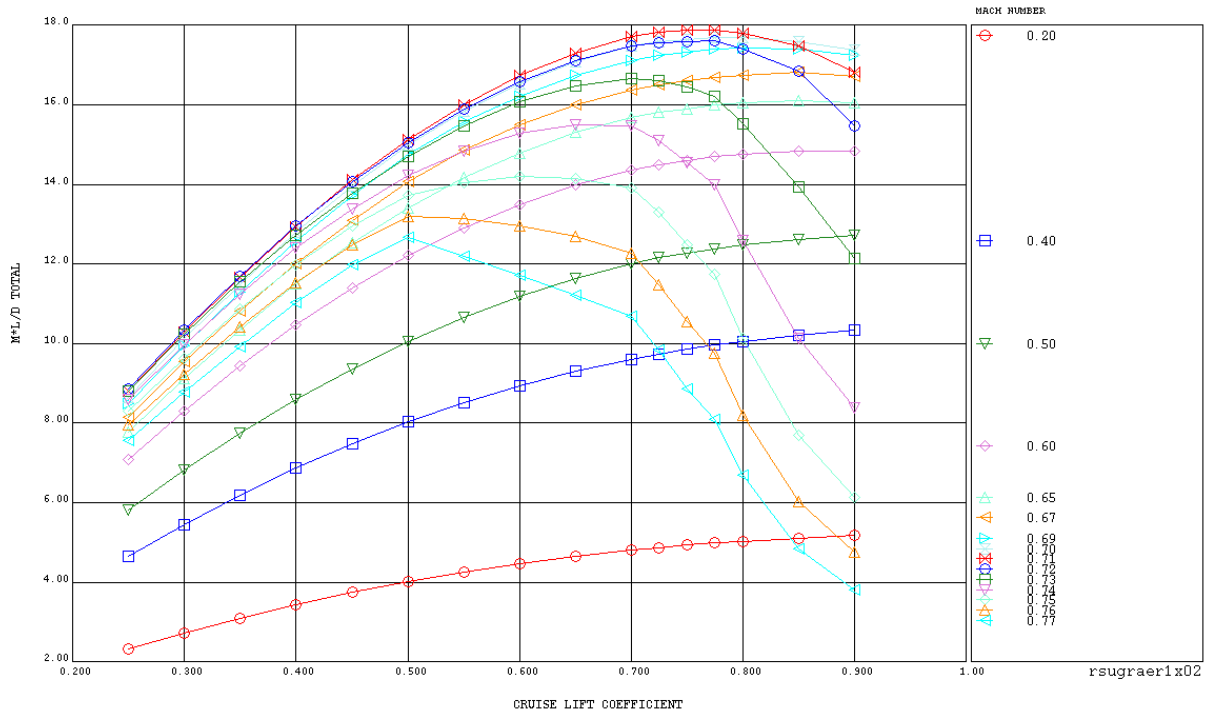


Figure 2.168 – 765-095 Rev D – $M \cdot L / D$ Total

Low Speed:

Figure 2.169 through Figure 2.171 show the low speed aerodynamic characteristics of the Truss Braced Wing. Higher fidelity analysis shown in Section 2.1.7 (with lifting struts and gear pods) was used to improve upon conceptual methods. Low speed data are trimmed as a function of angle of attack, lift coefficient, and drag coefficient at each flap detent. Low speed high lift devices on wing leading and trailing edges are deployed.

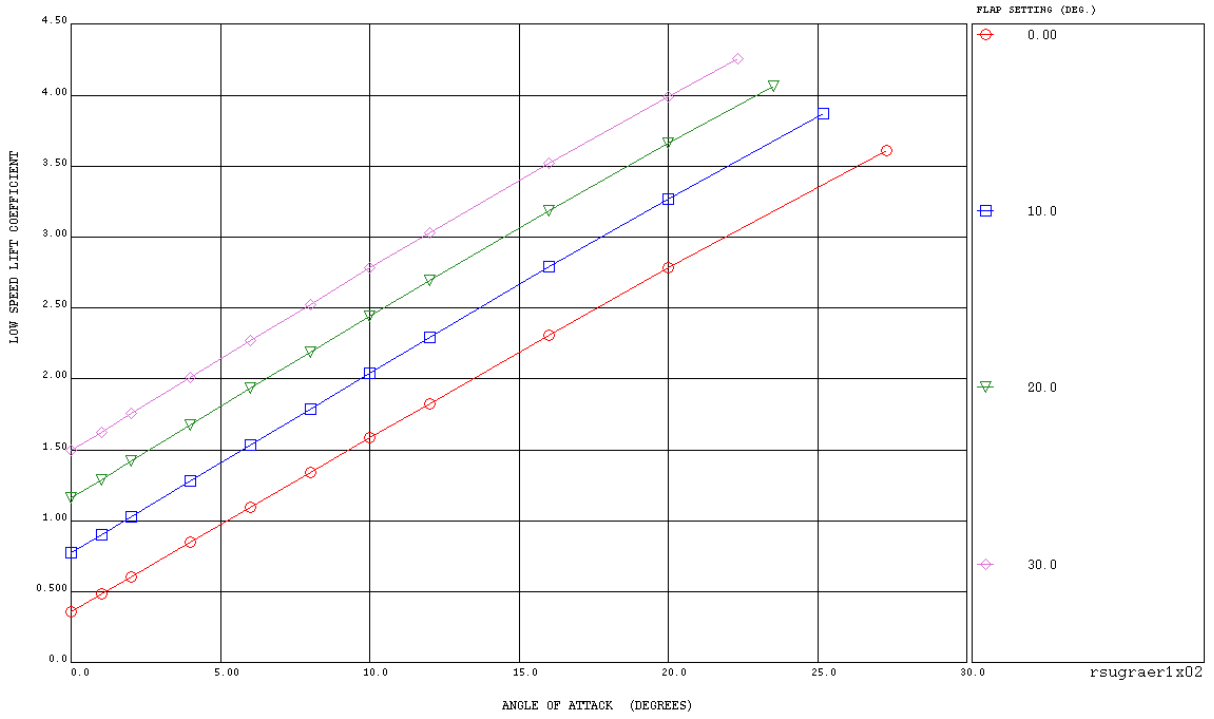


Figure 2.169 – 765-095 Rev D – Low Speed Lift Curve; Free Air

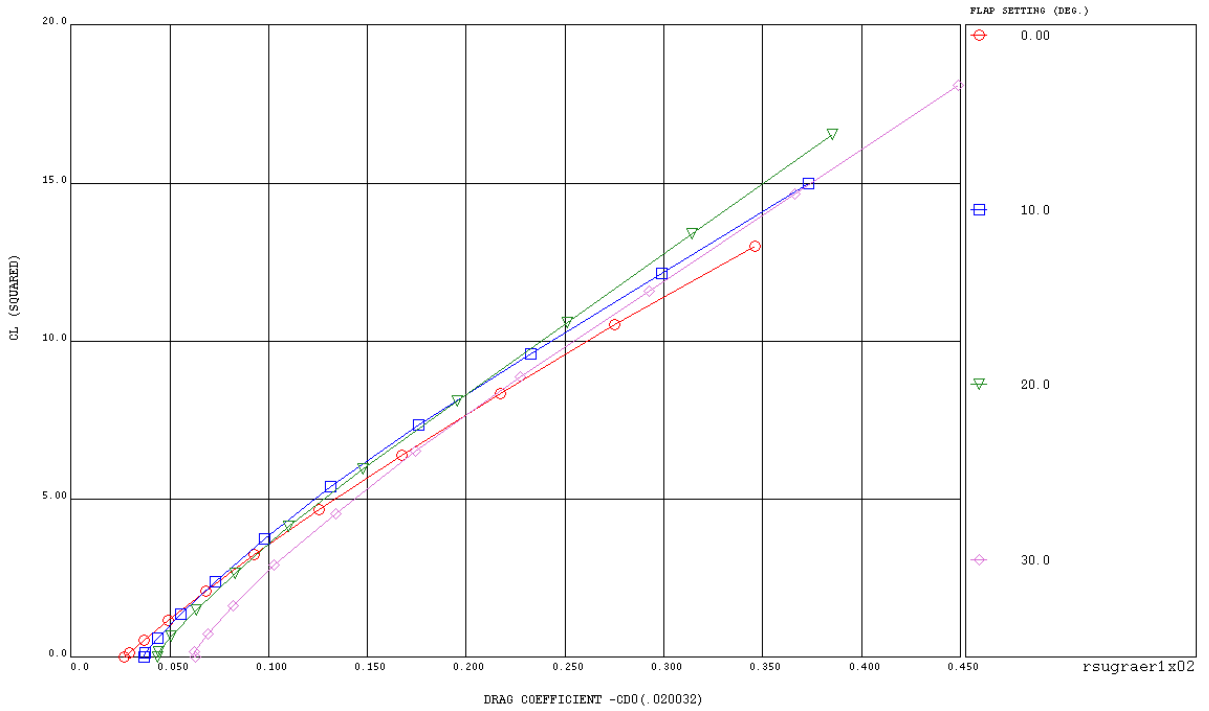


Figure 2.170 – 765-095 Rev D – Low Speed Polar; Free Air

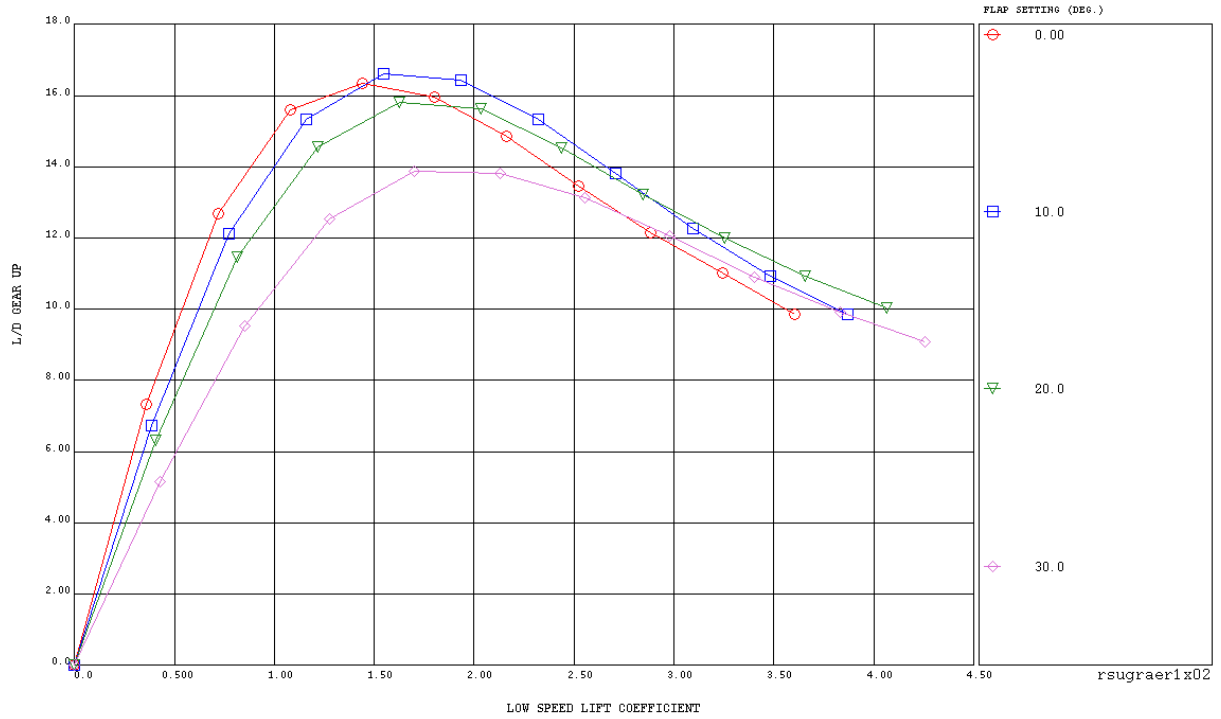


Figure 2.171 – 765-095 RevD – Low Speed Lift / Drag; Free Air

2.3.2 Mass Properties

The group weight statement for 765-095-Rev D is shown in Table 2.37. These weights include data generated with the aeroelastic FEM discussed in Section 2.1.8. The FEM data were essential for such a high aspect ratio strut-braced wing configuration. The group weight data was generated using a takeoff gross weight of 150,000 pounds, a first-cut estimate used to start the sizing process.

Table 2.37 – 765-095-RD Group Weight Statement

GROUP	WEIGHT (LB)	
	Ducted Fan	UDF
WING	16,670	16,740
TAIL	3,160	3,160
FUSELAGE	16,930	16,930
WING STRUT & MLG SUPT INSTL	3,680	3,680
LANDING GEAR	5,080	5,080
NACELLE & PYLON	4,830	4,650
PROPULSION	10,070	13,760
ENGINES	8,420	12,100
FUEL SYSTEM	1,650	1,660
FLIGHT CONTROLS	2,650	2,650
POWER SYSTEMS	4,070	4,070
AUXILIARY POWER UNIT	1,010	1,010
HYDRAULICS	760	760
ELECTRICAL	2,300	2,300
INSTRUMENTS	770	770
AVIONICS & AUTOPILOT	1,500	1,500
FURNISHINGS & EQUIPMENT	9,120	9,120
AIR CONDITIONING	1,440	1,440
ANTI-ICING	120	120
MANUFACTURER'S EMPTY WEIGHT (MEW)	80,090	83,670
OPERATIONAL ITEMS	7,210	7,210
OPERATIONAL EMPTY WEIGHT (OEW)	87,300	90,880
USABLE FUEL	31,900	28,300
DESIGN PAYLOAD	30,800	30,800
TAKEOFF GROSS WEIGHT (TOGW)	150,000	150,000

2.3.3 Performance and Sizing

The Boeing Mission Analysis Program (BMAP) is the principal tool used by Boeing Commercial Airplanes (BCA) to calculate mission performance such as payload, range, or fuel burn. It can analyze missions of varying complexity and has been validated to actual airplane performance. It has the capability to model complex tracks with enroute and alternate waypoints and complex profiles with multiple cruise segments including step and cruise climbs. It will calculate airplane performance including redispach, through-stop, radius, and extended-range twin-engine operations (ETOPS) capability.

Use of the Low Speed Performance System (LSPS) provides field length analysis. LSPS can calculate takeoff performance at any specified atmospheric condition (altitude and temperature within its atmospheric model) and includes One Engine Inoperative (OEI) in its calculations. Like BMAP, it is calibrated to existing commercial airplanes.

Vehicle performance and sizing is performed with Boeing’s Aircraft Design Navigator (ADNav) which encapsulates both mission performance (BMAP) and airfield performance calculations (LSPS). It provides the capability to scale engine thrust and wing area and provides the ability to size airplanes to their optimum sizes given a set of constraints (such as TOFL, ICAC, time and distance to climb, etc.). It also provides some data visualization tools. The sizing process is illustrated in Figure 2.172

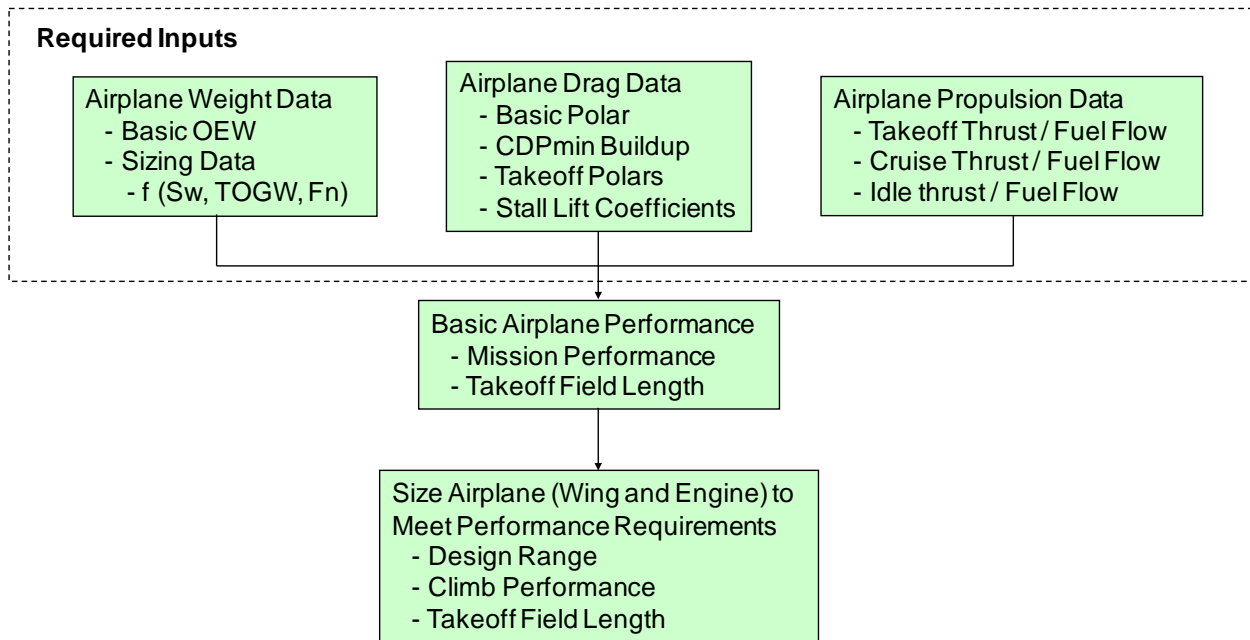


Figure 2.172 – Airplane Sizing Using ADNav

2.3.3.1 Sizing Requirements

A set of top level requirements for the SUGAR vehicles was generated from the future scenario previously reported in SUGAR Phase I (1). These top level requirements were turned into specific payload-range requirements which are illustrated in Figure 2.173. The figure has several points of interest called out.

1. The airplane is required to fly the average range at max payload (also maximum zero fuel weight). Max payload is required to be 15,200 pounds heavier than the payload from point 2. The range required is 900 nm.
2. The airplane is required to fly the maximum range at the average number of seats using 200 pounds per passenger and no revenue payload. This point must be achieved using less than 90% of the useable fuel. The range required is 3,500 nm.
3. This point will be used to calculate vehicle fuel burn performance and TOFL performance for the SUGAR program. This represents the point that represents how an operator would most commonly operate the vehicle class. This point is evaluated at a range of 900nm.

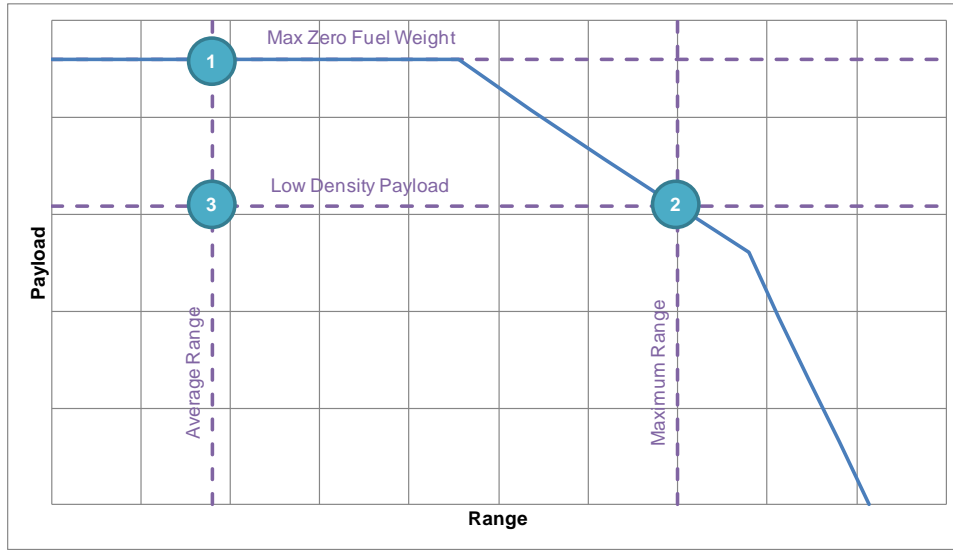


Figure 2.173 – Payload-Range Requirements

Both point 1 and 2 are required for sizing because airplane characteristics may change which point is critical. The mission profile for SUGAR 2035 concepts is shown in Figure 2.174. SUGAR High and Refined SUGAR are evaluated to the illustrated mission while SUGAR Free is flown with a non-advanced air traffic management system. These missions are further documented in Phase I (1).

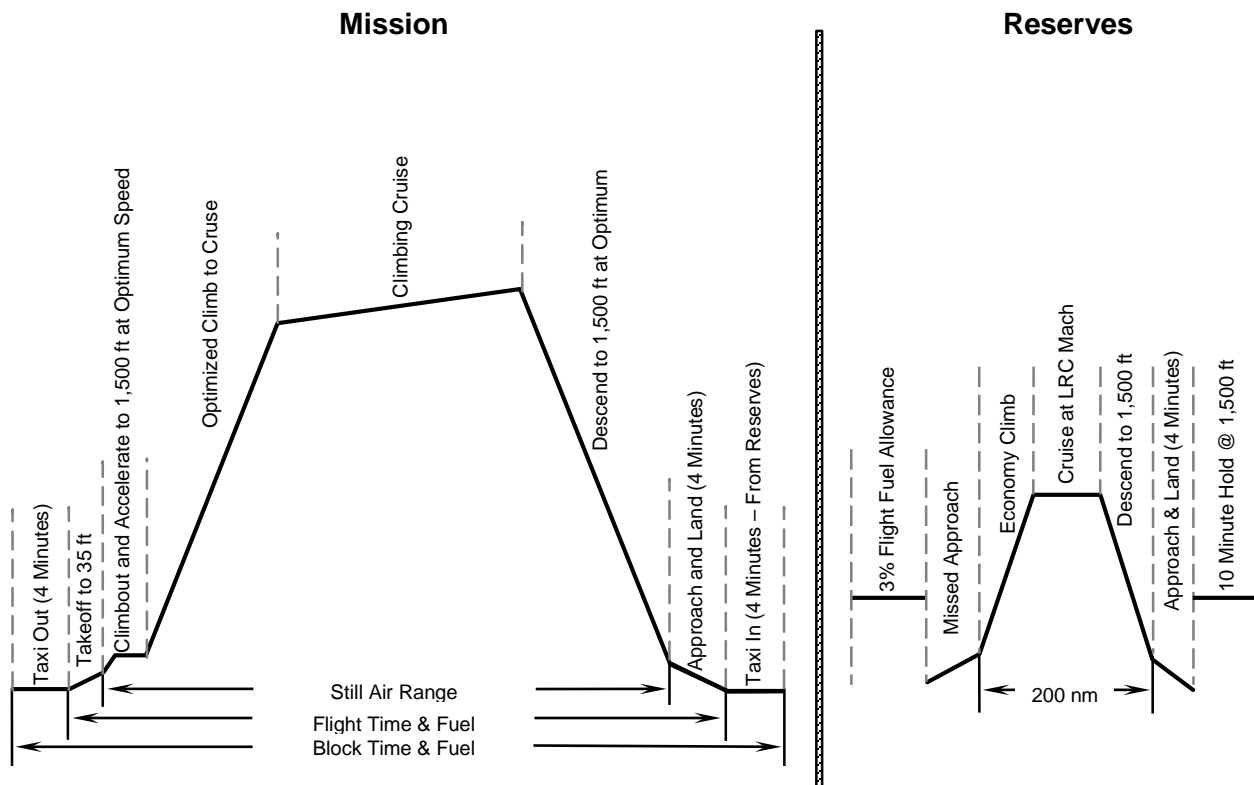


Figure 2.174 – 2030 Mission Profile with NextGen Air Traffic Management

2.3.3.2 *Sizing Results*

The performance of the SUGAR High configuration is shown in Table 2.38. There are several different sizing cases shown; working from left to right, the first two columns (ducted and unducted configurations) are referred to as As-Drawn meaning the performance was run at the reference wing area, thrust, and MTOW used to generate the underlying vehicle data. In this case, the thrust, wing area, and MTOW are higher than the mission requires. The next set of columns, which show a 5 and 10 percent fuel burn reduction for the Ducted and Unducted configurations respectively, is sized data for minimum fuel burn constrained by takeoff field length. The remaining two columns are sized with takeoff field length (inactive) and initial cruise altitude capability (ICAC) (active) constraints. The ICAC constraint requires the aircraft be able to climb to the altitude yielding best specific range (its optimum altitude). This constrained configuration shows a 0.7 and 1 percent increase in fuel burn relative to the ICAC unconstrained configurations. The ICAC constrained configurations are shown for all additional performance analysis.

The performance of the airplane is shown relative to the SUGAR Free baseline (configuration 765-093) in Table 2.39. This shows a 53.6 and 56 percent reduction for the SUGAR High and SUGAR High UDF respectively.

BMAP was exercised at various combinations of fuel and payload weights to generate a payload-range curve shown in Figure 2.175. This curve shows that the unducted fan variant does not meet the stated range requirements at the maximum payload condition with only 783 nautical miles of range. The airplane was not resized in an effort to maintain sizing criteria for consistency with the ducted fan airplane. The flat upper portion of the curve (at 46,000 lb. payload) represents the maximum zero fuel weight constraint of the airplane. The shallow sloped portion of the curve is set by Breguet range and the Maximum Takeoff Weight. The final region of the chart is set by the airplanes fuel volume limit.

Table 2.38 – 765-095 Rev D Mission Performance

Model Sizing Level		765-095-RD Ducted Fan As-Drawn	765-095-RD UDF As-Drawn	765-095-RD Ducted Fan Min Fuel	765-095-RD UDF Min Fuel	765-095-RD Ducted Fan ICAC Constraint	765-095-RD UDF ICAC Constraint
PASSENGERS / CLASS		154 / DUAL	154 / DUAL	154 / DUAL	154 / DUAL	154 / DUAL	154 / DUAL
MAX TAKEOFF WEIGHT	LB	150,000	150,000	137,200	137,400	138,300	130,000
MAX LANDING WEIGHT	LB	141,300	144,900	134,900	136,800	135,700	137,000
MAX ZERO FUEL WEIGHT	LB	133,300	136,900	126,900	128,800	135,700	137,000
OPERATING EMPTY WEIGHT	LB	87,300	90,900	80,900	82,800	81,700	83,000
FUEL CAPACITY REQ / AVIL	USG	5,154 / 5,416	4,604 / 5,416	4,172 / 4,272	3,917 / 4,427	4,213 / 4,212	3,968 / 4,145
ENGINE MODEL		gFan+2	gFan+2 UDF	gFan+2	gFan+2 UDF	gFan+2	gFan+2 UDF
FAN DIAMETER	IN	71	144	64	123	66	126
BOEING EQUIVALENT THRUST (BET)	LB	23,000	24,000	18,200	17,600	19,400	18,500
WING AREA / SPAN	FT ² / FT	1,478 / 170	1,478 / 170	1,210 / 154	1,248 / 156	1,195 / 153	1,178 / 152
ASPECT RATIO (EFFECTIVE)		19.56	19.56	19.56	19.56	19.56	19.56
OPTIMUM C _L		0.766	0.797	0.729	0.783	0.759	0.785
CRUISE L/D @ OPT C _L		25.249	25.936	24.117	25.135	23.995	24.741
DESIGN MISSION RANGE	NMI	4,260	3,850	3,500	3,500	3,500	3,500
PERFORMANCE CRUISE MACH		0.70	0.70	0.70	0.70	0.70	0.70
LONG RANGE CRUISE MACH (LRC)		0.70	0.70	0.70	0.70	0.70	0.70
THRUST ICAC (MTOW, ISA)	FT	40,400	42,300	36,500	37,600	37,700	38,200
TIME / DIST (MTOW, 35k FT, ISA)	MIN / NMI	19 / 119	20 / 122	27 / 170	33 / 206	23 / 147	29 / 181
OPTIMUM ALTITUDE (MTOW, ISA)	FT	40,800	41,500	37,400	39,500	37,700	38,200
BUFFET ICAC (MTOW, ISA)	FT	45,800	45,700	43,500	44,100	43,000	42,800
TOFL (MTOW, SEA LEVEL, 86 DEG F)	FT	5,990	5,530	8,200	8,190	7,680	8,180
APPROACH SPEED (MLW)	KT	100	101	108	107	109	111
BLOCK FUEL / SEAT (900 NMI)	LB	44.44	43.86	42.16	39.93	42.46	40.30

Table 2.39 – 765-095 Rev D Mission Performance Comparison

Model Sizing Level		765-093 SUGAR Free	765-095-RD Ducted Fan ICAC Constraint	765-095-RD UDF ICAC Constraint
PASSENGERS / CLASS		154 / DUAL	154 / DUAL	154 / DUAL
MAX TAKEOFF WEIGHT	LB	182,600	138,300	130,000
MAX LANDING WEIGHT	LB	149,400	135,700	137,000
MAX ZERO FUEL WEIGHT	LB	140,400	135,700	137,000
OPERATING EMPTY WEIGHT	LB	94,400	81,700	83,000
FUEL CAPACITY REQ / AVIL	USG	9,633 / 9,633	4,213 / 4,212	3,968 / 4,145
ENGINE MODEL		CFM56-7B27	gFan+2	gFan+2 UDF
FAN DIAMETER	IN	62	66	126
BOEING EQUIVALENT THRUST (BET)	LB	27,900	19,400	18,500
WING AREA / SPAN	FT ² / FT	1,406 / 121	1,195 / 153	1,178 / 152
ASPECT RATIO (EFFECTIVE)		10.41	19.56	19.56
OPTIMUM C _L		0.584	0.759	0.785
CRUISE L/D @ OPT C _L		17.997	23.995	24.741
DESIGN MISSION RANGE	NMI	3,680	3,500	3,500
PERFORMANCE CRUISE MACH		0.79	0.70	0.70
LONG RANGE CRUISE MACH (LRC)		0.79	0.70	0.70
THRUST ICAC (MTOW, ISA)	FT	36,200	37,700	38,200
TIME / DIST (MTOW, 35k FT, ISA)	MIN / NMI	23 / 148	23 / 147	29 / 181
OPTIMUM ALTITUDE (MTOW, ISA)	FT	34,900	37,700	38,200
BUFFET ICAC (MTOW, ISA)	FT	36,200	43,000	42,800
TOFL (MTOW, SEA LEVEL, 86 DEG F)	FT	8,190	7,680	8,180
APPROACH SPEED (MLW)	KT	126	109	111
BLOCK FUEL / SEAT (900 NMI)	LB	91.51 (Base)	42.46 (-53.6%)	40.30 (-56.0%)

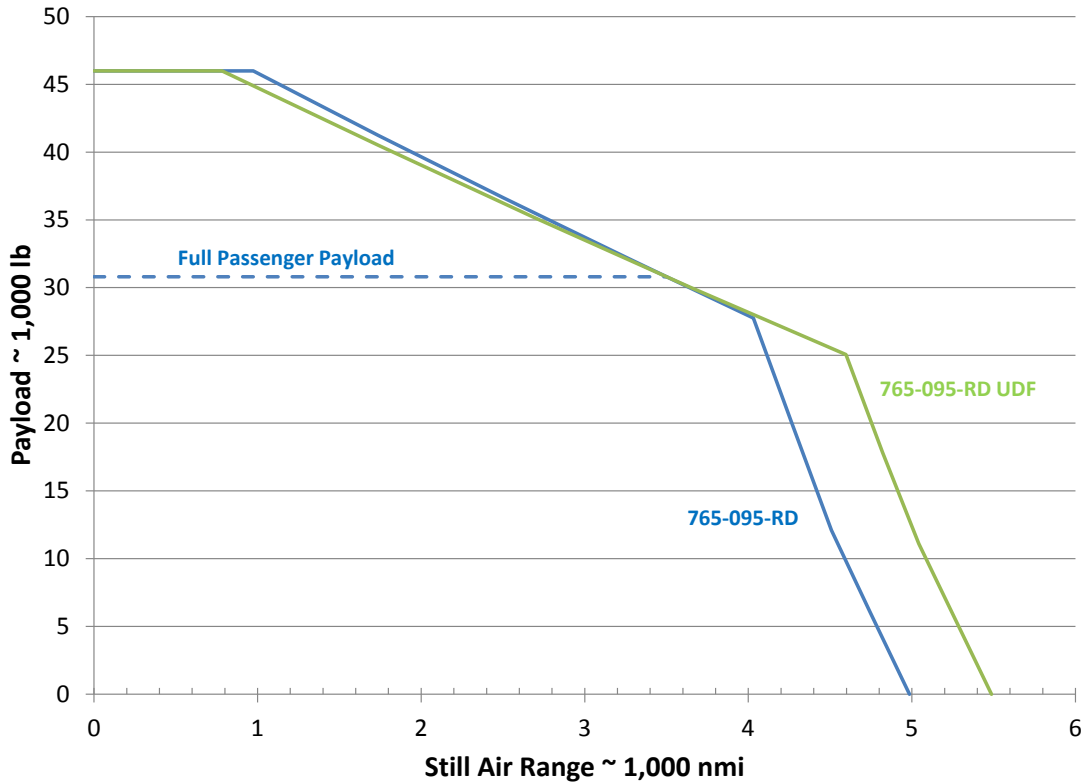


Figure 2.175 – 765-095 Sized Payload-Range Curve

Block Fuel for each configuration is compared to the SUGAR Free. NASA SFW Goals aim for a 60% reduction. Figure 2.176 shows the ducted and unducted configurations relative to these goals. The fuel burn per segment for the SUGAR High in comparison to SUGAR Free is shown in Figure 2.177 for the 900 nautical mile economic mission. Fuel burn as a function of range is illustrated by Figure 2.178.

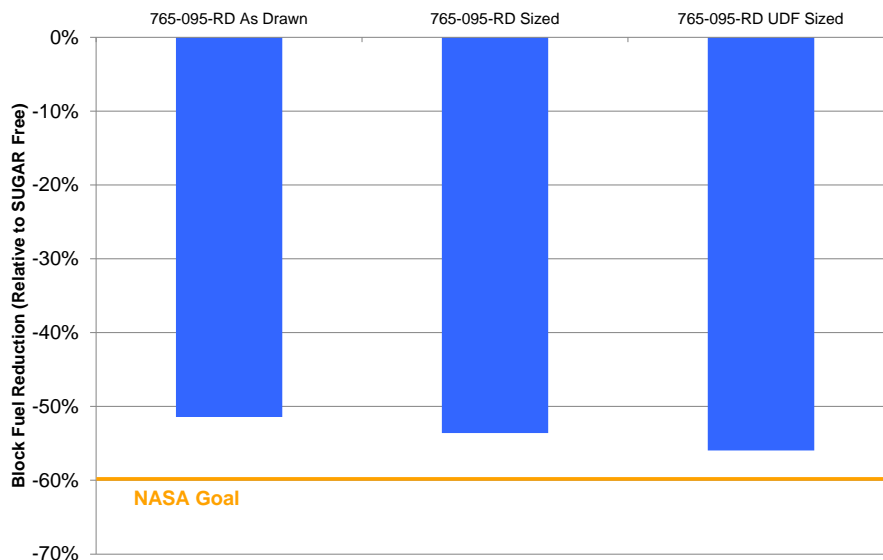


Figure 2.176 – Block Fuel Reduction Compared to NASA Goal

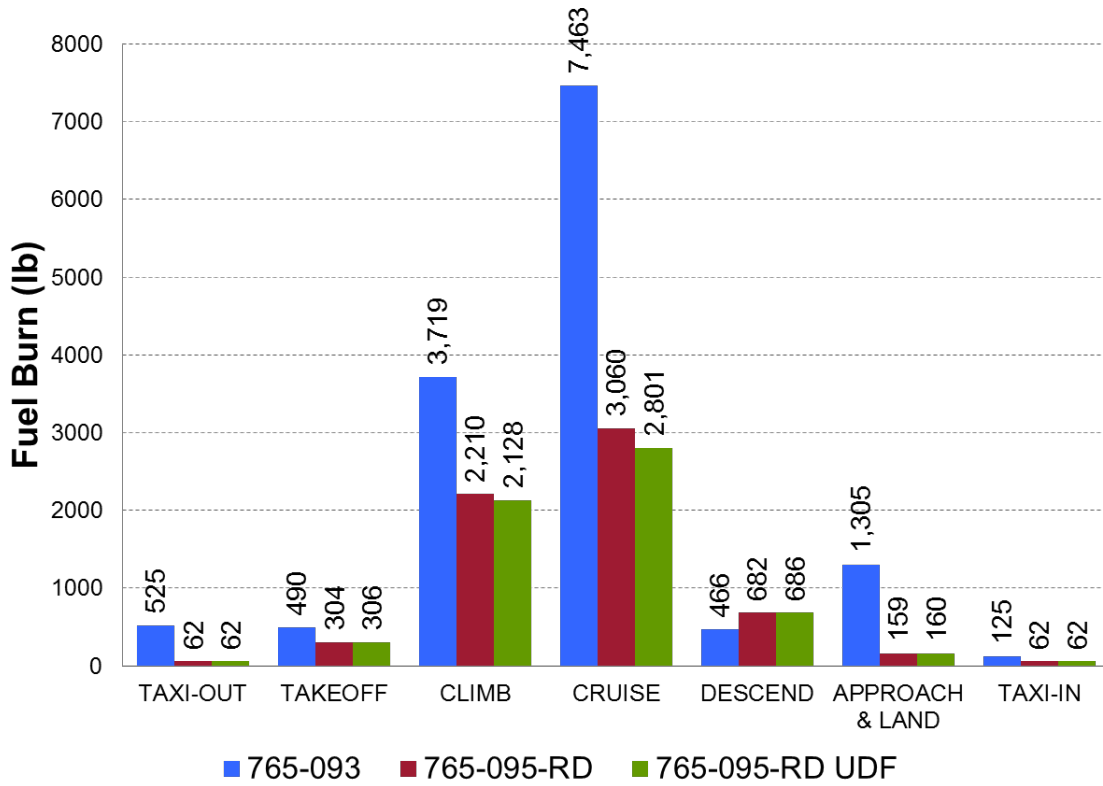


Figure 2.177 – Fuel Burn per Segment

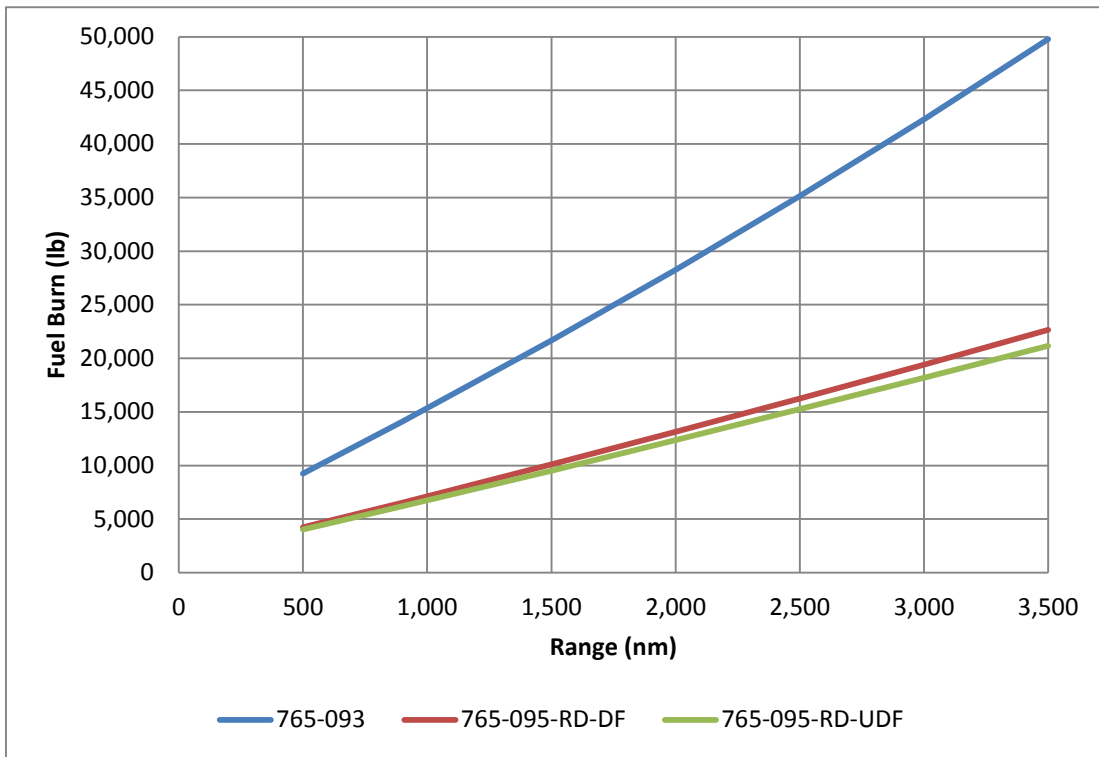


Figure 2.178 – Fuel Burn vs. Range

The sized group weights statement is shown below:

Table 2.40 – 765-095-RevD Sized Group Weights

GROUP	WEIGHT (LB)	
	Ducted Fan	UDF
WING	14,720	14,430
TAIL	3,160	3,160
FUSELAGE	16,790	16,690
WING STRUT & MLG SUPT INSTL	3,680	3,680
LANDING GEAR	4,640	4,340
NACELLE & PYLON	3,980	3,480
PROPULSION	8,360	10,890
ENGINES	6,820	9,350
FUEL SYSTEM	1,540	1,540
FLIGHT CONTROLS	2,280	2,250
POWER SYSTEMS	3,950	3,340
AUXILIARY POWER UNIT	1,010	1,010
HYDRAULICS	640	630
ELECTRICAL	2,300	2,300
INSTRUMENTS	770	770
AVIONICS & AUTOPILOT	1,500	1,500
FURNISHINGS & EQUIPMENT	9,120	9,120
AIR CONDITIONING	1,440	1,440
ANTI-ICING	100	100
MANUFACTURER'S EMPTY WEIGHT (MEW)	74,490	75,790
OPERATIONAL ITEMS	7,210	7,210
OPERATIONAL EMPTY WEIGHT (OEW)	81,700	83,000
USABLE FUEL	25,800	16,200
DESIGN PAYLOAD	30,800	30,800
TAKEOFF GROSS WEIGHT (TOGW)	138,300	130,000

2.3.4 Emissions

The LTO NOx emissions for the gFan+ Advanced Turbofan and UDF were assessed. The CAEP/6 requirements, characteristic LTO NOx, and margined estimates are listed in Table 2.41. Significant NOx emission improvements are shown, but fall short of the 20% of CAEP/6 goal and 80% reduction in cruise NOx goal.

Table 2.41 – gFan+ Advanced Turbofan and UDF LTO NOx Emissions

LTO NOx Emissions		
	gFan+	gFan+ UDF
CAEP/6, g/kN	72.5	59.8
Characteristic LTO NOx, g/kN	15.6	13.9
Margined Estimate, % CAEP/6	23.9%	25.7%

Mid-Cruise Emissions (CFM56-7B Baseline)		
	gFan+	gFan+ UDF
Absolute NOx Reduction	64.8%	66.3%

2.3.5 Stability and Control

Stability and control analysis focused on the lateral and directional control of the 765-095-RD Ducted Fan As-Drawn baseline. It is recognized that longitudinal analysis is also required to evaluate horizontal tail size and balance the airplane. A wing shift to balance the airplane is most likely necessary, but lateral/directional analysis was deemed to be higher priority. The airplane can be balanced in the next program phase, if additional low speed (slats and flaps extended) aerodynamic data become available.

Directional control analysis focused on engine out minimum control speed (V_{MC}). Both a V_{MCG} on-ground analysis and a one degree of freedom analysis of V_{MC} in air were performed. Engine data used were from the GE gFan+ ducted fan. Airplane geometry was for the baseline as-drawn 765-095-RD ducted fan configuration. Vertical tail aerodynamic data were based on the MD-80 aerodynamics model adjusted to 765-095 geometry (tail arm, tail area, wing span, and wing area). Conditions analyzed were for the 25 deg takeoff flap setting and angles-of-attack of 0.75 deg for V_{MCG} and 8.4 deg for V_{MC} . Table 2.42 summarizes the results of the analysis against FAR Part 25 airspeed requirements.

Table 2.42 – Engine Out Minimum Control Speed Results

FAR Part	Requirement	Speed (KEAS)
25.149(e)	Engine Out Minimum Control Speed Ground (V_{MCG})	94.6
25.149(b)	Engine Out Minimum Control Speed (V_{MC})	99.9
25.149(f)	Engine Out Minimum Control Speed Landing (V_{MCL})	Not Evaluated
25.107(a)(1)	Engine Failure Speed (V_{EF}) may not be less than V_{MCG}	120
25.107(b)(3)	Engine Out Climb Speed (V_2) may not be less than 1.10 times V_{MC}	126
25.107(e)(1)(ii)	Rotation Speed (V_R) may not be less than 105 percent of V_{MC}	122
25.149(c)	V_{MC} may not exceed 1.13 V_{SR} (Reference Stall Speed)	81.5
25.125(b)(2)(i)(B)	V_{REF} (Reference Landing Speed) may not be less than V_{MCL}	100

Most airspeed requirements are met, as indicated by the green color coding in the table. Unfortunately, the FAR part 25.149(c) requirement that V_{MC} not exceed 1.13 V_{SR} is not met. The stall speed used for takeoff analysis was 81.5 KEAS and 1.13 V_{SR} is 92.1 KEAS. The V_{MC} of 99.9 KEAS exceeds this value. There are two potential ways to solve this problem. Either the takeoff speeds need to be recalculated using a V_{SR} of 88.5 KEAS ($V_{MC}/1.13$), with resulting increases in takeoff distance, or directional control authority needs to be increased. Increasing directional control authority can be achieved by increasing the vertical tail area or by changing to a double hinged rudder design. Increasing vertical tail area may have a negative impact on crosswind landing capability and will increase the weight of the airplane. A double hinged rudder design is more complex and heavier than the current single hinged rudder. It is recommended that during the next phase of the program, takeoff field length be re-evaluated using higher takeoff speeds to see if field length requirements can still be met.

V_{MCL} with landing flap setting was not evaluated, but is not expected to be very much different from V_{MC} with takeoff flap setting. Assuming V_{MCL} is the same as V_{MC} , the FAR Part 25.125(b)(2)(i)(B) requirement that landing speed (V_{REF}) not be less than V_{MCL} is barely met. This requirement should be re-evaluated in the next program phase when better aerodynamic data are available.

Lateral control analysis focused on maximum steady state roll rate and time-to-bank 30 degrees. These analyses were performed with slats and flaps retracted because required low speed aerodynamic data was not available for the configuration. The effects of wing bending aeroelastics were investigated as part of this evaluation and were generated from the NASTRAN

FEM model. Roll moment of inertia also came from the FEM model for a full wing fuel state (high inertia).

Aerodynamic predictions were made using the Athena Vortex Lattice (AVL) code (15). 20 degrees was chosen as the maximum inboard and outboard aileron control surface deflections. Due to actuator hinge moment limiting at high speeds, data for similar airplanes show that available control surface deflection would be about $\frac{1}{2}$ the full range of deflection. The full aileron deflection for 765-095-RD was assumed to be 40 degrees. Because vortex lattice over-predicts control surface effectiveness, equivalent deflections were run based on aerodynamic data and AVL analysis from X-48C. For the inboard aileron, 14.2 deg of equivalent AVL deflection was calculated to produce the same rolling moment as 20 deg real world deflection. For the outboard aileron, 15.2 deg of equivalent AVL deflection produced the same rolling moment as 20 deg of physical deflection.

Because vortex lattice is not capable of predicting spoiler control effectiveness, MD-80 spoiler data were used. It was assumed that spoilers could deflect to their maximum angle of 60 degrees. No adjustments were made for spoiler area or span extent. This is partly due to the spoiler arrangement of 765-095-RD being considered notional. Inspection of 3-view drawings showed that the MD-80 spoiler arrangement has much less span extent and area than the currently drawn spoilers on 765-095-RD. Using the MD-80 spoiler effectiveness data should, therefore, be conservative and represent a lower bound on roll performance.

Requirements for steady state roll rate are documented in previous NASA studies (16). The steady state roll rate of 765-095-RD was evaluated for the inboard ailerons, outboard ailerons, and spoilers individually. Groupings of inboard ailerons and spoilers; and inboard ailerons, outboard ailerons, and spoilers were also investigated. Results are plotted in percentage (100% satisfies) of requirement in Figure 2.179.

The outboard ailerons, inboard ailerons, or spoilers, by themselves, cannot meet the steady state roll rate requirements. The low speed aileron reverses at some high Mach high dynamic pressure cases; the presumption is that outboard aileron would be locked out in those cases. Spoilers, by themselves, provide almost enough roll rate, but fail to meet the requirements at low dynamic pressures. Spoilers combined with either inboard ailerons, or both inboard and outboard ailerons meet all roll rate requirements.

Requirements for time-to-bank 30 degrees are documented (16) in previous NASA studies. The time-to-bank 30 deg of 765-095-RD was evaluated using a one degree of freedom roll simulation. Evaluations were performed for the inboard ailerons, outboard ailerons, and spoilers individually. Groupings of inboard ailerons and spoilers; and inboard ailerons, outboard ailerons, and spoilers were also investigated. The results are also illustrated in Figure 2.179.

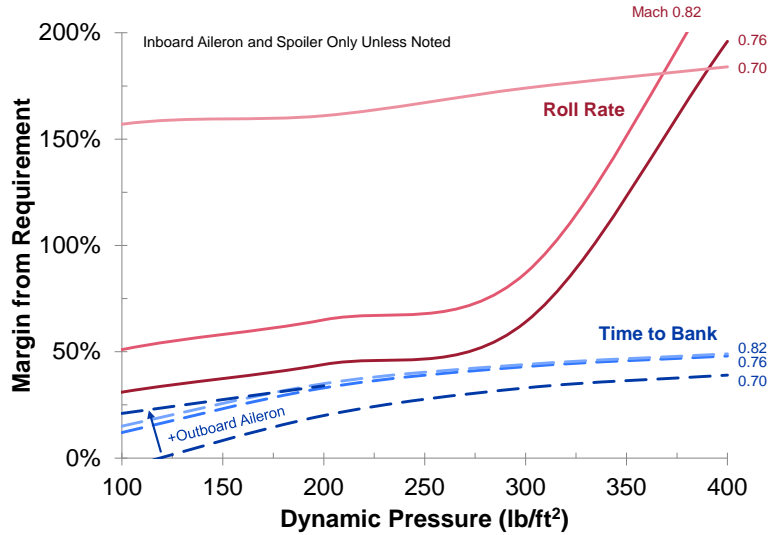


Figure 2.179 – Maximum Steady State Roll Rate and Time to Bank vs. Requirements

Like the roll rate requirement, outboard ailerons, inboard ailerons, or spoilers, by themselves, cannot meet the time-to-bank requirements. The cases for outboard ailerons at high dynamic pressure have aileron reversal. Spoilers, by themselves, provide almost enough control power, but fail to meet the requirements at low dynamic pressures. Spoilers combined with inboard ailerons, almost meet the requirements, but fail at the lowest Mach and dynamic pressure. Only spoilers combined with both inboard and outboard ailerons meet all time-to-bank 30 degree requirements. This justifies the inclusion of all of these control surfaces on the airplane. Aeroelastics on the high aspect ratio wing do not seem to limit the ability to meet the roll requirements.

2.4 Technology Plans and Roadmaps

The team has updated some of the technology plans that were developed in Phase I. The following updated technology plans are included in this section:

- Advanced Engine Technologies
- Advanced Subsystems
- Aerodynamic Technologies for Performance
- Airframe Acoustic Technologies
- Engine Acoustic Technologies
- NextGen Air Traffic Management
- Structural Concepts
- Structural Materials
- High Span TBW Technology Integration

These two plans are not included in this report but are included in Final Report Volume II Hybrid Electric Design Exploration:

- Hybrid Electric Engine
- High Performance Batteries

2.4.1 Advanced Engine Technologies

Goals and Objectives:

Develop enabling materials and methods for improved component performance

Performance Area and Impact:

Noise, Fuel burn, Emissions

Technical Description:

Develop propulsion enabling materials, cooling technology and component technology to support continued advancements in gas turbine efficiency, weight, and power

Major Milestones:

- Subscale alloy process development
- Full scale alloy development
- Final alloy ready for engine use
- Man tech milestones--TBD
- Test of gen 1, 2, 3 CMC components
- Tests of seals and bearings components
- Tests of variable fan nozzle concepts
- Tests of modulated cooling concepts
- Tests of advanced Active Clearance Control concepts
- Low emissions combustor cup, sector, full annular rig, and demo engine tests
- Overall program: program provides an "onramp" for demo engine test of technology concepts every 2 years

Dependency:

- Need suitable mule engine(s) to use as dedicated engine test asset
- Need a contingency plan for acquiring a backup asset should a catastrophic test failure occur

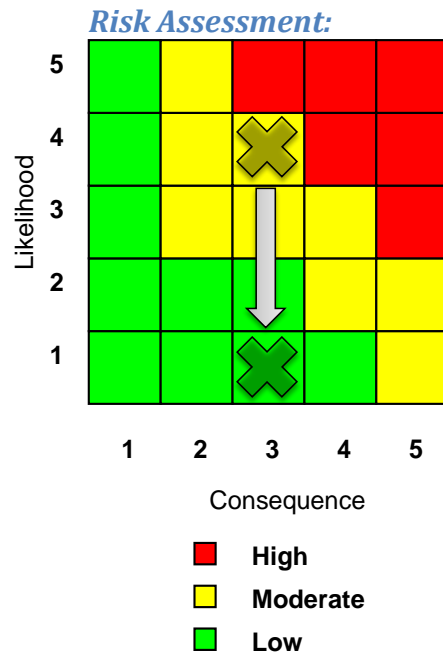


Figure 2.180 – Advanced Engine Technologies Risk Assessment

Notes:

- Program centered around multiple fast-paced builds of dedicated engine test vehicle
- 3 parallel materials development programs – 10 year sustained
- 2 parallel man. Tech programs – 10 year sustained
- Base engine is off-the-shelf
- Yields TRL6 by 2030
- Program for continuous improvement of low-emissions combustion technology
- PMC = polymer matrix composites
- CMC = ceramic matrix composites

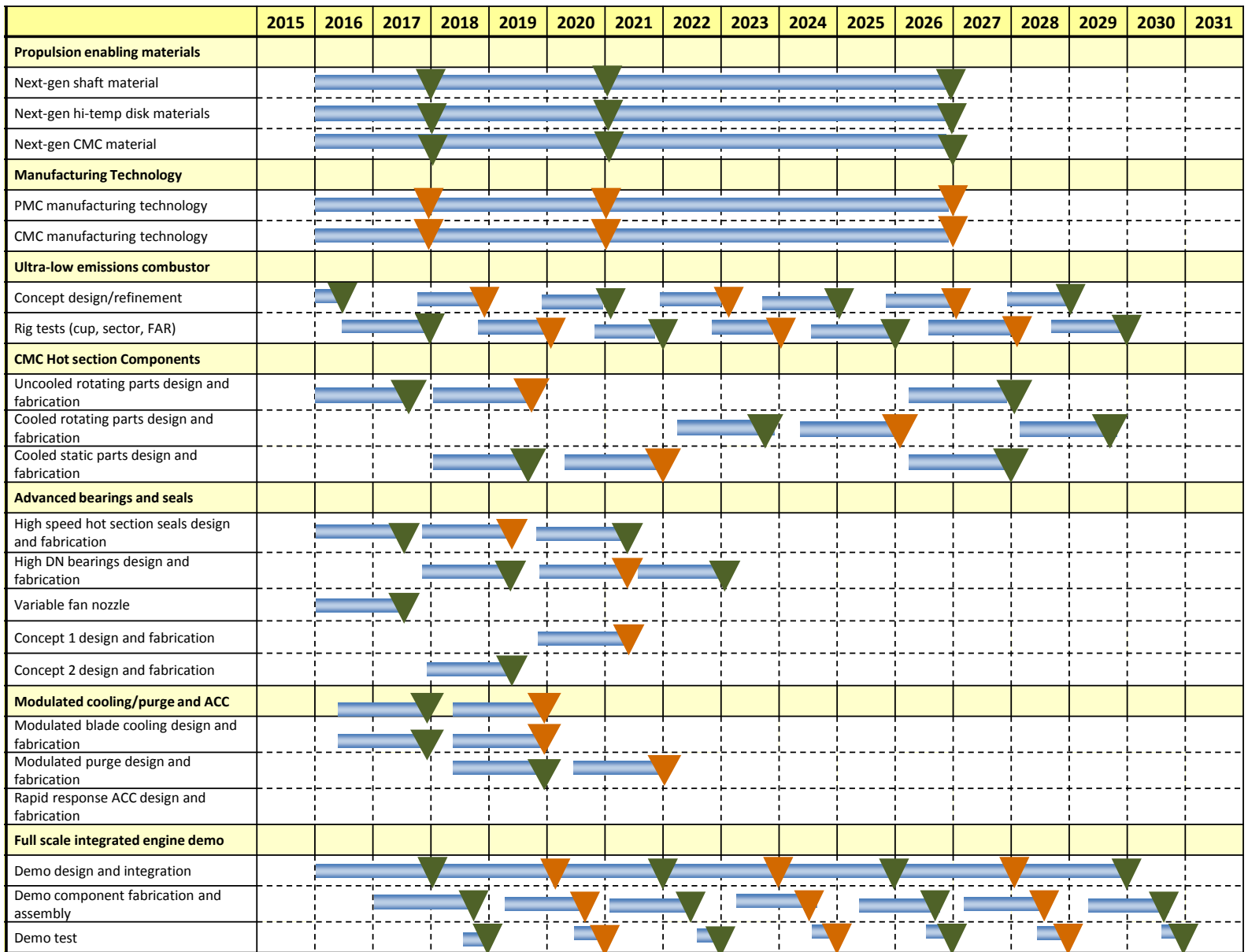


Figure 2.181 – Advanced Engine Technologies Roadmap*

2.4.2 Advanced Subsystems

Goals and Objectives:

Significantly improve weight and reliability of aircraft subsystems

Performance Area and Impact:

Reduced airplane weight, improved system reliability

Technical Description:

- Adaptive Power Management
- Diesel APU
- EMA Actuators
- Fiberoptic Control Architecture
- Lightweight Thermal Technology
- Integrated Computing Networks

Current TRL

2 to 4

Major Milestones:

- | | |
|--|------|
| • Diesel APU certification | 2017 |
| • Fiberoptic control system certification | 2021 |
| • Integrated computing network 3.0 certification | 2022 |
| • Adaptive power management system certification | 2024 |
| • Lightweight thermal technology certification | 2025 |
| • EMA Actuators Flight Demo | 2026 |
| • Integrated computing network 4.0 certification | 2031 |

Dependency:

- Integrated Airplane Systems Architecture

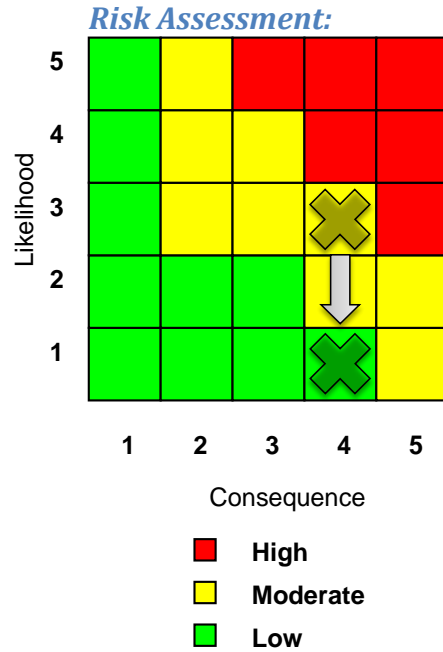


Figure 2.182 – Advanced Systems Risk Assessment

Success Criteria:

Table 2.43 – Advanced Subsystems Success Criteria

Task Number	Task Name	Success Criteria	Alternate Steps if Unsuccessful
1	Adaptive Power Management	Certification	Revert to current SOA
2	Diesel APU	Certification	Revert to advanced turboshaft APU Use highly integrated propulsion and power system to eliminate APU Use fuel cell APU (additional development time required)
3	EMA Actuators	Certification	Revert to current SOA
4	Fiberoptic Control Architecture	Certification	Revert to current SOA
5	Lightweight Thermal Technology	Certification	Revert to current SOA
6	Integrated Computing Networks -Generation 3.0	Certification	Revert to current SOA
7	Integrated Computing Networks -Generation 4.0	Certification	Revert to generation 3.0 architecture

TRL	Task	2010	2011	2012	2013	2014	2015	2016	2017	2018	2019	2020
	1 Adaptive Power Management											
3	1.1 Intelligent Energy Management Architecture											
4	1.2 Adaptive Load Management Models and Simulators											
5	1.3 Intelligent Components											
5	1.4 Self-powered passenger control units											
5	1.5 Self-powered wireless sensors											
6	1.6 High Power Energy Harvesting											
7	1.7 Prototype Testing and Demonstration											
8	1.8 Qualification and Certification tests											
9	1.9 Flight Ready											
	2 Diesel APU											
4	2.1 Breadboard demo in sub-atmospheric test chamber											
5	2.2 Ground test of prototype scaled unit											
6	2.3 Prototype test on the ETD at altitude											
7	2.4 Beta unit demonstration											
8	2.5 Qualified through certification tests											
9	2.6 Flight proven											
	3 EMA Actuators											
8	Hybrid control (Conventional EMA)											
9	Integrated Flight Demo (Conventional EMA)											
6	High Temp Superconducting (HTS) Motor EMA											
7	Integrated HTS Based EMA Ground Demo											
9	Integrated HTS Based EMA Flight Demo											
	4 Fiberoptic Control Architecture											
2	4.2 Technology Concept and/or Application Formulated											
3	4.3 Analytical and Experimental Critical Function and/or Characteristic Proof-of-Concept											
4	4.4 Component and/or Breadboard Validation in Laboratory Environment											
5	4.5 Component and/or Breadboard Validation in Relevant Environment											
6	4.6 System/Subsystem Model or Prototype Demonstration in a Relevant Environment											

TRL	Task		2010	2011	2012	2013	2014	2015	2016	2017	2018	2019	2020
7	4.7	System Prototype Demonstration in a Target Environment											
8	4.8	System Completed & Flight Qualified through Test and Demonstration											
9	4.9	System Flight Proven through Successful Operation											
	5	Lightweight Thermal Technology											
	5.1	Integrated Dynamic Models											
3	5.2	Total Energy Management Models											
4	5.3	Integrated Power/Thermal/EMI Dynamic models											
5	5.4	Total Energy Management Lab Integration											
6	5.5	Prototype Testing and Demonstration											
7	5.6	Certification											
8	5.7	Flight Ready											
9	6	Integrated computing Networks – Generation 3.0											
	6.1	Component and/or Breadboard Validation in Laboratory Environment											
	6.2	Component and/or Breadboard Validation in Relevant Environment											
4	6.3	System/Subsystem Model or Prototype Demonstration in a Relevant Environment											
5	6.4	System Prototype Demonstration in Target Environment											
6	6.5	System Completed & Flight Qualified through Test and Demonstration											
7	6.6	System Flight Proven through Successful Operation											
8	7	Integrated Computing Networks – Generation 4.0											
9	7.1	Technology Concept and/or Application formulated											
	7.2	Analytical and Experimental Critical Function and/or Characteristic Proof-of-Concept											
	7.3	Component and/or Breadboard Validation in Laboratory Environment											
2	7.4	Component and/or Breadboard Validation in Relevant Environment											
3	7.5	System/Subsystem Model or Prototype Demonstration in a Relevant Environment											
4	7.6	System Prototype Demonstration in Target Environment											
5	7.7	System Completed & Flight Qualified through Test and Demonstration											
6	7.8	System Flight Proven through Successful Operation											

Figure 2.183 – Advanced Subsystems Technologies Roadmap (1 of 2)

TRL	Task	2021	2022	2023	2024	2025	2026	2027	2028	2029	2030	2031
	1 Adaptive Power Management											
3	1.1 Intelligent Energy Management Architecture											
4	1.2 Adaptive Load Management Models and Simulators											
5	1.3 Intelligent Components											
5	1.4 Self-powered passenger control units											
5	1.5 Self-powered wireless sensors											
6	1.6 High Power Energy Harvesting											
7	1.7 Prototype Testing and Demonstration											
8	1.8 Qualification and Certification tests											
9	1.9 Flight Ready											
	2 Diesel APU											
4	2.1 Breadboard demo in sub-atmospheric test chamber											
5	2.2 Ground test of prototype scaled unit											
6	2.3 Prototype test on the ETD at altitude											
7	2.4 Beta unit demonstration											
8	2.5 Qualified through certification tests											
9	2.6 Flight proven											
	3 EMA Actuators											
8	Hybrid control (Conventional EMA)											
9	Integrated Flight Demo (Conventional EMA)											
6	High Temp Superconducting (HTS) Motor EMA											
7	Integrated HTS Based EMA Ground Demo											
9	Integrated HTS Based EMA Flight Demo											
	4 Fiberoptic Control Architecture											
2	4.2 Technology Concept and/or Application Formulated											
3	4.3 Analytical and Experimental Critical Function and/or Characteristic Proof-of-Concept											
4	4.4 Component and/or Breadboard Validation in Laboratory Environment											
5	4.5 Component and/or Breadboard Validation in Relevant Environment											
6	4.6 System/Subsystem Model or Prototype Demonstration in a Relevant Environment											

TRL	Task		2021	2022	2023	2024	2025	2026	2027	2028	2029	2030	2031
7	4.7	System Prototype Demonstration in a Target Environment											
8	4.8	System Completed & Flight Qualified through Test and Demonstration											
9	4.9	System Flight Proven through Successful Operation											
	5	Lightweight Thermal Technology											
	5.1	Integrated Dynamic Models											
3	5.2	Total Energy Management Models											
4	5.3	Integrated Power/Thermal/EMI Dynamic models											
5	5.4	Total Energy Management Lab Integration											
6	5.5	Prototype Testing and Demonstration											
7	5.6	Certification											
8	5.7	Flight Ready											
9	6	Integrated computing Networks – Generation 3.0											
	6.1	Component and/or Breadboard Validation in Laboratory Environment											
	6.2	Component and/or Breadboard Validation in Relevant Environment											
4	6.3	System/Subsystem Model or Prototype Demonstration in a Relevant Environment											
5	6.4	System Prototype Demonstration in Target Environment											
6	6.5	System Completed & Flight Qualified through Test and Demonstration											
7	6.6	System Flight Proven through Successful Operation											
8	7	Integrated Computing Networks – Generation 4.0											
9	7.1	Technology Concept and/or Application formulated											
	7.2	Analytical and Experimental Critical Function and/or Characteristic Proof-of-Concept											
	7.3	Component and/or Breadboard Validation in Laboratory Environment											
2	7.4	Component and/or Breadboard Validation in Relevant Environment											
3	7.5	System/Subsystem Model or Prototype Demonstration in a Relevant Environment											
4	7.6	System Prototype Demonstration in Target Environment											
5	7.7	System Completed & Flight Qualified through Test and Demonstration											
6	7.8	System Flight Proven through Successful Operation											

Figure 2.184 – Advanced Subsystems Technologies Roadmap (2 of 2)

2.4.3 Aerodynamic Technologies for Performance

Goals and Objectives:

Develop and implement aerodynamic technologies enabling the design of airplanes in 2030 timeframe. These technologies will contribute to the 30% improvement in fuel efficiency relative to current fleet.

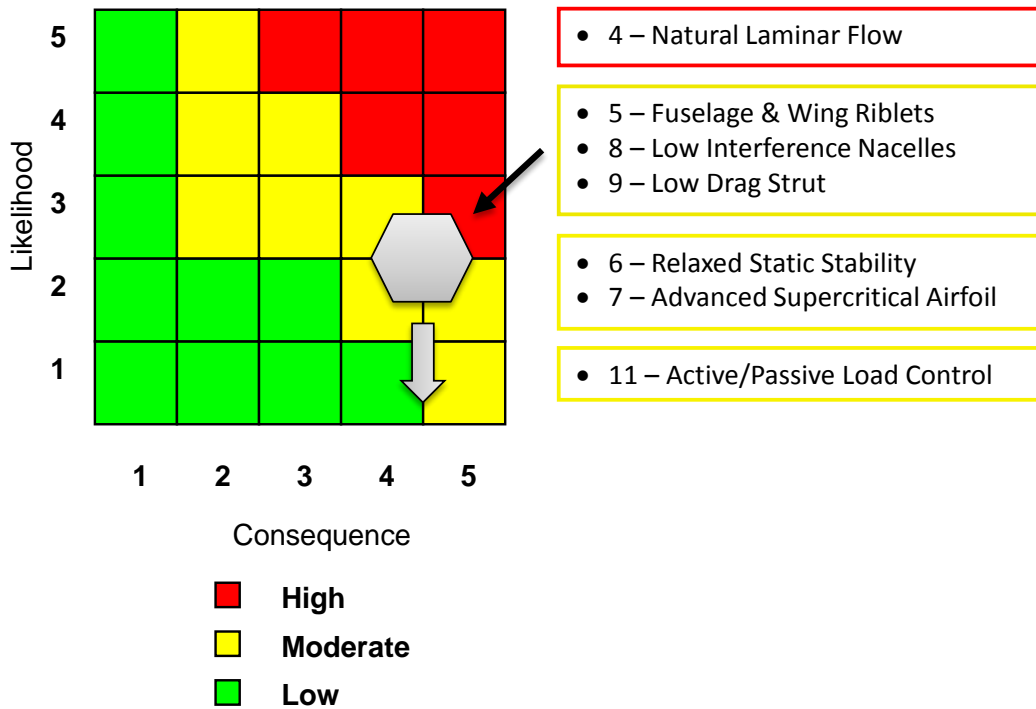
Performance Area and Impact:

Improved airplane performance through drag reduction

Technical Description:

- Aerodynamic technologies have been identified to provide significant improvement toward an Airplane in 2030 (N+3) timeframe.
- Laminar flow on any component reduces skin friction drag and pressure drag on the laminarized area.
- Riblets reduce skin friction drag by modifying turbulent structure in the turbulent boundary layer.
- Improve design integration of Nacelles in the presence of wings to reduce interference drag.
- Improve design integration of Strut braced configuration in the presence of wings and body to reduce interference drag.
- Reduced static stability reduces trim drag and increased CLmax tail designs reduce tail area and weight.
- Wing design to accommodate active/passive aeroelastic response for load control allows tailoring of wing spanloads to improve overall mission performance. This technology is shared with Structures.

Risk Assessment



Major Milestones:

- Natural laminar flow wing design without HLFC systems to achieve a viable configuration. Roadmap will address passive/active systems to achieve Aerodynamic goals. Identify system benefits for go-no-go. 2020
- Integration of low interference drag struts on high span wing configurations. Improvement in interference drag is significant. Identify system benefits for go-no-go. 2020
- Advanced Super-critical wings with improved efficiency. Identify system benefits for go-no-go. 2025
- Design, implement and demonstrate achievable drag improvements of Riblets on fuselage and wings. Identify system benefits for go-no-go. 2025
- Integration of low interference drag nacelles on high span wing configurations. Improvement in interference drag is significant. Identify system benefits for go-no-go. 2025
- Incorporate aggressive relaxed static stability and improve empennage performance. Identify system benefits for go-no-go. 2025
- Collaborate on integration of active/passive aeroelastic response for load control. Identify system benefits for go-no-go. 2025

Dependency:

- Configuration Development
- Technologies impact on each other (one technology could prevent another technology from maturing)

Success Criteria:

Task Number	Task	Success Criteria	Alternative steps if unsuccessful
1	Near term Aero Design & Testing	Verify performance improvements	Design with lower aero performance
2	Laminar Flow		
	Passive LFC	NLF laminar design matches Active LFC	Achieve 50% of an Active LFC laminar Run
	Active LFC	Achieve Laminar to shocks with low power consumption	Establish break even points between NLF/Passive/Active
3	Low Interference Drag Struts	Integrate strut into wing-body for only strut parasite drag	Establish low interference levels
4	Advanced Super-Critical Wing	Target 3% airplane drag improvement while attaining high design lift coefficient	Achieve 50% of target drag improvement
5	Riblet Integration	Target 2% – 3% airplane drag improvement	
6	Low Interference Drag Nacelles	Integrate nacelle/pylon to wing body for only nacelle/pylon parasite drag	Establish low interference levels
7	Relaxed static stability Increased CLmax Empennage	Achieve neutral static stability to reduce tail size. Improve empennage CLmax to reduce tail size	Demonstrate some reduction in tail size
8	Aeroelastic Load Control	Span load traded for Aerodynamics and structural efficiencies to improve overall mission performance	Achieve improvement for one discipline

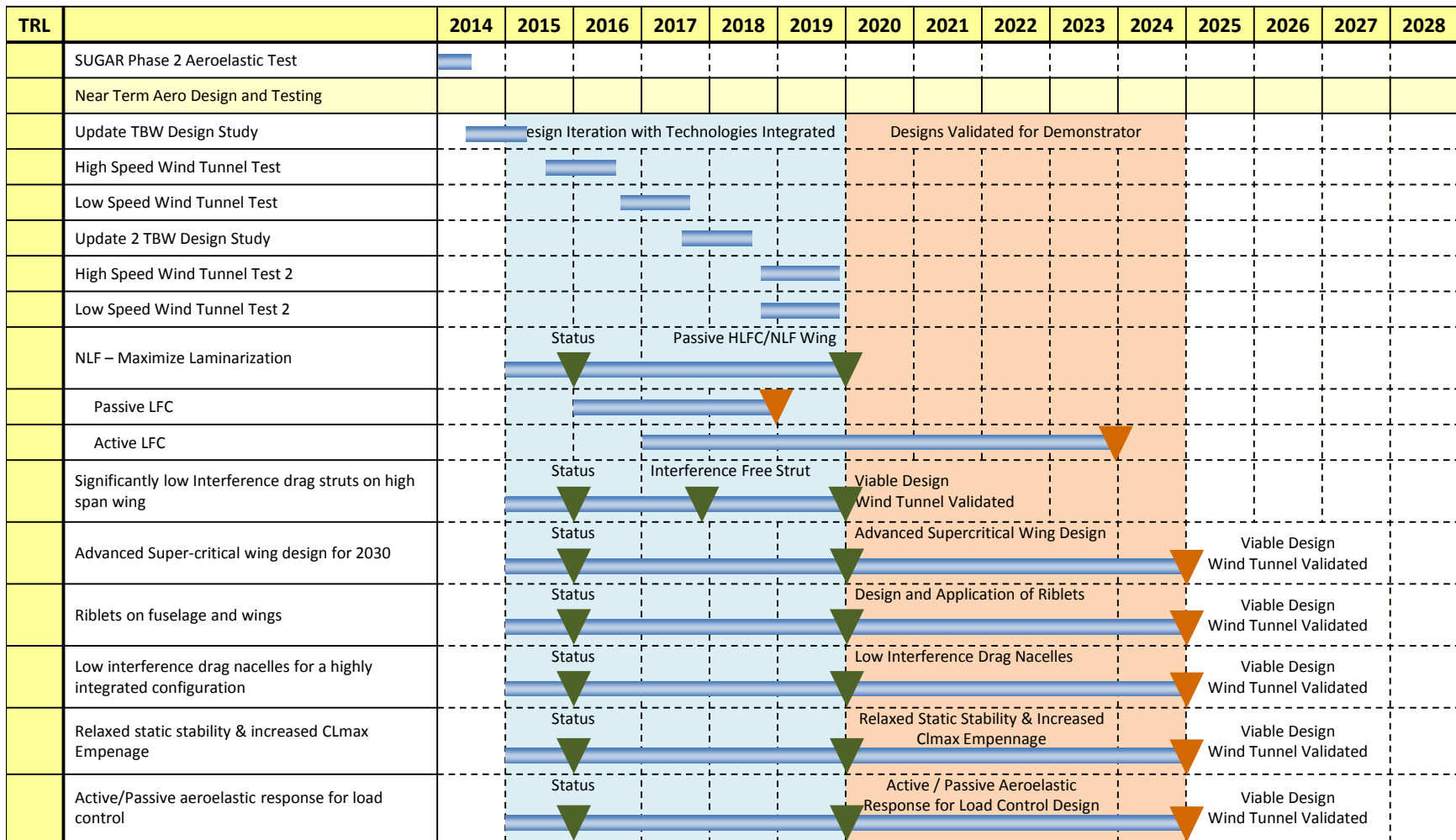


Figure 2.185 – Aerodynamic Technologies Roadmap

2.4.4 Airframe Acoustic Technologies

Goals and Objectives:

Develop airplane designs and technologies that reduce airframe noise and increase shielding of engine noise, in order to meet future strict noise regulations in airport environments

Performance Area and Impact:

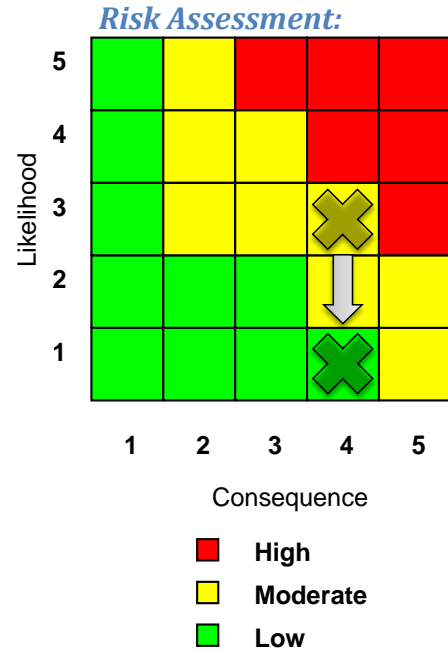
- Engine noise dominance at take-off (cutback and sideline), and airframe noise dominance at approach
- Impact on Aerodynamics, Propulsion, and Airframe Design

Technical Description:

- Develop inherently quiet landing gear designs (includes main and nose gear)
- Develop inherently quiet high-lift system designs with good aerodynamic characteristics (includes leading and trailing edge devices, and wing trailing edge)
- Develop integrated engine-airframe designs with inherent shielding (includes jet, inlet and aft-fan)
- Develop technologies to reduce landing gear noise, high-lift system noise, jet noise, and aft-fan noise
- Develop technologies to maximize engine noise shielding (includes shielding of jet, inlet, and aft-fan)
- Evaluate and down-select design ideas and technology concepts using the following: (a) acoustics integrated into multidisciplinary design, (b) airframe noise and engine noise shielding testing including model-scale and full-scale flight tests, and (c) development of tools for acoustic design, analysis, and prediction of airframe noise and engine noise shielding

Major Milestones:

- | | |
|--|-----------|
| • Acoustic design, analysis, and prediction tools (Landing Gear) | 2018 |
| • Acoustic design, analysis, and prediction tools (Shielding) | 2019 |
| • Acoustic design, analysis, and prediction tools (High-Lift System Tools) | 2022 |
| • Selection of promising designs and technology concepts for model-scale testing | 2016/2020 |



- Model-scale acoustic testing for initial assessments and candidate down-selection 2018/2019/2022
- Selection of best airframe designs and technology concepts for full-scale flight testing 2018/2019/2022
- Full-scale flight testing for final validation and TRL8 assessment of best airframe designs and technology concepts 2026

Dependency:

- Airplane design and development (cross-effect and reaction to engine design, high-lift design and airplane performance)
- Facilities for model-scale testing
- Platform (testbed) for full-scale flight testing
- CFD resources

Success Criteria:

Task Name	Success Criteria	Alternate Steps if Unsuccessful
Quiet Landing Gear Design	5 dB reduction in gear noise	More testing with alternate concepts or use of lowest attained reduction level
	Landing Gear design tool	Alternate approach/methodology or use of existing gear noise prediction tools
Advanced Airframe and Engine Design and Integration for Shielding Optimization	5 dB reduction in jet and aft-fan noise	More testing with alternate concepts or use of lowest attained reduction level
	15-20 dB cumulative shielding benefit (sum of jet, inlet, and aft-fan shielding)	More testing with alternate concepts or use of highest attained shielding benefit
	Shielding design tool	Alternate approach/methodology or use of existing shielding prediction tools
Advanced Acoustic Design for High-Lift Systems	8-10 dB combined reduction	Use of lowest existing high-lift noise levels
	High-Lift System design tool	Use of existing noise prediction tools
Full-Scale Flight Testing for Validation and Assessment of TRL8	Agreement between model-scale and full-scale results; realizing most of the expected benefits	Adjustment/extrapolation of existing data
		Conservative use of model-scale benefits

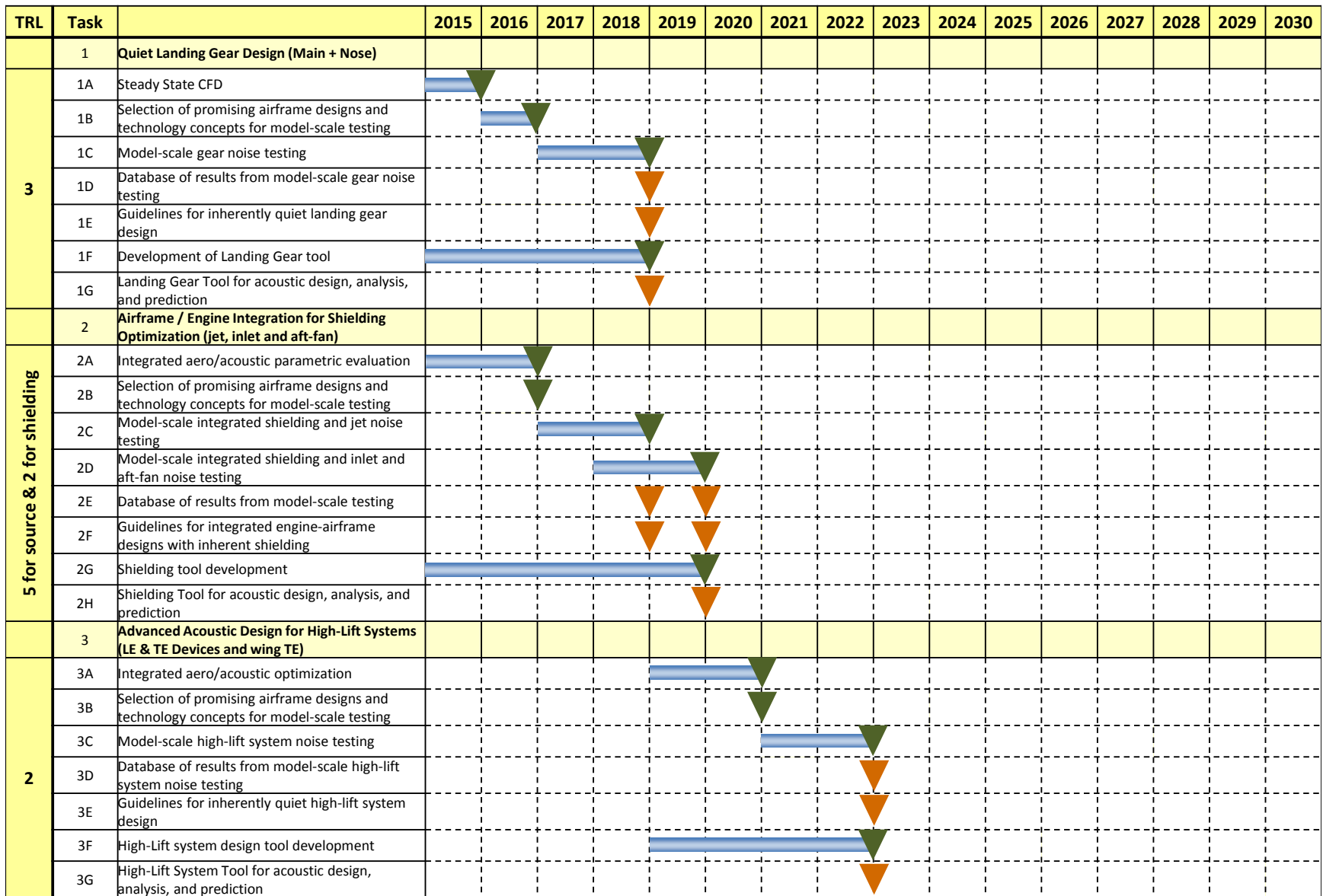


Figure 2.186 – Airframe Acoustic Technology Roadmap (1 of 2)

TRL	Task	2015	2016	2017	2018	2019	2020	2021	2022	2023	2024	2025	2026	2027	2028	2029	2030
	4 Full-Scale Flight Testing for Validation and Assessment of TRL8																
	4A Selection of best airframe designs and technology concepts for full-scale flight testing (for landing gear, jet, inlet, aft-fan, and high-lift)					▼	▼		▼								
	4B Flight testing for landing gear noise reduction					▬			▼								
	4C Database of results from full-scale gear noise testing								▼								
	4D TRL8 low noise landing gear (quiet design and noise reduction technology integration)								▼								
	4E Flight testing for jet noise reduction and shielding					▬			▼								
	4F Database of results from full-scale integrated shielding and jet noise testing								▼								
	4G TRL 8 high jet noise shielding (quiet design and noise reduction technology integration)								▼								
	4H Flight testing for inlet noise and aft-fan noise reduction and shielding					▬			▼								
	4I Database of results from full-scale integrated shielding and inlet and aft-fan noise testing								▼								
	4J TRL 8 high inlet and aft-fan noise shielding (quiet design and noise reduction technology integration)								▼								
	4K Flight testing for high-lift system noise reduction									▬			▼				
	4L Database of results from full-scale high-lift system noise testing												▼				
	4M TRL8 low noise high-lift system (quiet design and noise reduction technology integration)												▼				
	4N Flight testing for combined total noise reduction and shielding												▬		▼		

Figure 2.187 – Airframe Technology Roadmap (2 of 2)

2.4.5 Engine Acoustic Technologies

Goals and Objectives:

Develop new and innovative designs and methods to reduce propulsion system noise

Performance Area and Impact:

Engine Acoustic Properties

Technical Description:

Two pronged approach to develop a suite of near-term, mostly passive technologies and far-term aggressive suppression technologies

Major Milestones:

- Overall program: program provides an "onramp" for demo engine test of technology concepts every 2 years
- Ongoing design studies / data reduction / methods improvement throughout program
- Phase I – advanced/passive noise treatments full scale tests (typically 2 design/build/test iterations), best funding fit with N+2 2023
- Phase II – advanced/active noise treatments subscale/rig design/build/test cycles (3), plus full scale design/build/test cycles (2), best funding fit with N+3 2030
- Early thrusts of N+3 acoustic work: 1) sustained work on high-performance bulk absorbers, 2) open rotor noise reduction, Basic physics of fluidics and flow control 2023
- Mid-phase thrusts expanded to include Unconventional UHB, soft/active elements, and non-axisymmetric exhausts 2025
- Far term focus on low noise combustor, shape memory alloy 2029

Dependency:

- Need dedicated engine asset(s) to use as testbed
- Variable fan nozzle is not shown (appears on advanced engine tech roadmap)

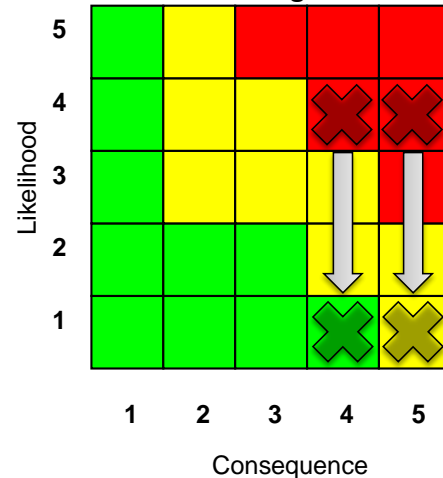
Notes:

- 10-yr sustained development of bulk and tailored absorbers
- Development program utilizes multiple builds of an engine test asset
- Hold pace of 1 engine build and test every 2 years

Risk Assessment:

Passive Technologies: 4 x 4

Active Technologies: 4 x 5



■ High
■ Moderate
■ Low

- Early program focused on full scale demos of incremental/moderate risk concepts
- Early program focused on subscale/rig demos of aggressive and high risk concepts
- Later program focused on full scale demo of aggressive/high risk projects
- Each technology gets 2 build/test cycles (can adjust as needed based on results: most promising concepts-->More builds, less promising-->fewer builds)
- Continuous effort to incorporate results into methods and design practices
- Variable fan nozzle is not shown (appears on advanced engine tech roadmap)

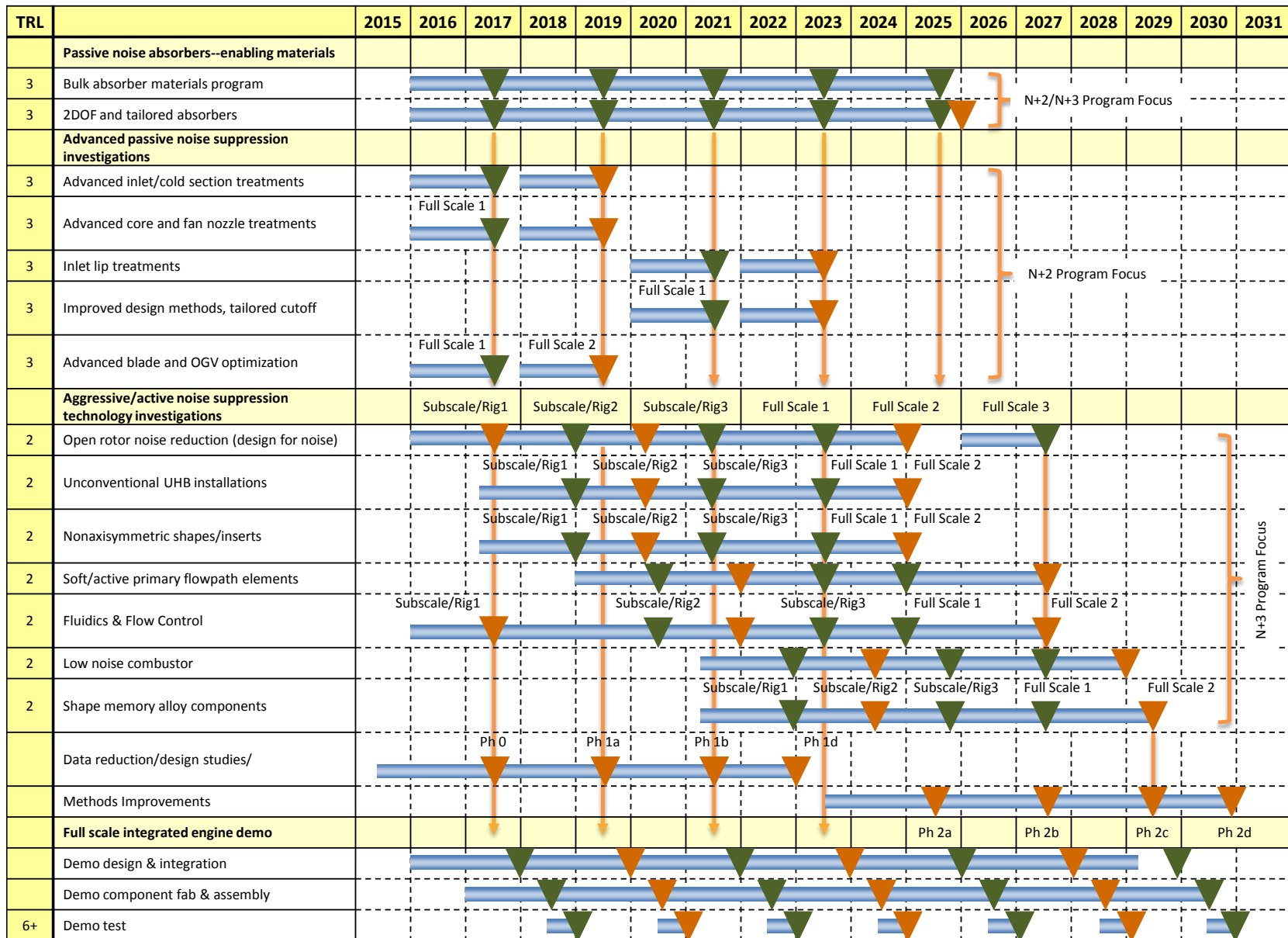


Figure 2.188 – Engine Acoustic Technologies*

2.4.6 NextGen Air Traffic Management

Goals and Objectives:

The goal of this project is to integrate avionics components into the aircraft in order to make it compatible with the Next generation Air Transportation System (NextGen). This research and development plan seeks to increase capacity, reduce delays, and improve safety throughout the ATS through technological improvements both on the ground and in the air.

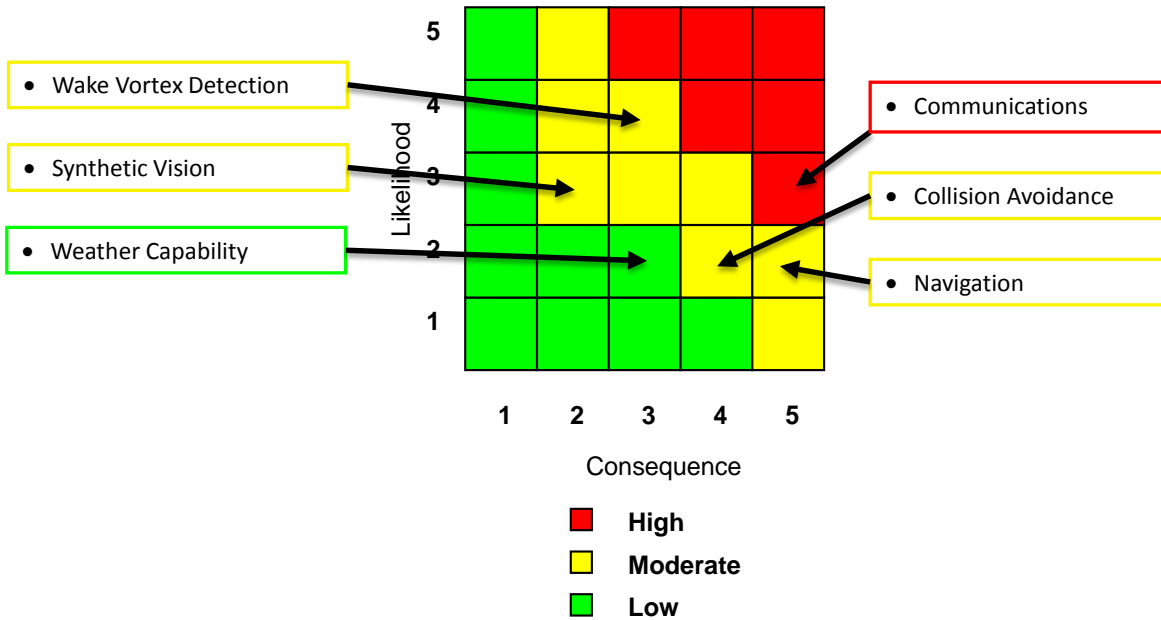
Performance Area and Impact:

- LTO NO_x Substantial Reduction (reduced taxi time)
- Fuel Burn Substantial Reduction (17% for current technology vehicles)
- Cruise Emissions Substantial Reduction (17% for current technology vehicles)
- System Capacity Substantial Increase (increased capacity at airport and increase airports)

Technical Description:

NextGEN as a program encompasses all the aircraft and ground related improvements that must be accomplished in order to realize the benefits to fuel efficiency, capacity and safety. For the purposes of this roadmap the technology is limited to the on-aircraft components only. Overall these new concepts will impact every phase of flight in some way. For example, increased situational awareness of other aircraft will allow for reduced taxi times. Better aircraft positioning data and route planning will allow for a more fuel optimized climb and reduced separation requirements. Improved collision avoidance will enable optimal climb and cruise climb trajectories. Better weather detection means that pilots can optimize their route in flight to find the compromise in avoiding the weather while still retaining a fuel efficient trajectory. Increased communications and optimized planning will allow for better descent profiles to save fuel, increase safety, and reduce noise.

Risk Assessment:



Major Milestones:

- Integrate Ground/Air Voice/Data Network 2025
- Trajectory Negotiation Automated 4 D Ts 2020
- Airborne Collision Avoidance 2020
- Aircraft-Aircraft Weather Information Sharing 2025
- Wake Detection and Avoidance Protocols 2015
- Synthetic Vision Systems 2018

Dependency:

- Ground Communications Architecture
- Integrated Route Planning and Optimization
- Airport Operations Improvements

Success Criteria:

Task Number	Task Name	Success Criteria	Alternate Steps if Unsuccessful
1	Communications	Aircraft and ground controllers can share information and voice communications simultaneously	Current SoA
2	Navigation	Ability of the controller to accurately predict and control the location of aircraft at any point in the flight profile	Current SoA
3	Collision Avoidance	Significant reduction of unnecessary in-flight alerts and collision risk	Current SoA
4	Weather Capability	Aircraft-Aircraft weather detection and information sharing	Current SoA
5	Wake Vortex Detection	Aircraft wake prediction based off type of aircraft and atmospheric conditions allows for decreased separation distance	Current SoA
6	Synthetic Vision	Synthetic and enhanced vision aids available to pilots to enable operation in reduced visibility conditions	Current SoA

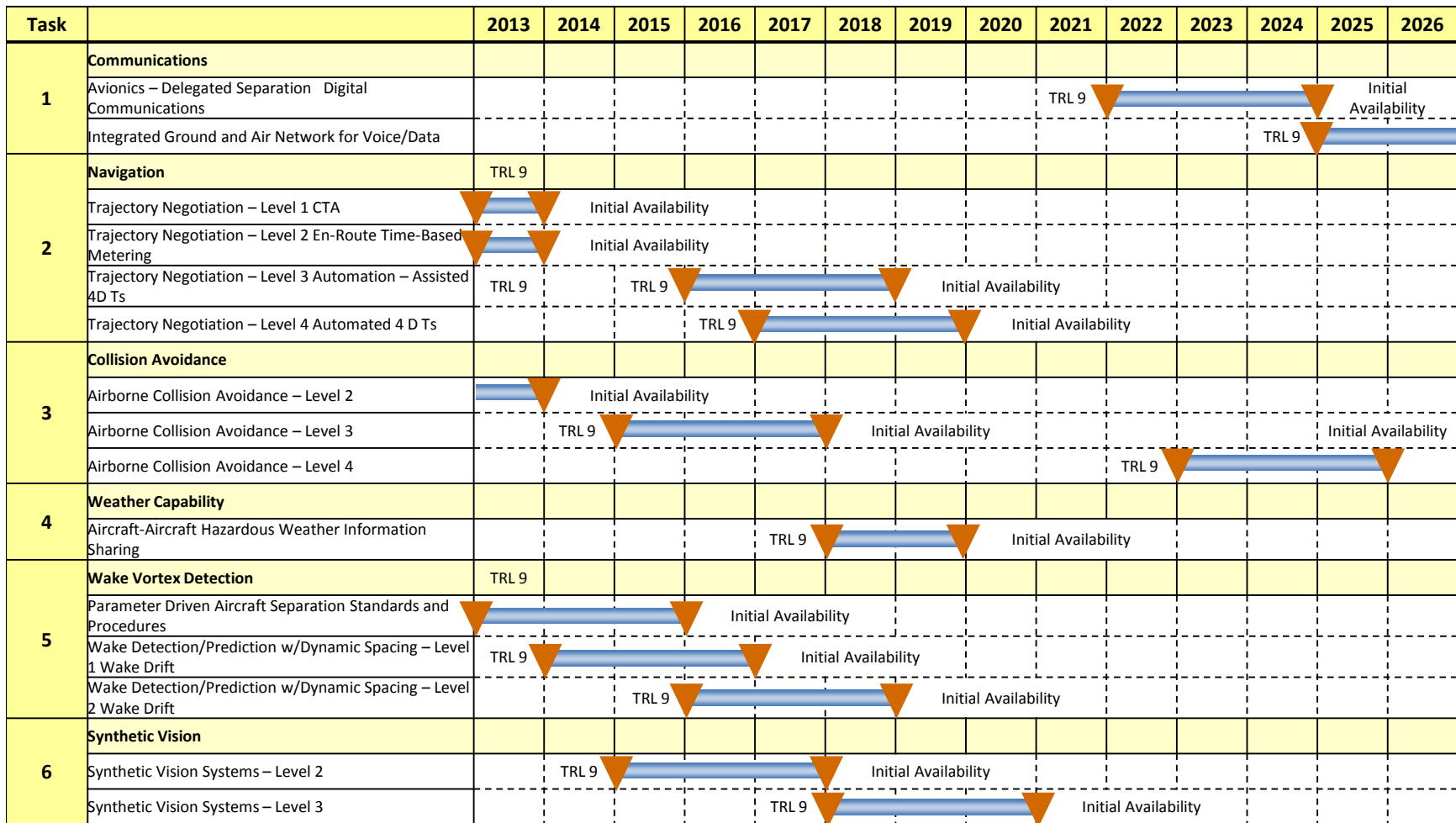


Figure 2.189 – Next Generation Air Traffic Management Technical Roadmap

Task		2013	2014	2015	2016	2017	2018	2019	2020	2021	2022	2023	2024	2025	2026
1	Communications														
	Applied Research on Integrated Voice/Data and Air/Ground Network Communications											TRL 6		TRL 9	
2	Navigation														
	Applied Research on 3D RNA V/RNP Procedures				TRL 9				TRL 6			TRL 9			
	Applied Research on Low Cost INS														
	Applied Research on Required 4D Intent Data	TRL 6			TRL 9										
4	Weather Capability														
	Applied Research on Improved Weather Sensing and Forecasting Models			TRL 6		TRL 9									
5	Wake Vortex Detection														
	Dynamic Wake Management for Single Runway Operation		TRL 9												
	Applied Research on Assessing and Predicting Wake Severity		TRL 9												

Figure 2.190 – Next Generation Air Traffic Management Operational Roadmap

2.4.7 Structural Concepts

Goals and Objectives:

Implement advanced structural technologies currently under development enabling design, fabrication and operation of advanced high performance structural systems without the conservatism inherent in current structures.

Structural designs will include integrated systems functionality which will benefit both airplane systems operations as well lighter weight structures.

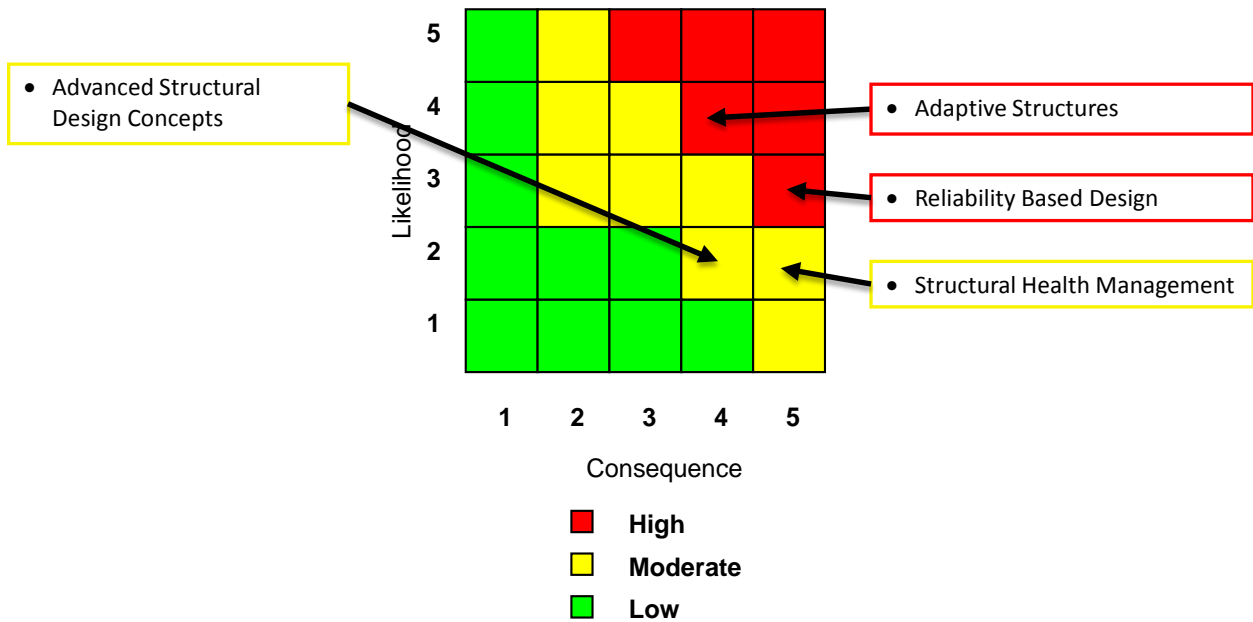
Performance Area and Impact:

- Primary, structural weight (OWE). Secondary, systems components weights (OEW)
- Secondary, support operations of advanced aerodynamics and control technologies to reduce drag and reduce noise

Technical Description:

- Reliability based design (RBD) and certification – quantify and actively manage structural design conservatism minimize excess weight while increasing airplane structural reliability
- Structural Health Management (SHM) – know and manage the current state of the structures health throughout its life cycle
- Advanced design concepts – design optimized structures using new design tools, advanced materials, fabrication and maintenance concepts
- Multifunctional structures (MFS) – integrate system functionality into structures to reduce overall airplane weight and increase operational reliability through distributed redundancy
- Adaptive structures – highly distributed actuation and sensing will enable airplanes to conformally change shape during flight to optimize L/D across a broad range of flight conditions

Risk Assessment



Major Milestones:

- Define objective function forms for each of the selected technologies
- Develop a complete objective function form integrating all the selected technologies
- Perform multidisciplinary optimization that maximizes airplane level performance for one or more N+3 configurations

Dependency:

None

Success Criteria:

Task Number	Task Name	Success Criteria	Alternate Steps if Unsuccessful
1	RBD Analysis and Certification	Use of probabilistic design methods for balanced design conservatism	Use of probabilistic design methods for secondary structure
2	Structural Health Management	Broad area monitoring of structure	Loads monitoring and structural hot spot detection (minimal weight improvement)
3	Advanced Structural Design Concepts	New structural concepts enable reduced weight	Conventional design
4	Multifunctional Structures	Structure with highly integrated systems functionality	Limited integration of wiring and thermal paths
5	Adaptive Structures	Reduced weight and complexity of conformal control surfaces and high lift systems	Reduce weight and complexity of rigid control and high lift surfaces

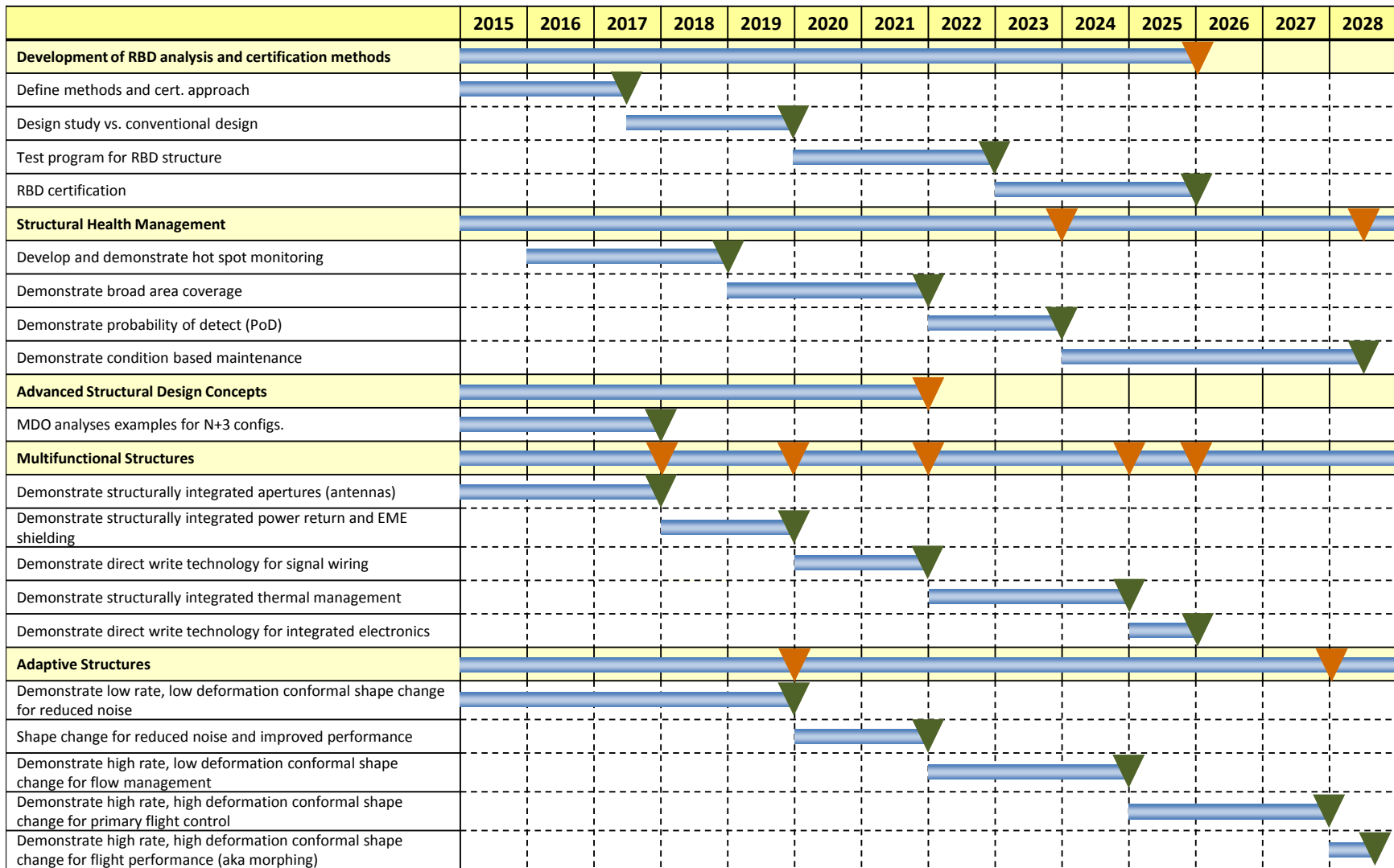


Figure 2.191 – Structural Concepts Technology Roadmap

2.4.8 Structural Materials

Goals and Objectives:

Implement advanced materials with greatly improved properties are needed to support the N+3 SUGAR configurations. Improved specific strength and specific stiffness are needed to enable very thin, very high aspect ratio wings.

Performance Area and Impact:

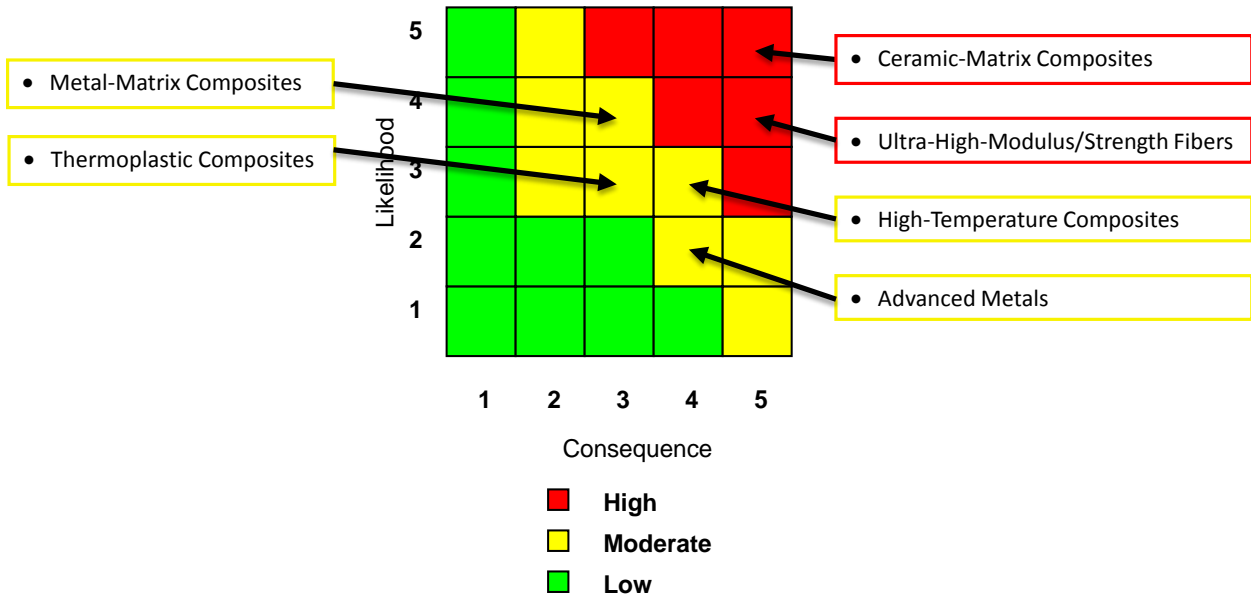
Primary, structural weight (OWE). Secondary, systems components weights (OEW)

Secondary, support operations of advanced aerodynamics and control technologies to reduce drag and reduce noise

Technical Description:

- Ultra-High-Modulus, Ultra-High-Strength Fibers – Carbon or other fibers that provide significant increase in specific strength or specific stiffness for improvement in both strength driven structure such as fuselage and lower wing surfaces, and stiffness driven structures such as wing upper surface. Thin wing loads, including dynamic loads such as gust and maneuver loads, and aeroelastic considerations will dictate to what extent improved strength is needed vs. improved stiffness
- Metal-Matrix Composites – titanium matrix composites to provide lower weight for very high strength applications such as landing gear
- Very Tough Composites – Resin systems with greatly reduced susceptibility to impact damage and reduced curing temperatures to support lower cost
- Thermoplastic Composites – thermoplastic resin systems support low cost manufacturing
- High-Temperature Polymer Composites – Composite matrix systems capable of sustained operation at temperatures above 350F for use near engine and exhaust
- Layer-by-Layer/Multifunctional nanocomposites for structures with integrated sensors and electronics to support structural health management and loads monitoring/active control
- Ceramics/CMC Durable ceramic and ceramic matrix composites for elevated temperature load bearing structure

Risk Assessment:



Major Milestones:

- Identify target applications/requirements for enhanced materials
- Identify new material chemistries for development
- Develop and refine processing methods
- Scale-up for manufacturing

Dependency:

None

Success Criteria:

Task Number	Task Name	Success Criteria	Alternate Steps if Unsuccessful
1	Ultra High Modulus Ultra High Strength Fibers	Very high aspect ratio wing designs not driven by sizing for aeroelasticity and gust/maneuver loads	Active control of aeroelastic response and loads alleviation
2	Metal Matrix Composites	Lightweight landing gear structures	Conventional materials, e.g., stainless steel
3	Very Tough Composites	Composite structure weight not driven by fracture toughness	Structural health management/prognosis to reduce fracture critical structural weight
4	Thermoplastic Composites	Sufficient strength for use in loaded secondary structures	Continued use of thermoset composites
5	High Temperature Polymer Composites	Use in engine nacelles	Titanium or high temperature aluminum depending on application
6	Layer-by Layer-Multifunctional Nanocomposites	Lightweight broad area sensing and distributed processing	Higher weight sensors and electronics
7	Ceramics/Ceramic Matrix Composites	Use in engines and nacelles	High temperature metals

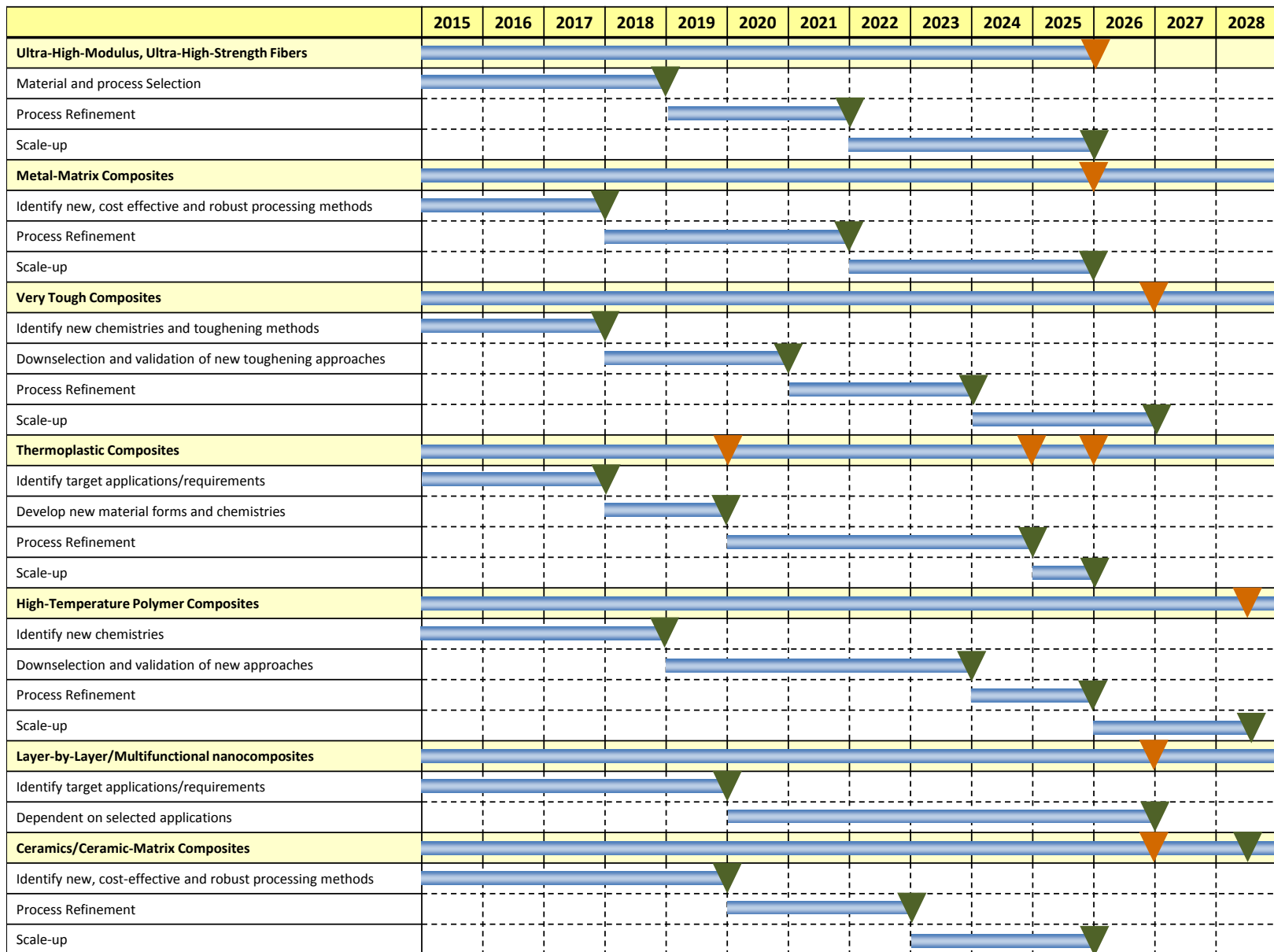


Figure 2.192 – Structural Materials Technology Roadmap

2.4.9 High Span TBW Technology Integration

Goals and Objectives:

Develop and integrate technologies required to enable a high speed truss-braced wing.

Performance Area and Impact:

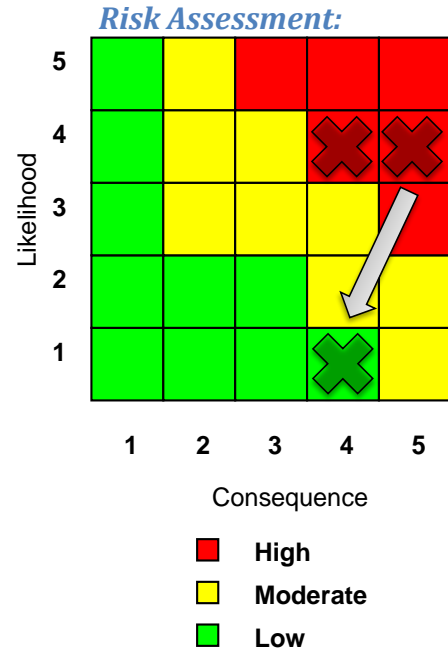
Enable integration of high span truss braced wing allowing very high aspect ratio wings for low induced drag and natural laminar flow

Technical Description:

- Ultra-High-Modulus, Ultra-High-Strength Fibers
- Low interference drag struts
- Low interference drag nacelles for a highly integrated configuration
- Active/Passive aeroelastic response for load control
- Advanced high cruise CL supercritical wing design
- Layer-by-Layer/Multifunctional nanocomposites
- Natural laminar flow wing design

Major Milestones:

- | | |
|---|------|
| • Ultra High Modulus fibers production ready | 2025 |
| • Integration of low interference drag struts on high span wing configurations. Improvement in interference drag is significant and results in significant system benefits. | 2020 |
| • Integration of low interference drag nacelles on high span wing configurations. Improvement in interference drag is significant and results in significant system benefits. | 2025 |
| • Integration of active/passive aeroelastic response for load control. Identify system benefits are significant. | 2025 |
| • Layer-by-Layer/Multifunctional nanocomposites production ready | 2027 |
| • Natural laminar flow wing design without HLFC systems to achieve a viable configuration. Roadmap will address passive/active systems to achieve Aerodynamic goals and results in significant system benefits. | 2020 |
| • Initial flight test verification (optional – could be replaced by focused ground demonstrations with some increase in integration risk) | 2019 |



- Flight test verification with additional technologies (laminar flow and advanced materials (optional – could be replaced by focused ground demonstrations with some increase in integration risk)

2024

Dependency:

Items are interdependent to achieve viable high aspect ratio truss-braced wing design.

Success Criteria:

Task Number	Task Name	Success Criteria	Alternate Steps if Unsuccessful
1	Natural Laminar Flow	NLF laminar design matches Active LFC	Achieve 50% of an Active LFC laminar Run
2	Low Interference Drag Struts	Integrate strut into wing-body for only strut parasite drag	Establish low interference levels
3	Advanced Supercritical Wing Design	Target 3% airplane drag improvement while attaining high design lift coefficient	Achieve 50% of target drag improvement
4	Low Interference Drag Nacelles	Integrate nacelle/pylon to wing body for only nacelle/pylon parasite drag	Establish low interference levels
5	Active/Passive Aeroelastic Load Control	Span load traded for Aerodynamics and structural efficiencies to improve overall mission performance	Achieve improvement for one discipline
6	Multifunctional Nanocomposites	Lightweight broad area sensing and distributed processing	Higher weight sensors and electronics
7	Ultra High Modulus and Strength Fibers	Very high aspect ratio wing designs not driven by sizing for aeroelasticity and gust/maneuver loads	Active control of aeroelastic response and loads alleviation
8	Vehicle Technology Integration	Integrated vehicle design with advanced technology suite	Integrated vehicle design with all achieved technology advancements
9	Flight Test Verification	Aero performance targets achieved. Structural analysis matches observed response.	Fix problems of design with lower performance
10	Pre-Certification Analysis and Testing	Verification that TBW can be designed to meet existing or modified certification criteria (Ditching, bird strike, crash loads, structural redundancy, etc.)	Additional design, testing, and discussion with FAA to discuss certification criteria. Possible weight penalties.

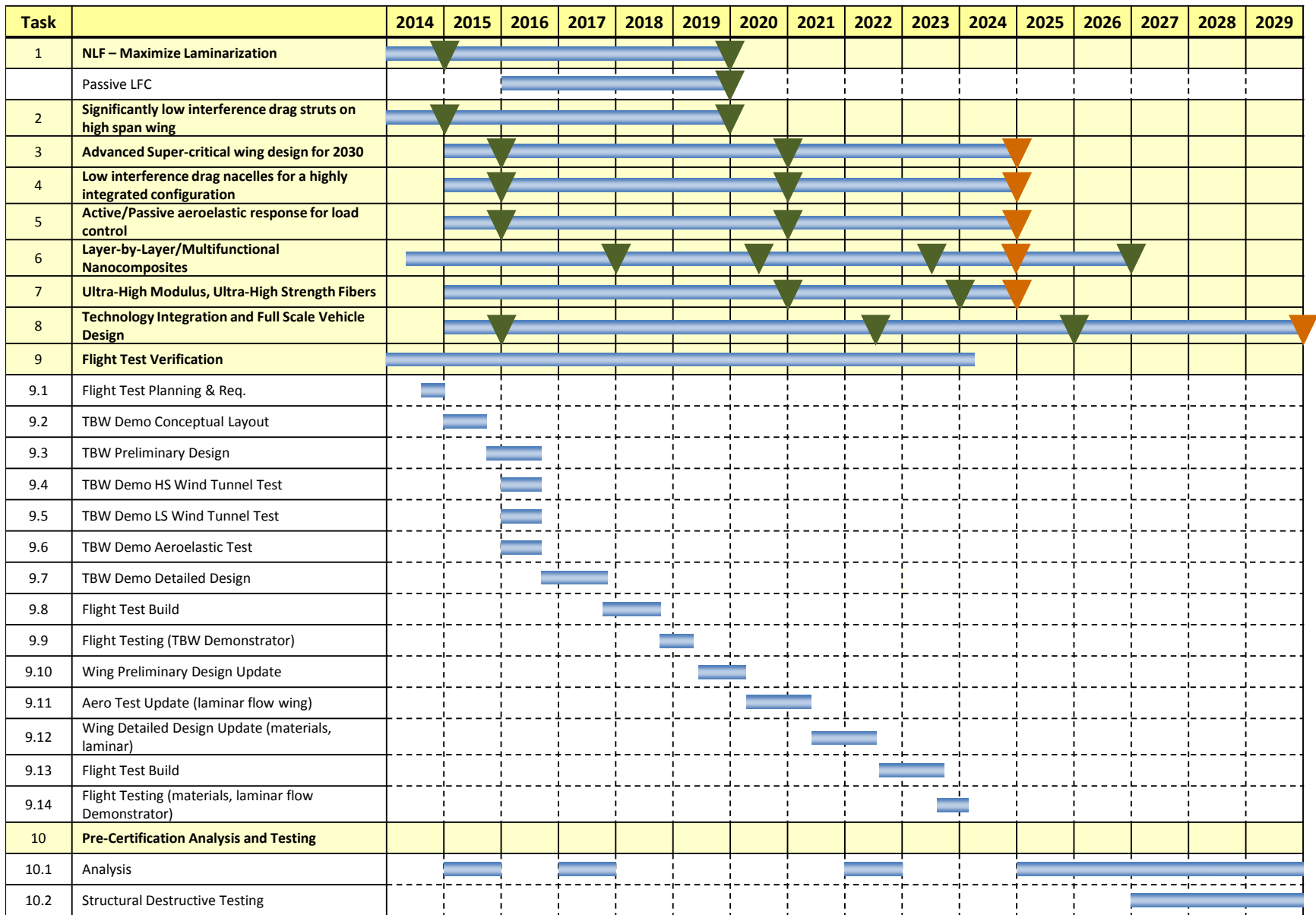


Figure 2.193 – High Span Truss Braced Wing Technology Integration Roadmap

3.0 Truss-Braced Wing Aeroelastic Experiment

This section provides an overview for the SUGAR TBW aeroelastic wind tunnel aeroelastic test (Task 3.1) which was tested in the NASA TDT from Dec 2013 through April 2014. Details of the test are documented in Volume III of this report. The basis for this test was the detailed FEM sizing/optimization performed in Task 2.1 (Section 2.0). This task produced a detailed FEM which met all strength, buckling, and flutter constraints. The results showed significant structural weight benefits of a truss-braced wing with minimal weight penalty to pass flutter.

The primary goal of the aeroelastic wind tunnel task was to validate the flutter results. The secondary goal was to investigate benefits of closed loop flutter suppression control laws. For assessing flutter suppression, the objective was to quantify the flutter speed increases and investigate control law effect on gust loads.

The Task 2.1 model chosen for the wind tunnel test is the configuration which has the strut attached at the front spar and sized with 1.09 V_d flutter constraints. The 1.09 V_d model is slightly softer than the full flutter margin 1.15 V_d model and therefore would facilitate the demonstration of aeroelastic instabilities in the tunnel. The V strut configuration which has a strut attached to the wing front spar and another strut attached to the rear spar showed the most structural weight benefit. This configuration wasn't chosen for the test due to concerns about drag and aerodynamic interference of the extra strut. Validating the flutter results for the front spar configuration should validate the flutter results on the V strut configuration since both analyses use the same methods.

The test was performed on a dynamically scaled half model in R134 heavy gas. Dynamically scaled components include the wing, strut, and jury strut. Nearly rigid components include the fuselage, flow through nacelle, and engine pylon. The model was fixed on the electronic turn table which allowed angle of attack to vary. The model was tested open loop and closed loop using a hydraulically actuated inboard and outboard control surface. The model was instrumented with 22 accelerometers, 10 strain gages and 2 RVDT's to measure control surface deflection. Testing was carried out between Mach =.6 to $M=.94$ for angles of attack from -3 to 5 degrees.

3.1 Dynamic Scale Factors and Requirements

The test was a dynamically scaled aeroelastic side mounted half span model tested in R134 heavy gas at the Transonic Dynamics Tunnel (TDT) 16-by-16 foot transonic wind tunnel located at the Langley Research Center in Hampton, Virginia.

When building a dynamic scaled wind tunnel model (WTM), several pieces of full scale aircraft information must be generated and transmitted to the model vendor. Those items are aircraft geometry, mass, stiffness and the scaling factors.

The model basic scale factors (length, density, and velocity) were selected to balance several considerations including TDT operating envelope, TDT test section size, and model manufacturability. All other scale factors are derived from the three basic scale factors. Scale factors for the test are shown in Table 3.1.

Table 3.1 – Scale Factors

Basic Scale Factors		Derived Scale Factors				
Length	Density	Mass	Accel	Force	Stiffness	Frequency
0.150	1.1000	0.003713	1.8103	0.006721	1.5122E-4	3.4740
Velocity		Linear	Rotational	Moment of Inertia	Time	Dyn. Press.
0.5211		0.04481	0.001008	8.3531e-5	0.2879	0.2987

	Weight (lb)	Span (ft)	Mach	Dyn. Press. (psf)	Density (s/cf)	Velocity (fps)	Re
Full Scale Half Span	29,530	85	0.8200	542.47	0.001451	864.6	4.35E7
Model Scale Half Span	109.6	12.75	0.8200	162.03	0.001597	450.5	5.07E6

The detailed structural finite element model (FEM) was used as the starting point for the SUGAR wind tunnel model. The FEM was developed for calculating structural loads and performing structural design, and is based on the Outer Mold Lines (OMLs) defined by the aerodynamics group. The target (baseline) equivalent beam stiffnesses were calculated to match the stiffness distributions of the detailed FEM model. Equivalent beam full scale wing, strut and jury stiffness for scaling are shown in Figure 3.1 through Figure 3.3. The figures also show the elastic axis location of the equivalent beams.

The mass of the wing is broken up into 19 sections as shown in Figure 3.4. The inboard control surface was broken up into 4 sections and the outboard control surface has 6 sections. The weight, C.G. and inertia for each section matching the full fuel mass case are listed in Table 3.2. In order to meet the stiffness requirements for the strut & jury strut, the target scaled weight could not be met. So, an estimate of the model beam’s weights (strut & jury strut) was scaled to full size thus requiring about 1,490 pounds to be added to the detailed FEM. The additional strut and jury strut mass was shown to have negligible impact on flutter results.

The goal of the analysis was to make a beam-rod FEM to become the “as built” analytical model of the WTM. This analytical model would be used in all aspects of aeroelastic analyses to verify

that the model was safe to operate in the wind tunnel. The first step in achieving this goal was to create a full scale beam-rod FEM using the mass and stiffness that was presented in the previous section. A comparison of the full scale Detailed FEM and the Beam-Rod FEM is shown Figure 3.5. Flutter results of these two full scale FEMs are shown in Figure 3.6; the Beam-Rod results match the Detailed FEM very well.

The second step toward achieving an “as built” analytical model, was accomplished by applying the scaling factors to the full scale model thus “shrinking it” to the same size as the WTM. Coordinating with the model vendor to determine what changes were achievable and match what was manufactured was critical. The “as built” FEM was updated as the design matured. Analysis was conducted throughout the model construction time period and updates to the “as built” FEM were being made.

The SUGAR WTM was attached to the Oscillating Turntable (OTT) mount residing on the east wall of the TDT test section. A beam-rod FEM of the OTT was provided by NASA so it could be incorporated into the analysis. Wind tunnel boundary conditions have been studied to try and keep similitude with the free flying vehicle symmetric flutter mechanism. A comparison of flutter results for the free-free detailed FEM and half model of the detailed FEM with the wind tunnel boundary conditions are shown in Figure 3.7. Flutter speeds have changed but the flutter mechanism is still a combination of the same primary modes. Also, as shown in Figure 3.8, the wind tunnel boundary conditions cause a small change in primary mode shapes but the modes are similar to the free-free modes. The z deflection for the plots is the average front and rear spar deflection. The torsional slope is the difference between the z deflection at the front spar and rear spar divided by the x distance between the spars. Since we have good similitude with the fixed boundary conditions we were able to simplify the test versus a free flying model or a pitch and plunge free arrangement.

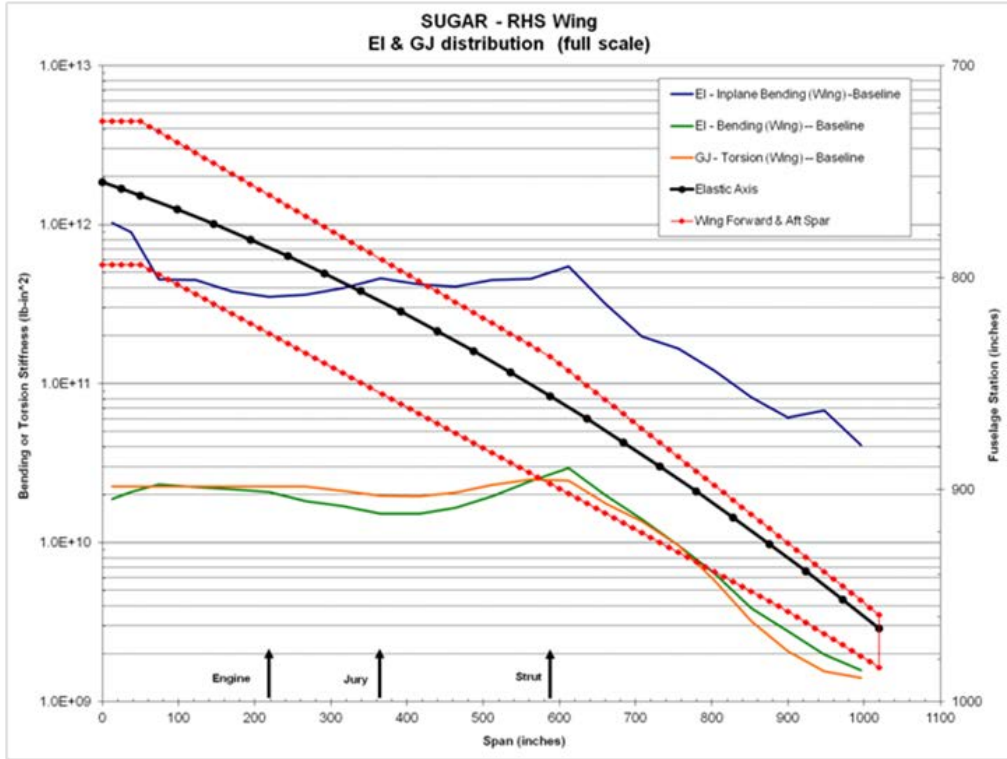


Figure 3.1 – Full Scale Wing Stiffness

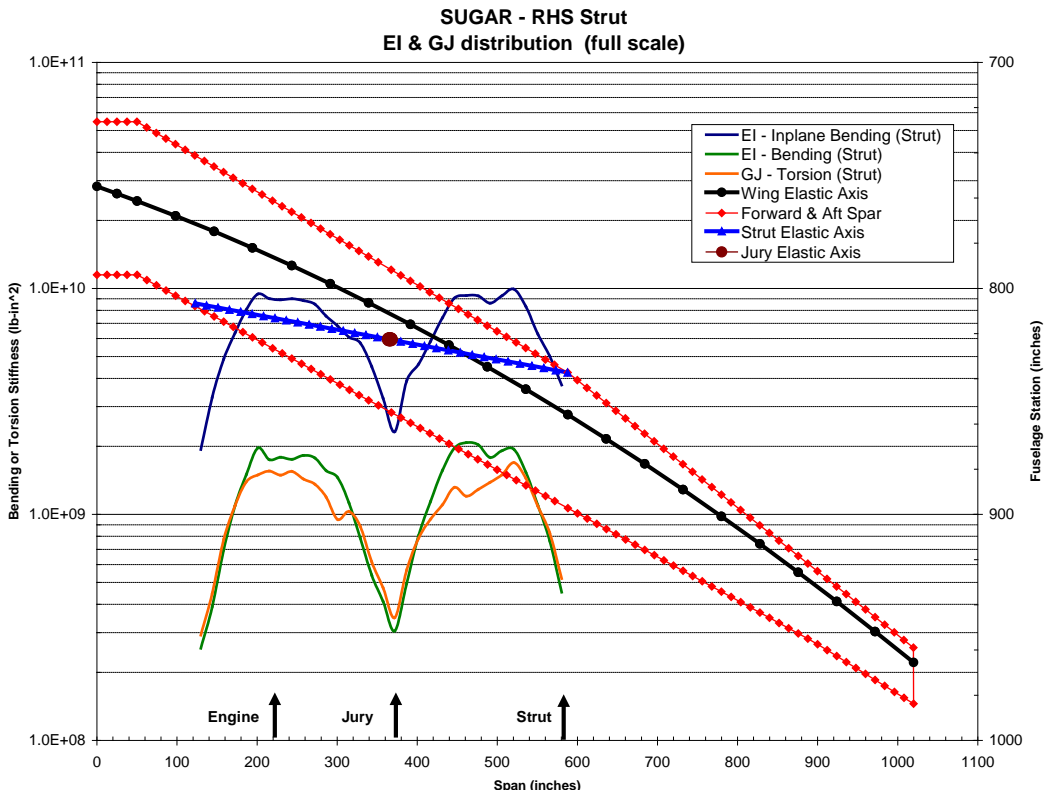


Figure 3.2 – Strut Full Scale Stiffness

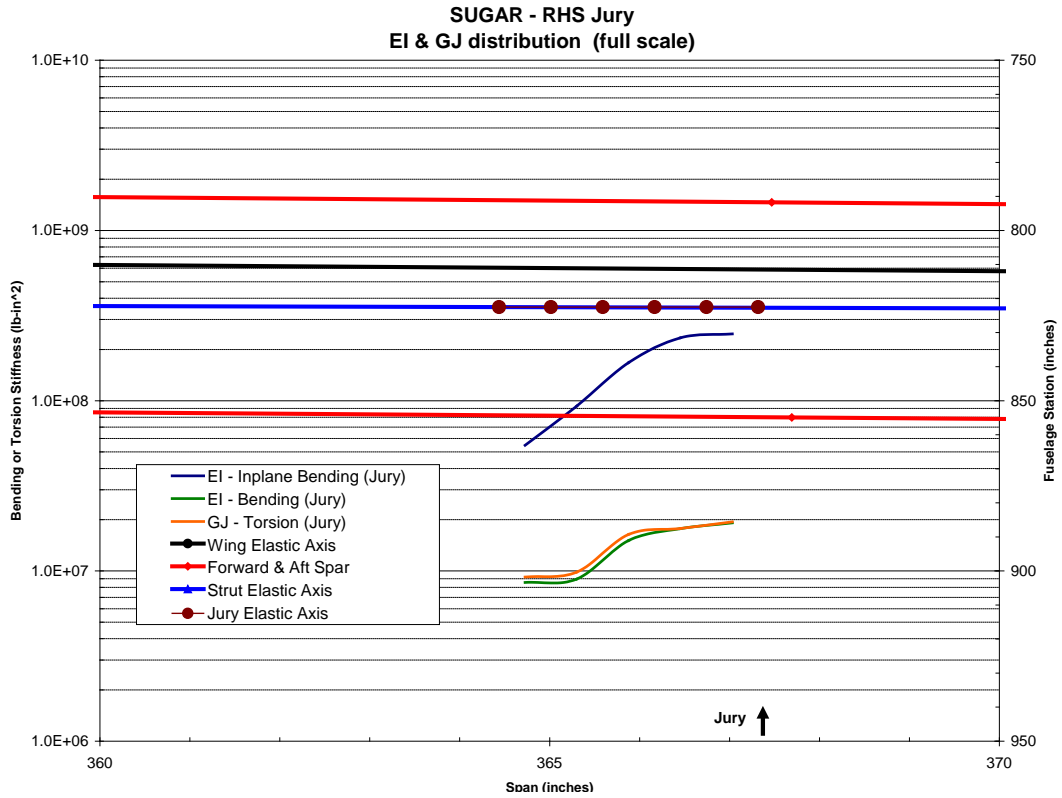


Figure 3.3 – Full Scale Jury Full Scale Stiffness

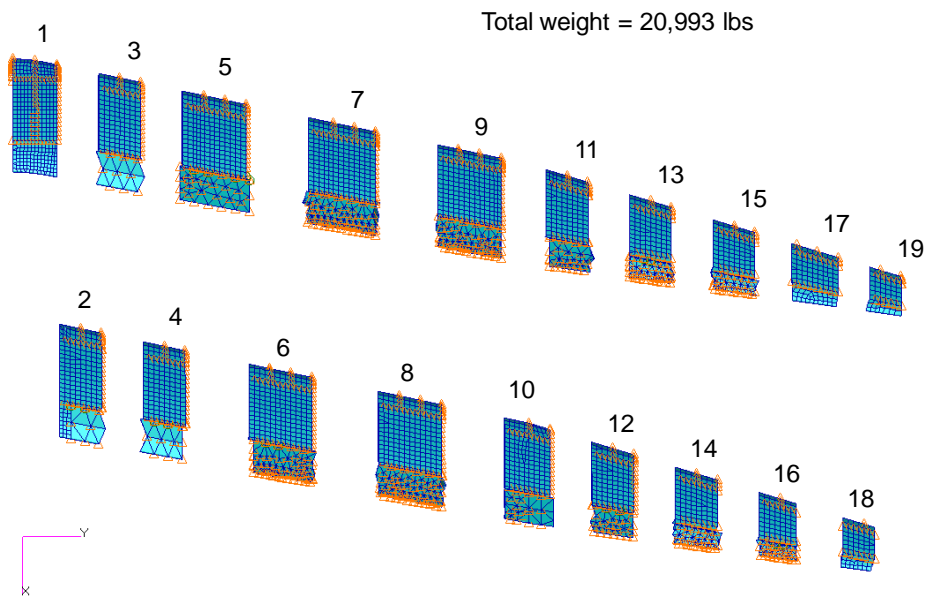


Figure 3.4 – Wing Mass Section Breakdown

Table 3.2 – Wing Full Scale Mass Distribution

DESCRIPTION	WT (LBS)	F.S. (X)	B.L. (Y)	W.L. (Z)	IROLL (IX)	IPITCH (IY)	IYAW (IZ)
----- Section 1	1732.10	761.52	33.56	302.61	414592	1237980	1558053
----- Section 2	1455.30	770.92	82.91	298.90	297412	992694	1236341
----- Section 3	1426.50	779.76	131.27	297.44	281779	943257	1174338
----- Section 4	1431.00	789.31	179.31	296.18	284031	940680	1172434
----- Section 5	2157.80	801.35	239.68	294.54	1005435	1421339	2346573
----- Section 6	2072.90	815.35	312.71	292.53	892266	1335313	2152403
----- Section 7	2078.20	830.71	387.65	290.82	938457	1343348	2199588
----- Section 8	1985.50	846.16	460.80	289.15	866233	1295008	2078732
----- Section 9	2043.40	860.42	532.84	287.36	919577	1319290	2148786
----- Section 10	1450.60	868.95	595.91	285.52	313832	799207	1049634
----- Section 11	357.00	887.68	637.46	289.40	80032	318255	380653
----- Section 12	1337.10	896.36	702.13	286.97	223995	529852	698115
----- Section 13	320.40	911.57	732.77	286.78	69726	213793	272707
----- Section 14	260.10	919.84	781.15	285.18	55006	156995	204410
----- Section 15	227.50	931.13	828.50	283.81	48032	117981	160751
----- Section 16	187.20	943.69	873.47	282.48	28565	82872	108022
----- Section 17	200.90	947.87	921.66	280.79	54768	58943	110049
----- Section 18	119.50	959.00	967.01	279.58	13811	27294	39380
----- Section 19	150.00	966.98	1004.00	278.48	19709	25854	43664
TOTAL	20993.00	829.44	374.86	292.06	6807258	13159955	19134633

MOMENTS OF INERTIA (ABOUT C.G.)

IROLL=	1163441478	LB*IN ² OR	251118	SLUG*FT ²
IPITCH=	63431253	LB*IN ² OR	13691	SLUG*FT ²
IYAW=	1224779989	LB*IN ² OR	264357	SLUG*FT ²

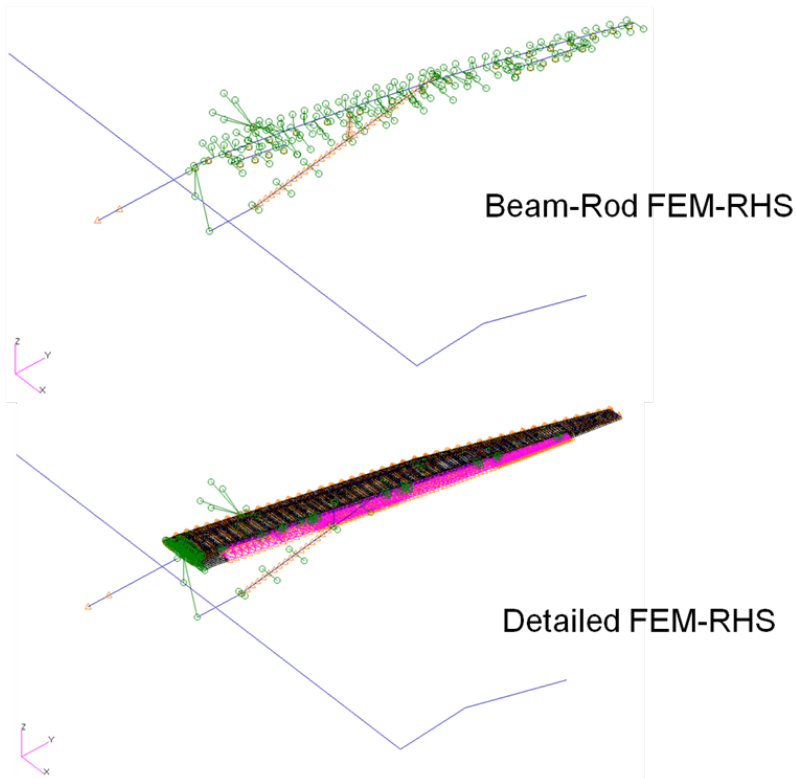


Figure 3.5 – Full Scale Beam Rod and Detailed FEMS

Sol 145 Results Comparison: Beam-Rod and Detailed FEM - Mach=0.82

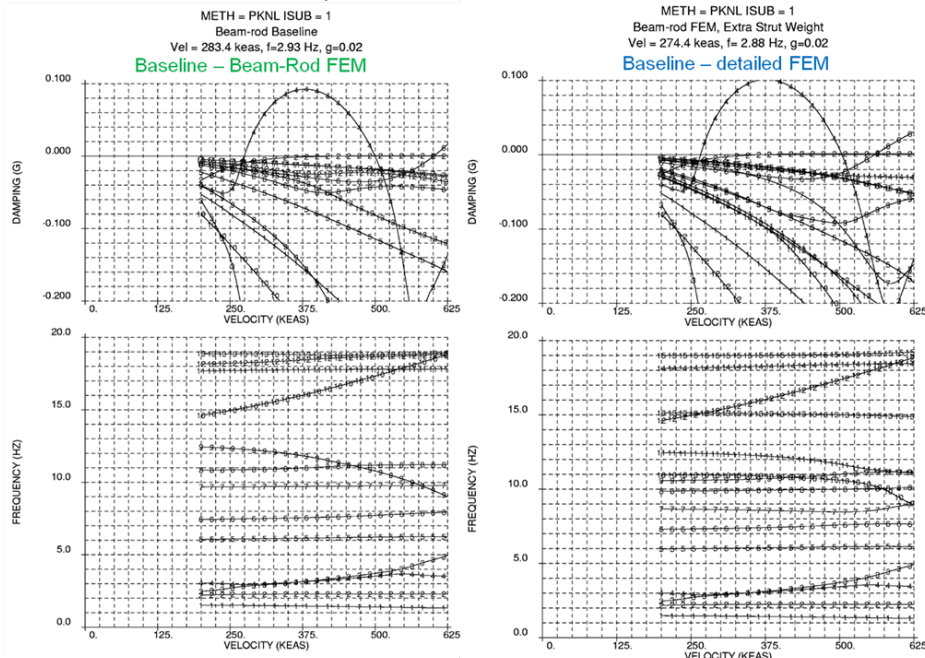


Figure 3.6 – Flutter Result Comparison of Full Scale Detailed FEM to Beam Rod FEM

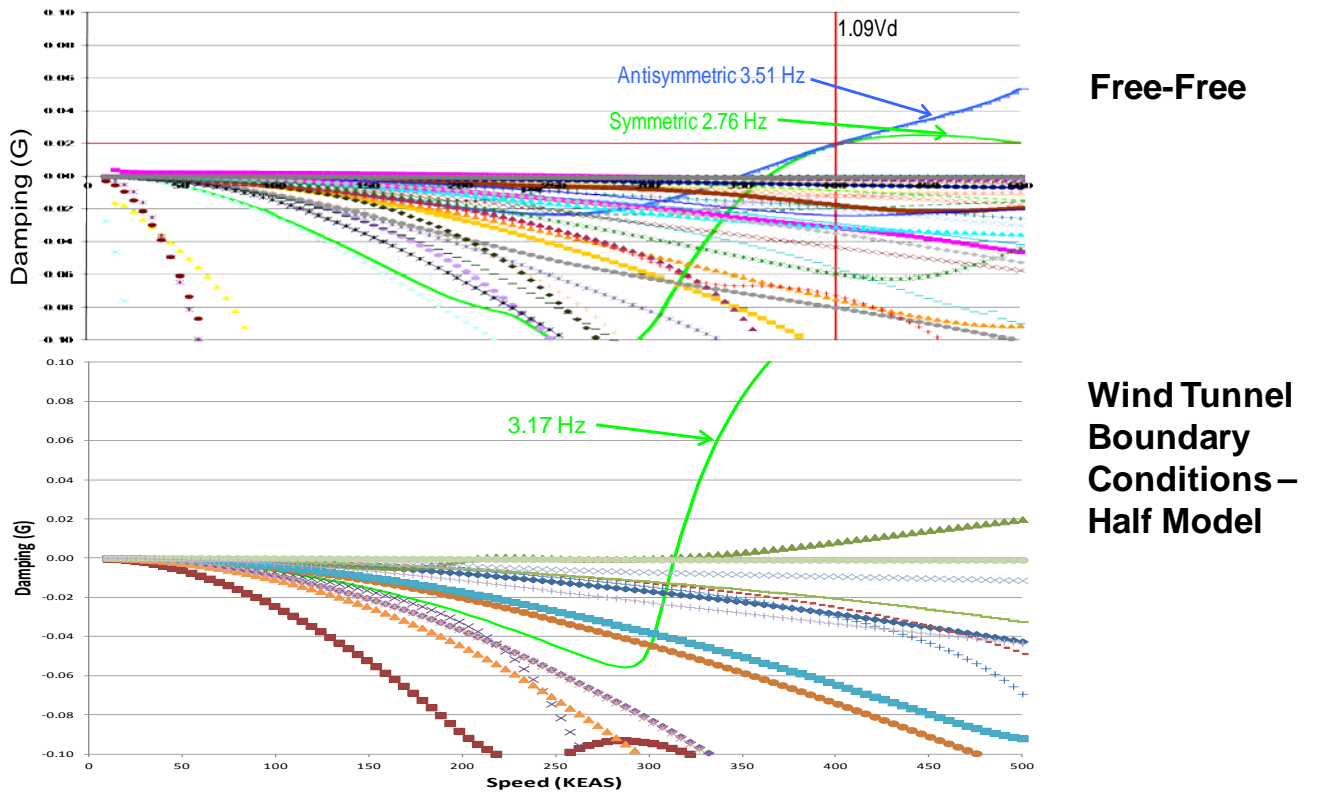


Figure 3.7 – Boundary Condition Study Flutter Comparison

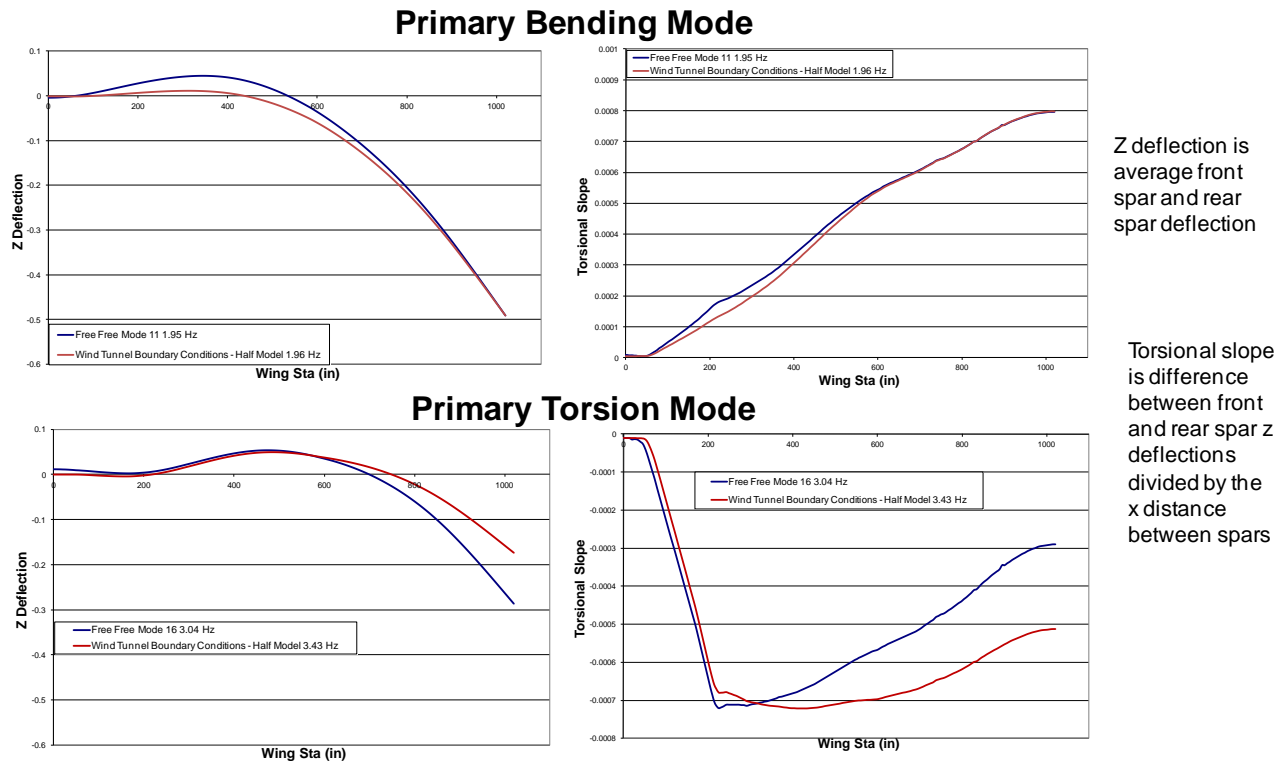


Figure 3.8 – Boundary Condition Study Mode Shapes

3.1.1 Full Scale vs. Test Scale Configuration Differences

This section describes configuration differences between the full scale analysis model and the test model. First, as shown in Figure 3.9 tunnel integration concerns required a fuselage length reduction from 18.7 ft to 13.4 ft. This change had no appreciable effect on the flutter results. The engine/nacelle position was moved 12.5 inches aft and 5 inches down during the full scale vehicle development. The tested position is a more realistic position for the engine/pylon. This difference did change the flutter solution but didn't change the primary flutter mechanism. Finally, as the test analysis model was updated to the as built mass distribution the unstable flutter damping decreased to the point where it might not be larger than the inherent structural damping. Therefore, as shown in Figure 3.10, six ballast weights of just under 3 pounds were added to aft section of the main spar. The ballast weights brought the flutter damping back to an acceptable level. The ballast weight for each station is tabulated in Table 3.3.

Table 3.3 – Model Ballast Weights

Location	Flutter mass design 9/17				Local inertia terms		
	Weight	Xcg	Ycg	Zcg	Ixx	Iyy	Izz
	lbs	in	in	in	lbs-in ²	lbs-in ²	lbs-in ²
1	2.92	123.22	40.77	45.06	1.80	4.10	5.50
2	2.92	124.35	46.61	44.91	1.81	4.10	5.50
3	2.92	126.56	58.89	44.58	1.80	4.10	5.50
4	2.92	127.75	67.60	44.44	1.75	4.15	5.50
5	2.92	129.66	77.32	44.20	1.81	4.10	5.50
6	2.92	132.95	91.17	43.63	2.01	4.09	5.50

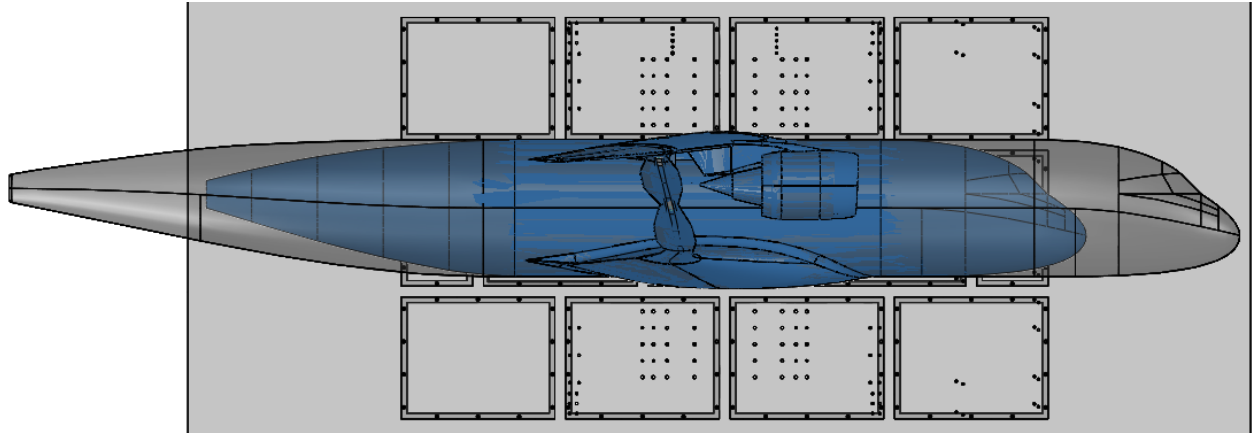


Figure 3.9 – Fuselage Length Reduction

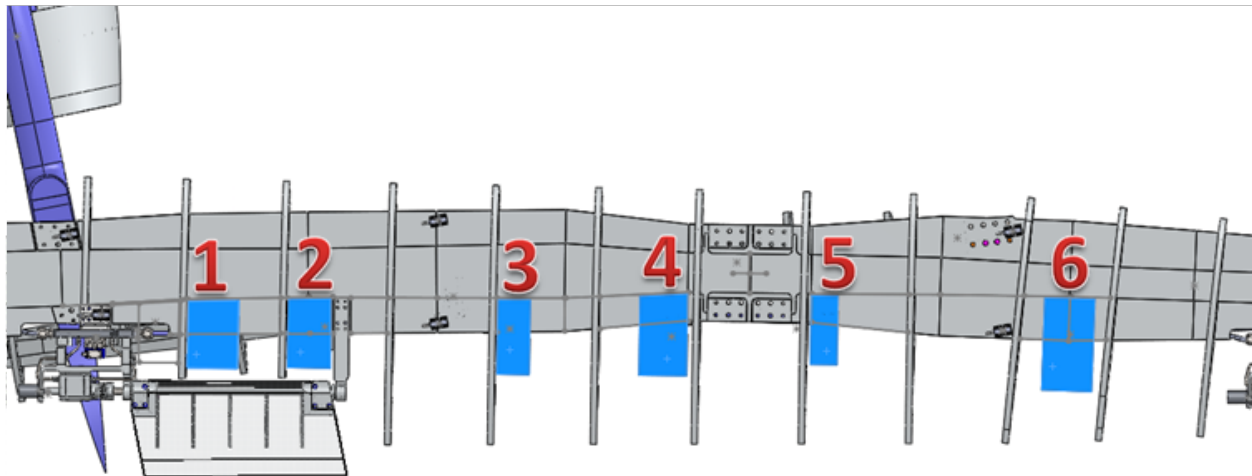
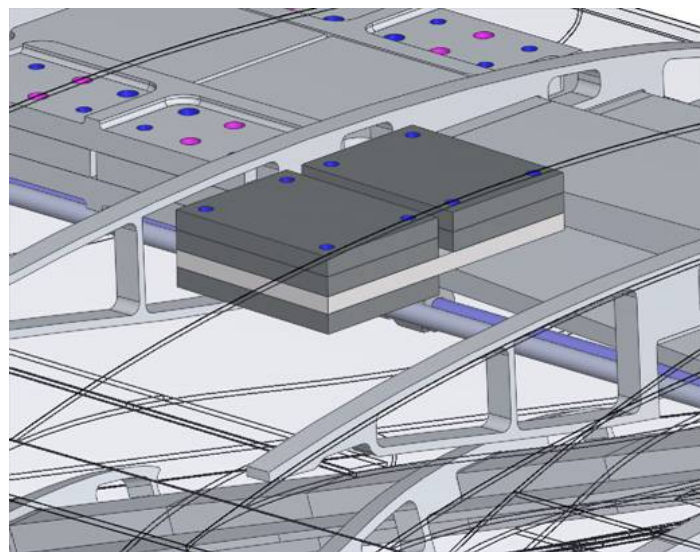


Figure 3.10 – Flutter Ballast Weights

3.2 Model Design and Analysis

The main features of the model are shown in Figure 3.11. The model features the cruciform wing and strut beam, H section jury beam, rigid fuselage, flow through nacelle, and 2 actively

controlled trailing edge surfaces. The model uses a classical flutter model construction approach, where a single internal beam represents the entire stiffness composition of a wing or strut member, and segmented skins are used for an aerodynamic fairing that does not contribute additional stiffness. The process used to develop equivalent beam cross sections to meet the stiffness requirements is shown in Figure 3.12. The large span wing couldn't be machined as a single piece, so there are two wing beams with a joint in the middle. Stiffness requirements were met for the wing, strut, and jury. Mass requirements were met for the wing. Based on classic flutter model construction, model strut and jury mass estimates exceed scaled requirements. However, the extra mass was shown to be inconsequential to flutter results and acceptable for test.

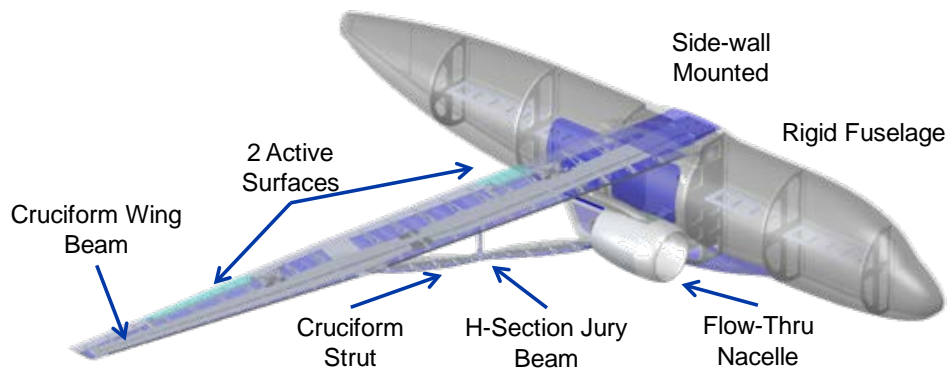
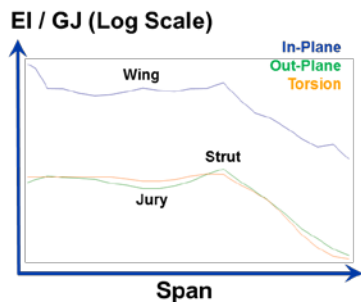


Figure 3.11 – Wind Tunnel Model Overview

Scaled Stiffness Targets → Section Solver → Initial CAD Layout



Y-location [in]	out-plane EI11	in-plane EI22	torque GJ
1.875	2.86E+06	1.55E+08	3.40E+06
5.636	3.15E+06	1.35E+08	3.40E+06
11.134	3.51E+06	6.83E+07	3.40E+06
18.344	3.38E+06	6.76E+07	3.40E+06
25.541	3.28E+06	5.75E+07	3.40E+06
32.823	3.16E+06	5.30E+07	3.40E+06

Boeing SUGAR - Cruciform Cross-Section Solver				
	Center Block		Side Blocks	
Variables [in]	2A	2B	2a	2b
	0.817	0.382	0.214	0.101
Current Section Properties	Yna [in]	lopX [in^4]	lipz [in^4]	J [in^4]
	NA	0.0038	0.029	0.0114
Target Section Properties	Yna [in]	lopX [in^4]	lipz [in^4]	J [in^4]
	NA	0.0039	0.0293	0.0115
Section Property Error	Total [in]	lopX [in^4]	lipz [in^4]	J [in^4]
	-9.7619E-08	-0.00004	-0.00029	-0.000115
Error %	-3.0	-1.00	-1.00	-1.00
Solver Constraints				
Description	Variable	V > Than	V < Than	
Total Height [in]	Htot	0.375	0.825	
Total Width [in]	Wtot	0.500	9.000	
Side Block Width [in]	Wsb	0.125	6.000	
Side Block Thickness [in]	Tsb	0.100	0.101	
Out-plane error [%]	lopX	0.99	1.01	
In-plane error [%]	lipz	0.99	1.01	
Torsional error [%]	J	0.99	1.01	

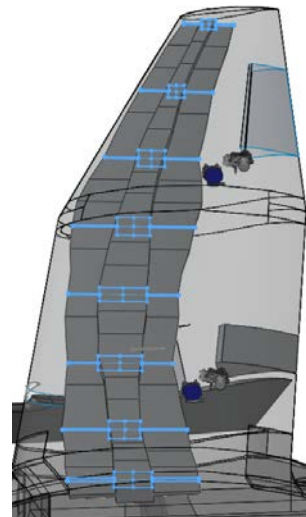


Figure 3.12 – Equivalent Beam Design

Actuator system design (Figure 3.13) was based on a successful system used for a number of actively controlled flutter models, including the Boeing joined-wing sensorcraft free-flying model,

and consisted of a high flow Moog servovalve, a custom designed hydraulic actuator, a coupler, and a RDVT sensor. Large hinge moment and high bandwidth requirements for flutter suppression were challenges for the control system design. The coupler wasn't able to fit within the OML so a small cutout in the skin was made for its accommodation.

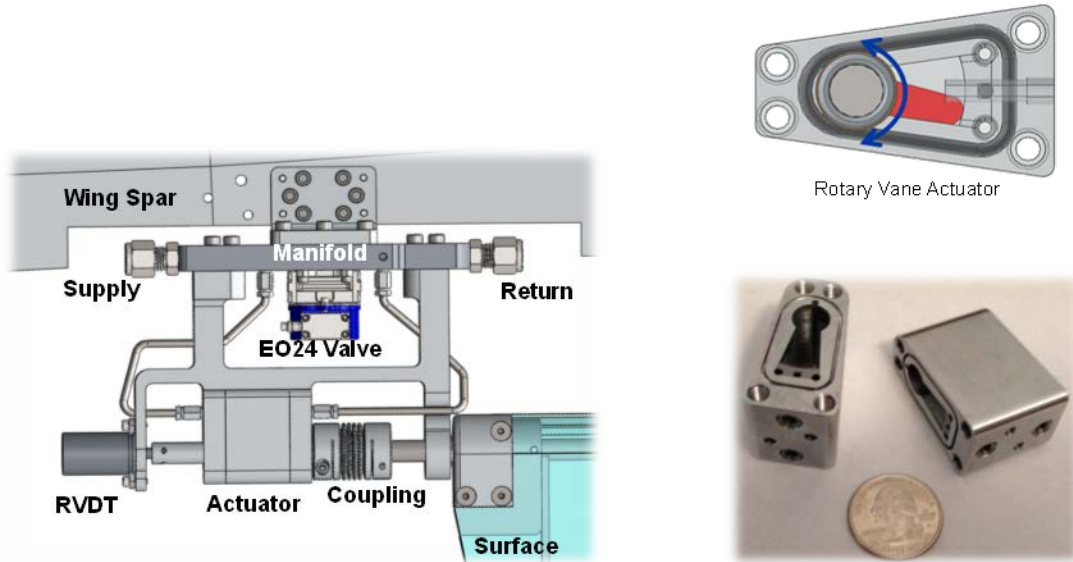


Figure 3.13 – Control System Design

The mounting structure attaches to the electronic turn table and wing spar and strut as shown in Figure 3.14. A summary of the model instrumentation which included 22 accelerometers, 10 strain gages, and 2 RVDT's is shown in Figure 3.15. The model was designed to have the NASA model systems criteria required safety margin for the five design conditions shown in Figure 3.16.

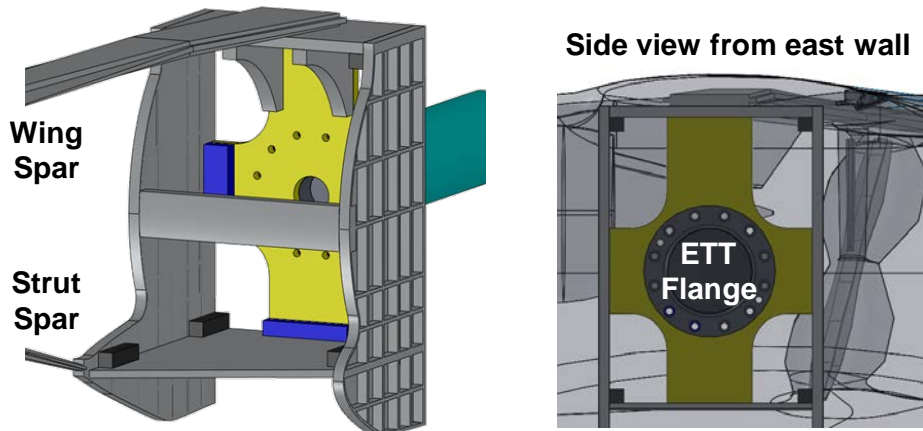


Figure 3.14 – Wind Tunnel Model Mounting Structure

Validation testing included actuator characterization, coupling strength strain gage calibration, mass properties verification, and GVTs. Actuator characterization involved recording the control surface position as it was commanded to sweep through a range of frequencies. Results showed actuator performance was adequate for flutter suppression control laws. A test was completed to determine hinge moment capability of the coupler, as spatial constraints forced the selection of an undersized component. The coupler hinge moment capability is lower than the actuator and close to some conservatively derived maximum hinge moment requirements. Strain gages were calibrated by recording values with a known applied load, and correlation with the finite element analysis result of each test case. The same loads were applied at a few times during testing to make sure individual strains remained consistent. The model was weighed to make sure it matched the analysis model. GVTs were conducted in the model prep area, and in the tunnel with and without skin tape. There were also multiple GVTs over the course of the test to verify that the model behavior was consistent. A comparison of the GVT results to the analysis model is documented in Section 3.6.

3.3 Dynamic Aeroelastic State Space Model

The current process for state space model construction takes the analysis modes and unsteady doublet lattice aerodynamics and generates a dynamic aeroelastic which is used to develop control laws. Unsteady aerodynamics is represented by a P-transform method in the time domain requiring no additional aero states. Multiple models were generated as the analysis FEM matured. Final models were based on FEM19 which was used to generate the tested control laws. Models included 40 states for 20 flexible modes up to 100 Hz. Models contain outputs at all accelerometer locations consisting of displacement, rate, and acceleration in all three coordinate directions and rotational displacement and rate about all three coordinate directions. Models contain inputs consisting of the inboard and outboard wing trailing edge control surface deflection, rate, and acceleration to accommodate coupling actuator dynamics. Final FEM19 models include 13 dynamic pressures at Mach = 0.75 and two dynamic pressures at Mach = 0.6, 0.65, and 0.7

3.4 Control Law Design

The following sections document the development of the control laws for the TBW TDT wind tunnel test.

3.4.1 Overview

Two separate control law designs were developed and tested closed-loop at the TDT. The first design was developed for a pair of System Identification (SysID) models of the TBW model. The SysID models were derived from control surface sweeps performed in open-loop testing. The second control law was designed for the FEM19 State Space Model (SSM) dynamics. Both control law designs were based on Linear Quadratic Regulator (LQR) design techniques with a Kalman

Filter state estimator. Both sets of control laws are actually comprised of several point designs (2 SysID models and 18 SSMs) and employ a “nearest neighbor” algorithm based on Mach and dynamic pressure (Q) to perform “gain scheduling”. Figure 3.17 shows where the various models (SysID and SSMs) were defined in relation to the pre-holiday flutter boundaries. Both designs proved to be robust to variations in Mach, Q, and angle of attack (AOA).

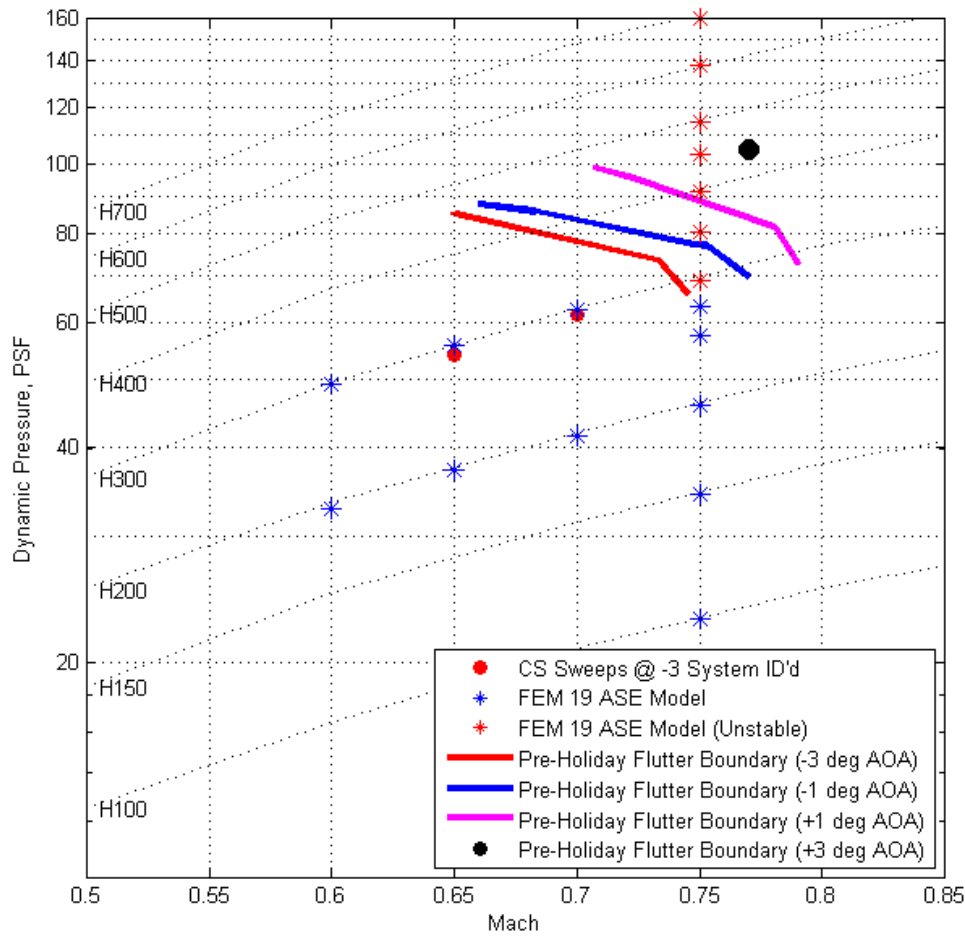


Figure 3.17 – Model Definition Points

3.4.2 System Identification Model Development

The SysID methods employed to derive the two models were based on methods developed previously for the Aerodynamic Efficiency Improvement program. The SysID method uses an optimizer to tune the simulation model to match the test data collected in the control surface sweeps. The derived models were based on open-loop control surface sweeps at Mach 0.65, Q 53.9 psf (TDT Run 10, Tab Points 529 and 530) and Mach 0.7, Q 61.6 psf (Run 10, Tab Points 551 and 552). All of the sweeps were performed at an AOA of -3°. The FEM19 SSMs were used as a

starting point in the process. The up side to the SysID modeling is that if the process converges to a solution, you have a high degree of confidence in the model. The down sides to this approach to model generation are the necessity for open-loop control surface sweeps and the large amount of memory and processor capacity required. Each of these models took over a day to generate, even given the fairly accurate starting point. The original plan for the TDT tests was to forgo the SysID step in order to save time and just use the FEM models for designing the controller. The variation in the TBW model's GVT data from pre-holiday to post-holiday provided both more time to develop the SysID models and the desire to make sure more wind tunnel time wasn't lost tuning the controller once testing began.

A comparison of the SysID model's mode frequencies and damping is shown in Table 3.4. Figure 3.18 shows a comparison of the Mach 0.65 SysID model to its FEM19 SSM counterpart for the inboard control surface to the outboard wing tip (forward) accelerometer (Z axis). In general, the SysID and FEM19 models agree fairly well, but the FEM19 models tend to be more attenuated in the 5 to 10 Hz range.

Table 3.4 – SysID to FEM19 Model Comparison - Frequency & Damping

Mach 0.65			
SysID Freq (Hz)	FEM19 Freq (Hz)	SysID Damping	FEM19 Damping
5.67	6.03	0.0082	0.0081
6.24	6.02	0.0724	0.0773
9.78	9.98	0.0189	0.0207
11.03	10.91	0.0219	0.0277
19.56	18.74	0.0252	0.0205
25.79	25.67	0.0682	0.0105
28.04	27.77	0.0010	0.0117
28.33	28.37	0.0102	0.0267
29.36	28.87	0.0023	0.0122
38.62	38.62	0.0090	0.0090
40.21	40.21	0.0231	0.0231
46.92	46.92	0.0106	0.0106
48.09	48.09	0.0231	0.0231
61.52	61.52	0.0064	0.0064
68.32	68.32	0.0082	0.0082
76.34	76.34	0.0088	0.0088
82.76	82.76	0.0158	0.0158
87.47	87.47	0.0083	0.0083
93.16	93.16	0.0068	0.0068
95.11	95.11	0.0079	0.0079

Mach 0.70			
SysID Freq (Hz)	FEM19 Freq (Hz)	SysID Damping	FEM19 Damping
5.70	6.03	0.0063	0.0066
6.35	6.14	0.0717	0.0806
9.99	10.20	0.0122	0.0106
10.93	10.78	0.0392	0.0397
19.59	18.78	0.0238	0.0214
26.73	25.63	0.0124	0.0119
28.22	27.78	0.0011	0.0121
28.60	28.39	0.0227	0.0286
29.38	28.84	0.0017	0.0134
38.64	38.64	0.0092	0.0092
40.21	40.21	0.0257	0.0257
46.94	46.94	0.0109	0.0109
48.05	48.05	0.0263	0.0263
61.52	61.52	0.0066	0.0066
68.32	68.32	0.0085	0.0085
76.35	76.35	0.0094	0.0094
82.80	82.80	0.0174	0.0174
87.48	87.48	0.0086	0.0086
93.16	93.16	0.0071	0.0071
95.12	95.12	0.0082	0.0082

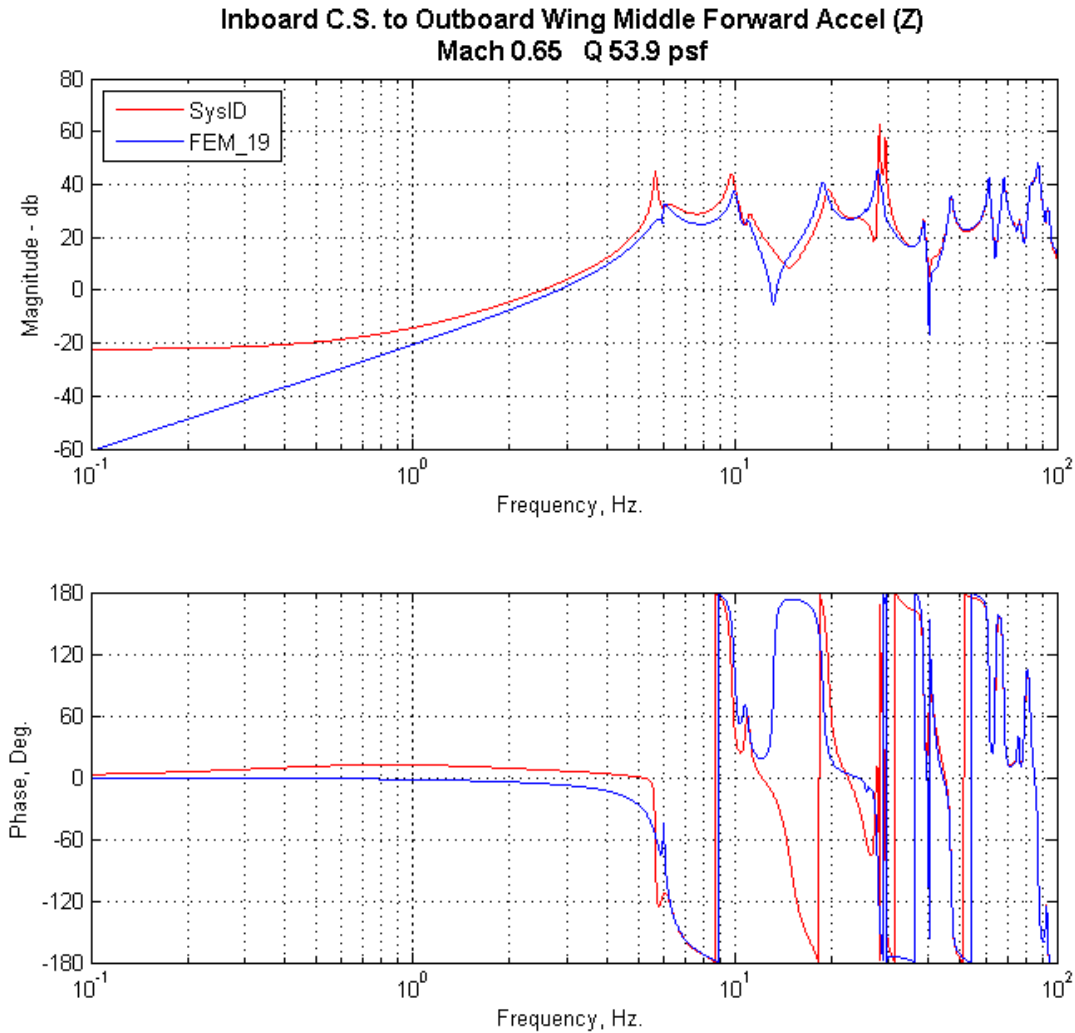


Figure 3.18 – Bode Plot Comparison of SysID Model to FEM19 SSM

3.4.3 SysID Simulation

The SysID version of the Simulink simulation is shown in Figure 3.19. From the beginning, the simulation architecture designed so that inserting the controller in the TDT’s dSpace control system would be as easy as possible. For the sake of clarity, the controller interfaces depicted in the figures have been simplified to just their core components. The actuator block (shown in orange) contains the model of the actuators. The outputs of the actuator are the inputs to the plant (control surface positions, velocities, and accelerations) and the sensed position of the control surfaces (the RVDT signals). The actuator model is followed by the plant (in state space form), the outputs of which (Y) are the accelerometer readings. The primary inputs to the SysID controller are the accelerometer readings (filtered through the dSpace system) and the RVDT signals. The current tunnel Mach and Q are input for nearest neighbor gain scheduling.

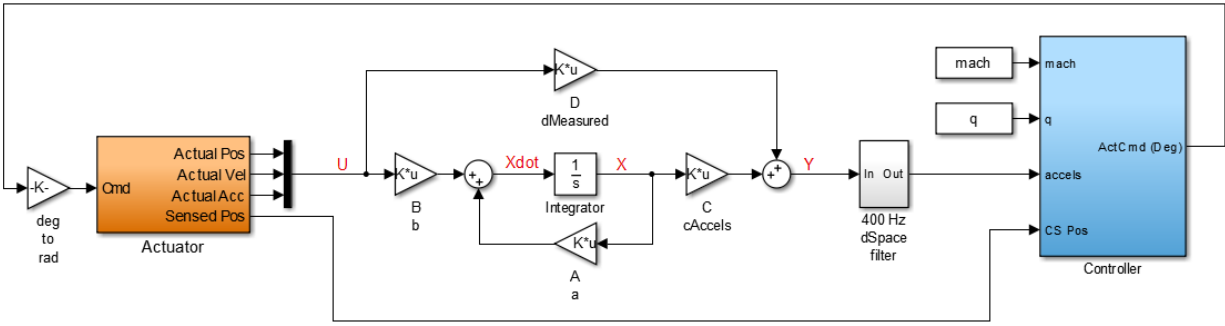


Figure 3.19 – SysID Simulation

3.4.4 SysID Control Law Design

Figure 3.20 shows the controller design for the SysID system, again slightly simplified. A nearest neighbor algorithm is used to determine which set of gains / state space model to use this pass through the controller. There is some hysteresis built into the algorithm to prevent bouncing between the point designs when the tunnel is near a boundary condition. All of the gains, etc., are predetermined to minimize computational overhead and make the controller block as fast as possible. Tests showed the controller needed to be run at 500 Hz minimum, but the dSpace system was able to run at 1,000 Hz for the tests.

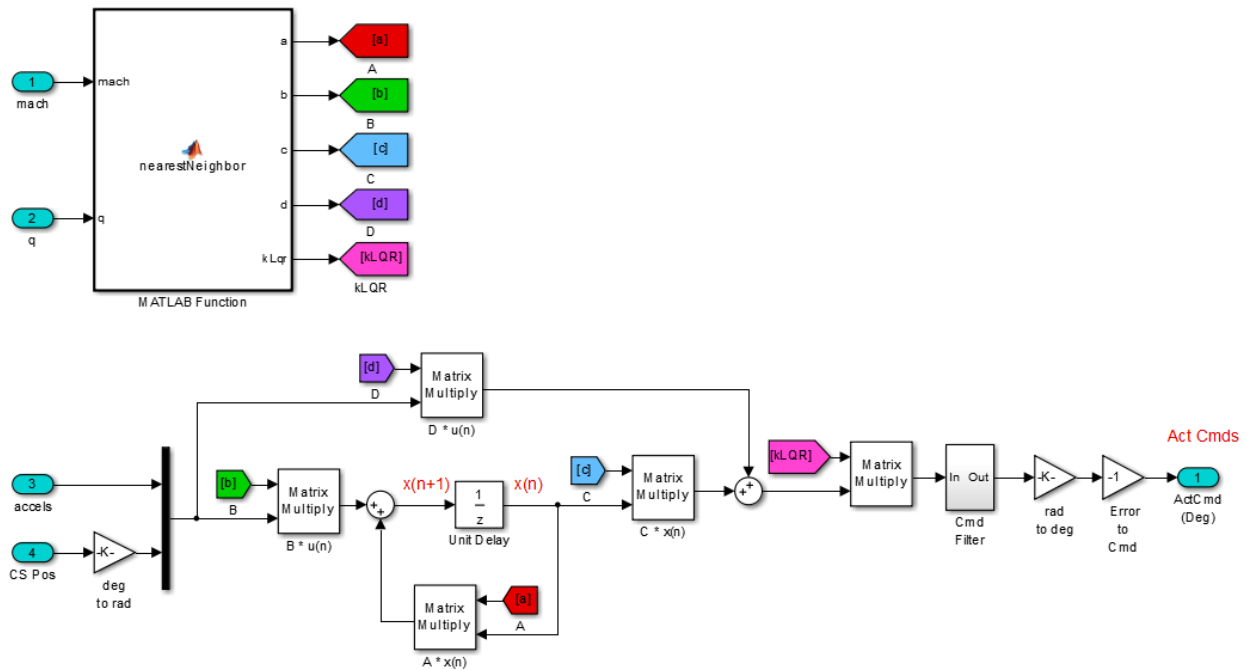


Figure 3.20 – SysID Controller

The sensed control surface positions and filtered accelerometer outputs are combined and fed through a Kalman filter state space estimator to calculate the estimator outputs (\hat{x}). The

resulting outputs from the estimator (\hat{X}) are multiplied by the LQR gains. A “Cmd Filter” is then applied to obtain the two control surface commands for output to the actuators.

The estimator coefficients are derived by first designing the full order estimator gains. The gains are then applied to the SysID model to form a state space model. The state space model is reduced to 10 states (“balanced” reduction) and discretized at the dSpace frequency, 1000 Hz, with “tustin” pre-warping.

The LQR gains are derived using a full order LQR design process primarily weighting the first 5 modes (10 states) with heaviest weighting on the 10 and 20 Hz modes.

The “Cmd filter” is second order, 15 Hz, 0.65 damping, “tustin” pre-warping, that has been discretized to 1000 Hz.

The weightings for the LQR gains were tuned to achieve our primary goal of actively damping the 10 Hz flutter mode while maintaining good stability margins. Figure 3.21 and Figure 3.22 show the resulting Bode plots for both the inboard and outboard control surfaces at the Mach 0.65 condition. The plots show the 10 Hz mode has been attenuated approximately 9 db in the inboard loop and approximately 15 db in the outboard loop. In Figure 3.23, the Nichols plots for the both of the control surface loops, show the robust margins of 9 db gain and 45° phase (depicted as black diamond shapes in the plot) have been maintained. Figures 3.24, 3.25, and 3.26 show similar plots for the Mach 0.7 condition. This condition is closer to the flutter condition and as such was harder to control resulting in slightly lower, but still acceptable, margins. The final designs were simulated in the time domain and proved to be stable.

SysID Bode Plot - Inboard Loop Mach 0.65 Q 53.9 psf

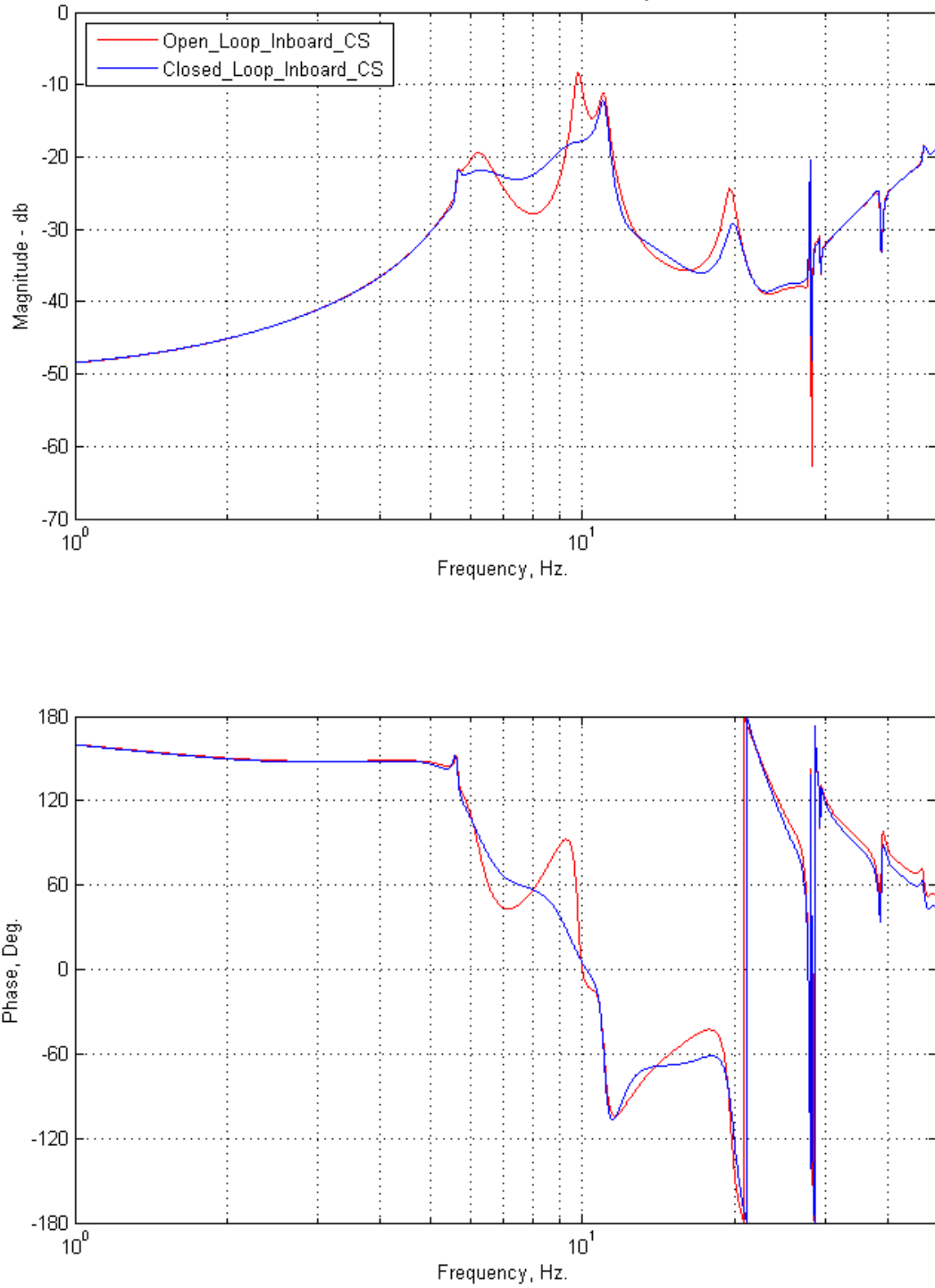


Figure 3.21 – Inboard Control Surface Open-Loop/Closed-Loop Bode Plot Comparison (Mach 0.65)

SysID Bode Plot - Outboard Loop Mach 0.65 Q 53.9 psf

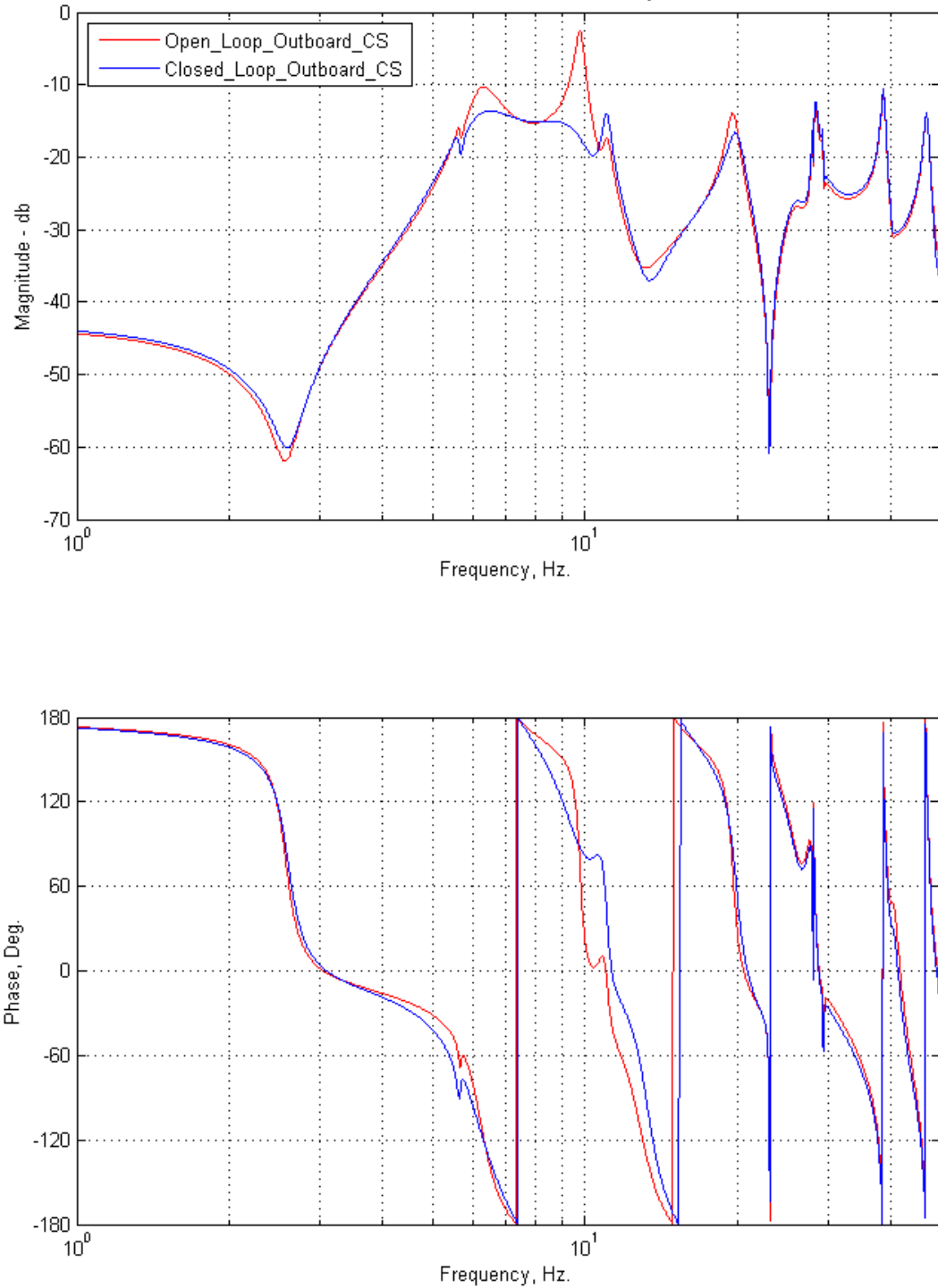


Figure 3.22 – Outboard Control Surface Open-Loop/Closed-Loop Bode Plot Comparison (Mach 0.65)

SysID Nichols Plot - Both Loops Mach 0.65 Q 53.9 psf

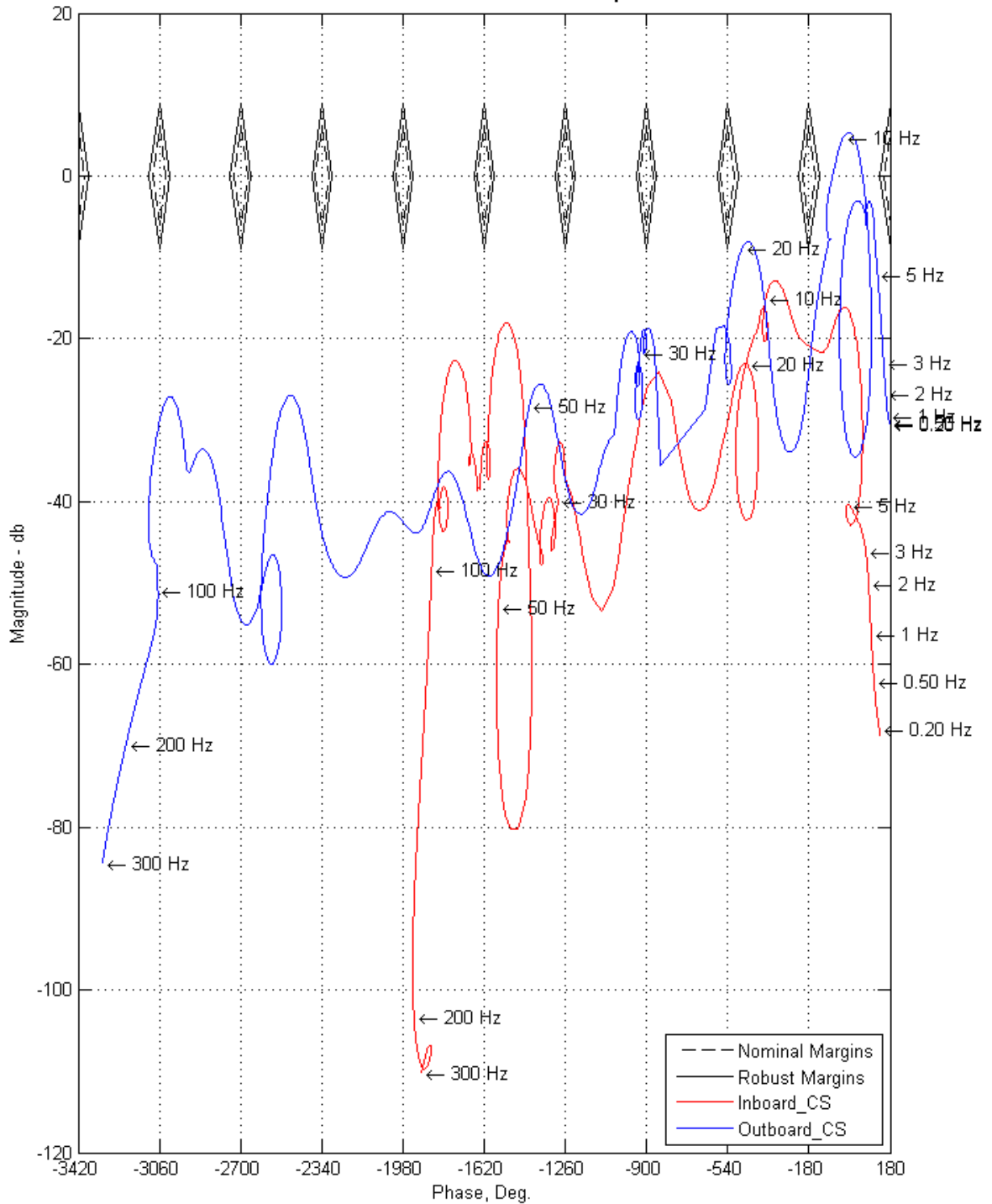


Figure 3.23 – SysID Mach 0.65 Nichols Plot

SysID Bode Plot - Inboard Loop Mach 0.70 Q 61.6 psf

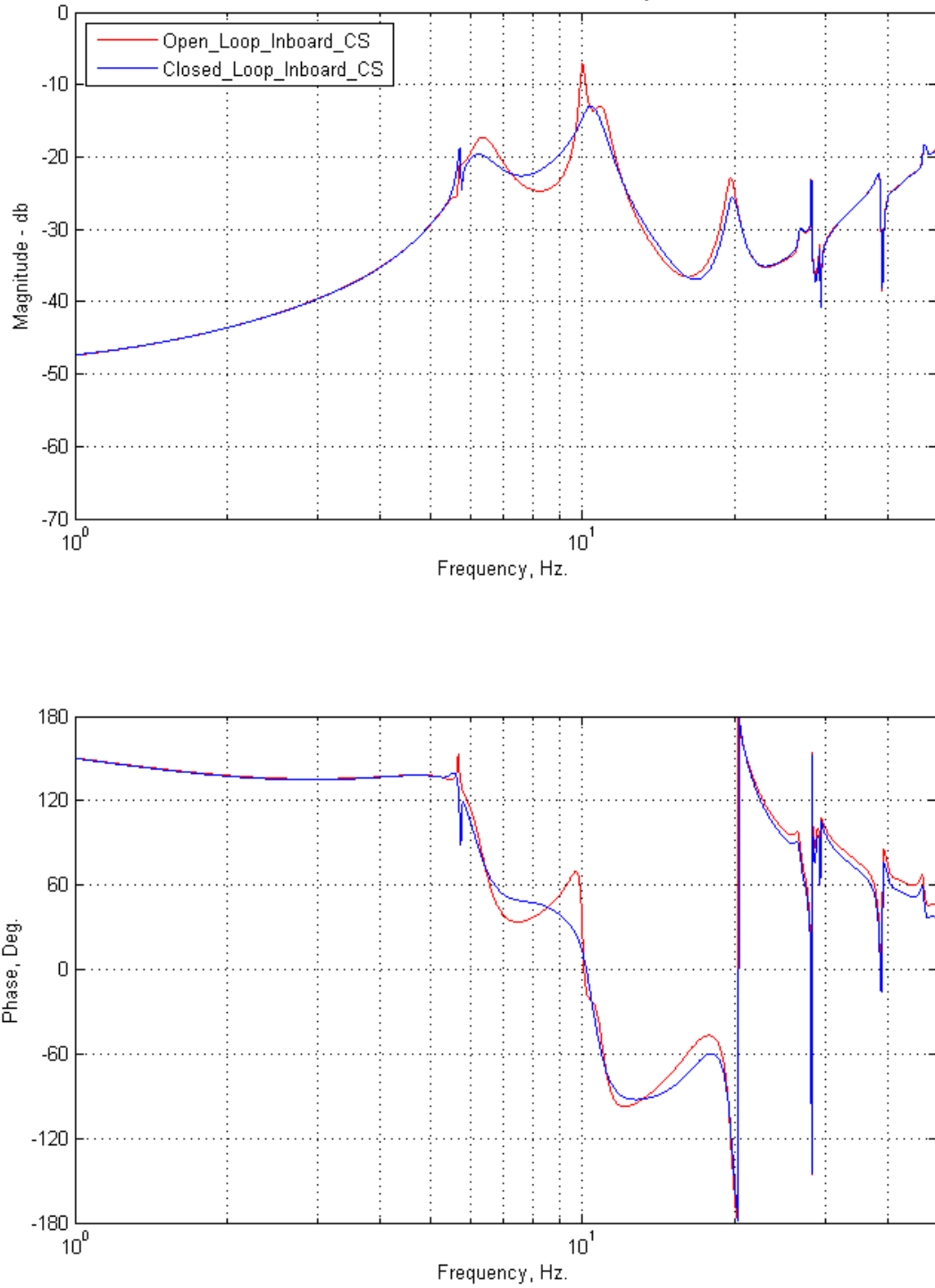


Figure 3.24 – SysID Inboard Control Surface Open-Loop/Closed-Loop Bode Plot Comparison (Mach 0.7)

SysID Bode Plot - Outboard Loop Mach 0.70 Q 61.6 psf

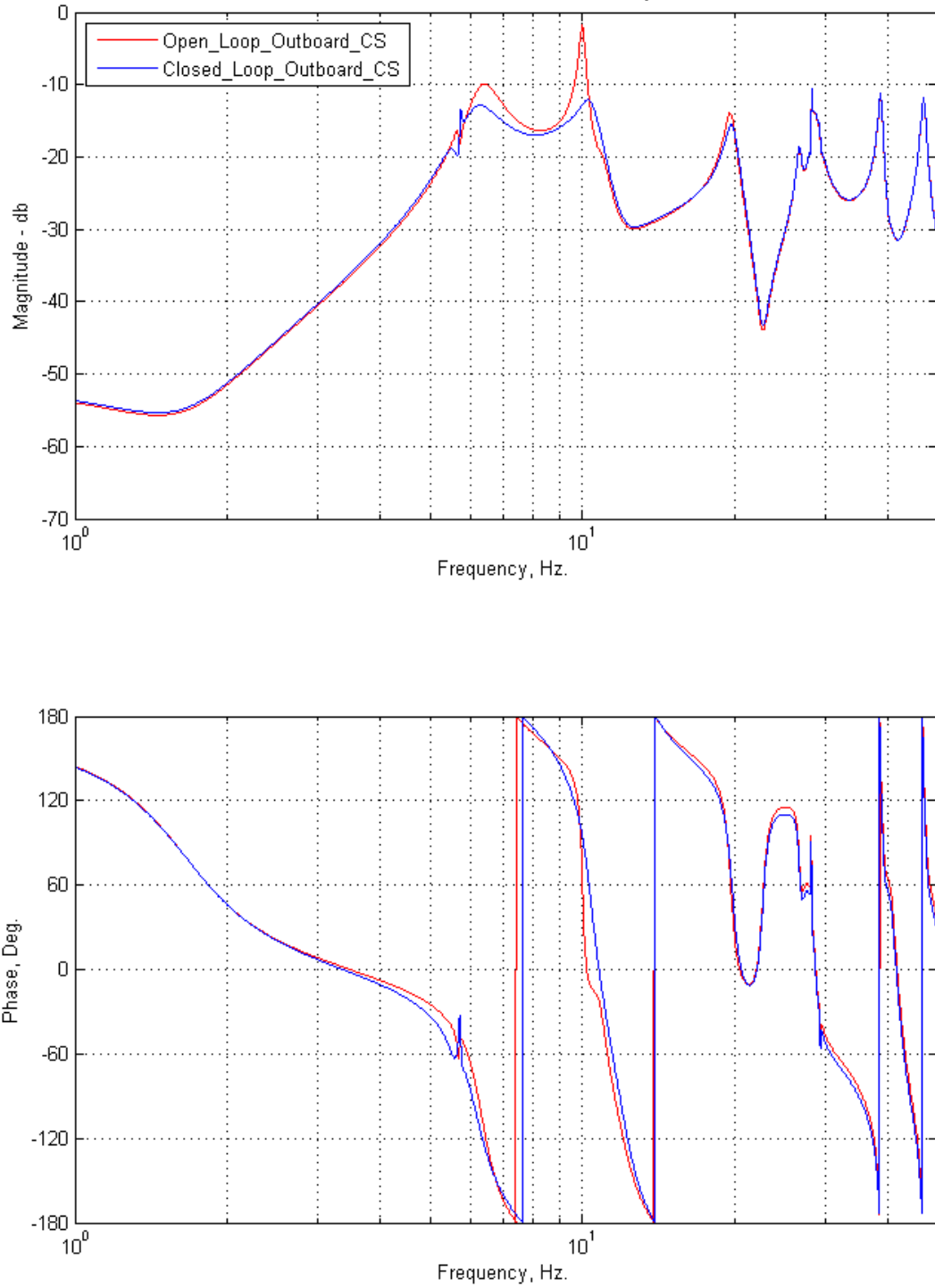


Figure 3.25 – SysID Outboard Control Surface Open-Loop/Closed-Loop Bode Plot Comparison (Mach 0.7)

SysID Nichols Plot - Both Loops Mach 0.70 Q 61.6 psf

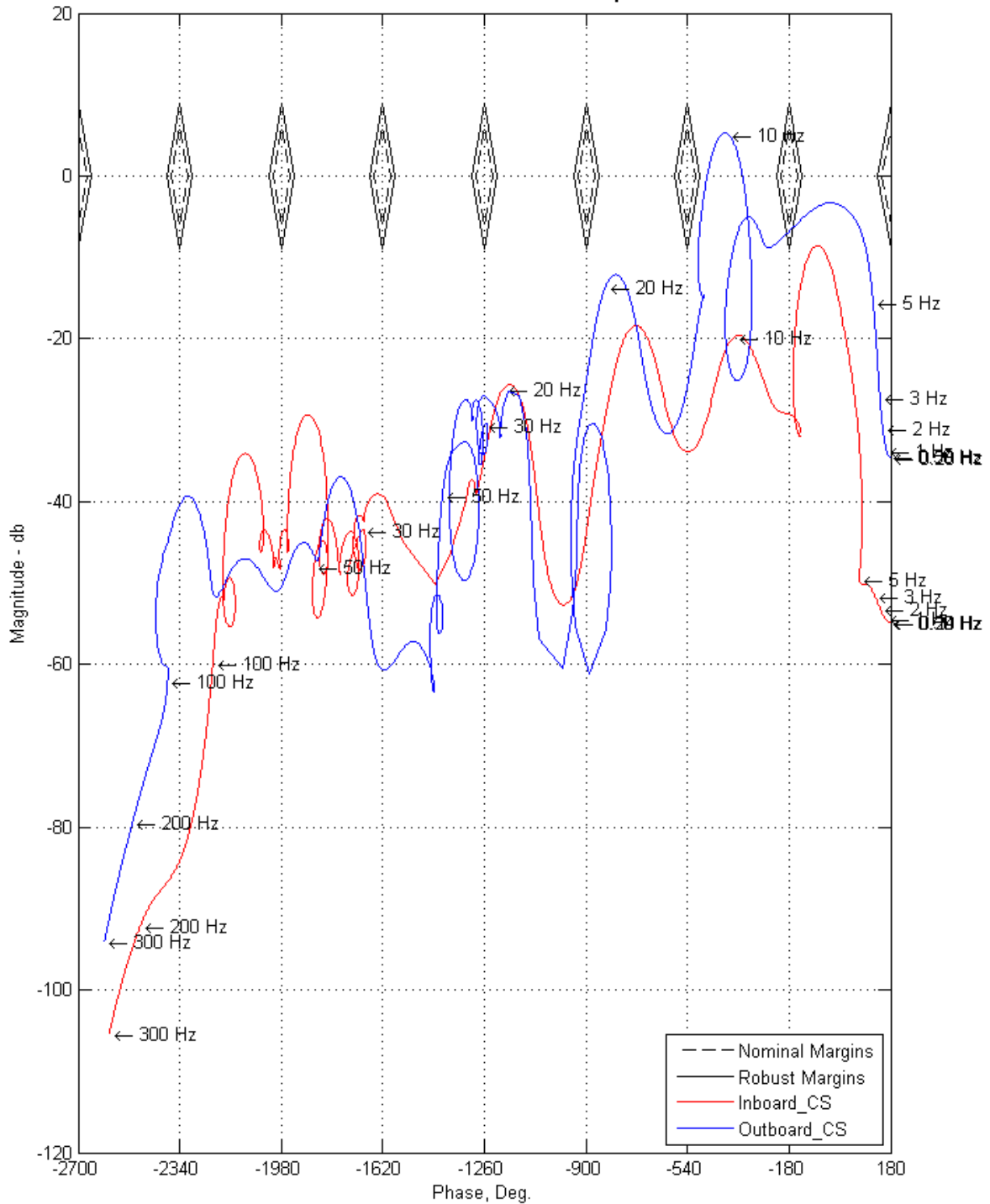


Figure 3.26 – SysID Mach 0.7 Nichols Plot

3.4.5 SysID Wind Tunnel Testing

Code was inserted in the controller to gather data that could be used to validate the stability margins derived from the simulation against actual test data. Unfortunately, the data gathered was too noisy to quantifiably validate the simulation. Figure 3.27 shows one of the better plots of this data. The plot compares the stability margins derived from one of the early TDT runs (Run 48, Tab Point 2354, Mach 0.7, Q 61.2 psf) to the expected simulation results.

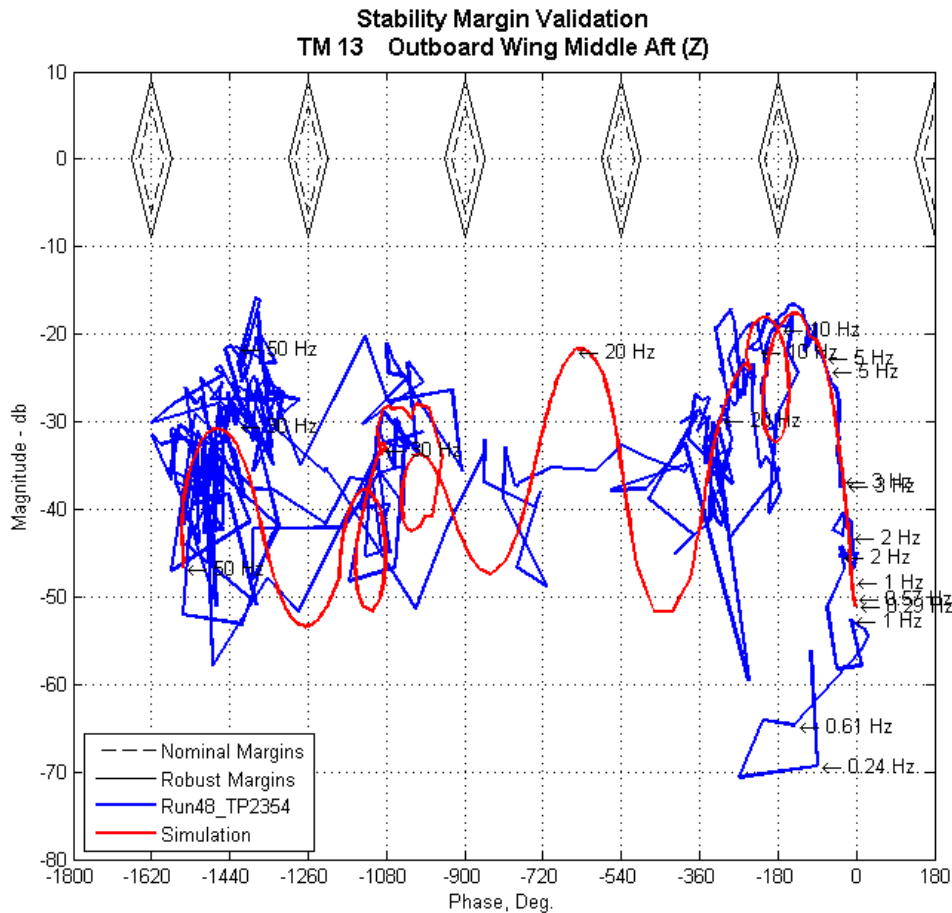


Figure 3.27 – Sample Tunnel Data Stability Margin Comparison

An example of the controller actually controlling flutter is shown in Figure 3.28. The TDT operators have the ability to turn the controller on and off in real time and the plot shows one of these occasions where the TBW is in a flutter condition. The data in red shows the wing beginning to flutter, while the data in blue shows flutter being controlled. The SysID controller supported TDT runs 48 through 54 where Mach varied from 0.23 up to 0.81, Q varied between 10 and 97 psf, and AOA varied from -3° to 1° . Almost all of testing with the SysID controller was based on the one design point at Mach 0.65, Q 53.9 psf, and entailed no gain scheduling. In all these cases where the controller was engaged, flutter was controlled.

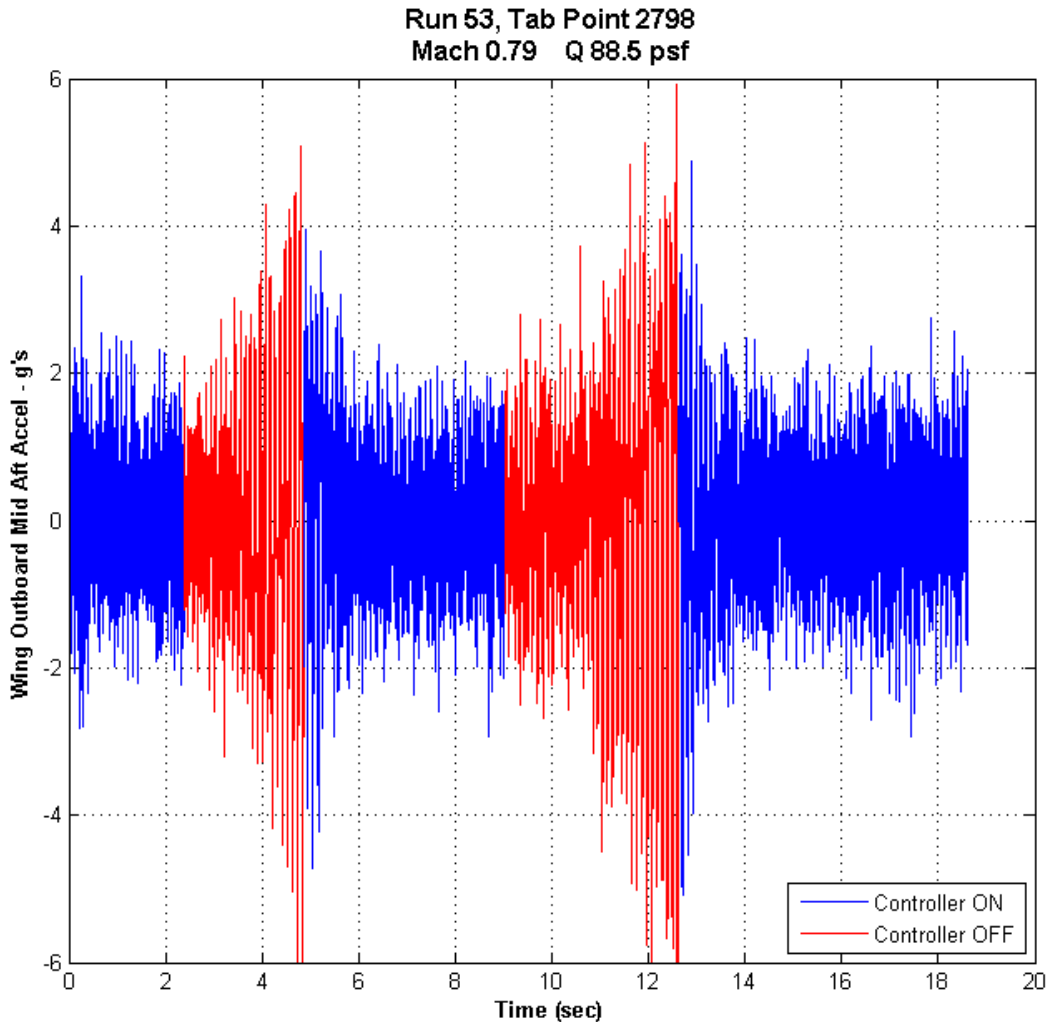


Figure 3.28 – SysID Controller – Open-loop/Closed-loop Demonstration

3.4.6 FEM19 Simulation and Control Law Design

Since a functioning controller was in place, there was time to attempt to design a new controller based on the FEM19 SSMs. Based on experience with the SysID gain design process, some changes were incorporated for the FEM19 controller. The FEM19 simulation architecture is essentially the same as the SysID version. The main difference is that the actuator commands are fed back within the controller, so the RVDT outputs are no longer required to be input to the controller. Figure 3.29 shows the FEM19 simulation.

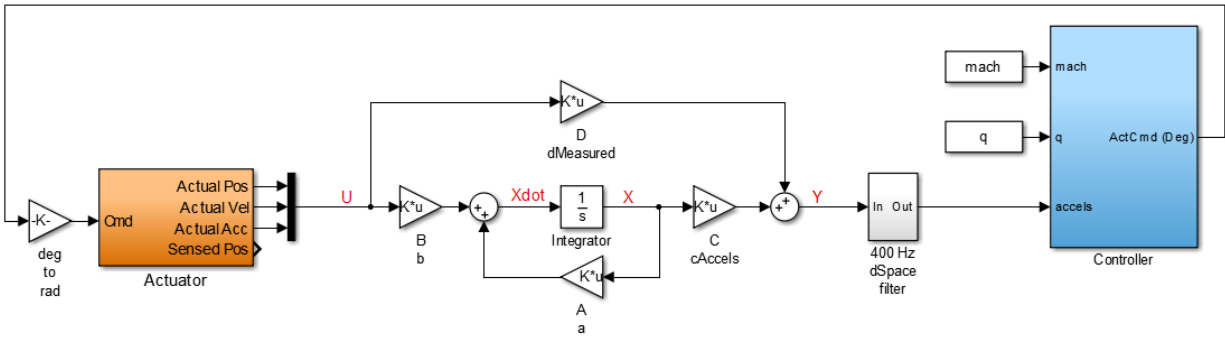


Figure 3.29 – FEM19 Simulation

The FEM19 controller architecture (Figure 3.30) is “essentially” the same as the SysID controller. The major difference is the actuator commands are fed back instead of using the RVDT signals. The other obvious change is the lack of LQR gains in the diagram. The gains are there, they’ve just been embedded in the estimator’s realization prior to calculating the estimator coefficients. Also, a 15° limit is imposed on the actuator commands and the hysteresis in the nearest neighbor algorithm was modified such that the states and actuator commands could be zeroed out briefly when transitioning between design points. The “Cmd filter” frequency was increased to 40 Hz (second order, 40 Hz, 0.65 damping, “tustin” pre-warping, that has been discretized to 1000 Hz).

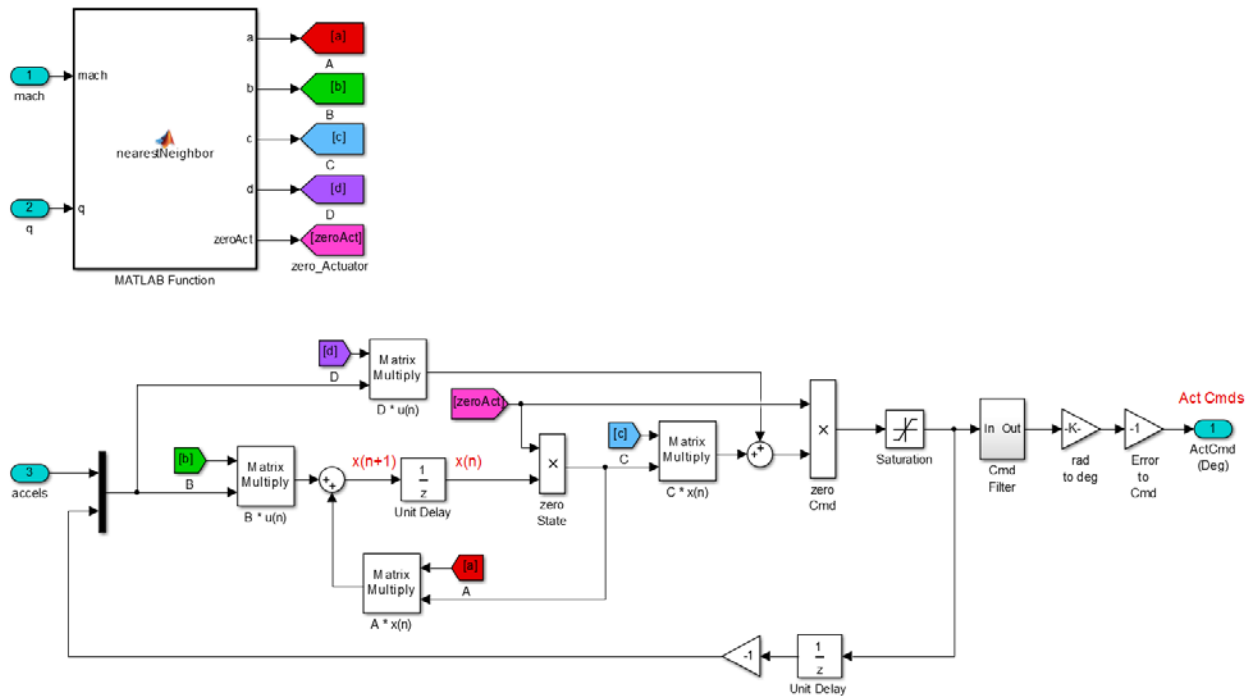


Figure 3.30 – FEM19 Controller

The process for deriving the LQR and estimator gains is fundamentally different from the SysID version. In order to increase stability margins, the FEM19 SSM was augmented with a pair of

second order filters (40 Hz, 0.98 damping) to model the two actuator's states and allow the LQR process to put gains on them. In order to keep the LQR gains on the actuator's states in check, the system was augmented with a pair of third order filters effectively penalizing very high gains to prevent driving the actuator bandwidth too high because of its inherent non-linearities. The third order filter is a second order filter (10 Hz, 0.6 damping) over a second order filter (100 Hz, 0.7 damping) multiplied by a first order filter (101 Hz). The LQR gains are derived using a full order LQR design process on the augmented model primarily weighting the first 5 modes with heaviest weighting on the 10 Hz flutter mode. It was found that heavily weighting the third state of the third order filter kept the actuator gains within the desired range.

The estimator gains are calculated and the LQR gains are embedded into estimator to form a new state space model. This model is reduced (balanced reduction) to 20 states (10 modes) and discretized at 1000 Hz.

The weightings for the LQR gains were tuned to actively damp the 10 Hz flutter mode while maintaining good stability margins. Figures 3.31, 3.32, and 3.33 show the resulting Bode and Nichols plots at the Mach 0.7 condition. The plots show that the 10 Hz mode has been attenuated about 7 db in the inboard loop and about 6 db in the outboard loop, but the robust margins (9 db and 45°) were maintained. In fact, the robust margins were maintained for all but the two most unstable cases (Mach 0.75, Q 137.7 psf and Mach 0.75, Q 160.6 psf) and the nominal margins (6 db and 30°) were maintained in those cases.

FEM19 Bode Plot - Inboard Loop Mach 0.70 Q 62.4 psf

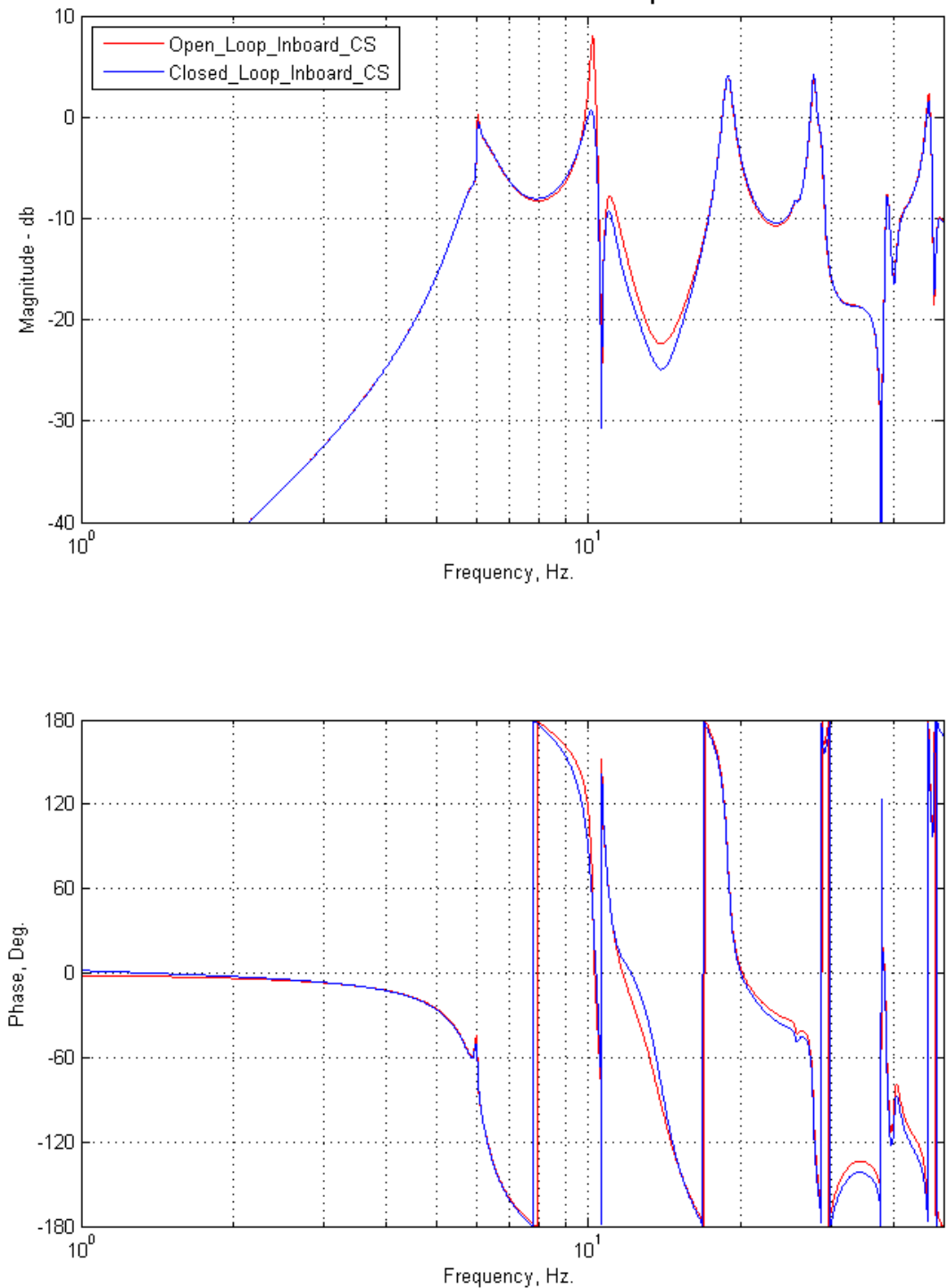


Figure 3.31 – FEM19 Inboard Control Surface Open-Loop/Closed-Loop Bode Plot Comparison (Mach 0.7)

FEM19 Bode Plot - Outboard Loop Mach 0.70 Q 62.4 psf

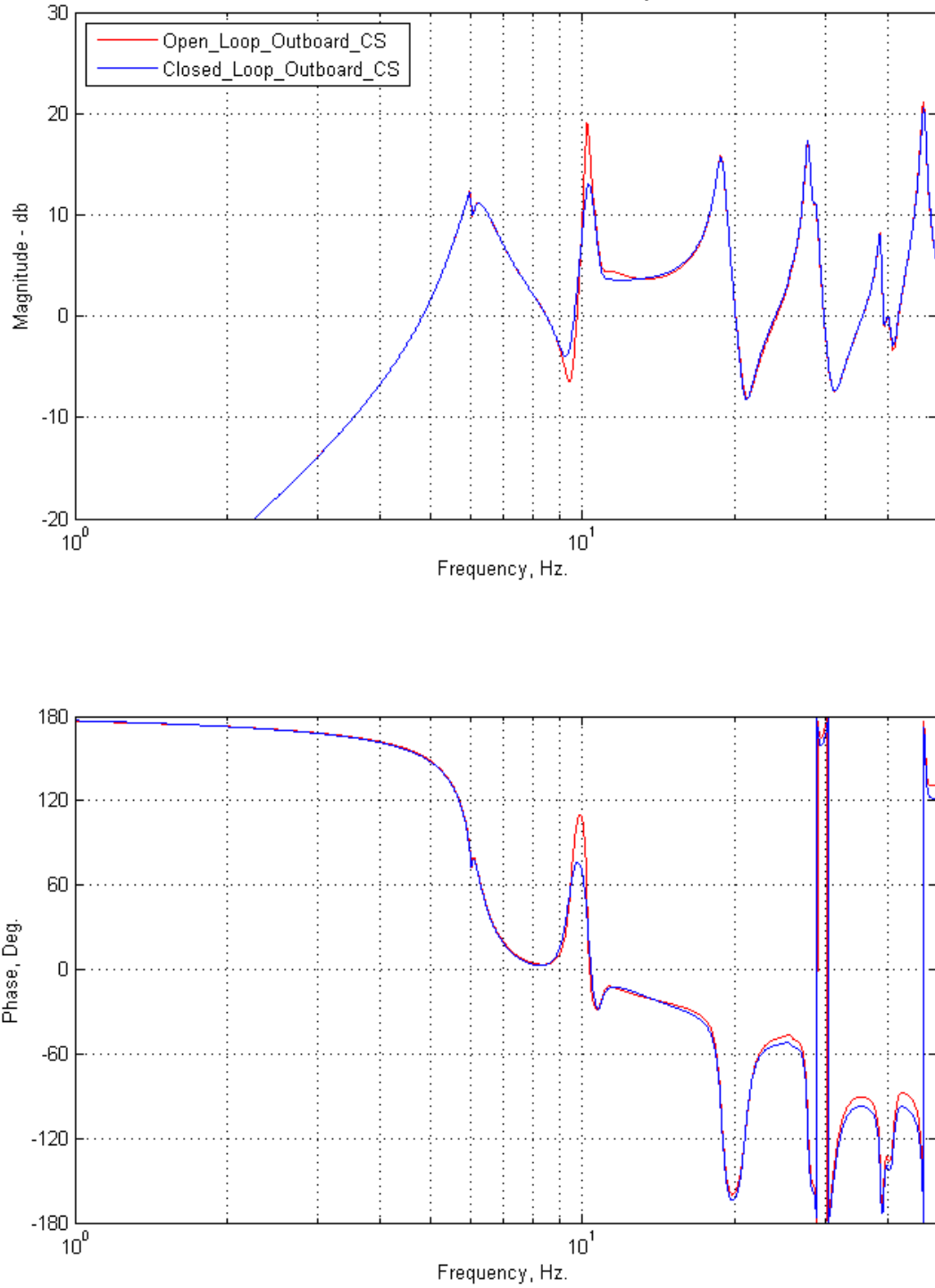


Figure 3.32 – FEM19 Outboard Control Surface Open-Loop/Closed-Loop Bode Plot Comparison (Mach 0.7)

FEM19 Nichols Plot - Both Loops Mach 0.70 Q 62.4 psf

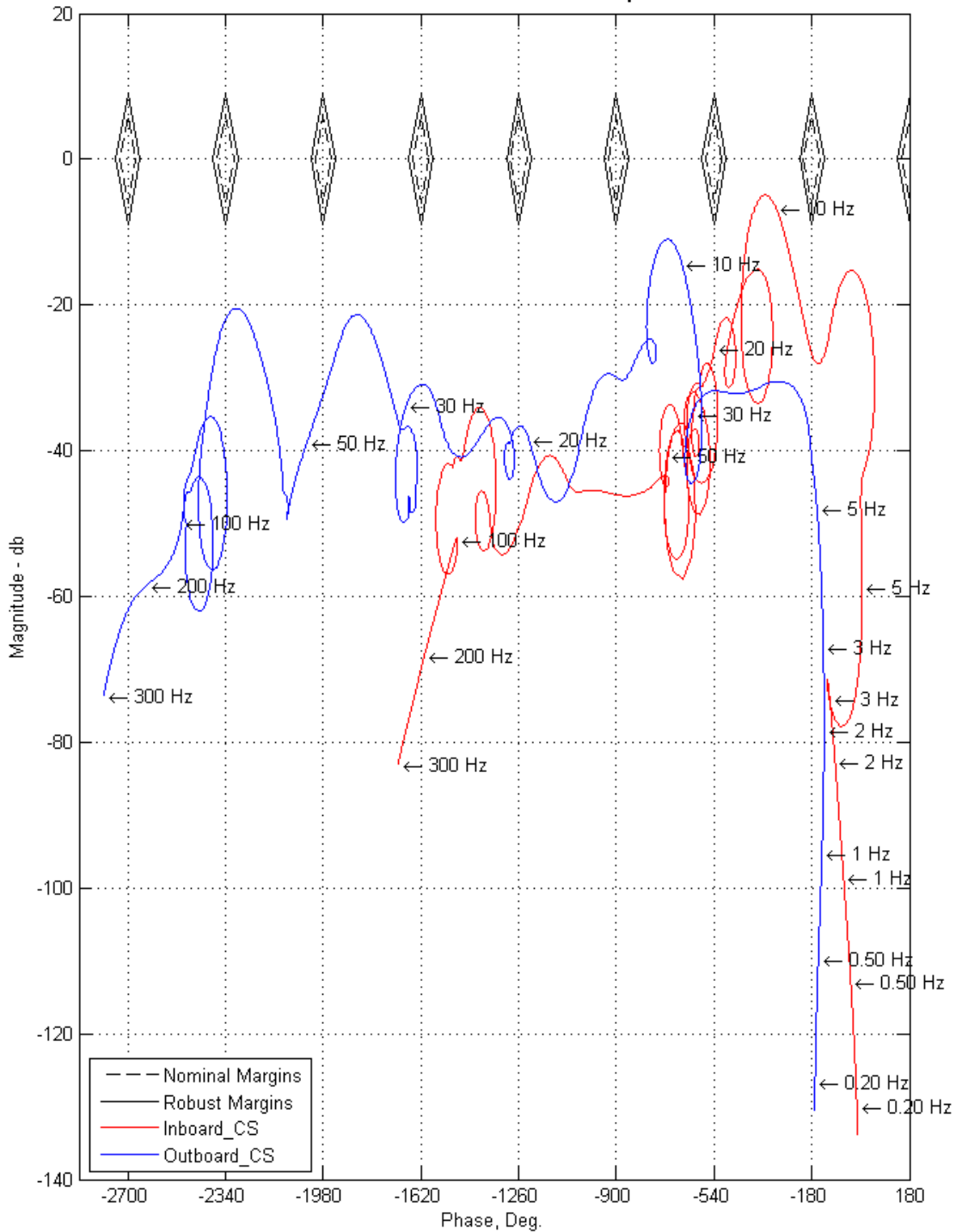


Figure 3.33 – FEM19 Mach 0.7 Nichols Plot

The final designs were tested in the time domain. Figure 3.34 shows a comparison of the simulated time responses, with the control loops open and closed, for one of the unstable cases (Mach 0.75, Q 68.9 psf). As expected, the open loop accelerations grow unbounded.

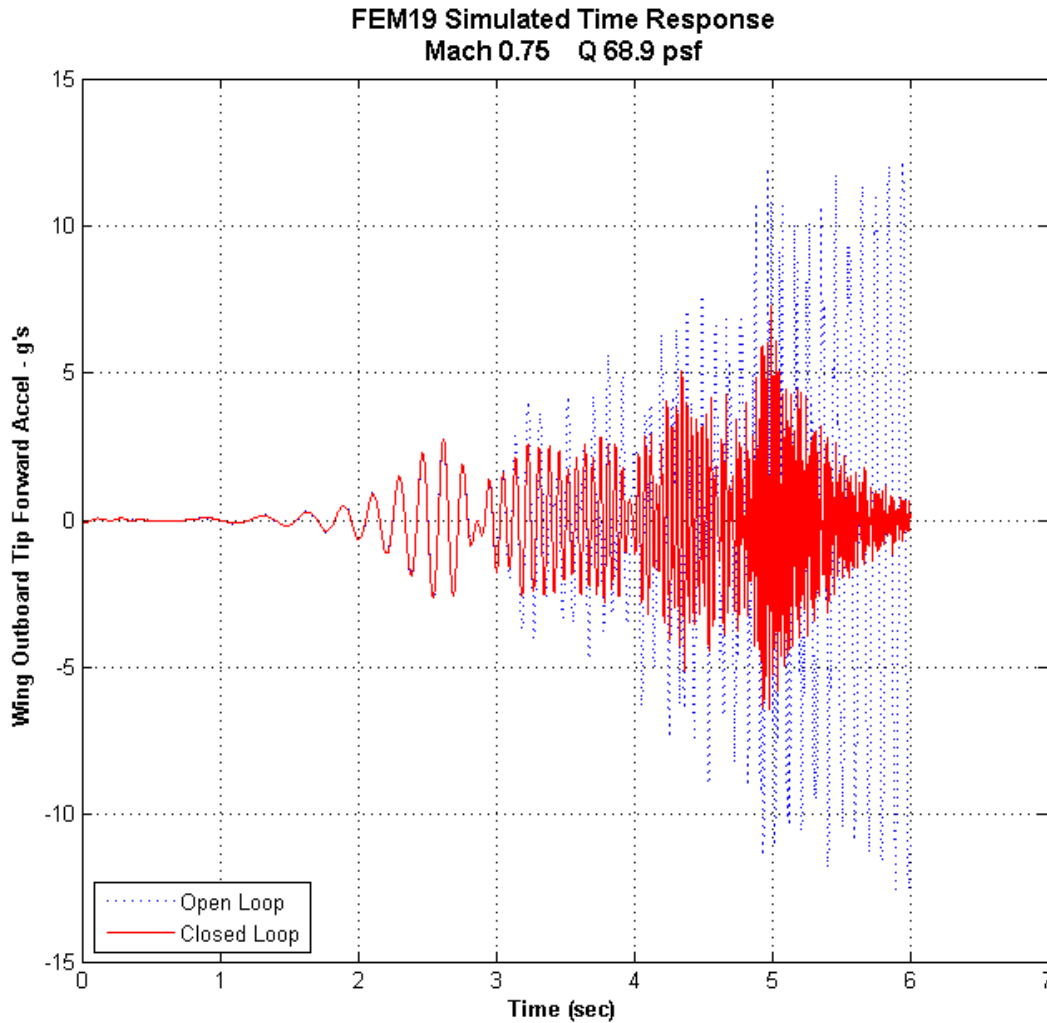


Figure 3.34 – FEM19 Simulated Time Response

3.4.7 FEM19 Wind Tunnel Testing

Figure 3.35 shows an example of the controller controlling flutter at an unstable condition. Again, the data in red shows the wing beginning to flutter when the controller is turned off and the data in blue shows controller damping out the flutter. The FEM19 controller supported TDT runs 55 through 63 where Mach varied from 0.35 up to 0.83, Q varied between 21 and 115 psf, and AOA varied from -3° to 5° .

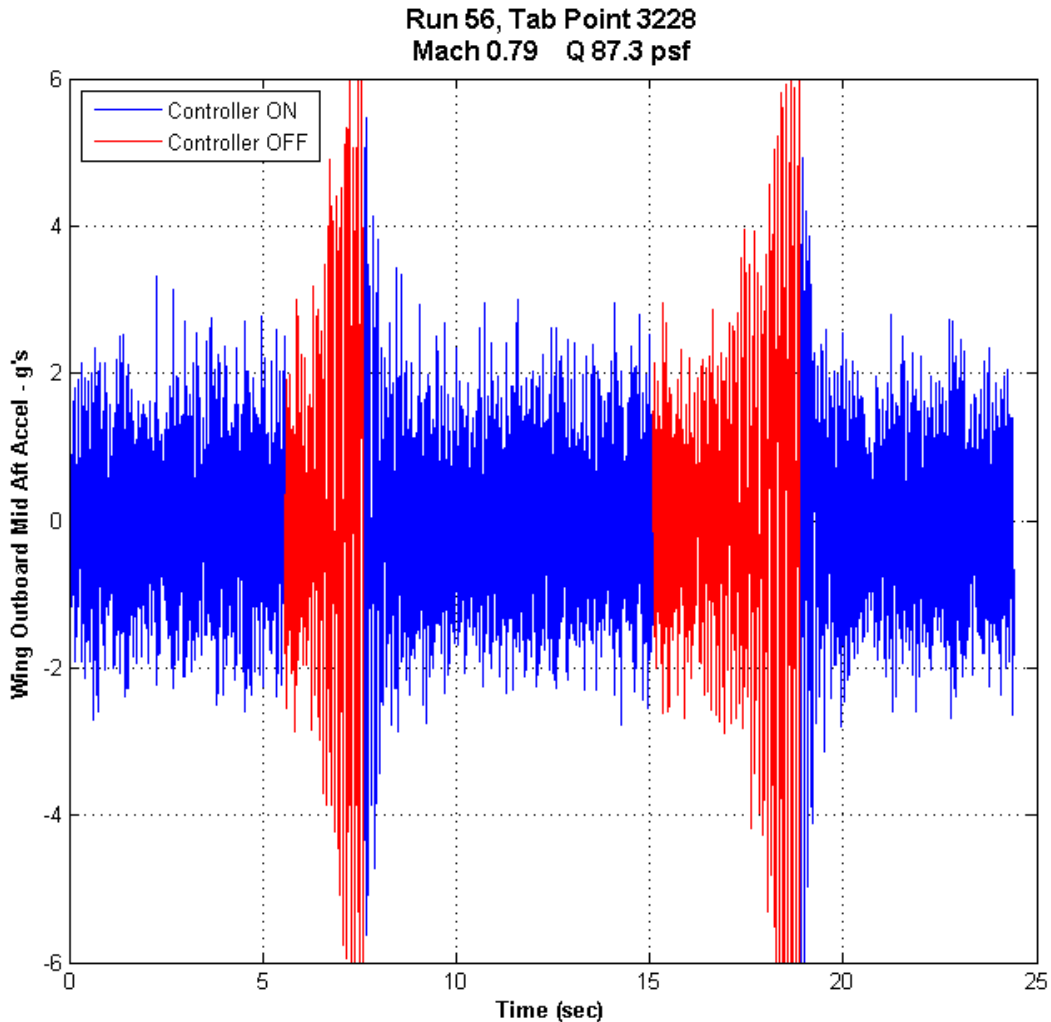


Figure 3.35 – Fem19 Controller – Open-loop/Closed-loop Demonstration

3.4.8 System Identification Model Development – Version 2

With two functioning controllers in hand, a decision was made to try and develop a controller based on control surface sweeps at an unstable point. In order to do this, of course, a controller would have to be functioning at the time to keep flutter attenuated. Data was acquired, but several issues prevented the models from converging to a solution. Large amplitude, high frequency sweeps were required to overcome the inherent noise in the system. However, the combination of amplitudes and frequencies required were too high for the actuators which became flow rate limited. Also, some unexpected non-linearities became apparent in the data that could not be accounted for in the SysID process. Between the actuator limitations, the inherent noise in the system, and the non-linearities, the SysID process failed to converge on a solution.

3.4.9 Conclusions

The main conclusion that can be drawn from this control law effort is that the LQR design process worked very well in this instance, allowing the 10 Hz flutter mode to be targeted directly in the gain design process. The cycle time for iterations was reduced and the ability to switch from the SysID models over to the FEM models was very smooth. The FEM19 SSMs based on the pre-holiday model proved to be sufficient for designing a robust control system, potentially reducing the need for open-loop testing in the future. Flutter suppression was demonstrated with two different control systems that proved to be very robust over a wide range of Mach, Q, and AOA.

3.5 Test Procedures

Test points investigated include flutter points, control surface sweeps, gust vane oscillation points, and control surface dwells.

Flutter points involve slowly increasing Mach and dynamic pressure along constant pressure H lines while visually monitoring model vibration as well as PSDs and time histories for signs of instability. A bypass valve is opened at any signs of instability and the tunnel winds down. An example of an unstable open loop flutter point is shown in Figure 3.36. The plot is a time history of the nacelle pylon accelerometer.

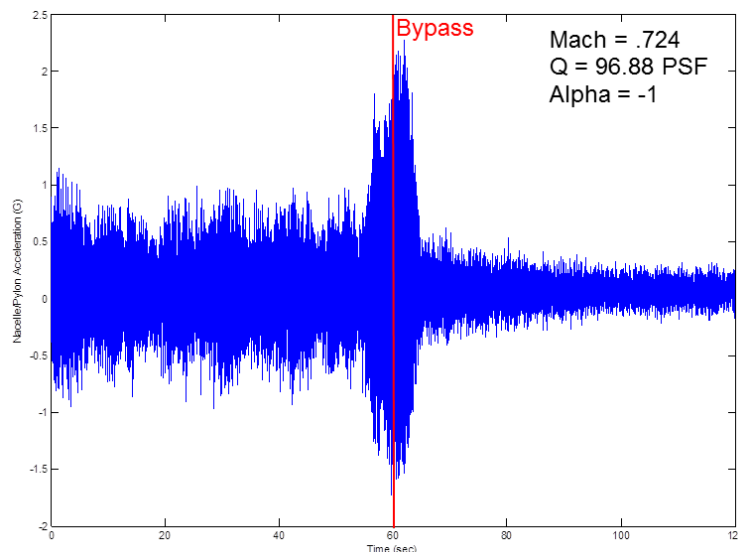


Figure 3.36 – Unstable Open Loop Flutter Point

Flutter points were run both open and closed looped. Once the control laws allowed the Mach and dynamic pressure to increase past the open loop flutter boundary a technique was used to open the loop and quickly close the loop and see if the open loop system looked stable. This technique allowed for determining the back side of the Mach dip open loop flutter boundary.

Control surface sweeps involve running a fixed amplitude sweep from 0 to 30 Hz to generate the data required for the system ID control laws. The sweeps were run inboard alone, outboard

alone, and both inboard and outboard. The sweeps were run both open loop and closed loop. The response due to the control sweeps for the closed loop point in the open loop unstable region was lost in the overall noise and insufficient for system ID.

The gust vanes were oscillated both open and closed loop to investigate the control laws effect on gust loads.

Control surface dwells involve oscillating the control surface at the 10 Hz flutter frequency and then stopping the oscillation and recording the response. This technique allows for a good estimate of system damping in the open loop stable region.

3.6 Test Results

Testing was broken up into pre-holiday open loop testing and post-holiday closed loop testing.

3.6.1 GVT and FEM Correlation

GVTs were run to correlate our analysis model to the test frequencies and mode shapes. The final preholiday in tunnel GVT results were compared to the pretest FEM18 analysis model results. A comparison of the analysis and test frequencies and modal assurance criteria is shown in Figure 3.37. The two primary flutter modes are second bending mode 3 and first torsion mode 4. The GVT vs. FEM18 frequencies are significantly different and the mode 3 MAC was 0.9. FEM19 was created to better match the preholiday GVT result. This was mostly accomplished by removing the electronic turn table model we had attached to the FEM. In addition, small changes to the wing stiffness were required. A comparison preholiday GVT and FEM 19 is shown in Figure 3.38. This shows a very good comparison between test and analysis. After the preholiday testing a cutout was made in a fairing at the root of the strut. It was suspected that there wasn't enough clearance between the strut root joint and the fairing and some fouling was occurring. This was tested by looking at GVT results with and without a wedge added which contacted the fairing. The cut out and wedge are shown in Figure 3.39. A summary of GVT frequencies showing which GVTs the FEMS are based on is shown in Table 3.5. The table shows significant difference in Mode 3 frequencies pre and post holidays. Part of the difference is due to the post-holiday cutout in the strut root fairing. The GVT results with the wedge included don't get all the way back to the preholiday values. FEM20 was created by updating stiffnesses again to match the post-holiday GVT results. The post-holiday GVT is compared to FEM20 in Figure 3.40. Again, there is good correlation between test and analysis.

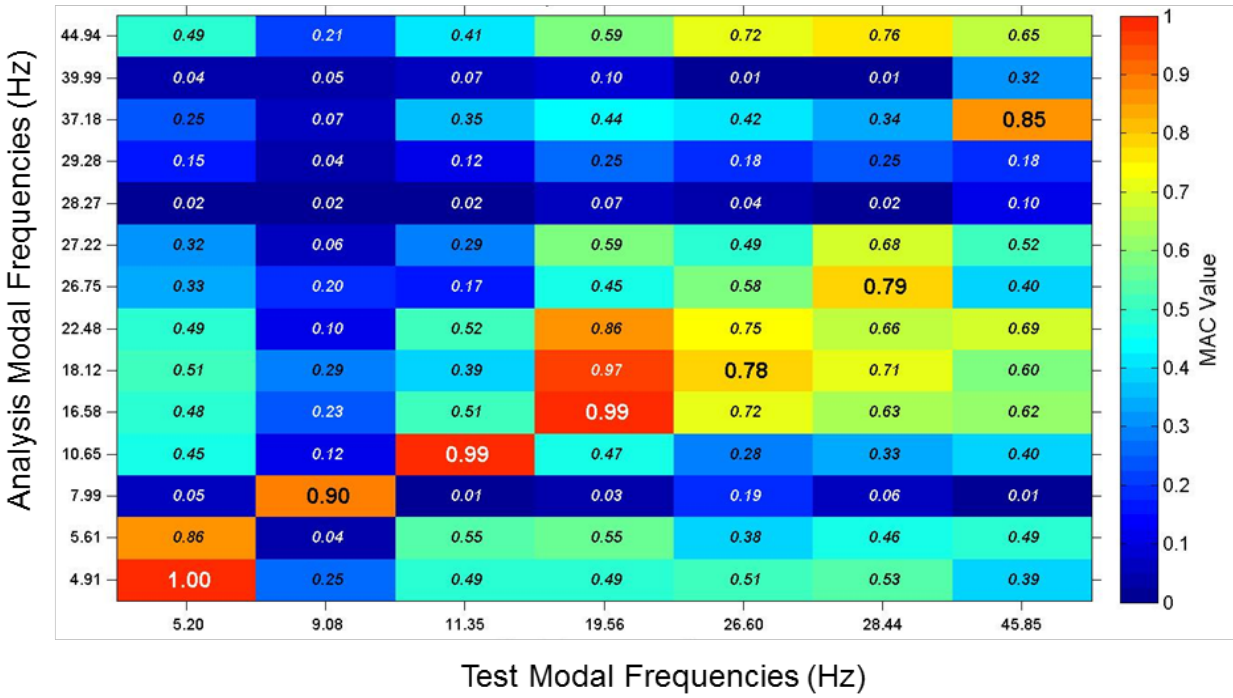


Figure 3.37 – Pre-Holiday GVT vs. FEM18

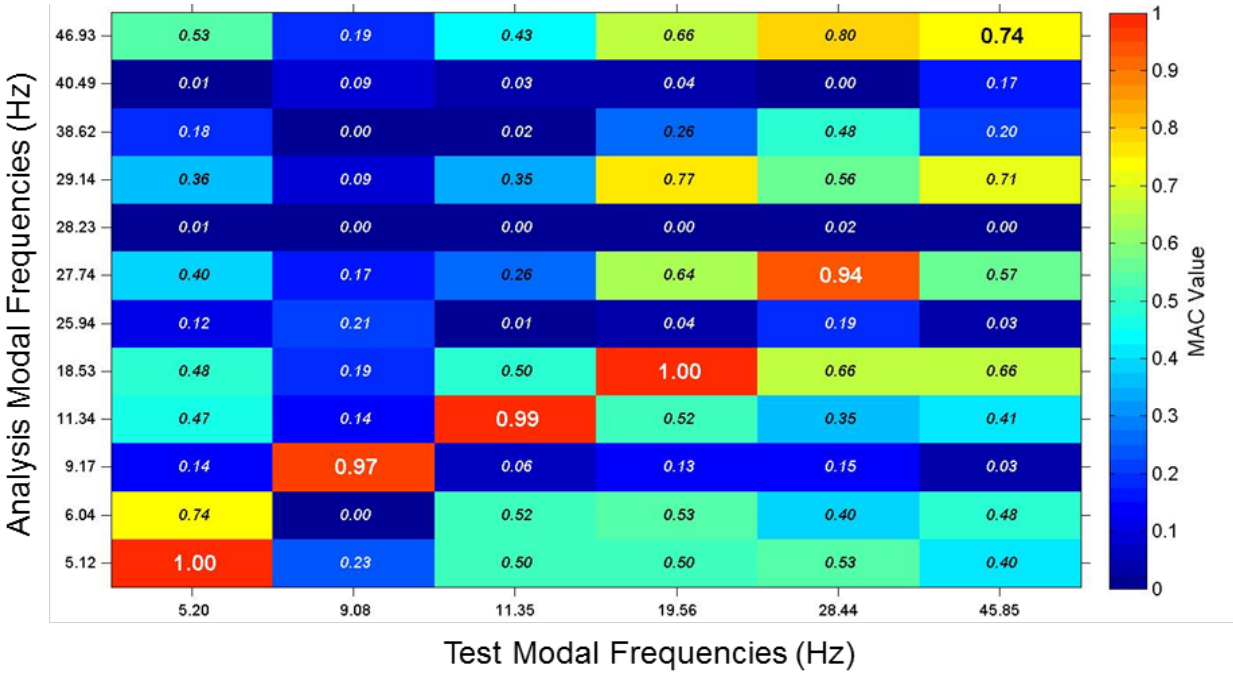


Figure 3.38 – Pre-Holiday GVT vs. FEM19

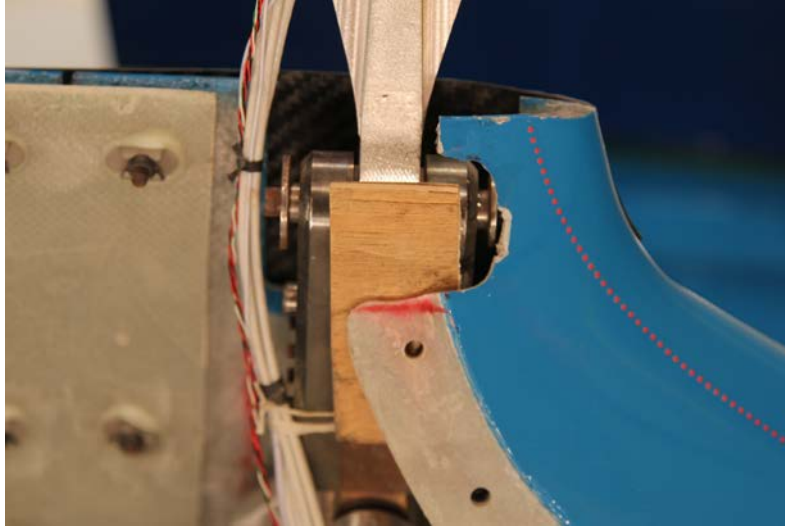


Figure 3.39 – Strut Root Fairing Cutout and Wedge

Table 3.5 – GVT Frequency Summary

	FEM 19							FEM 20						
Run Point	2	36	37	39	39	39	41	41	41	41	43	43	43	43
Mode				2VPP	2.25V	1.5V	Wedge			Wedge		Wedge	Wedge	Wedge
1	5.20	5.38	5.16	5.14	5.14	5.16	5.18	5.11	5.16	5.19	5.08	5.14	5.14	5.15
3	9.10	8.47	8.61	8.60	8.65	8.61	9.04	8.68	8.46	8.70	8.43	8.72	8.75	8.73
4	11.35	11.28	11.34	11.35	11.34	11.37	11.42	11.35	11.25	11.28	11.14	11.18	11.19	11.19
5	19.57	19.45	18.95	18.80	18.78	18.84	19.19	18.69	18.70	19.04	18.62	19.04	19.09	19.12
7	28.45	29.60	28.05	27.95	27.96	28.03	28.54	29.22	27.60	28.01	27.83	28.13	28.16	28.17

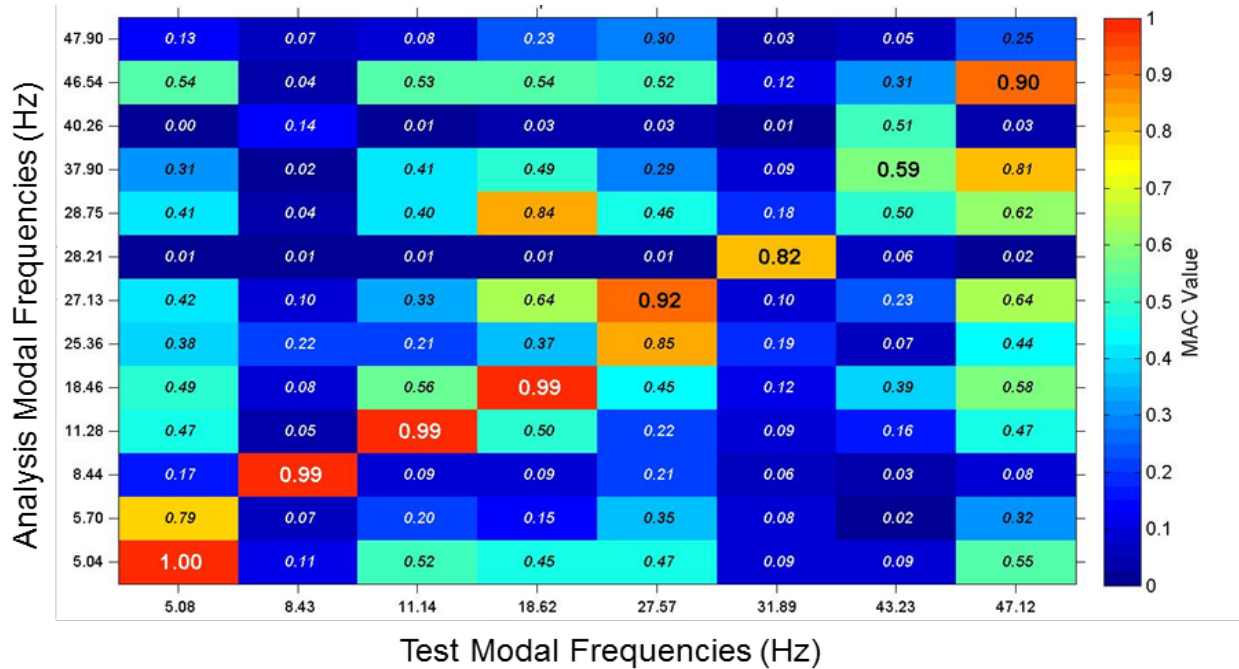


Figure 3.40 – Post-Holiday GVT vs. FEM20

3.6.2 Doublet Lattice Aerodynamic Correction Factors Update

To improve the test vs. analysis comparisons, the doublet lattice static aerodynamic correction factors, described in Section 2.1.8.5, were updated to better match all the test mean wing strain gage results. This was done for Mach numbers 0.7, 0.75, and 0.82. Figure 3.41 shows the improved correlation with test results for the outboard root strain gage at Mach = 0.7.

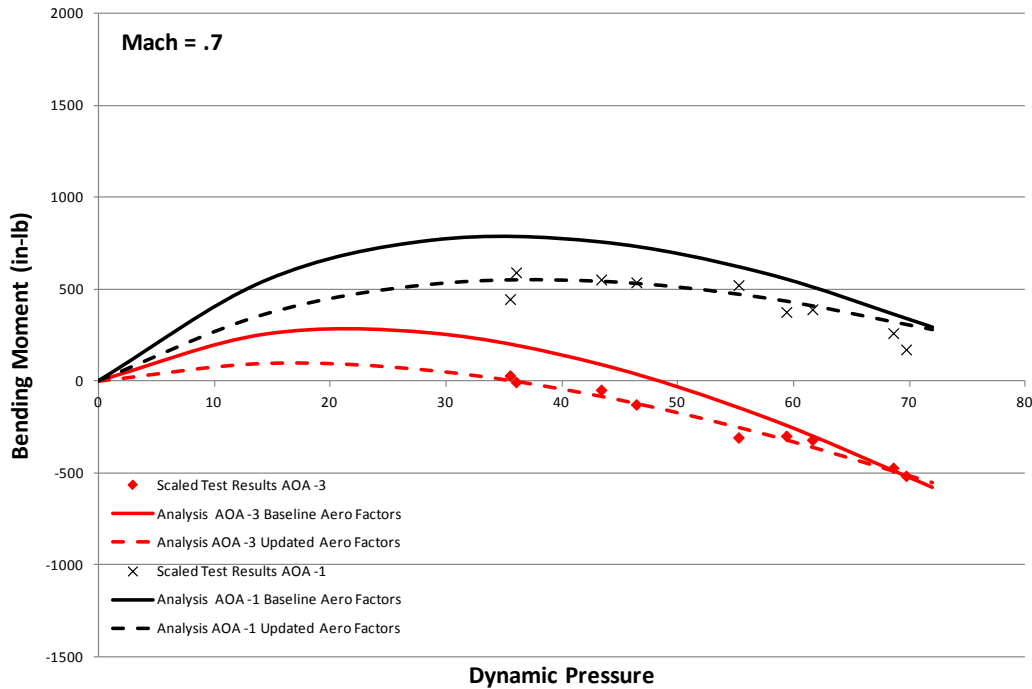


Figure 3.41 – Updated Static Aero Factors

3.6.3 Pre-Holiday Flutter Points

All the pre-holiday flutter points at alpha -3 are shown in Figure 3.42. Blue Xs are stable and red Xs are unstable. The pre-holiday unstable points for four angles of attack are shown in Figure 3.43. The results show a significant variation with angle of attack. This is in contrast to traditional linear flutter results which don't change for different angles of attack or loads. This angle of attack variation is unique to the truss braced wing due to its large in-plane loads and reduced stiffness of the inboard wing.

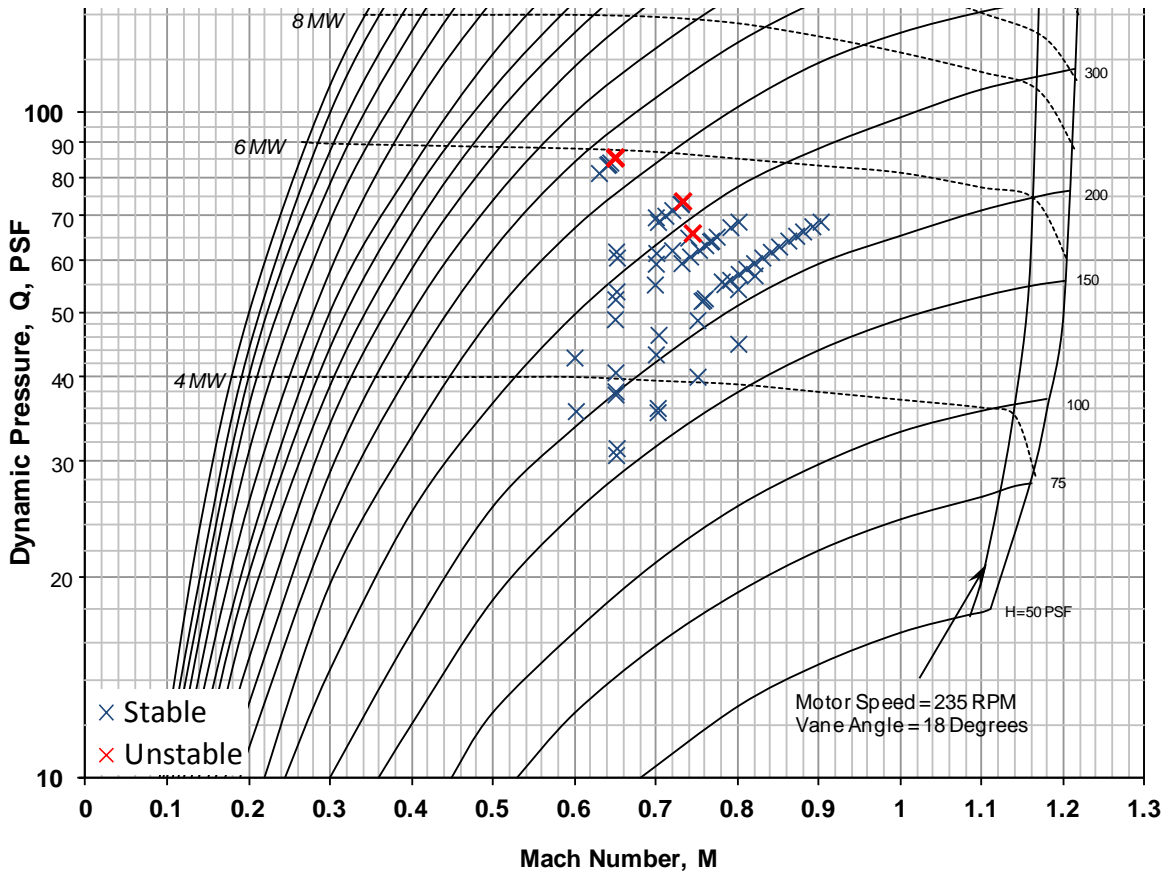


Figure 3.42 – Pre-Holiday Flutter Test Results Alpha=-3

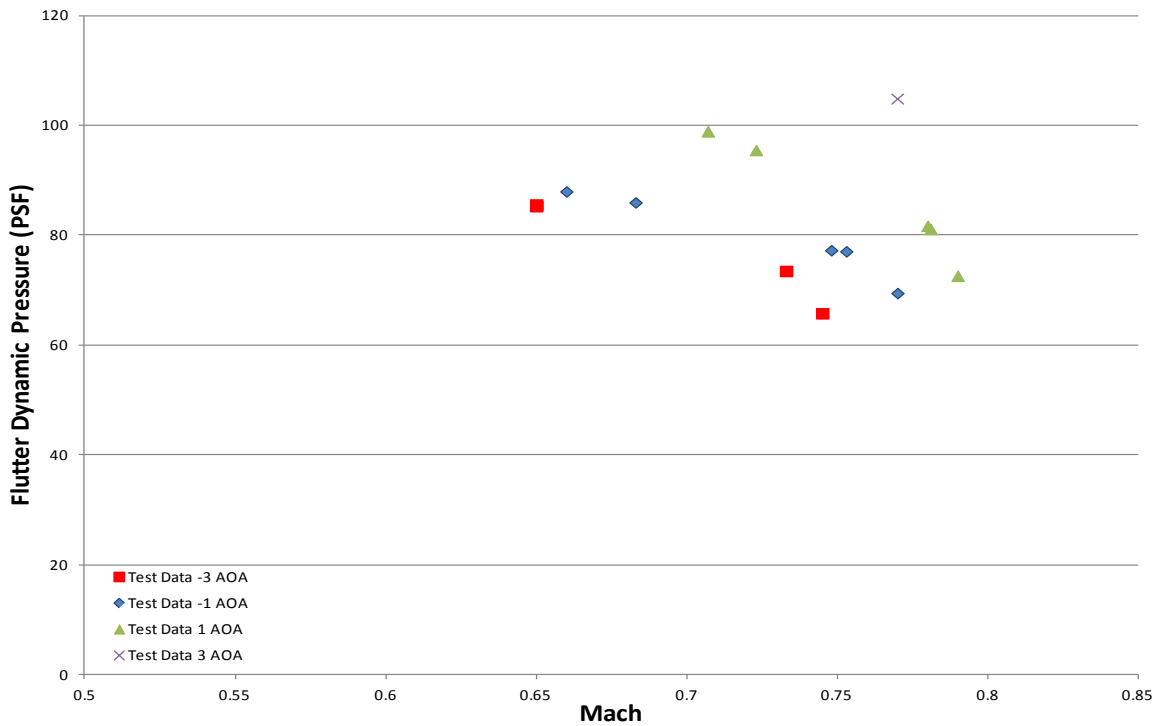


Figure 3.43 – Pre-Holiday Unstable Points

3.6.4 Non-linear Flutter Method

A method to include preload and large displacement effects in the flutter analysis is shown in Figure 3.44. The process starts by generating loads in Nastran solution 144. Next the loads are applied to the model in a Nastran solution 106 nonlinear run including the large displacement parameter. Finally the linear solution 145 is run from a restart of the stiffness and mass matrix output from the 106 run.

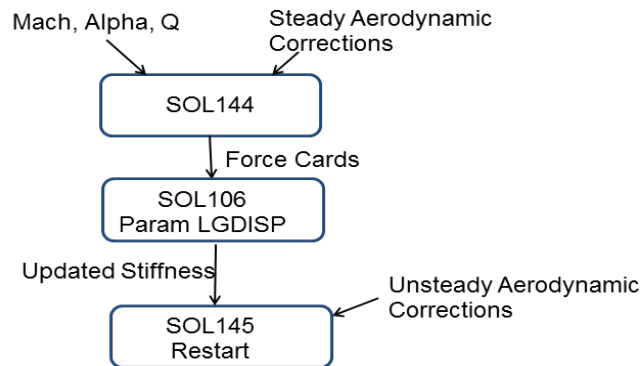


Figure 3.44 – Preload and Large Displacement Flutter

3.6.5 Pre-Holiday Flutter Test vs. Analysis

Pre-holiday flutter comparison between test and analysis is shown in Figure 3.45. The comparison is with the static corrections from Section 3.6.2 used in the solution 144 analysis, and no corrections to the doublet lattice unsteady aerodynamics for the flutter solution 145 analysis. The black line shows the traditional linear 145 solution. The analysis including the preload and large displacements predicts an angle of attack trend which matches the test data. The analysis also is accurate in predicting the minimum flutter speed at each angle of attack for this configuration. The Mach trend using the theoretical doublet lattice does not match the test data.

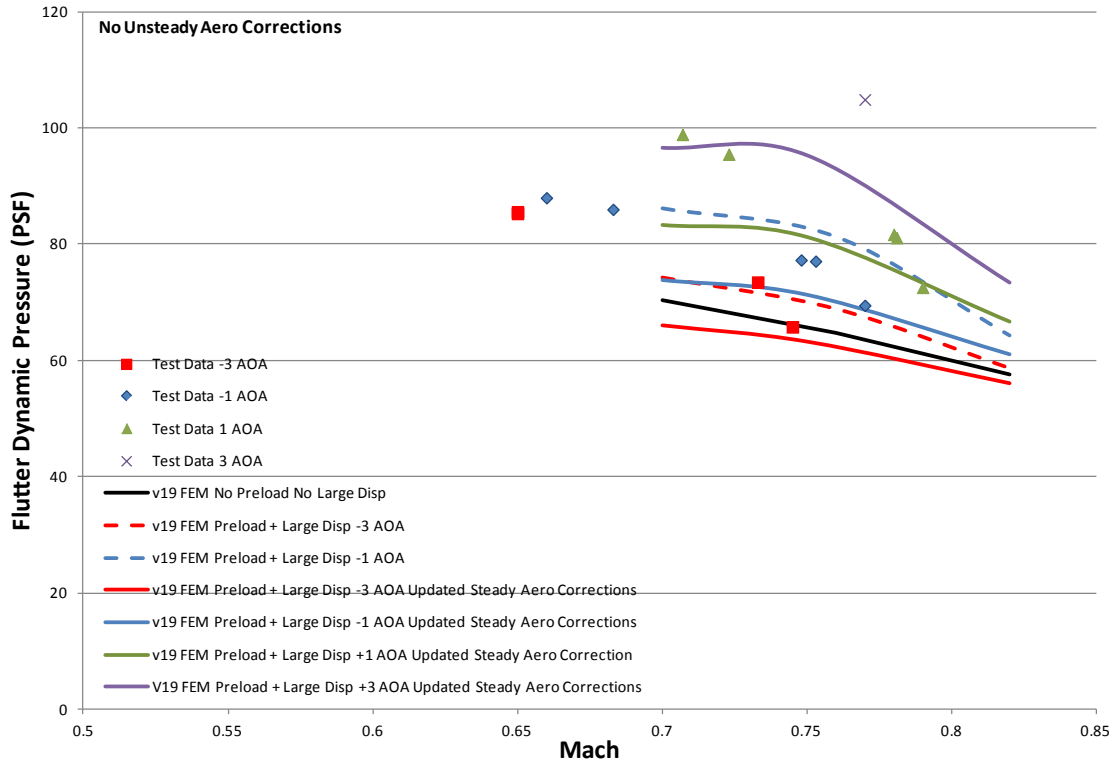


Figure 3.45 – Pre-Holiday Test vs. Analysis

3.6.6 Post-Holiday Flutter Points

Post-holiday alpha -3 flutter points are shown in Figure 3.46. At alpha -3 degrees, stable points were found at dynamic pressures above the unstable region. The pre-holiday and post-holiday flutter test results are shown in Figure 3.47. The trends are very similar. The post-holiday flutter speeds have increased as would be expected due to the increase separation between the primary modes post-holiday. The post-holiday analysis vs. test is shown in Figure 3.48. Again, angle of attack trend and minimum flutter speed modeled well.

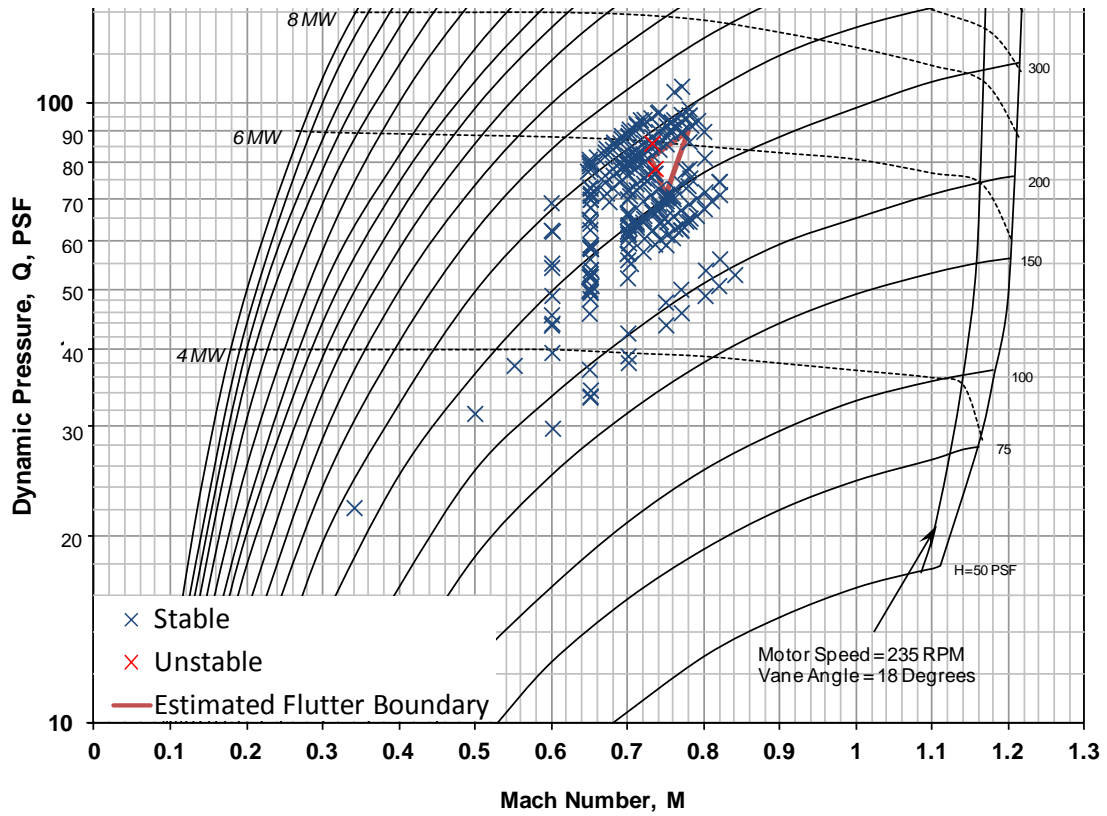


Figure 3.46 – Post-Holiday Flutter Points Alpha -3

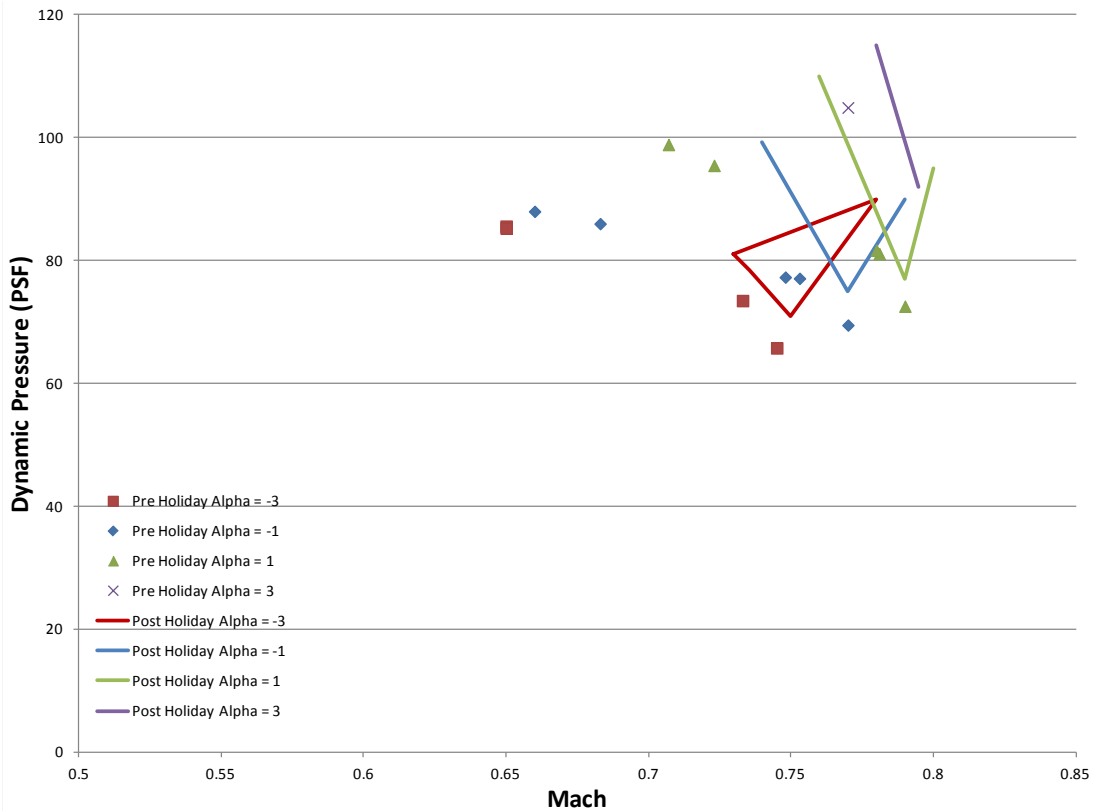


Figure 3.47 – Pre-Holiday vs. Post-Holiday Test Results

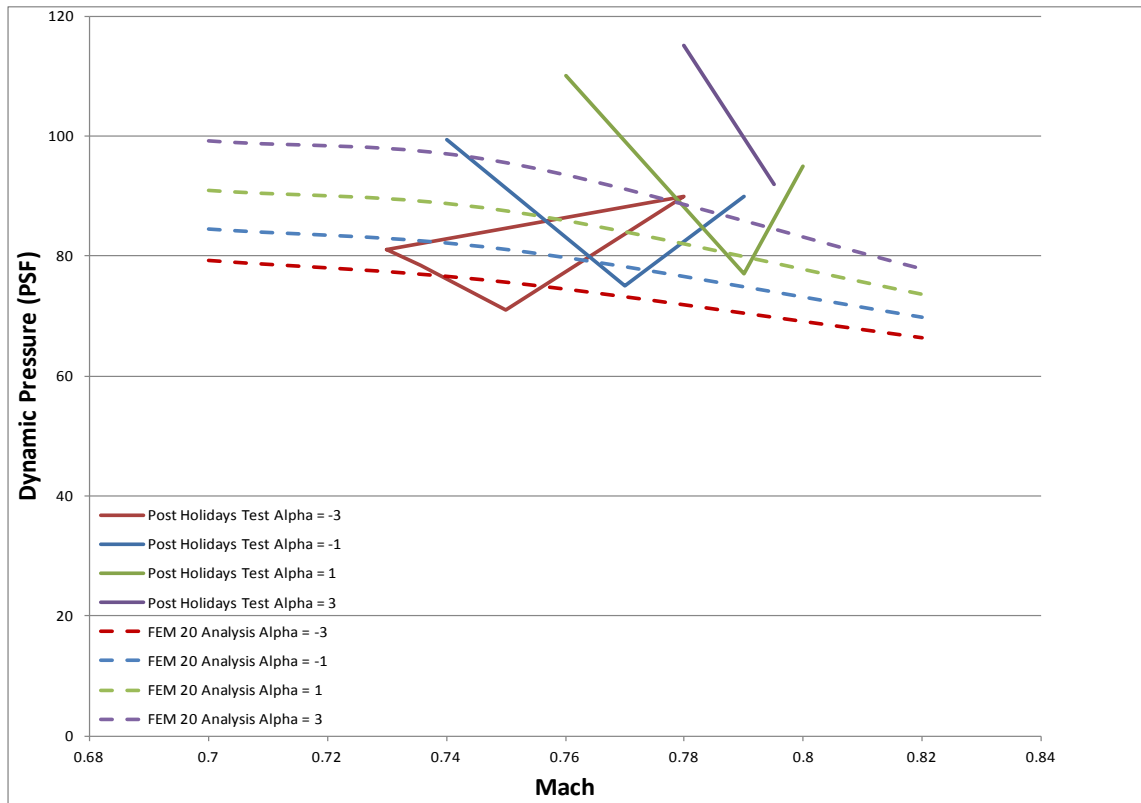


Figure 3.48 – Post Test Analysis vs. Test

3.6.7 Post-Holiday Stable Flutter Point Root Mean Square

The post-holiday stable flutter points root mean square (RMS) results for the wing tip, nacelle pylon, outboard strut, and wing root accelerometers were calculated and documented in Volume III of this report. The plots show a sharp rise in RMS as the flutter boundary is approached except the strut gage. The strut gage peaks at lower Mach numbers than the flutter boundary. The strut gage peaks between $M = 0.72$ to $M = 0.74$. The $\alpha = -3$ results show peak RMS values in the high Q region above the unstable region.

3.6.8 Post-Holiday Dwell Points Damping Estimates

Dwell time history decays were recorded at some 102 points, varying in Angle Of Attack (AOA), Mach, and/or dynamic pressure. A technique, scripted in Matlab, of fitting a set of damped sine waves to the decay response was employed to access modal damping. The analysis technique and results are documented in Volume III of this report. The results show the damping values getting smaller as the flutter boundary is approached. There is also a section of low damping that occurs at lower Mach numbers and Q than the flutter boundary. Damping then increases as the Mach and Q increases before reducing again before the flutter boundary. Some of the estimated values show small positive damping. It should be noted that all dwell points were stable and the positive damping means there was a limit cycle oscillation or the model was approaching flutter onset. These positive damping results illustrate the difficulty in estimating

damping using the test data. The values were positive in the time slice analyzed but the results would've been negative if a different time slice was chosen.

3.6.9 Closed Loop Flutter

Control laws for both system ID and FEM19 SSM were successful in suppressing flutter. The control laws were robust and suppressed flutter for a variety of Mach, dynamic pressures, and angle of attacks investigated. The post-holiday test results for $\alpha = -1$ are shown in Figure 3.49. The results show the stable closed loop test points going through the open loop unstable region and staying stable to much higher dynamic pressures.

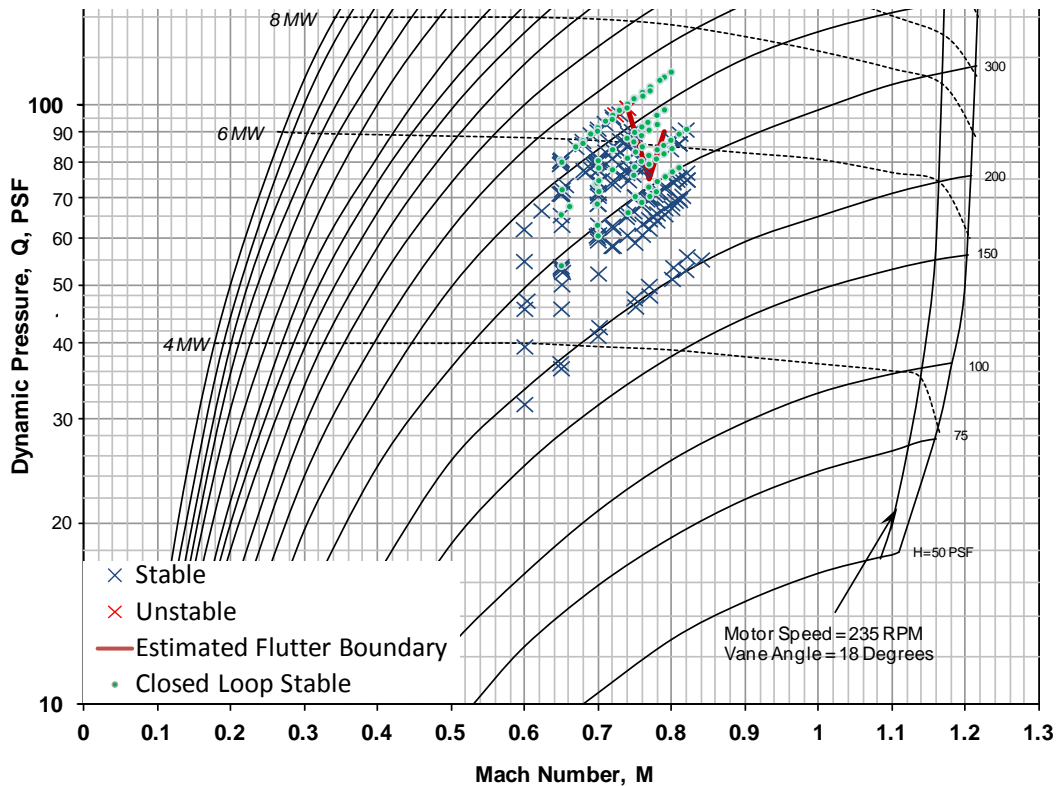


Figure 3.49 – Post-Holiday Test Results Alpha = -1

3.6.10 Closed Loop Gust

A comparison of open and closed loop gust response RMS for the inboard wing strain gage $M = .75$, $Q = 64$, and $\alpha = +1$, is shown in Figure 3.50. The gust responses were recorded as the airvane oscillation system (AOS) was swept from 0.5 to 13.5 Hz in 100 seconds, then a dwell at 13.5 Hz for 10 seconds, followed by a sweep from 13.5 Hz to 0.5 Hz in 60 seconds. The control laws used for the plotted results were based on the FEM19 SSM. The results show a peak response at the first bending mode and a smaller peak at the second bending mode. The second bending mode is a primary flutter mode and its gust response grows as the Mach and dynamics pressure approach the unstable region. The flutter suppression designed control laws show a large amount of gust load alleviation (GLA) at the second bending peak and a small amount of load alleviation

everywhere else. A PSD type gust analysis would show some amount of GLA since the resulting load is a result of input gusts at all frequencies. A tuned discrete gust critical at the flutter frequency would show significant GLA while a tuned gust critical at other frequencies would show a small amount of GLA.

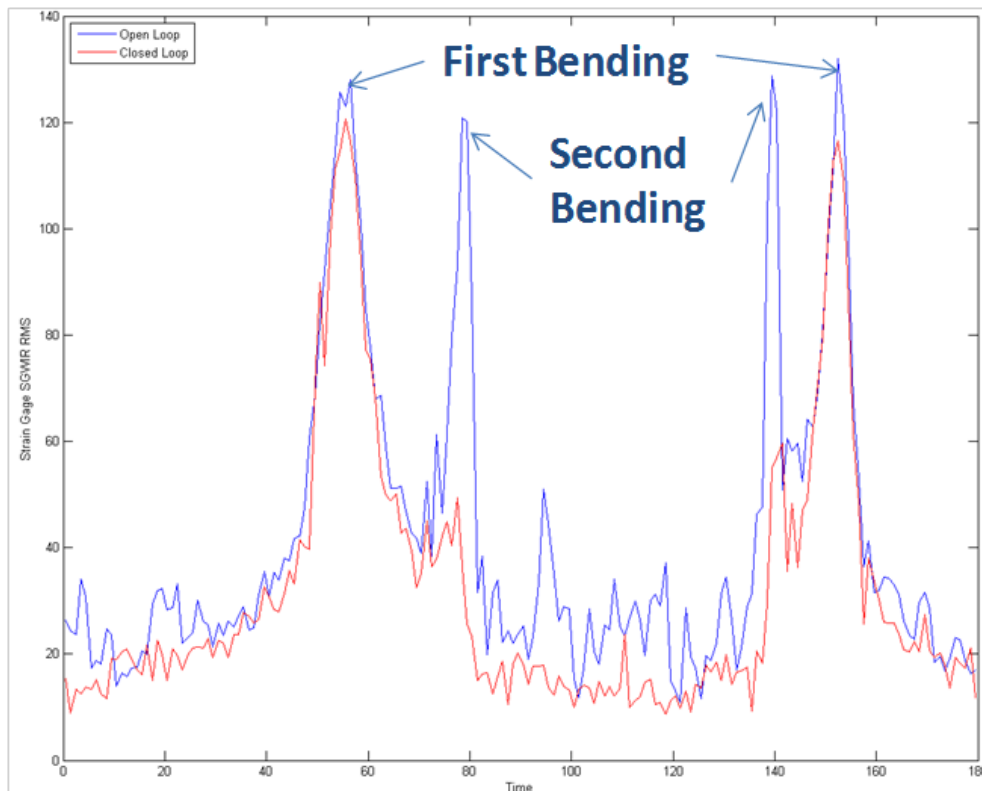


Figure 3.50 – Gust Response RMS Mach = .75, Q = 64, Alpha = +1

3.7 Conclusions

Analysis accurately predicted the flutter mechanism would be a coalescence of Mode 3 and Mode 4 at around 10 Hz. Flutter results showed significant variation with different angles of attack. Angle of attack variations are modeled fairly accurately using a method which accounts for preload and large displacement effects. The analysis using theoretical doublet lattice aerodynamics does not produce the sharp decrease in flutter speed with Mach but is fairly accurate in predicting minimum flutter speed. These predictions may not be accurate for different TBW vehicle geometries and/or aerodynamic configurations. No evidence was found of strut buffet causing vibration problems. Flutter suppression was successfully demonstrated using control laws derived from test system ID data and analysis models. Even though the control laws were designed for flutter suppression, the control laws do provide some gust load alleviation as well.

4.0 Advanced Aero Technologies Experiment

A wind tunnel test with a turbulent and a laminar airfoil was conducted in the NASA Langley 0.3m TCT facility. The test was two dimensional. The turbulent airfoil was for reference. The laminar airfoil was from the mid span region of the SUGAR strut braced wing configuration. The intent was to measure the airfoil characteristics of the laminar flow airfoil and use the information to create a data base that could be used to estimate performance of configurations that use laminar flow airfoils.

Pressure, force, and moment data from the test did not compare well to expectations. Testing in such a small tunnel relied on adaptive tunnel walls to conform to the streamlines around the model. This Wall Adaptation System (WAS) appeared to have difficulty converging to the streamlines when airflow became transonic.

Another goal was to demonstrate laminar flow drag benefit and verify a laminar flow design. Some laminar flow was shown to be present using Temperature Sensitive Paint, however wakes from the small regions of laminar flow mixed with the wakes from turbulent regions before arriving at the wake rake probes aft of the model. This made measuring the drag reduction for the laminar region difficult.

4.1.1 Test Preparation

In addition to the two face-to-face meetings between Boeing and the tunnel facility personnel in 2012, all test preparation was handled by scheduled telephone conversations and emails throughout the year. Planning for tunnel conditions, rake positions, and run rates was based on past experiences of the tunnel facility personnel. Alpha schedules, Mach and Reynolds Number requirements were based on airplane requirements. Temperature sensitive paint and data reduction requirements were handled by the tunnel facility.

4.1.2 Model Design and Fabrication

The wind tunnel models were designed and fabricated by Micro Craft in Tullahoma, TN. Inputs from Boeing and the tunnel facility personnel were solicited for the design. The 7 inch chord was slightly larger in size compared to past models that had been tested in the tunnel facility. The slightly larger scale allowed for the correct dimensioning of the trailing edge thicknesses of both airfoils and allowed the installation of a trailing edge pressure tap. The model was machined from 13-8 stainless steel. A non-removable lower surface cover plate was employed to allow the routing of the surface pressure orifices used to calculate aerodynamic characteristics. An orifice diameter of 0.020 was chosen to minimize aerodynamic interference. Additionally, all cover plate fasteners were inserted from the lower surface of the model to also minimize interference on the upper surface.

4.1.3 Testing

The test plan was set up for three airfoil configurations based on two airfoil geometries. The first configuration was a reference airfoil designed with pressure gradients that are typical of airfoils with a turbulent boundary layer flow over nearly the entire chord. This airfoil was designated as T1. The T1 airfoil was only tested with transition fixed using glass beads. Transition would likely take place on the forward portion of the airfoil even without the glass beads but the transition position could vary with Mach or angle-of-attack. The beads were added to ensure that transition always occurred at the same location. The second and third configurations were based on an airfoil specifically designed for laminar flow. This airfoil was designated as L1. At the cruise lift coefficient the boundary layer flow on the L1 airfoil was expected to remain laminar from the leading edge aft to the shock due to a favorable pressure gradient. The L1 airfoil without boundary layer transition trips was the second planned configuration. The L1 airfoil with fixed transition trips was the third planned configuration. The T1 and L1 airfoils are similar. The L1 airfoil was based on the T1 airfoil. The three dimensional SUGAR truss braced wing uses the L1 airfoil for a significant percentage of its span.

The wind tunnel test took place in the 0.3 Meter wind tunnel at NASA Langley. The test section of the 0.3 Meter wind tunnel is 13 inches square. The airfoil models create a two dimensional shape by spanning the test section wall to wall with the same airfoil. The T1 and L1 airfoil chords are 7 inches long. The decision to use such a large model in a small test section was based on the wind tunnels ability to adapt the shape of the ceiling and floor of the wind tunnel to the shape of the streamlines that exist around the airfoil. The ceiling and floor are supported by 21 jacks that can be moved by the Wall Adaptation System (WAS) in an iterative manner until the shape of the ceiling and floor converge to the theoretical shape of streamlines in free air. The jacks have a maximum displacement of plus or minus three inches. In the NASA 0.3 Meter bookkeeping system this test was Test Number 559. Installation of one of the airfoil models in the tunnel is shown in Figure 4.1.

The airfoil models are not mounted on a balance. Lift, drag, and pitching moment data are obtained from pressure data. Airfoil lift and pitching moment were integrated from a chordwise distribution of static pressure taps. The pressure taps were spaced so close to each other in the chordwise direction that they were split into three rows to allow more room between the taps. One of the pressure rows is in the center of the airfoil model, 6.5 inches from each of the tunnel walls. The other two rows are 1 inch away on either side of the center row.

Drag data is obtained from a wake rake, illustrated in Figure 4.2. The wake rake consists of an arm with 9 total pressure probes that span half of the tunnel. Probe 1 is in the center of the tunnel and the other 8 probes are equally spaced from the center of the tunnel to the wall where the arm is mounted. The wake arm can be moved up and down in very small increments to map

the wake at 9 different locations. The total pressure wake rake is located 1.5 chord lengths downstream of the airfoil model trailing edge.



Figure 4.1 – Installation of 2D Airfoil Model in 0.3 meter Transonic Cryogenic Tunnel

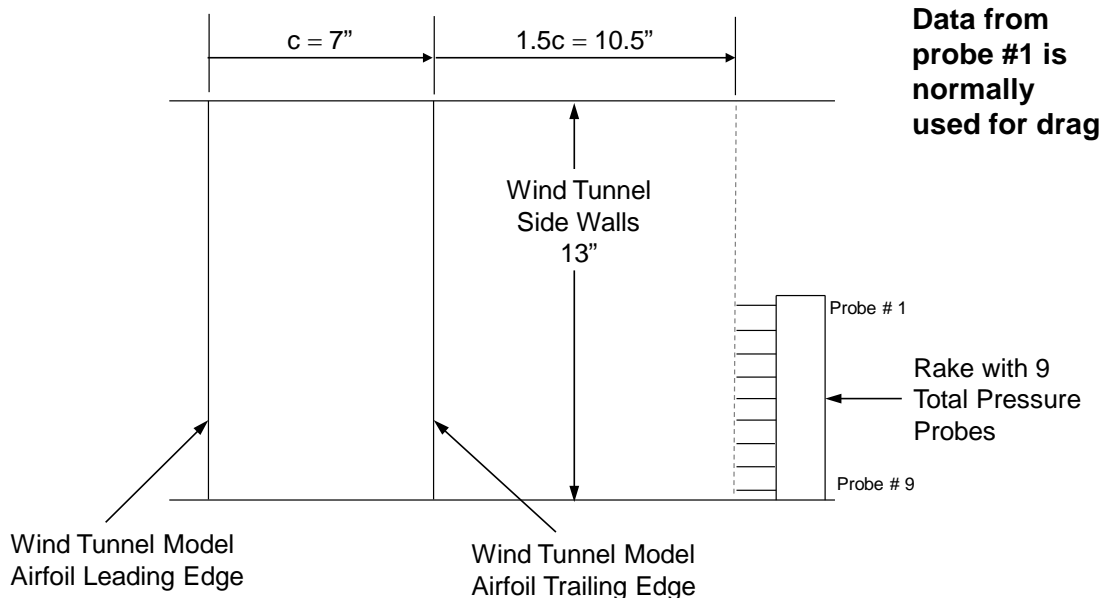


Figure 4.2 – Wake Rake Arrangement

The wind tunnel test was unintentionally divided into two entries. The first entry took place in late August of 2012. The model was installed and three data runs were completed on August 22nd and 23rd before testing was halted due to tunnel anomalies involving the wall adaptation system. It was determined that jack 7, a ceiling unit near the leading edge of the model, had seized. Another problem found during inspection was that the ceiling was not flat when all the jacks were commanded to be at their zero location. The test was stopped while NASA determined a solution.

The test resumed in mid-October after NASA completed a “tune-up” of the tunnel by servicing and re-aligning many of the ceiling jacks. The second entry went much smoother. The Wall

Adaptation System worked much better, but still caused problems on occasion. Forty two more data runs were completed during the second entry from October 10th through November 8th. The total number of runs during the test was 81, but many of these were not data runs.

4.1.4 Test Results and Analysis

0.3 Meter Lift and Drag Measurements

CFD data was compared to the wind tunnel data to check for data quality. The CFD data was obtained from a 2D Bauer-Garabedian full potential code with a Cohen-Reshotko laminar boundary layer and a Nash-Macdonald turbulent boundary layer. This Garabedian code (Program H) has compared well with wind tunnel data from past 2D airfoil tests. The CFD and wind tunnel data were expected to be close. At subsonic conditions the airfoil pressure distributions predicted by CFD and measured in the wind tunnel compare well, however the comparison is not as close at transonic conditions (due to Mach number or lift coefficient). Figure 4.3 shows the difference in shock strength and location between CFD and the wind tunnel at two lift coefficients at Mach 0.70. At the low lift coefficient the pressures compare reasonably well. At the high lift coefficient the shock in the wind tunnel is significantly stronger and further aft. A likely source of the problem with the pressure distribution comparisons is the position of the wind tunnel walls; apparently the walls adapt well at subsonic conditions but seemingly not as well at transonic conditions.

A comparison of lift curves between CFD and the wind tunnel raises additional questions about the wall adaptation system. Figure 4.3 contains a comparison of lift curves from the 0.3 Meter wind tunnel and CFD at three different Mach numbers. At a given angle-of-attack the lift in the 0.3 Meter wind tunnel is always greater than CFD. Some of this is caused by the shock strength problem, but at Mach 0.5 the airflow is subsonic and the wind tunnel lift curve is still shifted. The reason for the mismatch has not been found but the problem could be related to upwash imposed by the Wall Adaptation System. Figure 4.4 shows how the walls adapted for the T1 airfoil at a Mach number of 0.72 and a C_L of 0.822. The average slope of the upper and lower wall in front of the model could be regarded as an upwash angle. For this condition the average slope or upwash was about 6 degrees. This imposed upwash angle is high compared to typical values and may be the reason for the upward shift of the lift curves.

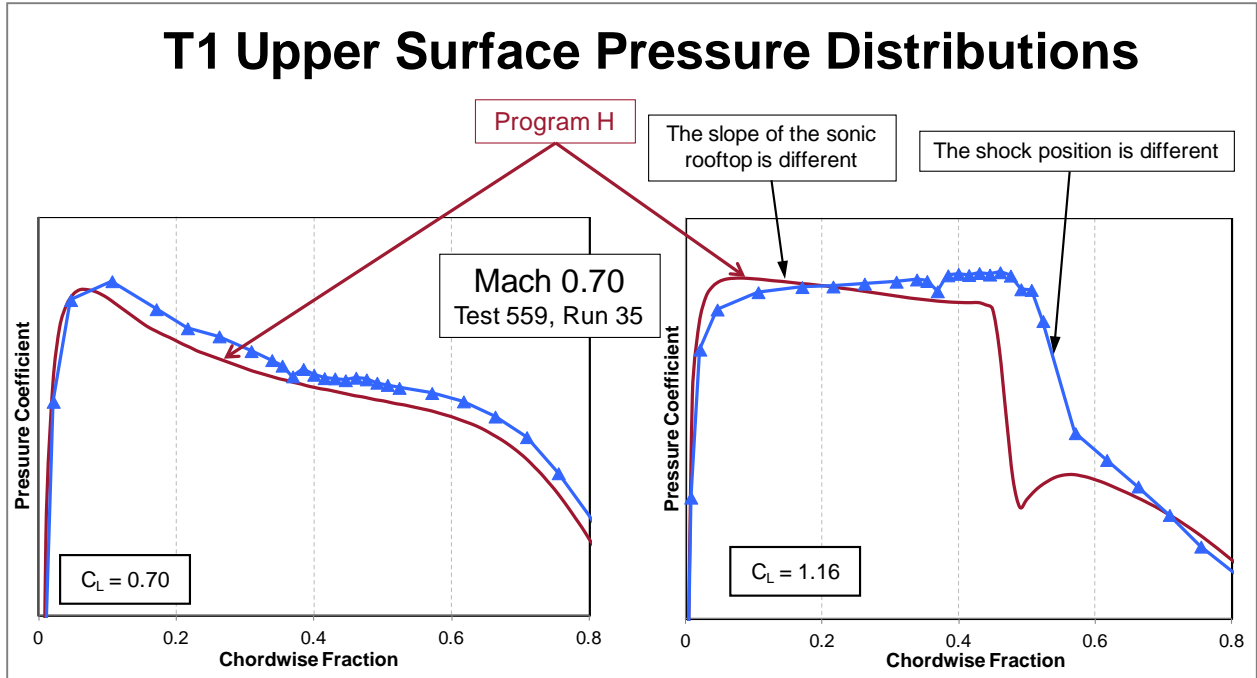


Figure 4.3 – Airfoil T1 CFD and Wind Tunnel Upper Surface Pressure Distributions

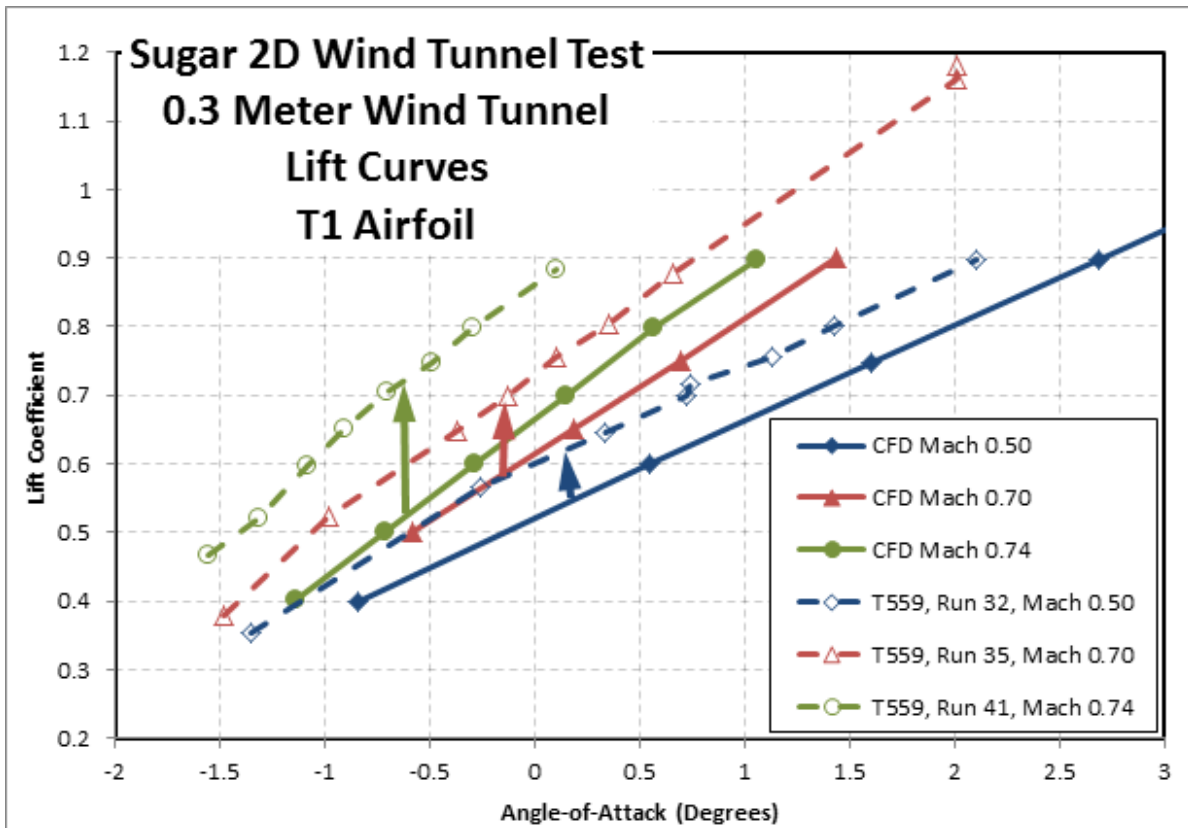


Figure 4.4 – Lift Curve Comparison, T1 Airfoil

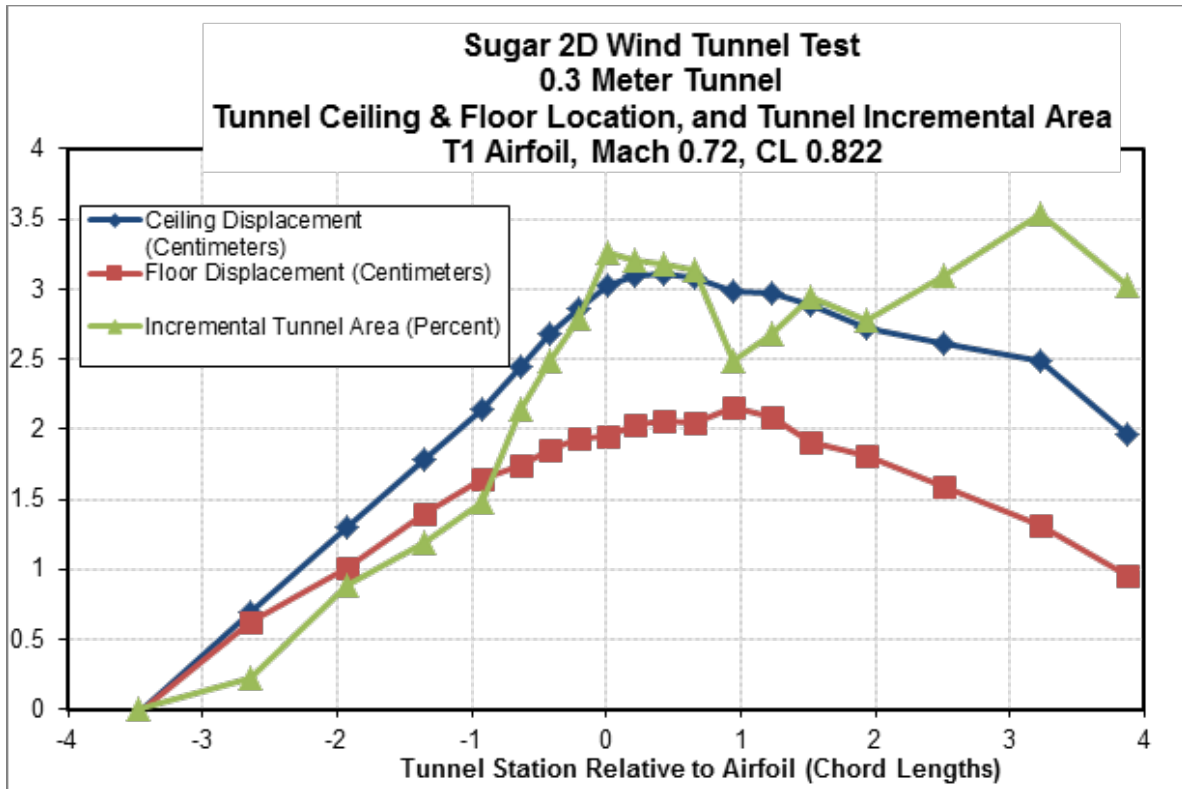


Figure 4.5 – Tunnel Ceiling and Floor Displacement

The shock strength problem is also evident in the drag polars at high lift coefficients. A comparison of drag polars for Mach 0.5, 0.7, and 0.74 is shown in Figure 4.6. The drag from the 0.3 Meter wind tunnel and CFD compare well at low Mach numbers and low lift coefficients, but at conditions where a strong shock exists the drag in the wind tunnel is too large.

The excessive shock strength in the wind tunnel also affects the drag divergence Mach number of the airfoil at constant lift coefficient. The performance of the airfoil in the 0.3 Meter wind tunnel was clearly inferior to the CFD prediction, as shown in Figure 4.7.

The lift coefficient where shock induced flow separation becomes significant is referred to as the buffet onset lift coefficient. The trend of buffet onset lift coefficient with Mach number is called the buffet onset boundary, which may limit the maximum cruise altitude of an aircraft. Two common methods to predict buffet onset lift coefficient involve the chordwise location of the shock and the divergence of the airfoil trailing edge pressure with increasing lift coefficient. Using these methods with data from the 0.3 Meter wind tunnel and from CFD produced the buffet onset boundaries for the L1 airfoil shown in Figure 4.8. It can be seen that the buffet onset boundary from the 0.3 Meter wind tunnel data is significantly lower than the CFD prediction.

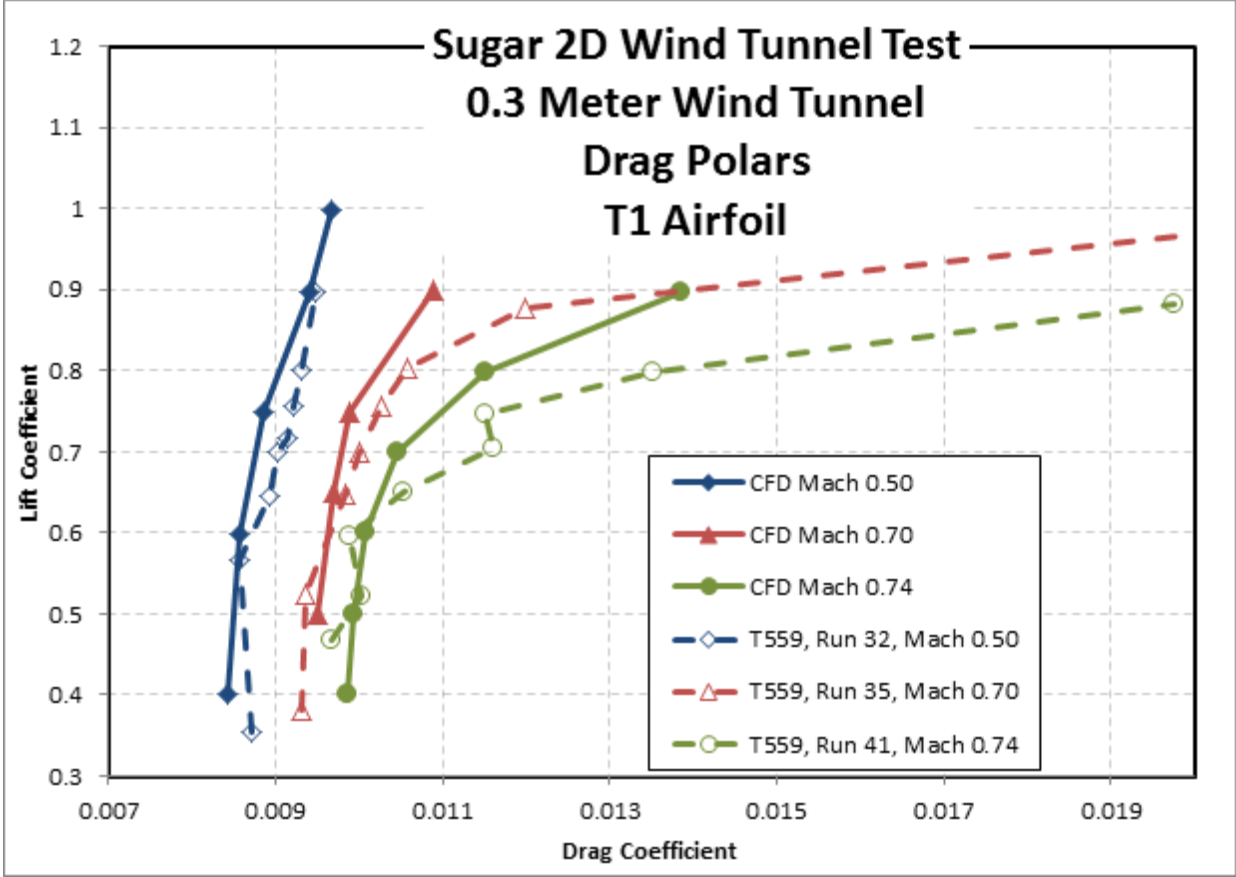


Figure 4.6 – Drag Polar Comparison, T1 Airfoil

Airfoil T1 Drag Divergence Compared to Program H

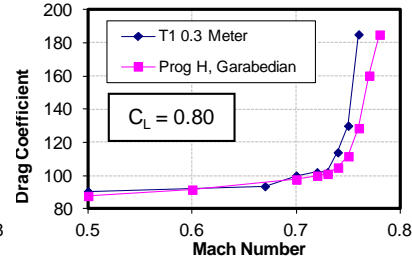
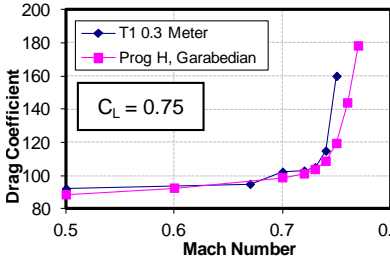
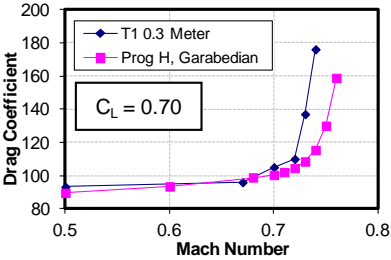
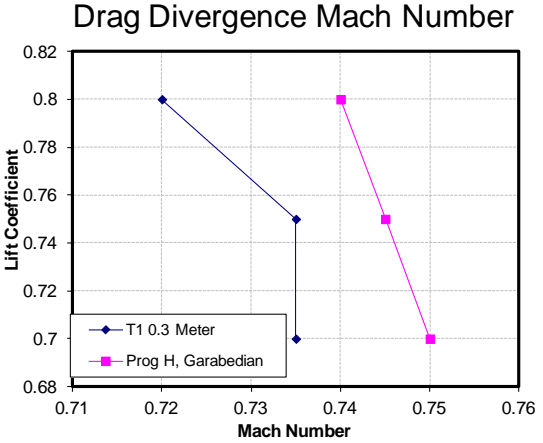


Figure 4.7 – Airfoil T1 Drag Divergence Compared to CFD

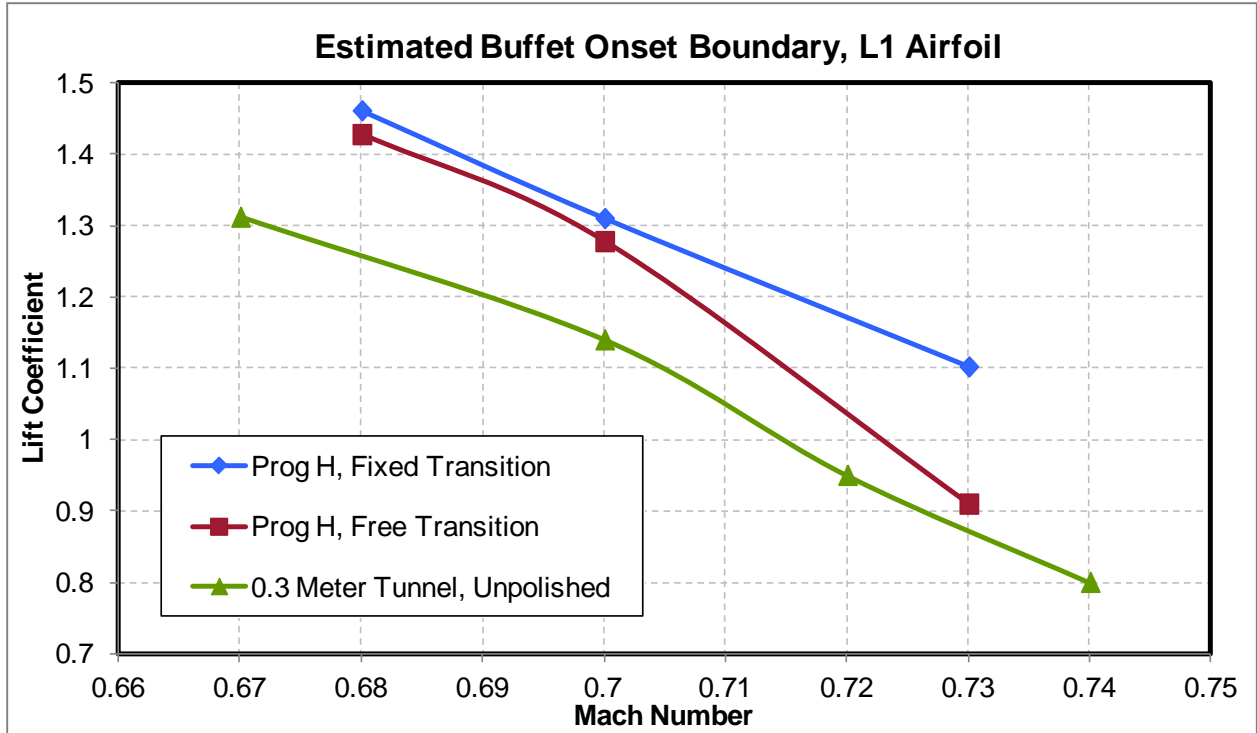


Figure 4.8 – Airfoil L1 Estimated Buffet Onset Boundary

Drag data from all 9 of the wake rake probes were compared to evaluate the consistency of the drag measured across the span. Figure 4.9 shows a loss of two-dimensionality of the flow in the 0.3 Meter wind tunnel as the shock gains strength with increasing lift coefficient. The high drag from Probe 9 may indicate that the airflow on the tunnel side walls has separated. The flow in the wind tunnel is beginning to have a three dimensional characteristic at high lift coefficients which invalidates the concept of two-dimensional sectional aerodynamic characteristics.

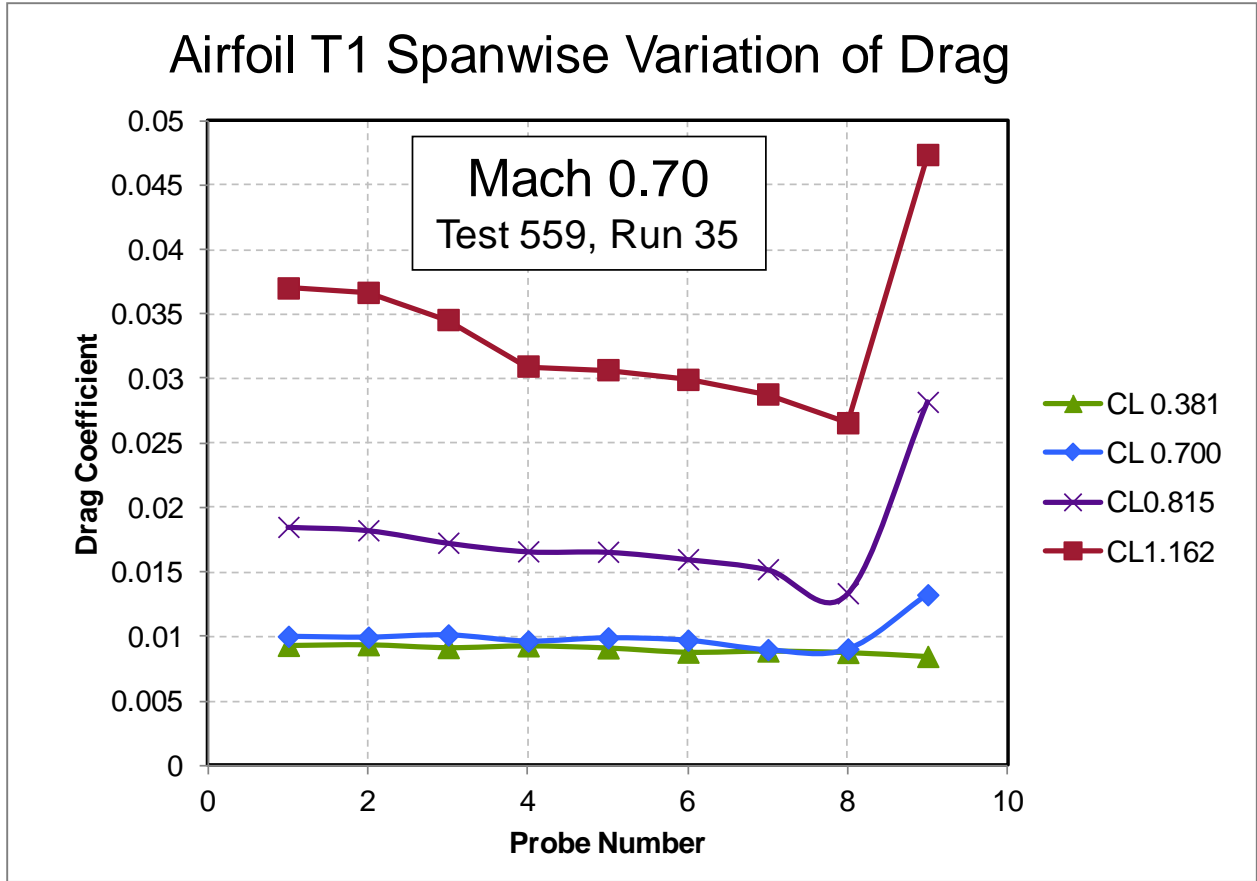


Figure 4.9 – Spanwise Variation of Drag

Figure 4.10 shows a hysteresis problem with the 0.3 Meter wind tunnel lift and drag data. The measured forces coming back down in angle of attack do not match the data going up in angle of attack. Inadequacy of the Wall Adaption System could be the cause of the hysteresis.

Wind Tunnel Lift and Drag Hysteresis (T1 airfoil, Run 35, Mach 0.70)

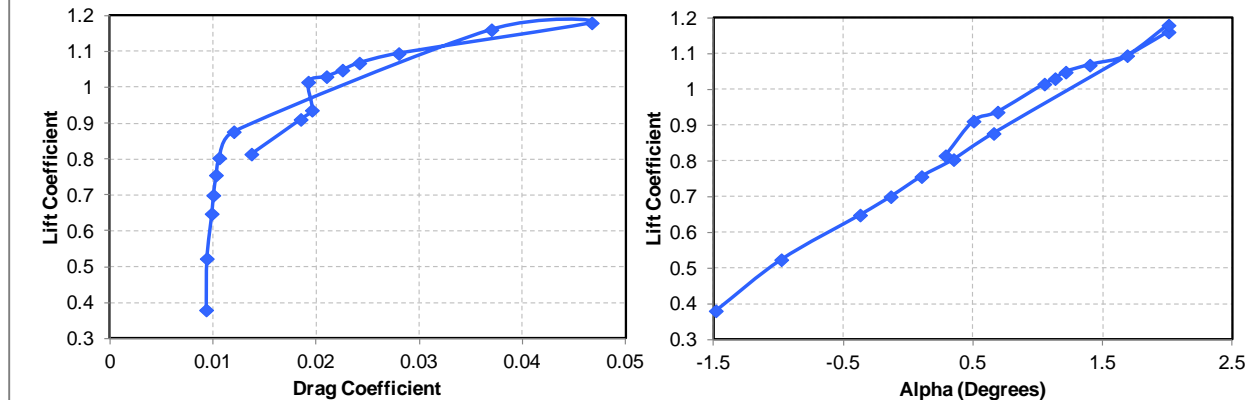


Figure 4.10 – Wind Tunnel Lift and Drag Hysteresis

Results from two dimensional transonic airfoil testing in the 0.3 Meter wind tunnel cannot be used with confidence primarily because of the problem with excessively high recompression shock strength. One of the main reasons for testing is to find the limits of airfoil performance. This performance cannot be properly measured if the shock strength is incorrect. Even increments between airfoils cannot be used because the wall adaptation system may alter shock strength on one airfoil more than on another airfoil.

Laminar Flow

Some laminar boundary layer flow was achieved on the L1 airfoil and confirmed using Temperature Sensitive Paint (TSP). Laminar flow is indicated by the dark regions in Figure 4.11. Laminar flow made it back to the shock for a small portion of the airfoil in the middle of the picture. The results shown in Figure 4.11 were only achieved after the leading edge was polished; initial runs with TSP did not indicate any laminar flow. The TSP paint felt smooth after application but apparently it was not smooth enough to support laminar flow until it was polished.

Results from the wind tunnel did not indicate any drag reduction due to laminar flow on the L1 airfoil. Laminar flow should have resulted in a large drag reduction. The drag for the T1 and L1 airfoils is shown in Figure 4.12, Figure 4.13 and Figure 4.14. CFD predictions are shown in the left hand plots. Drag measured in the wind tunnel is shown in the right hand plots. The CFD data predicts no drag reduction for L1 if both T1 and L1 are fully turbulent, but a large drag reduction for L1 if it is laminar. The wind tunnel results do not show any drag reduction for L1 before and after the leading edge was polished.

The absence of drag reduction due to laminar flow is likely due to the small area where laminar flow was achieved and the mixing that occurred before the airflow reached the wake rake probes.

Referring back to Figure 4.11 it can be seen that the boundary layer at the leading edge is laminar, but as the airflow moves aft most of this begins to transition to a turbulent boundary layer indicated by the disappearing dark wedges of laminar flow. Fully laminar flow back to the shock location only extends over about 20% of the span in the middle of the picture where the dark region stops in more of a straight line. By the time the airflow got to the wake rake station the boundary layer wakes from the laminar and turbulent regions were fully mixed. As shown in Figure 4.2, the wake rakes were 1.5 chords downstream of the airfoil trailing edge, and the dark wedges of laminar flow shown in Figure 4.11 faded away before even reaching the trailing edge of the airfoil.

Note that only about half of the model span is shown in Figure 4.11. The half span is 6.5 inches so the extent of fully laminar flow is only about 1.3 inches wide. It is possible that laminar flow was not achieved near the sides of the tunnel due to interference from the tunnel walls, and that laminar flow was not achieved in the center of the tunnel due to interference from the pressure taps on the model.

Laminar flow did affect the wakes measured in the wind tunnel. The drag levels calculated from all the wake rakes are shown in Figure 4.15 for one condition with and without laminar flow. There is a variation in the drag that is a function of the where the probes are located along the trailing edge, and the variation in drag is different with and without laminar flow. The largest region of laminar flow was in front of Probes 4 and 5 which measured an increase in drag, however Probes 7 and 8 measured a drag reduction. It is possible that the smaller wakes from the laminar region moved outboard as they moved aft of the model trailing edge. More investigation is needed. Note that the laminar run was Run 77 with the leading edge polished, indicated by transition off in Figure 4.15. The drag value that is typically used is from probe 1 in the center of the tunnel.

Run 67, Point 1709
 (M = 0.70, R = 10x10⁶, AOA = -0.74, C_l = 0.67)

- Darker regions indicate laminar flow
- As the laminar and turbulent regions mix wedges are formed with angles of about 7 degrees
- Pressure taps and tunnel walls cause the airflow to become turbulent

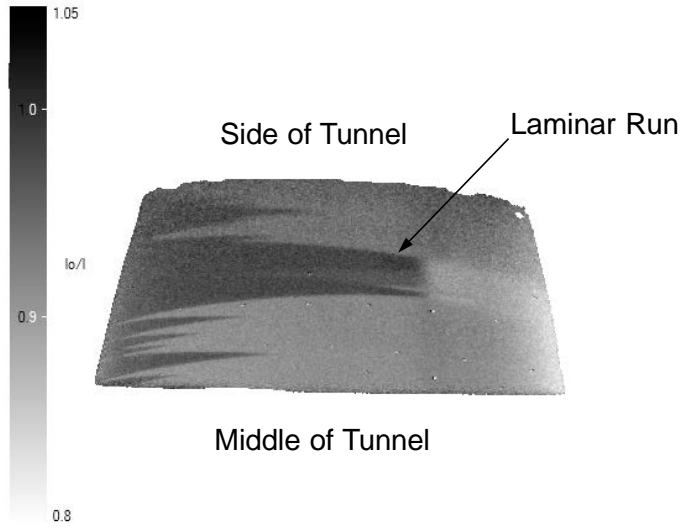


Figure 4.11 – Temperature Sensitive Paint Photo

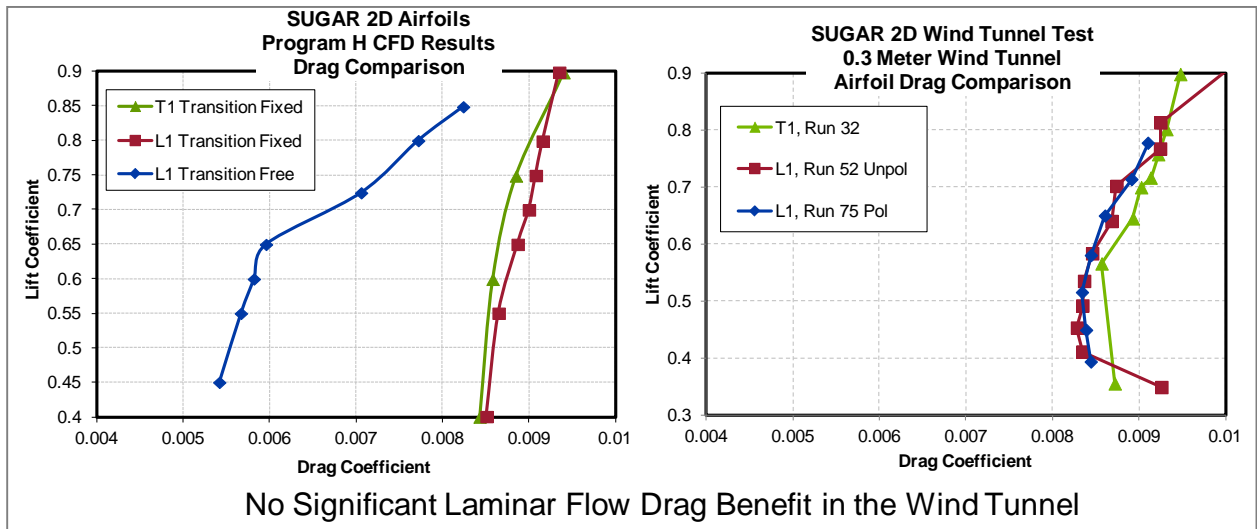


Figure 4.12 – CFD and Wind Tunnel L1 versus T1 Drag Comparison – Mach 0.50

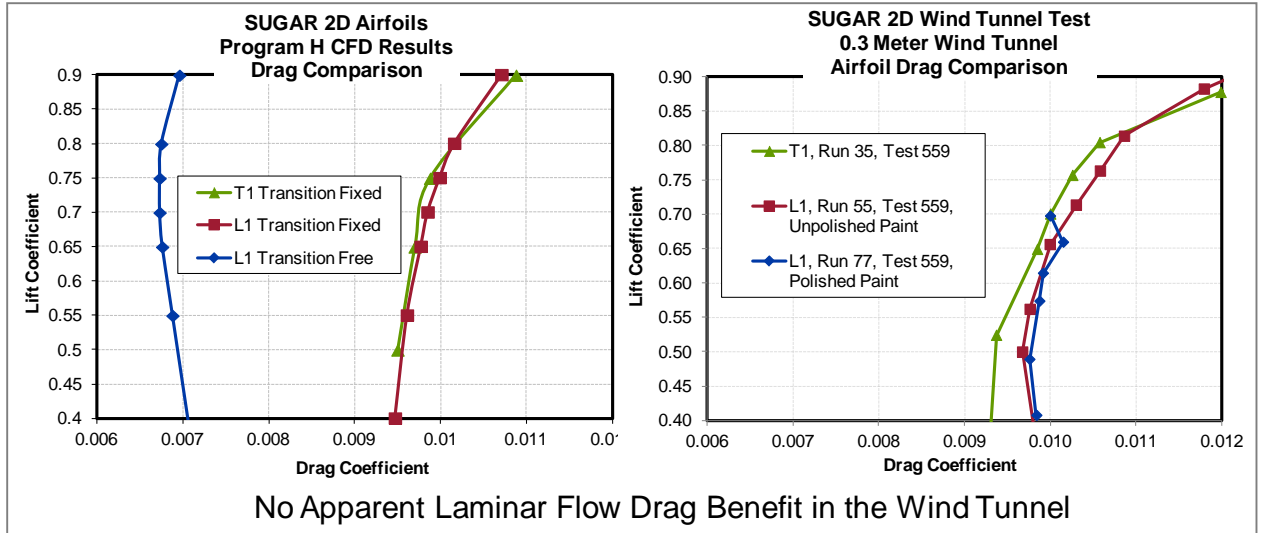


Figure 4.13 – CFD and Wind Tunnel L1 versus T1 Drag Comparison – Mach 0.70

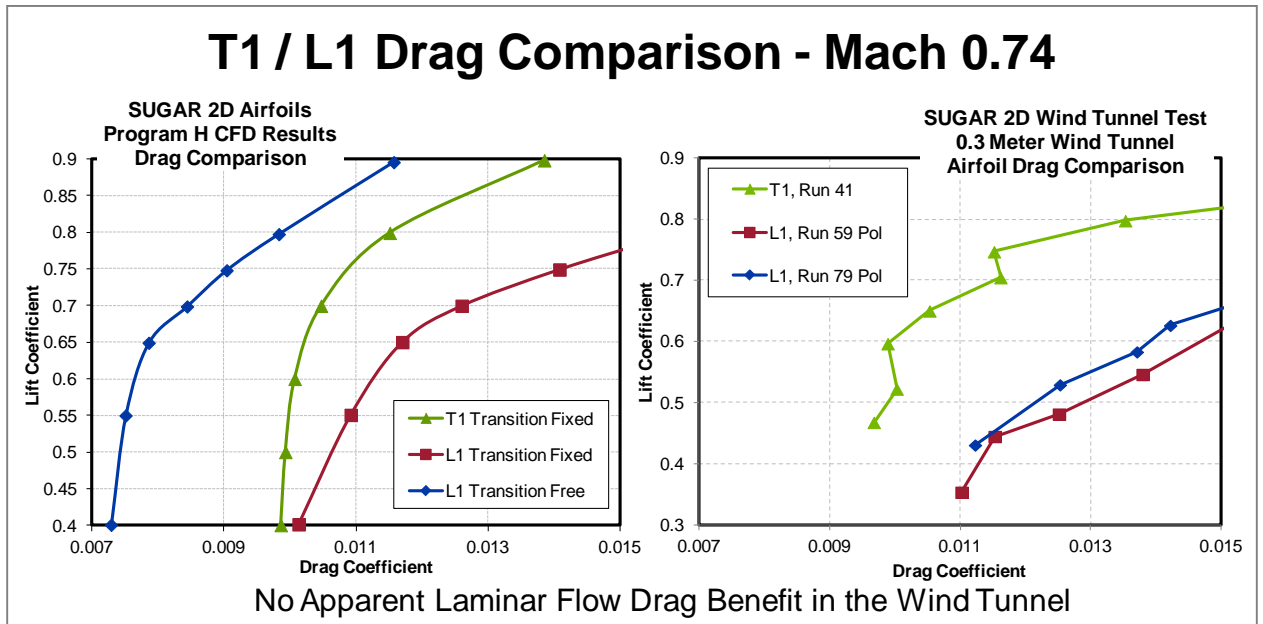


Figure 4.14 – CFD and Wind Tunnel L1 versus T1 Drag Comparison – Mach 0.74

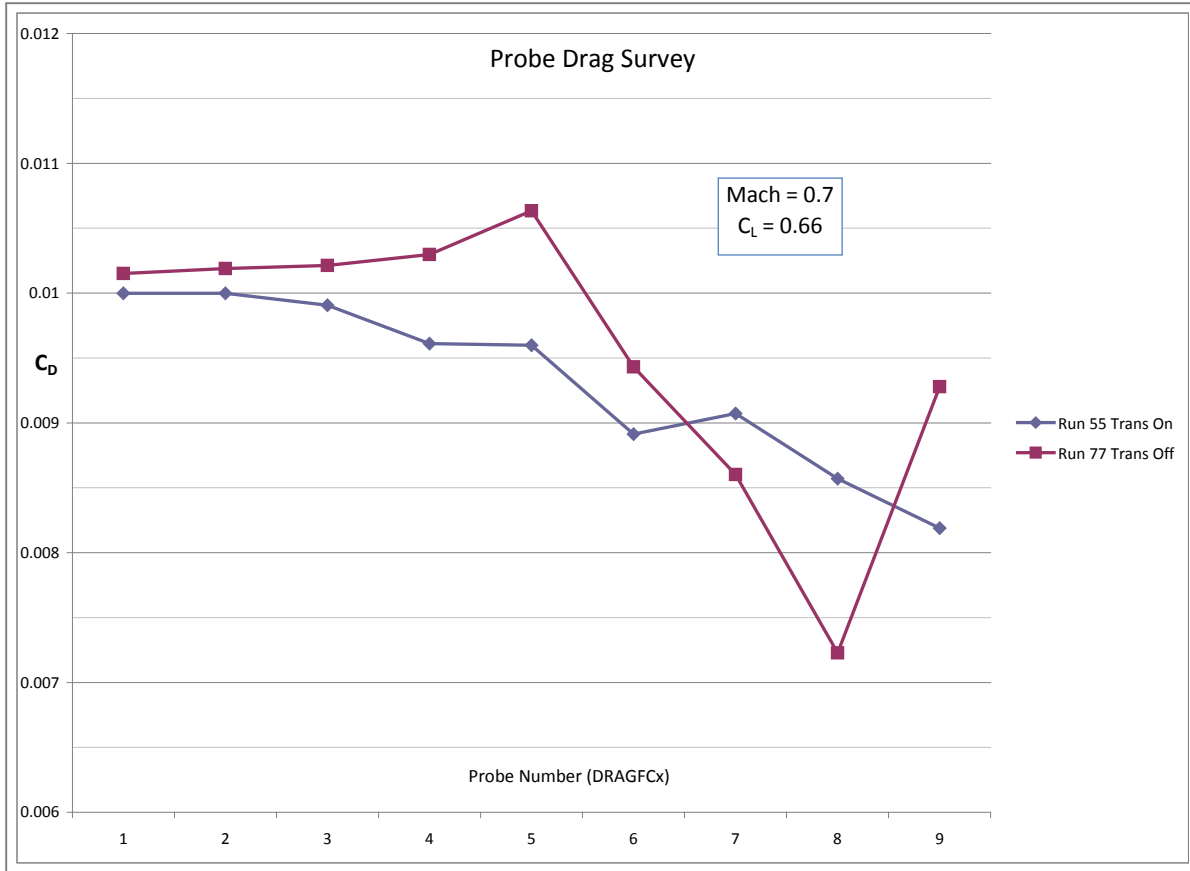


Figure 4.15 – Airfoil L1 Drag Comparison for All Probes

4.1.5 Recommendations

A second entry in the in the 0.3 Meter wind tunnel was not recommended primarily because of the problem with excessively strong shocks in the tunnel. The tunnel is small enough that a strong shock likely chokes the airflow in half of the tunnel, and the wall adaptation system does not have the sufficient capability to compensate.

Another reason to recommend against a second entry is the difficulty in achieving fully laminar flow over a large enough spanwise region to be able to measure the drag benefit of laminar flow. An airfoil model without any pressure taps may achieve fully laminar flow over a sufficiently large enough region in the mid span of the model, but lift and pitching moment data would not be obtained.

One proposal is to perform a “tune-up” for the floor jacks similar what was done to the ceiling jacks last September. It is felt that a “tune-up” might make the tunnel work more efficiently; the wall adaptation system may work faster. However, the problem with shock strength will still be present.

5.0 Summary

The team has made significant accomplishments in all areas of truss braced wing technology development.

Working with the Georgia Tech/Virginia Tech multi-disciplinary optimization (MDO) environment has led to a successful wing planform optimization. This helped define the geometry of the 765-095-RD SUGAR High truss braced configuration that was then detailed by Boeing. This configuration was used for a variety of analyses including low speed and high speed aerodynamics, and a detailed FEM. The geometry was also used as the starting point for work on the update to the hybrid electric configuration and acoustic analysis in Task 2.2.

This geometry was also used to provide airfoil shapes for the testing in the NASA TCT facility (Task 3.2) that was eventually completed in November 2012 after some test difficulties. The geometry and the completed FEM analysis were used by NextGen to design the aeroelastic model that was tested in 2013 and 2014 in the NASA TDT facility (Task 3.1).

All analysis tasks were completed, performance and sizing was updated, technology development roadmaps were updated, the aeroelastic wind tunnel test was completed, and all results were documented in this final report and the aeroelastic test report (Volume III – Truss Braced Wing Aeroelastic Test Report).

5.1 Technical Results

Fuel burn and energy use is reduced by 54% compared to the SUGAR Free current technology Baseline (Goal 60%). The Phase II SUGAR High aircraft is better than Phase I (39% reduction in Phase I), mostly due to lighter wing structure. Use of the unducted fan version of the engine reduces fuel burn and energy by 56% (Goal 60%).

Airport compatibility analysis establishes feasibility of a folding wing aircraft without strong adverse impact on airport usage.

Aeroelastic impacts on TBW design are manageable and updated wing weight is less than assumed in Phase I. Analysis accurately predicted the flutter mechanism. Flutter results showed significant variation with different angles of attack. Angle of attack variations are modeled fairly accurately using a method which accounts for preload and large displacement effects. The analysis using theoretical doublet lattice aerodynamics does not produce the sharp decrease in flutter speed with Mach but is fairly accurate in predicting minimum flutter speed. These predictions may not be accurate for different TBW vehicle geometries and/or aerodynamic configurations. Flutter suppression was successfully demonstrated using control laws derived from test system ID data and analysis models.

5.2 Conclusions

- SUGAR High has made good progress and is coming close to NASA emissions and fuel burn goals.
- The unducted fan version of the engine, when integrated on the TBW airframe, provides additional improvements over the turbofan configuration.
- High span folding wings are likely to be compatible with most airports of interest. They pose surmountable operational and limited infrastructure challenges.
- Although Mach 0.7 minimizes fuel burn, higher cruise speed should be considered for its increase in productivity and thus higher economic value.
- Flutter analysis of TBW designs need to include pre-load and large displacement non-linear effects.
- Flutter suppression was successfully demonstrated on a TBW configuration.

5.3 Recommendations

Implement the next steps in TBW technology development plan, including:

- Conduct a wing design update. Analyze and design features of strut, jury, and attachment joints to meet structural criteria and aerodynamic drag targets. Consider both $M=0.7$ and 0.8 designs.
- After the design update, conduct high speed and low speed aerodynamic wind tunnel tests.
- Investigate higher fidelity unsteady aeroelastic tools to better predict the flutter boundary of TBW design.
- Conduct initial planning for a possible TBW demonstrator aircraft.

References

1. **Bradley, Marty K. and Droney, Christopher K.** *Subsonic Ultra Green Aircraft Research: Phase I Final Report*. s.l. : NASA, 2011. CR-2011-216847.
2. **Bradley, Marty and Droney, Christopher K.** *SUGAR Phase II: N+4 Advanced Cocnept Development*. s.l. : NASA, 2012.
3. **Federal Aviation Administration.** Special Conditions: Airbus Model A380-800 Airplane, Crashworthiness. Docket No. NM319; Special Conditions No. 25-321-SC.
4. —. Electronic Code of Federal Regulations. *Government Printing Office*. [Online] January 11, 2012. [Cited: January 13, 2012.] http://ecfr.gpoaccess.gov/cgi/t/text/text-idx?c=ecfr&sid=96784884300b9846bc7a9ce5f552f5d3&tpl=/ecfrbrowse/Title14/14cfr25_main_02.tpl. Part 25.
5. **Aerodrome Design and Operations.** 2009. Vols. Annex 14, Volume 1, Fifth Edition.
6. **Federal Aviation Administration.** "*Airport Design*" *Advisory Circular*. s.l. : U.S. Department of Transportation, Sep. 29, 1989. AC 150/5300-13.
7. —. *Optimization of Airspace and Procedures in the Metroplex*. s.l. : FAA, 2011. NG10_041.
8. **Development of Framework for Truss-Braced Wing Conceptual MDO.** Bhatia, M., Mason, W. H., Schetz, J. A., and Kapania, R. K. Orlando, Florida : AIAA, 2010. 51st AIAA/ASME/ASCE/AHS/ASC Structures, Structural Dynamics, and Materials Conference.
9. **Aerospace Systems Design Laboratory, Georgia Institute of Technology.** *Aircraft Life Cycle Cost Analysis (ALCCA) Version 6.0*. Atlanta : s.n., 2001.
10. **Adminstration, U.S. Energy Information.** *Annual Energy Outlook 2012 with Projections to 2035*. 2012. DOE/EIA-0383(2012).
11. **Hess, J. L., Friedman, D. M. and Clark, R. W.** *Calculation Of Compressible Flow About Three-Dimensional Inlets With Auxiliary Inlets, Slats And Vanes By Means Of A Panel Method*. s.l. : NASA, 1985. NASA CR-174975; MDC J3789.
12. **Valarezo, W. O. and Chin, V. D.** *Maximum Lift Prediction for Multielement Wings*. Reno : AIAA, 1992. AIAA 92-0401.
13. **Niu, C. Y. Michael.** *Airframe Structural Design: Practical Design Information and Data On Aircraft Structures*. s.l. : Adaso Adastra Engineering Center, 1999. 9627128090.

14. NASA. NASA Subsonic Fixed Wing Project Overview. [Online] 2012. http://www.aeronautics.nasa.gov/fap/2012-PRESENTATIONS/SFW_2012_508.pdf.
15. Drela, Mark. AVL. [Online] MIT. <http://web.mit.edu/drela/Public/web/avl/>.
16. Rossito, Ken and et al. *HSCT Flight Control System Requirements Specification; Version No. 5.0*. s.l. : NASA, 1999. CRAD-9408-TR-6043.

Volume I – Appendix A – Georgia Tech Direct Design Framework for Airfoil Design

Sayan Ghosh, Graduate Research Assistant
Hongjun Ran, Research Engineer II
Michelle Kirby, Civil Aviation Division Chief
Dimitri Mavris, Principal Investigator

Aerospace Systems Design Laboratory
Guggenheim School of Aerospace Engineering
Georgia Institute of Technology
Atlanta, GA 30332-0150
<http://www.asdl.gatech.edu>

1 Abstract

A framework for the direct design of airfoils has been developed to generate globally optimized airfoils for a given target performance. The framework uses a *Particle Swarm Optimization (PSO) Method*, based on stochastic evolutionary dynamics, for global optimization. To generate smooth and realistic airfoil shapes with few design variables, Kulfan's Class/Shape Transformation (CST) method has been used. Cost function and performance calculation of the candidate airfoil is done using MSES, which is a coupled viscous/inviscid Euler method code with two-equation boundary layer formulation. The framework has been extended to generate a family of airfoils with different thicknesses from any given baseline airfoil. The uniqueness of the framework is that it

- combines the direct airfoil design method with a global optimization method
- does not require any prior user expertise to predict target pressure distributions on airfoils
- is fully automated and can be modified for any target performance and constraints
- can be used to generate a family of airfoils for a range of thicknesses

The framework has also been extended for multi-objective and multi-design-point optimization by integrating PSO with the Pareto Optimality principle.

2 Introduction

With the current focus on green aviation, the design of Natural Laminar Airfoils (NLF) for civil aviation transonic flight has become one of the major challenges for the designer. Though traditional NLF airfoils, including NACA 6-digit airfoils, have been used successfully for general aviation, their benefit is limited to a narrow usable lift range. Moreover, uncertainty in performance caused by surface roughness due to contamination or change in flow conditions has become one of the major issues. A computational framework has been developed to design optimized robust airfoils and improve the current generation of NLF.

Traditionally, aerodynamic shape optimization of an airfoil starts from a knowledge of the boundary layer properties and understanding the relationship between the pressure distribution and the airfoil geometry. In the inverse design approach, a desired flow property is specified along some boundary, e.g., a surface pressure distribution or velocity distribution, and an optimizer is then employed to modify the shape of the airfoil to attain the target flow property. The problem is well posed if the target distribution is formulated in terms of design variables while satisfying the constraints. One of the major disadvantages of this method is that the designer needs to have enough experience to specify the desired flow profile along the surface. In other words, the designer needs to represent his or her design needs via the surface flow properties. In another approach, called the direct design method, some objective is quantified as a function of design variables, e.g., lift to drag ratio. One of the major advantages of this method is that the designer does not have to rely on experience and knowledge of the surface pressure distribution in order to formulate the desired flow profile. In the direct design method an analysis code is linked with an optimizer that varies the design variables, which modifies the shape, to attain the target performance while maintaining constraint feasibility.

Optimization algorithms can be broadly categorized into gradient based and non-gradient based methods. Though gradient based methods are generally faster, for multi-modal problems like airfoil optimization, the optimizer may lead to a local optimum based on the initial starting point. One way to solve this problem is to start the optimizer with different initial conditions and then select the best airfoil. Among non-gradient based methods, some of the commonly used population based stochastic methods are Genetic Algorithms (GA) and Particle Swarming Optimization (PSO) methods. These methods start with an initial population which spans the entire design space and tries to reach globally optimized designs by different mechanisms. Although these methods are expensive, they are theoretically guaranteed to achieve

globally optimized solutions if enough population members and generations are used. The efficiency of population based stochastic methods varies from problem to problem, but in general a GA is preferred for discrete design variables and PSO for continuous design variables.

Keeping in mind the pros and cons of the various methods discussed above, a direct design method has been used with particle swarming optimization in the airfoil design framework. The three major components in the framework are an airfoil parameterization module, airfoil analysis module, and an optimizer. The framework is completely modular and is parametric in nature. This enables the user to modify or replace any method of parameterization, airfoil analysis, or optimizer very easily. During the development process two versions of the framework were developed; one for single-objective design (SOD) optimization and a second for multi-objective design (MOD) optimization using the Pareto Optimality Principle. Although SOD can be used for multi-objective design with weighted cost functions and Overall Evaluation Criteria (OEC), MOD generates a series of optimized airfoils, thus allowing the designer to select multiple airfoils depending on their preferences.

3 Parameterization

There are numerous methods available for shape parameterization of an airfoil shape. Some of the well known methods are

- Discrete Points
- Bezier or B-Spline
- “Free-Form” Representation
- Numerically derived orthogonal basis function
- Polynomial Surface Representation
- Cubic Spline Control Point Representation

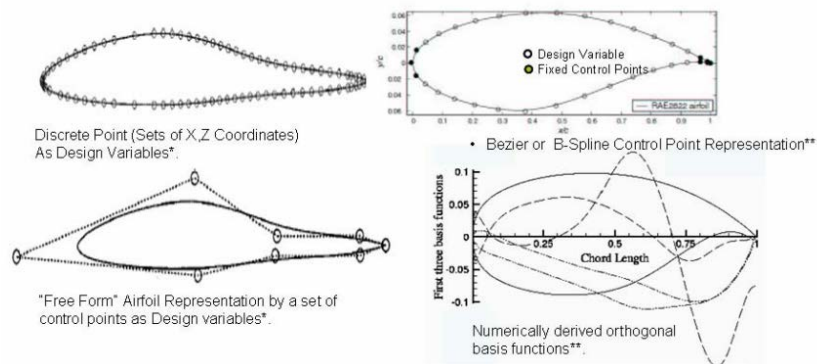


Figure 1 Methods of Airfoil Parameterization

Each of these methods has their own advantages and disadvantages. Some of the problems are

- High number of design variables
- Discontinuous / irregular geometry
- Inaccurate representation of the leading edge and trailing edge
- Limited design space

For aerodynamic design problems with high geometric sensitivity, like natural laminar flow airfoil design, there is a need for a parameterization method which can generate smooth airfoils. The parameterization method also needs to be physically intuitive so the user can specify physical parameters like leading edge radius, boat tail angle, etc. From the optimization point of view, the parameterization method needs to represent the design space with as few design variables as possible. Kulfan's class/shape transformation (CST) parameterization method, being one of the ideal methods fulfilling all of these requirements, has

been used for airfoil parameterization. The CST parameterization method defines a basic shape with a class function and modifies it to the desired shape with a shape function. The CST method can efficiently model any airfoil in the entire design space.

3.1 Class/shape transformation (CST) parameterization method for airfoil

The general form of the mathematical expression for an airfoil shape is given as:

$$\frac{z}{c} = \sqrt{\frac{x}{c}} \left(1 - \frac{x}{c}\right) \sum \left[A_i \left(\frac{x}{c}\right)^i \right] + \frac{x}{c} \frac{\Delta z_{TE}}{c}$$

Defining “class function”, $C(x/c)$ as

$$C\left(\frac{x}{c}\right) = \left(\frac{x}{c}\right)^{N1} \left[1 - \frac{x}{c}\right]^{N2}$$

and “shape function” as

$$S\left(\frac{x}{c}\right) = \sum \left[A_i \left[\frac{x}{c}\right]^i \right]$$

An airfoil can be represented by

$$\frac{z}{c}\left(\frac{x}{c}\right) = C\left(\frac{x}{c}\right) S\left(\frac{x}{c}\right) + \frac{x}{c} \frac{\Delta z}{c}$$

with $N1 = 0.5$ and $N2 = 1.0$ for the class function.

One way to represent the shape function for an airfoil is with Bernstein polynomials. A Bernstein polynomial of order n consist of “ $n+1$ ” terms, with the r^{th} term defined as

$$S_{r,n}(x) = K_{r,n} x^r (1-x)^{n-r}$$

where

$$K_{r,n} = \binom{n}{r} \frac{n!}{r!(n-r)!}$$

Then the shape function is defined as

$$S\left(\frac{x}{c}\right) = \sum A_i S_{i,n}$$

where coefficients A_i are scaling factors which can be used as design parameters. Details of the method are given in [1].

The higher the order of Bernstein polynomial used to define the airfoil, the better the representation of the airfoil surface. However, this is accompanied by the cost of a larger number of design variables.

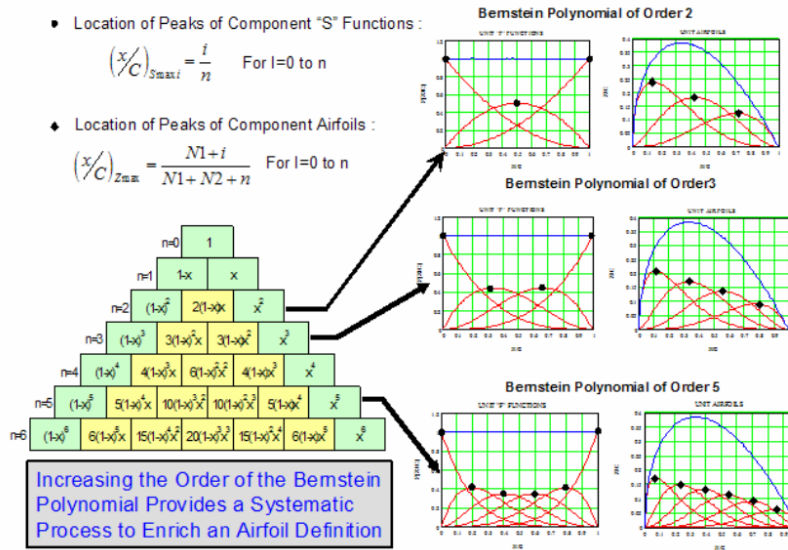


Figure 2 Effect of BP order on airfoil shape

Although in the current work the CST method has been used to parameterize airfoil, any other parameterization method can be easily incorporated in the design framework due to the modular nature of the tool.

4 Airfoil Analysis

In the framework MSES has been used to carry out aerodynamic analysis of airfoils as well as calculation of the transition location. MSES is a coupled viscous/inviscid Euler method for airfoil design and analysis. It employs a streamline based Euler discretization. It uses a two-equation boundary layer formulation which is coupled through the displacement thickness and solves simultaneously with a full Newton method. A full laminar bubble model in the boundary layer formulation is used for low Reynolds number flow representation. The turbulent transition prediction is carried out using spatial-amplification theory based on the Orr-Sommerfield equation. Some of the capabilities of MSES are

- Subsonic, Transonic and Supersonic Single and Multi-Element Airfoil Analysis
- Automatic grid generation using a streamline coordinate solution, allowing the grid to adapt to the evolving flow field
- Forced or free boundary layer transition
- Transitional separation bubble modeling
- Lift and drag predictions to just beyond $\max C_l$
- Blunt trailing-edge treatment

5 Particle Swarming Optimization

The optimizer starts with randomly distributed particles in the design space known as a swarm. Each particle is modeled by a vector of design parameters representing a particular design. Every individual of the swarm in a multidimensional space has a position and a velocity vector. These particles fly through hyperspace and remember the best position that they have seen. Members of a swarm communicate good positions to each other and adjust their own position and velocity vector based on these good positions. There are two main ways this communication is accomplished: (i) "swarm best" that is known to all (ii)

“local bests” are known in neighborhoods of particles. Updating of the position and velocity vector are done at each iteration as follows:

$$v_{i+1} = \omega v_i + c_1 r_1 (\hat{x}_i - x_i) + c_2 r_2 (\hat{x}_g - x_i)$$

Where

- x is the position and v is the velocity vector of the individual particle. The subscripts i and $i+1$ stand for the recent and the next (future) iterations, respectively.
- ω is the inertial constant. Good values are usually slightly less than 1.
- c_1 and c_2 are constants that control how much the particle is directed towards good positions. Good values are usually right around 1.
- r_1 and r_2 are random values in the range $[0,1]$.
- \hat{x} is the best design that the particle has seen.
- \hat{x}_g is the global best seen by the swarm.

The current work used a variant of PSO called Repulsive Particle Swarm method for single objective optimization (RPSO). In RPSO, there is an additional chaotic term added to the velocity of each particle which is effective in finding the global optimum in very complex search spaces, particularly when the process is caught in a local optimum.

The PSO algorithm has also been extended to handle multi-design point optimization. To handle multiple objectives, a Multi-Objective Particle Swarm Optimization (MOPSO) algorithm has been used which integrates Pareto dominance principles into a PSO algorithm for generating Pareto-optimal solutions. A Crowding distance mechanism with a mutation operator has been used to maintain the diversity of non-dominated solutions in the external archive [2].

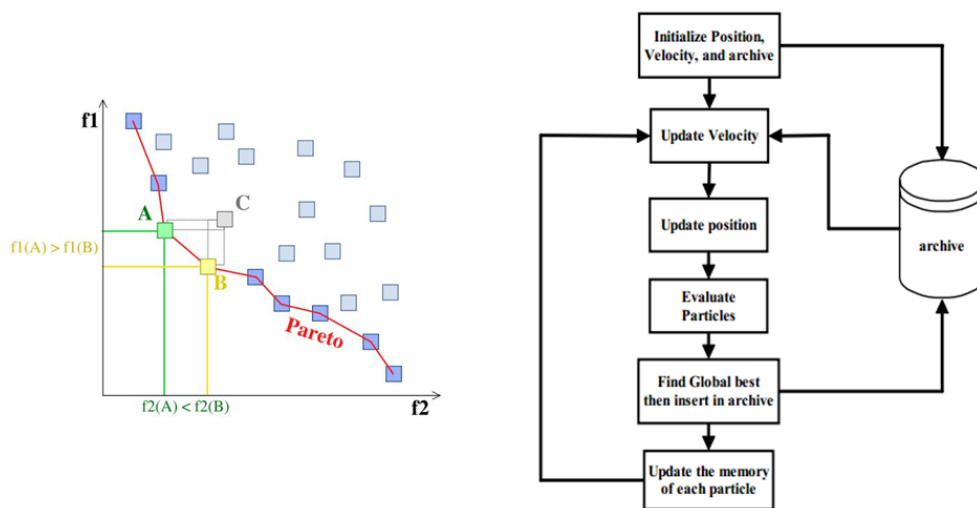


Figure 3 MOPSO Process

5.1 Quasi-Random Number Sequence

The random number generator is generally used to create an initial swarm population for the optimizer. Sometimes the random generation does not evenly distribute the particles in the design space, thus biasing the optimizer to regions of the space where particles are clustered together. In the framework the *Hammersley quasi-random* sequence has been used to generate the initial population. Since this is a quasi-random sequence, it generates a well distributed population which covers the design space evenly.

Testing has shown that the quasi-random sequence generator produces similar solutions with different trials.

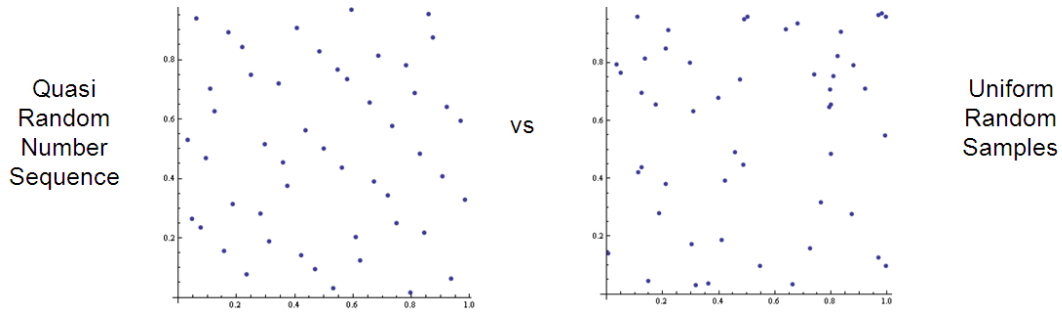


Figure 4 Comparison of Random number generator

6 Aerodynamic Airfoil Design Framework

6.1 Input Required

The input parameters required by the framework can be broadly classified into three categories: optimizer input, constraints and objective function, and flight conditions, as listed below.

6.1.1 Optimizer Inputs:

- Number of design variables:** In the current framework, BP coefficients are the design variables. Fitting different categories of airfoils with the CST method, it has been found that Bernstein polynomials of order 6 to 12 fit most of the surfaces with residuals on the order of 10^{-4} and R^2 of above 0.99. In general, surfaces with high modal shapes like the lower surface of supercritical airfoils require BPs on the order of 10 or above. Although using a larger number of coefficients can reduce the residual, they increase the sensitivity drastically. This is because small changes in coefficients cause large changes in shape. Using a higher number of design variables can also drive the optimizer towards unacceptable higher modal (wavy) shapes.

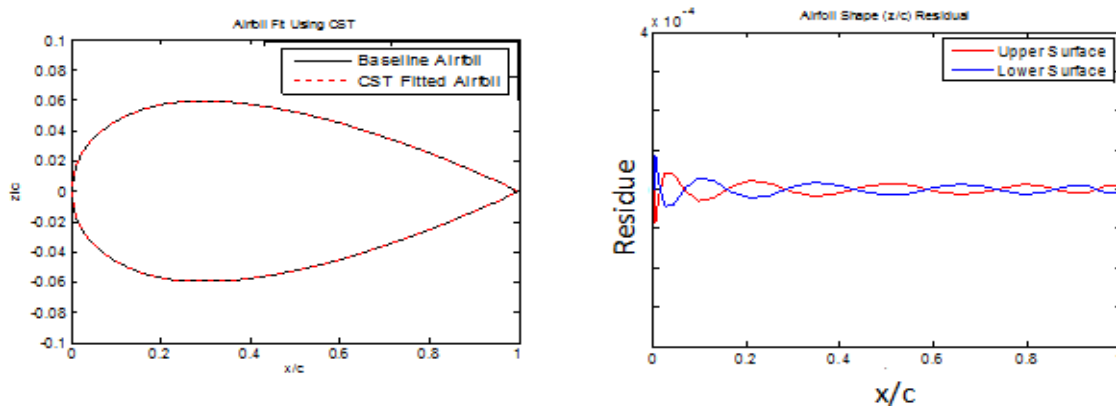


Figure 5 NACA0012 fit CST method and residue plot (BP order= 8)

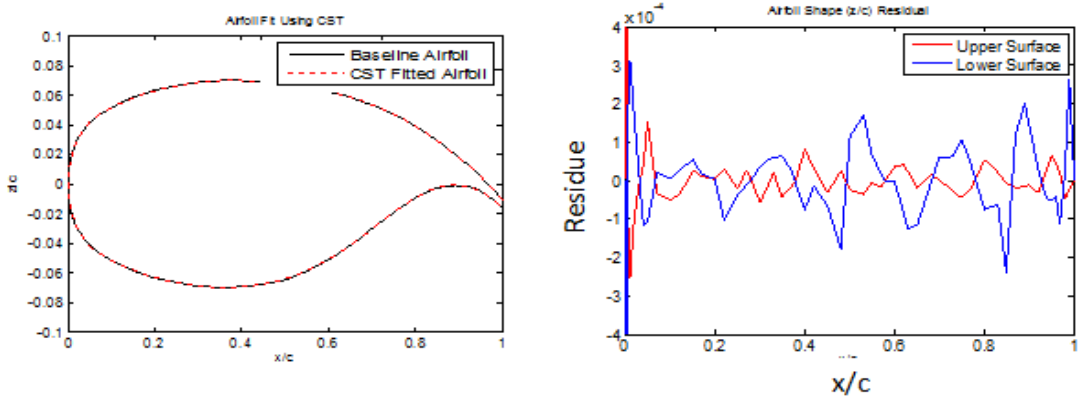


Figure 6 NASA SC(2)-0714 fit CST method and residue plot (BP order= 12)

- **Swarm Population size:** Small population sizes require more iterations (generations) to converge whereas larger populations take a longer time to compute each generation. Based on the user's experience a population size of 100 to 200 is recommended.
- **Size of randomly chosen neighbor** (for SO optimizer only): 10 to 30% of the initial population size is recommended.
- **Number of steps for local search by tunneling** (for SO optimizer only): Steps of 3 to 5 is recommended.
- **Maximum number of generations with same Global Best** (for convergence): 50 to 100 are recommended.
- **Maximum number of overall generations:** As high as 500 is recommended.
- **Percentage perturbation of design variables (BP coefficients) about the baseline airfoil to create the design space:** This defines the initial design space for the optimization process. The initial swarm of particles is generated by perturbing the baseline airfoil with user-defined percentage perturbation of the BP coefficients. Analytically, change in BP coefficients by x% leads to change in thickness by x%. Since each BP coefficient represents different modes of geometry, perturbing each coefficient with different values leads to different shapes and thickness. An initial population of airfoils generated from a baseline airfoil with 13.25% thickness and $\pm 10\%$ BP perturbation is shown below. As seen in the histogram plot, the design space ranges from 12.25% c to 14% c which corresponds to change in thickness of -7.5% c to +5.6% c.

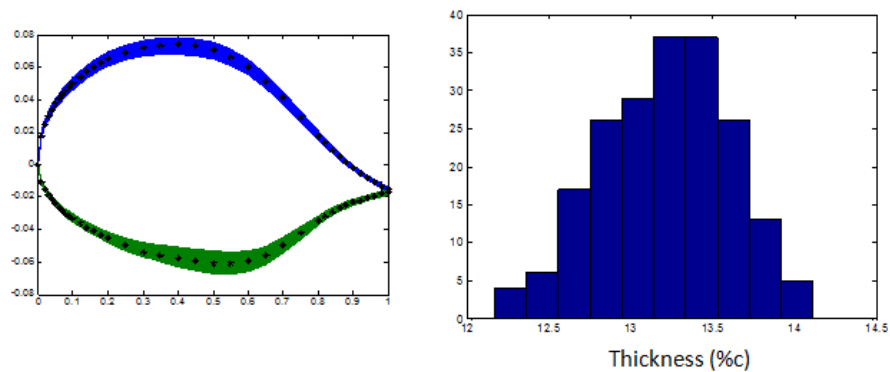


Figure 7 Design space with BP perturbation of 10%

Although the optimizer should theoretically be able to reach the global optimum solution for a given unconstrained problem, a well defined design space is recommended for two reasons. First, an optimized airfoil that is close in shape to the baseline airfoil should be generated to maintain the characteristics of the baseline airfoil. Second, it is desirable to avoid airfoils with wavy shapes and shapes with upper-lower surface crossover. Unacceptable airfoil shapes in the initial population lead to failure of cases, thus causing inefficiency in the optimization process. In general a higher percentage of BP perturbation also leads to upper-lower surface crossover for airfoils with a thin trailing edge. To avoid this, a BP perturbation of 10 to 20% is recommended.

6.1.2 Constraints and Target Function:

- Maximum thickness
- Minimum thickness
- Minimum Cl required
- Maximum trailing edge thickness
- Target Performance (Currently Cl/Cd or $Cl^{3/2}/Cd$)

6.1.3 Flight Condition(s):

- Number of flight conditions (only one for SO optimizer)
- Angle of attack at each flight condition
- Altitude at each flight condition
- Mach number at each flight condition

6.2 Process Flow

The process flow of the framework is shown in the flow chart below. The framework reads in a baseline airfoil, design parameters, and constraints. It generates the BP coefficients of the baseline airfoil, which act as design variables. The baseline BP coefficients are then randomly perturbed to a maximum of user specified percentage perturbation to generate the initial swarm of particles. At each generation, airfoil analysis is carried out to calculate the cost function of each particle. A local tunneling search is also carried out, where the performance of each particle is calculated along its velocity direction to get the best position. After the performance is calculated at each generation, the global best and the local best is calculated. If the global best does not change for N generations, the optimizer terminates. Else, the particles communicate with each other, modify their velocity vectors, and move to the new position. The whole process is then repeated.

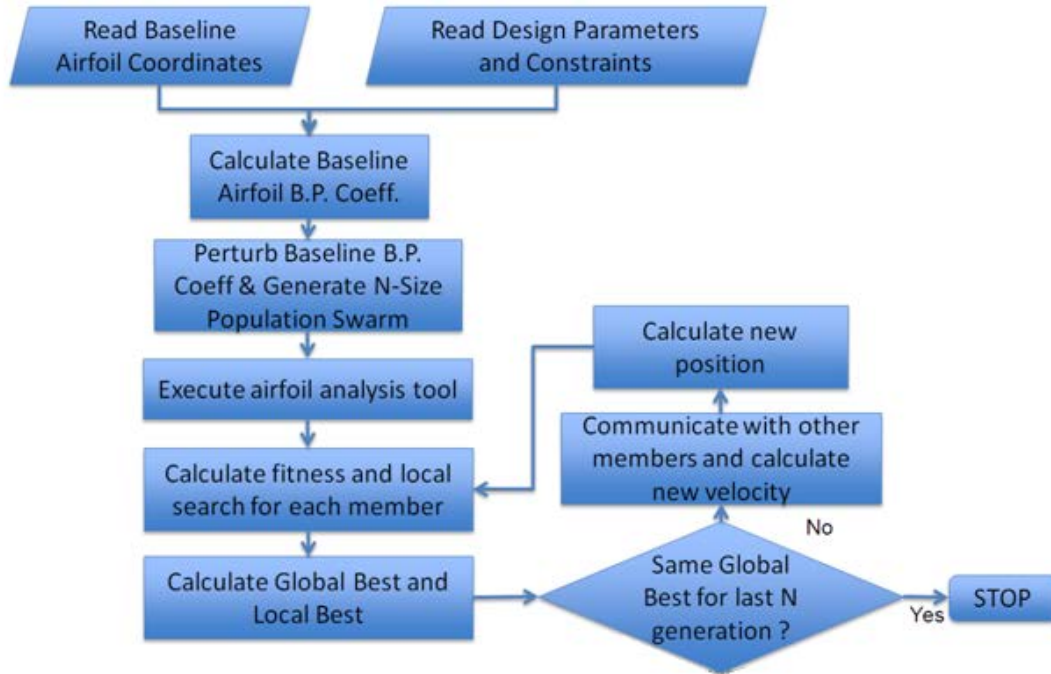


Figure 8 Process Flow of framework

In addition to the above mentioned process, the multi-objective optimizer, MOPSO, performs a few more steps. Depending upon the number of design conditions, multiple analyses are carried out for a given particle in the MOPSO method. After the fitness calculation in each generation, MOPSO archives the particles which have Pareto dominance, and these particles form the Pareto Frontier. In addition to global best and local best positions, the velocity vector of all particles is also influenced by the particles at the Pareto frontier. Finally, the user is provided choices based on the number of airfoils that lie on the Pareto Frontier.

7 Results

Case 1: Single Design Point Optimization: Optimization has been carried out with the H213 airfoil as the baseline at a design angle of attack of 2° , Mach number = 0.7, and altitude = 30,000 ft. A thickness constraint of $\pm 5\%$ of baseline and minimum lift coefficient of Cl_{baseline} has been used. Maximization of $Cl^{3/2}/Cd$ has been used as the cost function. To attain at least 50% laminar flow, a transition trip of $Xtr_{\text{up}} = 0.5c$ for upper surface and $Xtr_{\text{lo}} = 0.3c$ for the lower surface has been used.

Three trials have been carried out with a particle population size of 100. As seen in the plot below, shapes of the optimized airfoils from each trial are very close to each other. Similarity in trends has also been found in the pressure distribution. All of the optimized airfoils have lift coefficients higher than the baseline, and the performance ($Cl^{3/2}/Cd$) has improved by almost 100%.

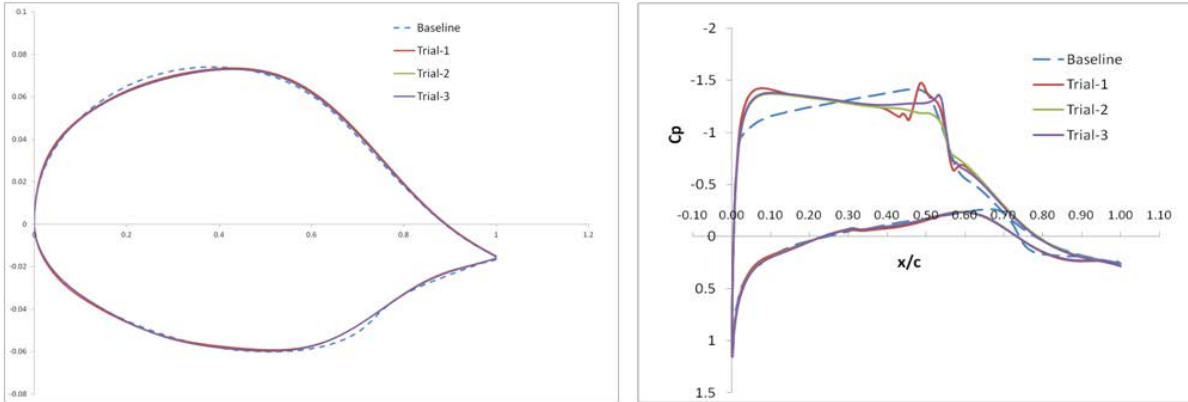


Figure 9 Airfoils optimized from H213

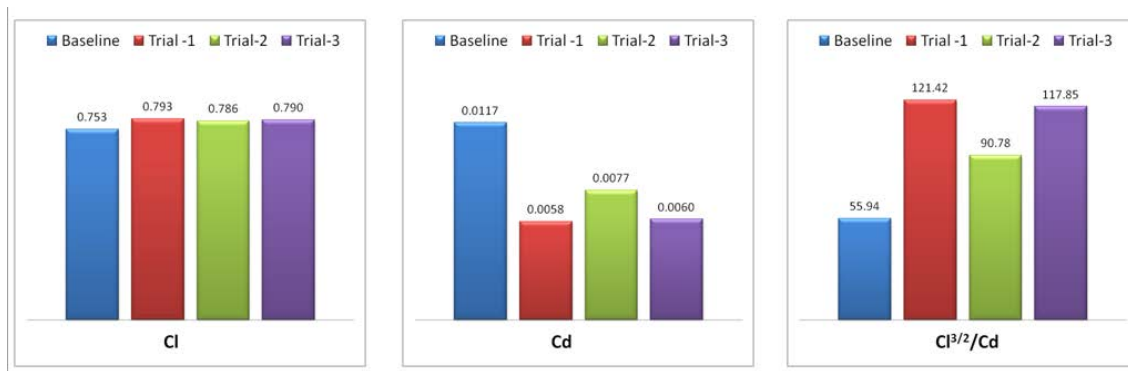


Figure 10 Performance of optimized airfoils with respect to baseline (H213) airfoil

Off-design-condition performance:

Analysis of an optimized airfoil (trial-1) has been carried out at off-design Mach numbers of 0.6 and 0.8 and at various angles of attack. It has been found that performance of the optimized airfoil is better than the baseline airfoil around the design angle of attack for Mach numbers of 0.7 and higher. The baseline performs relatively better than the optimized airfoil for lower Mach numbers. Nevertheless, the optimized airfoil has been found to be robust close to the design condition.

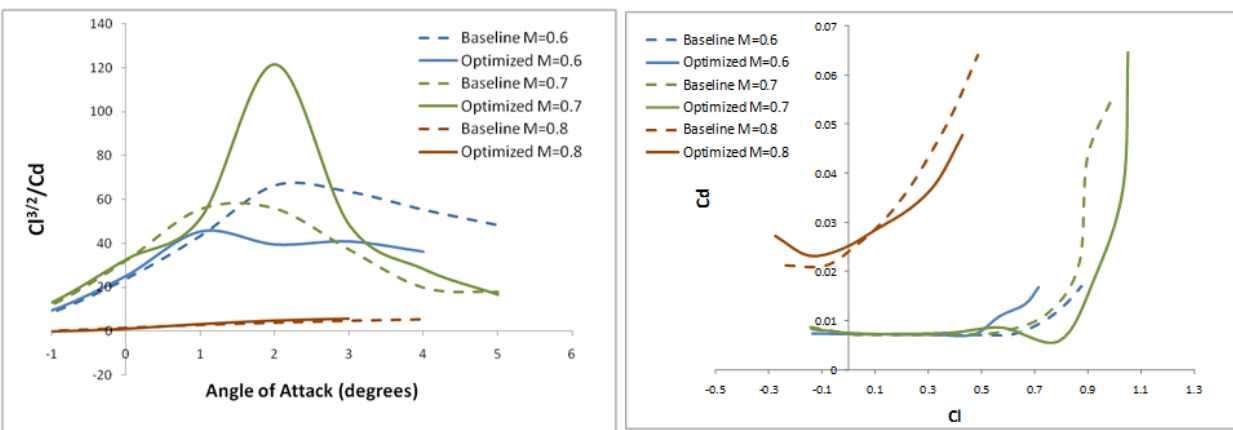


Figure 11 Off-design performance of optimized airfoil

Case 2: Family of optimized thick airfoils: Optimization has been carried out to generate thick/thin airfoils from a given baseline airfoil. One option is to scale up/down the baseline airfoil to a desired thickness and then optimize the scaled airfoil. The second option is to scale up/down the baseline airfoil in steps, optimize the intermediate airfoil, and then use the optimized airfoil as the baseline for the next step. The second method generates a family of optimized thick airfoils from a given baseline.

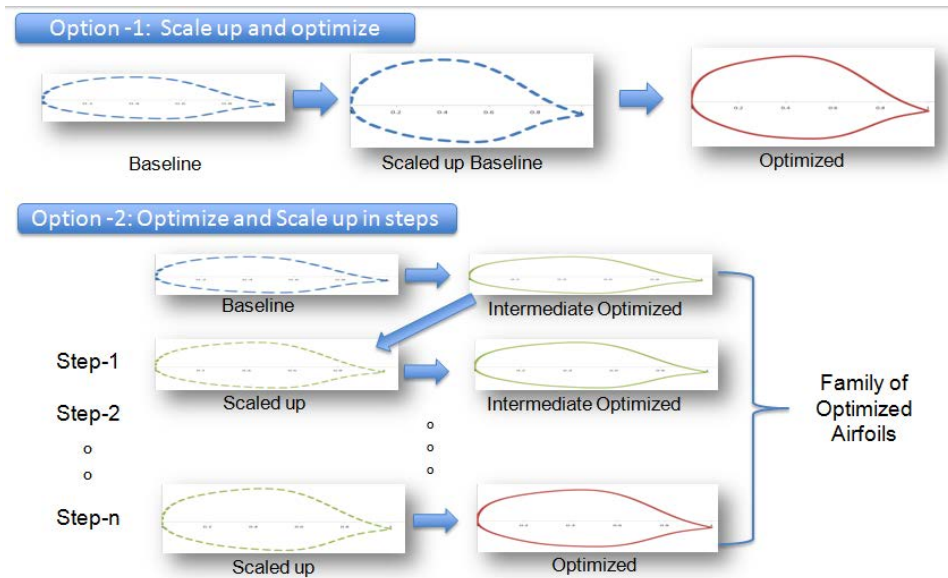


Figure 12 Design strategy for thick/thin airfoils

The second option has been used to generate optimized airfoils for thicknesses from 12 to 17%. The H213 airfoil (13.25% thick) has been used as a baseline. Design angle of attack of 2° with Mach number of 0.7 and altitude of 30,000 ft has been used. A turbulent transition point of 0.5c for the upper surface and 0.3c for the lower surface has been used to attain at least 50% laminar flow for the upper surface. The optimized airfoil and performance improvement is shown in the plot below. The performance of the optimized airfoil has been found to be improved by more than 100% in some of the cases. The percentage improvement was higher for thicker airfoils.

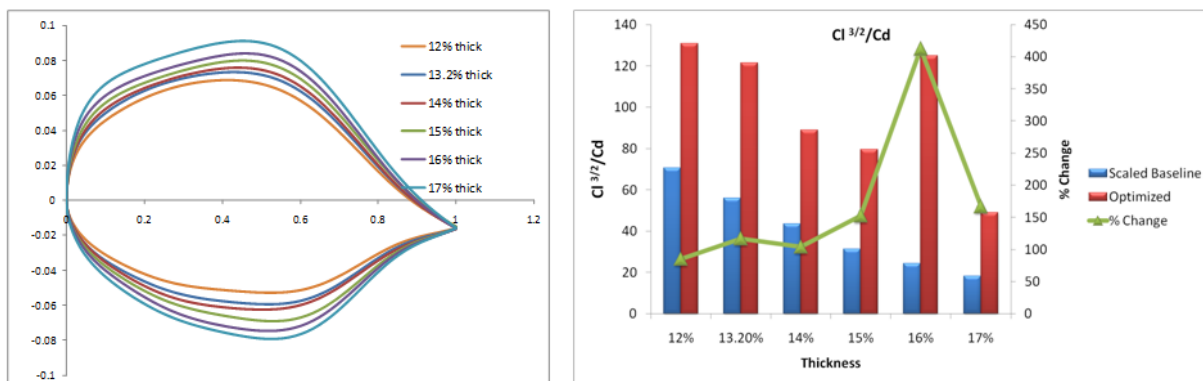


Figure 13 Family of optimized thick airfoils

The optimized airfoils were then analyzed at off-design angles of attack at a Mach number of 0.7 and altitude of 30,000 ft. The optimized airfoil improves performance at the design angle of attack, but at off-design angle of attack, performance degrades significantly, as seen in the plot below. It has been found

that the optimized airfoils were highly sensitive at off-design angles of attack causing flow instability and early transition.

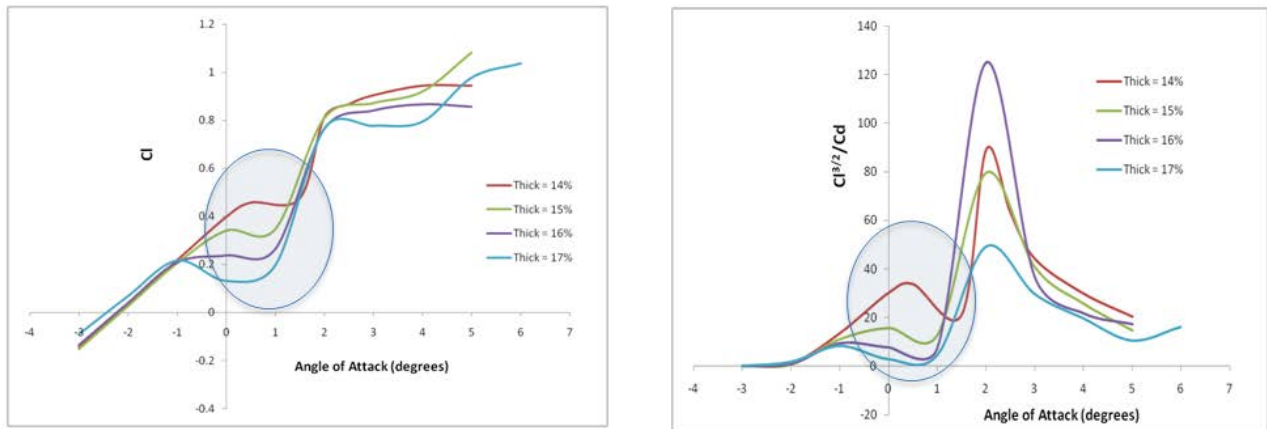


Figure 14 Degradation of performance of optimized airfoils at off design condition

To analyze the worst-case scenario, analyses have been carried out using optimized airfoils with turbulent transition location at $0.2c$ for the upper surface. As seen in the plot below, the performance of the optimized airfoils was sharply degraded for this lower turbulent transition location.

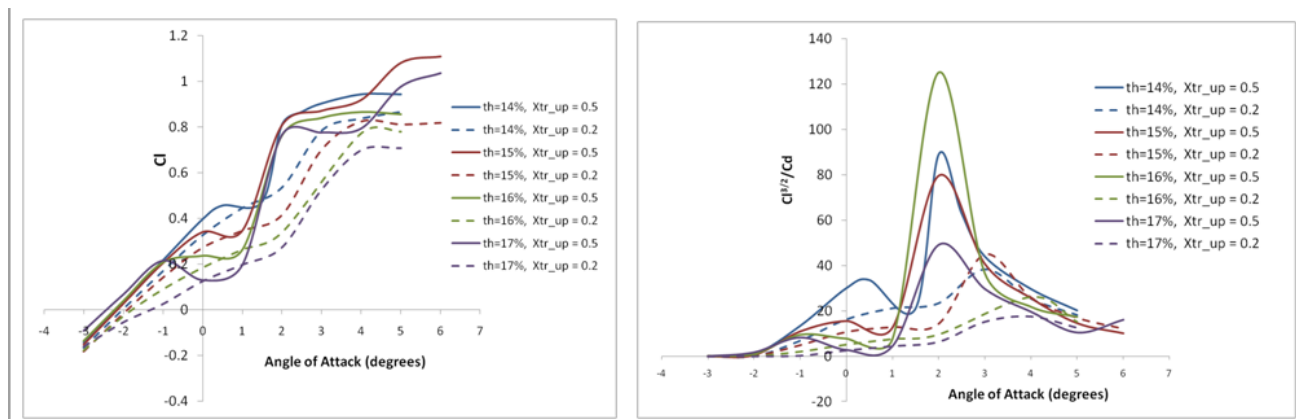


Figure 15 Degradation of performance of optimized airfoil at early transition

Based on the above results, the design strategy has been revised to optimize airfoils for lower transition location ($0.2c$ or lower) and then select the airfoil with maximum laminar flow in free transition among the best candidate airfoils in the final population. The new design strategy has been carried out to optimize airfoils for 14% thickness with cost function of maximizing Cl/Cd at a design angle of attack of 2° , Mach number = 0.7, and altitude of 30,000 ft. The five best airfoils have been selected from the final population. Analysis of all selected airfoils has been carried out for a number of angles of attack while keeping the transition location for the upper surface at $0.2c$. As seen in the plots below, the selected airfoils are similar in shape, and all of them perform better than the baseline airfoil at and around design angles of attack.

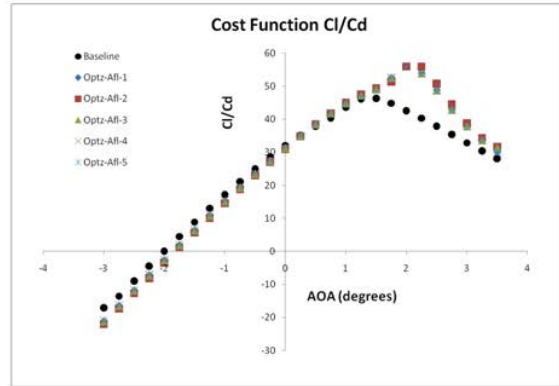
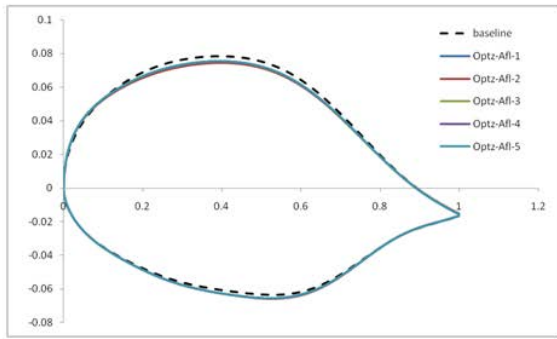


Figure 16 Optimized airfoil and performance with revised design guideline

Optimized airfoils have also been analyzed at free transition to calculate the performance and natural turbulent transition location. As seen in the plots below, the airfoils have been found to be robust at and around the design angle of attack with free transition location close to the baseline at around 0.5c.

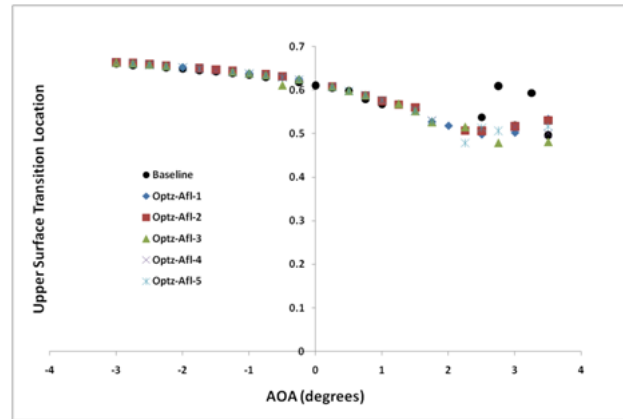
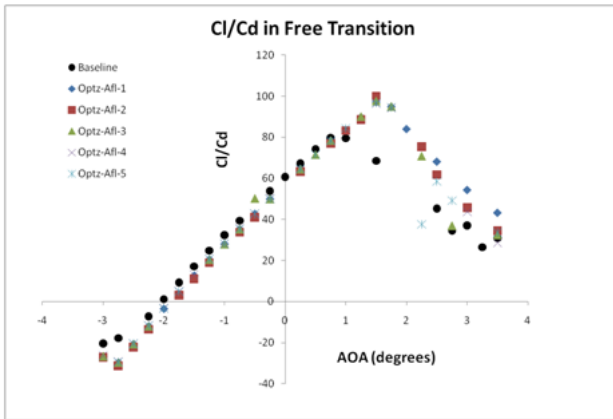


Figure 17 Performance of optimized airfoils at free transition

The results found above support the revised design strategy of designing airfoils for a lower transition point. Thus, this design guideline has been used for all studies mentioned below.

Case 3: Optimization with new design guideline: Optimization of a 14% thick airfoil has been carried out with the H213 airfoil as the baseline at Mach number = 0.7 and altitude = 30,000 ft with design angles of attack of 1.0°, 1.5° and 2.0° to verify the new design guideline. The optimized airfoils at each design angle of attack and performance of the airfoils at various angles of attacks is plotted below. It has been found that the leading edge radius of the optimum decreases as the design angle of attack increases. Each airfoil has been optimized at its respective design angle of attack while performing better or close to the baseline at off-design angles of attack. Comparison of pressure distributions and moment coefficients with the baseline is also shown below. All of the optimized airfoils have lower pressures at the leading edge, suggesting flow acceleration at the leading edge. The pitching moment of the optimized airfoil at 1.5° has been found to be close to the baseline, whereas the other airfoils have slightly higher pitching moments. Free transition performance also demonstrated robustness of the optimized airfoils; all of the airfoils have free transition location at 0.5c or higher. The airfoil optimized at 1.0° has a slightly earlier transition location compared to the others. This is due to early shock formation on that particular

airfoil. The robustness of the airfoils designed at different angles of attack supports the new design guidelines.

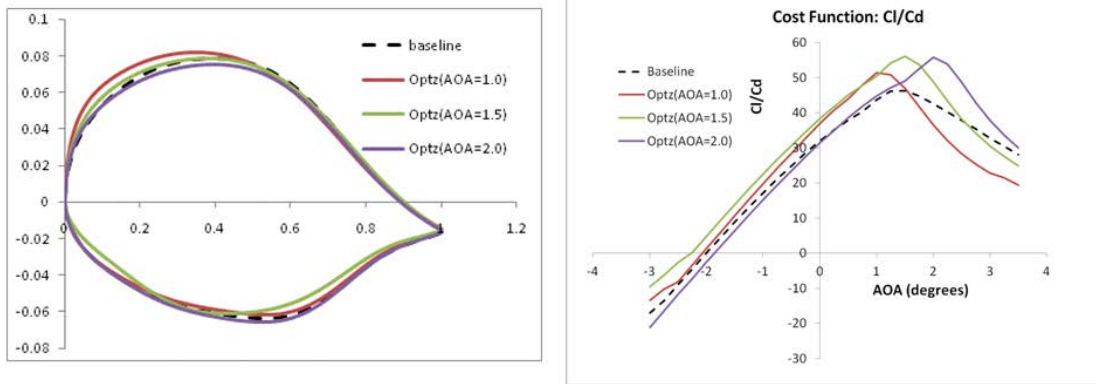


Figure 18 Optimized airfoils at angle of attack of 1.0°, 1.5° and 2.0° respectively

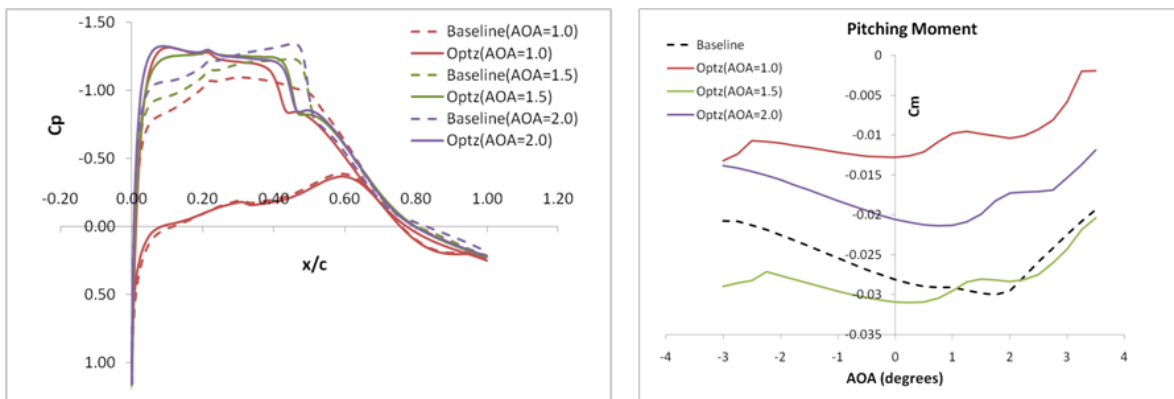


Figure 19 Pressure distribution and pitching moment of optimized airfoils

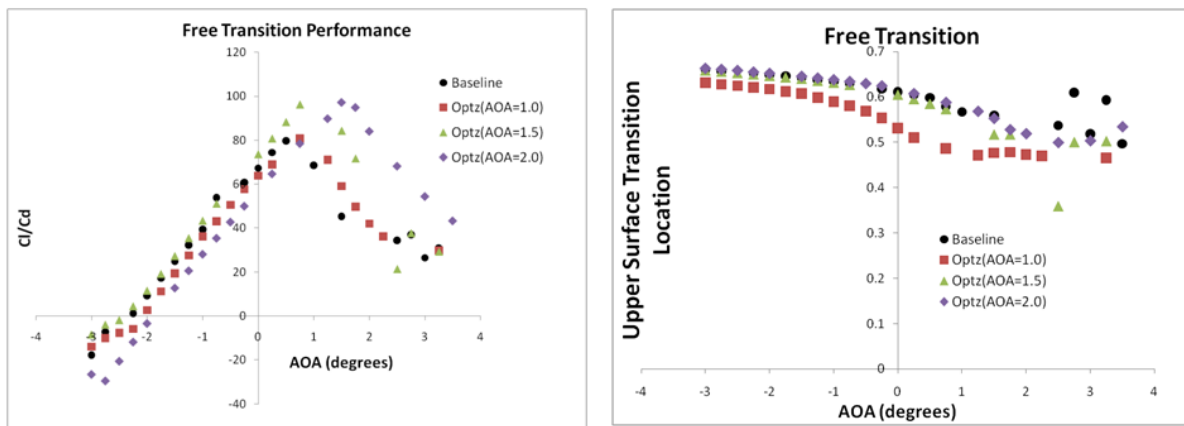


Figure 20 Free transition performance of optimized airfoils

Case 4: Multi-design-point optimization: Multi-design-point optimization has been carried out to generate 14% thick airfoils at design angles of attack of 1.0° and 2.0° , with the H213 airfoil as the baseline airfoil, at Mach number = 0.7 and altitude = 30,000 ft. For this optimization problem Multi-Objective Particle Swarming Optimization (MOPSO) has been used. The target function of maximizing Cl/Cd has been used for optimization. The evolution of the Pareto Front with generations is shown below. Three airfoils from the Pareto Front have been selected for further analysis. The three airfoils have been referred to as Optz-AA (best airfoil at 1.0°), Optz-BB (best airfoil at 2.0°) and Optz-AB (compromised solution).

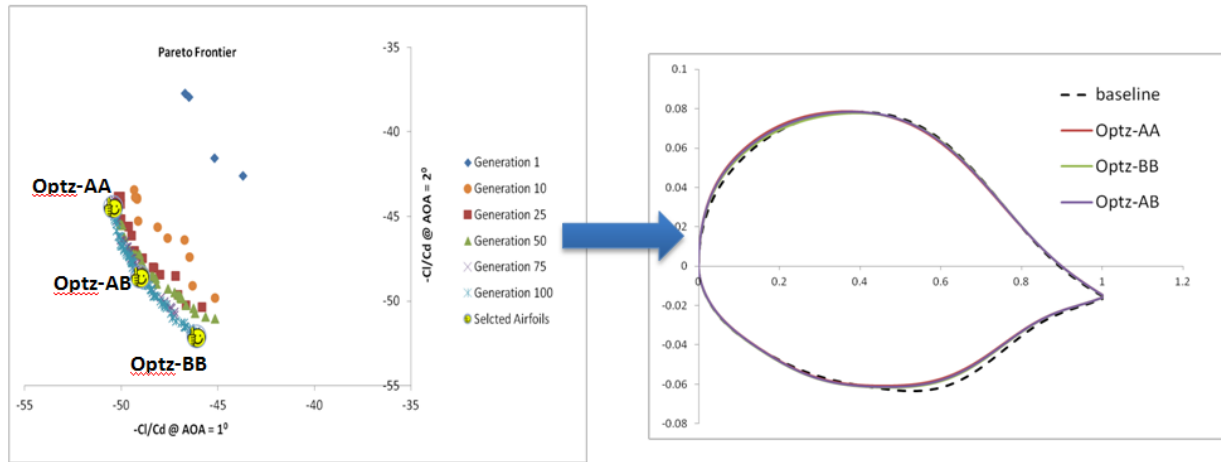


Figure 21 Evolution of Pareto Front with generation and selection of optimized airfoils

As seen in the Cl/Cd vs angle of attack plot below, Optz-AA performs best at 1.0° while Optz-BB performs best at 2.0° . Optz-AB, being the compromised solution, obtains the best at both 1.0° and 2.0° . All of the three airfoils have been found to have free transition location at around 0.5c.

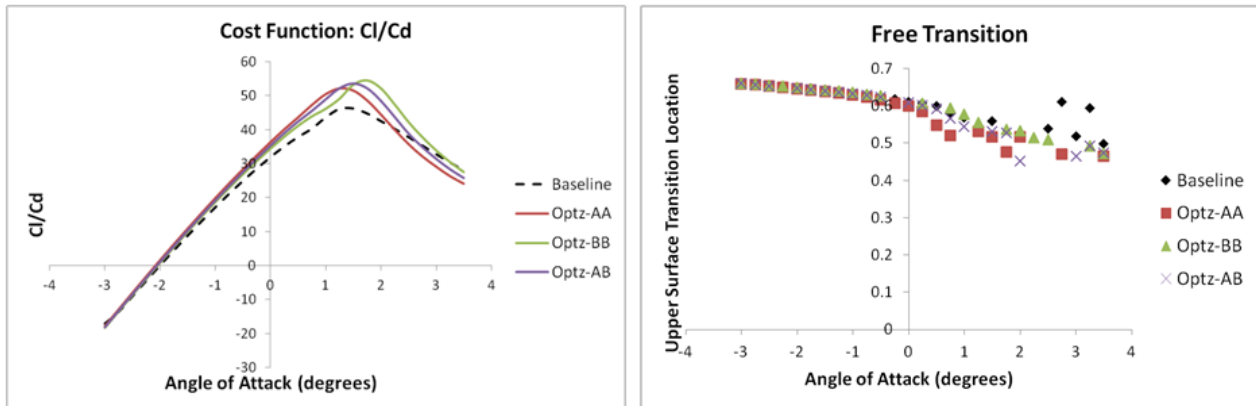


Figure 22 Performance and transition location of optimized airfoils

Comparison of pressure distributions shows improvement in pressures at the leading edge while maintaining a pressure profile similar to the baseline. The shock location was found to move forward for all of the optimized airfoils at an angle of attack of 2.0° , which is also evident in an earlier transition location compared to the baseline.

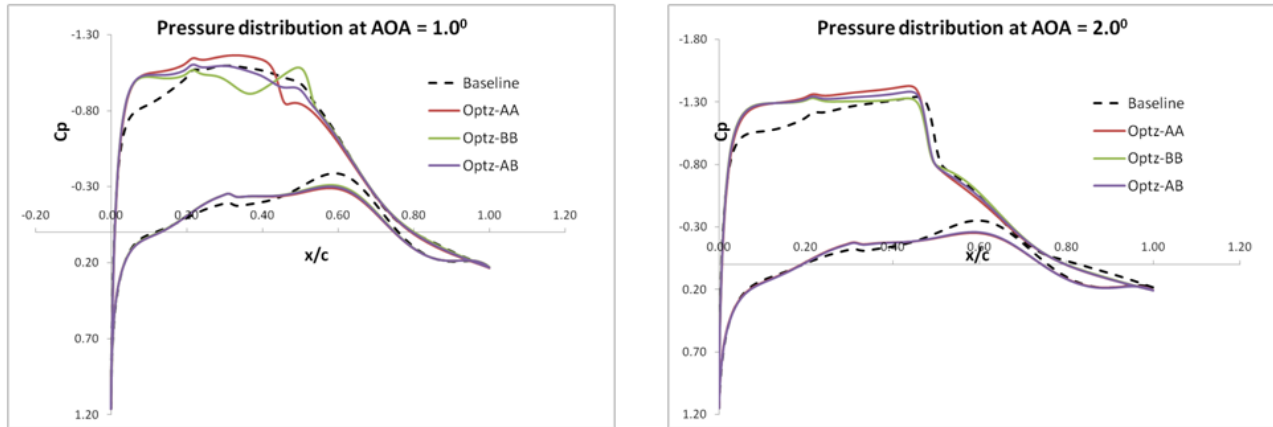


Figure 23 Pressure distribution of optimized airfoils

Pitching moments of all of the optimized airfoils has been found to be close to baseline airfoil.

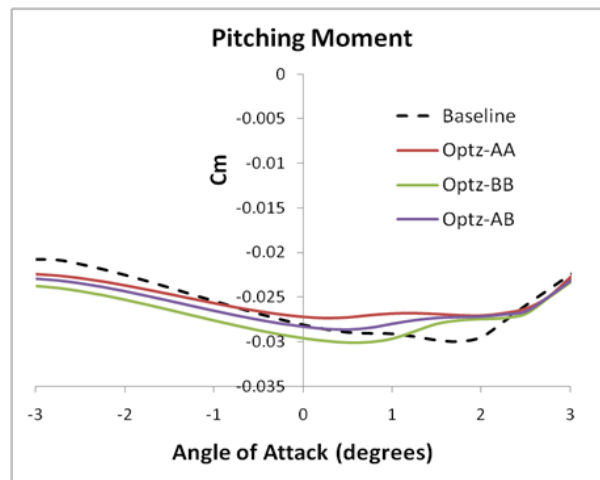


Figure 24 Pitching moment variation with angle of attack of optimized airfoils

Case 5: Comparison of Multi-design-point optimization: Two additional multi-design-point optimizations of the 14% thick airfoil have been carried out and compared with the case 4 airfoil. The first one has been carried out with design points at 1.5° and 2.0° and the second one at 1.0° , 1.5° , and 2.0° . All of the other parameters were set to the same values as in case 4. To select an airfoil from the Pareto frontier, the closest Euclidean distance from the target optimum airfoil has been used. For the current case, target optimum performance is equal to 20% improvement in the baseline performance at a given angle of attack.

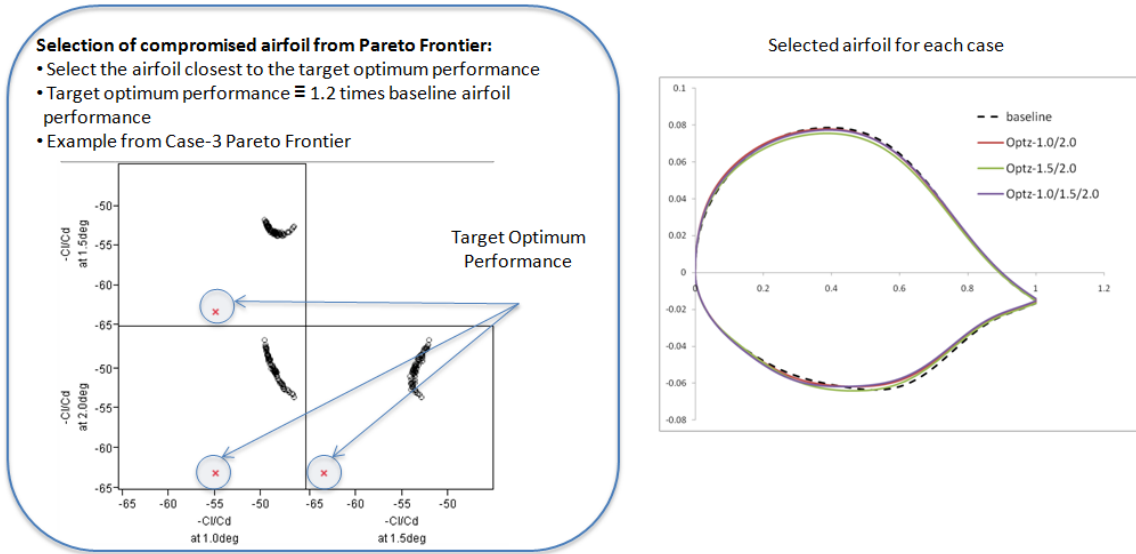


Figure 25 Selection procedure of optimized airfoils and selected optimized airfoils

As seen in the plot below, the performance of each of the optimized airfoils is very close to each other. Each of the airfoils has been driven towards obtaining the best compromised solution at their multi-design-point angles of attack. All of the airfoils have almost the same pitching moment at various angles of attack while Optz-1.0/1.5/2.0 have the lowest of all.

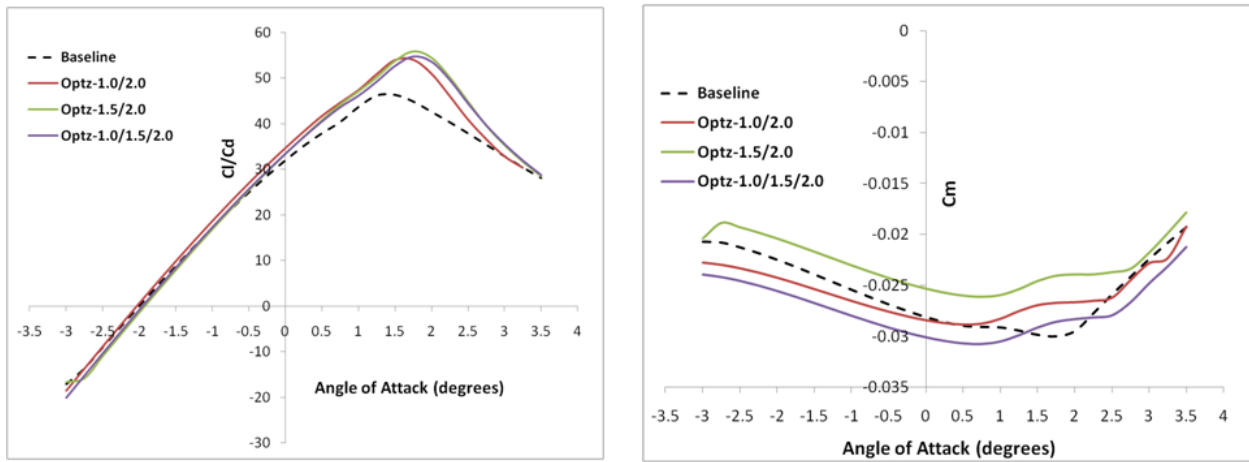


Figure 26 Performance of selected optimized airfoils and pitching moment variation

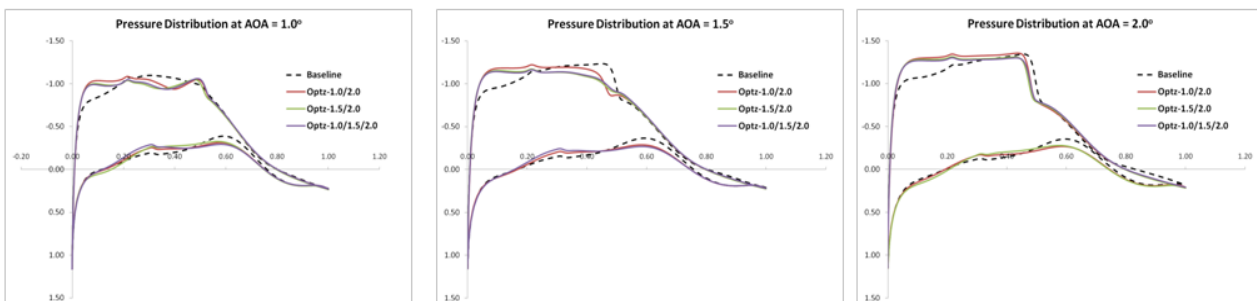


Figure 27 Pressure variation of optimized airfoils

8 Conclusion

A framework for the direct design of airfoils has been developed to generate globally optimized airfoils. The significance of the method is that it

- combines the direct airfoil design method with a global optimization method
- does not require any prior expertise to predict target pressure distributions on airfoils
- is fully automated and can be modified for any target performance objective and constraints
- has the capability to generate families of optimized airfoils with a range of thickness from a given baseline airfoil
- has also been extended to multi-design-point optimization

9 Reference:

- 1) Brenda M. Kulfan and John E. Bussoletti, "Fundamental" Parametric Geometry Representations for Aircraft Component Shapes", 11th AIAA/ISSMO Multidisciplinary Analysis and Optimization Conference, September 2006, Portsmouth, Virginia.
- 2) Carlo R. Raquel and Prospero C. Naval, Jr. 2005. An effective use of crowding distance in multiobjective particle swarm optimization. In Proceedings of the 2005 conference on Genetic and evolutionary computation (GECCO '05), Hans-Georg Beyer (Ed.). ACM, New York, NY, USA, 257-264. DOI=10.1145/1068009.1068047 <http://doi.acm.org/10.1145/1068009.1068047>
- 3) Kulfan, B., "Universal parametric geometry representation method", Journal of aircraft, American Institute of Aeronautics and Astronautics, 2008, 45, 142-158
- 4) Lane, K. & Marshall, D., "Inverse Airfoil Design Utilizing CST Parameterization", 48th AIAA Aerospace Sciences Meeting, 2010.
- 5) Liebeck, R. H., "Design of Subsonic Airfoils for High Lift", Journal of Aircraft, 1978, 15 no.9, 547-561
- 6) Morris, A.; Allen, C. & Rendall, T., "Aerodynamic Optimisation of Modern Transport Wing using efficient Variable Fidelity Shape Parameterisation", Proceedings 47th AIAA Aerospace Sciences Meeting, 2009
- 7) Cella, U.; Quagliarella, D.; Donelli, R. & Imperatore, B., "Design and Test of the UW-5006 Transonic Natural-Laminar-Flow Wing, Journal of Aircraft", Citeseer, 2010, 47, 783-795
- 8) Driver, J., "Optimal Aerodynamic Shape Design with Transition Prediction," M.A.Sc. thesis, University of Toronto, 2005.
- 9) Driver, J., and Zingg, D. W., "Optimized Natural-Laminar-Flow Airfoils," AIAA Paper2006-247, Reno, Jan. 2006.
- 10) Gopalarathnam, A. & Selig, M. Low-speed natural-laminar-flow airfoils: Case study in inverse airfoil design Journal of aircraft, 2001, 38, 57-63
- 11) Jepson, J. & Gopalarathnam, A. "Incorporation of aircraft performance considerations in inverse airfoil design", Journal of aircraft, American Institute of Aeronautics and Astronautics, 2005, 42, 199-207
- 12) Jun, S.; Jeon, Y.; Rho, J. & Lee, D., "Application of collaborative optimization using response surface methodology to an aircraft wing design", 10th AIAA/ISSMO Multidisciplinary Analysis and Optimization Conference, 2004

10 Code / Executable

Parametric_Airfoil.exe

Purpose: Reads in any airfoil geometry and calculates the Bernstein polynomial coefficient of order NB and writes to the file 'BPcoeff.txt'.

Command: *Parametric_Airfoil.exe (space) NB*

Support File: 1) Airfoil Data point file in 'baseline.txt'

```
***** dy for upper and lower surface *****
-0.00067  -0.00567
***** upper and lower Surface BP Coeff *****
0.08298  -0.04755
0.09595  -0.03802
0.09051  -0.00559
0.12892  -0.13219
0.06950   0.02857
0.15979  -0.11965
0.09308  -0.10999
0.17579  -0.01120
0.30095   0.19685
```

BP_AirfoilGen.exe

Purpose: Reads in BP coefficients from 'BPcoeff.txt' and calculates the coordinates of the corresponding airfoil. The executable also needs the 'baseline.txt' file to calculate the initial shift in leading edge position of the baseline airfoil.

Command: *BP_AirfoilGen.exe (space) NewAirfoilName.txt*

Support Files: 1) BPcoeff.txt 2) Baseline.txt

airfoil_optz.exe

Purpose: It is the driver code to run single objective airfoil design optimization using the PSO algorithm. The optimizer needs a baseline airfoil, target function, and maximum perturbation (in terms of BP coefficient) to globally optimize the baseline airfoil in the given design space. The design point is given in terms of angle of attack, altitude, and Mach number. Minimum thickness, maximum thickness, and maximum trailing edge thickness are used as constraints. Currently, minimum lift coefficient thickness is also being used. The cost function currently being used is $(Cl^{3/2}/Cd - Target)^2$. The target function can be modified very easily in the source code. To define the initial design space, a Bernstein polynomial coefficient perturbation factor is used. The perturbation factor is the maximum change in BP coefficient from the baseline coefficient in percentage. All of the design parameters are input through 'designparameter.txt'.

```

***** RESTART FLAG = 0-> Initialize; = 1-> Restart**
0
***** Bernstein Polynomial Order *****
8
***** ANGLE OF ATTACK in degrees *****
2.0
***** MACH Number *****
0.7
***** ALTITUDE in feet *****
30000.0
***** Airfoil Geometry BP Coefficient % perurbation ***
5.0
***** Airfoil Target Thickness (%)*****
13.25
***** Airfoil Minimum Thickness Constraint (%)*****
13.1
***** Airfoil Maximum Thickness Constraint (%)*****
13.4
** Airfoil Maximum Trailing edge Thickness Constraint (%)*
0.132
***** Target Cost Function *****
150.0
***** Target CLmin*****
0.7525

```

Some of the defaulted values for the optimizer are the number of initial population (set to 100), the number of randomly selected neighbors (set to 30), local search tunnel steps (set to 3), and max iterations (set to 400). These variables can be easily modified in the source code.

Note: Some other airfoil analysis variables like transition tripping point location have to be directly modified in the airfoil analysis code (MSES used here).

Command: *airfoil.optz.exe*

Support Files: 1) designparameter.txt 2) baseline.txt 3) Parametric_airfoil.exe 4) BP_AirfoilGen.exe

The optimized airfoil is written to '*optimized_airfoil.txt*'.

Volume I – Appendix B – Georgia Tech Wing Planform Design Tool Theory and Test Cases

Ryan Jacobs, Graduate Research Assistant
Hongjun Ran, Research Engineer II
Michelle Kirby, Civil Aviation Division Chief
Dimitri Mavris, Principal Investigator

Aerospace Systems Design Laboratory
Guggenheim School of Aerospace Engineering
Georgia Institute of Technology
Atlanta, GA 30332-0150
<http://www.asdl.gatech.edu>

Wing Planform Design Tool Theory and Test Cases

I. Introduction

During the aircraft conceptual design stage, the lifting-surface planforms must be sized for particular mission capabilities and performance objectives. Lifting-surface performance predictions may be obtained by employing historical data analyses, analytic methods, or low-fidelity analyses. The use of historical data could be unreliable for the design of *novel* aircraft configurations, whereas analytic methods and low-fidelity analyses may only provide crude approximations. High-fidelity tools, such as Reynolds averaged Navier-Stokes computational fluid dynamics (CFD) methods have developed to the point where full aircraft configurations can be analyzed routinely. But due to the level of geometric detail, time, and resources required for useful CFD solutions, it is still restrictive in the early design phases. The current work attempts to bridge the gap by applying a modern lifting-line method, developed by Phillips and Snyder,¹ to multiple-lifting-surface configurations and by extending it to transonic speeds.

The modern lifting-line method is based on vortex potential flow, thus, applications have been limited to inviscid and incompressible flow conditions. The accuracy of the method has been shown for swept wings at low speeds in Ref. 1, but it has not demonstrated numerical predictions for multiple-lifting-surface cases or attempted an extension to transonic speeds. In this work, it is assumed that incorporation of viscous, compressible airfoil data will enable application of the modern lifting-line method to flight conditions in the compressibility dominated transonic regime. The key concept behind this assumption is that the induced velocity produced by a vortex may not be greatly influenced by compressibility. This concept is partially based on the work by Aboelkassem and Vatisas,² where it was shown that compressibility affects the radial and axial velocity components of a strong vortex but not the tangential velocity.

The first part of this paper provides a brief summary of the modern-lifting line method. This method is capable of analyzing individual or multiple-lifting-surface systems with arbitrary sweep, dihedral, twist, and chord length distribution. Results are then presented for validation cases, and discrepancies between lifting-line predictions and experimental data are identified. Possible sources for the discrepancies are discussed. Finally, the methodology for the planform design tool is presented.

Nomenclature

\bar{c}	Local aerodynamic mean chord length
C_D	Drag coefficient of lifting-surface(s) based on wing reference area
C_L	Lift coefficient of lifting-surface(s) based on wing reference area
C_d	Airfoil drag coefficient
C_l	Airfoil lift coefficient
dA	Local differential planform area
dF	Differential aerodynamic force vector
$d\mathbf{l}$	Directed differential vortex filament length vector
\mathbf{r}	Radius vector from a vortex filament to an arbitrary point in space
\mathbf{u}_a	Unit vector normal to local chord line

\mathbf{u}_n	Unit vector parallel to local chord line
\mathbf{u}_∞	Dimensionless freestream velocity vector
\mathbf{V}_∞	Freestream velocity vector
\mathbf{v}	Dimensionless induced velocity
α	Angle of attack
Γ	Vortex strength
Λ	Leading edge sweep angle
ρ	Density of freestream flow

Subscript

i, j	Horseshoe vortex indices
1,2	Horseshoe vortex nodal points

II. Modern Lifting-Line Model

The fundamental physical model of the modern lifting-line method involves the synthesis of a finite lifting-surface by discrete horseshoe vortex filaments, as shown in Figure 1. Adjacent horseshoe vortex corners are illustrated as being spaced apart, but this is simply for the purpose of visualization. With the exception of the wing tips, the inboard corner of one horseshoe vortex is coincident with the outboard corner of the adjacent horseshoe vortex. The bound portion of each horseshoe vortex is aligned with a constant-chord position, typically chosen to be quarter-chord, and the trailing segments of each horseshoe vortex are aligned with the freestream flow direction.

Figure 2a illustrates the geometry of a segment of an arbitrarily curved, infinite vortex filament. In the figure, \mathbf{r} is a radius vector from the directed segment of the filament $d\mathbf{l}$ to point P . The Biot-Savart law, Eq. (1),³ is employed to calculate the velocity induced at a point P by the vortex filament with circulation strength Γ .

$$d\mathbf{v} = \frac{\Gamma}{4\pi} \frac{d\mathbf{l} \times \mathbf{r}}{|\mathbf{r}|^3} \quad (1)$$

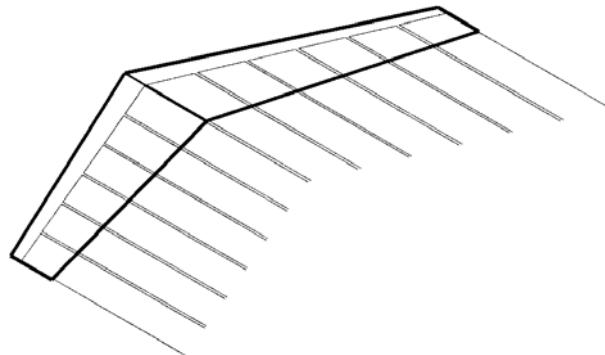


Figure 1. Example distribution of horseshoe vortex filaments along the quarter-chord line of a finite lifting-surface (from Ref. 1).

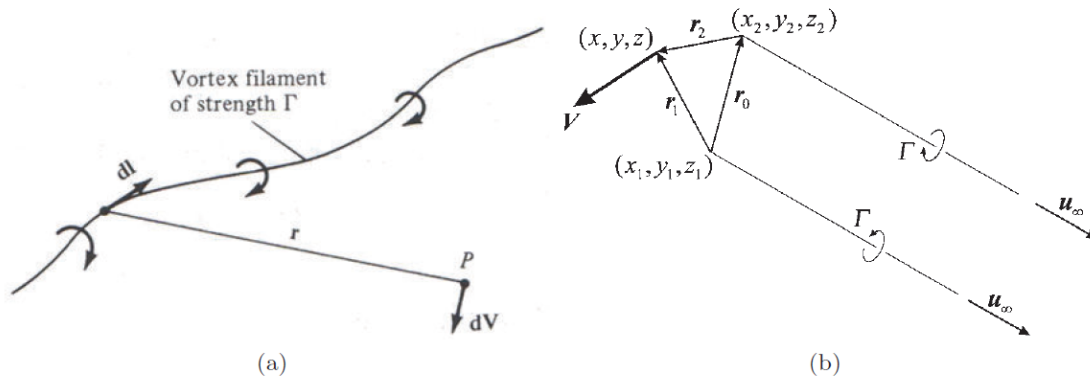


Figure 2. Vortex filament geometry (a) (from Ref. 3) and horseshow vortex geometry (b) (from Ref. 1).

A detailed view of a horseshoe vortex is shown in Figure 2b. The element is composed of two semi-infinite segments following the \mathbf{u}_∞ direction and a bound segment following the \mathbf{r}_0 direction. Application of Eq. (1) to a horseshoe vortex in a uniform freestream flow and an arbitrary point in space results in the velocity vector computed using Eq. (2). Note that with the exception of Eq. (1), all ensuing equations are from Ref. 1.

$$\mathbf{V} = \frac{\Gamma}{4\pi} \left[\frac{\mathbf{u}_\infty \times \mathbf{r}_2}{r_2(r_2 - \mathbf{u}_\infty \cdot \mathbf{r}_2)} + \frac{(r_1 + r_2)(\mathbf{r}_1 \times \mathbf{r}_2)}{r_1 r_2 (r_1 r_2 + \mathbf{r}_1 \cdot \mathbf{r}_2)} - \frac{\mathbf{u}_\infty \times \mathbf{r}_1}{r_1(r_1 - \mathbf{u}_\infty \cdot \mathbf{r}_1)} \right] \quad (2)$$

When lifting-surfaces are modeled using N discrete horseshoe vortex elements, Eq. (2) is used to find the velocity induced by each element on all others, if the vortex strengths are known. Since these strengths are not known anteriorly, a system of N equations are required to relate the strengths to known properties of the lifting-surfaces. The vortex lifting law, Eq. (3), is employed for this purpose.

$$d\mathbf{F} = \rho \Gamma \mathbf{V} \times d\mathbf{l} \quad (3)$$

The local velocity at horseshoe vortex j is the combination of the freestream and total induced velocity generated by the N vortices in the system. In this formulation, i and j are simply two different horseshoe element control points in the system. Using Eq. (2), the local velocity at a control point located anywhere on the bound segment of horseshoe vortex j is

$$\mathbf{V}_j = \mathbf{V}_\infty + \sum_{i=1}^N \frac{\Gamma_i \mathbf{V}_{ij}}{\bar{c}_i} \quad (4)$$

where the dimensionless induced velocity induced at control point j by horseshoe vortex i is

$$\mathbf{V}_{ij} \equiv \begin{cases} \frac{\bar{c}_i}{4\pi} \left[\frac{\mathbf{u}_\infty \times \mathbf{r}_{i2j}}{r_{i2j}(r_{i2j} - \mathbf{u}_\infty \cdot \mathbf{r}_{i2j})} + \frac{(r_{i1j} + r_{i2j})(\mathbf{r}_{i1j} \times \mathbf{r}_{i2j})}{r_{i1j} r_{i2j} (r_{i1j} r_{i2j} + \mathbf{r}_{i1j} \cdot \mathbf{r}_{i2j})} - \frac{\mathbf{u}_\infty \times \mathbf{r}_{i1j}}{r_{i1j}(r_{i1j} - \mathbf{u}_\infty \cdot \mathbf{r}_{i1j})} \right], & i \neq j \\ \frac{\bar{c}_i}{4\pi} \left[\frac{\mathbf{u}_\infty \times \mathbf{r}_{i2j}}{r_{i2j}(r_{i2j} - \mathbf{u}_\infty \cdot \mathbf{r}_{i2j})} - \frac{\mathbf{u}_\infty \times \mathbf{r}_{i1j}}{r_{i1j}(r_{i1j} - \mathbf{u}_\infty \cdot \mathbf{r}_{i1j})} \right], & i = j \end{cases} \quad (5)$$

In Eq. (5), \bar{c}_i is merely used to nondimensionalize the induced velocity. The bound vortex segment contribution is removed from Eq. (5) when $i = j$ because a straight vortex filament does not induce a velocity along its own length.

Combining Eqs. (3) and (4), the aerodynamic force at the differential spanwise section control point i is

$$\mathbf{dF}_i = \rho \Gamma_i \left(\mathbf{v}_\infty + \sum_{j=1}^N \frac{\Gamma_j}{\bar{c}_j} \mathbf{v}_{ji} \right) \times \mathbf{dl}_i \quad (6)$$

If the local airfoil section lift as a function of angle of attack is known at control point i , then the aerodynamic force for a differential spanwise section, based on airfoil data, is expressed as

$$|\mathbf{dF}_i| = \frac{1}{2} \rho V_\infty^2 C_{l_i} dA_i \quad (7)$$

Prandtl's hypothesis that each spanwise section of a finite lifting-surface has a lift equivalent to an airfoil with the same circulation can now be applied. Setting the magnitude of the force vector from Eq. (6) equal to Eq. (7), and with some algebra, the result is

$$2 \left| \left(\mathbf{v}_\infty + \sum_{j=1}^N \mathbf{v}_{ji} G_j \right) \times \zeta_i \right| G_i - C_{l_i} = 0 \quad (8)$$

where

$$\mathbf{v}_\infty \equiv \frac{\mathbf{V}_\infty}{V_\infty}, \quad \zeta_i \equiv \bar{c}_i \frac{\mathbf{dl}_i}{dA_i}, \quad G_i \equiv \frac{\Gamma_i}{\bar{c}_i V_\infty}$$

In order to use a table lookup or computation for the airfoil lift coefficient, the local angle of attack must be known at each control point, and this angle is calculated using Eq. (9).

$$\alpha_i = \frac{(\mathbf{v}_\infty + \sum_{j=1}^N \mathbf{v}_{ji} G_j) \cdot \mathbf{u}_{ni}}{(\mathbf{v}_\infty + \sum_{j=1}^N \mathbf{v}_{ji} G_j) \cdot \mathbf{u}_{ai}} \quad (9)$$

Eq. (8) must be solved as a system of N nonlinear equations in order to compute the vortex strengths. This is achieved by implementing Newton's method. Once converged, the vortex strengths are utilized to find the total force and moment vectors for each lifting-surface. Since the N horseshoe vortices can be placed on as many surfaces as necessary, the system's solution accounts for interactions between lifting-surfaces.

III. Lifting-line results

The modern lifting-line method has been employed for analysis of two configurations with multiple lifting-surfaces, two transonic transport aircraft models, and a swept wing model in transonic flow. The multiple-lifting-surface cases serve to validate the method's ability to capture interference effects, and the transonic cases demonstrate its competency for modeling compressible flight conditions. Each lifting-surface was composed of multiple 2D sections, and airfoil polars were generated by one of the airfoil design and analysis codes XFOIL4 and MSES.5 Both codes are capable of modeling compressible, viscous flows, but XFOIL is unreliable at transonic speeds.

During the validation process, it was discovered that the lifting-line method accurately accounts for lift reduction due to sweep but not the reduction in drag. Thus, as an approximation, all the MSES airfoil pressure drag data was modified for sweep using a rule of cosine method presented in Ref. 6. The effective airfoil drag was computed using Eq. (10), below.

$$C_{d_{effective}} = C_{d_{friction}} + C_{d_{pressure}} \cos^3 \Lambda \quad (10)$$

A. Wing-Canard Configuration

The first multiple-lifting-surface test case is a rectangular wing and canard configuration, as shown in Figure 3. This model was tested in the NASA Ames 7 × 10 foot wind tunnel by Feistel, Corsiglia, and Levin,⁷ to study wing-canard positioning. Two canard longitudinal stagger positions were tested along with three vertical wing positions. Both lifting-surfaces were constructed from the NASA/LANGLEY LS(1)-0413 (GA(W)-2) airfoil section, and the canard was mounted with an incidence of 2° relative to the wing. Neither surface had sweep or dihedral. The wind tunnel Reynolds number based on wing chord was 1.4×10^6 and the dynamic pressure was 60 lb/ft².

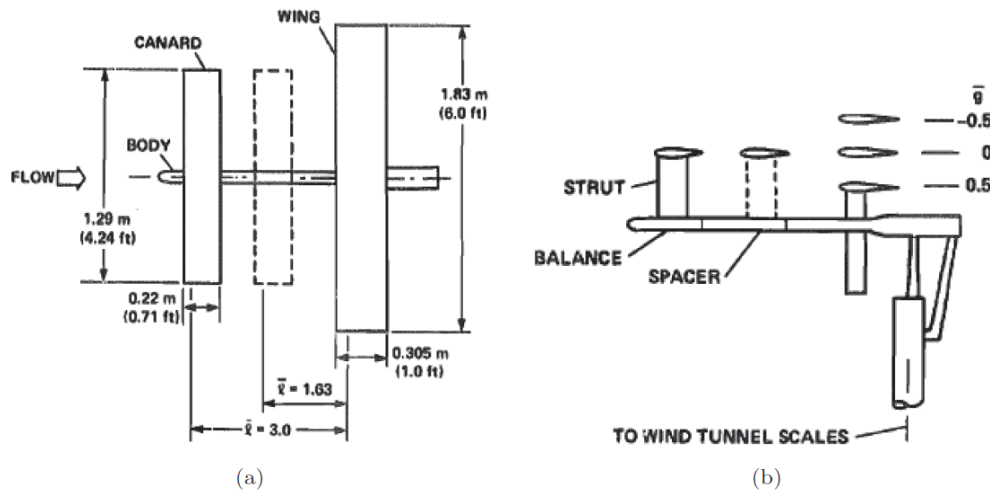


Figure 3. Wing-canard model top view (a) and side view (b) (from Ref. 7).

The short-stagger, high-wing setup was chosen as the most challenging validation case because significant interference effects between the wing and canard were exhibited in the wind tunnel. The less difficult configurations were also analyzed and results showed good agreement,

but they are not reported here. Figure 4 shows the results of the experiment and the lifting-line code for this case. All airfoil polars used to analyze the wing-canard model were generated by XFOIL. The lifting-line prediction in Figure 4a agrees well with the wind tunnel data over the majority of positive angles of attack up to stall. However, the code predicted stall at an angle of attack beyond the experimental result. Individual measurements for the wing and canard are also shown, and although the lifting-line method did not accurately predict the lift on each surface, the sum of the two is acceptable. The drag polar lifting-line data in Figure 4b demonstrate decent concurrence with the experiment for moderate lift values. Wind tunnel wall corrections were not applied to the data, and this may have been a large factor in the discrepancy at higher lift values.

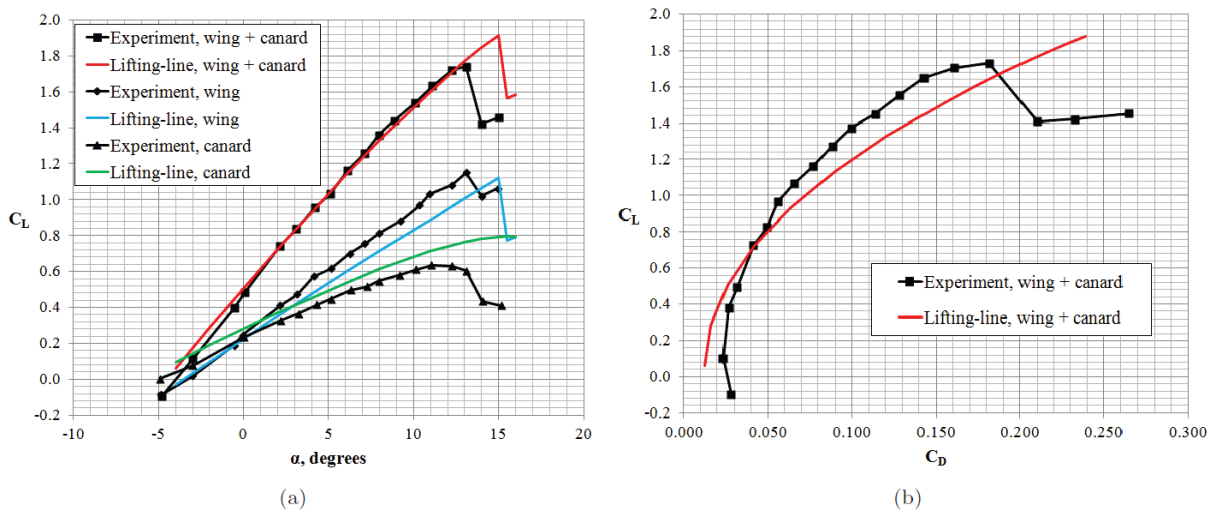


Figure 4. Wing-canard lift-curve comparison (a) and drag polar comparison (b) for the short-stagger, high-wing configuration.

B. Three-Lifting-Surface Business Jet

The second multiple-surface case is a typical business jet geometry with the addition of a canard, as can be seen in Figure 5. The model was tested in the Texas A&M University 2.13 × 3.05 meter low-speed wind tunnel by Ostowari and Naik⁸ using a 0.15 scale model. The test Reynolds number based on wing mean aerodynamic chord was 1.3×10^6 and the dynamic pressure was 45 lb/ft². The aspect ratios of the wing, horizontal tail, and canard were 7.2, 4, and 5.3, respectively. The wing was constructed from a modified NACA 64A109 airfoil and had a dihedral of 2.5° and no twist. The quarter-chord wing sweep was 12.7°. The horizontal tail and canard were constructed from the NACA 64A008 airfoil and neither had dihedral or twist. Quarter-chord sweep angles for the horizontal tail and canard were 25° and 30°, respectively. The incidence of the horizontal tail and canard were variable. Two canards were used for the test; one with a span equivalent to the horizontal tail span, and another with a span of 75% of the horizontal tail span. The horizontal tail was tested at two vertical gap positions, as illustrated in Figure 5. Also, the fuselage was built with a removable extension for testing two stagger lengths between the wing and canard.

A lifting-line analysis was performed on the business jet model with short fuselage stagger, high horizontal tail at -2° incidence, and the large canard at 0° incidence. The precise modifications applied to the wind tunnel model wing airfoil were not known, thus, a standard

NACA 64A109 airfoil geometry was used in the analysis. All airfoil polars were generated using MSES, which had difficulty converging at post-stall angles of attack. A comparison of the wind tunnel data and lifting-line analysis is in Figure 6. It is evident that the lifting-line method accurately predicted the lift values in the linear region of the curve, but the solution did not provide correct stall behavior. The lifting-line code was known to be sensitive near stall for one lifting-surface, so the erratic behavior in the plot was not unexpected considering that this is a system of three surfaces with complex interactions. Additionally, it is suspected that the lack of airfoil data at post-stall angles of attack played a strong role in this behavior. When airfoil data was not available at a particular angle of attack, the lifting-line code extrapolated airfoil lift values based on the nearest lift-curve slope. An appropriate comparison of drag data was not possible for this case since the fuselage was present in the wind tunnel tests.

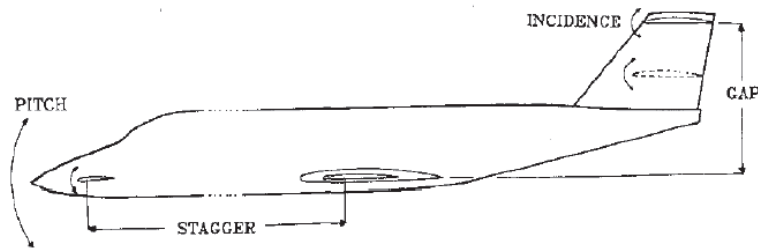


Figure 5. Business jet geometry (from Ref. 8).

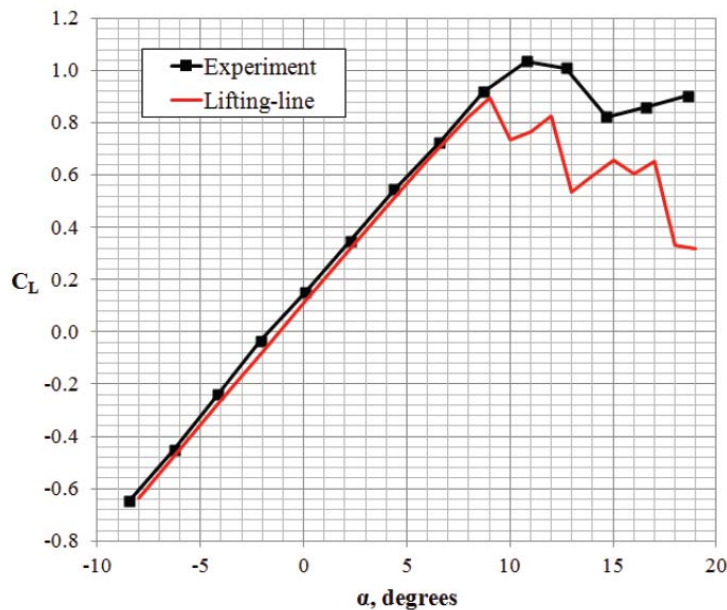


Figure 6. Business jet lift-curve comparison for the short fuselage, high horizontal tail, and large canard model.

C. High Aspect Ratio Supercritical Wing with Fuselage

The first transonic case that the lifting-line code was validated against is a supercritical wing and fuselage model, designated as SCW-1a in a wind tunnel investigation by Bartlett.⁹ All wind

tunnel tests were performed in the NASA Langley 8 foot transonic pressure tunnel. The SCW-1a model had an aspect ratio of 11.954, and the aircraft model geometry is illustrated in Figure 7. The tests were run at various Mach numbers and a unit Reynolds number of 5×10^6 per foot. Boundary-layer transition was fixed on all of the model components.

For the lifting-line analysis, the SCW-1a wing geometry was modeled with three supercritical airfoils using the coordinates provided in Ref. 9. All airfoil polars were generated by MSES using the prescribed transition locations also found in the report. The inboard airfoil section defined at the wing-body intersection was used to model the wing at the aircraft model centerline. Lifting-line analyses were executed for Mach numbers of 0.6, 0.7, 0.75, and 0.8, and the lift-curve results are shown in Figure 8. Although the lifting-line prediction did not capture all of the minor non-linearity present in the wind tunnel data, the agreement at Mach 0.6 and 0.7 is excellent. The portion of the Mach 0.75 lift curve below approximately 2.5° angle of attack also shows a favorable match but premature stall was predicted. At Mach 0.8, the lifting-line method did not predict a lift-slope match as well as at lower Mach numbers. Drag polars were not compared because of the presence of the fuselage in the wind tunnel model.

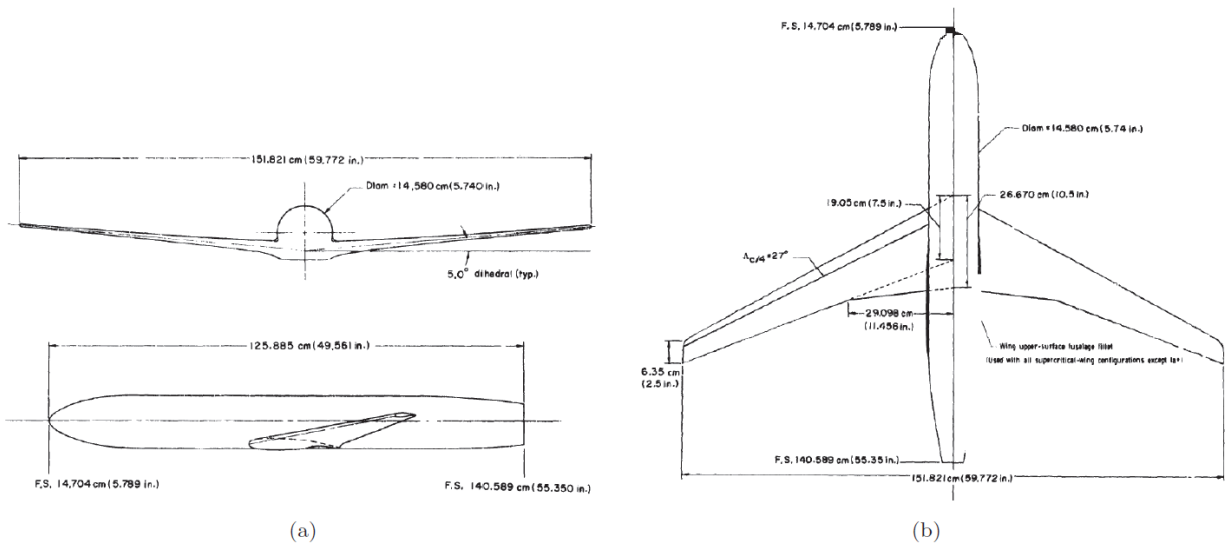


Figure 7. SCW-1a geometry front and side views (a) and top view (b) (from Ref. 9).

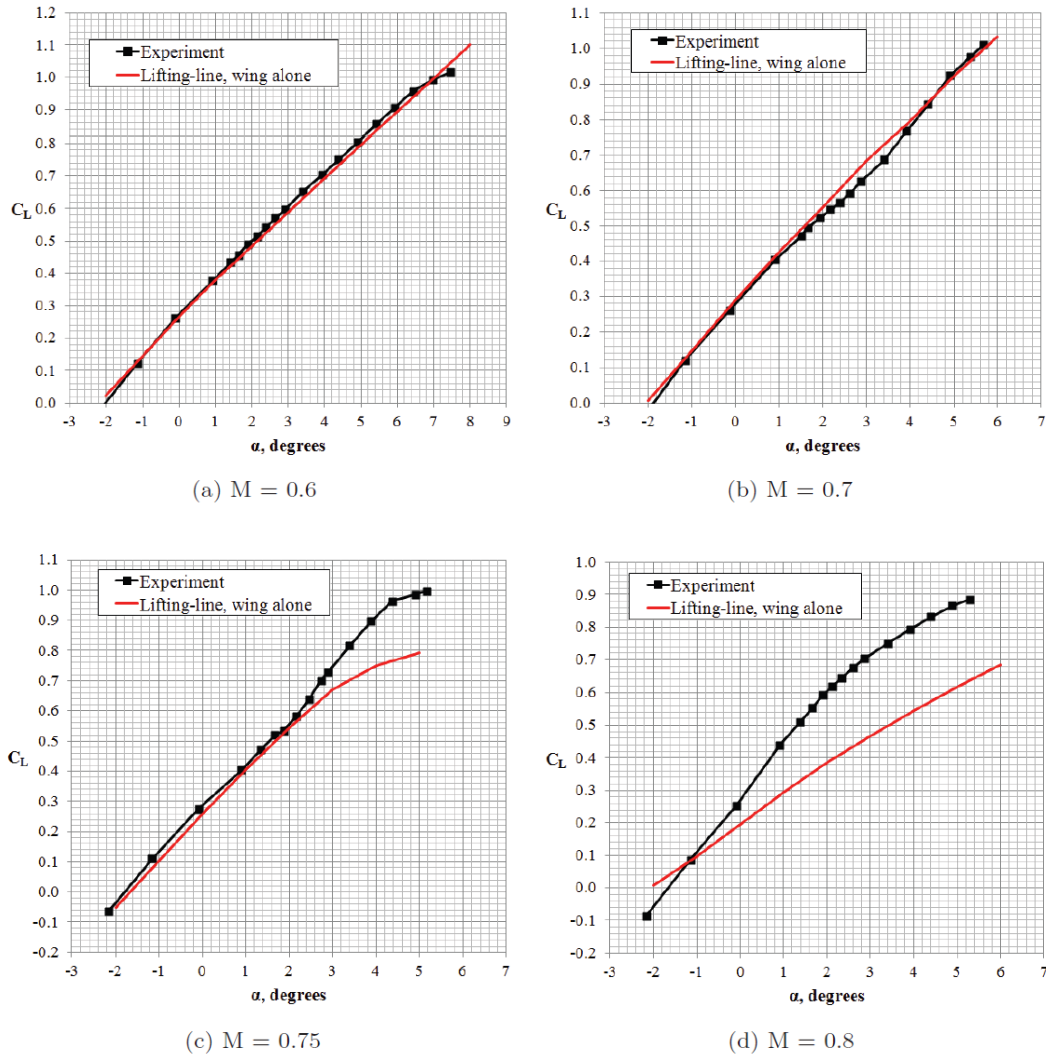


Figure 8. SCW-1a lift-curve comparisons.

D. Wing-body Configuration from the 1st AIAA CFD Drag Prediction Workshop

The wing-body model used for analysis in the 1st AIAA CFD Drag Prediction Workshop was selected as a transonic test case for the lifting-line method. The German Aerospace Research Center DLR-F4 geometry, seen in Figure 9, and wind tunnel results from three sources were documented by Redeker¹⁰ for use as a CFD validation test case. The wind tunnel tests were carried out at a range of transonic Mach numbers and at a Reynolds number based on wing mean geometric chord of 3×10^6 . Boundary-layer transition was fixed on the fuselage as well as the upper and lower wing surfaces.

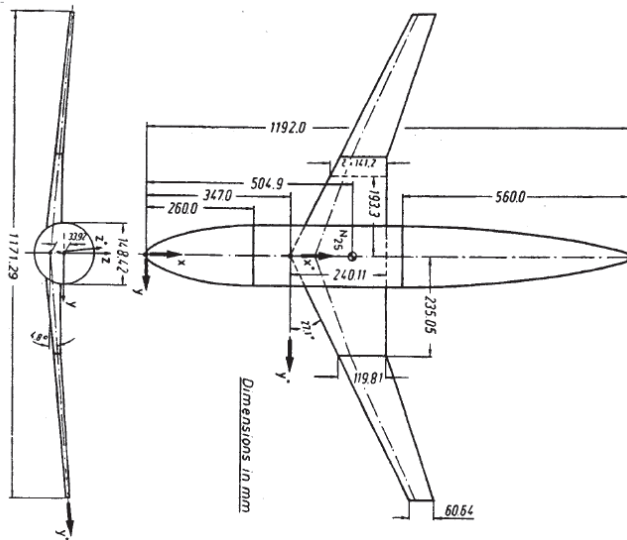


Figure 9. DLR-F4 wing-body geometry (from Ref. 10).

The DLR-F4 wing was modeled for the lifting-line analysis using four airfoils, and the coordinates for each airfoil were supplied as part of the workshop. All airfoil polars were computed with MSES using the fixed transition locations documented in Ref. 10. The inboard airfoil section defined at the wing-body intersection was used at the aircraft model centerline in the absence of a fuselage. A lifting-line analysis was completed for Mach numbers 0.6, 0.75, and 0.8, and the lift curves and drag polars are in Figure 10, Figure 11, and Figure 12. All experimental data in Figure 10 and Figure 12 are from the NLR-HST tests documented in Ref. 10. The drag polars shown include the lifting-line results for the wing-alone as well as with the addition of body-alone experimental drag of 90 counts for all Mach numbers. Adding the body drag in this manner is a conservative estimate considering that the drag of the wing that would be hidden by the fuselage was included in the lifting-line analyses.

For the Mach 0.6 case, the lift values in Figure 10a were slightly over-predicted over the entire curve. However, the lift-curve slope for a linear curve fit between -2° and 3° angle of attack was $\frac{\partial C_L}{\partial \alpha} = 0.0912$ per degree for the lifting-line result and $\frac{\partial C_L}{\partial \alpha} = 0.0929$ per degree for the wind tunnel data. The Mach 0.6 drag predictions in Figure 10b follow the wind tunnel trend very well. The Mach 0.75 lifting-line results were compared with all of the workshop CFD data as well as the wind tunnel data, as can be seen in Figure 11. Similar to the previous test case results, the lifting-line method predicted an early stall in Figure 11a. A linear curve fit of the wind tunnel data from -2° to 1° angle of attack resulted in a lift-curve slope of $\frac{\partial C_L}{\partial \alpha} = 0.1216$ per degree while the lifting-line slope was $\frac{\partial C_L}{\partial \alpha} = 0.1019$ per degree. A linear curve fit of the lifting-line results from -3° to -1° angle of attack was also computed and the result matched the wind tunnel value of $\frac{\partial C_L}{\partial \alpha} = 0.1216$ per degree. The drag predictions in Figure 11b deviated at higher lift values but are still acceptable for design purposes. A trend similar to that seen in the previous case was found for the Mach 0.8 lift-curve results in Figure 12a as well. A majority of the lift values were under-predicted, and the shape of the curve was not well-matched. The drag predictions in Figure 12b were high even before the body drag was added. This trend was caused by the under prediction of lift compared with the wind tunnel results.

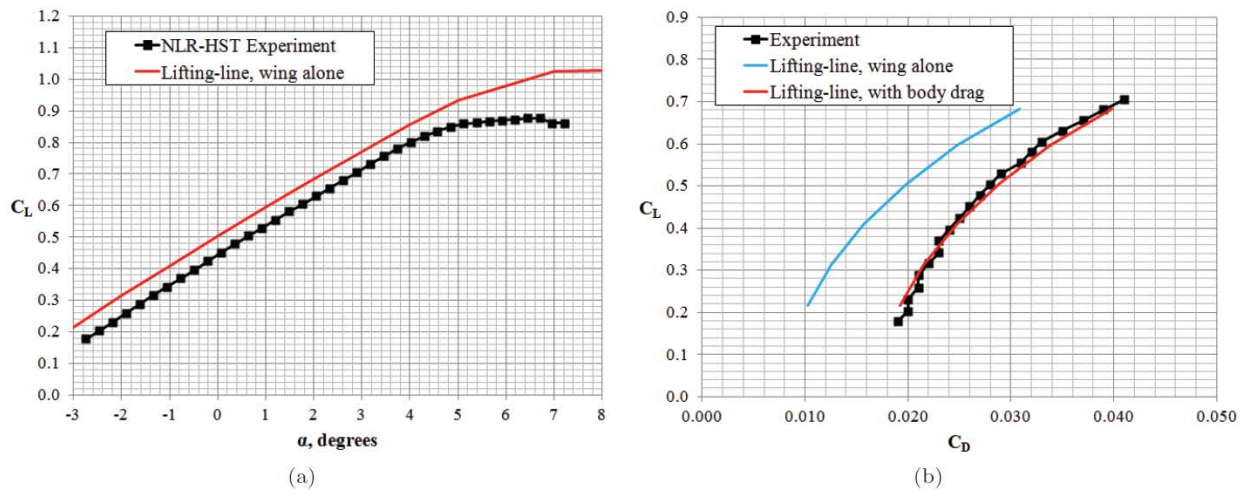
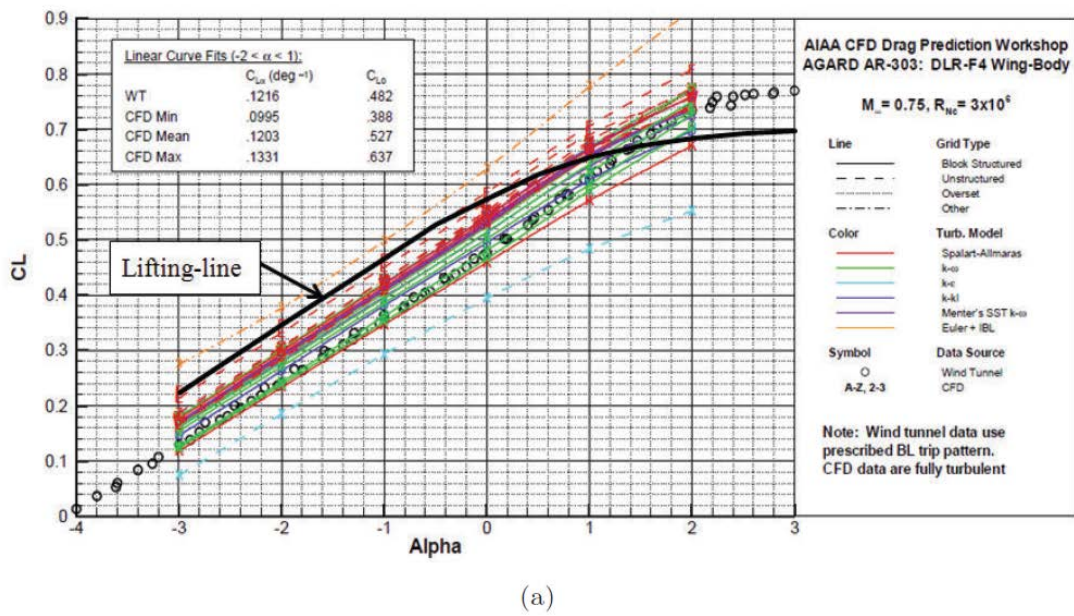
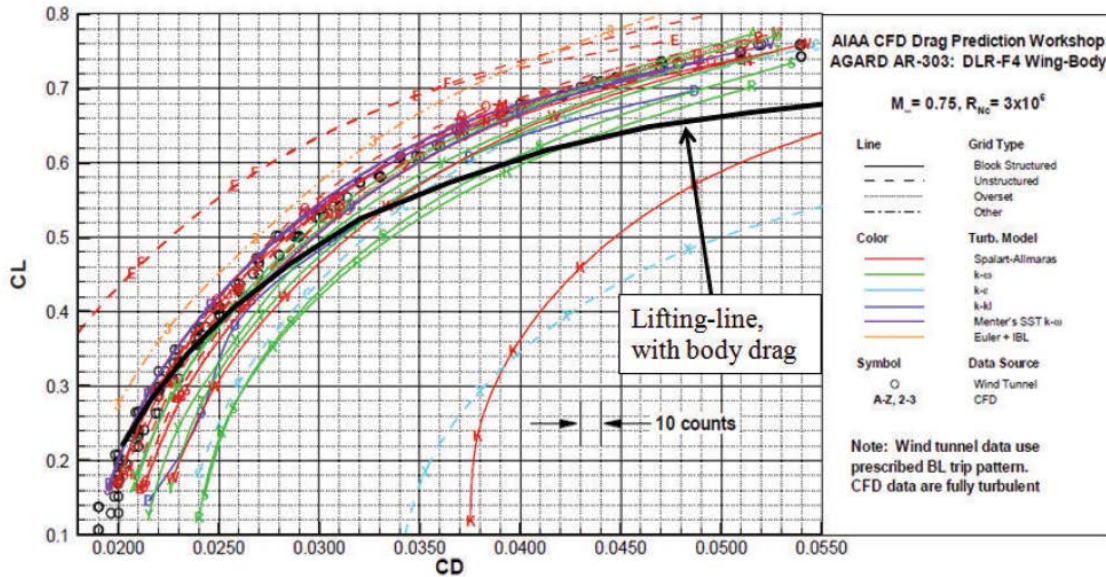


Figure 10. DLR-F4 lift curves (a) and drag polars (b) for $M = 0.6$.



$$M_\infty = .75, R_{Nc} = 3 \times 10^6$$



(b)

Figure 11. DLR-F4 lift curves (a) and drag polars (b) for $M = 0.75$ (original plots from Ref. 11).

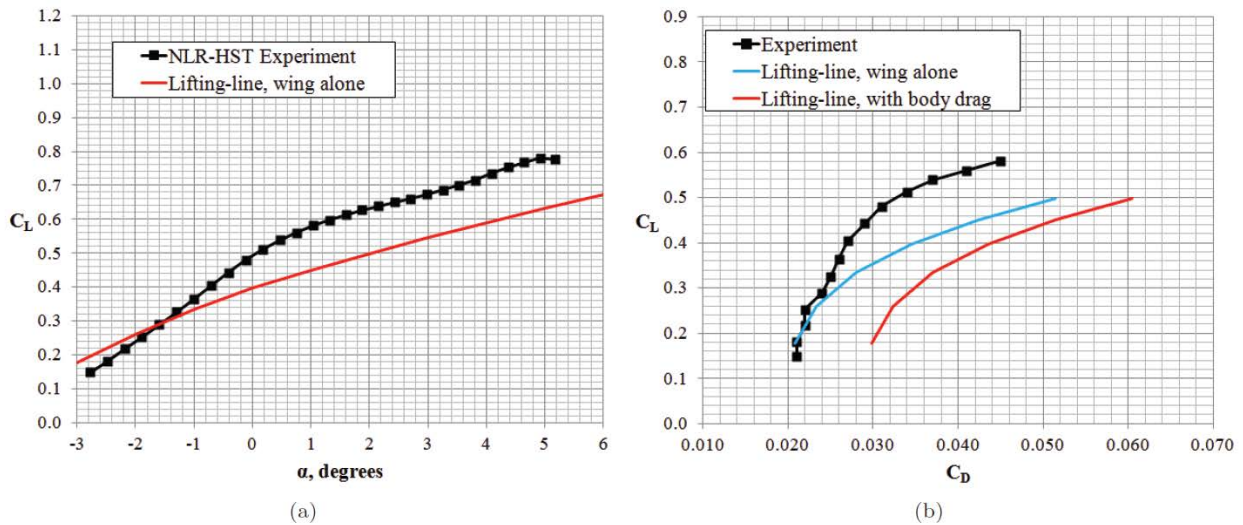


Figure 12. DLR-F4 lift curves (a) and drag polars (b) for $M = 0.8$.

E. Transonic Swept Wing

The final validation case is a swept, tapered wing wind tunnel model. The model is from an experimental investigation by Polhamus and King¹² in which the aerodynamic characteristics of three wings with different aspect ratios were evaluated. The wings were constructed from NACA 63₁012 airfoils and swept back 45°. The wing model selected for validation had an aspect

ratio of 8 and a taper ratio of 0.45. Tests were performed in the NASA Langley 7- by 10-foot tunnel at Mach numbers ranging from 0.7 to 1.15 and a Reynolds number of 570,000.

Ref. 12 did not report fixed boundary-layer transition points. A transition location of 15% chord was assumed for the MSES airfoil analysis. Lifting-line analyses were completed for Mach numbers 0.7, 0.8, and 0.9. The results comparisons are shown in Figure 13, Figure 14, and Figure 15. The Mach 0.7 lifting-line lift curve and drag polar demonstrated excellent agreement with the trends seen in the experimental data. Although the lift values were slightly over-predicted at positive angles of attack, the shape of the stall curve was followed very well. The Mach 0.8 predictions are promising because the lift-curve slope predicted by the lifting-line method is not significantly different from the experimental data. The drag polar at Mach 0.8 was predicted accurately up to a lift coefficient of approximately 0.12, but beyond this point, the drag was over-predicted. At Mach 0.9, the lift curve was predicted with more accuracy than shown for the previous transonic cases. However, the drag polar demonstrated a large over-prediction at all lift values.

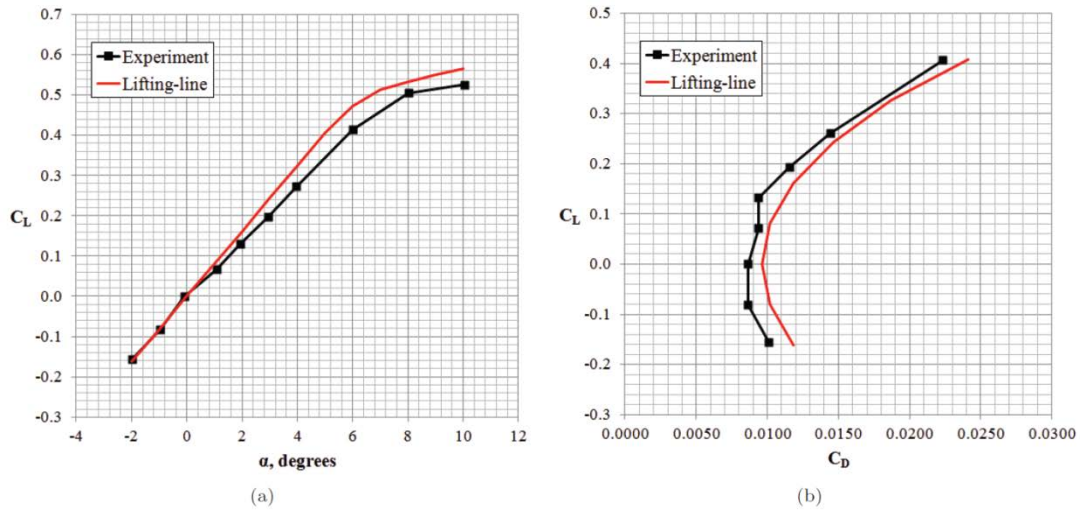


Figure 13. Transonic swept wing lift curves (a) and drag polars (b) for $M = 0.7$.

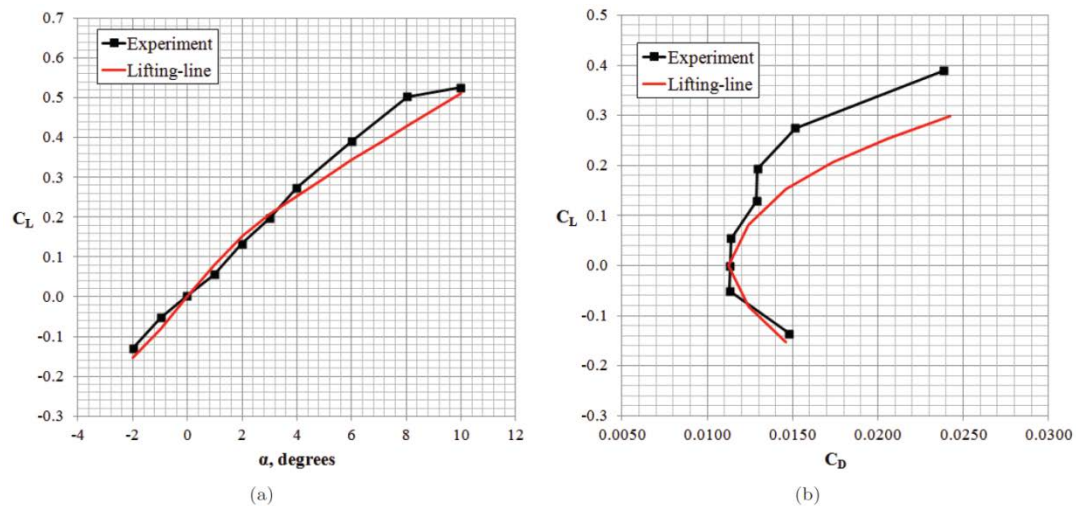


Figure 14. Transonic swept wing lift curves (a) and drag polars (b) for $M = 0.8$.

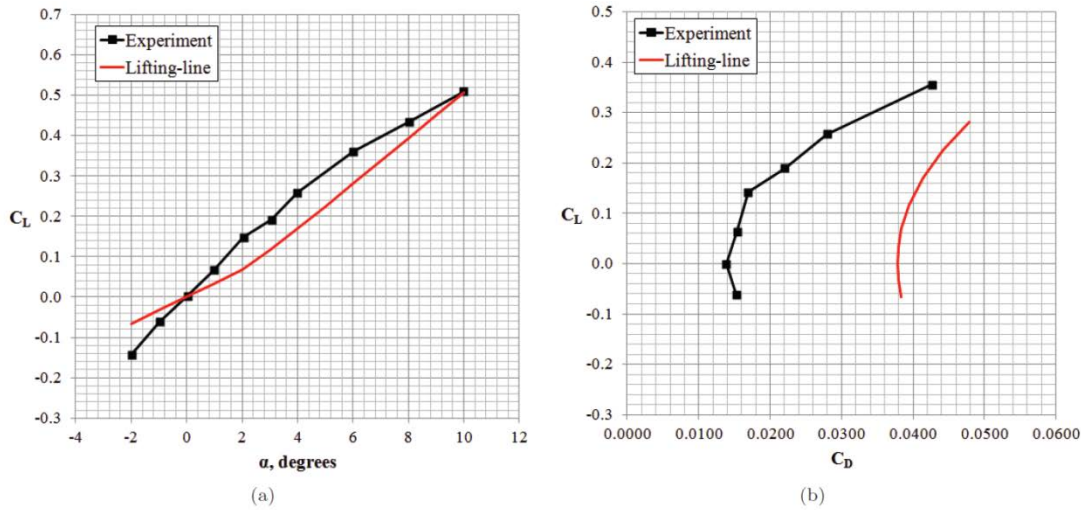


Figure 15. Transonic swept wing lift curves (a) and drag polars (b) for $M = 0.9$.

IV. Discussion of Lifting-Line Test Case Results

The largest discrepancies observed in the multiple-lifting-surface cases were present in the stall region of the lift curves. For the wing-canard model, the late stall prediction was apparent in the individual wing and canard contributions. This was most likely caused by late stall predictions from XFOIL. The drag polar prediction may have also been affected by the airfoil data. As previously mentioned, the three-lifting surface business jet case exhibited an erratic stall curve, but this wasn't completely unanticipated. However, predictions for both cases were excellent in the linear regions of the lift curves. The wing-canard model also exhibited discrepancies in the individual component lift curves. Further work should include additional verification of the method's capability to capture interference effects.

The transport-type aircraft model predictions were satisfactory at lower transonic speeds, but they diverged from experimental data as the Mach number increased above 0.75. It is suspected that a combination of problems created the degradation of the results at higher Mach numbers. One major consideration is that the fuselage was not and could not be included in the lifting-line analyses. With increasing Mach number, the fuselage interference effects may have become quite significant. In a commercial transport design study by Jameson,¹³ he notes that the fuselage can contribute approximately 15% of the total aircraft lift. The design speed range in the study was between Mach numbers 0.8 and 0.9. In an experimental study by Danforth and O'Bryan,¹⁴ static pressure was measured with a wing-tip boom installed on a fighter aircraft wind tunnel model. The freestream Mach number was set at various transonic speeds. The results showed a deviation in the pressure coefficient measured at the boom, due to fuselage effects, beginning at approximately Mach 0.75. A similar trend could have affected the results for the transonic transport-type aircraft comparisons. Future work should compare CFD predictions for the transport-type aircraft models with and without the fuselage present. A method for modeling a fuselage must also be addressed. Although discrepancies were present in the lifting-line results, it is encouraging that the method predicted lift and drag values at Mach 0.75 within the range of

CFD computations from the 1st AIAA CFD Drag Prediction Workshop (see Figures 11a and 11b). The last validation case provided evidence that the lift-curve slope can be predicted at transonic speeds with more accuracy when a fuselage is not present. However, the drag polar discrepancies were larger as the Mach number increased for the final two cases. It is suspected that this was due to the MSES airfoil drag predictions.

Each test case presented in this work took no more than a few hours to set up the geometry inputs, run the airfoil analyses, and execute the lifting-line code. As a comparison, multiple days would be required for CFD geometry creation, meshing, and solution convergence. With further validation and verification and incorporation of a fuselage modeling method, this tool will serve as a powerful conceptual design tool.

V. Planform Design Tool

The modern lifting-line code serves as the foundation for the planform design capability. In fact, the planform design code simply generates a seed geometry and executes an optimizer which receives objective function values from the modern lifting-line code. This portion of the report explains how the design tool is set up.

A. Optimization Routine

The optimization routine, developed by Vanderplaats,¹⁵ employs sequential quadratic programming with the modified method of feasible directions for solving the direction-finding subproblem. For one-dimensional search, the optimizer uses polynomial interpolation with bounds. Gradients are obtained by a forward difference formula using a step size of 0.1% of the design variable, with 0.001 being the lower bound on the step size. The objective function options available include maximization of either C_L/C_D or $C_L^{3/2}/C_D$.

B. Fixed Inputs

Many inputs to the modern lifting-line code have been fixed in the planform design tool. The following is a complete list of these inputs:

- Airfoil data
- Flight Mach number and altitude (incorporated in airfoil data)
- Number of lifting surfaces
- Spans and reference areas of all lifting surfaces
- Relative locations of all lifting surfaces
- Configuration angle of attack
- Number of spanwise breaks for each lifting surface
- Spanwise distribution of the input airfoils (the order they follow as a function of span)
- Number of horseshoe vortex elements used to synthesize each lifting surface
- Angle between trailing edge and aircraft centerline out to a set break location for Yehudi (optional)

C. Design Variables

The available design variables offer full flexibility of the planform geometry. Note that the optimizer normalizes each of these variables for use in the optimization routine. Chord lengths are normalized by an average chord, which is calculated as reference area divided by span. Additionally, the tip chord length is calculated during the optimization to ensure that a fixed reference area is maintained. Design variables include the following:

- Break span positions (normalized by half of the span)
- Chord length at each break other than the tip (normalized by average chord)
- Sweep angle at each break (normalized by half of the span)
- Dihedral angle at each break, out of the page in Figure 16 (normalized by half of the span)
- Twist angle at each break (normalized by a reference value of 10°)

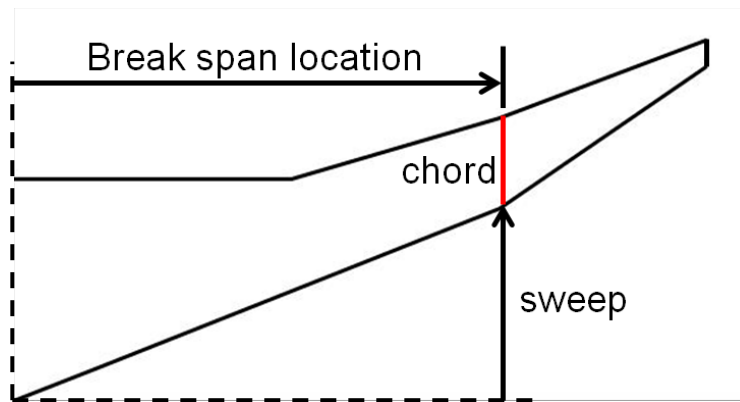


Figure 16. Illustration of design variable definitions.

If a Yehudi is present in the design, the code will not change the span location of breaks that are part of the Yehudi portion of the wing. Also, the chords, sweeps, and dihedrals of breaks that are part of the Yehudi will be calculated to maintain straight leading and trailing edges. Outboard of the Yehudi, the design variables are treated normally.

D. Constraints

The flexibility offered by the design variables can often lead to undesirable solutions. Thus, constraint options have been implemented in the planform design code to enable more control. The available constraints include:

- Minimum leading edge sweep angle
- Minimum dihedral angle
- Maximum and minimum configuration C_L
- Minimum taper ratio
- Maximum and minimum twist angle
- Require each chord length to be smaller than the adjacent inboard chord length (optional)

- For a Yehudi geometry, require the root chord length to be at least as long as the baseline geometry

In addition to the above list, four options are available for controlling the leading and trailing edge sweeps. The options are listed below from most to least flexible.

- Variable sweep at each break location
- Maintain straight leading edge
- Maintain straight leading edge and trailing edge
- Fixed leading edge sweep angle

E. Initialization

Two planform options are offered for initialization of the wing geometry; with Yehudi or straight and tapered. In both cases, all leading edge sweeps and dihedrals are set at the input minimum constraints. The initialized root chord length is set to the baseline, and the tip chord is calculated using the input starting taper ratio. All intermediate chords are computed based on linear interpolation. Then, all chord lengths are scaled to satisfy the input reference area.

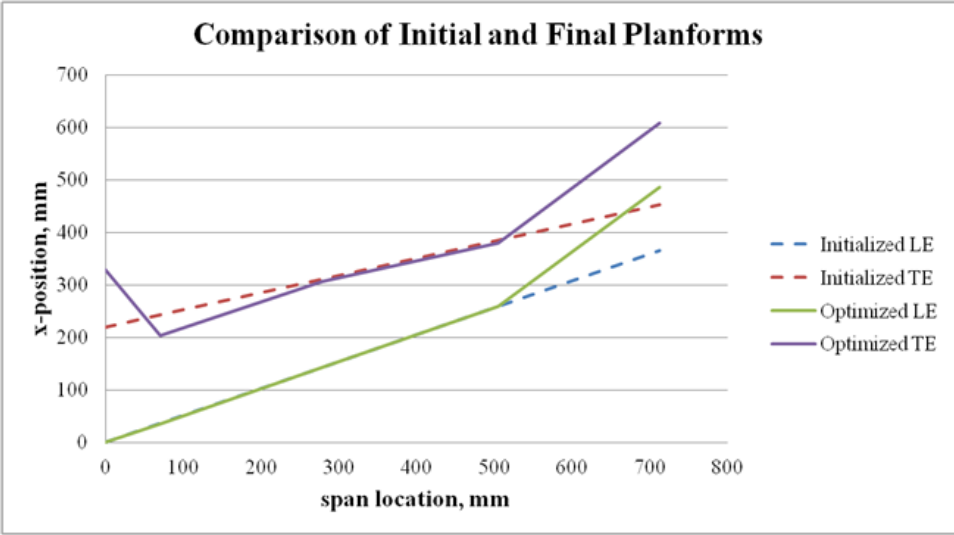
VI. Planform Design Tool Sample Results

A sample case has been optimized with various settings to test the design tool. The baseline model used is the DLR-F4 geometry from Ref. 10. The minimum allowable leading edge sweep was set at the baseline value of 27.1° , and the dihedral angle was set to be fixed for all optimization runs at the baseline value of 4.8° . Bounds were set on the twist angles just outside of the maximum and minimum present in the baseline geometry of 5.3° and 0.3° . Flight conditions were fixed at a Reynold's number of 3×10^6 , Mach number of 0.75, and configuration angle of attack of -2° . The objective function maximized for all cases is C_L/C_D , with the baseline value being 24.01. All airfoil data used in the optimizations is identical to that used in the validation study from section III-D of this report.

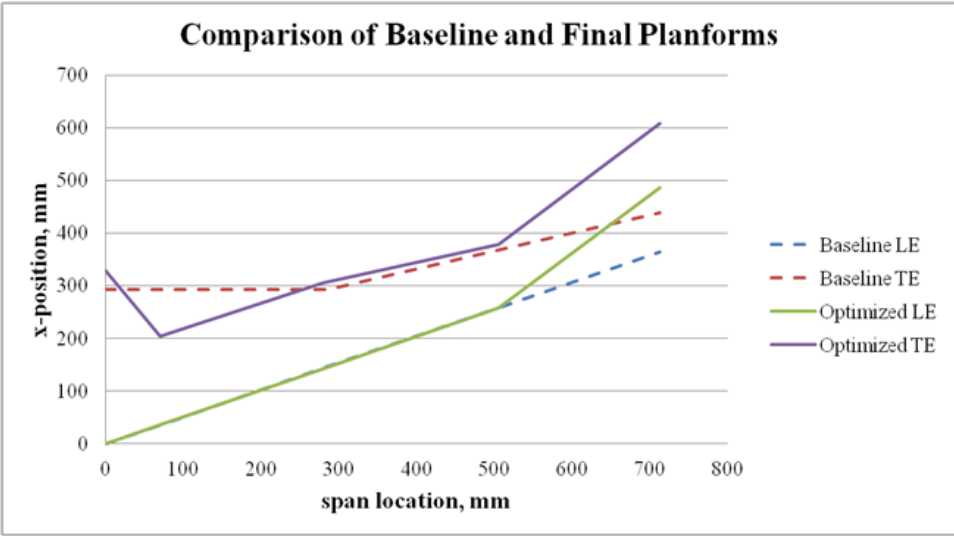
A. Straight and Tapered Wing Initialization

The following optimization test cases were initialized with a straight and tapered wing planform. Cases are presented for each of the sweep options: variable sweep at each break, maintaining straight leading edge, fixed leading edge sweep, and maintaining straight leading edge and trailing edge.

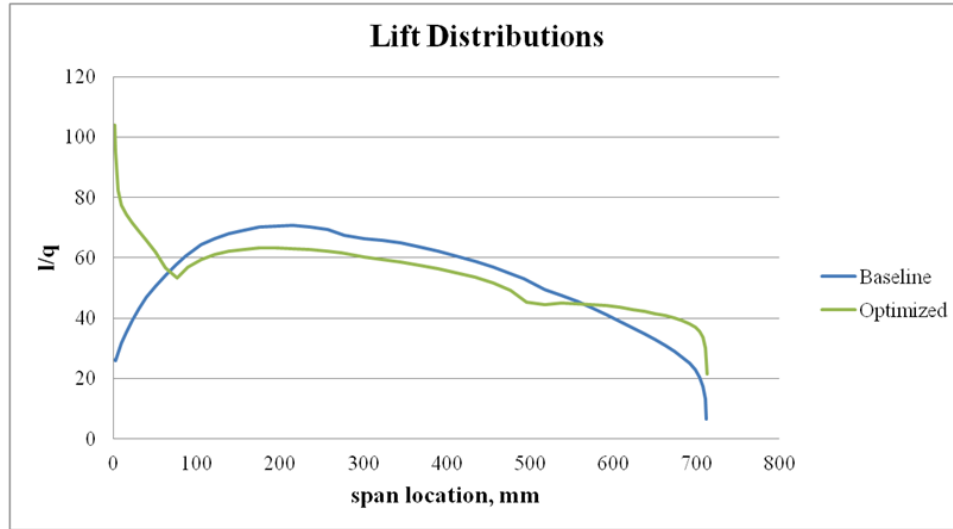
The first test case was set up for variable sweep at each break with C_L constrained to lie between the baseline value of 0.356 and 0.365. The initialized planform had a taper ratio of 0.4. The results of the optimization are shown in Figure 17. As anticipated, the flexibility in sweeps and the fact that structural considerations were ignored allowed the optimizer to produce a geometry that is probably not practical. However, the gain in the objective for this case was 5.9%.



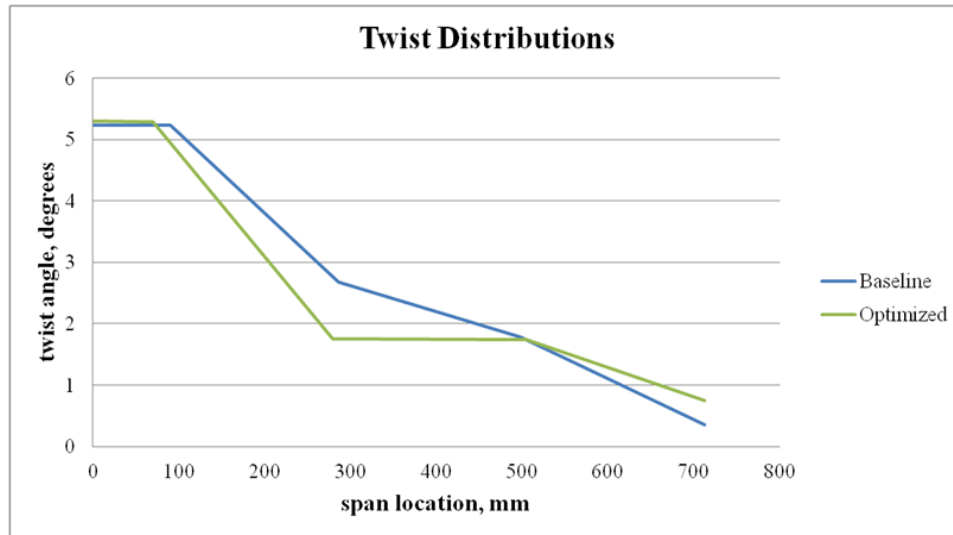
(a)



(b)



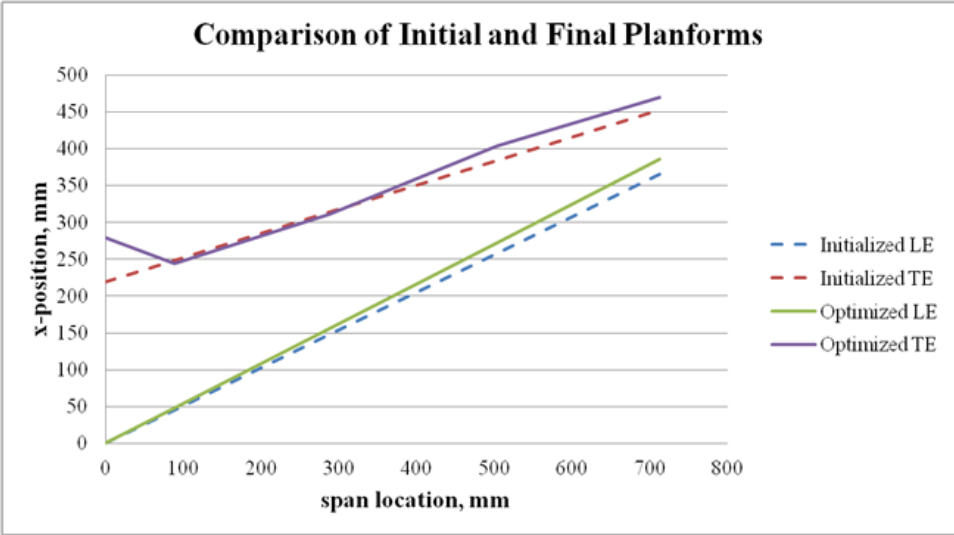
(c)



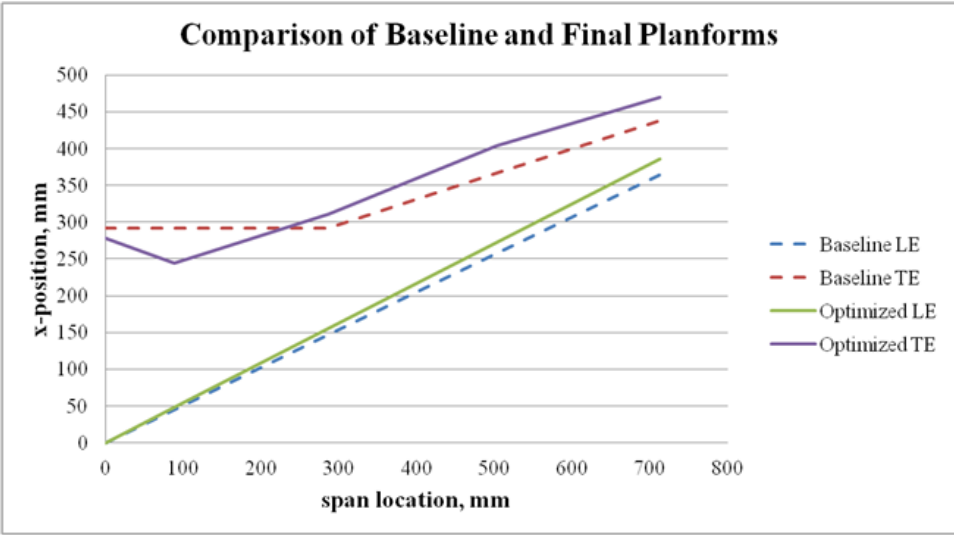
(d)

Figure 17. Optimization results for straight and tapered initialization with variable sweep at each break.

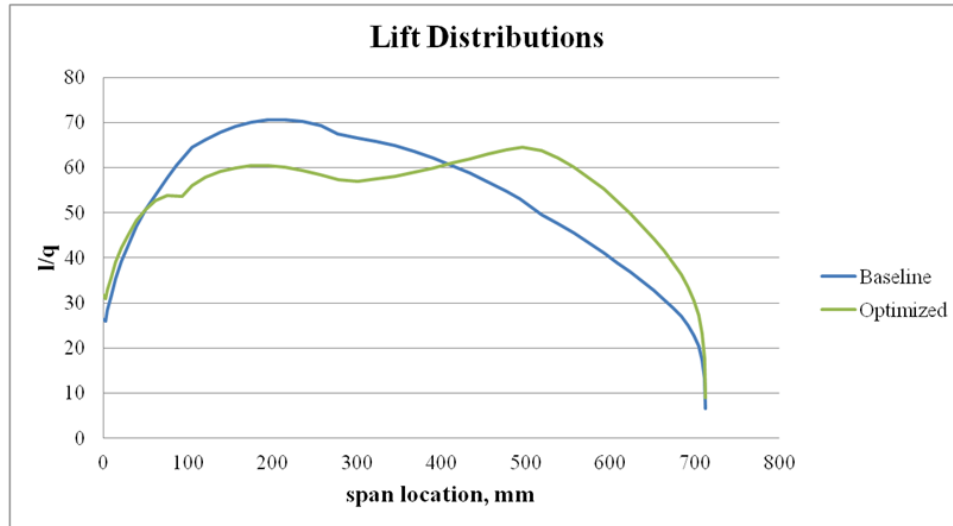
The next test case was set up to maintain a straight leading edge with C_L constrained to lie between the baseline value of 0.356 and 0.365. The initialized planform had a taper ratio of 0.4. The results of the optimization are shown in Figure 18. It is apparent that requiring a straight leading edge produced a geometry that looks more reasonable. A flaw in this design is the high twist angle at approximately 70% span which results in high outboard loading. The gain in the objective for this case was modest at 0.3%.



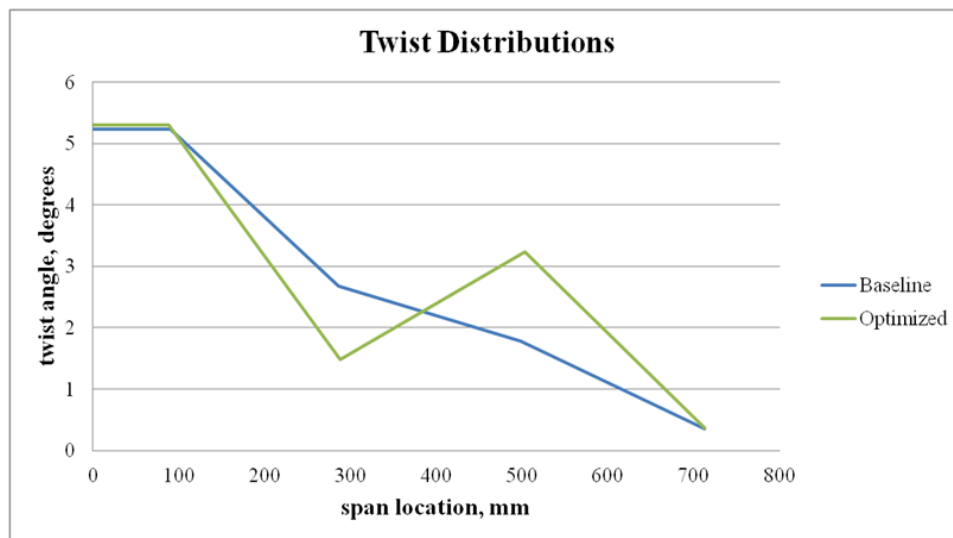
(a)



(b)



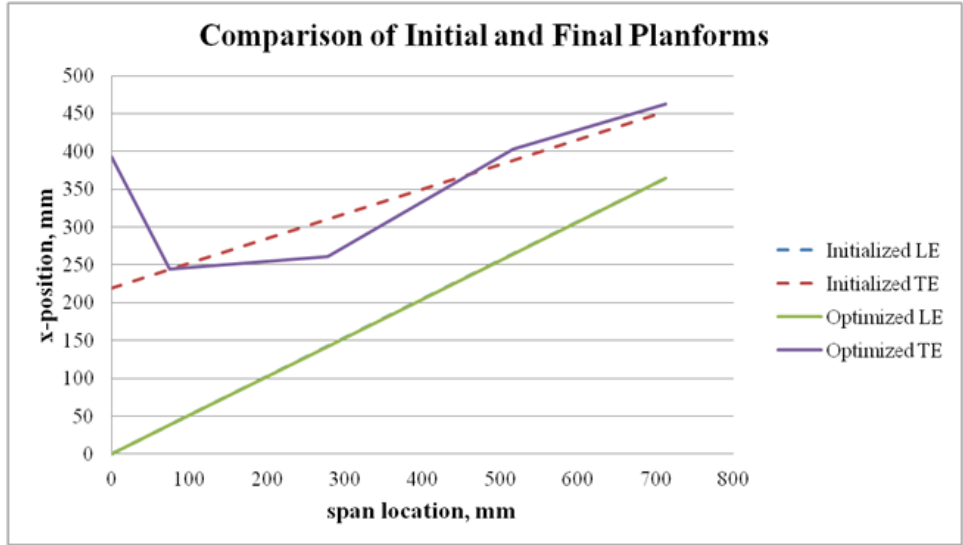
(c)



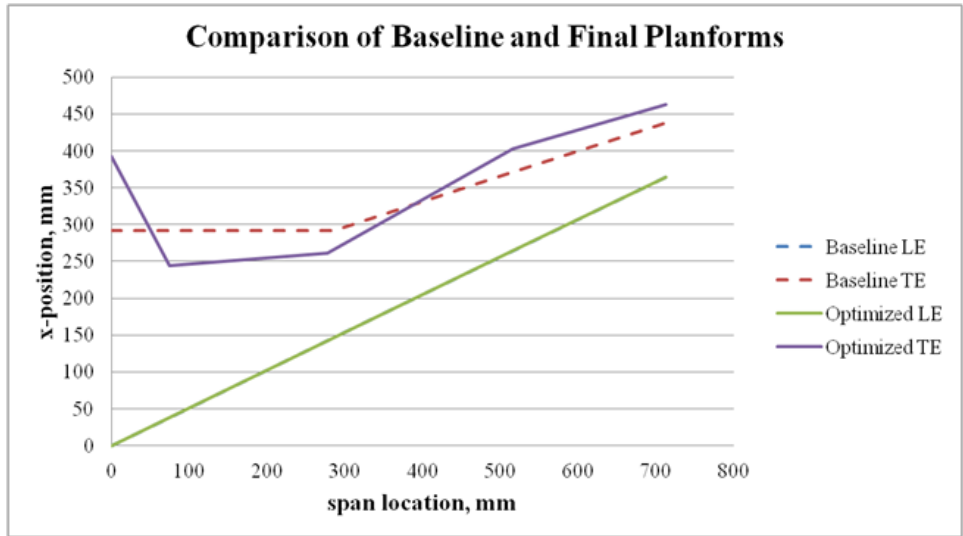
(d)

Figure 18. Optimization results for straight and tapered initialization with straight leading edge.

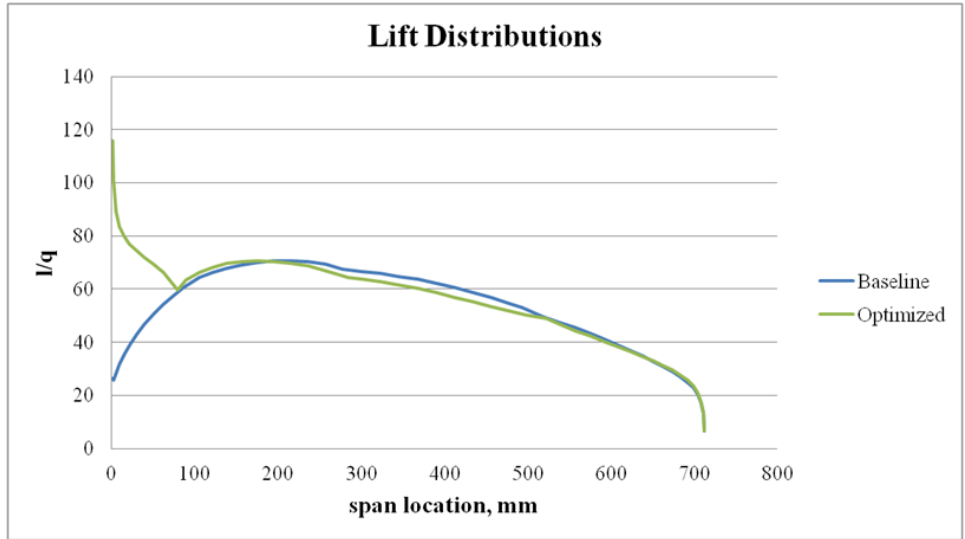
The following test case was set up to maintain a fixed leading edge with C_L constrained to lie between the baseline value of 0.356 and 0.37. The initialized planform had a taper ratio of 0.4. The results of the optimization are shown in Figure 19. This optimized planform demonstrates that the optimizer exploited sensitivities of the chord length variables in the absence of sweep variables. The gain in the objective for this case was the most impressive at 16.4%.



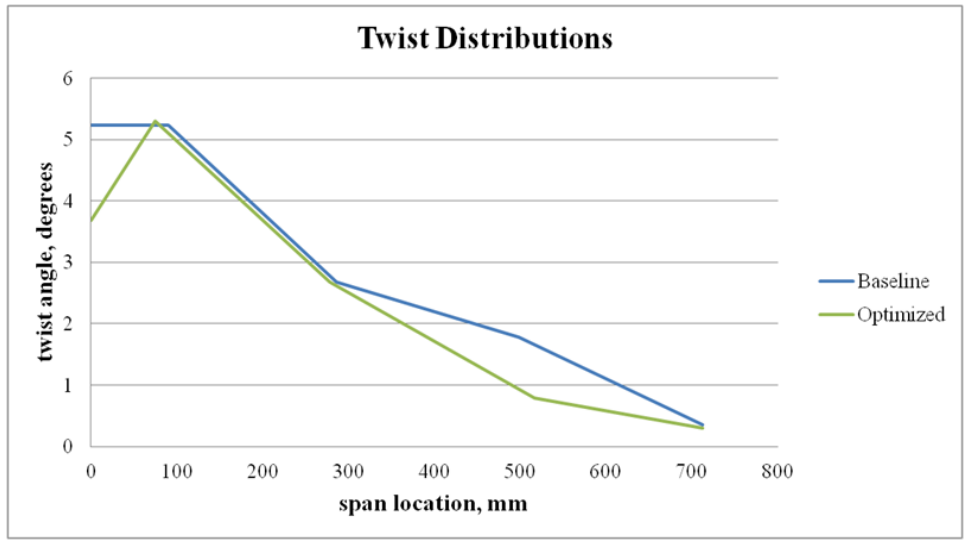
(a)



(b)



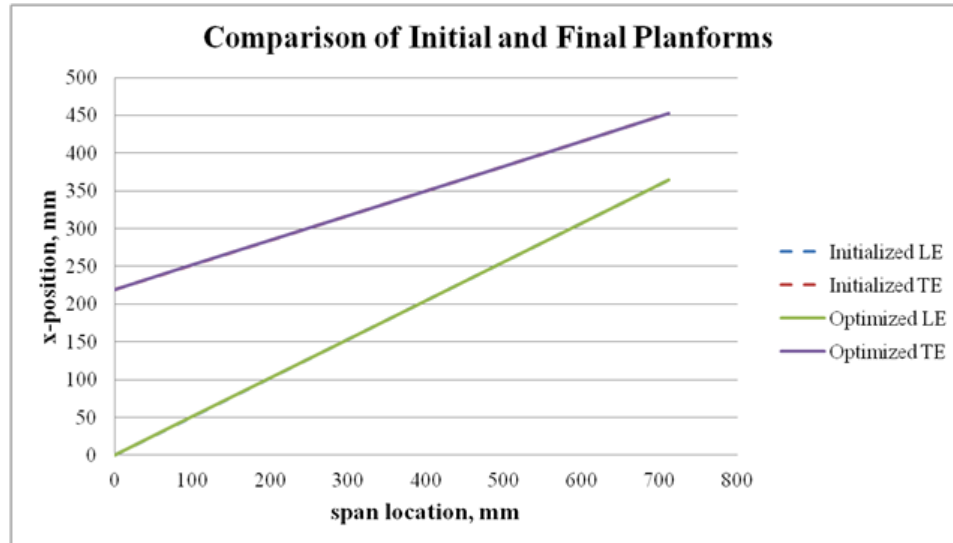
(c)



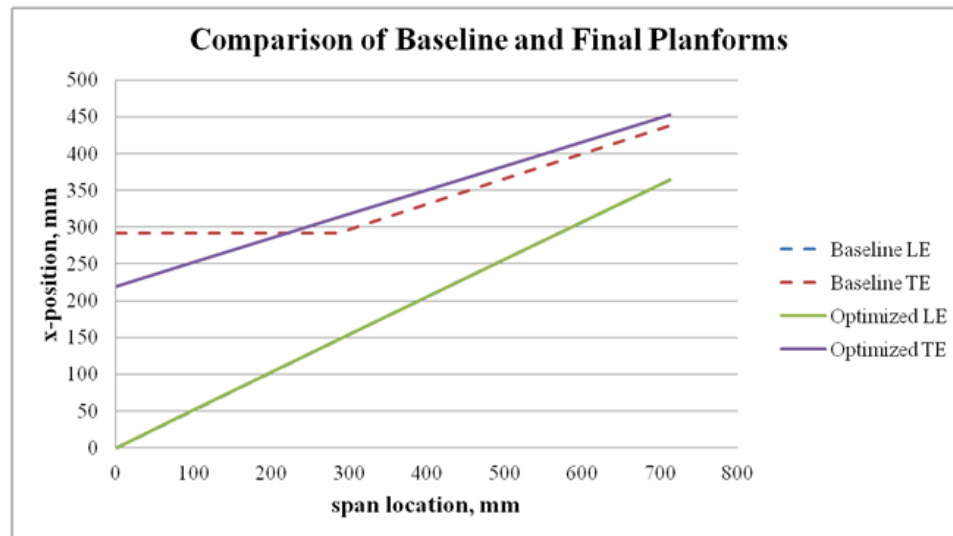
(d)

Figure 19. Optimization results for straight and tapered initialization with fixed leading edge.

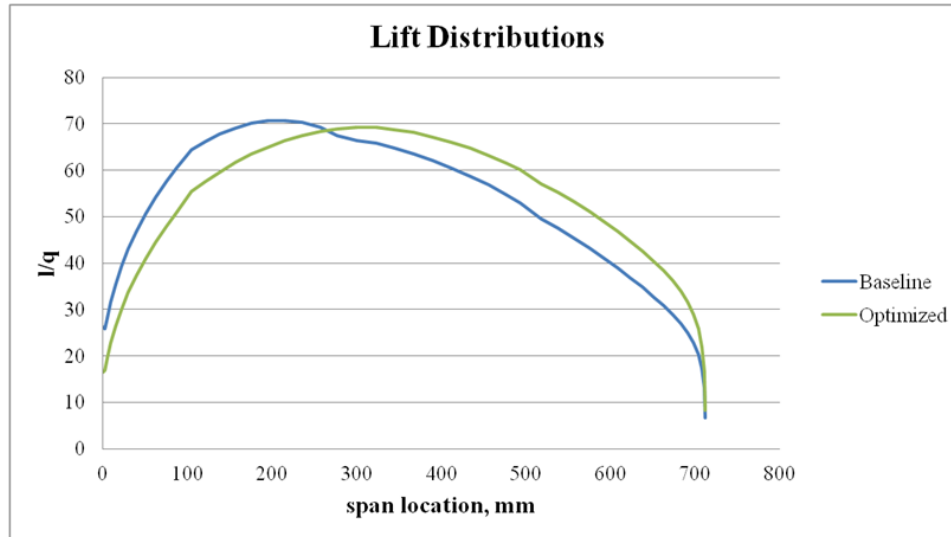
The next test case was set up to maintain a fixed leading edge and trailing edge with C_L constrained to lie between the baseline value of 0.356 and 0.365. The initialized planform had a taper ratio of 0.4. The results of the optimization are shown in Figure 20. This optimized planform did not change significantly from the initialized planform. This is attributed to the seed geometry, as will be shown in the next case. The change in the objective for this case was -1.6%.



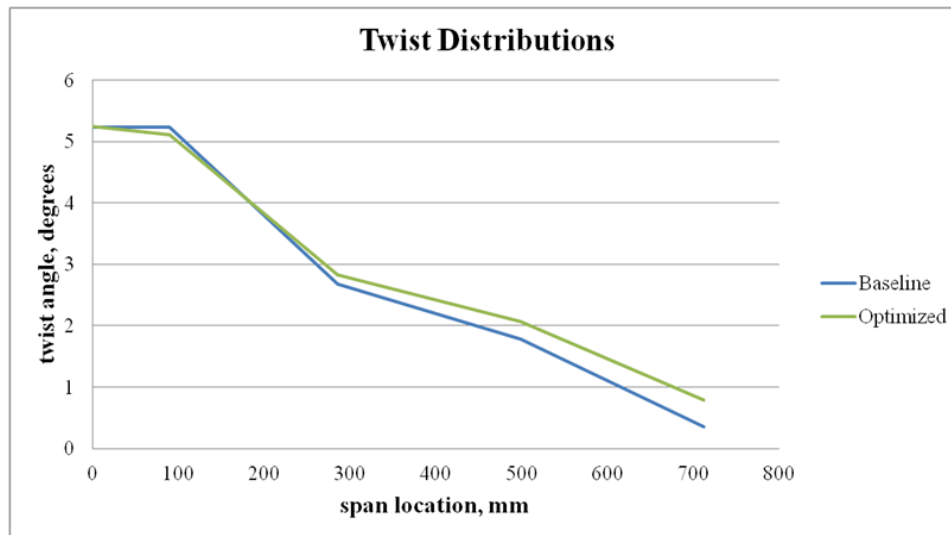
(a)



(b)



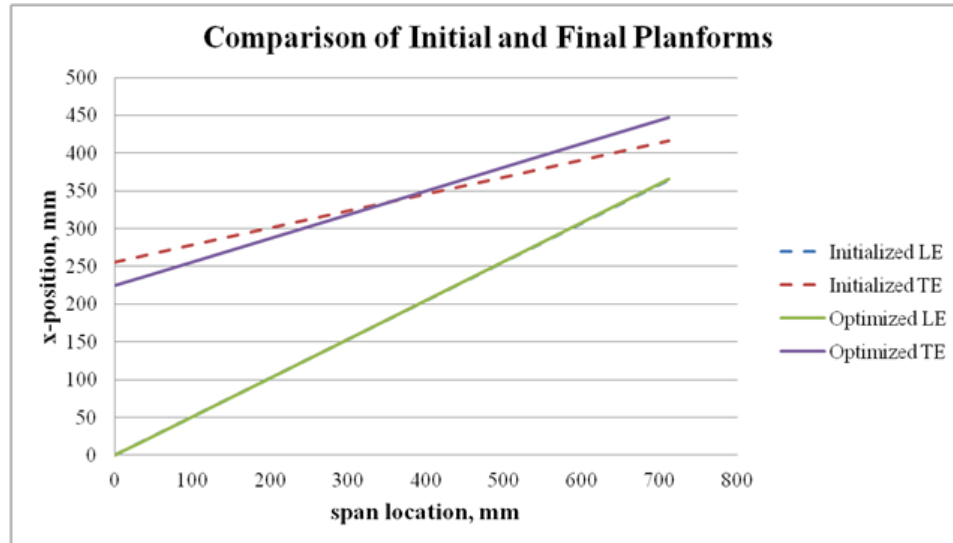
(c)



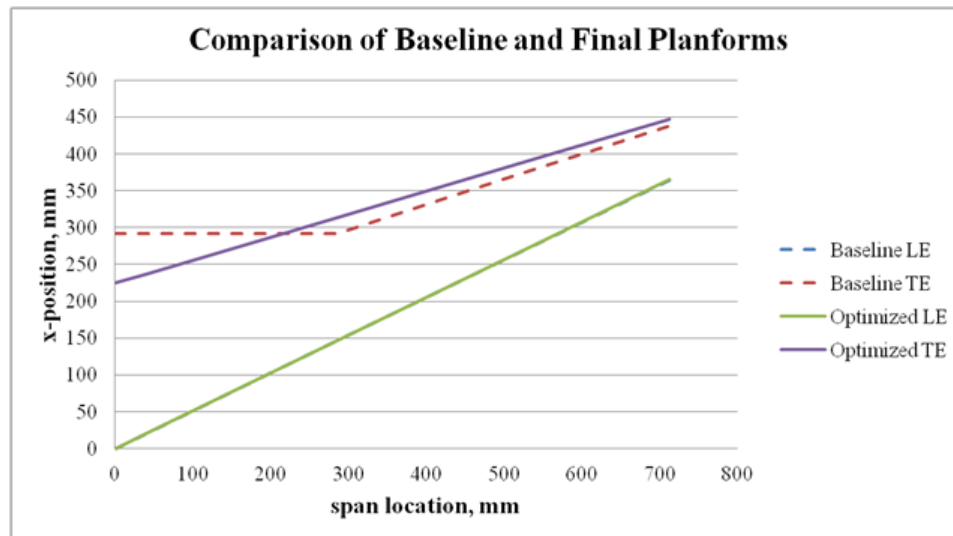
(d)

Figure 20. Optimization results for straight and tapered initialization with straight leading edge and trailing edge (initialized taper ratio = 0.4).

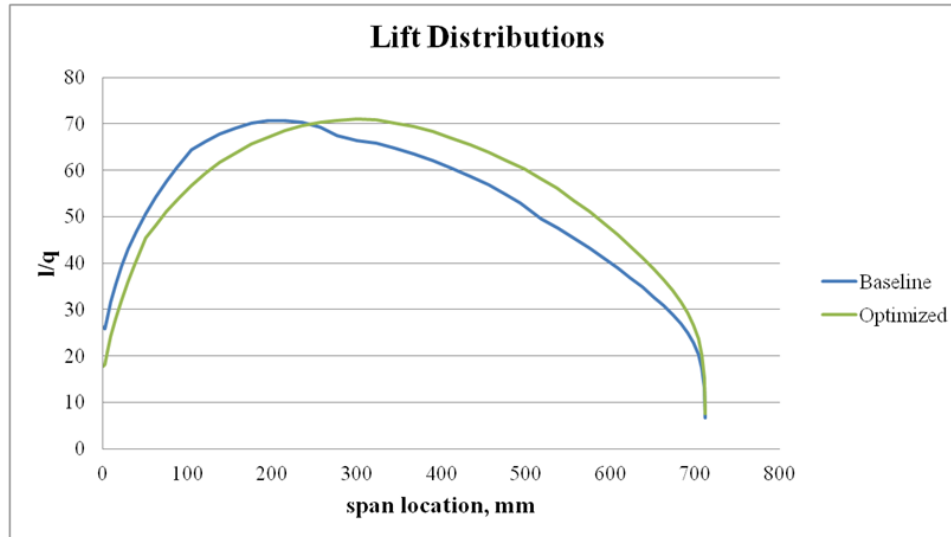
The final straight and tapered test case was set up to maintain a fixed leading edge and trailing edge as well, with C_L constrained to lie between the baseline value of 0.356 and 0.37. However, for this case the initialized planform had a taper ratio of 0.2. The results of the optimization are shown in Figure 21. This optimized planform changed much more significantly from the initialized planform. Initializing the geometry with a taper ratio of 0.2 and increasing the maximum C_L constraint facilitated improvement of the objective. The gain in the objective for this case was 0.8%.



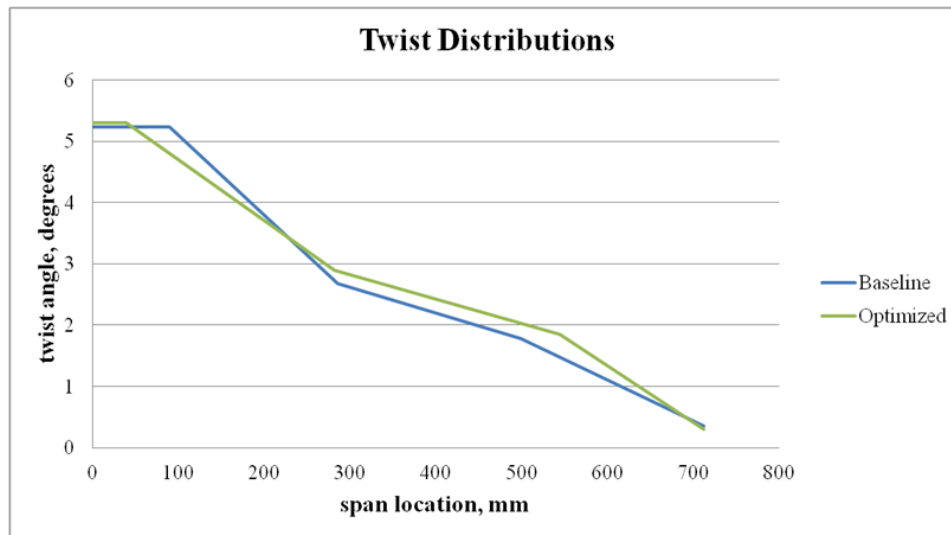
(a)



(b)



(c)



(d)

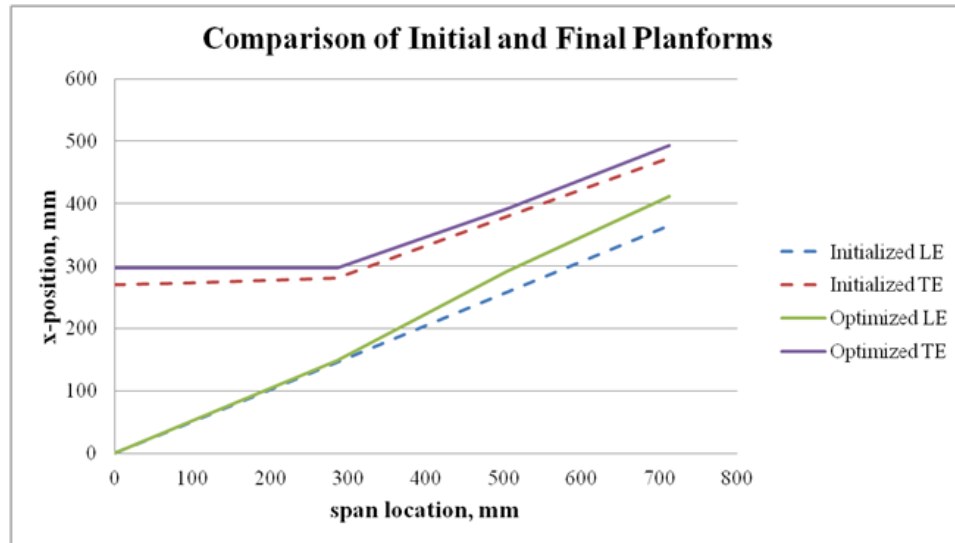
Figure 21. Optimization results for straight and tapered initialization with straight leading edge and trailing edge (initialized taper ratio = 0.2).

B. Wing with Yehudi Initialization

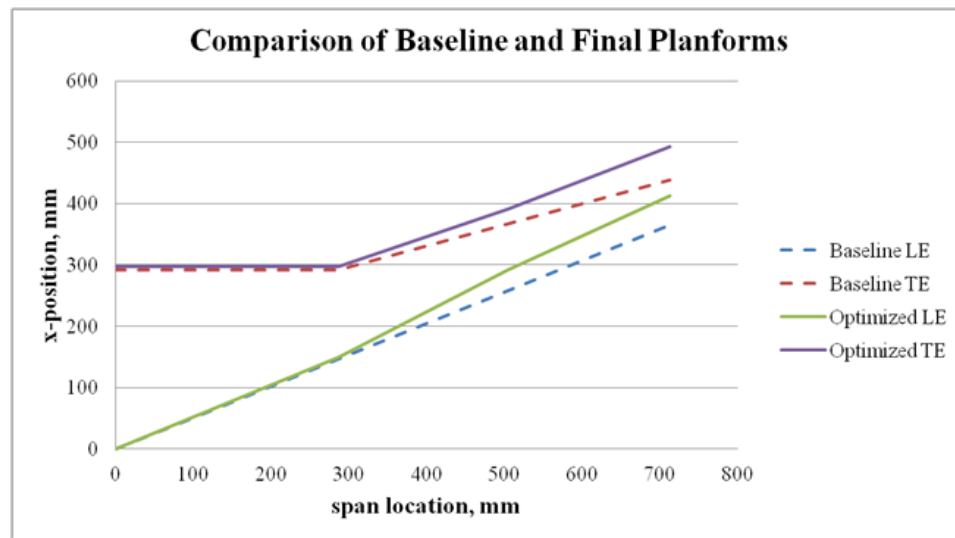
The following optimization test cases have been initialized with a Yehudi and straight and tapered outboard section planform. As in the previous section, cases are presented for each of the sweep options: variable sweep at each break, maintaining straight leading edge, fixed leading edge sweep, and maintaining straight leading edge and trailing edge.

The first Yehudi test case was set up for variable sweep at each break, not including the break between the root and Yehudi break, with C_L constrained to lie between the baseline value of 0.356 and 0.37. The initialized planform had a taper ratio of 0.4. The results of the

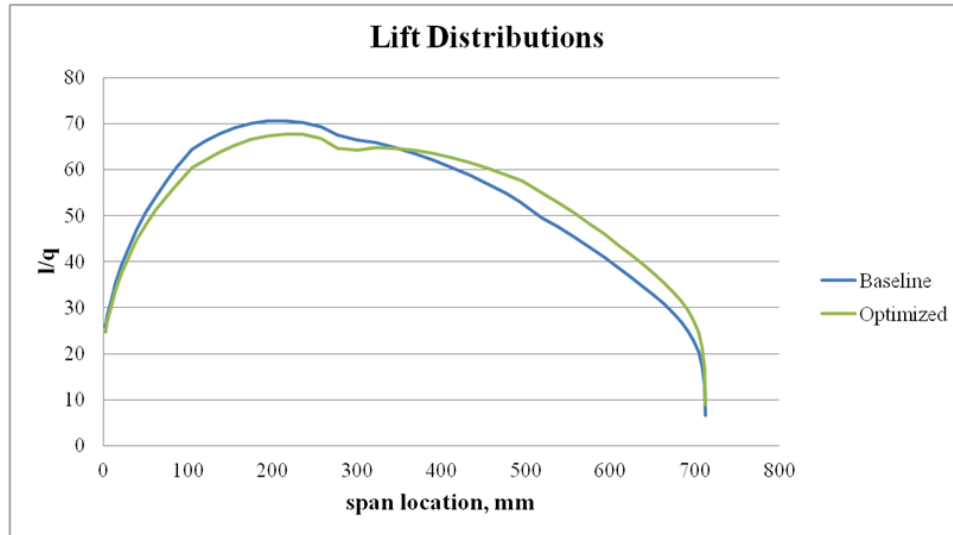
optimization are shown in Figure 22. The constraint of maintaining the Yehudi layout facilitated a more realistic optimized planform. The gain in the objective for this case was 1.1%.



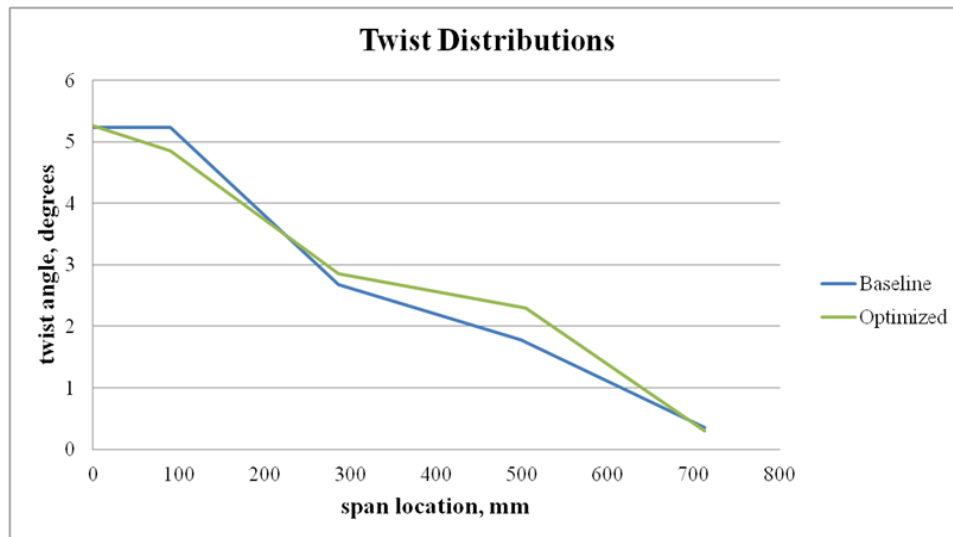
(a)



(b)



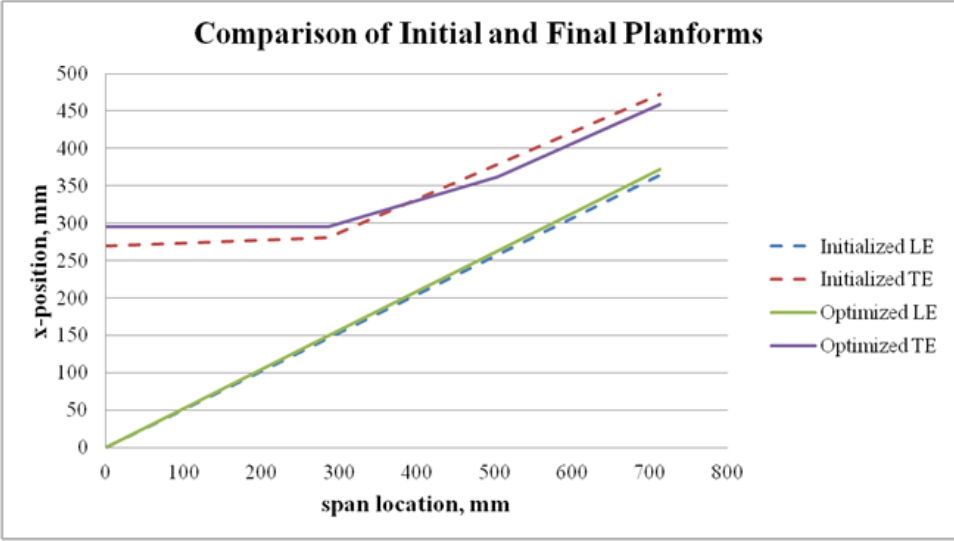
(c)



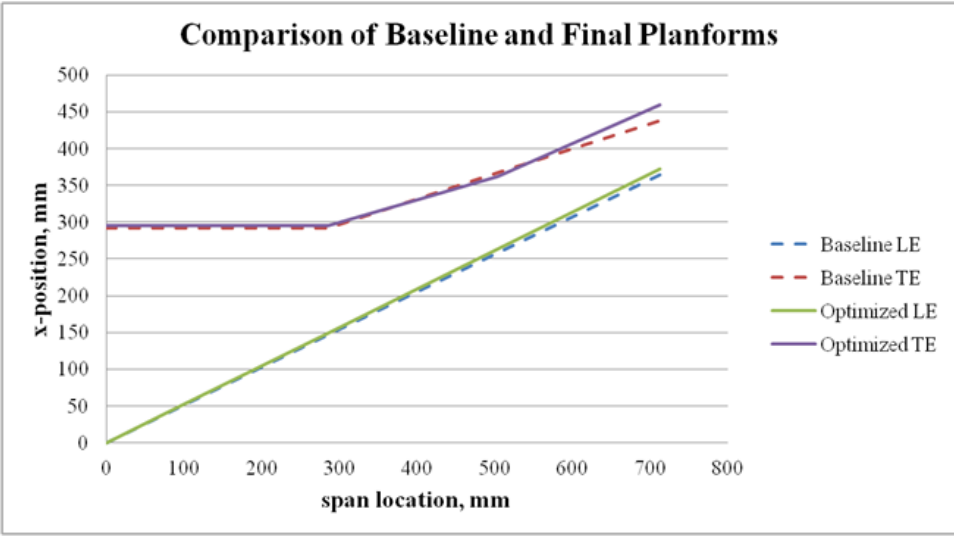
(d)

Figure 22. Optimization results for Yehudi initialization with variable sweep at each break.

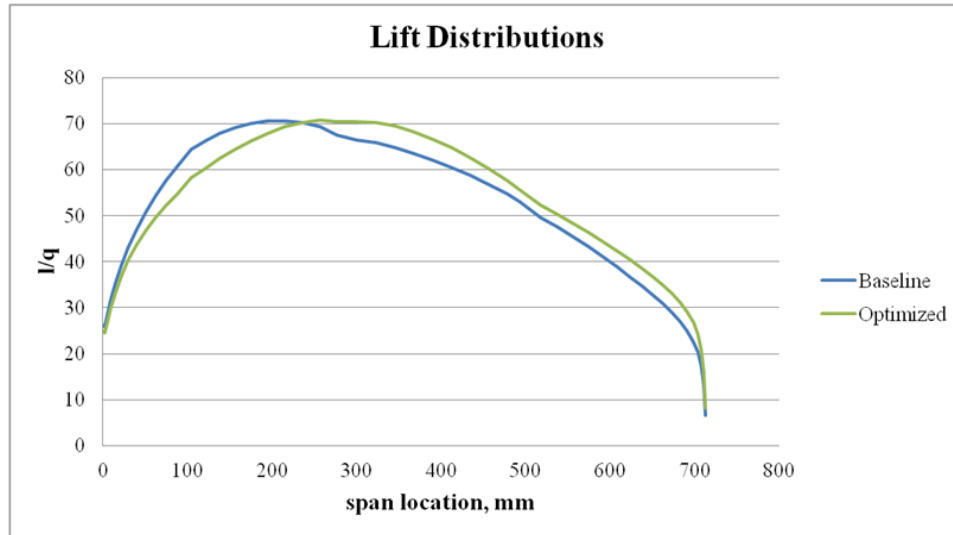
The next Yehudi test case was set up to maintain a straight leading edge with C_L constrained to lie between the baseline value of 0.356 and 0.37. The initialized planform had a taper ratio of 0.4. The results of the optimization are shown in Figure 23. As expected based on the previous case, the optimizer very slightly swept the leading edge. The gain in the objective for this case was 0.5%.



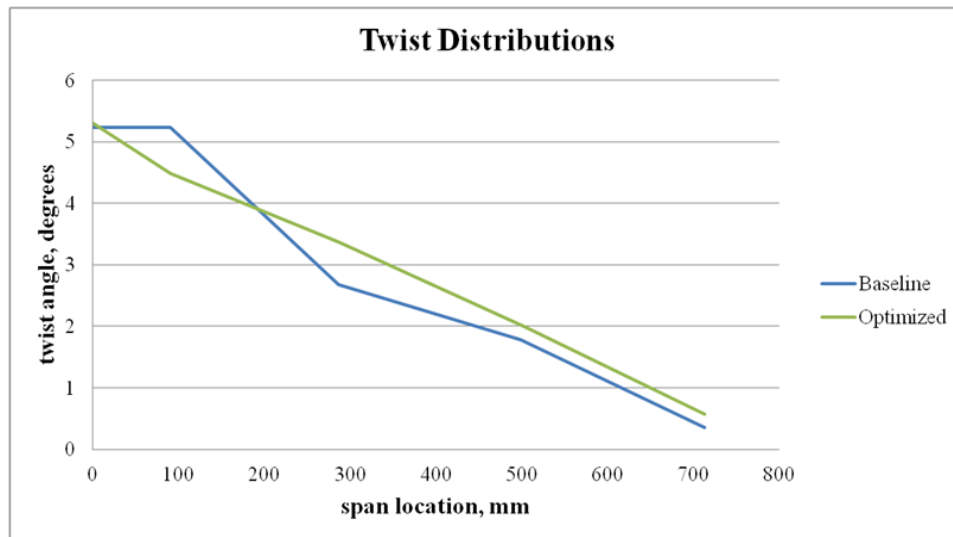
(a)



(b)



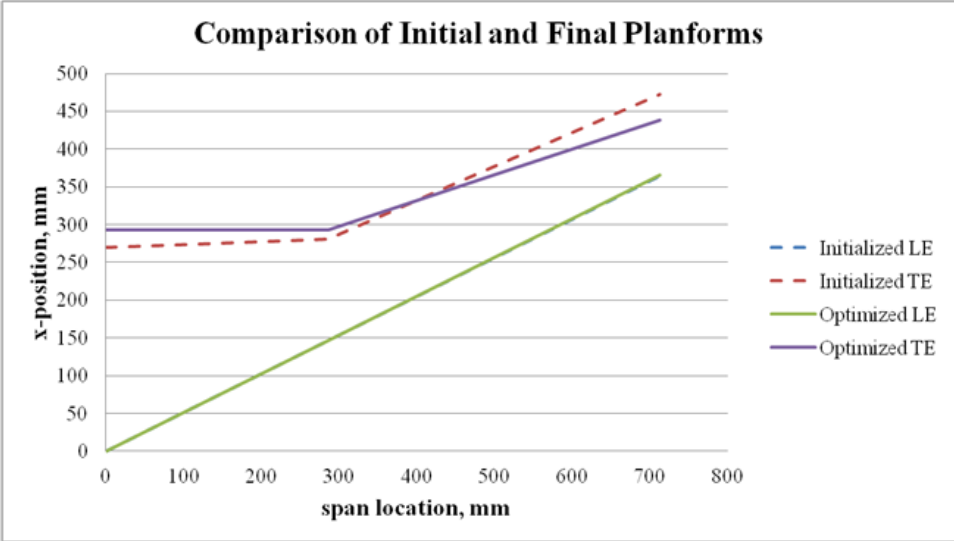
(c)



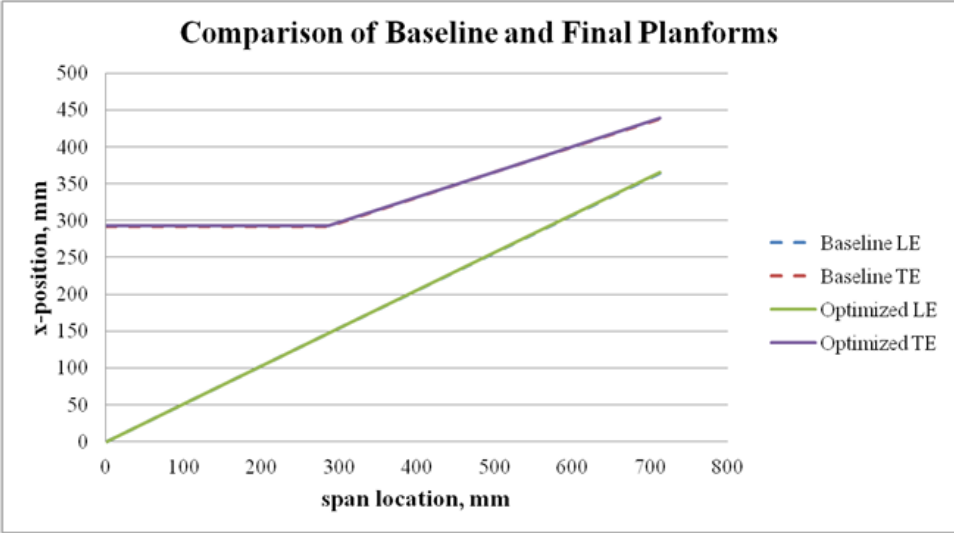
(d)

Figure 23. Optimization results for Yehudi initialization with straight leading edge.

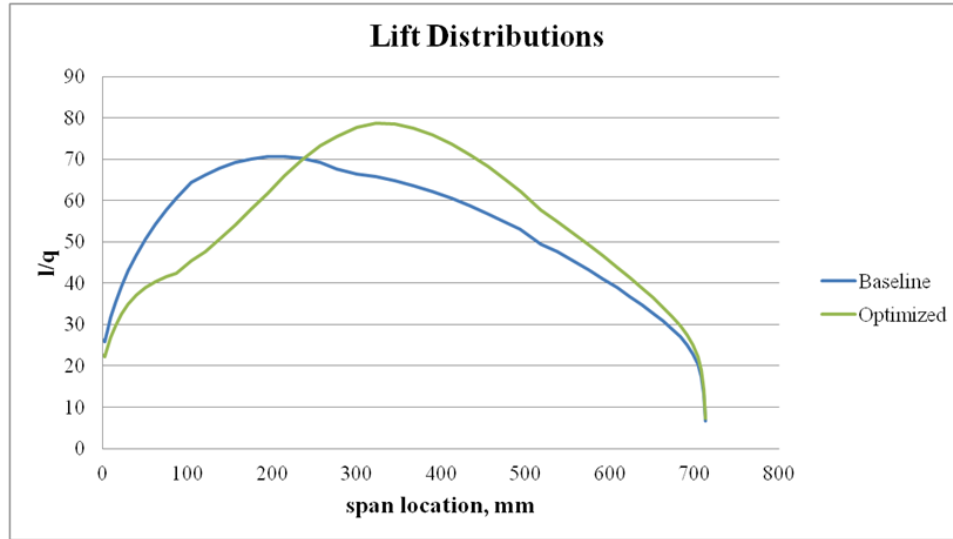
The following Yehudi test case was set up to maintain straight leading and trailing edges with C_L constrained to lie between the baseline value of 0.356 and 0.36. The initialized planform had a taper ratio of 0.4. The results of the optimization are shown in Figure 24. The optimized solution planform is not much different than the baseline, but the twist distribution was significantly altered relative to the baseline. The difference in the objective for this case was -2.9%.



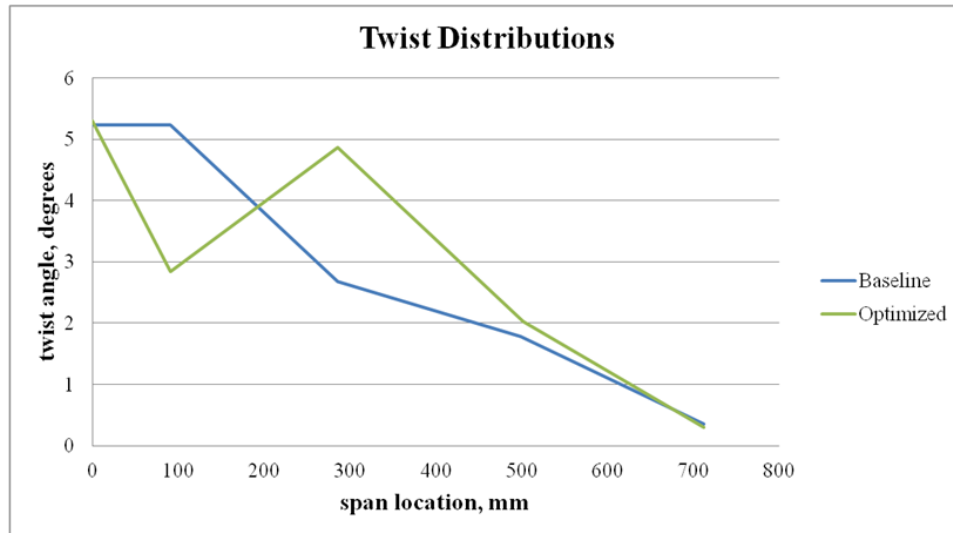
(a)



(b)



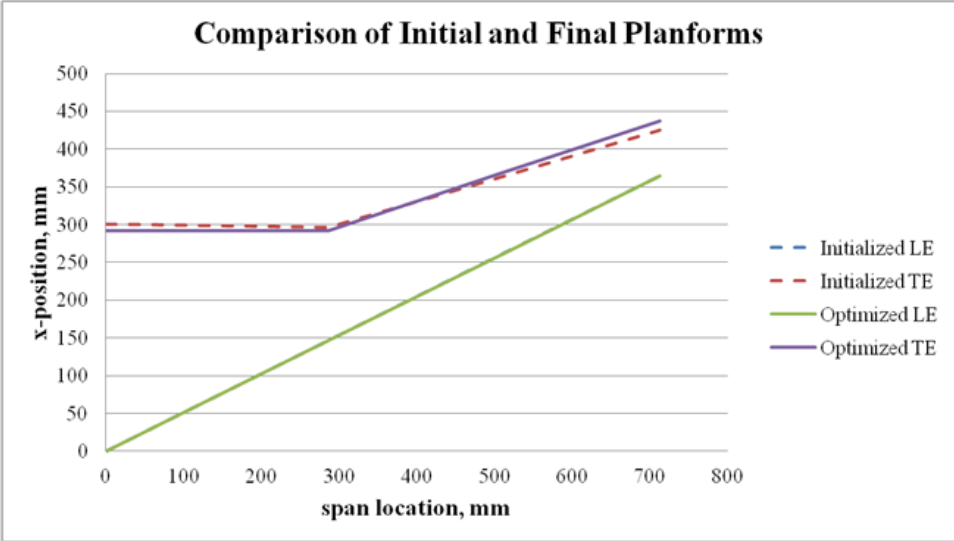
(c)



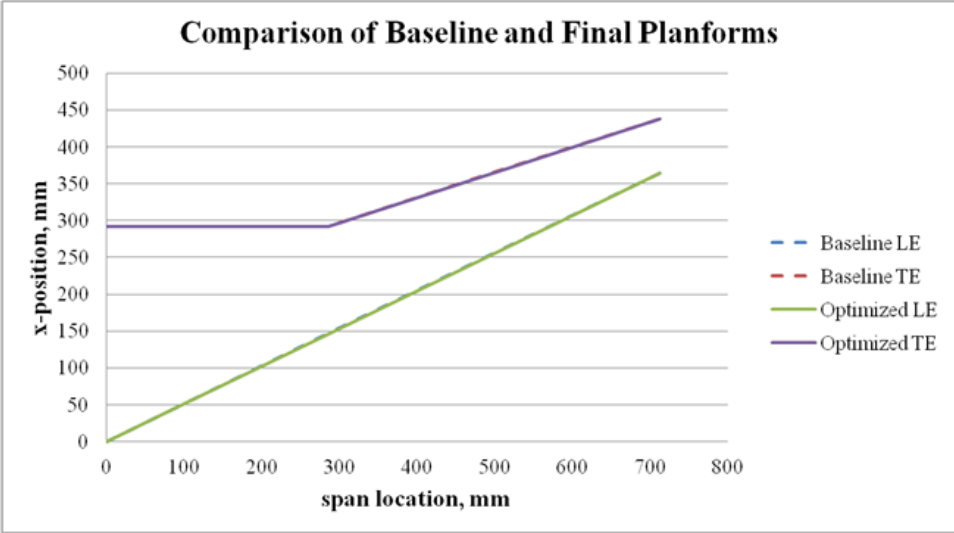
(d)

Figure 24. Optimization results for Yehudi initialization with straight leading edge and trailing edge (initialized taper ratio = 0.4).

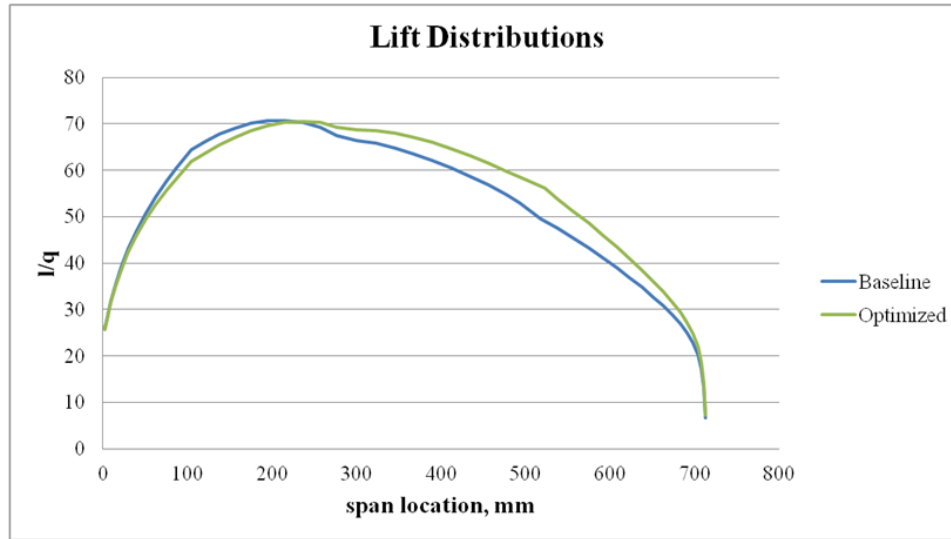
The next Yehudi test case was set up to maintain straight leading and trailing edges as well, with C_L constrained to lie between the baseline value of 0.356 and 0.37. The initialized planform had a taper ratio of 0.2. The results of the optimization are shown in Figure 25. Once again a much improved solution is found by choosing a different initial taper ratio and broadening the C_L constraint range. The difference in the objective for this case was 2.5%.



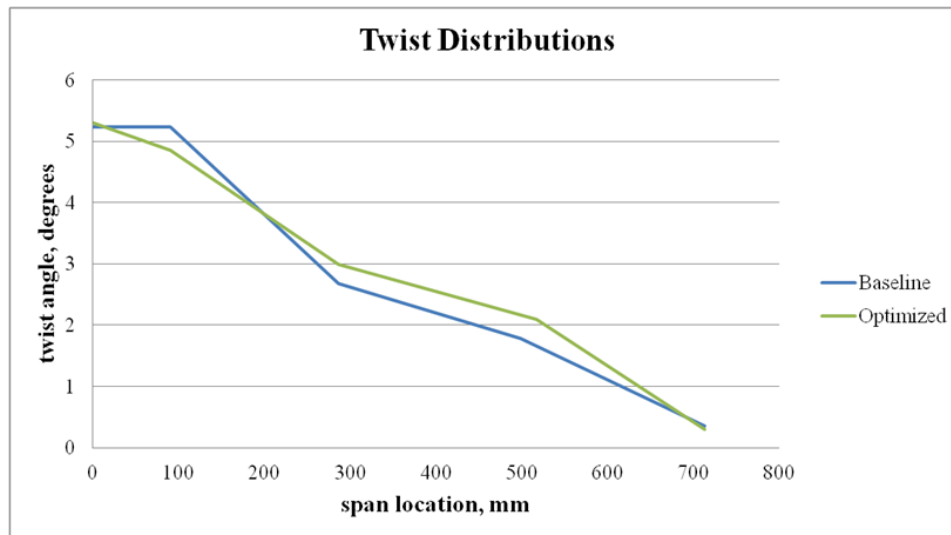
(a)



(b)



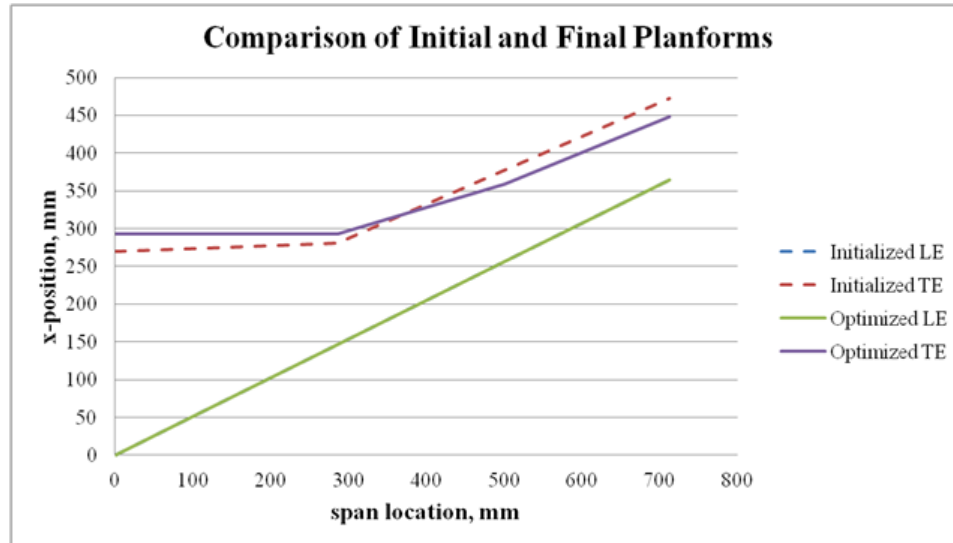
(c)



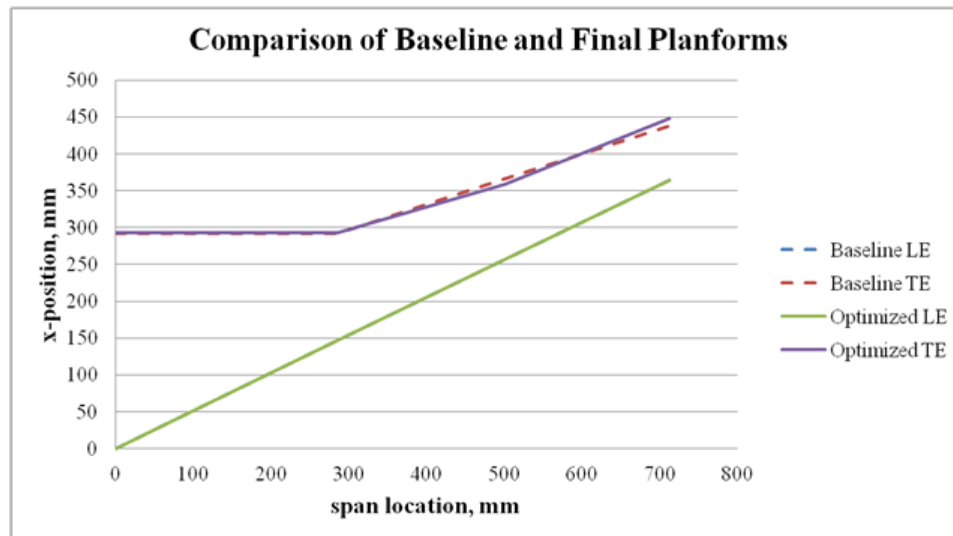
(d)

Figure 25. Optimization results for Yehudi initialization with straight leading edge and trailing edge (initialized taper ratio = 0.2).

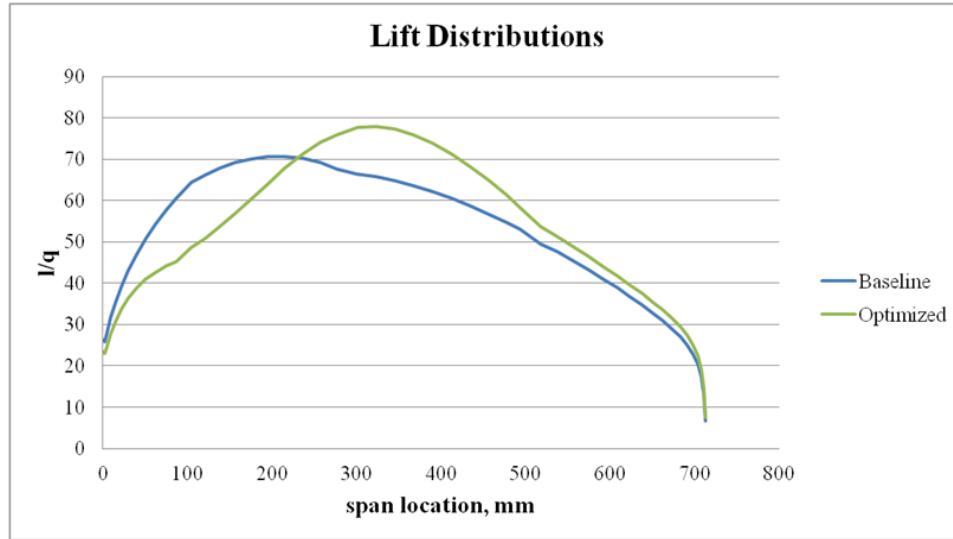
The next Yehudi test case was set up to maintain a fixed leading edge with C_L constrained to lie between the baseline value of 0.356 and 0.37. The initialized planform had a taper ratio of 0.4. The results of the optimization are shown in Figure 26. The optimized solution planform is slightly different than the baseline, but the twist distribution was significantly altered relative to the baseline. The difference in the objective for this case was -2.4%.



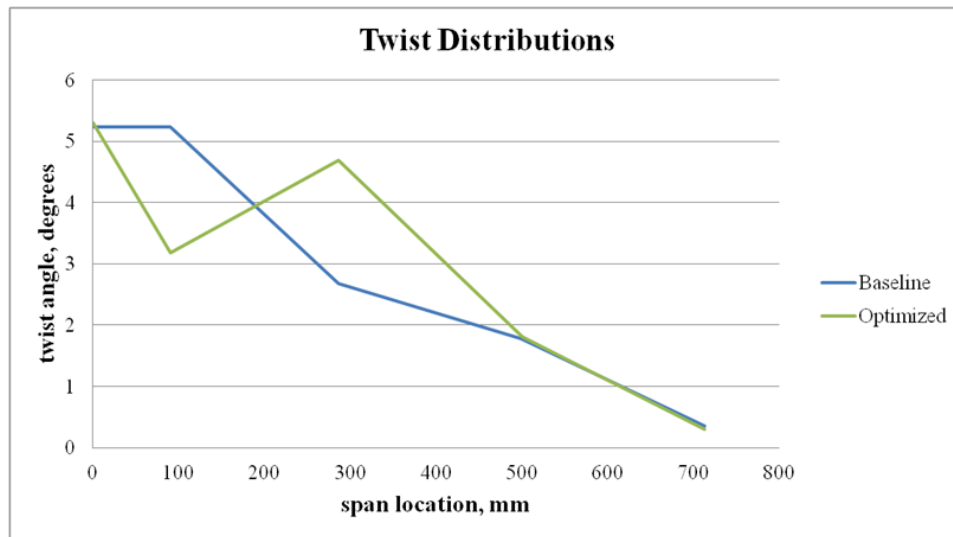
(a)



(b)



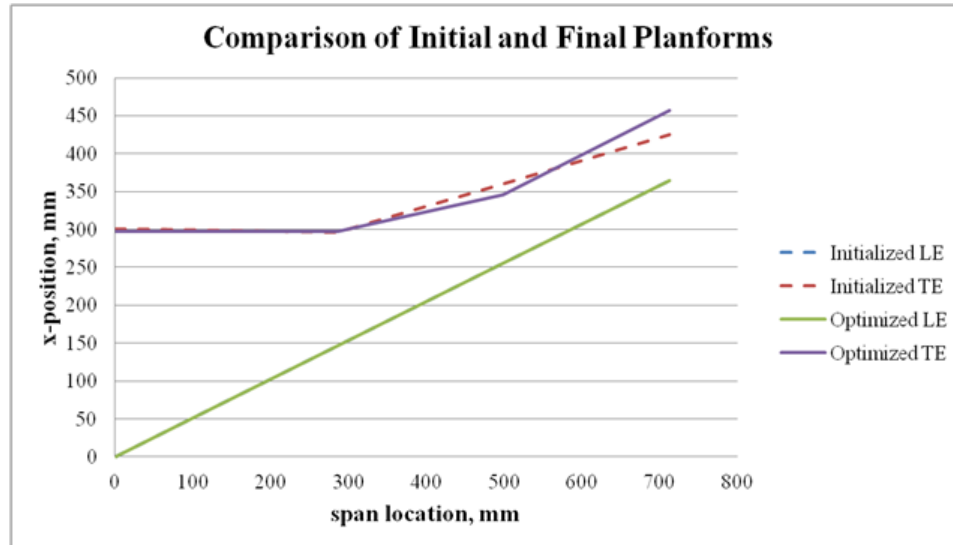
(c)



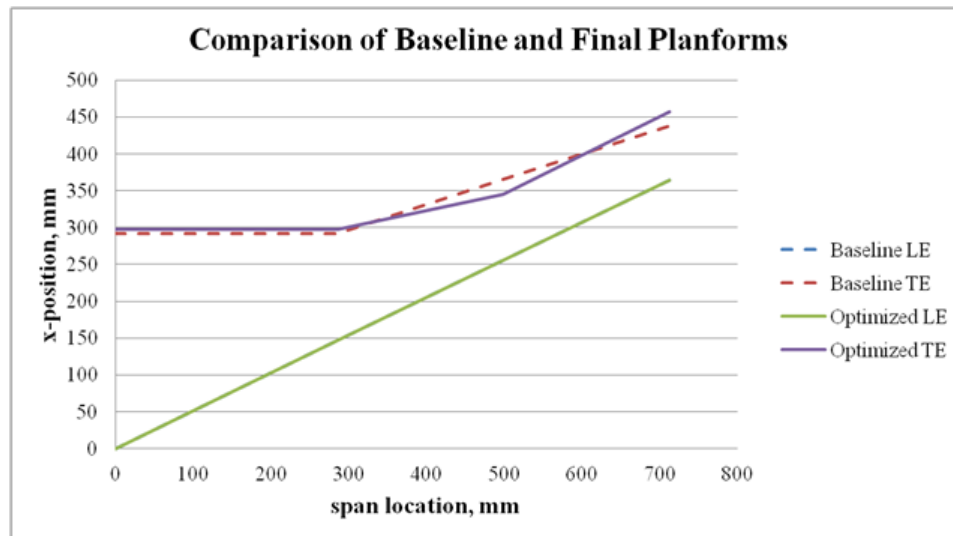
(d)

Figure 26. Optimization results for Yehudi initialization with fixed leading edge (initialized taper ratio = 0.4).

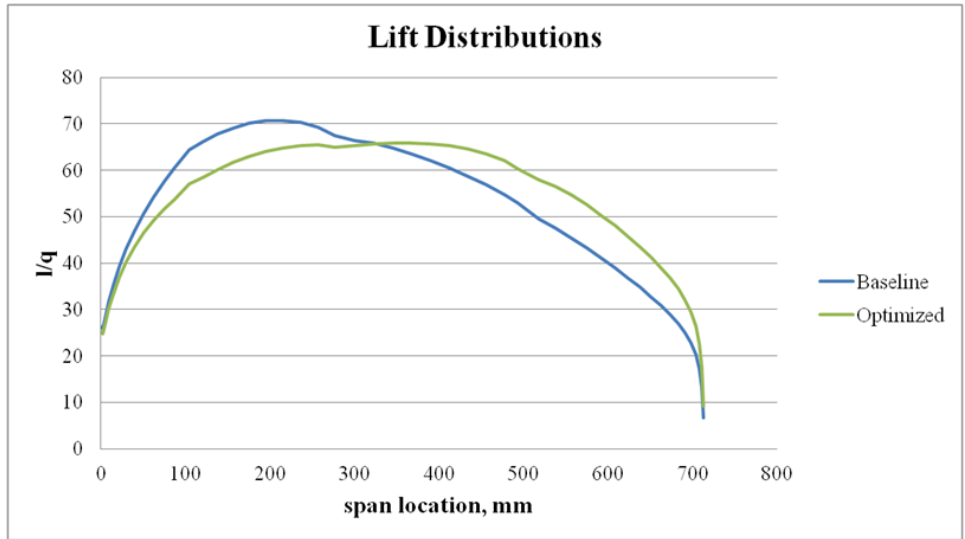
The next Yehudi test case was set up to maintain a fixed leading edge with C_L constrained to lie between the baseline value of 0.356 and 0.37. The initialized planform had a taper ratio of 0.2. The results of the optimization are shown in Figure 27. The optimized solution planform is different than the baseline in the outboard region, and the twist distribution is much different than the baseline. But, the difference in the objective for this case was 0.0%.



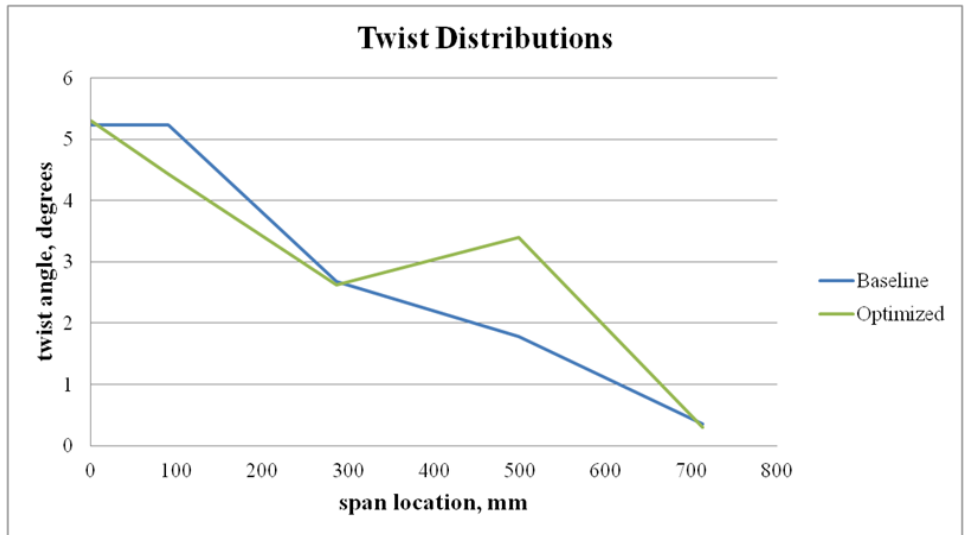
(a)



(b)



(c)



(d)

Figure 27. Optimization results for Yehudi initialization with fixed leading edge (initialized taper ratio = 0.2).

References

- ¹Phillips, W. F. and Snyder, D. O., "Modern Adaptation of Prandtl's Classic Lifting-Line Theory," *AIAA Journal of Aircraft*, Vol. 37, No. 4, 2000, pp. 662-670.
- ²Aboelkassem, Y. and Vatisas, G. H., "New Model for Compressible Vortices," *Journal of Fluids Engineering*, Vol. 129, No. 8, 2007, pp. 1073-1079.
- ³Anderson, J. D., *Fundamentals of Aerodynamics*, 4th ed., McGraw-Hill, New York, 2007, pp. 400.
- ⁴Drela, M., *XFOIL User's Guide, Version 6.96*, MIT Department of Aeronautics and Astronautics, 2001
- ⁵Drela, M., *A User's Guide to MSES 3.04*, MIT Department of Aeronautics and Astronautics, 2006
- ⁶Cella, U., Quagliarella, D., Donelli, R., and Imperatore, B., "Design and Test of the UW-5006 Transonic Natural-Laminar-Flow Wing," *AIAA Journal of Aircraft*, Vol. 47, No. 3, 2010, pp. 783-795.
- ⁷Feistel, T. W., Corsiglia, V. R., and Levin, D. B., "Wind-Tunnel Measurements of Wing-Canard Interference and a Comparison with Various Theories," SAE Technical Paper, 1981.
- ⁸Naik, D. and Ostowari, C., "Experimental Study of Three-Lifting-Surface Configuration," *AIAA Journal of Aircraft*, Vol. 25, No. 2, 1987, pp. 106-112.
- ⁹Bartlett, D. W., "Wind Tunnel Investigation of Several High Aspect-Ratio Supercritical Wing Configurations on a Wide-Body-Type Fuselage," NASA TM X-71996, 1977.
- ¹⁰Redeker, G., "DLR-F4 Wing-Body Configuration," *A Selection of Experimental Test Cases for the Validation of CFD Codes*, AGARD Report AR-303, Aug. 1994.
- ¹¹Levy, D. W., "AIAA CFD Drag Prediction Workshop Data Summary and Comparison," Anaheim, CA, June 9-10, 2001. [http://aaac.larc.nasa.gov/tsab/cfdlarc/aiaa-dpw/Workshop1/pdf/Summary_Levy.pdf. Accessed 11/01/2011.]
- ¹²Polhamus, E. C. and King, T. J., "Aerodynamic Characteristics of Tapered Wings Having Aspect Ratios of 4, 6, and 8, Quarter-Chord Lines Swept Back 45°, and NACA 631A012 Airfoil Sections," NACA RM L51C26, 1951.
- ¹³Jameson, A., "Re-engineering the design process through computation," *35th AIAA Aerospace Sciences Meeting & Exhibit*, Reno, NV, Jan. 6-9, 1997.
- ¹⁴Danforth, E. C. B. and OBryan T. C., "Error in Airspeed Measurement Due to Static-Pressure Field Ahead of the Wing Tip of a Swept-Wing Airplane Model at Transonic Speeds," NACA RM L5L28, 1951.
- ¹⁵Vanderplaats, Garret N. *Multidiscipline Design Optimization*. Monterey, CA: Vanderplaats Research & Development, 2007. Print.

THE BOEING COMPANY

Volume I – Appendix C – Virginia Tech Nonlinear FEM Analysis

1.0 Effect of In-Plane Loads

The TBW Team at Virginia Tech has already performed the following flutter studies on both the SUGAR TBW Full Model and Wind-tunnel Model (WTM) under in-plane loads:

- Validation of the flutter results of the SUGAR Full Model already obtained by the Boeing Company
- Investigation of the effects of in-plane stresses obtained from linear static analysis on the flutter results of SUGAR Full Model
- Investigation of the effects of in-plane stresses obtained from nonlinear static analysis on the flutter results of the in-house Strut-Braced Wing
- Traditional flutter analysis of the unloaded SUGAR WTM beam-rod FEM
- Wing deflection and axial forces investigation of the SUGAR WTM beam-rod FEM
- Investigation of Effects of in-plane loads on flutter boundaries of the SUGAR WTM using both linear and nonlinear analysis
- Influence of physical parameters on the pre-stressed flutter boundaries of the SUGAR WTM
- Influence of in-plane loads on modal frequencies and model shapes of the SUGAR WTM using both linear and nonlinear analysis
- Comparisons of flutter dynamic pressures of new SUGAR WTM FEM versions, FEM V19 and V20, with NASA TDT experimental results

1.1 Validation of Flutter Results of the SUGAR Full Model

The aim was to validate the Boeing Company obtained results using commercially obtainable flutter analysis software like NASTRAN and ZAERO. Although using NASTRAN for validation was rather straightforward, the use of ZAERO for the SUGAR input files was complex because there were NASTRAN WFACT files that incorporate the Lift and Moment corrections for compressible flow (including for Mach number 0.82). These corrections were obtained from steady CFD results performed by the Boeing Company. The correct method to incorporate these corrections in NASTRAN unsteady aerodynamics module was utilized for transonic flutter analysis of the SUGAR TBW WTM.

However, ZAERO *was* used to validate the NASTRAN results – without applying the correction factors – and shows good agreement. The flutter analyses were done for the full fuel and the residual fuel cases. The V-g plots for both the cases have been shown in Figure 2.147.

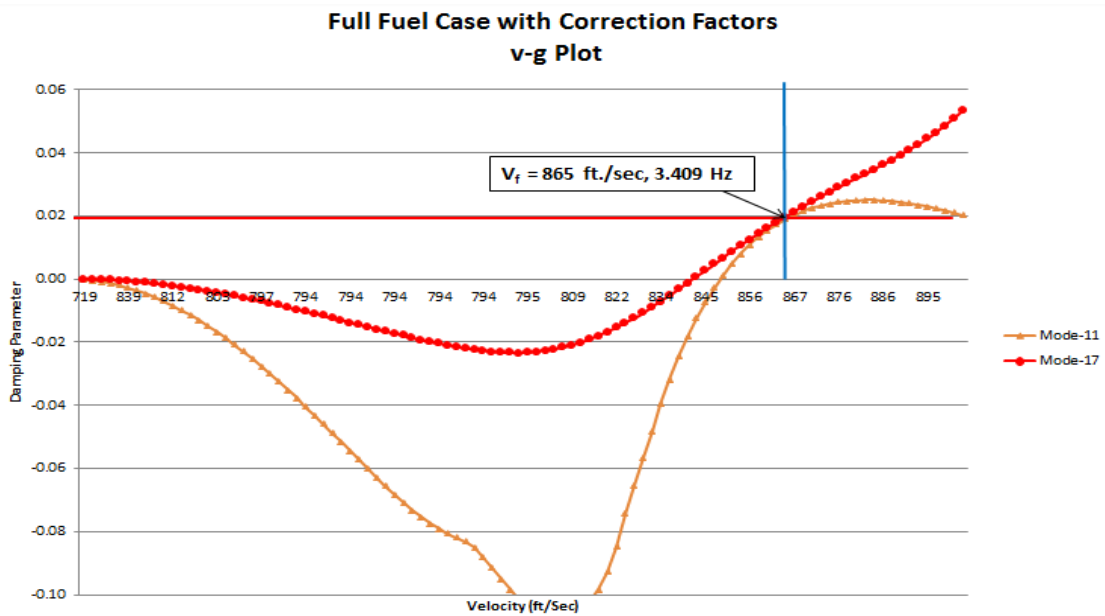


Figure 2.1 – V-g Plot for Full Fuel Case with Correction Factors

Figure 2.148 and Figure 2.149 show mode 17 and mode 10, respectively the anti-symmetric torsion and bending modes.

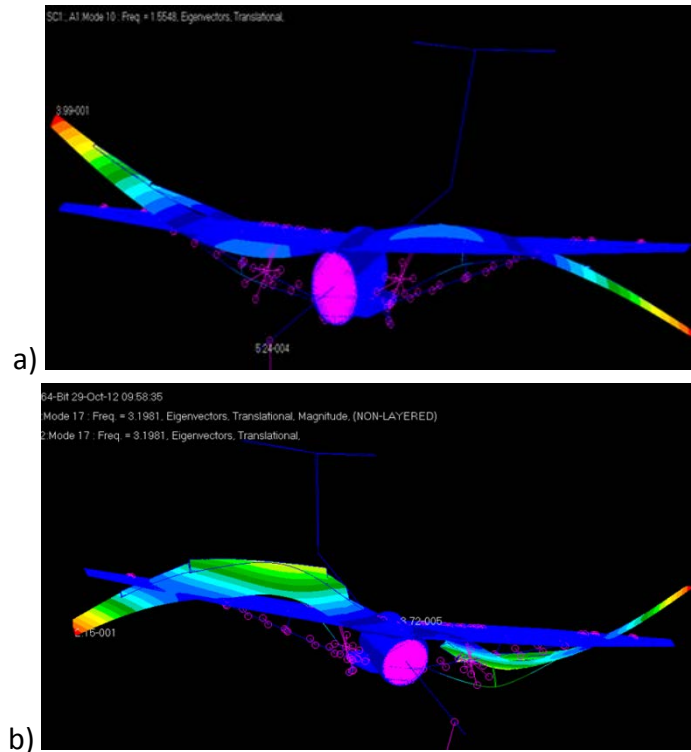


Figure 2.2 – Primary Flutter Modes for Full Fuel Case a) Mode 10: 1.554 Hz, b) Mode 17: 3.198 Hz.

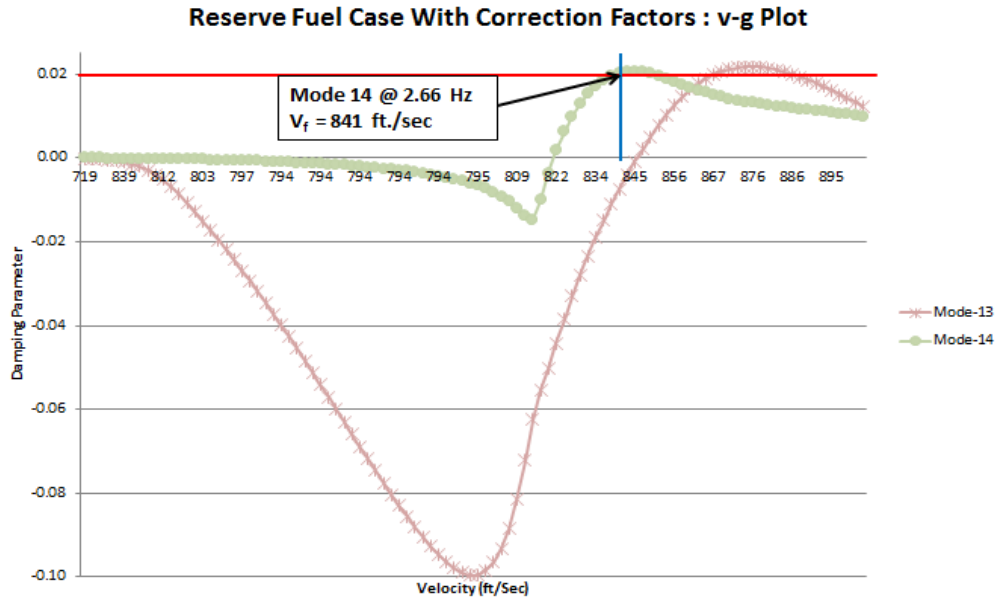


Figure 2.3 – V-g Plot for Residual Fuel Case with Correction Factors

Table 2.1 – Results for Full Fuel Case

Full Fuel case (Boeing results reproduced in col. 2) : Mach = 0.82 at 2% damping				
ω_f , (Hz.)	With correction factors		Without correction factors	
	NASTRAN	ZAERO	NASTRAN	ZAERO
	3.409 (Mode 17)	-	3.404 (Mode 17)	3.420 (Mode 17)
V_f , (ft./sec)	865 fps @ 15687 ft.	-	822 fps @ 29084 ft.	825 fps @ 27167 ft.

Table 2.2 – Results for Full Fuel Case

Reserve Fuel case: Mach = 0.82 at 2% damping				
ω_f , (Hz.)	With correction factors		Without correction factors	
	NASTRAN	ZAERO	NASTRAN	ZAERO
	2.747 (Mode 14)	-	2.697 (Mode 13)	2.797 (Mode 10)
V_f , (ft./sec)	841 fps @ 22813 ft.	-	830 fps @ 25882 ft.	822 fps @ 28158 ft.

1.2 The effects of In-Plane Stresses Obtained from Linear Static Analysis on the Flutter Results of the SUGAR Full Model

Flexible wing structures, like the truss-braced wing configurations, develop in-plane stresses, due to applied lift and inertia relief loads, which can change the geometric stiffness of the structure, thereby changing its natural frequencies. Two load cases were considered, 2.5 g and -1 g (with a factor of safety of 1.5), to investigate the effects of the in-plane stresses on the structural natural modes and on aircraft flutter speed. Results were obtained primarily with

NASTRAN; ZAERO was used for this analysis only for cases where no CFD correction factors for lift and moment were applied, with these results subsequently validated by running NASTRAN for the same cases. The results obtained for the full fuel case and the reserve fuel case with the correction factors applied are shown in Figure 2.150 and Figure 2.151. Table 2.27 and Table 2.28 show the values of the results for the full fuel and the residual fuel cases, respectively, with the correction factors applied to both of them. Table 2.29 shows the effect of in-plane stresses on flutter speed obtained without any correction factors by using ZAERO and NASTRAN.

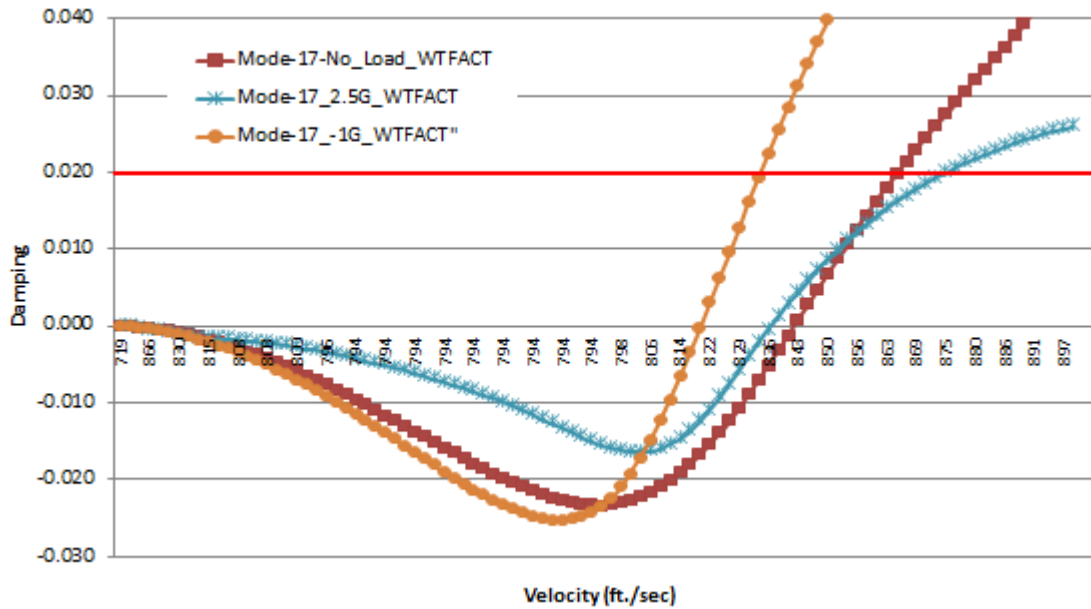


Figure 2.4 – V-g Plot for Full Fuel Case with Correction Factors

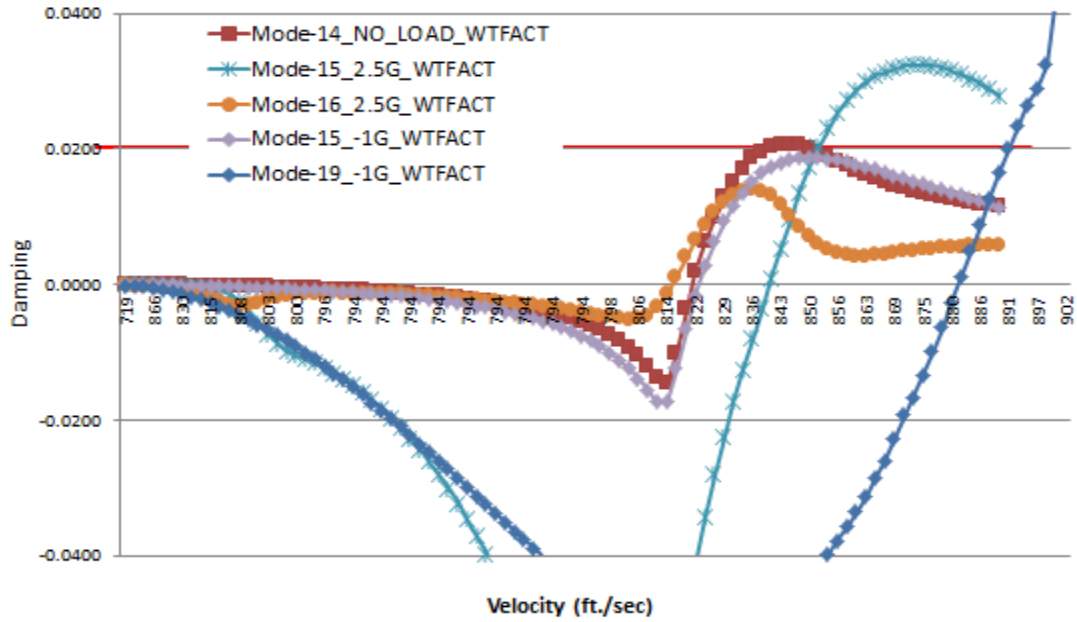


Figure 2.5 – V-g Plot for Reserve Fuel Case with Correction Factors

Table 2.3 – Results for Full Fuel Case

Full Fuel case with Correction factors				
Damping		No load	2.5 g	-1 g
2%	Mode	17	17	17
	ω_f (Hz.)	3.409	2.933	3.263
	V_f (ft./s)	865	875	835
Full Fuel case with Correction factors				
Damping		No load	2.5 g	-1 g
2%	Mode	17	17	17
	ω_f (Hz.)	3.409	2.933	3.263
	V_f (ft./s)	865	875	835

Table 2.4 – Results for Residual Fuel Case

Reserve Fuel case with Correction factors				
Damping		No load	2.5 g	-1 g
0%	Mode	14	16	15
	ω_f (Hz.)	2.665	2.696	2.653
	V_f (ft./s)	821	817	824
2%	Mode	14	15	19
	ω_f (Hz.)	2.747	2.779	5.247
	V_f (ft./s)	841	852	891

Table 2.5 – Results for Flutter without Correction Factors

Results obtained without Correction factors							
Damping	No load		2.5 g		-1 g		
Full Fuel Case							
0%		NASTRAN	ZAERO	NASTRAN	ZAERO	NASTRAN	ZAERO
	Mode	17	17	14	10	17	18
	ω_f (Hz.)	3.404	3.420	2.792	2.762	3.216	3.245
	V_f (ft./s)	822	826	839	824	798	810
Reserve Fuel case							
2%		NASTRAN	ZAERO	NASTRAN	ZAERO	NASTRAN	ZAERO
	Mode	13	10	15	9	19	20
	ω_f (Hz.)	2.697	2.798	2.68	2.775	5.10	5.073
	V_f (ft./s)	830	822	822	814	856	852

1.3 The Effects of In-Plane Stresses Obtained From Nonlinear Static Analysis on the Flutter Results of In-house Strut-Braced Wing

High aspect ratio truss-braced wings are slender flexible structures that undergo large deformation due to applied loads (like the lift and pitching moment distribution), which linear static analysis may not portray accurately. The approach discussed in this section was to perform nonlinear static analysis of the TBW aircraft and then to investigate the effects of the resultant in-plane stresses on the flutter results. The procedure is similar to that discussed in section 2.1.8.10.2; however, the initial static analysis is performed by including geometric nonlinearities.

Initially, several in-house strut braced wing designs were used as test cases to observe the effects of large structural deformations on the flutter analysis; these results showed considerable effect on the flutter speed. Such analysis is still to be performed for the SUGAR FEM and will comprise the future work to be performed at Virginia Tech.

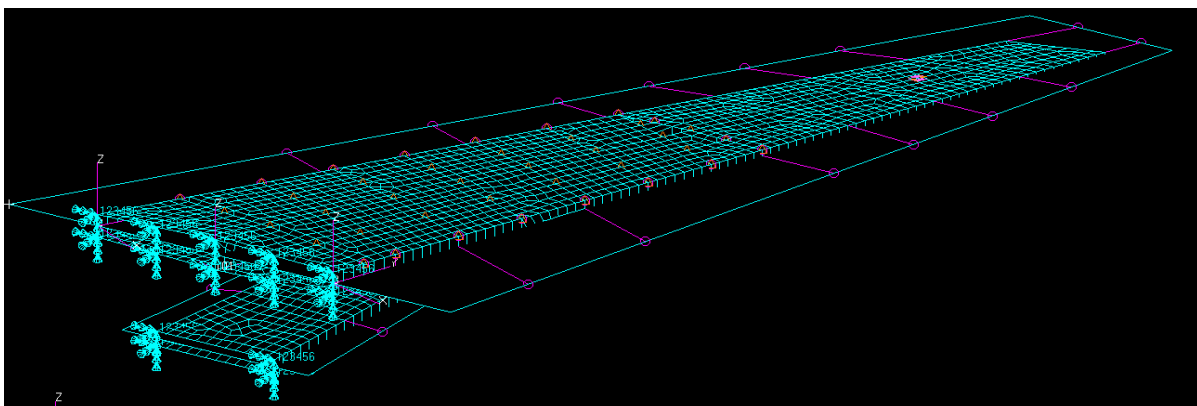


Figure 2.6 – Finite Element Model for SBW Test Case

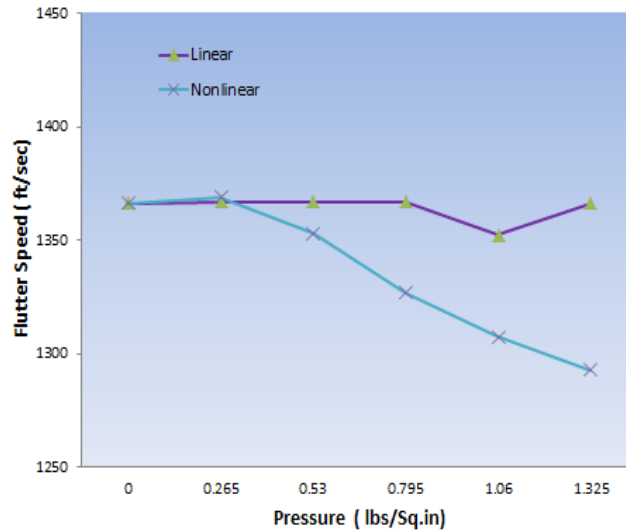


Figure 2.7 – Variation of Flutter with Distributed Pressure on the Wing Planform for Linear and Nonlinear Analysis

Table 2.6 – Comparison of Linear and Nonlinear Flutter Speeds for In House SBW Design

Pressure Distribution Applied 1.325 lbs/Sq.in				
	Linear		Nonlinear	
	NASTRAN	ZAERO	NASTRAN	ZAERO
Mode	2	2	2	2
ω_f (Hz.)	14.61	14.64	12.5	12.65
V_f (ft./s)	1333	1366	1280	1292

1.4 The Effect of in-plane loads on modal and flutter results of SUGAR TBW Wind Tunnel Model

As part of the NASA SUGAR research program, a wind tunnel model has been designed, fabricated and tested in the NASA TDT during late 2013 and early 2014. One of the test goals was to evaluate the performance of a scaled model up to the point of flutter instabilities and to implement active flutter control. The flutter analysis presented here was developed to predict the aeroelastic behavior of the WTM under a variety of flight conditions planned for the wind tunnel test. The specific beam-rod finite element model utilized for the present study was developed by the Boeing Company with the purpose of simulating the TBW wind tunnel model, as shown in Figure 2.153. The structural characteristics of the FEM were updated to reflect the WTM stiffness distribution as constructed. There are six ballasts with each mass 2.92 lbs. located at the wing spar to improve the modal similitude with the full-scale FEM. In-plane loads were obtained by performing static structural analysis under flight loads and self-weight. Geometrically nonlinearities should be considered in the static analysis due to the large aspect ratio, 9.52, of the WTM. So, nonlinear static analysis was implemented for in-plane loads. It is also interesting to examine the linear static analysis for in-plane loads for its potential to provide useful estimate of flutter dynamic pressure at reduced computational expense. So,

both linear and nonlinear static analyses were performed for in-plane loads of the WTM under different Mach numbers and AoAs.

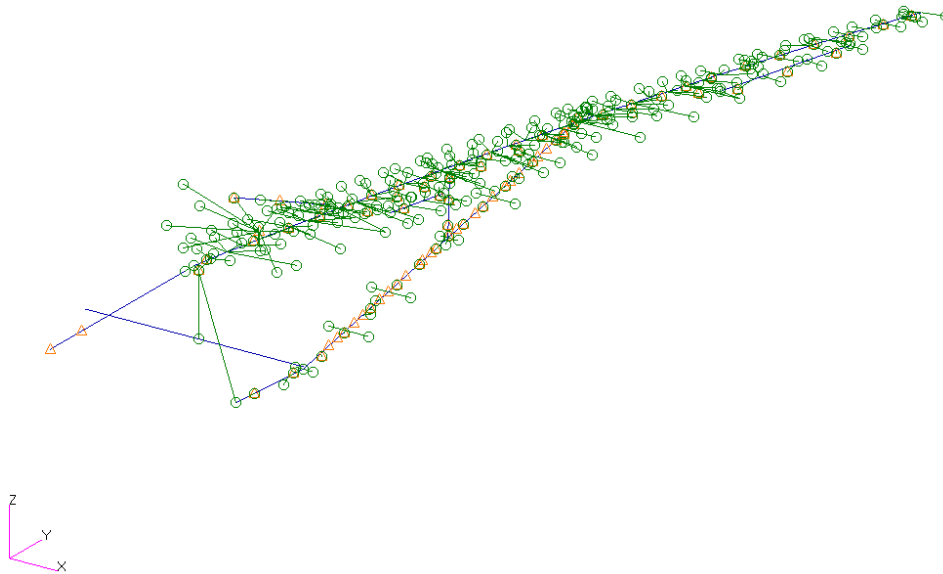


Figure 2.8 – The beam-rod FEM, developed by The Boeing Company, used for the present aeroelastic analysis

The flight conditions utilized for the SUGAR TBW WTM flutter analysis are based on previous MDO studies of the full-scale aircraft model when subjected to the flutter speed constraint of $1.09V_d$ (Refer to Phase I final report). Results for the full-scale aircraft indicated that the critical Mach number for flutter was 0.82, when weight factors are applied for both steady and unsteady aerodynamic pressure. The aerodynamic weighting factors, also called correction factors, are obtained from computational fluid dynamics (CFD) analyses which can capture compressibility and shock behavior lacking in the doublet-lattice method (DLM) in NASTRAN. The weight factors constitute “panel by panel” corrections to the pressure magnitude and also to the lift curve slope. The key behavior captured through addition of the weight factors is the aft shift in center of pressure (C_p) due to transonic effects. This aft shift in C_p , especially beyond Mach 0.82, alleviates the flutter instability at higher Mach numbers. The flutter analysis utilized a non-looping matched-point method, also known as the PKNL method in NASTRAN. The flutter search included density ratios and velocities spanning the flight envelope. Reduced frequencies were chosen from 0.001 to 10.0 in order to cover the frequency range of interest.

The flow chart shown in Figure 2.153 with several analysis steps was developed to conduct pre-stressed flutter analysis of the SUGAR TBW WTM. Axial forces in the wing components, the main wing, the jury and the strut have considerable effect to the modal information and flutter boundary. These axial forces were caused by the flight loads and self-weight of the WTM. The obtained axial forces were considered as in-plane loads in the subsequent modal analysis and flutter analysis. Flight loads were obtained by performing static aeroelastic analysis (Step

①②③④), and then using linear/nonlinear static analysis to compute the axial forces under such flight loads (Step ⑤). Incremental stiffness due to the pre-stress was then incorporated to the structural stiffness to conduct modal analysis and flutter analysis (Step ⑥ and ⑦). Once the pre-stressed flutter solution is obtained, the dynamic pressure at this new flutter velocity is used as an improved estimate for input to the calculation of flight loads in Step ④. Iteration is performed on Steps ④⑤⑥ and ⑦ until the flutter dynamic pressure converges. The allowed convergence criterion in this problem for flutter dynamic pressure is 0.1 psf.

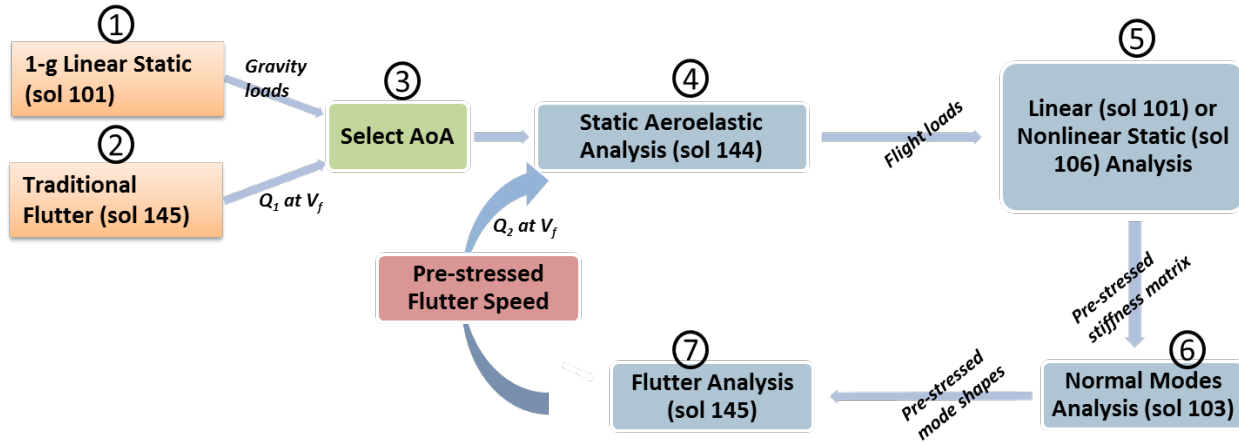


Figure 2.9 – The flow chart of the NASTRAN based nonlinear aeroelastic solution sequence used for the present work

It takes time to manually input all the data required to obtain the theoretical predictions of the flutter boundaries for all the tests conducted in the wind tunnel for a large set of Mach numbers and angles of attack (AoAs). So, it is necessary to automate the process of analysis, including generating the flight loads, stresses, incremental stiffness matrix, modal information and flutter results, including the determination of the flutter velocity or the flutter dynamic pressure. The flow chart shown in Figure 2.153 was programmed in MATLAB to perform aeroelastic analysis of the SUGAR WTM to find the flutter boundary of a pre-stressed WTM. The pre-stressed flutter dynamic pressure is defined as the dynamic pressure obtained from Step ⑦ which should be exactly the same or very little less than the input dynamic pressure in Step ④. This method is called as the **Iterative Method**.

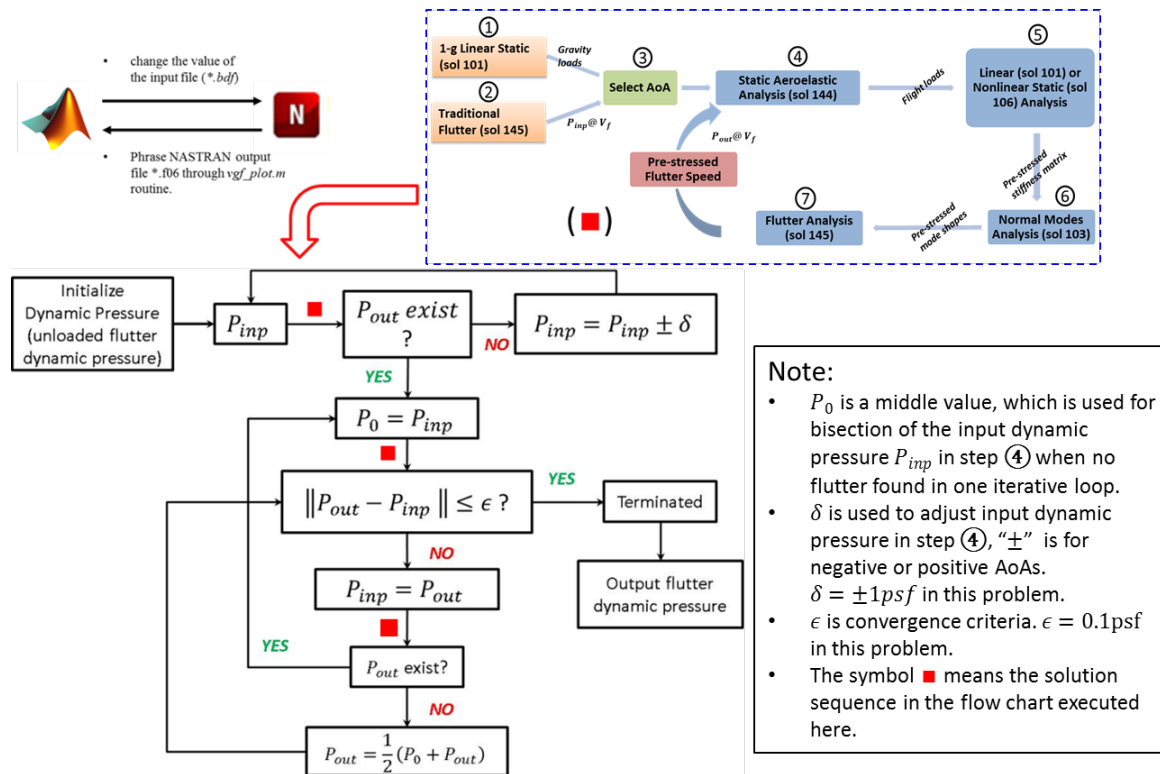


Figure 2.10 – Iteration framework used to find the flutter boundary in MATLAB environment using NASTRAN based solution sequences for flutter analysis

One alternative method is the **Discrete Method** as seen in Figure 2.153. In this method, a series of separate calculations are performed to obtain the flutter damping corresponding to the input velocity/dynamic pressure in the static aeroelastic analysis, followed by linearly interpolating the data in the V-g plot to find the flutter velocity or flutter dynamic pressure. This method was mainly developed to validate the results obtained from the iterative method and to cope with the cases with no convergence obtained when using the iterative method. To implement the discrete method, it's necessary to point out the flutter mode in advance to obtain the structural damping at that mode, and then plot the V-g graph using the structural damping and input velocity/dynamic pressure. However, the flutter mode could be different at different Mach numbers and AoAs. It's because that incremental stiffness generated could have different influence on the modal information and flutter boundary under different dynamic pressures and AoAs that cause the shift of normal modes. So, it is not easy to recognize the critical mode in advance when using the discrete method for all the cases. However, the flutter speed could be more efficiently obtained once the critical mode is fixed by using parallel computing for the discrete method for all cases. But when compared with the work using the iterative method, more computations needed to interpolate an accurate flutter speed from V-g plot. In this work, the iterative method was used as primary method to find out the open-loop flutter boundaries of the WTM under in-plane loads, and the discrete method was used for

validation and as an alternative method for cases where convergence could not be obtained when using the iterative method.

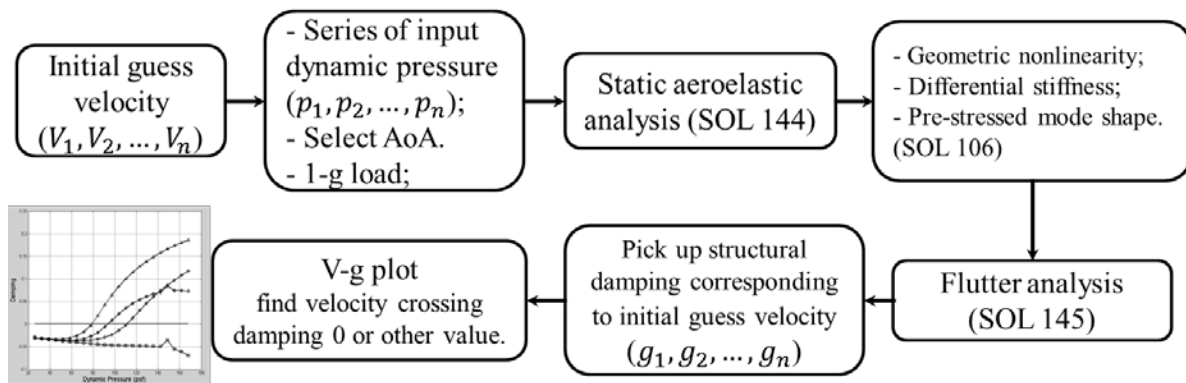


Figure 2.11 – Flow chart of the discrete method utilized for computing flutter dynamic pressure

The above SUGAR WTM FEM and analysis procedures were utilized to generate results across a range of AoAs. Parametric studies were performed to examine the influence of aerodynamic weighting factors and ballast mass on flutter boundary at Mach No. 0.82. As a preliminary step, analysis of the unloaded model was performed to provide a baseline for comparison to pre-stressed analyses results. The weight factors are always applied to the steady aerodynamic pressures in the static aeroelastic analysis in the following work to generate the flight loads in transonic flow regardless of the analysis types. The steady aerodynamic weighting factors could also be used as weight factors for the unsteady aerodynamic pressure. Flutter dynamic pressure of the cases with weight factors used for the unsteady aerodynamic pressure was examined to validate the use of the steady aerodynamic weighting factors for unsteady aerodynamic pressure. The case w/WF and w/o WF in the subsequent work means that there are weight factors and no weight factors employed for DLM based unsteady aerodynamic pressure in the flutter analysis, respectively. Flutter boundaries of new WTM FEM versions, FEM V19 and V20, were calculated at Mach No. 0.7, 0.76 and 0.82 at AoA ranging from -3 degrees AoA to 3 degrees AoA. Comparisons of flutter predictions with test results were conducted and some conclusions were made in the summary part.

1.5 Traditional flutter analysis of the unloaded SUGAR WTM

To investigate the influence of in-plane loads on the modal information and flutter boundaries, it's necessary to perform modal analysis and flutter analysis of the unloaded SUGAR WTM. This analysis is considered as a baseline for comparisons to the subsequent pre-stressed modal analysis and flutter analysis. Modal analysis and flutter analysis of the unloaded SUGAR WTM is a single step in MSC NASTRAN Solution Sequence 103 and 145, since no flight loads and gravity loads are considered. The first 4 mode shapes and corresponding natural frequencies were shown in Figure 2.153. The first 4 modes are 1st outboard wing bending mode, 1st inboard wing

bending mode, 2nd bending mode and 1st torsion mode, respectively. V-g plot and V-f plot of the flutter analysis were shown in Figure 2.153 and Figure 2.153. From these two graphs, it was found that the 2nd bending mode (mode 3) and 1st torsion model (mode 4) contribute to the flutter instability. 2% modal damping was included in the flutter analysis. From the V-g plot, we can find the curve of mode 3 in the V-g plot crosses zero damping line and produces flutter instability at approximately 120 KEAS.

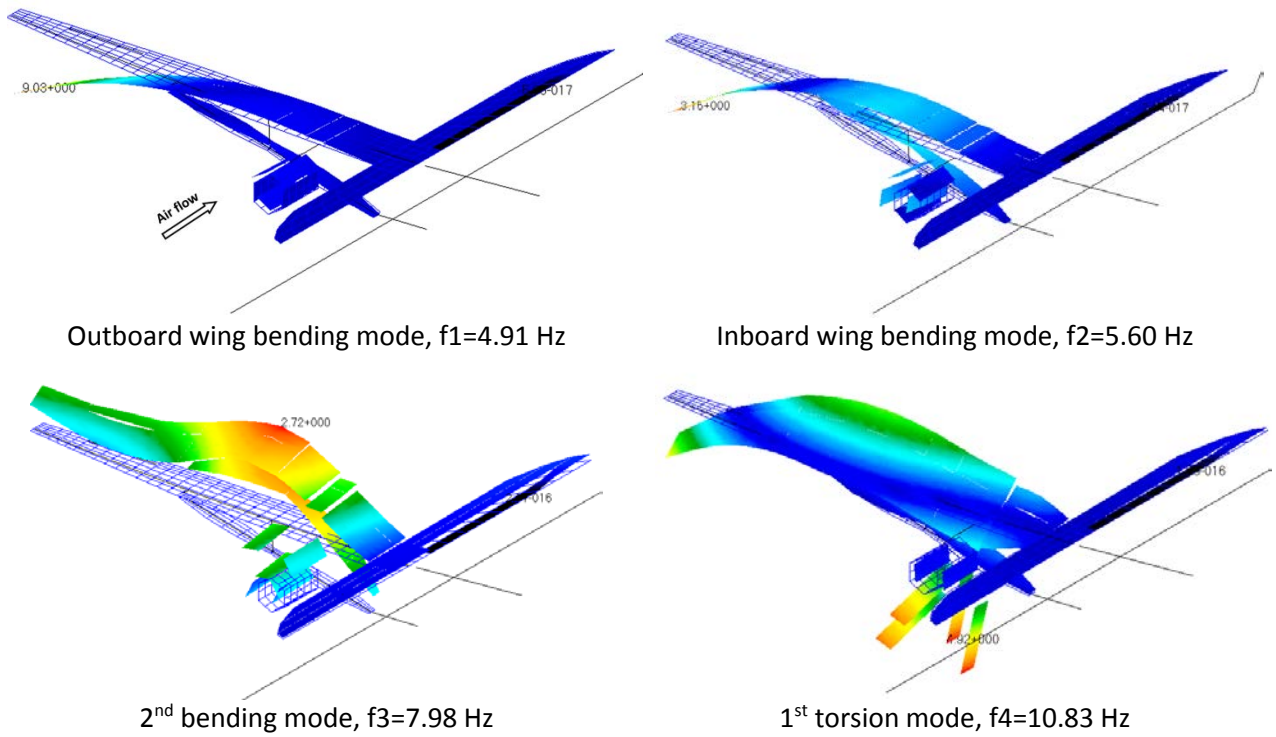


Figure 2.12 – The first 4 mode shapes, spline from beam-rod FEM, of the unloaded model FEM V18 with ballast masses 2.92 lbs.

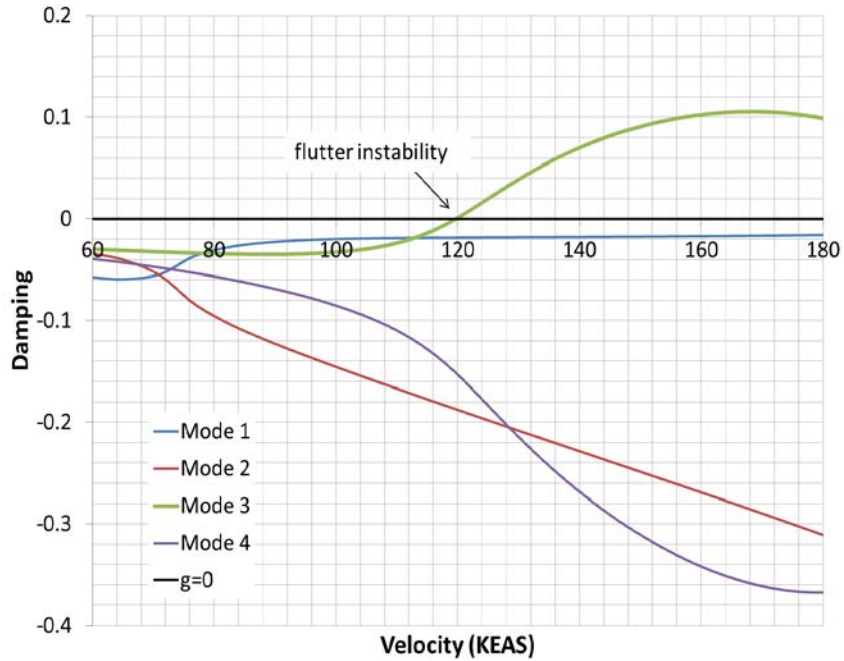


Figure 2.13 – The velocity vs. structural damping (V-g) plot for the unloaded model indicating that the curve of mode 3 crosses zero damping line (flutter instability) at approximate 120 KEAS

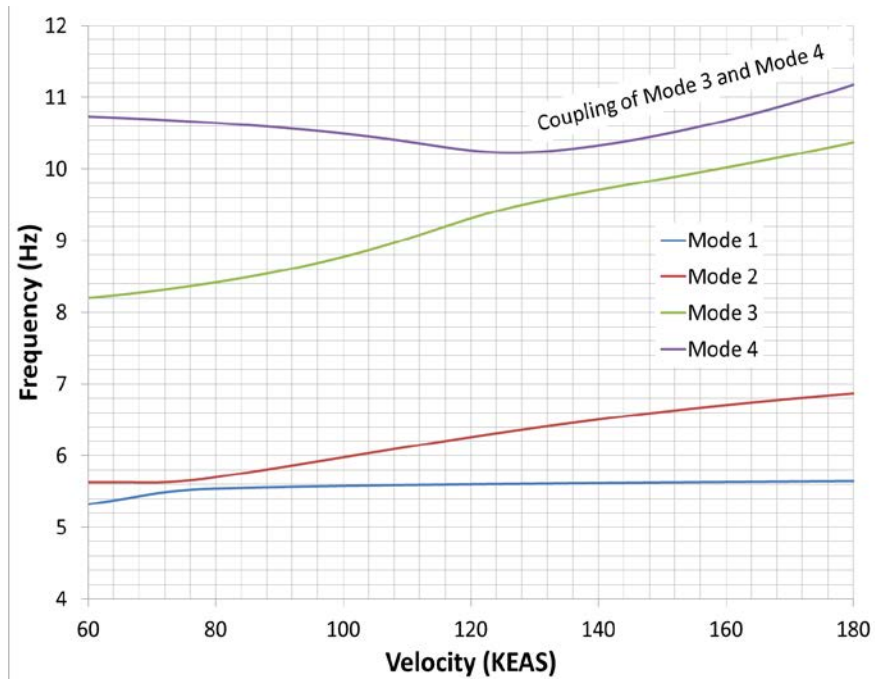


Figure 2.14 – The velocity vs. frequency (V-f) plot for the unloaded model indicating that modes 3 and 4 are coupling to cause the flutter instability

1.6 Wing deflection and axial forces investigation of the SUGAR WTM

Variations of the deflections of the beam model of the SUGAR WTM with AoA were investigated using both linear and nonlinear analysis as shown in Figure 2.153. It was seen that beam deflections of the WTM are close to each other using both linear and nonlinear analysis for each AoA. For positive AoAs, the magnitudes of beam deflections as obtained from a linear analysis are a bit larger than those as obtained from a nonlinear analysis. However, for negative AoAs, the magnitude of beam deflection as obtained from a nonlinear analysis is a bit larger than that obtained from a linear analysis.

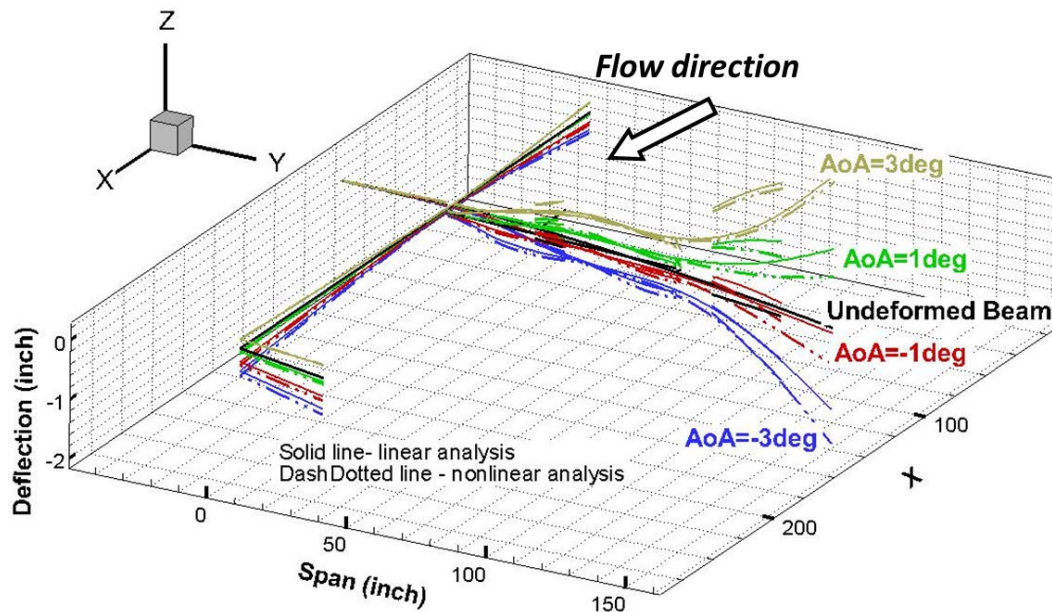


Figure 2.15 – Wing deflections of the beam model of the SUGAR TBW WTM at AoA = -3, -1, 1 and 3 degrees, Mach No. 0.82 and ballast mass 2.92 lbs. using both linear and nonlinear analysis (Scale Factor:20)

The axial forces in the three different components, the jury, the strut and the inboard wing, of the TBW WTM were also investigated as seen in Figure 2.153. The variation of the axial forces with AoA in these three components is shown in Figure 2.153. The axial forces in these representative elements are normalized with respect to the weight of the WTM without mounting system, about 529 lbs. It was shown that the in-plane load in each component varies linearly with AoA regardless of the analysis types. The axial forces, obtained from the nonlinear analysis, in the jury and the inboard wing are larger than those obtained from the linear analysis, but opposite of that in the strut. It was also found that the value of the axial force in the jury for this TBW WTM design is much less than the axial forces in the strut and the inboard wing. The jury and the inboard wing come under compression as the AoA increases, whereas, the strut remains in tension as the AoA increases. Different axial forces were generated at some different AoAs when using linear and nonlinear static analysis. So, it's necessary to examine the

influence of in-plane loads obtained from linear and nonlinear static analysis to the flutter boundaries.

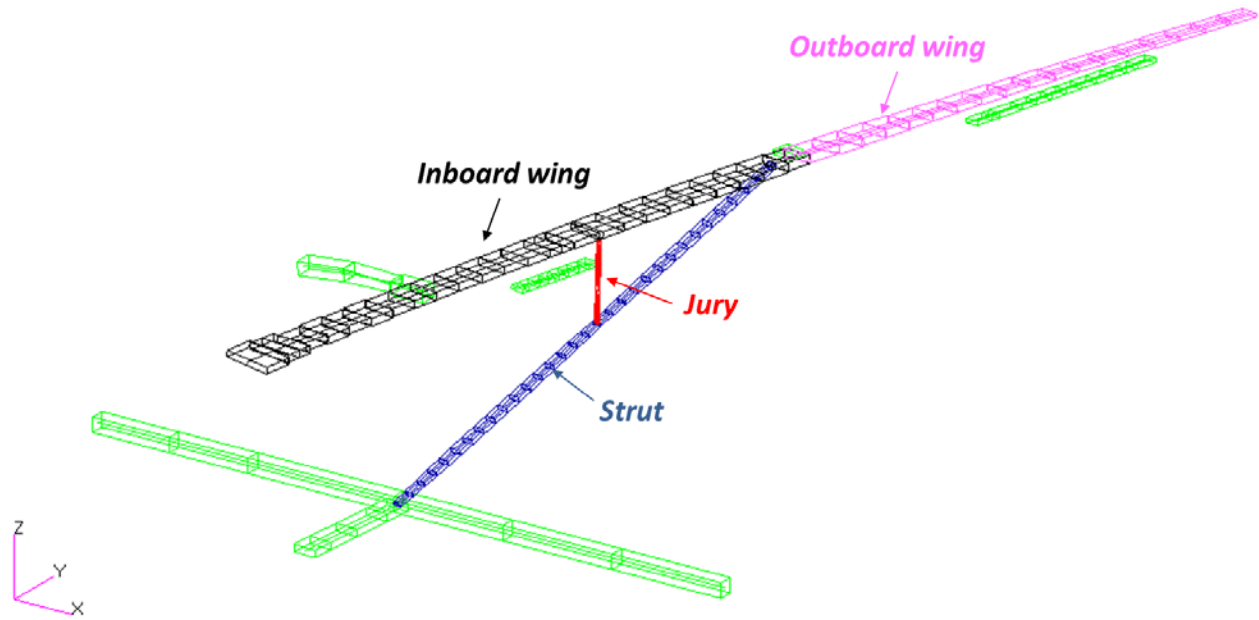


Figure 2.16 – The selected three wing components of the SUGAR TBW WTM, the inboard wing, the jury and the strut with equivalent rectangle cross sections

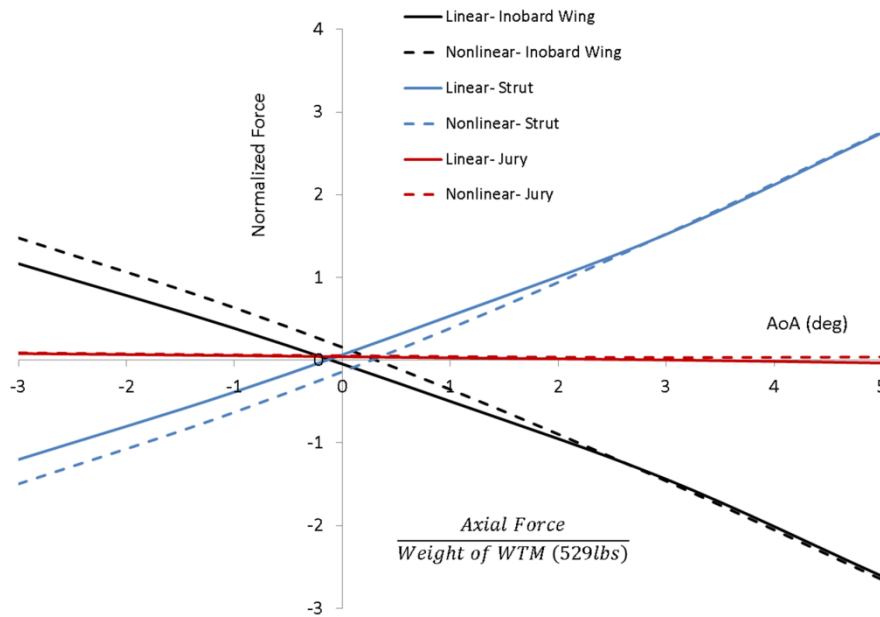


Figure 2.17 – Variation of axial force with AoA for the jury, the inboard wing and the strut at Mach No. 0.82 and ballast mass 2.92 lbs using both linear and nonlinear analysis

1.7 Flutter analysis of the SUGAR WTM under in-plane loads using both linear and nonlinear analysis

To examine the accuracy of employing the iterative method for pre-stressed flutter analysis, a comparison of flutter speed of the case under Mach 0.82 and 1 degree AoA at 4 different analysis types using the iterative method and the discrete method was conducted. The 4 different analysis types mean that using linear and nonlinear analysis, w/ and w/o weight factors applied to the unsteady aerodynamic pressure. The output data from the iterative method and the discrete method are plotted in Figure 2.153 and Figure 2.153, respectively. The flutter dynamic pressures from the two plots are tabulated in Table 2.31. The table shows that the values of the flutter dynamic pressure calculated by the two methods are almost same. Another case, the same flight conditions but under -1 degree AoA, was also chosen to validate the flutter dynamic pressure obtained from the iterative method. The results were shown in Table 2.32. We can see that the two sets of results obtained from the discrete method and the iterative method are also similar. Good agreement was achieved when using the iterative method and the discrete method for both of the cases. Parallel computing was utilized for the discrete method provided that the critical mode remains unchanged. For instance, mode 3 (2nd bending mode) was the critical mode for the SUGAR WTM. However, the normal modes were shift as the compressive stress and tensile stress in wing components generated at higher AoAs and dynamic pressures. We can not point out which two mode numbers would couple to cause the flutter in advance when using the discrete method for higher AoA. It takes time when post-processing structural damping from all modes involved in flutter analysis. It was also found that more computations needed to give an accurate estimate of flutter boundary when using the discrete method although parallel computing was utilized in the discrete method. By comparing the computation numbers in the Figure 2.153 and Figure 2.153, it's cheaper when using the iterative method for the cases of linear analysis and the case of w/o WF applied to the unsteady aerodynamic pressure in the flutter analysis. So, the iterative method was used as the primary method in the subsequent work of the other two WTM FEM versions to calculate the flutter speed under in-plane loads.

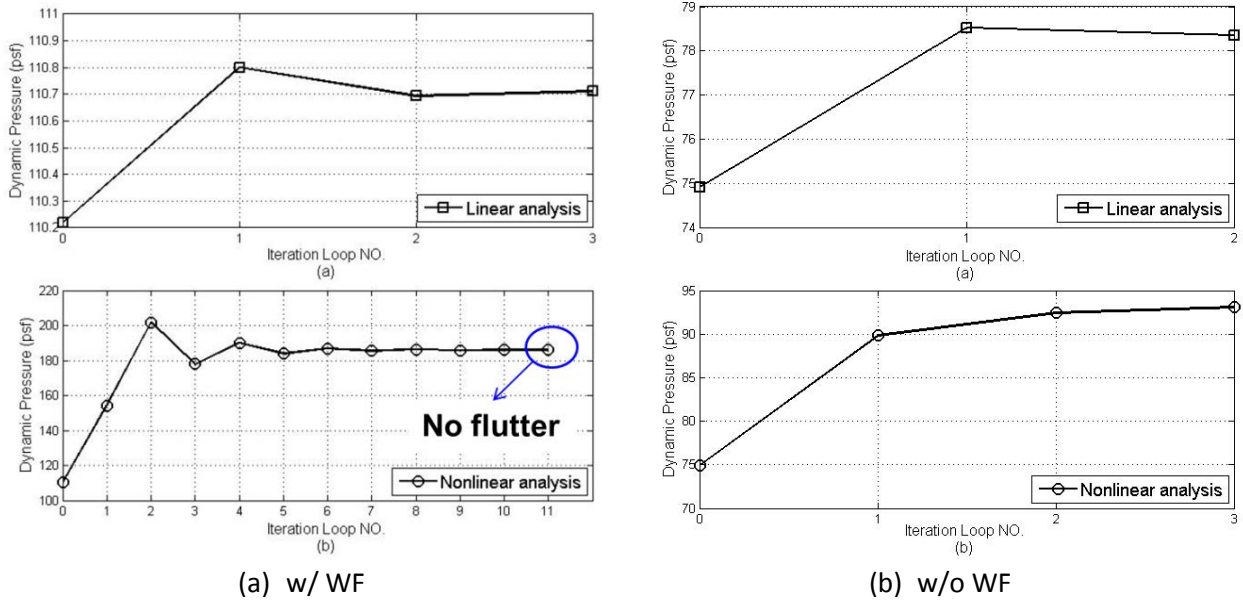


Figure 2.18 – Iteration history of flutter dynamic pressure using linear and nonlinear analysis, Mach=0.82, ballast mass 2.92 lbs., AoA=1deg. (a) w/ WF used on unsteady aerodynamic pressure, (b) w/o WF used on unsteady aerodynamic pressure

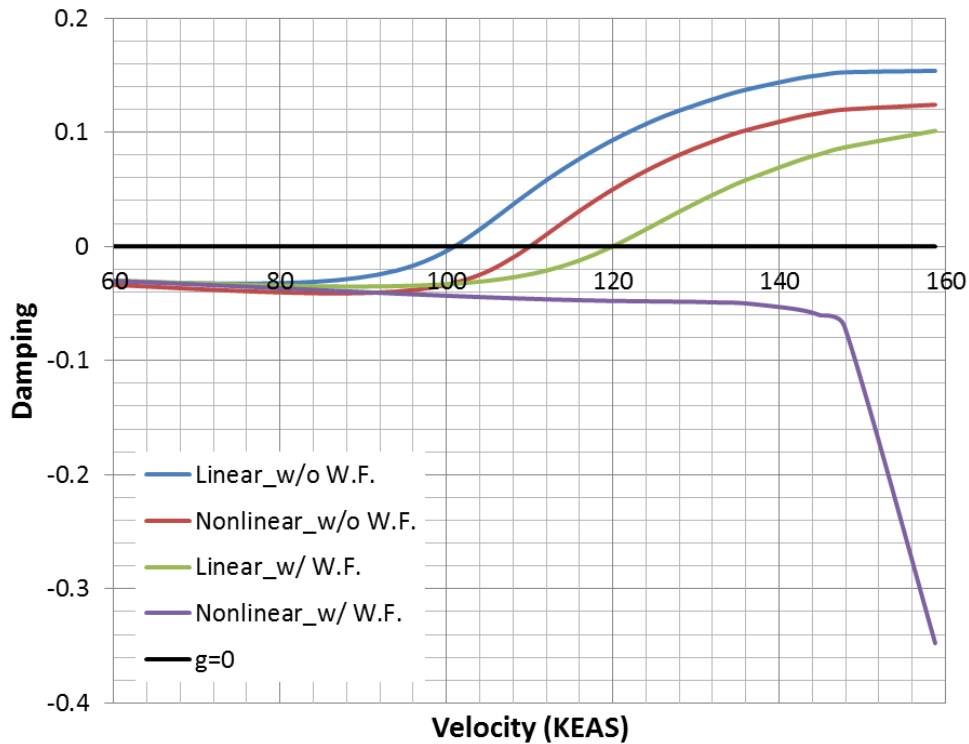


Figure 2.19 – Flow velocity vs. damping for the case of 1 degree AoA. Linear and nonlinear analysis provided with and without weight factors (23 initial guess of velocities, 6 cores used in parallel computing)

Table 2.7 – Flutter dynamic pressure(psf) using both linear and nonlinear analysis under Mach=0.82, AoA=1deg, ballast mass of 2.92 lbs. w/ and w/o WF applied to the unsteady aerodynamic pressure

Method	w/ WF		w/o WF	
	Linear	Nonlinear	Linear	Nonlinear
Iteration Method	110.71	N/F	78.36	93.06
Discrete Method	110.69	N/F	78.36	93.34

* N/F means No Flutter Predicted

Table 2.8 – Flutter dynamic pressure(psf) using both linear and nonlinear analysis under Mach=0.82, AoA=-1deg, ballast mass of 2.92 lbs. w/ and w/o WF applied to the unsteady aerodynamic pressure

Method	w/ WF		w/o WF	
	Linear	Nonlinear	Linear	Nonlinear
Iteration Method	100.01	N/F	72.67	86.02
Discrete Method	99.87	N/F	72.62	86.15

* N/F means No Flutter Predicted

Pre-stressed flutter speed of the SUGAR WTM under Mach number 0.82 and different AoAs was calculated by using the iterative method for both linear and nonlinear analysis. The variation of the flutter speed with AoA at different analysis types w/ and w/o WF applied to the unsteady aerodynamic pressure was examined as shown in Figure 2.153. It was found that for the case of nonlinear analysis w/ WF, no flutter instability was observed at any AoA so that is not shown in the plot. The flutter speed for the unloaded WTM is shown by a horizontal line, since the pre-stress is not included and flutter speed is not a function of AoA. It can be seen that the variation of the predicted flutter speed increase with AoA regardless of the analysis type (linear or nonlinear, w/ or w/o WF). It can also be seen that analysis w/ WF results in a higher predicted flutter velocity than those obtained at the cases w/o WF.

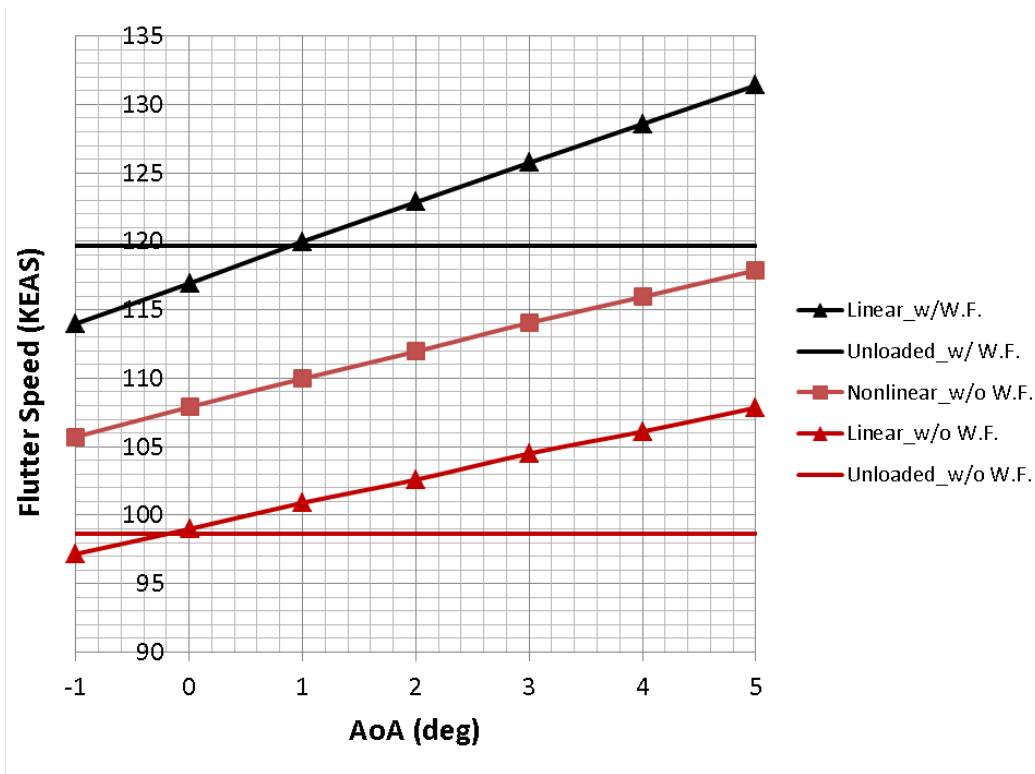


Figure 2.20 – Flutter Speed vs. AoA for analyses w/ and w/o WF applied to the unsteady aerodynamic pressure. Both linear and nonlinear results are provided for the case of Mach number 0.82 and ballast mass 2.92 lbs.

1.8 Influence of ballast mass on flutter speed

There are six ballasts located in the wing spar, which were developed for the WTM in order to improve modal similitude with the full-scale FEM. The locations of these six ballasts are shown in Figure 2.153. Each mass is nominally 2.92 lbs. As we know, both mass distribution and magnitude have significant influence on modal frequencies, mode shapes and, therefore, flutter behaviors. The flutter results shown in Figure 2.153 indicated that the highest fidelity analysis (nonlinear w/ WF on unsteady aerodynamic pressure) did not predict flutter instability within the intended flight envelope. Therefore, we investigated the influence of the ballast mass to the flutter boundary. We examined the flutter response as the ballast mass (6 locations at 2.92 lbs. each) was firstly increased by 50% (6 locations at 4.38 lbs. each) and then by 100% (6 locations at 5.84 lbs. each). The mass moments of inertia of the ballasts remain unchanged. The results in this section were generated at Mach 0.82 and included weight factors applied to the unsteady aerodynamic pressure.

Firstly, the flutter results of the unloaded model with three different ballast masses at Mach No. 0.82 were examined, shown in Figure 2.153. It can be seen that flutter speed is reduced by nearly 20% by doubling the ballast mass from 2.92 to 5.84 lbs. Although this is a significant change in the ballast mass, it only represents a 1.4% change to the overall structural weight including mounting system, and 3.36% change to the WTM weight without mounting system, as

indicated in the legend of Figure 2.153. This result illustrates that the flutter speed of the WTM can be very sensitive to even small changes in the ballast mass.

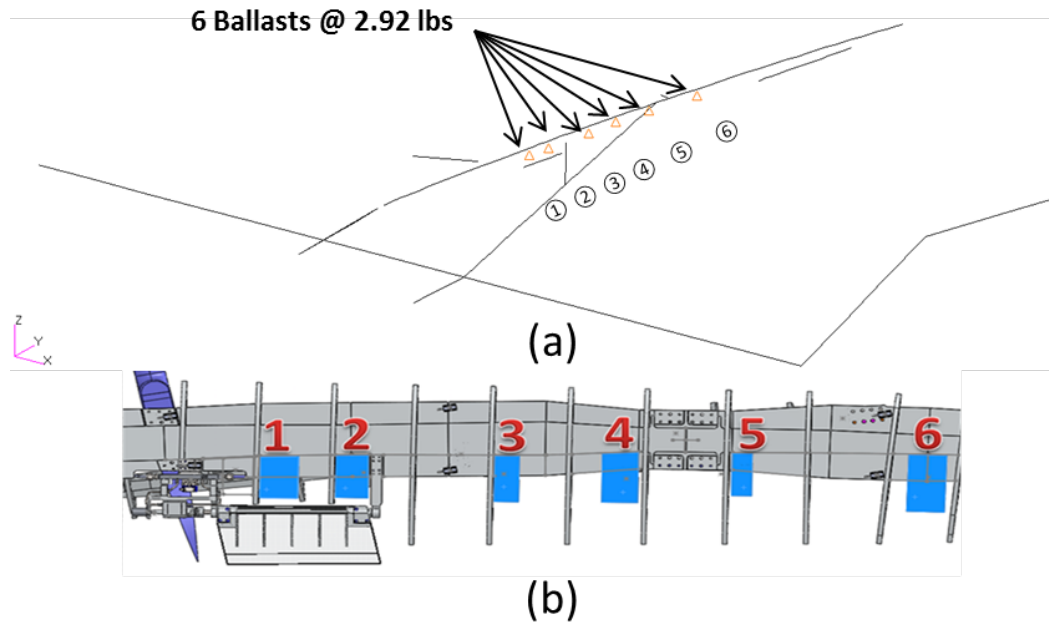


Figure 2.21 – Ballast mass added to the WTM to improve modal similitude with the full-scale aircraft

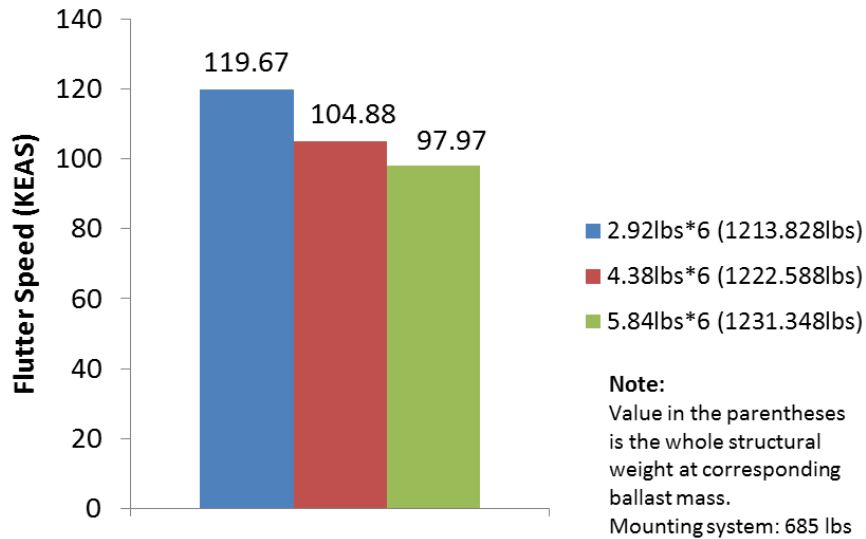


Figure 2.22 – Flutter speed of the unloaded model at different ballast masses for Mach No. 0.82

Secondly, the flutter results of the pre-stressed models with three different ballast masses using both linear and nonlinear analysis were computed as shown in Figure 2.153. All cases include unsteady aerodynamic weighting factors in flutter analysis. The flutter results obtained from linear analysis indicated the similar variation trend of the flutter speed with ballast mass

with that as shown in Figure 2.153, flutter speed is reduced by approximate 20% by doubling the ballast mass. For the flutter results obtained from nonlinear analysis, as noted previously for ballast mass of 2.92 lbs. in Figure 2.153, nonlinear analysis w/ WF's does not predict a flutter instability within the flight envelope. Therefore, the results in Figure 2.153(b) only include the ballast mass cases of 4.38/lbs. and 5.84/lbs., which did bring the flutter instability back within the planned test envelope. The response of these two mass cases indicates the previously seen behavior for flutter speed to increase with increasing AoA. The magnitude of the flutter speed reduction due to the increased ballast mass is similar to the previous cases for the unloaded model and the linear analyses. From this plot, it was concluded that the flutter boundary is very sensitive to the ballast mass.

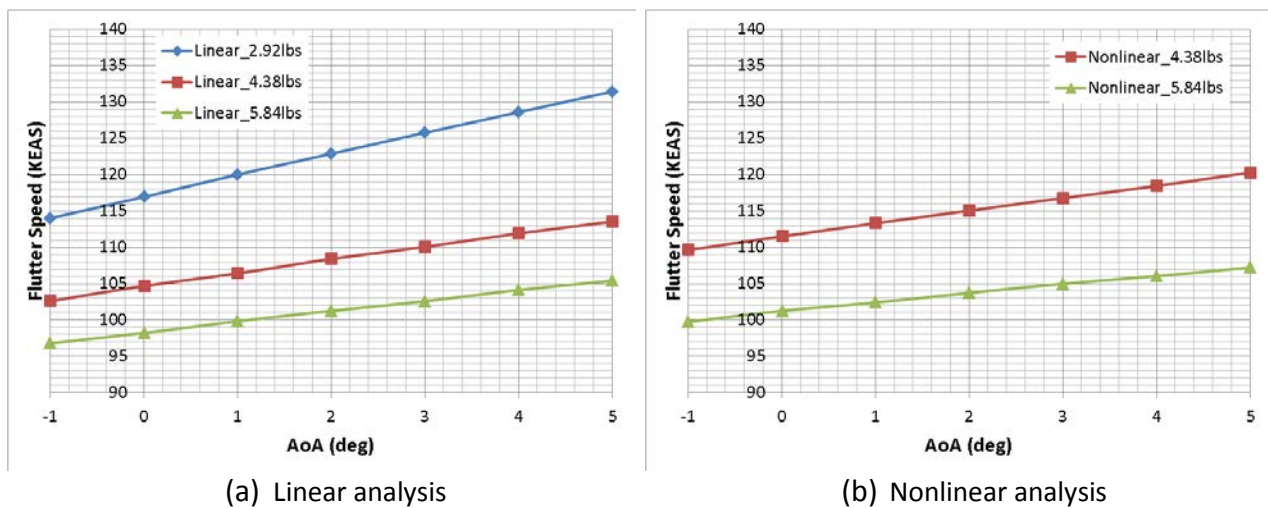
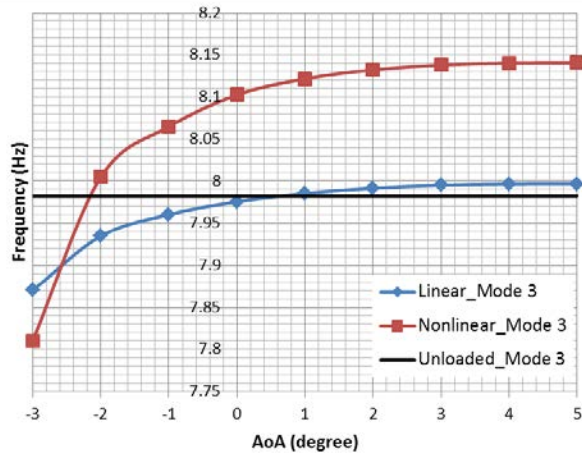


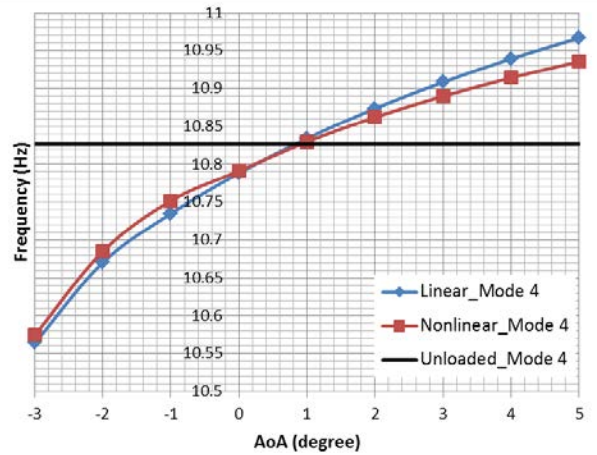
Figure 2.23 – Flutter speed of the pre-stressed model using (a) linear analysis, (b) Nonlinear analysis w/WF applied to the unsteady aerodynamic pressure in flutter analysis for the case of three different ballast masses for Mach No. 0.82

1.9 Modal information of the SUGAR WTM under in-plane loads using both linear and nonlinear analysis

As we known, the modal information was the base for flutter analysis. The change in modal frequencies and mode shapes could cause significant change to the flutter boundaries for the same model. So, it's necessary to study the modal frequencies and corresponding mode shapes cross the range of AoA and for various analysis types. The fundamental mechanism influencing flutter speed prediction involves the change in the modal frequency of the 2nd bending mode (mode 3) and 1st torsion mode (mode 4). The variations of the natural frequencies of these 2 modes with AoA are shown in Figure 2.153. Modal frequencies of the unloaded model are independent of AoAs, so a horizontal black line was plotted for the modal frequency of the mode 3 and mode 4 in the following two plots. The blue line and red line represent the variation of modal frequencies with AoA when using linear analysis and nonlinear analysis, respectively. The natural frequencies of mode 3 and mode 4 are approximately linearly varying with AoAs between -1 to 5 degrees, and they increases with AoA regardless of analysis types.



(a) Mode 3



(b) Mode 4

Figure 2.24 – Natural frequencies of (a) the third mode and (b) the fourth mode using both linear and nonlinear analysis w/o WF using on unsteady aerodynamic pressure at Mach number 0.82 with ballast mass 2.92 lbs.

Variations of the normalized modal frequencies with AoA using both linear and nonlinear analysis were investigated, and the results are shown in Figure 2.153. The frequency here was normalized with respect to the corresponding mode frequency of the unloaded model. The natural frequency of the 2nd bending mode (mode 3) increased by about 2.5% compared to that of the unloaded model up to 5 degrees AoA, whereas, the natural frequency of the 1st torsion mode (mode 4) increased by approximately 1% up to 5 degrees AoA. An increase in the modal frequency of mode 3 results in an increase in the flutter velocity.

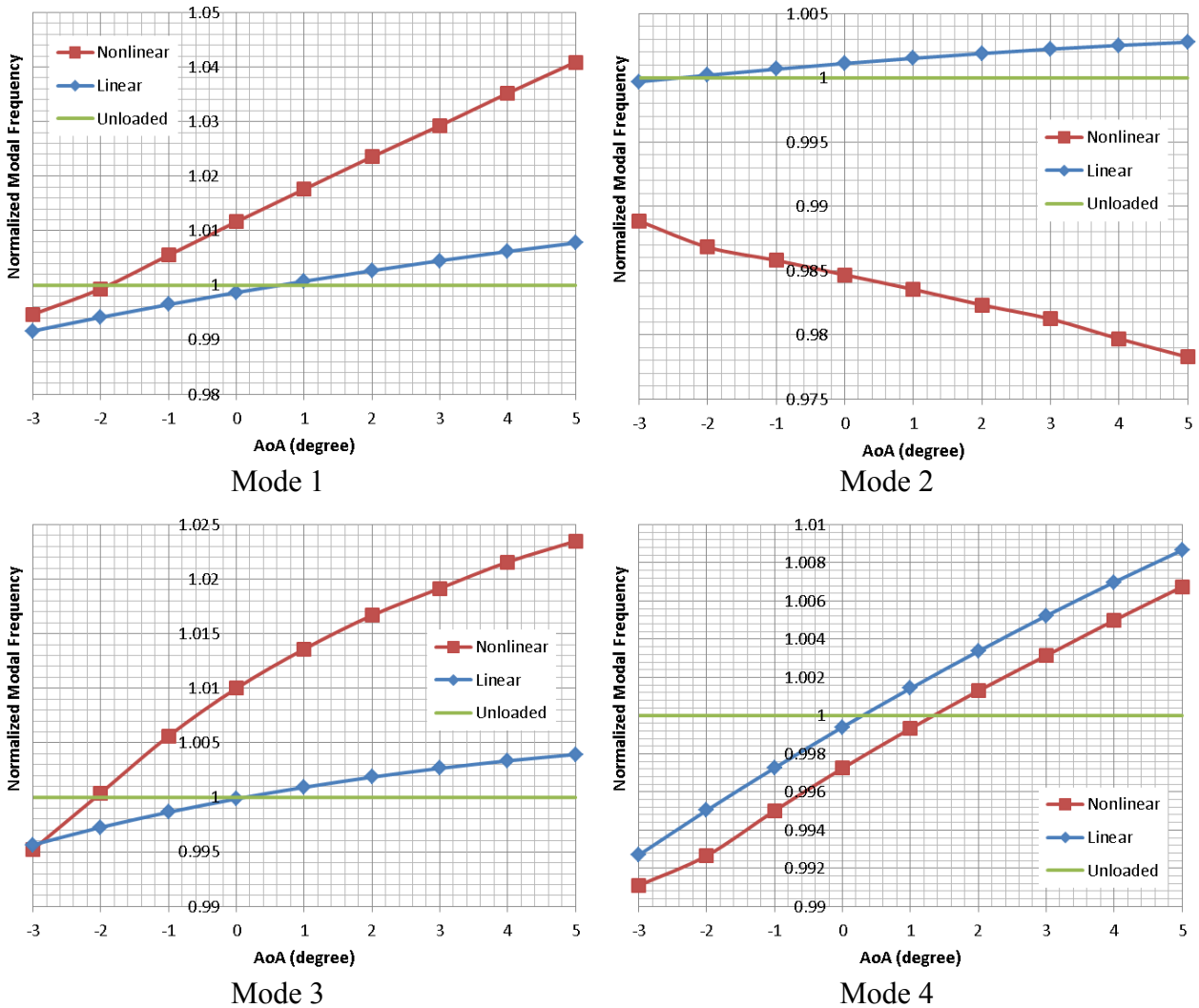


Figure 2.25 – Variation of the normalized modal frequencies of the first 4 modes (normalized with respect to the corresponding unloaded mode frequencies) with AoA using both linear and nonlinear analysis w/o WF used on the unsteady aerodynamic pressure under Mach number 0.82; with ballast mass 2.92 lbs.

The unsteady aerodynamic model, DLM based unsteady aerodynamic pressure, in NASTRAN depends on the structural mode shapes. The change of mode shapes could also influence the flutter boundary. Figure 2.153 shows comparisons of mode shapes of the first 4 modes of the unloaded and the pre-stressed models when using both linear and nonlinear analysis of one case with the flight condition at -1 degree AoA and Mach number 0.82. It was found that the first four mode shapes of the unloaded model and the linearly pre-stressed model are similar to each other. The mode shapes of the nonlinearly pre-stressed model are largely different from those of the unloaded model and the linearly pre-stressed model. It is the change of mode shapes and natural frequencies of the nonlinearly pre-stressed model that cause the change in flutter boundary of the WTM when using nonlinear analysis for different AoAs.

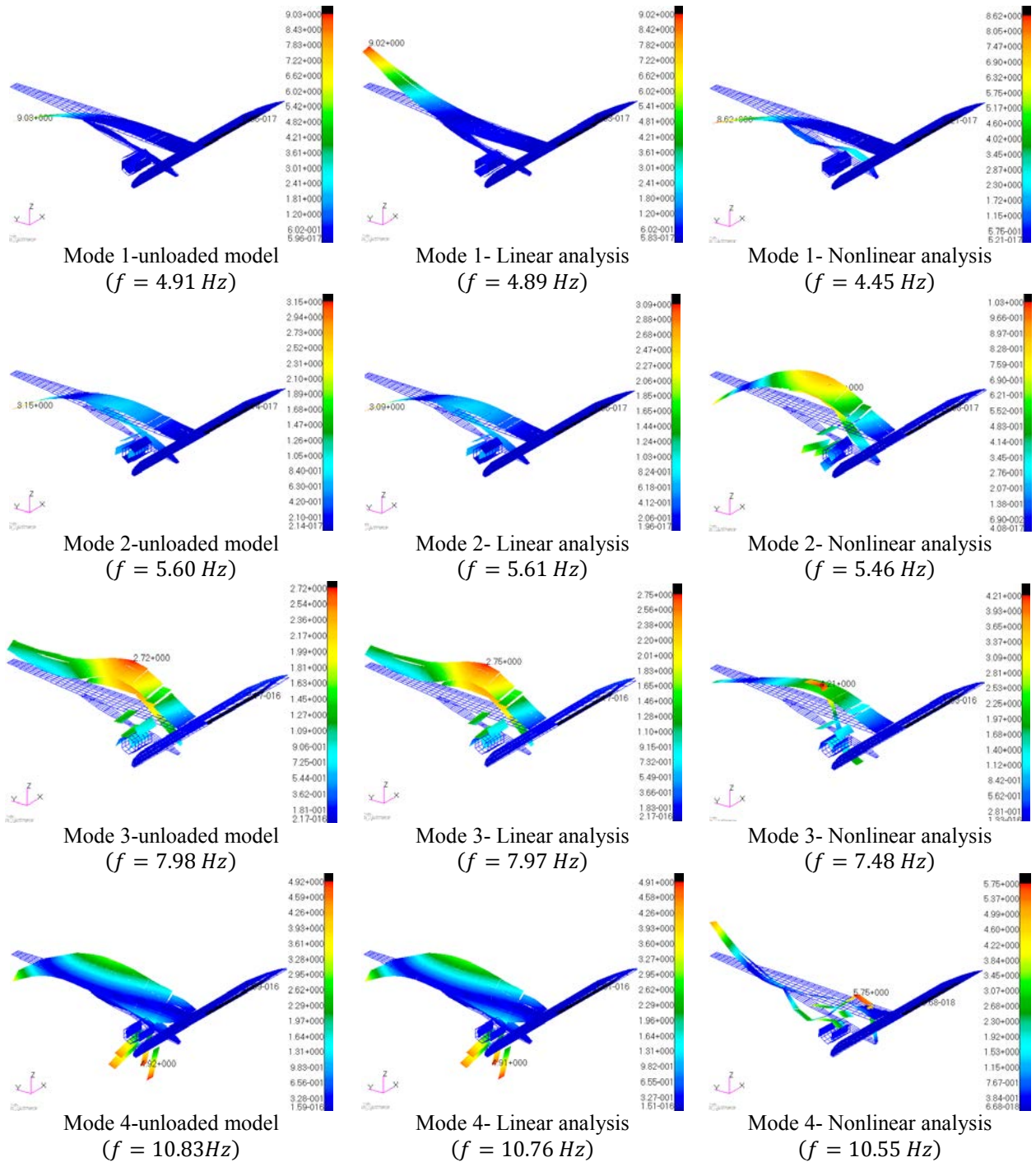


Figure 2.26 – The first 4 mode shapes of the unloaded model, the linear pre-stressed model and the nonlinear pre-stressed model at -1 degree AoA and Mach number 0.82

1.10 Flutter boundaries of FEM V19 and V20

The finite element model of the SUGAR wind tunnel model was updated to FEM V19 and FEM V20 based on GVT results by the Boeing Company. The steady aerodynamic weighting factors were also updated based on the wind tunnel tests. The Flutter boundaries for the latest FEMs with updated steady aerodynamic weighting factors were computed. It was validated that it is

not appropriate to employ steady aerodynamic weighting factors as the weight factors for unsteady aerodynamic pressure while performing a flutter analysis by comparing flutter predictions of FEM V18 with test results. So, no weight factors were included in the flutter analysis while performing aeroelastic analysis of the SUGAR wind tunnel model for FEM V19 and V20. This section mainly discusses how the flutter dynamic pressure varies with AoA ranging from -3 degrees to 3 degrees for FEM V19 and FEM V20 using both linear and nonlinear analysis w/o WF applied to the unsteady aerodynamic pressure.

Figure 2.153 shows the predicted flutter dynamic pressure for FEM V19 increases approximately linearly with AoA using both linear and nonlinear analysis with original weight factors only applied to the steady aerodynamic pressure, except for the results of the cases above -1 degree AoA using nonlinear analysis at Mach number 0.7 and 0.76. No flutter is predicted above 1 degree AoA using nonlinear analysis at Mach number 0.7 and 0.76. It was found that the flutter dynamic pressure decreases as the Mach number increases, which agrees with the phenomena of the transonic “dip” often seen in the relationship of flutter dynamic pressure with Mach number, caused by the transonic effects in a transonic flow.

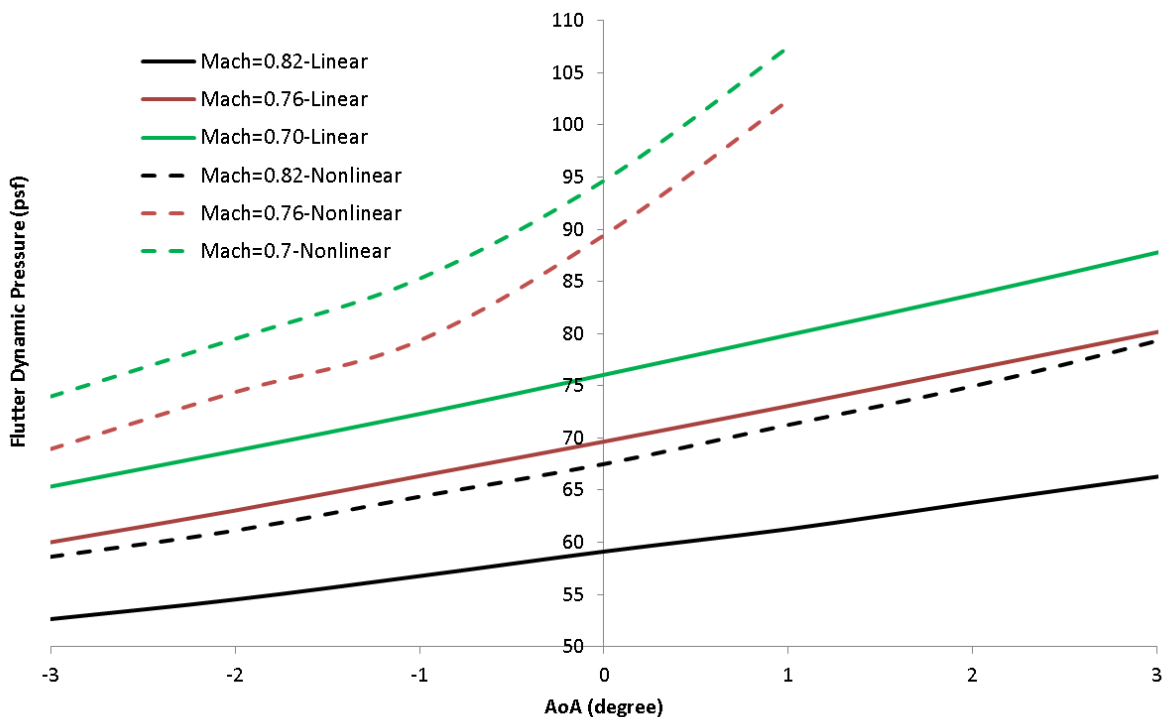


Figure 2.27 – Variation of the flutter dynamic pressure with the AoA for FEM V19 using both linear and nonlinear analysis, the original weight factors are only used to modify the steady aerodynamic pressure

Flutter dynamic pressure for FEM V19 was also calculated with updated weight factors applied to the steady aerodynamic pressure, as shown in Figure 2.153, which has the similar variation

with the AoA as seen in Figure 2.153. Flutter speed still decreases as the Mach number increases for different AoA. It was found that the flutter dynamic pressure is very close at Mach number 0.7 and 0.76 and AoA=3 degrees using nonlinear analysis. Results from the discrete method also show that these two results are very close to each other. By comparing the data in these two plots, Figure 2.153 and Figure 2.153, it was found that the flutter dynamic pressure decreases about 4% for the cases with updated steady aerodynamic weighting factors using both linear and nonlinear analysis for different AoAs compared with results obtained using the original weight factors of the same analysis type.

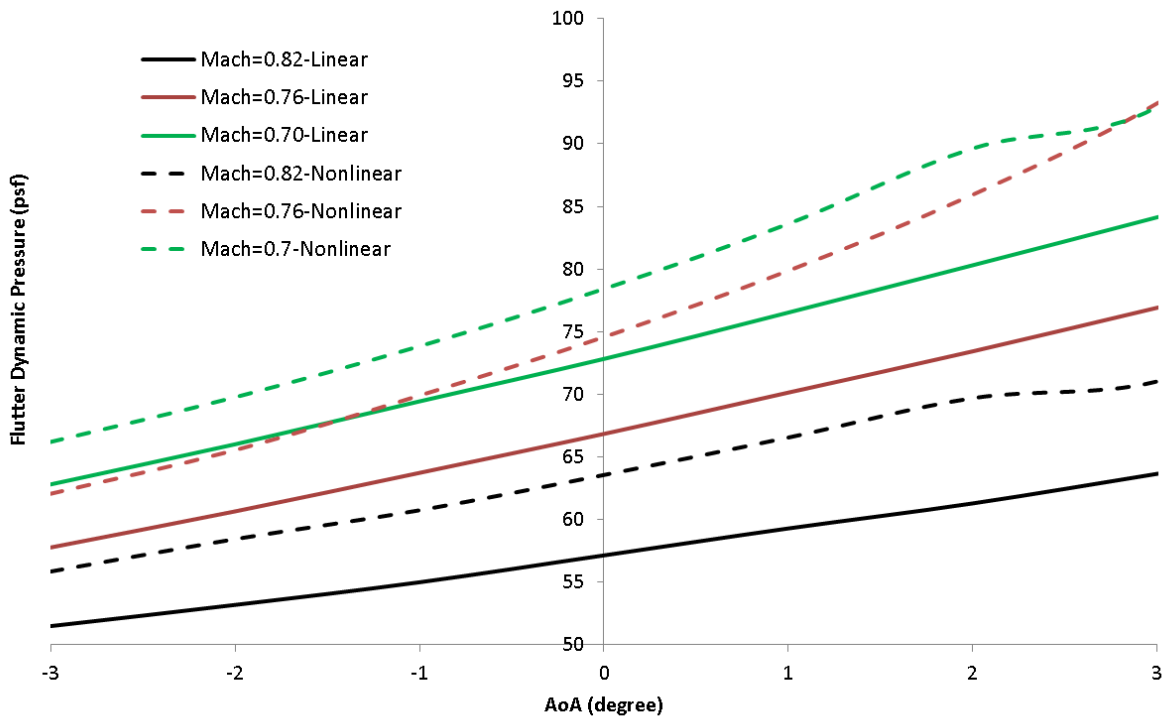


Figure 2.28 – Variation of the flutter dynamic pressure with AoA for FEM V19 using both linear and nonlinear analysis, the updated weight factors are only used to modify the steady aerodynamic pressure

Figure 2.153 shows that the flutter dynamic pressure increases linearly with AoA using both linear and nonlinear analysis, when using FEM V20, with updated weighting factors only applied to the steady aerodynamic pressure. With the change in the structural model from FEM V19 to V20, the flutter dynamic pressure increased by about 10 psf using the same analysis type. We also find again that the flutter dynamic pressure decreases as Mach number increases for different AoA, using both linear and nonlinear analysis.

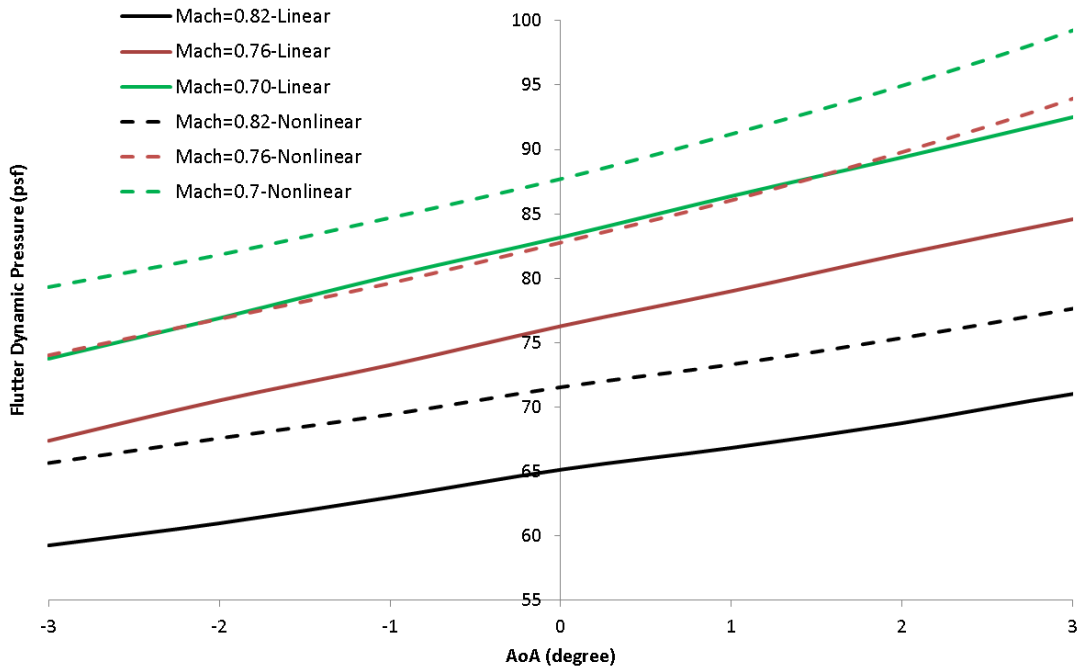


Figure 2.29 – Variation of the flutter dynamic pressure with AoA for FEM V20 using both linear and nonlinear analysis, the updated weight factors are only used to modify the steady aerodynamic pressure

1.11 Comparison of the experimental results and the theoretical predictions

Wind tunnel tests of the scaled SUGAR wind tunnel model were finished. Both Pre-holiday and post-holiday test results are presented here. Some open-loop flutter test results were obtained for -3, -1, 1 and 3 degrees AoA at Mach numbers ranging from 0.65 to 0.79. Comparisons between the experimental results (pre-holiday and post-holiday) and theoretical predictions are shown for three different versions of finite element model (FEM V18, FEM V19 and FEM V20).

1.11.1 Flutter results comparison of FEM v18

Figure 2.153 shows the flutter dynamic pressure of the pre-holiday experimental results and the theoretical predictions with the original weight factors without unsteady aerodynamic weighting factors in flutter analysis using both linear and nonlinear analysis. Results from nonlinear analysis are higher than the experimental results with difference around 20~35psf in absolute magnitude and around 30% in relative magnitude. Results from linear analysis were found to be closer to the experimental results. The variation of the flutter dynamic pressure with Mach number didn't agree well with the test results.

The flutter predictions obtained by including unsteady aerodynamic weighting factors, same with steady aerodynamic weighting factors, in flutter analysis, comparisons between theoretical predictions and pre-holiday experimental results were tabulated in Table 2.30. No

flutter was predicted at Mach number 0.76 using nonlinear analysis w/ WF applied to the unsteady aerodynamic pressure, and there was no flutter predicted above -3 degrees AoA at Mach number 0.70 and above -1 degree AoA at Mach number 0.82. The predictions were found not to agree with the experimental results, where there was flutter for -3, -1, 1 and 3 degrees AoA at Mach number ranging from 0.65 to 0.79 in the wind tunnel test. It appears that the steady aerodynamic weighting factors were not appropriate to be used as weight factors for the unsteady aerodynamic pressure.

Table 2.9 – Flutter dynamic pressure (psi) for FEM V18 calculated with the original weight factors employed to both steady and unsteady aerodynamic pressure using both linear and nonlinear analysis

AoA (deg)	Mach=0.7		Mach=0.76		Mach=0.82	
	Linear	Nonlinear	Linear	Nonlinear	Linear	Nonlinear
-3	83.48	103.15	85.46	N/F	89.69	110.13
-1	94.18	N/F	99.21	N/F	99.94	173.25
1	105.94	N/F	116.64	N/F	110.71	N/F
3	119.40	N/F	151.28	N/F	121.64	N/F

* N/F means No Flutter

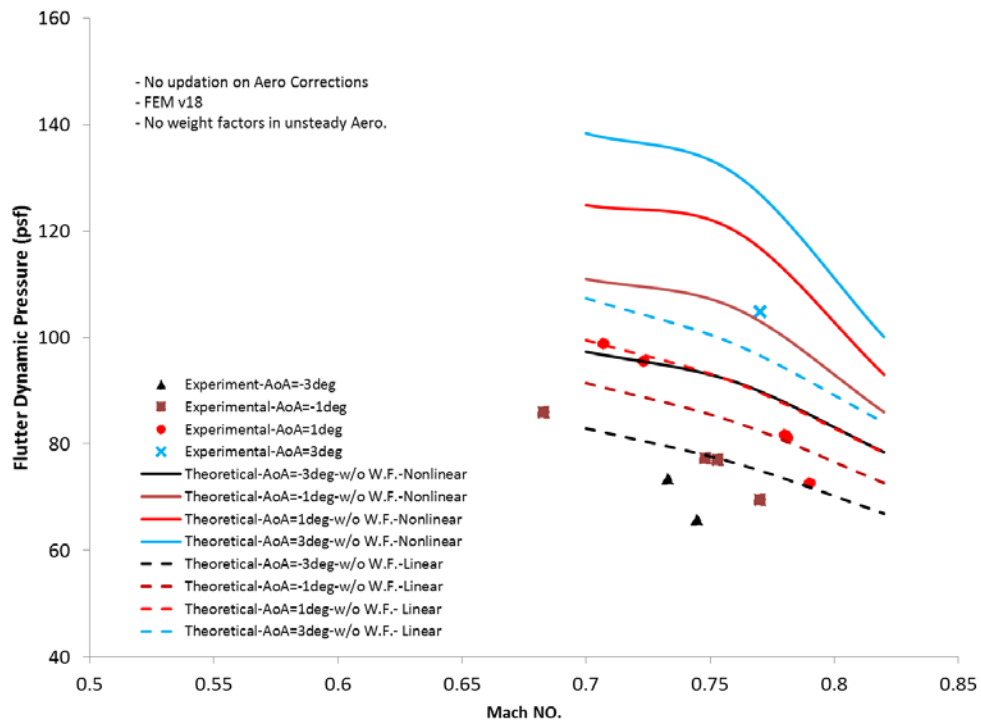


Figure 2.30 – Comparison of the pre-holiday experimental results with the theoretical predictions for FEM V18 using both linear and nonlinear analysis with the original weight factors applied to the unsteady aerodynamic pressure only

1.11.2 Flutter results comparison of FEM v19

Figure 2.153 shows the comparison between the pre-holiday experimental results and the theoretical predictions for FEM V19 using linear analysis with updated weight factors employed to correct the steady aerodynamic pressure only. It was found that the calculation of the flutter dynamic pressure was increased for FEM V19 with the updated weighting factors applied to the steady aerodynamic pressure. The differences between the theoretical predictions and the experimental results were reduced by about 3 psf for different AoA when compared with the results obtained using the original weighting factors applied to the steady aerodynamic pressure. However, there still exists large differences 4~20 psf (7%~20%) between the experimental results and the theoretical predictions. The variation of flutter dynamic pressure with Mach number didn't agree well with the experimental results after Mach number about 0.73.

Figure 2.153 illustrates the comparisons between the pre-holiday experimental results and the theoretical predictions for updated FEM V19 using nonlinear analysis with the updated weight factors applied to the steady aerodynamic pressure only. No flutter was predicted at 3 degrees AoA at Mach number 0.7 and 0.76. Comparing the results with flutter dynamic pressure obtained using the original weight factors, the flutter dynamic pressure using updated weight factors decreased by 3 to 23 psf for different AoA. The flutter dynamic pressures calculated using the original weight factors are higher than the experimental results by around 4~15 psf (4%~21%), whereas the flutter dynamic pressure calculated using the updated weight factors in this analysis type are less than the experimental results by around 4~15 psf (4%~16%). Both of the two theoretical variations of the flutter dynamic pressure with Mach number didn't match well with the experimental results after Mach number about 0.73.

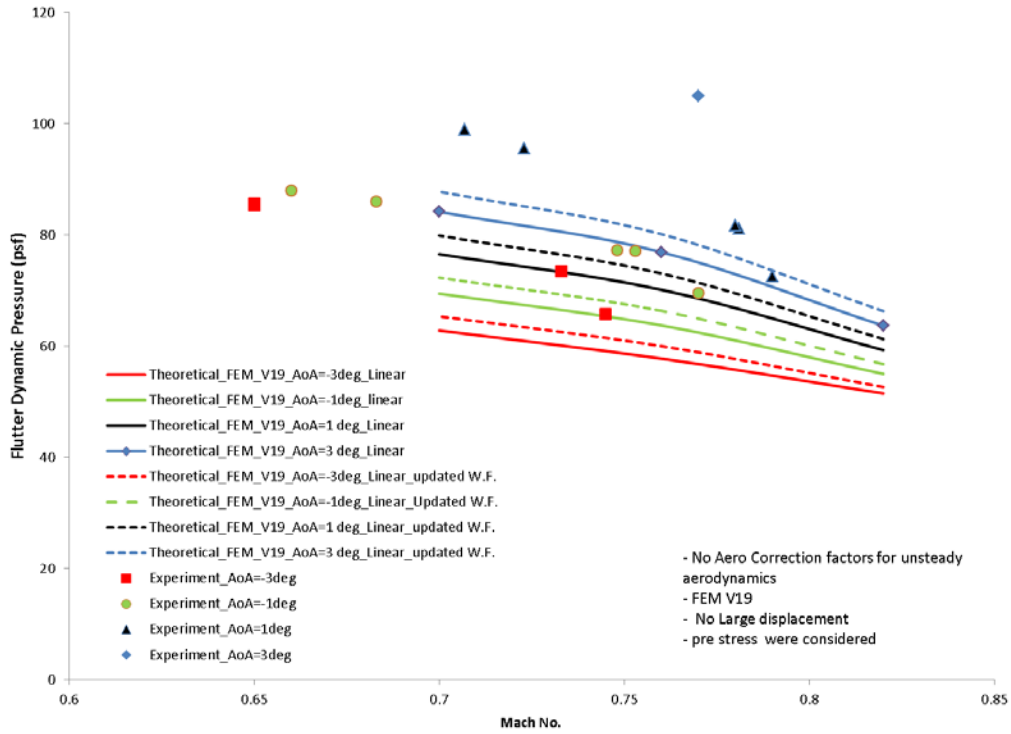


Figure 2.31 – Comparison of the experimental results with the theoretical predictions for FEM V19 using linear analysis with the updated weight factors applied to the steady aerodynamic pressure only

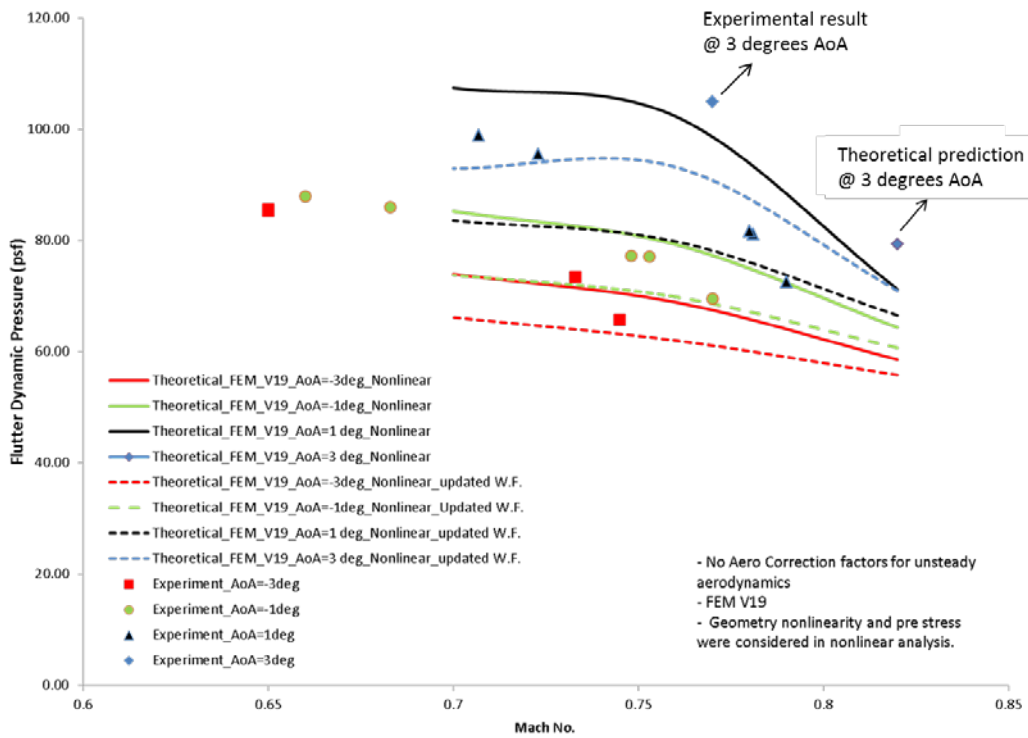


Figure 2.32 – Comparison of the experimental results with the theoretical predictions for FEM V19 using nonlinear analysis with the updated weight factors applied to the steady aerodynamic pressure only

1.11.3 Flutter results comparison of FEM v20

The finite element model of the SUGAR TBW WTM was updated based on the latest GVT results to FEM version 20. Figure 2.153 shows the comparison between the theoretical predictions and the post-holiday experimental results for the latest finite element model, V20. The flutter dynamic pressure was calculated with the updated weight factors applied only to the steady aerodynamic pressure and using a nonlinear analysis. No weight factors were applied to the unsteady aerodynamic pressure. Flutter dynamic pressure calculated with the updated weight factors are less than those obtained using the original weight factors by 2~10 psf (3%~13%) for the same analysis type.

It is seen that there exists a flutter “dip” in the experimental results of flutter dynamic pressure with Mach No. for each AoA. However, no flutter “dip” was observed in the theoretical predictions regardless of the analysis type in the flight envelope. Theoretical predictions for FEM v20 using nonlinear analysis with both the original WF and the updated WF applied to the steady aerodynamic pressure did not match well with the experimental results. Once again, it is felt that the unsteady aerodynamic weighting factors, including the time lag factors, to correct the DLM in NASTRAN should be investigated to capture the transonic effects in transonic flow.

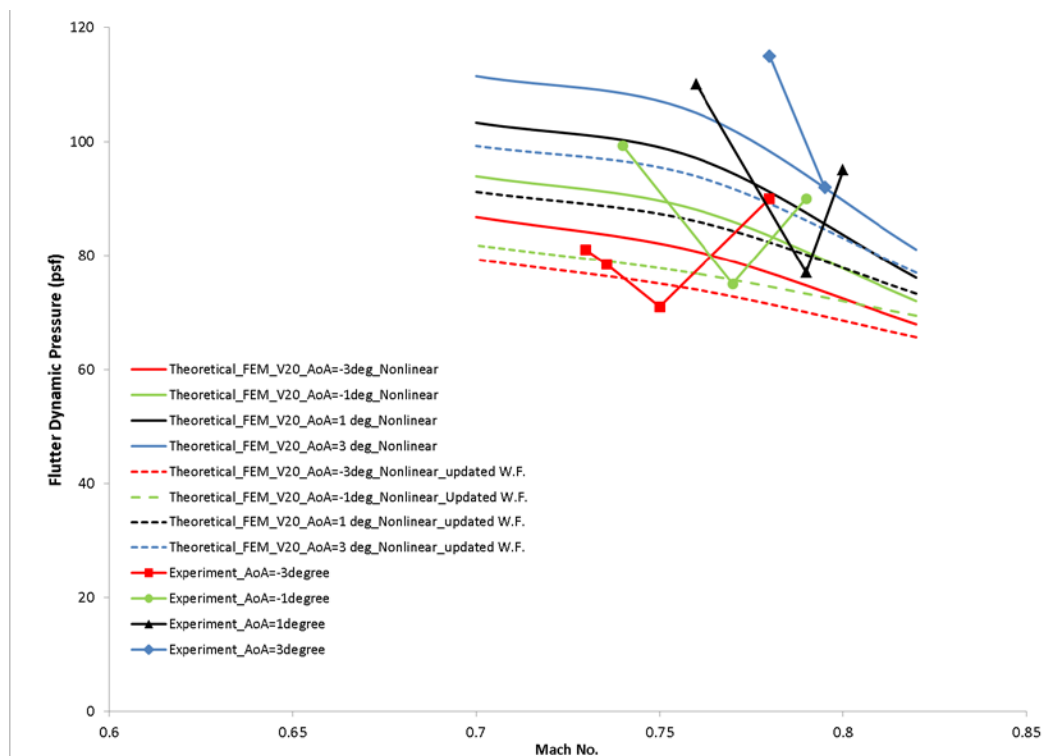


Figure 2.33 – Comparison of the updated experimental results with the theoretical predictions for FEM V20 using nonlinear analysis with both the original weight factors (Not label them in the legend) and the updated weight factors applied to the steady aerodynamic pressure only

1.12 Summary

We have described an iterative solution sequence using NASTRAN Flightloads to perform nonlinear aeroelastic analysis including structural nonlinearities and vehicle pre-stress due to flight loads and self-weight. The solution sequence was utilized to study the impact of transonic aerodynamic weighting factors, ballast mass, and AoA on flutter speed predictions. After that, nonlinear aeroelastic analyses of the SUGAR wind tunnel model with the latest finite element models with updated steady aerodynamic weighting factors were performed. We have also developed a discrete method for this problem. The discrete method was mainly used as an alternative method for cases without convergence when using the iterative method and as a validation tool for results obtained by using the iterative method.

Unlike the modal information and flutter boundaries slightly influenced by the in-plane loads for cantilevered wings, the modal frequencies and flutter boundaries of the TBW are sensitive to the in-plane loads. It was seen that flutter speed calculated under in-plane loads with the inclusion of aerodynamic weighting factors for unsteady aerodynamic pressure can increase the flutter margin prediction by 20% - 30% depending on AoA. The analysis has shown the importance of including structural geometric nonlinearities and in-plane loads when predicting the flutter boundary of nontraditional truss-braced wing aircraft. In the case of the SUGAR TBW WTM studied here, for high AoA the nonlinear analysis predicts an increased flutter margin of 20% - 30%, or in some cases, does not predict any flutter instability at all. The linear analysis, in general, did not provide the same prediction as the nonlinear analysis, and the variation of the flutter dynamic pressure with Mach number doesn't agree with the experimental results, and therefore may not be an adequate prediction for this particular TBW example. The values for linear analysis typically fell in between the unloaded results and the nonlinear ones.

The extreme sensitivity to ballast mass was demonstrated by evaluating several mass cases. It was shown that even small changes of 1.4% to the total vehicle weight or 3.36% change to the WTM weight can result in large changes to the flutter speed around 20%.

The physical mechanisms influencing the flutter boundary were investigated. It was shown that the inclusion of pre-stress can result in changes to the critical mode frequencies when using linear analysis, and both natural frequencies and mode shapes in the nonlinear analysis, and that in turn changes the flutter boundary.

We also examined that the in-plane loads linearly vary with AoA for each component of the wing. The in-plane loads in the jury are much less than axial forces in the strut and the inboard wing. The jury and the inboard wing come under compression as the AoA increases, whereas, the strut remains in tension as the AoA increases. The axial forces obtained from linear and nonlinear analysis contribute differently to the geometry stiffness in the subsequent pre-stressed modes and flutter analysis.

Steady aerodynamic weighting factors were found not to be appropriate to be used as weight factors for the unsteady aerodynamic pressure in the flutter analysis. Flutter boundaries were also calculated for two new FEM versions, FEM V19 and FEM V20, of the SUGAR wind tunnel model. The latest FEM version 19 combined with the updated steady aerodynamic weighting factors helped to reduce the differences between the theoretical predictions and the experimental results. However, the variations of flutter dynamic pressure with Mach number still does not agree well with the experimental results after Mach number about Mach 0.73. Comparisons between the theoretical predictions for FEM V20 and the updated experimental results of flutter dynamic pressure show that there was no flutter “dip” predicted in the calculated results. The flutter predictions for FEM V20 didn’t match quite well with the updated experimental results. So, it is necessary to study the weight factors and the associated time lag factors for unsteady aerodynamic pressure in a transonic flow. The aeroelastic studies with high-fidelity aerodynamic pressure considering both geometrical nonlinearities and aerodynamic nonlinearities of the TBW configurations are on investigation at Virginia Tech.

REPORT DOCUMENTATION PAGE

*Form Approved
OMB No. 0704-0188*

The public reporting burden for this collection of information is estimated to average 1 hour per response, including the time for reviewing instructions, searching existing data sources, gathering and maintaining the data needed, and completing and reviewing the collection of information. Send comments regarding this burden estimate or any other aspect of this collection of information, including suggestions for reducing this burden, to Department of Defense, Washington Headquarters Services, Directorate for Information Operations and Reports (0704-0188), 1215 Jefferson Davis Highway, Suite 1204, Arlington, VA 22202-4302. Respondents should be aware that notwithstanding any other provision of law, no person shall be subject to any penalty for failing to comply with a collection of information if it does not display a currently valid OMB control number.
PLEASE DO NOT RETURN YOUR FORM TO THE ABOVE ADDRESS.

1. REPORT DATE (DD-MM-YYYY) 01-04-2015		2. REPORT TYPE Contractor Report		3. DATES COVERED (From - To) February 2012 - June 2014	
4. TITLE AND SUBTITLE Subsonic Ultra Green Aircraft Research Phase II: Volume I – Truss Braced Wing Design Exploration				5a. CONTRACT NUMBER NNL08AA16B	
				5b. GRANT NUMBER	
				5c. PROGRAM ELEMENT NUMBER	
6. AUTHOR(S) Bradley, Marty K.; Droney, Christopher K.; Allen, Timothy J.				5d. PROJECT NUMBER	
				5e. TASK NUMBER NNL11AA00T	
				5f. WORK UNIT NUMBER 561581.02.08.07.11.02	
7. PERFORMING ORGANIZATION NAME(S) AND ADDRESS(ES) The Boeing Company 5301 Bolsa Ave, MC H017-D334 Huntington Beach, California 92647-2099				8. PERFORMING ORGANIZATION REPORT NUMBER	
9. SPONSORING/MONITORING AGENCY NAME(S) AND ADDRESS(ES) National Aeronautics and Space Administration Washington, DC 20546-0001				10. SPONSOR/MONITOR'S ACRONYM(S) NASA	
				11. SPONSOR/MONITOR'S REPORT NUMBER(S) NASA/CR-2015-218704/Volume I	
12. DISTRIBUTION/AVAILABILITY STATEMENT Unclassified - Unlimited Subject Category 05 Availability: NASA STI Program (757) 864-9658					
13. SUPPLEMENTARY NOTES Final Report Langley Technical Monitor: Erik D. Olson					
14. ABSTRACT This report summarizes the Truss Braced Wing (TBW) work accomplished by the Boeing Subsonic Ultra Green Aircraft Research (SUGAR) team, consisting of Boeing Research and Technology, Boeing Commercial Airplanes, General Electric, Georgia Tech, Virginia Tech, NextGen Aeronautics, and Microcraft. A multi-disciplinary optimization (MDO) environment defined the geometry that was further refined for the updated SUGAR High TBW configuration. Airfoil shapes were tested in the NASA TCT facility, and an aeroelastic model was tested in the NASA TDT facility. Flutter suppression was successfully demonstrated using control laws derived from test system ID data and analysis models. Aeroelastic impacts for the TBW design are manageable and smaller than assumed in Phase I. Flutter analysis of TBW designs need to include pre-load and large displacement non-linear effects to obtain a reasonable match to test data. With the updated performance and sizing, fuel burn and energy use is reduced by 54% compared to the SUGAR Free current technology Baseline (Goal 60%). Use of the unducted fan version of the engine reduces fuel burn and energy by 56% compared to the Baseline. Technology development roadmaps were updated, and an airport compatibility analysis established feasibility of a folding wing aircraft at existing airports.					
15. SUBJECT TERMS Aeroelastic testing; Control law; Dynamic scaling; Finite element analysis; Flutter suppression; Fuel burn; Laminar flow; Multidisciplinary optimization; Non-linear flutter; Unducted fan					
16. SECURITY CLASSIFICATION OF:			17. LIMITATION OF ABSTRACT	18. NUMBER OF PAGES	19a. NAME OF RESPONSIBLE PERSON
a. REPORT	b. ABSTRACT	c. THIS PAGE			STI Help Desk (email: help@sti.nasa.gov)
U	U	U	UU	378	19b. TELEPHONE NUMBER (Include area code) (757) 864-9658